

Special Issue Reprint

---

# Trends in Environmental Applications of Advanced Oxidation Processes

---

Edited by  
Juan José Rueda-Márquez, Javier Moreno-Andrés and Irina Levchuk

[mdpi.com/journal/catalysts](https://www.mdpi.com/journal/catalysts)

# **Trends in Environmental Applications of Advanced Oxidation Processes**



# Trends in Environmental Applications of Advanced Oxidation Processes

Editors

**Juan José Rueda-Márquez**

**Javier Moreno-Andrés**

**Irina Levchuk**



Basel • Beijing • Wuhan • Barcelona • Belgrade • Novi Sad • Cluj • Manchester

*Editors*

Juan José Rueda-Márquez  
Department of Environmental  
and Biological Sciences  
University of Eastern Finland  
Kuopio  
Finland

Javier Moreno-Andrés  
Department of  
Environmental Technologies  
University of Cadiz  
Cádiz  
Spain

Irina Levchuk  
Fine Particle and Aerosol  
Technology Laboratory (FINE)  
University of Eastern Finland  
Kuopio  
Finland

*Editorial Office*

MDPI  
St. Alban-Anlage 66  
4052 Basel, Switzerland

This is a reprint of articles from the Special Issue published online in the open access journal *Catalysts* (ISSN 2073-4344) (available at: [www.mdpi.com/journal/catalysts/special\\_issues/Environmental\\_Advanced\\_Oxidation\\_Processes](http://www.mdpi.com/journal/catalysts/special_issues/Environmental_Advanced_Oxidation_Processes)).

For citation purposes, cite each article independently as indicated on the article page online and as indicated below:

Lastname, A.A.; Lastname, B.B. Article Title. <i>Journal Name</i> <b>Year</b> , <i>Volume Number</i> , Page Range.
--

**ISBN 978-3-0365-8795-0 (Hbk)**

**ISBN 978-3-0365-8794-3 (PDF)**

**[doi.org/10.3390/books978-3-0365-8794-3](https://doi.org/10.3390/books978-3-0365-8794-3)**

© 2023 by the authors. Articles in this book are Open Access and distributed under the Creative Commons Attribution (CC BY) license. The book as a whole is distributed by MDPI under the terms and conditions of the Creative Commons Attribution-NonCommercial-NoDerivs (CC BY-NC-ND) license.

# Contents

About the Editors . . . . .	vii
Preface . . . . .	ix
<b>Juan José Rueda-Márquez, Irina Levchuk, Manuel Manzano and Mika Sillanpää</b> Toxicity Reduction of Industrial and Municipal Wastewater by Advanced Oxidation Processes (Photo-Fenton, UVC/H <sub>2</sub> O <sub>2</sub> , Electro-Fenton and Galvanic Fenton): A Review Reprinted from: <i>Catalysts</i> <b>2020</b> , <i>10</i> , 612, doi:10.3390/catal10060612 . . . . .	1
<b>Wamda Faisal Elmobarak, Bassim H. Hameed, Fares Almomani and Ahmad Zuhairi Abdullah</b> A Review on the Treatment of Petroleum Refinery Wastewater Using Advanced Oxidation Processes Reprinted from: <i>Catalysts</i> <b>2021</b> , <i>11</i> , 782, doi:10.3390/catal11070782 . . . . .	29
<b>He Lv, Yanan Liu, Yubin Bai, Hongpu Shi, Wen Zhou and Yaoning Chen et al.</b> Recent Combinations of Electrospinning with Photocatalytic Technology for Treating Polluted Water Reprinted from: <i>Catalysts</i> <b>2023</b> , <i>13</i> , 758, doi:10.3390/catal13040758 . . . . .	58
<b>Laura Ponce-Robles, Aránzazu Pagán-Muñoz, Andrés Jesús Lara-Guillén, Beatriz Masdemont-Hernández, Teresa Munuera-Pérez and Pedro Antonio Nortes-Tortosa et al.</b> Full-Scale O <sub>3</sub> /Micro-Nano Bubbles System Based Advanced Oxidation as Alternative Tertiary Treatment in WWTP Effluents Reprinted from: <i>Catalysts</i> <b>2023</b> , <i>13</i> , 188, doi:10.3390/catal13010188 . . . . .	90
<b>Michalis K. Arfanis, George V. Theodorakopoulos, Christos Anagnostopoulos, Irene Georgaki, Evangelos Karanasios and George Em. Romanos et al.</b> Photocatalytic Removal of Thiamethoxam and Flonicamid Pesticides Present in Agro-Industrial Water Effluents Reprinted from: <i>Catalysts</i> <b>2023</b> , <i>13</i> , 516, doi:10.3390/catal13030516 . . . . .	108
<b>Javier Moreno-Andrés, Iván Vallés, Paula García-Negueroles, Lucas Santos-Juanes and Antonio Arques</b> Enhancement of Iron-Based Photo-Driven Processes by the Presence of Catechol Moieties Reprinted from: <i>Catalysts</i> <b>2021</b> , <i>11</i> , 372, doi:10.3390/catal11030372 . . . . .	121
<b>Antia Fdez-Sanromán, Bárbara Lomba-Fernández, Marta Pazos, Emilio Rosales and Angeles Sanromán</b> Peroxymonosulfate Activation by Different Synthesized CuFe-MOFs: Application for Dye, Drugs, and Pathogen Removal Reprinted from: <i>Catalysts</i> <b>2023</b> , <i>13</i> , 820, doi:10.3390/catal13050820 . . . . .	136
<b>Marwa H. Shemy, Sarah I. Othman, Haifa E. Alfassam, Maha A. Al-Waili, Haifa A. Alqhtani and Ahmed A. Allam et al.</b> Synthesis of Green Magnetite/Carbonized Coffee Composite from Natural Pyrite for Effective Decontamination of Congo Red Dye: Steric, Synergetic, Oxidation, and Ecotoxicity Studies Reprinted from: <i>Catalysts</i> <b>2023</b> , <i>13</i> , 264, doi:10.3390/catal13020264 . . . . .	156
<b>Muhammad Nadir Saleem, Afzal Shah, Naimat Ullah, Jan Nisar and Faiza Jan Iftikhar</b> Detection and Degradation Studies of Nile Blue Sulphate Using Electrochemical and UV-Vis Spectroscopic Techniques Reprinted from: <i>Catalysts</i> <b>2023</b> , <i>13</i> , 141, doi:10.3390/catal13010141 . . . . .	181

<b>Sara El Hakim, Tony Chave and Sergey I. Nikitenko</b> Photocatalytic and Sonocatalytic Degradation of EDTA and Rhodamine B over Ti <sup>0</sup> and Ti@TiO <sub>2</sub> Nanoparticles Reprinted from: <i>Catalysts</i> <b>2021</b> , <i>11</i> , 928, doi:10.3390/catal11080928 . . . . .	<b>199</b>
<b>Linshuang Xue, Chenyi Yuan, Shipeng Wu, Zhen Huang, Zhen Yan and Stéphane Streiff et al.</b> Preparation of Mn-Doped Co <sub>3</sub> O <sub>4</sub> Catalysts by an Eco-Friendly Solid-State Method for Catalytic Combustion of Low-Concentration Methane Reprinted from: <i>Catalysts</i> <b>2023</b> , <i>13</i> , 529, doi:10.3390/catal13030529 . . . . .	<b>212</b>
<b>Yong-Ming Dai, Wu-Tsan Wu, Yu-Yun Lin, Hsiao-Li Wu, Szu-Han Chen and Jih-Mirn Jehng et al.</b> Photocatalytic CO <sub>2</sub> Reduction to CH <sub>4</sub> and Dye Degradation Using Bismuth Oxychloride/Bismuth Oxyiodide/Graphitic Carbon Nitride (BiO <sub>m</sub> Cl <sub>n</sub> /BiO <sub>p</sub> I <sub>q</sub> /g-C <sub>3</sub> N <sub>4</sub> ) Nanocomposite with Enhanced Visible-Light Photocatalytic Activity Reprinted from: <i>Catalysts</i> <b>2023</b> , <i>13</i> , 522, doi:10.3390/catal13030522 . . . . .	<b>227</b>

# About the Editors

## **Juan José Rueda-Márquez**

Juan José Rueda Márquez is a post-doctoral researcher in the Department of Environmental and Biological Sciences at the University of Eastern Finland. He completed his PhD at the University of Cadiz (Spain) in 2015. His research interests involve but are not limited to advanced wastewater treatment technologies for industrial (petrochemical, pulp and paper, etc.) and municipal wastewater treatment. He co-authored 21 papers in international peer-reviewed journals (h-index 15, 1018 citations, source: SCOPUS). He has participated in various academic and industry-involved research projects, including EU-funded projects, and as a PI in a project funded by the Academy of Finland.

## **Javier Moreno-Andrés**

Javier Moreno-Andrés holds a Ph.D. in Marine Science and Technology from the University of Cadiz (Spain). In the post-doctoral stage, Dr. Moreno moved to the Polytechnic University of Valencia (Spain), and he also enjoyed being a visiting researcher at NIOZ (Netherlands), Aalto University (Finland), and CCMAR (Portugal). He currently works at the University of Cadiz as an Emerging Principal Investigator. He is also actively involved in understanding the motivations and concerns of Early Career Researchers through participation in related working groups, such as Young Water Professionals (IWA) or OYSTER (Euromarine). His research focuses on assessing environmental technologies for water purification, mainly based on UV-based processes and Advanced Oxidation Processes. His research interests are to acquire deeper knowledge in treating non-traditional source waters such as seawater or brackish water, i.e., from the maritime perspective. Some examples can be derived from maritime transport, the aquaculture industry, or the increasing episodes of Harmful Algal Blooms and related biotoxins. In this regard, Dr. Moreno co-authored 36 articles in international peer-reviewed journals (h-index 16). He has participated in various research projects; currently, Dr. Moreno is leading three projects dedicated to minimizing marine pollution from maritime transport as Principal Investigator.

## **Irina Levchuk**

Irina Levchuk is currently a postdoctoral researcher in the Department of Environmental and Biological Sciences at the University of Eastern Finland. Previously, she was a postdoctoral researcher at Aalto University, Finland (2018–2021) and a Junior Researcher at LUT, Finland, where she obtained her PhD (2011–2016). Her research mainly deals with Advanced Oxidation Processes (photocatalysis, UV/H<sub>2</sub>O<sub>2</sub>, catalytic wet peroxide oxidation, etc.) for the decomposition of persistent organic pollutants, contaminants of emerging concern (CECs), and inactivation of pathogens in industrial and urban wastewater. She published 28 peer-reviewed articles in international journals (h-index 17, 1188 citations, source: SCOPUS) and 6 book chapters. She has participated in eight projects, in some of which as a principal investigator.





# Preface

Welcome to this reprint on Advanced Oxidation Processes (AOPs) and their diverse environmental applications. We are delighted to present a compilation of published research papers and reviews that delve into the promising world of AOPs and their significant contributions to solving various environmental challenges. Comprehensive reviews are presented on specific AOP technologies, focusing on their applications in specific sectors. For example, researchers have examined the potential of electrospinning, a technique that produces nanofibers, in enhancing AOPs for pollutant degradation. Furthermore, the articles explore the utilization of AOPs in sectors like petroleum refineries and wastewater treatment plants, discussing their efficiency, cost-effectiveness, and environmental benefits. Also, a dedicated chapter is focused on the application of AOPs for toxicity reduction. Researchers have explored using AOPs to transform and degrade toxic compounds into less harmful substances, mitigating the adverse effects on aquatic organisms and ecosystems. These reviews provide valuable insights into the diverse applications of AOPs and offer guidance for future research and industrial implementations.

The application of AOPs for the removal of organic pollutants such as Contaminants of Emerging Concern, pesticides, or dyes from water matrices of diverse origin is featured in the present reprint as specific chapters. The diverse studies, in this regard, demonstrate the versatility of AOPs in treating water matrices from various sources, including industrial, agricultural, and municipal wastewater.

Two chapters are dedicated to the innovative application of AOPs in the field of greenhouse gas reduction. The featured articles delve into the catalytic capabilities of AOPs for converting carbon dioxide (CO<sub>2</sub>) into methane (CH<sub>4</sub>), a process that offers a potential solution for carbon capture and utilization. Additionally, researchers have explored the catalytic combustion of low-concentration methane to remove it in coalbed gas before emission, which presents a significant challenge in environmental and industrial settings.

We would like to express our sincere appreciation to the authors of the published articles for their outstanding contributions to this compilation. We also extend our gratitude to the reviewers who dedicated their expertise and time to ensure the quality and accuracy of the published works.

We hope this collection of published articles provides readers with a comprehensive understanding of the potential and practical implications of AOPs in environmental remediation. It is our sincere desire that the knowledge shared within this special issue inspires further advancements in the field, leading to sustainable and efficient solutions for our environmental challenges.

We would like to acknowledge the financial support through the project TED2021-130994B-C31 and Grant IJC2020-042741-I funded by MCIN/AEI/10.13039/501100011033 and by the European Union NextGenerationEU/PRTR. In addition, to the project PID2021-123155OB-I00 funded by MCIN/AEI/10.13039/501100011033 and by “ERDF A way of making Europe”.

**Juan José Rueda-Márquez, Javier Moreno-Andrés, and Irina Levchuk**  
*Editors*



Review

# Toxicity Reduction of Industrial and Municipal Wastewater by Advanced Oxidation Processes (Photo-Fenton, UVC/H<sub>2</sub>O<sub>2</sub>, Electro-Fenton and Galvanic Fenton): A Review

Juan José Rueda-Márquez <sup>1,2,\*</sup>, Irina Levchuk <sup>2,3</sup>, Manuel Manzano <sup>2</sup>  and Mika Sillanpää <sup>4,5,6,\*</sup> 

<sup>1</sup> Department of Separation Science, School of Engineering Science, Lappeenranta-Lahti University of Technology LUT, Sammonkatu 12, 50130 Mikkeli, Finland

<sup>2</sup> Department of Environmental Technologies, INMAR-Marine Research Institute, Faculty of Marine and Environmental Sciences, University of Cádiz, Poligono Rio San Pedro s/n, Puerto Real, 11510 Cadiz, Spain; irina.levchuk@aalto.fi (I.L.); manuel.manzano@uca.es (M.M.)

<sup>3</sup> Department of Chemical and Metallurgical Engineering, School of Chemical Engineering, Aalto University, Kemistintie 1, P.O. Box 16100, FI-00076 Espoo, Finland

<sup>4</sup> Institute of Research and Development, Duy Tan University, Da Nang 550000, Vietnam

<sup>5</sup> Faculty of Environment and Chemical Engineering, Duy Tan University, Da Nang 550000, Vietnam

<sup>6</sup> School of Civil Engineering and Surveying, Faculty of Health, Engineering and Sciences, University of Southern Queensland, West Street, Toowoomba, QLD 4350, Australia

\* Correspondence: juan.rueda.marquez@lut.fi (J.J.R.-M.); mikaetapiosillanpaa@duytan.edu.vn (M.S.)

Received: 5 May 2020; Accepted: 28 May 2020; Published: 1 June 2020

**Abstract:** The application of Fenton-based advanced oxidation processes (AOPs), such as photo-Fenton or electro-Fenton for wastewater treatment have been extensively studied in recent decades due to its high efficiency for the decomposition of persistent organic pollutants. Usually Fenton-based AOPs are used for the degradation of targeted pollutant or group of pollutants, which often leads to the formation of toxic by-products possessing a potential environmental risk. In this work, we have collected and reviewed recent findings regarding the feasibility of Fenton-based AOPs (photo-Fenton, UVC/H<sub>2</sub>O<sub>2</sub>, electro-Fenton and galvanic Fenton) for the detoxification of real municipal and industrial wastewaters. More specifically, operational conditions, relevance and suitability of different bioassays for the toxicity assessment of various wastewater types, cost estimation, all of which compose current challenges for the application of these AOPs for real wastewater detoxification are discussed.

**Keywords:** wastewater; advanced oxidation processes (AOPs); photo-Fenton; toxicity; bioassays; costs

## 1. Introduction

Industrial and urban wastewater effluents are considered to be among the most important sources of aquatic pollutants [1]. Due to advances in analytical chemistry, increasingly more pollutants can be identified and quantified at very low concentrations [2]. Negative impacts, such as neuroendocrine, mutagenic and health effects on the aquatic environment, have been reported recently for contaminants even at low concentrations [3–5].

Wastewater treatment plants (WWTP) play the role of a barrier preventing the release of contaminants into the aquatic environment. Most wastewater treatment plants carry out conventional treatment which includes, in the best case, a tertiary step. In practice, the main objectives of tertiary step are removal of nutrients, turbidity and pathogens. As a result, such processes as coagulation, sand and membrane filtration, chlorination and UVC disinfection are applied. However, these processes are

not effective enough for resistant and recalcitrant pollutant elimination. In accordance with recent studies, traditional urban and industrial WWTPs are not always efficient for the removal of various organic pollutants such as contaminants of emerging concern (CECs) [6], which cause its release into the aquatic environment and damage the stability of ecosystems. In addition, the current directive concerning urban wastewater treatment [7] does not include methodology and control for modern contaminants discharge. Therefore, tertiary treatment of wastewater effluents should aim not only at nutrients, particulate matter removal and disinfection, but also emerging pollutants elimination is needed in order to avoid the discharge of these specific pollutants into the aquatic environment [8].

Among the available technologies for organic pollutants removal suitable for the post-treatment of wastewater effluents are advanced oxidation processes (AOPs) which have received significant attention in recent decades. Generally, AOPs are recommended when the level of chemical oxygen demand (COD) is low which makes AOPs suitable for tertiary treatment for the majority of wastewater effluents [9].

The efficiency of AOPs is usually evaluated based on the chemical analysis of treated water, including the concentration of pollutants (such as emerging compounds), total organic carbon (TOC), COD, etc. However, decomposition of pollutants occurring during AOPs leads to the formation of by-products. These by-products are not always known and not easy to identify due to required sophisticated analytical equipment, for instance, liquid chromatography coupled with time of flight mass spectrometry (LC-TOF MS) [10]. Thus, the chemical analysis might not be the best and not the only way to assess the effectiveness of AOPs. It should also be noted that by-products generated during the AOPs can be more toxic than parental compounds [11–15]. Therefore, chemical analysis alone for the evaluation of the efficiency of AOPs may produce inconclusive results and should be accompanied by toxicity assessment when possible.

In the majority of the studies devoted to wastewater treatment by AOPs, the toxicity assessment is conducted when the optimal conditions of the applied process are already selected (based on maximum COD removal, for example). This is done in order to confirm that no toxic effect is generated for a particular species at chosen optimal conditions. However, some studies do not include toxicity assessment after COD reduction which does not mean that the water could be safe for discharge (as some toxic by-products can possibly be generated). Therefore, toxicity bioassays could also be used for the selection of the optimal condition of the process, especially when the objective is to produce non-toxic wastewater effluent for species indigenous in the receiving aquatic environment.

Among various AOPs used for the detoxification and purification of wastewater, Fenton-based processes such as photo-Fenton is emerging as most studied and one of significant promise. Thus, photo-Fenton is listed among the best available techniques for wastewater treatment in the textile industry [16]. Moreover, the Technology Readiness Level (TRL) of photo-Fenton process for water treatment was reported to be 8 (system complete and qualified) [17], which is only one level below the maximum (TRL 9 “System proven in operational environment”). Judging from the results obtained from Scopus database (Figure 1), the interest in the evaluation of the toxicity of water treated by Fenton-based AOPs is increasing and continues to grow nowadays. However, only about 7% of studies concerned with the toxicity assessment of real (based on real wastewater matrix) wastewater treated by Fenton-based AOPs (Figure 1). Early findings in this area of research were reported in excellent review [18].

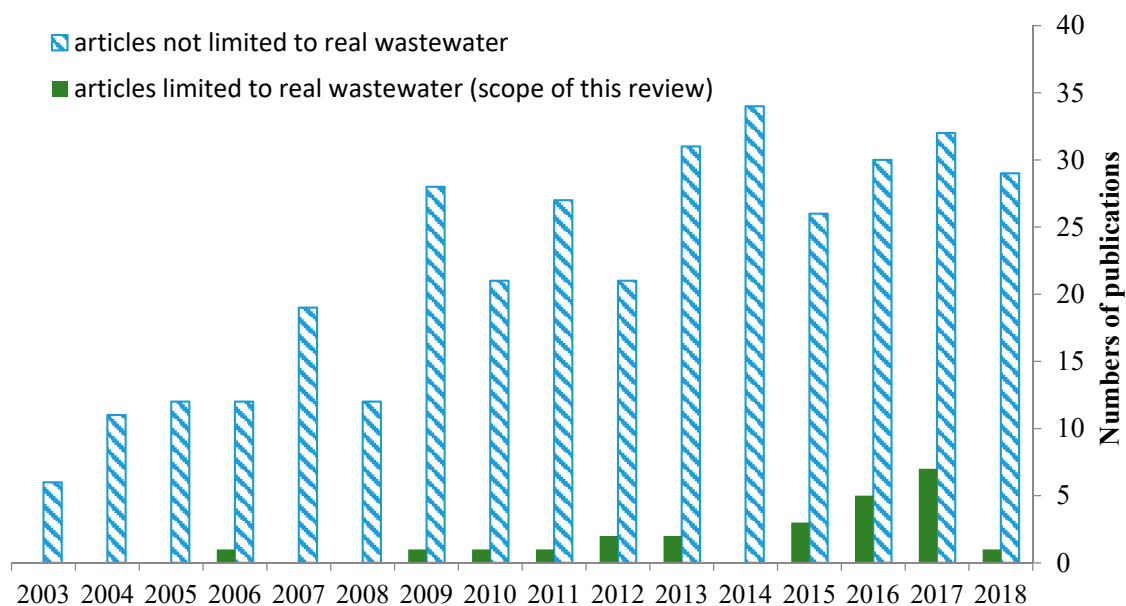


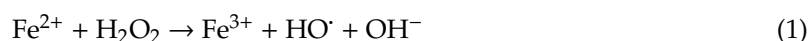
**Figure 1.** Number of scientific publications per year containing keywords (Scopus): “Fenton”, “wastewater” and “toxicity” in the title and/or keywords of article (blue). Number of articles in which real wastewater matrix was used (green).

The main goal of this work is to summarize and critically discuss the recent findings regarding the feasibility of photo-Fenton, UVC/H<sub>2</sub>O<sub>2</sub> (in presence of iron), electro-Fenton and galvanic Fenton AOPs for the detoxification of real industrial or urban wastewater (or wastewater matrix). It is important to emphasize that in this review, studies, in which the toxicity assessment was applied for model wastewater were not discussed. Relevant scientific articles for this review were selected using Science Direct, Scopus, Google Scholar and NCBI databases. Obtained literature list was checked manually with the purpose to leave studies, in which (i) only real or synthetic wastewater (municipal and/or industrial wastewater matrix) was used; (ii) toxicity assessment was performed before and after (or during) Fenton-based AOPs. It should be noticed that list of articles used for this review was limited to those published in peer-reviewed journals in English language.

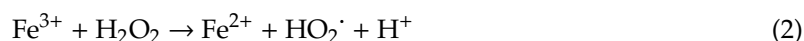
## 2. Photo-Fenton Process for Wastewater Detoxification

### 2.1. Main Principles of Photo-Fenton

The Fenton process was called after Henry J.H. Fenton [19], who discovered it during the degradation of tartaric acid in the presence of H<sub>2</sub>O<sub>2</sub> and Fe<sup>2+</sup> as a catalyst. Nowadays there are two generally accepted mechanisms of Fenton reactions [20]. The first mechanism, known as “free radical” or “classical” mechanism was suggested in 1934 by Haber and Weiss [21] and further investigated by Barb et al. [22–24]. In this mechanism, formation of hydroxyl radicals (HO·) is considered as a crucial step leading to series of reactions [25], main of which are presented below (reactions 1–4). Generation of hydroxyl radicals occurs during reaction of iron(2+) with hydrogen peroxide (reaction 1).



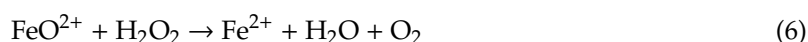
Reduction of iron(3+) to iron(2+) takes place in accordance with reaction 2. This reaction can be rate-limiting as it is significantly slower than reaction 1 [25].



Scavenging of hydroxyl radicals by iron(2+) and H<sub>2</sub>O<sub>2</sub> (reactions 3 and 4) takes place as shown below.

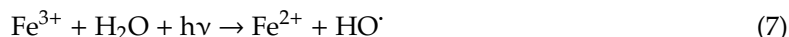


According to the “non-classical” Fenton mechanism, ferryl moiety (Fe = O) is generated during reaction between iron(2+) and hydrogen peroxide. Ferryl moiety can be formed when some chelated forms of iron (polycarboxylate and/or macrocyclic ligand) reacts with H<sub>2</sub>O<sub>2</sub> [25]. It should be mentioned that some organic pollutants possess capability of chelating iron [25], which possibly may lead to formation of ferryl moieties. The ferryl ions were first suggested as an active oxidant by Bray and Gorin [26]. Reactions representing non-classical Fenton pathway are shown below (reactions 5 and 6).



Fenton processes applied in water treatment usually require hydrogen peroxide/iron molar ratio between 100 and 1000 [25]. Commonly reported optimum pH of Fenton reaction is around 3, which can be explained by speciation of iron [25]. When the pH of the water decreases (2.5–3), the performance of the Fenton process increases due to the higher solubility of iron(3+) in water. At a pH lower than 2.5, the formation of iron complexes such as [Fe(H<sub>2</sub>O)<sub>6</sub>]<sup>2+</sup> may occur, as a result, the reaction with H<sub>2</sub>O<sub>2</sub> becomes slower and consequently less oxidizing species are generated. At basic pH, iron reacts with hydroxide ions (HO<sup>-</sup>) leading to precipitation in the form of iron hydroxide Fe(OH)<sub>2</sub> or Fe(OH)<sub>3</sub>. Precipitated iron does not react with H<sub>2</sub>O<sub>2</sub> [27]. More detailed consideration of Fenton process mechanism can be found in distinguished papers [25,27,28].

The Fenton process is significantly enhanced when UV radiation is introduced (photo-Fenton) [29]. Under these conditions, additional reactions take place, namely the photo-reduction of iron(3+) to iron(2+) as shown in reaction 7 ( $\lambda < 600$  nm) and the photolysis of hydrogen peroxide, (UV/H<sub>2</sub>O<sub>2</sub>) in reaction 8 ( $\lambda < 310$  nm) [30].



The conventional photo-Fenton process usually occurs at a pH of approx. 3.0, molar ratio of H<sub>2</sub>O<sub>2</sub>/iron between 2 and 150 and molar ratio of H<sub>2</sub>O<sub>2</sub>/COD between 1 and 3.5 [31–33]. One of the main drawbacks of the conventional photo-Fenton process is the low pH of the water. The pH adjustment (around pH 3) is a relatively easy operation on the laboratory scale, but it is generally regarded as not economically feasible for application on the industrial scale (especially taking into account subsequent neutralization of water and separation of generated sludge). A photo-Fenton reaction can also occur under circumneutral pH (6.5–7.5) in water containing naturally present or added chelating agents, forming dissolved organic complexes of iron [34,35]. It is noteworthy that the concentration of iron in the water can be considerably lower when photo-Fenton is applied compared to the Fenton process (in absence of adequate light) due to the importance of fast iron recycling (reaction 7). Moreover, iron removal may not be required if it is below the established discharge limit.

It should be mentioned that UV/H<sub>2</sub>O<sub>2</sub> treatment applied for real wastewater (UV/H<sub>2</sub>O<sub>2</sub>/RWW) can also include photo-Fenton mechanism. This can be explained by the fact that presence of naturally dissolved iron in urban and industrial wastewaters might favor the mechanism of photo-Fenton process as it was previously reported [36]. According to the literature, photo-Fenton may occur even at very low concentrations ( $\mu\text{g L}^{-1}$ ) of dissolved iron in water [37]. For instance, it was demonstrated that 0.05–0.09 mg L<sup>-1</sup> (50–90  $\mu\text{g L}^{-1}$ ) of natural iron content was sufficient to drive an efficient photo-Fenton process [37]. In all articles on UV/H<sub>2</sub>O<sub>2</sub> included in this review, the concentration of total dissolved iron was in the same range or above that reported in [36,37]. For instance, total dissolved iron concentration in

urban wastewater at one of the largest wastewater treatment plant in Finland (2015–2018) varied from 8.30–9.31 mg L<sup>-1</sup> (influent) and 0.32–0.47 mg L<sup>-1</sup> (effluent) [38–41]. Concentration of iron in industrial wastewaters varies significantly depending on the type of industry and other factors. It should be noticed that when UVC lamps are used, the dominant mechanism for radical generation might not be photo-Fenton, while it can be assumed that in presence of naturally available iron (in case of real wastewaters) photo-Fenton reactions may also take place. In order to distinguish these processes, UV/H<sub>2</sub>O<sub>2</sub> in presence of iron was called as UV/H<sub>2</sub>O<sub>2</sub>/RWW in this review.

## 2.2. Types of Wastewater

The types of wastewater used for detoxification by photo-Fenton and/or UV/H<sub>2</sub>O<sub>2</sub>/RWW treatment in the last ten years are shown in Figure 2.

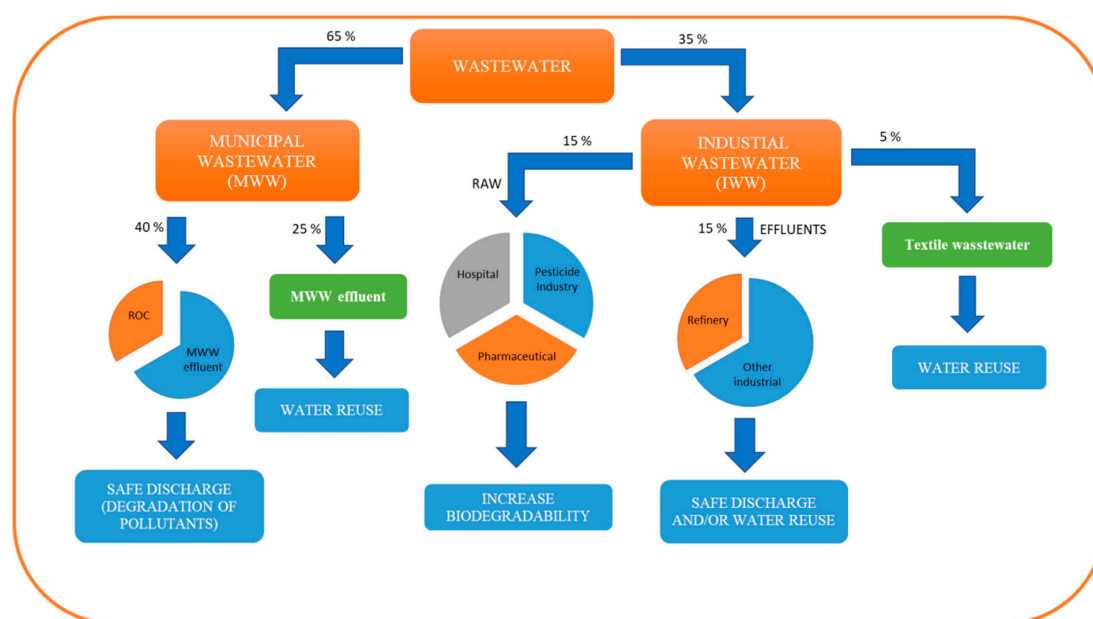


**Figure 2.** Schematic presentation of types of wastewater used for detoxification by photo-Fenton and/or UV/H<sub>2</sub>O<sub>2</sub>/real waste water (RWW) in the last ten years.

Approx. 35% of the reviewed articles on photo-Fenton were conducted with industrial wastewater (IWW) from such sectors as refinery, textile, pesticide and pharmaceutical. Influent and effluents of industrial wastewater treatment plants were used. Therefore, the concentration of organic pollutants in IWW varied greatly. The reported results suggest that photo-Fenton treatment can be successfully applied as IWW pre-treatment (before the biological process) causing the increase of its biodegradability [42] as well as post-treatment (after biological process) of IWW effluents leading to the degradation of organic pollutants and the decrease of toxicity [43]. Interestingly, among the reviewed articles, there are studies reporting that the quality of IWW effluent after photo-Fenton was in agreement with the legal requirements (physical, chemical and microbiological parameters) for IWW reuse [43,44]. Moreover, solar photo-Fenton was reported to be efficient not only for the detoxification of textile wastewater but also for its successful reuse in the dyeing and washing stages of the process [15].

As can be seen from Figure 2, the majority of articles (65%) were performed with municipal wastewater treatment plant effluents (MWW) and its concentrates. In general, DOC and COD values for the studied MWW effluents varied in a range of 7–23 mg L<sup>-1</sup> and 26–83 mg L<sup>-1</sup>, respectively. These values were higher for the concentrates obtained from MWW effluents, being 37–53 mg L<sup>-1</sup> for DOC and 105–200 mg L<sup>-1</sup> for COD. The highest COD values were observed for raw hospital wastewater (COD, 1350 mg L<sup>-1</sup>). It was demonstrated that photo-Fenton is efficient



as a pre-treatment step (before biological process) of raw hospital wastewater for increasing its biodegradability and detoxification [45] and a post-treatment step (after biological process) of MWW effluents and concentrates for the elimination of pollutants and the detoxification of water [12,46]. The application of the additional post-treatment of MWW effluents, such as the photo-Fenton process in general leads to the decomposition of organic pollutants and detoxification of water. Therefore, such effluents are becoming more attractive for water reuse, especially in areas with water scarcity. Among the reviewed literature there are studies for MWW effluent reuse using UV/H<sub>2</sub>O<sub>2</sub>/RWW treatment [47–49].

It should be mentioned that in 35% of the reviewed articles devoted to the detoxification of wastewater by photo-Fenton adjustment of pH and/or decreasing concentration of carbonates was performed (for example by the addition of H<sub>2</sub>SO<sub>4</sub>). Carbonates or hydrogencarbonate present in wastewater can play the role of hydroxyl radical scavengers, as shown in reactions 9 and 10 [9].



Therefore, the elimination of carbonates and/or hydrogencarbonates can significantly enhance the performance of photo-Fenton treatment. Taking into consideration that the pH of wastewater treated by photo-Fenton is close to neutral, the acidification of wastewater in order to increase the solubility of iron(3+) and/or eliminate hydrogencarbonates might be associated with relatively high cost on the industrial scale as well as sludge generation. It can be expected that more studies will be conducted in the future on the detoxification of wastewater by the photo-Fenton process at near neutral pH.

### 2.3. Operational Conditions

#### 2.3.1. Concentration of Iron in Wastewater

Iron concentration in wastewater is of high importance for the performance of Fenton or the photo-Fenton process. As mentioned above, the amount of iron required for photo-Fenton process is significantly lower than that for classical Fenton. In reviewed articles, two main approaches were used: (i) addition of iron to the wastewater and (ii) without iron addition (UV/H<sub>2</sub>O<sub>2</sub>/RWW process with iron naturally present in the wastewater). Taking into account that iron is often present in many types of wastewaters, in some cases, its concentration might be sufficient for successful photo-Fenton treatment aiming at removal of low concentrations of organic contaminants and disinfection (as it was mentioned above, 50 µg L<sup>-1</sup> was reported to be sufficient for photo-Fenton process [36]).

The concentration of added iron in industrial and municipal wastewater treated by photo-Fenton varied from 5 to 168 mg L<sup>-1</sup>, whereas when iron was not added to the wastewater its concentrations were generally at µg L<sup>-1</sup> level (~60–220 µg L<sup>-1</sup>). An optimal concentration of iron reported for the photo-Fenton detoxification of municipal wastewater treatment plant effluents, reverse osmosis and nanofiltration concentrates was in the range of 5–60 mg L<sup>-1</sup>, while the most commonly used concentrations were 5 or 20 mg L<sup>-1</sup>. For raw hospital wastewater (IWW), a higher iron concentration was applied (135 mg L<sup>-1</sup>). In general, the iron concentration applied for the detoxification of industrial wastewater by photo-Fenton was higher than that for municipal wastewater, varying in a range of 20–168 mg L<sup>-1</sup>. When a relatively high concentration of iron is required for the process, iron removal should be conducted after the application of the Fenton or photo-Fenton process in order to achieve discharge limits of iron in wastewater effluents. Maximum permissible concentrations of iron in surface waters (receiving wastewater effluents) are established based on toxicity data and other relevant parameters. To the best of our knowledge, there are only a few studies concerned with the toxicity assessment of iron for aquatic organisms [50–54]. In a recent study, the final chronic value of 251 µg L<sup>-1</sup> was estimated for iron(3+) at a circumneutral pH based on a toxicity assessment on a taxonomically diverse group of organisms and a mesocosm study [54]. The maximum permissible discharge of

iron in wastewater treatment plant effluents is calculated for each case, so the concentration of iron should not exceed the maximum permissible concentration at the control point. In the United States, the recommended iron concentration of  $1 \text{ mg L}^{-1}$  should be achieved at the end of the initial dilution zone (general and designated use of water) for the protection of aquatic life [55]. According to the general industrial wastewater discharge standards suggested by the Water Environment Partnership in Asia (WEPA), the discharge limit for iron for industrial wastewater is  $2 \text{ mg L}^{-1}$  [56]. Taking into account the concentrations of added iron in reviewed studies, it is questionable as to whether the residual iron concentration in treated wastewater (after wastewater neutralization when needed) can be in agreement with what is suggested by the WEPA limits.

### 2.3.2. Concentration of $\text{H}_2\text{O}_2$ in Wastewater

Another important parameter for photo-Fenton wastewater treatment is  $\text{H}_2\text{O}_2$  concentration. The weight ratio of  $\text{H}_2\text{O}_2/\text{Fe}$  varied from 2.5 to 25 (80% of reviewed articles) and from 40 to 105 (20% of articles) when iron was added prior to treatment. Generally, there are two different ways of adding  $\text{H}_2\text{O}_2$  to the reaction: (i) adding the optimal concentration fully before the beginning of treatment [57], and (ii) adding a part of the required amount of  $\text{H}_2\text{O}_2$  before and during the process (usually when added  $\text{H}_2\text{O}_2$  is consumed, the next part is added) [12]. An optimal concentration of  $\text{H}_2\text{O}_2$  reported for the photo-Fenton detoxification of municipal wastewater effluents and its reverse osmosis and nanofiltration concentrates varied from 50 to  $102 \text{ mg L}^{-1}$ . For the photo-Fenton detoxification of the raw hospital wastewater concentration of  $\text{H}_2\text{O}_2$  was four times higher ( $5400 \text{ mg L}^{-1}$ ) than the initial COD value ( $1350 \text{ mg L}^{-1}$ ). In the reviewed studies, the concentration of  $\text{H}_2\text{O}_2$  added to industrial wastewater for the photo-Fenton process varied from 136 to  $6273 \text{ mg L}^{-1}$ . Such a huge variation can be possibly explained by the significant difference in the initial TOC and COD levels of industrial wastewaters.

In the majority of reviewed articles devoted to the detoxification of wastewater using the photo-Fenton process (>70%) concentration of residual  $\text{H}_2\text{O}_2$  (not consumed during photo-Fenton treatment) after treatment was monitored. In some cases, residual  $\text{H}_2\text{O}_2$  can be as high as  $1000 \text{ mg L}^{-1}$  [42]. It is noteworthy that the presence of residual  $\text{H}_2\text{O}_2$  in wastewater effluent can be a problem for water reuse or safe discharge due to the high toxicity of this compound even at low concentrations [58]. Therefore, residual  $\text{H}_2\text{O}_2$  should be eliminated from treated wastewater before discharge or reuse. In the reviewed works, two main approaches were implemented in order to avoid the presence of residual  $\text{H}_2\text{O}_2$  in treated water, namely the addition of relatively small concentrations of  $\text{H}_2\text{O}_2$  (which can be fully consumed during the process) and filtration through activated carbon. It was reported that the decomposition of  $\text{H}_2\text{O}_2$  is catalyzed by activated carbon [59–62]. Therefore, this process can be defined as catalytic wet peroxide oxidation (CWPO), which is one of AOPs. The CWPO can be considered to be beneficial post-treatment step after the photo-Fenton process leading to the removal of residual  $\text{H}_2\text{O}_2$  as well as residual hydrophobic organic contaminants.

### 2.3.3. Irradiation Sources

Irradiation sources are introduced to the Fenton reaction in order to increase the reaction rate, which occurs mainly due to photo-reduction of iron(3+) to iron(2+) (reaction 7;  $\lambda < 600 \text{ nm}$ ) and the photolysis of hydrogen peroxide ( $\lambda = 254 \text{ nm}$ ).

The most common UV sources applied for photo-Fenton and/or UV/ $\text{H}_2\text{O}_2$ /RWW water purification in industrial or semi industrial scale are UVC mercury based lamps. Depending on the pressure of mercury vapor, low pressure (LP, 0.01 mbar or 1 Pa) and medium pressure (MP, 1 bar or 100 kPa) lamps can be differentiated. Two main types of LP lamps can be distinguished: pure mercury lamps (standard) and mercury amalgam (usually mercury/indium) [63]. The introduction of LP amalgam lamps to the market was extremely beneficial due to higher specific UVC flux per unit arc length (up to  $1000 \text{ mW cm}^{-1}$ ) in comparison with standard LP lamps ( $<200 \text{ mW cm}^{-1}$ ) [63,64]. The main characteristics of MP and LP amalgam lamps are presented in Table 1.

**Table 1.** Main parameters of low pressure (LP) (amalgam) and medium pressure (MP) lamps [63].

Parameters	LP Amalgam Lamp	MP
UV spectrum	monochromatic (254 nm)	polychromatic (200–600 nm)
Operating temperature (°C)	90–120	500–950
Electrical power (W)	40–500	400–60000
Operation costs	relatively low	high
Amount of liquid mercury (mg):	0	up to 300
Specific UVC flux (W/cm)	<1	<35
UVC efficiency (%)	35–40	5–15
Life-time (h)	<16000	<5000

As can be seen in Table 1, LP lamps emit a wavelength of 254 nm which is suitable for H<sub>2</sub>O<sub>2</sub> breaking into oxidizing species. In case of an MP lamp, the emission is polychromatic but most of the spectrum (>280 nm) is not relevant for H<sub>2</sub>O<sub>2</sub> decomposition. The main advantage of an MP lamp is the specific UVC flux per unit arc length, which can reach 35 W cm<sup>-1</sup>. However, the UVC efficiency of an MP lamp is about three times lower than that of an LP amalgam lamp. Moreover, the lifetime of LP amalgam lamps is about three times higher than an MP lamp, which obviously affect the cost. However, if the space is limited, an MP lamp can be used due to high UVC output and a compact reactor design. In our earlier work, we observed that the electricity consumption of MP lamp was about six times higher than that of an LP lamp, while the degradation performance of organic pollutants was similar [43]. Moreover, in case of refinery wastewater treatment by UV/H<sub>2</sub>O<sub>2</sub>/RWW, the formation of toxic phenolic by-product was detected when an MP lamp was applied which was not the case with an LP lamp [43], suggesting that pathways of organic contaminant degradation varies when different types of lamps are utilized. Similar results were reported earlier for drinking water [65]. In summary, the achieved results indicate that LP lamps are more beneficial than MP lamps. It is noteworthy that the intensity of the lamp is not provided in some articles; moreover, the elimination of organic pollutants is represented as a function of time. The contact time is a useful parameter for the selection of the optimal conditions of the process in case an experimental set-up and wastewater matrix are the same. However, the authors of the present paper believe that the contact time might not be an appropriate parameter when the performance of photo-Fenton and/or UV/H<sub>2</sub>O<sub>2</sub>/RWW treatment, applied to different wastewaters using various experimental set ups, should be compared. The UVC dose, encompassing the contact time and intensity of irradiation, would be more suitable parameter allowing to compare various studies. Among the reviewed studies devoted to the detoxification of wastewater using photo-Fenton and/or UV/H<sub>2</sub>O<sub>2</sub>/RWW treatment, LP and MP lamps were used as the radiation source in approx. 39% and 28% of the articles, respectively. In one study [42] high pressure mercury vapor lamp was used as a source of UVA. However, it should be noticed that use of these conventional UV lamps leads to generation of highly toxic wastes at the end of their useful life time. Hence, alternative and more environmentally friendly irradiation sources, such as light emitting diodes (LEDs) and natural solar irradiation may be used in the future. Considering that 128 countries signed the Minamata Convention on Mercury [66], the use of light emitting diodes (LEDs) is becoming more attractive. Taking into account rapid development of LED technology and advances achieved in this field in recent years it may be expected that more studies will be conducted in the future using LEDs as irradiation source.

Approx. 33% among the reviewed studies on photo-Fenton wastewater detoxification were conducted using natural solar light as the radiation source. It should be mentioned that the solar photo-Fenton process can be activated by low global irradiance values (200 W m<sup>-2</sup>) when relatively low concentration of iron and H<sub>2</sub>O<sub>2</sub> are present (0.5 mg L<sup>-1</sup> Fe<sup>2+</sup>/5 mg L<sup>-1</sup> H<sub>2</sub>O<sub>2</sub>) in water [67].

#### 2.4. Toxicity

Both acute and chronic bioassays were applied for the toxicity assessment of wastewater treated by the photo-Fenton process. Bacteria [15,45,68,69], seawater invertebrates [42], freshwater invertebrates [70], microalgae [46], freshwater vertebrates [49], seawater vertebrates [46] and plants

(phytotoxicity assay) were used in the last ten years for the toxicity assessment of wastewater treated by photo-Fenton and/or UV/H<sub>2</sub>O<sub>2</sub>/RWW. In 60% of the reviewed studies, the toxicity of wastewater decreased after the application of the photo-Fenton and/or UV/H<sub>2</sub>O<sub>2</sub>/RWW process, especially when added H<sub>2</sub>O<sub>2</sub> was fully consumed and/or post-treatment step such as CWPO, leading to the elimination of residual H<sub>2</sub>O<sub>2</sub> and some trace pollutants, was applied. It is noteworthy that residual H<sub>2</sub>O<sub>2</sub> may significantly elevate the toxicity of the water after treatment [43]. Therefore, caution should be applied in the interpretation and comparison of results of various studies on wastewater detoxification by photo-Fenton because in some studies residual H<sub>2</sub>O<sub>2</sub> is eliminated before the toxicity assessment [42] while in others it is not [43]. The question regarding H<sub>2</sub>O<sub>2</sub> removal prior conducting toxicity bioassays before, during and after the photo-Fenton process may arise. The authors of the present paper tend to believe that in case when the goal is to determine possible toxic effect of treated wastewater to the receiving environment, the water sample should not be modified before toxicity assessment, i.e., the residual H<sub>2</sub>O<sub>2</sub> (if any) should not be removed. However, if the goal of the study is to determine the toxic effect of generated during the process by-products the elimination of H<sub>2</sub>O<sub>2</sub> before toxicity assessment might be relevant. A toxicity assessment during the photo-Fenton treatment of wastewater was performed in approx. 30% of the reviewed works. In all of these studies, residual H<sub>2</sub>O<sub>2</sub> was eliminated prior to the toxicity evaluation. However, a significant increase of toxicity during the photo-Fenton process was observed in MWW effluents with *Vibrio fischeri* [12] and *Lactuca sativa* [13], and in IWW with *Vibrio fischeri* [14] and *Alivibrio fischeri* [15]. These results generally may be ascribed to the formation of more toxic by-products during the photo-Fenton process than parental contaminants and their possible synergetic effect. Another interesting aspect when analyzing the results of toxicity tests is that chelating agents might be added in order to perform photo-Fenton at a near neutral pH [34]. However, as reported in a recent study [70], the addition of certain concentrations of chelating agents such as (S,S)-Ethylenediamine-N,N'-disuccinic acid trisodium salt (EDDS) can be the toxic.

The types of IWW treated by the photo-Fenton process for its detoxification are shown in Figure 2. Bioassays with *Vibrio fischeri*, *Alivibrio fischeri*, *Photobacterium phosphoreum*, *Artemia salina*, *Daphnia magna*, *Paracentrotus lividus* and *Sparus aurata larvae* were used for the assessment of wastewater toxicity before, after and during photo-Fenton treatment. All the above-mentioned toxicity assays were sensitive for IWW. Interestingly, *Daphnia magna* was too sensitive to pharmaceutical wastewater. Thus, after 24 h of exposure all of the organisms were dead not only in the untreated pharmaceutical wastewater, but also in the water samples taken during and after photo-Fenton treatment (hydrogen peroxide was removed from water samples prior toxicity test) [14].

The toxicity tests used for the assessment of hospital and MWW detoxification efficiency by the photo-Fenton process were *Vibrio fischeri*, *Daphnia magna*, *Tetrahymena thermophila*, *Carassius auratus* L., *Sorghum saccharatum*, *Lepidium sativum*, *Sinapis alba*, *Lactuca sativa*, *Spirodela polyrhiza*, *Sparus aurata larvae*, *Paracentrotus lividus* and *Isochrysis galbana*. Among the reviewed articles, the most commonly applied toxicity bioassay for MWW effluents was a standardized *Vibrio fischeri* bioluminescence test with 5, 15 and 30 min incubation time (ISO 11348). Such parameters as short duration required for analysis, well-defined protocols, reproducibility and sensibility, as well as cost efficiency were reported among the main advantages of this test [71–74]. However, it was demonstrated that the standard *Vibrio fischeri* bioluminescence test underestimates or even fails to detect the toxicity of chemical compounds interfering in the biosynthetic process due to insufficient incubation time (acute toxicity assessment) [75,76]. Interestingly, a long-term (chronic toxicity assessment) *Vibrio fischeri* bioassay (7 h and 24 h) was reported to overcome this limitation [76]. This might probably be explained by insignificant acute toxic effect and measurable chronic toxicity of pollutants in MWW on *Vibrio fischeri*. Moreover, the standard *Vibrio fischeri* bioassay cannot always provide relevant biological or ecological information [77]. Thus, *Vibrio fischeri* is marine bacteria, so the results of this test might be irrelevant for the toxicity assessment of wastewater discharged to the freshwater body (not an adequate environment for this species). The *Vibrio fischeri* bioassay was reported to be not sensitive for spiked and naturally present pollutants in MWW effluents before and after photo-Fenton treatment [13,49,69].

These findings are in agreement with another study which demonstrated that effluents from nine different WWTPs were not toxic to *Vibrio fischeri* [78]. It should be noted that some authors reported growth stimulation (hormesis) of *Vibrio fischeri* in MWW effluents [46,68]. However, in some cases, a *Vibrio fischeri* bioassay was reported to be sensitive for MWW effluents, its concentrates and hospital wastewater treated by the photo-Fenton process [45,70,79]. This might be explained by the presence of residual H<sub>2</sub>O<sub>2</sub> in water during the toxicity assessment [79] or additional toxicity due to the added chelating agent [70] or significantly higher concentrations of pollutants in WW [45].

Another commonly used toxicity bioassay is the *Daphnia magna* (freshwater invertebrate) immobilization test. High sensitivity, relatively low cost and ease of use were reported among the main advantages of this bioassay [80]. It was only in one study that a *Daphnia magna* bioassay was reported to be not sensitive to MWW effluent before and after photo-Fenton treatment (residual concentration of H<sub>2</sub>O<sub>2</sub> was in the range of 15–20 mg L<sup>-1</sup>) [68], while in other studies this test was sensitive enough [13,70,81]. However, it was suggested by Koivisto in 1995 that this excellent bioassay might not be ecologically relevant since *Daphnia magna* is not a representative zooplankton species [80]. Interestingly, a bioassay with *Tetrahymena thermophyla* was reported to be more sensitive than that with *Daphnia magna* (48 h) for MWW effluents [13].

Toxicity tests with different types of fish are well known and widely used because of high sensitivity. However, fish bioassays are usually time consuming, requiring special equipment and a skilled operator [82]. Shu and co-authors studied the endocrine disruption effect on goldfish (*Carassius auratus* L.) exposed to MWW effluent (untreated, after UV/H<sub>2</sub>O<sub>2</sub>/RWW and after GAC) [49]. The results of this study revealed acute and sub-chronic endocrine disruptors in the kidney, liver and spleen of goldfish exposed to untreated effluent. Interestingly, the UV/H<sub>2</sub>O<sub>2</sub>/RWW treatment was not efficient due to the negative acute (7 days) toxicological impact on goldfish (spring, summer and autumn). The efficiency of the UV/H<sub>2</sub>O<sub>2</sub>/RWW process for the elimination of a sub-chronic (60 days) impact was changing depending on the season. Thus, in spring, no significant difference was observed for the sub-chronic toxic effect between reuse water and water after the UV/H<sub>2</sub>O<sub>2</sub>/RWW process. However, during the summer season, the potential of UV/H<sub>2</sub>O<sub>2</sub>/RWW treatment for the remediation of the estrogenic impact in the spleen and kidney of goldfish was observed. These results were attributed to the seasonal variations of estrogenic substances composition in water [49]. Another study by Singh and co-authors reported that 7 days of exposure (acute toxicity) of goldfish to the xenobiotics present in MWW effluent led to the down-regulation of innate immune responses [48]. It was also demonstrated that goldfish have habituated to MWW effluent after 60 days of exposure (sub-chronic). It was suggested that the UV/H<sub>2</sub>O<sub>2</sub>/RWW treatment applied for filtered MWW effluent may be insufficient for the complete elimination of pollutants (xenobiotics), which may alter the physiology of aquatic organisms in the receiving water body [48]. Moreover, cytokine and cytokine gene expression were suggested to be promising parameters for the safety assessment of MWW effluents subjected to further reuse or safe discharge [48]. Another useful tool for the evaluation of MWW effluent water quality is the goldfish olfaction test reported by Blunt and co-authors [47]. They found that goldfish may “smell” MWW effluents and the exposure of fish to effluents affects the olfactory responses. Interestingly, sub-chronic exposure of goldfish to UV/H<sub>2</sub>O<sub>2</sub>/RWW treated MWW effluent does not impair olfactory responses, whereas the opposite was true for untreated effluent [47].

Bioassays with plants can be considered as a useful tool for WW effluents quality control, especially in case MWW effluent is used for agricultural irrigation. Among the main advantages of a bioassay with plants, availability of various evaluation endpoints (root growth, shoot growth, germination rate, etc.) and cost-efficiency can be mentioned. However, generally, a long time is needed (4–6 days) to obtain results [82]. Michael and co-authors evaluated the phytotoxic potential of MWW effluent spiked with antibiotics (µg L<sup>-1</sup>) during solar photo-Fenton treatment using *Sorghum saccharatum* (monocotyl Sorgho), *Lepidium sativum* (dicotyl garden cress) and *Sinapis alba* (dicotyl mustard) as indicator species [81]. Root growth was a more sensitive parameter than seed germination. The phytotoxicity of MWW effluent was decreased after the applied photo-Fenton process (residual H<sub>2</sub>O<sub>2</sub> was eliminated from

water samples before toxicity assessment and pH was neutralized), suggesting the possible reuse of wastewater for agricultural irrigation. The phytotoxicity assessment of MWW effluent before and after solar photo-Fenton treatment using aquatic (*Spirodela polyrhiza*) and terrestrial (*Lactuca sativa*) plants was reported [13]. Interestingly, *Lactuca sativa* was more sensitive than *Spirodela polyrhiza*. The untreated MWW effluent resulted in the stimulation of root elongation attributed to the presence of nutrients in MWW, whereas in case of treated effluent the inhibition of root elongation was observed. The slight inhibition after treatment was ascribed to decrease the organic load and the generation of more toxic by-products [13]. It is noteworthy that growth stimulation often caused by MWW effluent should not be interpreted as an advantageous effect [13].

A battery of bioassays using different species at various trophic levels is known as an efficient tool for the evaluation of WW effluents quality and prediction of the possible effect on the species in the receiving aquatic environment [82]. It is also noteworthy that an adequate toxicity assessment can be achieved when the tested species are widespread, ecologically representative and indigenous to the receiving environment [46]. A battery of bioassays consisting of *Vibrio fischeri*, *Isochrysis galbana*, *Paracentrotus lividus* and *Sparus aurata* was developed for the toxicity assessment of MWW effluent discharged into the marine environment [46]. The *Paracentrotus lividus* was found to be the most sensitive species among those tested. While studying the detoxification of various MWW effluents by the application of UV/H<sub>2</sub>O<sub>2</sub>/RWW followed by CWPO, Díaz-Garduño and co-authors suggested the decrease of acute toxicity after applied treatment, but not harmless treated effluents for the receiving environment [46]. The efficiency of UV/H<sub>2</sub>O<sub>2</sub>/RWW followed by CWPO was reported to be higher than that of photobiotreatment (using microalgae) for the detoxification of MWW effluents using a battery of bioassays [8]. García and co-authors investigated the efficiency of raceway pond reactors for MWW effluent disinfection and detoxification by the solar photo-Fenton process and found that there was hardly any decrease of toxicity after treatment for the tested bioassays (*Vibrio fischeri*, *Daphnia magna*, *Tetrahymena thermophila*) [68]. The results of MWW effluent detoxification by photo-Fenton indicate the significance of a toxicity evaluation using a battery of bioassays for understanding the efficiency of the applied post-treatment methods.

Based on the reviewed studies, it can be suggested that standard bioassays and most widely used for municipal wastewater (*Vibrio fischeri*, *Daphnia magna*) are not always sensitive (Figure 3) for the pollutants present in municipal wastewater (not spiked with pollutants or EDDS).

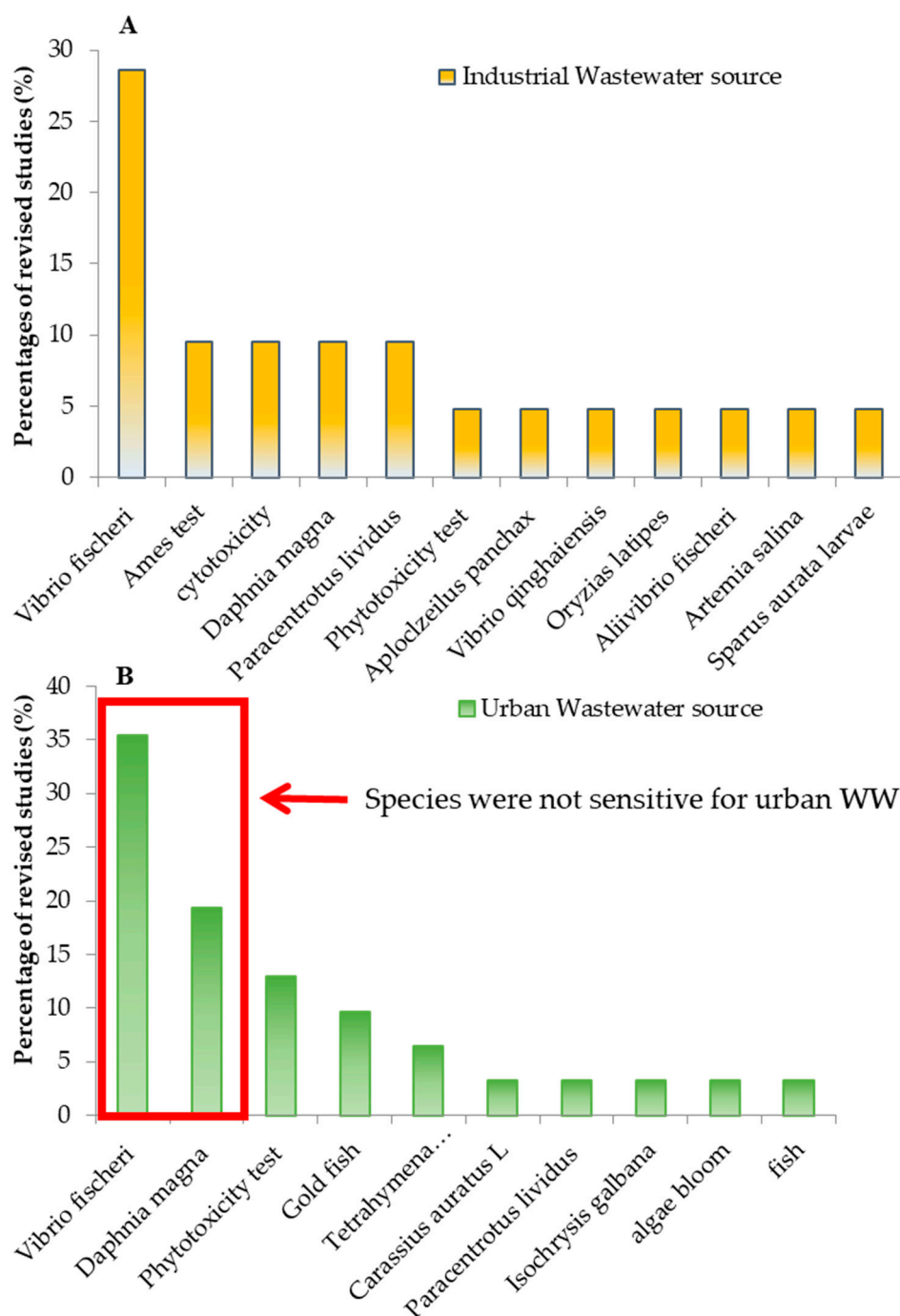


**Figure 3.** Schematic representation of species used for toxicity assessment in revised studies; A - for industrial wastewater and B - for urban wastewater.

### 2.5. Cost Estimation of Wastewater Treatment by the Photo-Fenton Process

One of the most promising AOPs for real applications nowadays is photo-Fenton and/or UV/H<sub>2</sub>O<sub>2</sub>/RWW treatment. The cost of this process was estimated in the majority (approx. 60%) of revised articles devoted to wastewater detoxification. There is much more literature available on cost estimation of photo-Fenton process [83–85], but in this review we have only considered studies, in which WW was used and toxicity assessment was conducted. The electrical consumption of the lamp is among the main contributors to the operational and maintenance (O&M) cost of the treatment. In reviewed articles, the electrical cost (generated by lamp) varied from €1.2 to €1.73 m<sup>-3</sup> when medium

pressure (MP) lamp was used, whereas these values were lower (€0.28 to €1.25 m<sup>-3</sup>) for treatment with low pressure (LP) lamps. The electrical cost is proportional to the performance of the lamp. Industrial scale MP lamps in general have a relatively low performance of approx. 15% [57], whereas the performance of laboratory scale MP lamps is even lower (approx. 4%). Commonly used LP lamps are more efficient reaching values of performance of approx. 25% and 50% in the laboratory and industrial scale, respectively [44,86]. It was demonstrated that coagulation as a pre-treatment can decrease the electrical cost of the photo-Fenton process (from 350 kWh m<sup>-3</sup> to 60–100 kWh m<sup>-3</sup>). Moreover, the combination of coagulation before photo-Fenton and filtration through activated carbon applied after was reported to decrease the energy cost further (45–50 kWh m<sup>-3</sup>) [79]. In case of solar photo-Fenton, the electrical cost (energy consumption) drastically decreases.

Various reagents are used in the photo-Fenton process, such as H<sub>2</sub>O<sub>2</sub>, iron salts (FeSO<sub>4</sub>) and reagents for acidification and neutralization (HCl, H<sub>2</sub>SO<sub>4</sub>, NaOH, etc.). The cost of H<sub>2</sub>O<sub>2</sub> was reported to be €0.7 kg<sup>-1</sup> [87]. Generally, in reviewed articles, the cost of H<sub>2</sub>O<sub>2</sub> required for the photo-Fenton process varied from €0.07 to €0.125 m<sup>-3</sup> with the exception of €0.93 m<sup>-3</sup> reported for hospital wastewater treatment. As mentioned before, two different approaches for conducting the photo-Fenton process are used: (i) with the addition of iron (Fe<sup>2+</sup> or Fe<sup>3+</sup>) or (ii) without iron addition (with naturally present iron in wastewater at µg L<sup>-1</sup> level). The most common reagent used as an iron source is FeSO<sub>4</sub>·7H<sub>2</sub>O and its cost varies from €0.074 to €0.27 kg<sup>-1</sup> in reviewed works. Depending on the required iron concentration for the photo-Fenton process, the cost of iron addition in reviewed works varied from €0.01 to €0.1 m<sup>-3</sup>. The acidification of wastewater is required for carrying out conventional photo-Fenton treatment. For this purpose, sulfuric acid is usually used. The price of this reagent is approx. €0.25 kg<sup>-1</sup> [85]. The cost of H<sub>2</sub>SO<sub>4</sub> addition in reviewed studies was estimated to be €0.01–€0.025 m<sup>-3</sup>. Generally, the cost of water neutralization (conducted by NaOH, €0.55 kg<sup>-1</sup>) and management of the generated sludge after photo-Fenton is not considered, which is of high importance for real applications. When chelating agents are used for the photo-Fenton process at neutral pH, the reagent cost increases significantly [70].

As shown in Table 2, the total O&M cost of photo-Fenton and/or UV/H<sub>2</sub>O<sub>2</sub>/RWW treatment (with UV lamps) varies from €0.44 to €2.18 m<sup>-3</sup>. The results of a recent study revealed that the O&M cost of UV/H<sub>2</sub>O<sub>2</sub>/RWW treatment of WW was five times higher when an MP lamp was used (€2.18 m<sup>-3</sup>) compared to LP lamp (€0.44 m<sup>-3</sup>), whereas the required UV dose and TOC elimination performance were similar [43]. Therefore, it can be suggested that the use of LP lamps, when possible, increases the economic feasibility of the process. Recently, operational costs (OPEX) for a full-scale implementation of UV/H<sub>2</sub>O<sub>2</sub>/RWW process for municipal wastewater effluent treatment in Sweden was calculated to be 0.064€ m<sup>-3</sup> (UV-dose 5000 J m<sup>-2</sup>; H<sub>2</sub>O<sub>2</sub> dose 20 mg L<sup>-1</sup>; dissolved iron 0.12 mg L<sup>-1</sup>, LP replacement every 1.5 years), from which about 35% was attributed to energy consumption [87]. This estimation is significantly lower than cost estimations performed in revised literature, which can be explained as follows: (i) estimation of operational costs is not very precise when it is based on laboratory scale experiments; (ii) the UV-dose required for removal of residual pharmaceuticals is lower than that needed for decrease of toxicity (safe discharge/water reuse).



**Table 2.** Operation and maintenance cost for photo-Fenton process and UV/H<sub>2</sub>O<sub>2</sub>/RWW.

AOP Process and References	Type of Radiation	Type of Wastewater/Initial TOC or COD	Main Objective	Total Cost
<i>UV lamps as radiation source</i>				
UV/H <sub>2</sub> O <sub>2</sub> /RWW + CWPO [57]	MP lamp	Synthetic industrial wastewater; TOC = 40 mg/L; COD = 150 mg/L	Safe discharge or water reuse	The cost of H <sub>2</sub> O <sub>2</sub> /UV + GAC was estimated to be €1.57 m <sup>-3</sup> (based on reagent and electrical consumption)
UV/H <sub>2</sub> O <sub>2</sub> /RWW + CWPO [43]	MP and LP lamps	Refinery effluent; TOC = 35 mg/L; COD = 128 mg/L	Safe discharge or water reuse	The operation and maintenance costs for H <sub>2</sub> O <sub>2</sub> /UVC + GAC using MP and LP lamps was estimated to be €2.18 m <sup>-3</sup> and €0.44 m <sup>-3</sup> , respectively.
UV/H <sub>2</sub> O <sub>2</sub> /RWW + CWPO [44]	LP lamp	Synthetic industrial wastewater; TOC = 40 mg/L; COD = 146 mg/L	Safe discharge or water reuse	The operation and maintenance cost of H <sub>2</sub> O <sub>2</sub> /UVC + GAC was estimated to be €0.59 m <sup>-3</sup>
UV/H <sub>2</sub> O <sub>2</sub> /RWW + CWPO [8]	LP lamp	Three types of urban wastewater effluents; TOC = 10–13.2 mg/L; COD = 75–85 mg/L	Safe discharge or water reuse	The operation and maintenance cost of H <sub>2</sub> O <sub>2</sub> /UVC + GAC was estimated to be €0.59 m <sup>-3</sup>
UV/H <sub>2</sub> O <sub>2</sub> /RWW [69]	LP lamp	Reverse osmosis concentrate; COD = 65 mg/L	Increase of biodegradability	The electrical energy per order (EE/O) was estimated to be around 50 kWh m <sup>-3</sup> (in optimal condition, 30 min) followed by biological treatment (consumption considered negligible).
UV/H <sub>2</sub> O <sub>2</sub> /RWW + BAC [79]	LP lamp	Reverse osmosis concentrate; COD = 105 mg/L	Safe discharge	The electrical energy dose (EED) required for each treatment was calculate. It included the EDD of H <sub>2</sub> O <sub>2</sub> production (10 kWh m <sup>-3</sup> ). H <sub>2</sub> O <sub>2</sub> /UV: ~350 kWh m <sup>-3</sup> H <sub>2</sub> O <sub>2</sub> /UV + BAC: ~60 kWh m <sup>-3</sup> Coagulation Al + H <sub>2</sub> O <sub>2</sub> /UV: ~100 kWh m <sup>-3</sup> Coagulation Fe + H <sub>2</sub> O <sub>2</sub> /UV: ~60 kWh m <sup>-3</sup> Coagulation Al + H <sub>2</sub> O <sub>2</sub> /UV + BAC: ~50 kWh m <sup>-3</sup> Coagulation Fe + H <sub>2</sub> O <sub>2</sub> /UV + BAC: ~45 kWh m <sup>-3</sup>
Photo-Fenton [45]	LP lamp	Hospital wastewater; TOC = 1050 mg/L; COD = 1350 mg/L	Increase of biodegradability	The operating cost concerning only electrical cost is \$0.52 m <sup>-3</sup> . The reagent cost was estimate to be \$0.01 m <sup>-3</sup> and \$0.93 m <sup>-3</sup> for FeSO <sub>4</sub> ·7H <sub>2</sub> O and H <sub>2</sub> O <sub>2</sub> , respectively. Total cost \$1.46 m <sup>-3</sup>
<i>Solar light as radiation source</i>				
Solar Photo-Fenton [68]	Natural solar light	Secondary urban wastewater effluent; COD = 65.1 ± 1.4 mg/L	Wastewater disinfection	Economical cost calculation was conducted based on simulation of chosen treatment using a secondary effluent flow of 400 m <sup>3</sup> d <sup>-1</sup> . The total cost was estimated to be €0.15 m <sup>-3</sup> (including operating and maintenance and reagent cost) for disinfection.

Table 2. Cont.

AOP Process and References	Type of Radiation	Type of Wastewater/Initial TOC or COD	Main Objective	Total Cost
<i>Solar light as radiation source</i>				
Solar Photo-Fenton [81]	Natural solar light	Municipal wastewater effluent; COD = 26 mg/L	Water reuse	Economical cost calculation was conducted based on simulation of full-scale unit of 150 m <sup>3</sup> d <sup>-1</sup> . The total cost evaluated was €0.85 m <sup>-3</sup> (including majority of electrical consumption, reagents, maintenance and investment costs).
Solar-Photo Fenton [70]	Natural solar light	(1) municipal WW effluent (direct treatment (DOC = 23 mg/L); (2) nanofiltration concentrate (DOC = 53 mg/L)	Safe discharge	The total cost (including amortization cost of solar collectors and membrane, operating and maintenance cost and reagents) of four different processes were: pH 3, direct MWW effluent: €0.53 m <sup>-3</sup> circumneutral pH, direct MWW effluent: €1.17 m <sup>-3</sup> pH 3, ROC MWW effluent: €0.48 m <sup>-3</sup> circumneutral pH, ROC MWW effluent: €0.76 m <sup>-3</sup>

For solar photo-Fenton, the total cost varied for conventional photo-Fenton at pH 3 (€0.48 to €0.53 m<sup>-3</sup>) and circumneutral photo-Fenton (€0.76 to €1.17 m<sup>-3</sup>). It is noteworthy that solar-photo Fenton was reported to be approx. €0.5 m<sup>-3</sup> (CPC solar field in case of 14,000 m<sup>2</sup>).

### 3. Electrochemical Technologies Based on Fenton

#### 3.1. Electro-Fenton

During the electro-Fenton process, the continuous in situ electrochemical generation of H<sub>2</sub>O<sub>2</sub> occurs in an acidic medium via oxygen reduction at cathode as shown in the reaction below [88].



The generated H<sub>2</sub>O<sub>2</sub> decomposition is catalyzed by iron ions according to a classical Fenton reaction. Simultaneously, the regeneration of iron(2+) at cathode occurs (reaction 12) [89].



Decomposition of organic pollutants occurs via classical Fenton's reaction and anodic oxidation at the anode surface [89]. Parameters such as the type of anode, current intensity, oxygen solubility, generation rate of hydrogen peroxide and pH are critical for the electro-Fenton process.

To the best of our knowledge, only four studies on electro-Fenton process for wastewater treatment published in the last ten years have reported results of toxicity assessment [89–92]. Interestingly, studies on wastewater detoxification applying heterogeneous and homogeneous electro-Fenton were conducted. The latter was performed with the addition of iron as a catalyst. In general, a relatively high concentration of iron was added, such as 0.55 mM [89] and 2 mM (ferrous sulfate) [91]. For the heterogeneous electro-Fenton process, Fe-zeolite Y [92] and waste rice straw-coal fly ash [91] were used as catalysts. Different types of electrodes, such as Ti/RuO<sub>2</sub>, graphite and boron-doped diamond, were used as an anode in reviewed works devoted to wastewater detoxification by the electro-Fenton process.

It should be noted that all of the reviewed studies on electro-Fenton were conducted with industrial wastewaters. Generally, the initial COD values of IWW effluents treated by electro-Fenton varied from 160 to 270 mg L<sup>-1</sup> except textile effluent with COD 1156 mg L<sup>-1</sup>. Acute and/or chronic bioassays with freshwater bacteria [92], freshwater invertebrate [91] and freshwater fish [89], as well as brackish and freshwater fish [90] were used for the toxicity assessment of wastewater before and after the electro-Fenton process. The acute toxicity of IWW effluents decreased after the application of electro-Fenton when *Aploclzeilus panchax*, *Vibrio qinghaiensis* and *Daphnia magna* bioassays were used. Interestingly, acute and chronic toxicity were reported to be significantly higher after Fenton and electro-Fenton treatment of coking wastewater effluent when an *Oryzias latipes* bioassay was used. These results suggest significant variations in sensitivity of the used species.

Despite the fact that only a few studies have addressed the detoxification of wastewater by the electro-Fenton process, the cost estimation was conducted at half of these. Thus, the total operational cost of the homogeneous electro-Fenton process was estimated to be \$9.75 per kg of removed COD [89]. It is important to mention that the average values reported for electrical energy consumption during electrochemical processes was 1.2 to 200 kWh m<sup>-3</sup> [93–96]. In terms of the cost per treated water for heterogeneous electro Fenton is around 0.78 CNY per ton of treated water (around €0.1 m<sup>-3</sup>) [91].

### 3.2. Galvanic Fenton

Galvanic Fenton was also applied for the detoxification of industrial wastewater [97]. Galvanic Fenton (GF) as Fenton technology can be suitable for wastewater with high turbidity, color, salinity and low biodegradability index [97]. The main principle of the system is based on corrosion of the metal (M) in an acidic environment, which leads to dissolution of the metal and production of hydrogen gas (reaction 13 and 14) [97].



To the best of our knowledge, only one study in last ten years was published with GF for wastewater treatment and toxicity assessment [97]. In published study iron—copper (Fe/Cu) electrodes were used as an anode and cathode. The ratio H<sub>2</sub>O<sub>2</sub>/Fe was 19:1 (7840 mg L<sup>-1</sup> of H<sub>2</sub>O<sub>2</sub> and 408 mg L<sup>-1</sup> of Fe). Toxicity tests with plant (*Lactuca sativa*) [97] were implemented. The treated wastewater was as toxic to *Lactuca sativa* as the untreated one [97]. Interestingly in this case, the concentration of residual H<sub>2</sub>O<sub>2</sub> in treated water was relatively high (40 mg L<sup>-1</sup>). A significant toxic effect (EC50 29.57%) for *Lactuca sativa* was reported to take place with an H<sub>2</sub>O<sub>2</sub> concentration of 1570 mg L<sup>-1</sup> [97].

The results reported in the last ten years on the topic are summarized in Table 3.

**Table 3.** Toxicity bioassays applied for assessment of wastewater detoxification after photo-Fenton, electro-Fenton and other Fenton-based advanced oxidation processes (AOPs).

AOP Process	Experimental Conditions	Type of the Water	Toxicity Assessment	Main Outcomes
	<i>Photo-Fenton and/or UV/H<sub>2</sub>O<sub>2</sub>/RWW</i>			
Photo-Fenton [45]	Laboratory scale (LP lamp 10 W). <i>Optimal conditions:</i> pH 3; COD:H <sub>2</sub> O <sub>2</sub> :Fe(II) 1:4:0.1; residual H <sub>2</sub> O <sub>2</sub> was 30 mg/L	Hospital wastewater. TOC 1050 mg/L, COD 1350 mg/L, pH 7.3	<i>Vibrio fischeri</i>	Drastic decrease of toxicity was observed after 2 h of photo-Fenton treatment at optimal conditions.
Photo-Fenton [42]	Laboratory scale (high pressure lamp; UVA 1100 W/m <sup>2</sup> ). <i>Optimal conditions:</i> H <sub>2</sub> O <sub>2</sub> 6273 mg/L; Fe <sup>2+</sup> 60 mg/L. Residual H <sub>2</sub> O <sub>2</sub> 1000 mg/L	Industrial WW from pesticide factory diluted 20–5% ( <i>v/v</i> )	<i>Artemia salina</i>	On the course of the treatment inhibition of <i>Artemia salina</i> decreased. <i>Artemia salina</i> inhibition was 13 ± 6% after treatment (60 min of contact time).
UV/H <sub>2</sub> O <sub>2</sub> /RWW [69]	Laboratory scale (LP lamp, 12.89 mJ/cm <sup>2</sup> ). <i>Optimal conditions:</i> H <sub>2</sub> O <sub>2</sub> 3 mM, pH 4	Reverse osmosis concentrate (ROC). DOC 21 mg/L; COD 65 mg/L; pH 8.5	<i>Vibrio fischeri</i>	The untreated ROC was non-toxic. After ROC treatment using UVC/H <sub>2</sub> O <sub>2</sub> /RWW (after 30 and 75 min of contact time) no toxicity was detected.
UV/H <sub>2</sub> O <sub>2</sub> /RWW [49]	Pilot scale (MP lamp, UV fluence of 1000 mJ/cm <sup>2</sup> ). <i>Optimal conditions:</i> 20 mg/L of H <sub>2</sub> O <sub>2</sub>	Municipal WW effluent. TOC 11 ± 2 mg/L; pH 7.4	<i>Carassius auratus</i> L. and <i>Vibrio fischeri</i>	<i>V. fischeri</i> showed no significant differences response to tested water. Applied UV/H <sub>2</sub> O <sub>2</sub> /RWW treatment was inefficient due to negative acute (7 days) toxicological impact.
UV/H <sub>2</sub> O <sub>2</sub> /RWW [48]	Pilot scale (MP lamp, UV fluence of 1000 mJ/cm <sup>2</sup> ). <i>Optimal conditions:</i> 20 mg/L of H <sub>2</sub> O <sub>2</sub>	Municipal WW effluent after ultrafiltration step (UF)	Gold fish innate immunity	Acute innate immune response deficiencies were reported for goldfish exposed to reuse water during 7 days. After sub-chronic exposure of fish to reuse water evaluated innate immunity parameters in kidney were at the same level as control sample (after GAC filtration).
UV/H <sub>2</sub> O <sub>2</sub> /RWW [47]	Pilot scale (MP lamp, UV fluence of 1000 mJ/cm <sup>2</sup> ). <i>Optimal conditions:</i> 20 mg/L of H <sub>2</sub> O <sub>2</sub>	Municipal WW effluent after ultrafiltration step (UF)	Gold fish	After acute exposure, olfactory impairment was observed after UV/H <sub>2</sub> O <sub>2</sub> /RWW treatment as well as for untreated reuse water. However, after sub-chronic exposure, olfactory impairment was not observed for UV/H <sub>2</sub> O <sub>2</sub> /RWW treated water,

Table 3. Cont.

AOP Process	Experimental Conditions	Type of the Water	Toxicity Assessment	Main Outcomes
<i>Solar Photo-Fenton</i>				
Solar photo-Fenton [70]	Pilot scale (CPC reactors). <i>Optimal conditions:</i> Fe(III):EDDS = 1:2; H <sub>2</sub> O <sub>2</sub> 50 mg/L; Fe(III) 0.1 mM for WWTP effluent and 0.2 mM for NF stream.	Two different types of water: (1) municipal WW effluent (direct treatment, D): DOC 23 mg/L; pH 7.5; (2) nanofiltration concentrate (NF concentrate, C): DOC 53 mg/L; pH 8.0;	<i>Vibrio fischeri</i> , <i>Daphnia magna</i>	Acute toxicity: Initial undiluted effluents were classified as slightly toxic for <i>V. fischeri</i> (Class II) and toxic for <i>D. magna</i> (Class III). All treated water samples were toxic for <i>V. fischeri</i> (Class III) and slightly toxic for <i>D. magna</i> (Class II), except NF concentrate (C + 0.4 mM of EDDS), which was highly toxic to <i>D. magna</i> (Class IV). Chronic toxicity: All initial and treated water samples (undiluted) exposed to <i>D. magna</i> for 21 day belonged to Class III. It should be noted that adaptation of resistant <i>D. magna</i> was observed when sufficient amount of DOC was available. The EDDS at studied concentrations increase the toxicity of water.
Solar photo-Fenton [68]	Pilot scale (CPC and raceway pond reactors (RPR)). <i>Optimal conditions:</i> pH set to 7, H <sub>2</sub> O <sub>2</sub> 50 mg/L and Fe <sup>2+</sup> 20 mg/L, 120 min.	Secondary effluent from municipal WWTP was used: DOC 18.9 ± 5.1 mg/L, COD 65.1 ± 1.4 mg/L, pH 7.7 ± 0.2	<i>Vibrio fischeri</i> , <i>Daphnia magna</i> and <i>Tetrahymena thermophila</i> .	Chronic toxicity for <i>T. thermophila</i> decreased after photo-Fenton treatment leading to slight growth stimulation. No acute toxicity was produced by secondary effluent before and after treatment for <i>D. magna</i> . Significant stimulation of <i>V. fischeri</i> growth was observed in secondary effluent before treatment, which decreased after treatment.
Solar photo-Fenton [14]	Pilot scale (CPC reactors). Photo- <i>Optimal conditions:</i> H <sub>2</sub> O <sub>2</sub> 66 mM, Fe <sup>2+</sup> 20 mg/L	Industrial pharmaceutical WW. DOC 775 mg/L, COD 3420 mg/L, pH 3.98	<i>Vibrio fischeri</i> , <i>Daphnia magna</i>	The toxicity of WW increased during the treatment followed by slight decrease. <i>D. magna</i> died in all wastewater samples after 24h of exposure.
Solar photo-Fenton [12]	Pilot plant (CPC reactors). <i>Optimal conditions:</i> for SE: Fe <sup>2+</sup> 5mg/L, H <sub>2</sub> O <sub>2</sub> 50 mg/L + 50 mg/L and t <sub>30w</sub> 336 min; for RE: Fe <sup>2+</sup> 5mg/L, H <sub>2</sub> O <sub>2</sub> 50 mg/L and t <sub>30w</sub> 276 min	Simulated WW (SE) and real municipal WW effluent (RE). The TOC of RE was 55 mg/L, pH 8.	<i>Vibrio fischeri</i>	SE: During photo-Fenton toxicity increased reaching EC <sub>50</sub> value (60 min) and disappearing in the end of the experiment (336 min). RE: During photo-Fenton, toxicity was increasing. The EC <sub>50</sub> value was reached after (25 min) and further increased during the treatment.

Table 3. Cont.

AOP Process	Experimental Conditions	Type of the Water	Toxicity Assessment	Main Outcomes
<i>Solar Photo-Fenton</i>				
Solar photo-Fenton [15]	Semi-pilot scale (CPC plant) <i>Optimal conditions:</i> 20 mg/L of Fe <sup>2+</sup> , H <sub>2</sub> O <sub>2</sub> 500 mg/L and pH 2.8.	Textile WW. DOC 92.4 ± 46 mg/L, COD 300 ± 99 mg/L, pH 6.9 ± 0.2	<i>Aliivibrio fischeri</i>	The EC <sub>50</sub> of initial WW was 30.3% (3 acute toxic units). After treatment (from 180 min) the value of toxic units decreased till 1 (non-toxic). After 90 min, toxicity started to increase (7.5 a. T.U. at 150 min).
Solar photo-Fenton [81]	Pilot scale (CPC plant). <i>Optimal conditions:</i> Fe <sup>2+</sup> 5 mg/L, H <sub>2</sub> O <sub>2</sub> concentration 75 mg/L,	Municipal WW effluent. DOC 7.45 mg/L, COD 26 mg/L, pH 6.8, Fe <sup>2+</sup> 0.29 mg/L	<i>Daphnia magna</i> and Phytotoxicity test ( <i>Sorghum saccharatum</i> , <i>Lepidium sativum</i> , <i>sinapis alba</i> ).	Seed germination inhibition was eliminated at the end of the treatment for all plants. Root and shoot inhibition was decreasing during the treatment. No toxic effect was observed for <i>D. magna</i> after 24 h of exposure to untreated effluent. During photo-Fenton treatment, the toxicity drastically increased reaching peak at 120 min. After 300 min of contact time, the toxicity effect for <i>D. magna</i> was lower than that in untreated wastewater effluent.
Solar photo-Fenton [13]	Pilot scale (RPR). UV 26 W/m <sup>2</sup> . <i>Optimal conditions:</i> 50 mg/L of H <sub>2</sub> O <sub>2</sub> ; 20 mg/L of iron x 3 times during experiment; pH 6.5	Municipal secondary WW effluent (filtered by 20 µm). DOC 20.6 mg/L, pH 7.6,	<i>Tetrahymena thermophyla</i> , <i>Daphnia magna</i> , <i>Lactuca sativa</i> (phytotoxicity); <i>Spirodela polyrrhiza</i> (phytotoxicity); <i>Vibrio fischeri</i>	The <i>T. thermophyla</i> was the most sensitive species, followed by <i>D. magna</i> and <i>L. Sativa</i> for initial wastewater. After 90 min of the treatment, 5% of immobilization of <i>D. magna</i> was observed. No toxic effect was observed for <i>T. thermophyla</i> during and after photo-Fenton process. For <i>L. Sativa</i> statistically significant inhibition of root elongation was observed after 20 min and 90 min of. The <i>V. fischeri</i> was not sensitive to initial and treated wastewater effluent.
Solar photo-Fenton [98]	Pilot scale. <i>Optimal conditions:</i> Fe <sup>2+</sup> 5 mg/L, H <sub>2</sub> O <sub>2</sub> 60 mg/L, pH 2.8, (photo-Fenton). TiO <sub>2</sub> 20 mg/L (photocatalysis)	Real municipal WW effluents. DOC 13–23 mg/L; COD 32–63 mg/L	<i>Vibrio fischeri</i>	No significant changes in toxicity of wastewater after treatment were detected.

Table 3. Cont.

AOP Process	Experimental Conditions	Type of the Water	Toxicity Assessment	Main Outcomes
<i>Combination of Photo-Fenton with other treatment processes</i>				
UV/H <sub>2</sub> O <sub>2</sub> /RWW + CWPO [57]	Laboratory scale (MP, 150W, 5.7 W <sub>UVC</sub> ). <u>Optimal conditions:</u> 320 mg/L of H <sub>2</sub> O <sub>2</sub> , UVC dose 7.51 Ws/cm <sup>2</sup> and 3.5 min of GAC.	Synthetic industrial WW prepared using matrix of urban WW effluent. TOC 40 mg/L; COD 150 mg/L	<i>Paracentrotus lividus</i> (embryo-larvae development, fertilization); <i>Vibrio fischeri</i>	<i>P. lividus</i> embryo-larvae development was the most sensitive test. The H <sub>2</sub> O <sub>2</sub> /UVC/RWW treatment increased the toxicity of initial water for both species. The toxicity drastically decreased after CWPO.
UV/H <sub>2</sub> O <sub>2</sub> /RWW + CWPO [44]	Laboratory scale (LP lamp, 2 W <sub>UVC</sub> ). <u>Optimal conditions:</u> 200 mg/L of H <sub>2</sub> O <sub>2</sub> , UVC dose 8.8 Ws/cm <sup>2</sup> and 2.3 min of GAC	Synthetic industrial WW based on matrix of urban WW. TOC 40 mg/L; COD 146 mg/L; pH 7.14	<i>Sparus aurata larvae</i> and <i>Vibrio fischeri</i>	The most sensitive specie was <i>Sparus aurata larvae</i> . The water after H <sub>2</sub> O <sub>2</sub> /UVC/RWW treatment was more toxic than final effluent (after CWPO step).
UV/H <sub>2</sub> O <sub>2</sub> /RWW + CWPO [43]	Laboratory scale (LP lamp, 2 W <sub>UVC</sub> and MP, 5.7 W <sub>UVC</sub> ). <u>Optimal conditions:</u> LP: 280 mg/L of H <sub>2</sub> O <sub>2</sub> , UVC dose 5.28 Ws/cm <sup>2</sup> and 6 min of GAC; MP: 175 mg/L of H <sub>2</sub> O <sub>2</sub> , UVC dose 6.57 Ws/cm <sup>2</sup> and 3.5 min of GAC	Industrial WW effluent from refinery company. TOC 35 mg/L; COD 128 mg/L; pH 7.14	<i>Paracentrotus lividus</i> (embryo-larvae development and fertilization) and <i>Vibrio fischeri</i>	The ranking of water toxicity from more to less toxic for <i>V. fischeri</i> was: effluent of H <sub>2</sub> O <sub>2</sub> /UVC (IV, TU) > Initial water (II, TU) > total effluent (0, TU). <i>P. lividus</i> fertilization test also showed same order of water toxicity. During H <sub>2</sub> O <sub>2</sub> /UVC/RWW process the toxicity of water increased 400 times in comparison with the initial wastewater. <i>P. lividus</i> embryo-larvae development was the most sensitive test. In this case, the toxicity ranking (starting from more toxic) was as follows: initial wastewater > H <sub>2</sub> O <sub>2</sub> /UVC/RWW effluent > final effluent.
UV/H <sub>2</sub> O <sub>2</sub> /RWW + CWPO [46]	Laboratory scale (LP lamp, 2 W <sub>UVC</sub> ). <u>Optimal conditions:</u> 50 mg/L of H <sub>2</sub> O <sub>2</sub> , UVC dose 6.00 Ws/cm <sup>2</sup> and 5 min of GAC	Different urban WW effluents: (D1) urban, (D2) Urban + industrial (D3) Urban + hospital. BOD <sub>5</sub> 10–13.2 mg/L; COD 75–83 mg/L; pH 7.42–8	<i>Paracentrotus lividus</i> (embryo-larvae development, fertilization), <i>Vibrio fischeri</i> and <i>Isochrysis galbana</i> , <i>Sparus aurata larvae</i> ,	The most sensitive endpoints were sea urchin larval development (D1 and D2) and mortality of fish larvae (3) for WWTP effluents. The PT-Value summarize that MBT treatment reduce the toxicity from highly toxic (pT index III and V) to slightly toxic (I and II).

Table 3. Cont.

AOP Process	Experimental Conditions	Type of the Water	Toxicity Assessment	Main Outcomes
<i>Combination of Photo-Fenton with other treatment processes</i>				
UV/H <sub>2</sub> O <sub>2</sub> /RWW + CWPO [8]	Laboratory scale (LP lamp, 2 W <sub>UVC</sub> ) <u>Optimal conditions</u> : The TOC/H <sub>2</sub> O <sub>2</sub> optimal ratio 5, UVC dose 6.00 Ws/cm <sup>2</sup> and 5 min of GAC.	WW effluents (1) urban (W1), (2) urban + hospital (W2), (3) urban + industrial (W3). COD 75–85 mg/L; pH 7.42–8	Different algae species (primary producer), <i>Daphnia</i> (invertebrate) and fish (vertebrate)	Toxicity drastically decrease after MBT treatment, reaching negligible risk (RQ < 0.01). Algae were the most sensitive species among tested. After MBT negligible risk was obtained for all tested effluent.
UV/H <sub>2</sub> O <sub>2</sub> /RWW + BAC [99]	Laboratory scale (LP lamp, irradiation 12.89 mJ/cm <sup>2</sup> ). <u>Optimal conditions</u> : 4 mM of H <sub>2</sub> O <sub>2</sub>	Reverse osmosis concentrated (ROC), DOC 44.6 ± 5.8 mg/L; COD 200 ± 27 mg/L; pH 7.8–8.4	<i>Vibrio fischeri</i>	It was observed that before and after treatment steps, ROC did not demonstrate toxic effect for <i>V. fischeri</i> . It was not specified if residual H <sub>2</sub> O <sub>2</sub> was eliminated from water samples prior toxicity assessment.
UV/H <sub>2</sub> O <sub>2</sub> /RWW + BAC [79]	Laboratory scale (LP lamp, 8.91 mJ/cm <sup>2</sup> ). <u>Optimal conditions</u> UVC dose 16.10 <sup>3</sup> mJ/cm <sup>2</sup> , H <sub>2</sub> O <sub>2</sub> 3mM (H <sub>2</sub> O <sub>2</sub> /UVC)	Reverse osmosis concentrate (ROC), DOC 37 mg/L; COD 105 mg/L; pH 7.7	<i>Vibrio fischeri</i>	<i>V. fischeri</i> test showed that initial ROC was not toxic. However, after the UVC/H <sub>2</sub> O <sub>2</sub> /RWW treatment the toxicity of water increased (EC <sub>50</sub> : 13%). After final BAC step no toxicity was observed.
<i>Homogeneous and heterogeneous electro-Fenton</i>				
Electro-Fenton process [89]	<u>Optimal conditions</u> : elapsed time 137 min, current 1.10 A, ferrous sulfate 0.55 mM.	Textile WW, pH 3, BOD 196 mg/L, COD 1156 mg/L	<i>Aploczeilus panclax</i>	The mortality reached 100% when organisms were exposed to untreated wastewater during 1 min. After applied treated no mortality was observed after 96 h.
Heterogeneous electro-Fenton process [92]	<u>Optimal conditions</u> : graphite anode and Fe-zeolite Y catalyst at neutral pH. Current density was 10 A/m <sup>2</sup> and cathodic potential −0.7 V	Coking wastewater effluent. pH 7.2, COD 225 mg/L, TOC 84 mg/L	<i>Vibrio qinghaiensis</i> sp. Nov.-Q67	The toxicity of effluent was decreased by 50–60% after applied treatment as compared to untreated wastewater.



Table 3. Cont.

AOP Process	Experimental Conditions	Type of the Water	Toxicity Assessment	Main Outcomes
<i>Homogeneous and heterogeneous electro-Fenton</i>				
Fenton and electro-Fenton [90]	Effluent was subjected different treatments such as Fenton, electro-Fenton and coagulation.	Effluent of coking WW (after treatment in anaerobic, anoxic and oxic reactors). COD 160 ± 27 mg/L, TOC 50 ± 10 mg/L, pH 6.5–7.5	embryos and larvae of <i>Oryzias latipes</i> (Japanese medaka)	The acute and chronic toxicity was significantly increased after Fenton and electro-Fenton treatment. The acute and chronic toxicity of MBR and coagulation effluents were lower. Endocrine disruption effect was not detected for MBR, Fenton and electro-Fenton effluents.
Heterogeneous electro-Fenton [91]	<u>Optimal conditions:</u> CPE 2.0 g/L, aeration rate 5 L/min, current density 10 mA/cm <sup>2</sup>	WW from typical azo dye WW plant. COD 270 ± 30 mg/L	<i>Daphnia magna</i>	Residual H <sub>2</sub> O <sub>2</sub> was removed from water samples by heating during 1 h. Acute toxicity significantly reduced during applied treatment.
<i>Galvanic Fenton</i>				
Galvanic Fenton [97]	<u>Optimal conditions:</u> pH 2.8, H <sub>2</sub> O <sub>2</sub> /Fe <sup>2+</sup> ratio 19:1 (H <sub>2</sub> O <sub>2</sub> 7840 mg/L and Fe <sup>2+</sup> 408 mg/L).	Industrial WW. pH 7.95, total COD 5264 mg/L, TOC 1744 mg/L, iron 1.48 mg/L	<i>Lactuca sativa</i>	The EC <sub>50</sub> value reported for raw WW was 64.05%, whereas this value after galvanic-Fenton was 65.07%. The residual H <sub>2</sub> O <sub>2</sub> after galvanic-Fenton was 40 mg/L.

#### 4. Conclusions

In this article, the feasibility of real municipal and industrial wastewater detoxification by Fenton-based advanced oxidation processes was reviewed. Based on the analyzed literature, it can be concluded that in general the application of Fenton-based AOPs for wastewater detoxification is feasible. However, it is of high importance to assess the toxicity of water on the course of AOP treatment because in the majority of cases the generation of more toxic than parental compounds occurs. It is important to mention that maximum process efficiency (in terms of COD and/or TOC removal) does not coincide with maximum detoxification.

Toxicity bioassays were demonstrated to be an efficient tool for the assessment of wastewater detoxification. Based on the reviewed studies, it can be suggested that standard bioassays and most widely used for municipal wastewater (*Vibrio fischeri*, *Daphnia magna*) are not always sensitive for the pollutants present in municipal wastewater (not spiked with pollutants or EDDS). Moreover, the use of single toxicity bioassay might not be sufficient for the evaluation of wastewater toxicity after the application of Fenton-based AOPs due to the large variation of sensitivity of different species. Hence, a battery of bioassays is more suitable for the estimation of treated wastewater toxicity. The use of biologically representative, widespread and indigenous species is among the main requirements for an adequate battery of bioassays leading to a realistic evaluation of the possible environmental risks of treated wastewater effluents. In recent years, the batteries of bioassays for the assessment of urban wastewater effluents discharged to the marine aquatic environment after pot-treatment by Fenton-based AOPs were developed. It is expected that future studies devoted to the detoxification of wastewater by Fenton-based AOPs will implement batteries of bioassays (including biosensors) for a more comprehensive evaluation of water toxicity. Additionally, from the reviewed literature on wastewater detoxification by photo-Fenton, it can be expected that future research will be conducted using a more realistic approach regarding wastewater pre-treatment avoiding when possible, the acidification of wastewater prior treatment, addition of excessive amount of reagents, removing residual H<sub>2</sub>O<sub>2</sub>, etc. This might enable not only a decrease of the operation and maintenance (O&M) costs but also the possible risks for organisms in the aquatic environment.

From the O&M cost point of view, the lowest O&M cost estimation reported for the detoxification of wastewater effluent in the scope of this review was €0.44 m<sup>-3</sup> (personnel cost was not included), whereas the average O&M cost of conventional treatment of municipal wastewater in WWTP with a flow of approx. 10,000 m<sup>3</sup> day<sup>-1</sup> is approx. €0.5–0.6 m<sup>-3</sup> (including personnel cost; southern Spain). Interestingly, it was reported that the O&M cost of wastewater detoxification by photo-Fenton can be significantly decreased when preliminary microfiltration, coagulation aiming at more economically feasible removal of organic matter (suspended and/or colloidal) and increasing of water transmittance is applied. Moreover, application of additional polishing step such as catalytic wet peroxide oxidation (CWPO) after photo-Fenton can remove residual hydrogen peroxide, reduce the toxicity and the cost of the treatment. The total cost (investment and maintenance costs for the period of 5 years) estimation of a full scale unit (150 m<sup>3</sup> day<sup>-1</sup>, equivalent to 1000 pe) for treatment of secondary urban wastewater effluent by solar photo-Fenton (removal of antibiotics and toxicity reduction) was reported to be €0.85 m<sup>-3</sup>.

**Author Contributions:** J.J.R.-M., and I.L., did the literature search, elaborated discussion and wrote the paper, M.M. and M.S., elaborated discussion. All authors have read and agreed to the published version of the manuscript.

**Funding:** This research was funded by ACADEMY OF FINLAND within the project “Combination of Advanced Oxidation Processes and Photobiotreatment for Sustainable Resource Recovery and Wastewater Reuse” as well as PoDoCo and MAA- JA VESITEKNIIKAN TUKI within the project “Application of Advanced Oxidation Processes (AOPs) for refinery wastewater with high phenol concentrations”. The APC was funded by the project “Combination of Advanced Oxidation Processes and Photobiotreatment for Sustainable Resource Recovery and Wastewater Reuse” (Academy of Finland).

**Conflicts of Interest:** The authors declare no conflict of interest.

## References

1. Venkatesan, A.K.; Halden, R.U. Wastewater Treatment Plants as Chemical Observatories to Forecast Ecological and Human Health Risks of Manmade Chemicals. *Sci. Rep.* **2014**, *4*, 3731. [CrossRef]
2. Stuart, M.; Lapworth, D.J.; Crane, E.; Hart, A. Review of risk from potential emerging contaminants in UK groundwater. *Sci. Total Environ.* **2012**, *416*, 1–21. [CrossRef]
3. Gagné, F.; Mélanie, D.; Marlène, F.; Michel, F. Effects of a municipal effluent on the freshwater mussel *Elliptio complanata* following challenge with *Vibrio anguillarum*. *J. Environ. Sci.* **2015**, *37*, 91–99.
4. Quinn, B.; Schmidt, W.; O'Rourke, K.; Hernan, R. Effects of the pharmaceuticals gemfibrozil and diclofenac on biomarker expression in the zebra mussel (*Dreissena polymorpha*) and their comparison with standardised toxicity tests. *Chemosphere* **2011**, *84*, 657–663. [CrossRef]
5. Quinn, B.; Gagné, F.; Blaise, C. Evaluation of the acute, chronic and teratogenic effects of a mixture of eleven pharmaceuticals on the cnidarian, *Hydra attenuata*. *Sci. Total Environ.* **2009**, *407*, 1072–1079. [CrossRef]
6. Gracia-Lor, E.; Sancho, J.V.; Serrano, R.; Hernandez, F. Occurrence and removal of pharmaceuticals in wastewater treatment plants at the Spanish Mediterranean area of Valencia. *Chemosphere* **2012**, *87*, 453–462. [CrossRef]
7. European Commission. *Seventh Report on the Implementation of the Urban Waste Water Treatment Directive (91/271/EEC)*; European Commission: Brussels, Belgium, 2013.
8. Díaz-Garduño, B.; Pintado-Herrera, M.; Biel-Maeso, M.; Rueda-Marquez, J.J.; Lara-Martín, P.A.; Perales, J.A.; Manzano, M.; Garrido-Pérez, C.; Martín-Díaz, M.L.; Garrido-Pérez, M.D.C. Environmental risk assessment of effluents as a whole emerging contaminant: Efficiency of alternative tertiary treatments for wastewater depuration. *Water Res.* **2017**, *119*, 136–149. [CrossRef]
9. Andreatti, R. Advanced oxidation processes (AOP) for water purification and recovery. *Catal. Today* **1999**, *53*, 51–59. [CrossRef]
10. Ferrer, I.; Writer, J.; Keen, O.; Lester, Y.; Padilla-Sánchez, J.A.; Fernández-Ramos, C.; Thurman, E.M. *LC-TOF-MS for the Identification of Environmental Metabolites and Degradation Products*; Elsevier: Amsterdam, The Netherlands, 2016; pp. 231–261.
11. Vela, N.; Calín, M.; Yáñez-Gascón, M.J.; Garrido, I.; Pérez-Lucas, G.; Fenoll, J.; Navarro, S. *Photocatalytic oxidation* of six pesticides listed as endocrine disruptor chemicals from wastewater using two different TiO<sub>2</sub> samples at pilot plant scale under sunlight irradiation. *J. Photochem. Photobiol. A Chem.* **2018**, *353*, 271–278. [CrossRef]
12. Klammerth, N.; Rizzo, L.; Malato, S.; Maldonado, M.I.; Agüera, A.; Fernández-Alba, A. Degradation of fifteen emerging contaminants at  $\mu\text{gL}^{-1}$  initial concentrations by mild solar photo-Fenton in MWTP effluents. *Water Res.* **2010**, *44*, 545–554. [CrossRef]
13. Freitas, A.M.; Rivas, G.; Campos-Mañas, M.C.; López, J.L.C.; Agüera, A.; Pérez, J.A.S. Ecotoxicity evaluation of a WWTP effluent treated by solar photo-Fenton at neutral pH in a raceway pond reactor. *Environ. Sci. Pollut. Res.* **2016**, *24*, 1093–1104. [CrossRef]
14. Sirtori, C.; Zapata, A.; Oller, I.; Gernjak, W.; Agüera, A.; Malato, S. Decontamination industrial pharmaceutical wastewater by combining solar photo-Fenton and biological treatment. *Water Res.* **2009**, *43*, 661–668. [CrossRef]
15. Starling, M.C.V.M.; Dos Santos, P.H.R.; De Souza, F.A.R.; Oliveira, S.C.; Leão, M.; Amorim, C. Application of solar photo-Fenton toward toxicity removal and textile wastewater reuse. *Environ. Sci. Pollut. Res.* **2016**, *24*, 12515–12528. [CrossRef]
16. European Commission. *Reference Document on Best Available Techniques (BREF) for the Textile Industry; Integrated Pollution Prevention and Control (IPPC)*; Brussels, Belgium, 2003.
17. Heras, S.F. *Comercialización E Implementación De Las Tecnologías De Oxidación Avanzada (Commercialization and Implementation of Advanced Oxidation Technologies)*; Universidad De Cantabria: Cantabria, Spain, 2016.
18. Rizzo, L. Bioassays as a tool for evaluating advanced oxidation processes in water and wastewater treatment. *Water Res.* **2011**, *45*, 4311–4340. [CrossRef]
19. Fenton, H.J.H. LXXIII.—Oxidation of tartaric acid in presence of iron. *J. Chem. Soc. Trans.* **1894**, *65*, 899. [CrossRef]
20. Barbusiński, K. Fenton reaction-controversy concerning the chemistry. *Ecol. Chem. Eng.* **2009**, *16*, 347–358.

21. Haber, F.; Weiss, J. The catalytic decomposition of hydrogen peroxide by iron salts. *Proc. R. Soc. Lond. Ser. A Math. Phys. Sci.* **1934**, *147*, 332–351.
22. Barb, W.G.; Baxendale, J.; George, P.; Hargrave, K.R. Reactions of Ferrous and Ferric Ions with Hydrogen Peroxide. *Nature* **1949**, *163*, 692–694. [CrossRef]
23. Barb, W.G.; Baxendale, J.; George, P.; Hargrave, K.R. Reactions of Ferrous and Ferric Ions with Hydrogen Peroxide. Part I—The ferrous ion reaction. *Trans. Faraday Soc.* **1951**, *47*, 462–500. [CrossRef]
24. Barb, W.G.; Baxendale, J.; George, P.; Hargrave, K.R. Reactions of ferrous and ferric ions with hydrogen peroxide. Part II.—The ferric ion reaction. *Trans. Faraday Soc.* **1951**, *47*, 591–616. [CrossRef]
25. Pignatello, J.J.; Oliveros, E.; Mackay, A. Advanced Oxidation Processes for Organic Contaminant Destruction Based on the Fenton Reaction and Related Chemistry. *Crit. Rev. Environ. Sci. Technol.* **2006**, *36*, 1–84. [CrossRef]
26. Bray, W.C.; Gorin, M.H. Ferrylion, a compound of tetravalent iron. *J. Am. Chem. Soc.* **1932**, *54*, 2124–2125. [CrossRef]
27. Mota, A.; Albuquerque, L.; Beltrame, L.C.; Chiavone-Filho, O.; Machulek, A., Jr.; Nascimento, C. Advanced oxidation processes and their application in the petroleum industry: A review. *Braz. J. Pet. Gas* **2009**, *2*, 3.
28. Oturan, M.A.; Aaron, J.-J. Advanced Oxidation Processes in Water/Wastewater Treatment: Principles and Applications. A Review. *Crit. Rev. Environ. Sci. Technol.* **2014**, *44*, 2577–2641. [CrossRef]
29. Pignatello, J.J. Dark and photoassisted iron(3+)-catalyzed degradation of chlorophenoxy herbicides by hydrogen peroxide. *Environ. Sci. Technol.* **1992**, *26*, 944–951. [CrossRef]
30. Pouran, S.R.; Aziz, A.A.; Daud, W.M.A.W. Review on the main advances in photo-Fenton oxidation system for recalcitrant wastewaters. *J. Ind. Eng. Chem.* **2015**, *21*, 53–69. [CrossRef]
31. Affam, A.C.; Kutty, S.R.M.; Chaudhuri, M. Solar photo-Fenton induced degradation of combined chlorpyrifos, cypermethrin and chlorothalonil pesticides in aqueous solution. *World Acad. Sci. Eng. Technol.* **2012**, *6*, 2.
32. Elmolla, E.S.; Chaudhuri, M. Effect of Photo-Fenton Operating Conditions on the Performance of Photo-Fenton-SBR Process for Recalcitrant Wastewater Treatment. *J. Appl. Sci.* **2010**, *10*, 3236–3242. [CrossRef]
33. Elmolla, E.S.; Chaudhuri, M. Photo-Fenton treatment of antibiotic wastewater. *Nat. Environ. Pollut. Technol.* **2010**, *9*, 365–370.
34. Clarizia, L.; Russo, D.; Di Somma, I.; Marotta, R.; Andreozzi, R. Homogeneous photo-Fenton processes at near neutral pH: A review. *Appl. Catal. B Environ.* **2017**, *209*, 358–371. [CrossRef]
35. Zuo, Y.; Hoigne, J. Formation of hydrogen peroxide and depletion of oxalic acid in atmospheric water by photolysis of iron(III)-oxalato complexes. *Environ. Sci. Technol.* **1992**, *26*, 1014–1022. [CrossRef]
36. Ndounla, J.; Spuhler, D.; Kenfack, S.; Wéthé, J.; Pulgarin, C. Inactivation by solar photo-Fenton in pet bottles of wild enteric bacteria of natural well water: Absence of re-growth after one week of subsequent storage. *Appl. Catal. B Environ.* **2013**, *129*, 309–317. [CrossRef]
37. Ndounla, J.; Pulgarin, C. Evaluation of the efficiency of the photo Fenton disinfection of natural drinking water source during the rainy season in the Sahelian region. *Sci. Total. Environ.* **2014**, *493*, 229–238. [CrossRef] [PubMed]
38. Castrén, J.; Korhonen, R.; Kuokkanen, A.; Lallukka, S.; Lehtinen, E.; Urho, A. *Jätevedenpuhdistus Pääkaupunkiseudulla 2015—Viikinmäen Ja Suomenojan Puhdistamot*; Helsinki Region Environmental Services Authority: Helsinki, Finland, 2016.
39. Castrén, J.; Kuokkanen, A.; Lallukka, S.; Lehtinen, E.; Blomberg, K. *Jätevedenpuhdistus Pääkaupunkiseudulla 2016—Viikinmäen Ja Suomenojan Puhdistamot*; Helsinki Region Environmental Services Authority: Helsinki, Finland, 2017; p. 72.
40. Graan, M.; Kuokkanen, A.; Lallukka, S.; Lehtinen, E.; Rossi, L.; Urho, A. *Jätevedenpuhdistus Pääkaupunkiseudulla 2017—Viikinmäen Ja Suomenojan Puhdistamot*; Helsinki Region Environmental Services Authority: Helsinki, Finland, 2018; p. 72.
41. Helsinki Region Environmental Services Authority. *Jätevedenpuhdistus Pääkaupunkiseudulla 2018—Viikinmäen ja Suomenojan Jätevedenpuhdistamot*; Helsinki Region Environmental Services Authority: Helsinki, Finland, 2019; p. 23.
42. Filho, B.; Da Silva, V.M.; Silva, J.D.O.; Machado, A.E.H.; Trovó, A. Coupling coagulation, flocculation and decantation with photo-Fenton process for treatment of industrial wastewater containing fipronil: Biodegradability and toxicity assessment. *J. Environ. Manag.* **2016**, *174*, 71–78. [CrossRef]

43. Rueda-Marquez, J.J.; Levchuk, I.; Salcedo, I.; Merino, A.A.; Manzano, M. Post-treatment of refinery wastewater effluent using a combination of AOPs (H<sub>2</sub>O<sub>2</sub> photolysis and catalytic wet peroxide oxidation) for possible water reuse. Comparison of low and medium pressure lamp performance. *Water Res.* **2016**, *91*, 86–96. [CrossRef]
44. Rueda-Marquez, J.J.; Sillanpää, M.; Pocostales, P.; Acevedo, A.; Manzano, M. Post-treatment of biologically treated wastewater containing organic contaminants using a sequence of H<sub>2</sub>O<sub>2</sub> based advanced oxidation processes: Photolysis and catalytic wet oxidation. *Water Res.* **2015**, *71*, 85–96. [CrossRef]
45. Kajitvichyanukul, P.; Suntronvipart, N. Evaluation of biodegradability and oxidation degree of hospital wastewater using photo-Fenton process as the pretreatment method. *J. Hazard. Mater.* **2006**, *138*, 384–391. [CrossRef]
46. Díaz-Garduño, B.; Rueda-Marquez, J.J.; Quiñones, M.A.M.; Garrido-Pérez, M.D.C.; Martín-Díaz, M.L. Are combined AOPs effective for toxicity reduction in receiving marine environment? Suitability of battery of bioassays for wastewater treatment plant (WWTP) effluent as an ecotoxicological assessment. *Mar. Environ. Res.* **2016**, *114*, 1–11. [CrossRef]
47. Blunt, B.; Singh, A.; Wu, L.; El-Din, M.G.; Belosevic, M.; Tierney, K.B. Reuse water: Exposure duration, seasonality and treatment affect tissue responses in a model fish. *Sci. Total. Environ.* **2017**, *607*, 1117–1125. [CrossRef]
48. Singh, A.; Havixbeck, J.J.; Smith, M.K.; Shu, Z.; Tierney, K.B.; Barreda, D.R.; El-Din, M.G.; Belosevic, M. UV and hydrogen peroxide treatment restores changes in innate immunity caused by exposure of fish to reuse water. *Water Res.* **2015**, *71*, 257–273. [CrossRef]
49. Shu, Z.; Singh, A.; Klammerth, N.; Mcphedran, K.; Bolton, J.R.; Belosevic, M.; El-Din, M.G. Pilot-scale UV/H<sub>2</sub>O<sub>2</sub> advanced oxidation process for municipal reuse water: Assessing micropollutant degradation and estrogenic impacts on goldfish (*Carassius auratus* L.). *Water Res.* **2016**, *101*, 157–166. [CrossRef]
50. Goettl, J.; Davies, P. Study of the Effects of Metallic Ions on Fish and Aquatic Organisms. *Water Pollution Studies Job Progress Report*, Federal Aid Project F-33-R-13. 1978; 6–40.
51. Sykora, J.; Smith, E.; Synak, M.; Shapiro, M. Some observations on spawning of brook trout (*Salvelinus Fontinalis*, mitchill) in lime neutralized iron hydroxide suspensions. *Water Res.* **1975**, *9*, 451–458. [CrossRef]
52. Cadmus, P.; Brinkman, S.F.; May, M.K. Chronic Toxicity of Ferric Iron for North American Aquatic Organisms: Derivation of a Chronic Water Quality Criterion Using Single Species and Mesocosm Data. *Arch. Environ. Contam. Toxicol.* **2018**, *74*, 605–615. [CrossRef]
53. Hazardous Materials. In *Quality Criteria for Water*; The US Environmental Protection Agency: Washington, DC, USA, 1976.
54. WEPA, Water Environment Partnership in Asia. Environmental Quality Standards for Water and Effluent Standard. Available online: <http://www.wepa-db.net/policies/law/laos/standards.htm> (accessed on 1 June 2019).
55. Boutet, C.; Chaisemartin, C. Propriétés toxiques spécifiques des sels métalliques chez *Austroptomobius pallipes pallipes* et *Orconectes limosus*. *CR Seances Soc. Biol. Fil.* **1973**, *167*, 1933–1938.
56. Brenner, F.J.; Cooper, W.L. Effect of suspended iron hydroxide on the hatchability and embryonic development of the coho salmon. *Ohio J. Sci.* **1978**, *78*, 34–38.
57. Rueda-Márquez, J.J.; Pintado-Herrera, M.G.; Martín-Díaz, M.L.; Acevedo-Merino, A.; Manzano, M.A. Combined AOPs for potential wastewater reuse or safe discharge based on multi-barrier treatment (microfiltration-H<sub>2</sub>O<sub>2</sub>/UV-catalytic wet peroxide oxidation). *Chem. Eng. J.* **2015**, *270*, 80–90. [CrossRef]
58. Drábková, M.; Matthijs, H.C.P.; Admiraal, W.; Marsalek, B. Selective effects of H<sub>2</sub>O<sub>2</sub> on cyanobacterial photosynthesis. *Photosynthetica* **2007**, *45*, 363–369. [CrossRef]
59. Georgi, A.; Kopinke, F.-D. Interaction of adsorption and catalytic reactions in water decontamination processes. *Appl. Catal. B Environ.* **2005**, *58*, 9–18. [CrossRef]
60. Oliveira, L.C.; Silva, C.N.; Yoshida, I.M.; Lago, R.M. The effect of H<sub>2</sub> treatment on the activity of activated carbon for the oxidation of organic contaminants in water and the H<sub>2</sub>O<sub>2</sub> decomposition. *Carbon* **2004**, *42*, 2279–2284. [CrossRef]
61. Lücking, F.; Köser, H.; Jank, M.; Ritter, A. Iron powder, graphite and activated carbon as catalysts for the oxidation of 4-chlorophenol with hydrogen peroxide in aqueous solution. *Water Res.* **1998**, *32*, 2607–2614. [CrossRef]

62. Rueda-Marquez, J.J.; Levchuk, I.; Sillanpää, M. Application of Catalytic Wet Peroxide Oxidation for Industrial and Urban Wastewater Treatment: A Review. *Catalysts* **2018**, *8*, 673. [CrossRef]
63. Schalk, S.; Adam, V.; Arnold, E.; Brieden, K.; Voronov, A.; Witzke, H. UV-lamps for disinfection and advanced oxidation-lamp types, technologies and applications. *IUVA News* **2005**, *8*, 32–37.
64. Heering, W. UV sources-basics, properties and applications. *IUVA News* **2004**, *6*, 7–13.
65. Hofman-Caris, R.C.; Harmsen, D.J.; Puijker, L.; Baken, K.; Wols, B.A.; Beerendonk, E.; Keltjens, L.L. Influence of process conditions and water quality on the formation of mutagenic byproducts in UV/H<sub>2</sub>O<sub>2</sub> processes. *Water Res.* **2015**, *74*, 191–202. [CrossRef]
66. Coulter, M.A. Minamata Convention on Mercury. *Int. Leg. Mater.* **2016**, *55*, 582. [CrossRef]
67. Mosteo, R.; Lopez, A.V.; Muzard, D.; Benitez, N.; Giannakis, S.; Pulgarin, C. Visible light plays a significant role during bacterial inactivation by the photo-fenton process, even at sub-critical light intensities. *Water Res.* **2020**, *174*, 115636. [CrossRef]
68. García, B.E.; Rivas, G.; Arzate, S.; Pérez, J.A.S. Wild bacteria inactivation in WWTP secondary effluents by solar photo-fenton at neutral pH in raceway pond reactors. *Catal. Today* **2018**, *313*, 72–78. [CrossRef]
69. Liu, K.; Roddick, F.A.; Fan, L. Impact of salinity and pH on the UVC/H<sub>2</sub>O<sub>2</sub> treatment of reverse osmosis concentrate produced from municipal wastewater reclamation. *Water Res.* **2012**, *46*, 3229–3239. [CrossRef]
70. Cuevas, S.M.; Oller, I.; Agüera, A.; Pérez, J.A.S.; Malato, S. Strategies for reducing cost by using solar photo-Fenton treatment combined with nanofiltration to remove microcontaminants in real municipal effluents: Toxicity and economic assessment. *Chem. Eng. J.* **2017**, *318*, 161–170. [CrossRef]
71. Galvez, J.B.; Fernández-Ibáñez, P.; Malato, S. Solar Photocatalytic Detoxification and Disinfection of Water: Recent Overview. *J. Sol. Energy Eng.* **2006**, *129*, 4–15. [CrossRef]
72. Ghosh, S.K.; Doctor, P.B.; Kulkarni, P.K. Toxicity of zinc in three microbial test systems. *Environ. Toxicol. Water Qual.* **1996**, *11*, 13–19. [CrossRef]
73. Nohava, M.; Vogel, W.R.; Gaugitsch, H. Evaluation of the luminescent bacteria bioassay for the estimation of the toxicological potential of effluent water samples—Comparison with data from chemical analyses. *Environ. Int.* **1995**, *21*, 33–37. [CrossRef]
74. Riisberg, M.; Bratlie, E.; Stenersen, J. Comparison of the response of bacterial luminescence and mitochondrial respiration to the effluent of an oil refinery. *Environ. Toxicol. Chem. A Int. J.* **1996**, *15*, 501–502. [CrossRef]
75. Backhaus, T.; Froehner, K.; Altenburger, R.; Grimme, L. Toxicity testing with *Vibrio fischeri*: A comparison between the long term (24 h) and the short term (30 min) bioassay. *Chemosphere* **1997**, *35*, 2925–2938. [CrossRef]
76. Froehner, K.; Backhaus, T.; Grimme, L. Bioassays with *Vibrio fischeri* for the assessment of delayed toxicity. *Chemosphere* **2000**, *40*, 821–828. [CrossRef]
77. Marugán, J.; Bru, D.; Pablos, C.; Catalá, M. Comparative evaluation of acute toxicity by *Vibrio fischeri* and fern spore based bioassays in the follow-up of toxic chemicals degradation by photocatalysis. *J. Hazard. Mater.* **2012**, *213*, 117–122. [CrossRef]
78. Hernando, D.; Fernandezalba, A.; Tauler, R.; Barceló, J. Toxicity assays applied to wastewater treatment. *Talanta* **2005**, *65*, 358–366. [CrossRef]
79. Umar, M.; Roddick, F.; Fan, L. Impact of coagulation as a pre-treatment for UVC/H<sub>2</sub>O<sub>2</sub>—biological activated carbon treatment of a municipal wastewater reverse osmosis concentrate. *Water Res.* **2016**, *88*, 12–19. [CrossRef]
80. Koivisto, S. Is *Daphnia magna* an ecologically representative zooplankton species in toxicity tests? *Environ. Pollut.* **1995**, *90*, 263–267. [CrossRef]
81. Michael, I.; Hapeshi, E.; Michael, C.; Varela, A.R.; Kyriakou, S.; Manaia, C.M.; Fatta-Kassinos, D. Solar photo-Fenton process on the abatement of antibiotics at a pilot scale: Degradation kinetics, ecotoxicity and phytotoxicity assessment and removal of antibiotic resistant enterococci. *Water Res.* **2012**, *46*, 5621–5634. [CrossRef]
82. Farré, M.; Barceló, D. Toxicity testing of wastewater and sewage sludge by biosensors, bioassays and chemical analysis. *TrAC Trends Anal. Chem.* **2003**, *22*, 299–310. [CrossRef]
83. Belalcázar-Saldarriaga, A.; Prato-Garcia, D.; Vasquez-Medrano, R. Photo-Fenton processes in raceway reactors: Technical, economic, and environmental implications during treatment of colored wastewaters. *J. Clean. Prod.* **2018**, *182*, 818–829. [CrossRef]

84. Soriano-Molina, P.; Plaza-Bolaños, P.; Lorenzo, A.; Agüera, A.; Sánchez, J.G.; Malato, S.; Pérez, J.A.S. Assessment of solar raceway pond reactors for removal of contaminants of emerging concern by photo-Fenton at circumneutral pH from very different municipal wastewater effluents. *Chem. Eng. J.* **2019**, *366*, 141–149. [CrossRef]
85. Pérez, J.A.S.; Román-Sánchez, I.M.; Carra, I.; Reina, A.C.; López, J.L.C.; Malato, S. Economic evaluation of a combined photo-Fenton/MBR process using pesticides as model pollutant. Factors affecting costs. *J. Hazard. Mater.* **2013**, *244*, 195–203. [CrossRef]
86. Rueda-Marquez, J.J.; Levchuk, I.; Uski, J.; Sillanpää, M.; Acevedo, A.; Manzano, M. Post-treatment of plywood mill effluent by Multi-Barrier Treatment: A pilot-scale study. *Chem. Eng. J.* **2016**, *283*, 21–28. [CrossRef]
87. Baresel, C.; Harding, M.; Junestedt, C. *Removal of Pharmaceutical Residues from Municipal Wastewater Using UV/H<sub>2</sub>O<sub>2</sub>*; IVL Swedish Environmental Research Institute Ltd.: Stockholm, Sweden, 2019.
88. Brillas, E.; Sirés, I.; Oturan, M.A. Electro-Fenton Process and Related Electrochemical Technologies Based on Fenton's Reaction Chemistry. *Chem. Rev.* **2009**, *109*, 6570–6631. [CrossRef]
89. Kaur, P.; Kushwaha, J.P.; Sangal, V.K. Transformation products and degradation pathway of textile industry wastewater pollutants in Electro-Fenton process. *Chemosphere* **2018**, *207*, 690–698. [CrossRef]
90. Zhu, X.; Chen, L.; Liu, R.; Liu, C.; Pan, Z. Biototoxicity evaluation of coking wastewater treated with different technologies using Japanese medaka (*Oryzias latipes*). *Environ. Sci. Process. Impacts* **2013**, *15*, 1391–1396. [CrossRef]
91. Zhuang, H.; Shan, S.; Guo, J.; Han, Y.; Fang, C. Waste rice straw and coal fly ash composite as a novel sustainable catalytic particle electrode for strengthening oxidation of azo dyes containing wastewater in electro-Fenton process. *Environ. Sci. Pollut. Res.* **2017**, *24*, 27136–27144. [CrossRef]
92. Li, H.; Li, Y.; Cao, H.; Li, X.; Zhang, Y. Advanced electro-Fenton degradation of biologically-treated coking wastewater using anthraquinone cathode and Fe-Y catalyst. *Water Sci. Technol.* **2011**, *64*, 63–69. [CrossRef]
93. Vlyssides, A.G.; Israilides, C.J. Detoxification of tannery waste liquors with an electrolysis system. *Environ. Pollut.* **1997**, *97*, 147–152. [CrossRef]
94. Vlyssides, A.G.; Loizidou, M.; Karlis, P.; Zorpas, A.A.; Papaioannou, D. Electrochemical oxidation of a textile dye wastewater using a Pt/Ti electrode. *J. Hazard. Mater.* **1999**, *70*, 41–52. [CrossRef]
95. Vlyssides, A.G.; Karlis, P.K.; Rori, N.; Zorpas, A.A. Electrochemical treatment in relation to pH of domestic wastewater using Ti/Pt electrodes. *J. Hazard. Mater.* **2002**, *95*, 215–226. [CrossRef]
96. Kushwaha, J.P.; Srivastava, V.C.; Mall, I.D. Organics removal from dairy wastewater by electrochemical treatment and residue disposal. *Sep. Purif. Technol.* **2010**, *76*, 198–205. [CrossRef]
97. Alcalá-Delgado, A.G.; Lugo-Lugo, V.; Linares-Hernández, I.; Miranda, V.M.; Fuentes-Rivas, R.M.; Ureña-Núñez, F. Industrial wastewater treated by galvanic, galvanic Fenton, and hydrogen peroxide systems. *J. Water Process. Eng.* **2018**, *22*, 1–12. [CrossRef]
98. Prieto-Rodríguez, L.; Oller, I.; Klammerth, N.; Agüera, A.; Rodríguez, E.M.; Malato, S.; Alberola, I.O. Application of solar AOPs and ozonation for elimination of micropollutants in municipal wastewater treatment plant effluents. *Water Res.* **2013**, *47*, 1521–1528. [CrossRef]
99. Lu, J.; Fan, L.; Roddick, F.A. Potential of BAC combined with UVC/H<sub>2</sub>O<sub>2</sub> for reducing organic matter from highly saline reverse osmosis concentrate produced from municipal wastewater reclamation. *Chemosphere* **2013**, *93*, 683–688. [CrossRef]



© 2020 by the authors. Licensee MDPI, Basel, Switzerland. This article is an open access article distributed under the terms and conditions of the Creative Commons Attribution (CC BY) license (<http://creativecommons.org/licenses/by/4.0/>).

Review

# A Review on the Treatment of Petroleum Refinery Wastewater Using Advanced Oxidation Processes

Wamda Faisal Elmobarak <sup>1</sup>, Bassim H. Hameed <sup>1</sup>, Fares Almomani <sup>1,\*</sup>  and Ahmad Zuhairi Abdullah <sup>2</sup>

<sup>1</sup> Department of Chemical Engineering, Qatar University, Doha P.O. Box 2713, Qatar; we1609816@student.qu.edu.qa (W.F.E.); b.hammadi@qu.edu.qa (B.H.H.)

<sup>2</sup> School of Chemical Engineering, Engineering Campus, University Sains Malaysia, Nibong Tebal 14300, Pulau Pinang, Malaysia; chzuhairi@usm.my

\* Correspondence: falmomani@qu.edu.qa; Tel.: +974-4403-4140

**Abstract:** The petroleum industry is one of the most rapidly developing industries and is projected to grow faster in the coming years. The recent environmental activities and global requirements for cleaner methods are pushing the petroleum refining industries for the use of green techniques and industrial wastewater treatment. Petroleum industry wastewater contains a broad diversity of contaminants such as petroleum hydrocarbons, oil and grease, phenol, ammonia, sulfides, and other organic composites, etc. All of these compounds within discharged water from the petroleum industry exist in an extremely complicated form, which is unsafe for the environment. Conventional treatment systems treating refinery wastewater have shown major drawbacks including low efficiency, high capital and operating cost, and sensitivity to low biodegradability and toxicity. The advanced oxidation process (AOP) method is one of the methods applied for petroleum refinery wastewater treatment. The objective of this work is to review the current application of AOP technologies in the treatment of petroleum industry wastewater. The petroleum wastewater treatment using AOP methods includes Fenton and photo-Fenton, H<sub>2</sub>O<sub>2</sub>/UV, photocatalysis, ozonation, and biological processes. This review reports that the treatment efficiencies strongly depend on the chosen AOP type, the physical and chemical properties of target contaminants, and the operating conditions. It is reported that other mechanisms, as well as hydroxyl radical oxidation, might occur throughout the AOP treatment and donate to the decrease in target contaminants. Mainly, the recent advances in the AOP treatment of petroleum wastewater are discussed. Moreover, the review identifies scientific literature on knowledge gaps, and future research ways are provided to assess the effects of these technologies in the treatment of petroleum wastewater.

**Keywords:** petroleum wastewater refinery; advanced oxidation process; fenton; photo-Fenton; ozonation

**Citation:** Elmobarak, W.F.; Hameed, B.H.; Almomani, F.; Abdullah, A.Z. A Review on the Treatment of Petroleum Refinery Wastewater Using Advanced Oxidation Processes. *Catalysts* **2021**, *11*, 782. <https://doi.org/10.3390/catal11070782>

Academic Editors: Irina Levchuk, Javier Moreno-Andrés and Juan José Rueda-Márquez

Received: 2 June 2021

Accepted: 23 June 2021

Published: 27 June 2021

**Publisher's Note:** MDPI stays neutral with regard to jurisdictional claims in published maps and institutional affiliations.



**Copyright:** © 2021 by the authors. Licensee MDPI, Basel, Switzerland. This article is an open access article distributed under the terms and conditions of the Creative Commons Attribution (CC BY) license (<https://creativecommons.org/licenses/by/4.0/>).

## 1. Introduction

Water is crucial for life since it is a fundamental necessity of all organisms. Fast industrial and economic growth have guided a rapid increase in population and development [1]. The world is observing growth and development in the industry, owing to the several industrial methods that are applied [2]. The industrial regions incessantly produce significant quantities of wastewater at high rates and generally dispose of the wastewater with no appropriate management and treatment [3,4]. Petroleum refineries and industries are crucial from an economic development perspective [5]. Petroleum refineries are meeting the difficulty of how to dispose this wastewater.

Wastewater produced by petroleum industries includes various kinds of organic and inorganic contaminants, for example sulfides, phenol, BTEX, hydrocarbons, heavy metals, etc. [6]. Huge amounts of harmful materials are produced through petroleum industry activities, for example through the oil production process, oil refinery, transportation, storage, etc., which are all unsafe for the environment and human health [6]. The treatment of wastewater produced from the petroleum industry includes different processes that



comprise physical, chemical, and biological methods [7]; however, the majority of these techniques are ideal to match certain treatment requirements for every application and generally do not recommend the treatment to separate the various groups of compounds [8].

The chemical oxidation method is one of the techniques used for wastewater treatment, and it can be classified into two types: conventional chemical treatments and advanced oxidation processes [9]. Advanced oxidation methods are highly efficient techniques needed for the treatment of several wastewater types, including the oil and gas industry, pharmaceutical industries wastewaters, etc. In previous years, several works have been carried out to examine the efficiency of advanced oxidation processes in the treatment of different wastewater types that contain recalcitrant and toxic pollutants [10]. AOPs are defined as the methods that depend on the production of hydroxyl free radicals, which have great electrochemical oxidant power and strong oxidizing potential [11,12]. The great oxidizing potential allows them to easily oxidize and degrade nearly all organic compounds to  $H_2O$ , carbon dioxide ( $CO_2$ ), and inorganic ions, through dehydrogenation or hydroxylation. In general, AOPs are extensively employed in petroleum wastewater treatment for decreasing organic materials, the removal of certain contaminants, and sludge treatment [13]. The possibility of AOPs being used for wastewater treatment is improved by their capability to generate hydroxyl radical ( $OH\bullet$ ) via various methods.

The very common AOP method types studied for wastewater treatment involve heterogeneous photocatalytic oxidation [14], ozonation processes ( $O_3$ ) [15], Fenton and photo-Fenton reaction [16,17], and electrochemical oxidation [18]. These methods are favorable in the treatment of wastewater containing different organic and inorganic pollutants. According to previous reviews, several combinations of various AOPs are more effective in comparison to a single oxidation process, owing to the production of additional radicals and excessive energy efficiency. Moreover, the utilization of heterogeneous and homogeneous catalysts and energy-dispersing elements considerably improves the degradation of the wastewater. Wang et al. [19] summarized hydrogen peroxide ( $H_2O_2$ ),  $O_3$ , ultraviolet (UV)/ $H_2O_2$  or  $O_3$ ,  $O_3/H_2O_2$ , and photo-Fenton processes and their use in wastewater treatment. Furthermore, Chen et al. [20] and Ani et al. [21] reported a review on the basics of the heterogeneous photocatalytic degradation of organic pollutants and stated the benefits of utilizing titanium as an effective material for the removal of organic contaminants by applying advanced oxidation processes. Azizah and Widiya [22] reviewed the application of  $H_2O_2/UV$  and  $H_2O_2/UV/O_3$  advanced oxidation process methods in synthetic residual fluid catalytic cracking (RFCC) wastewater to verify the suitable condition of AOPs to meet the phenol separation ranges. It is found that a high phenol degradation of 93.75% was achieved by using the  $H_2O_2/UV/O_3$  AOP process with a  $H_2O_2$  amount of 1000 ppm; this clarified that the  $H_2O_2/UV$  method requires extended time and greater  $H_2O_2$  amounts for the removal of phenols from these wastewater types to levels below the target. Lofrano et al. [23] propose a generally updated review of AOPs in antibiotics removal considering physio-chemical and toxicity implications. They discussed the technical and economic problems, and the environmental compatibility of effluents.

An environmentally friendly preparation of  $TiO_2$  nanoparticles supported by microwaves from titanium tetrachloride and water was carried out by de Oliveira et al. for the treatment of petroleum refinery effluent [24]. The highest rates of TOC separation were achieved below pH conditions of 10 and a catalyst dosage of 100 mg/L in 90 min of reaction time. The catalyst demonstrated steadiness for four cycles. The attained data revealed that the produced catalyst is a favorable material for the separation of remaining recalcitrant organic material from petroleum refinery effluent.

As far as the authors are aware, there are different studies on the treatment of petroleum refinery wastewater using the different types of an advanced oxidation process method as a tertiary treatment to disinfect and degrade the wastewater compounds and reuse the treated wastewater for different purposes. Therefore, the objective of the review is to present the different methods of the advanced oxidation process and its use in petroleum refinery wastewater treatment. The review reports that the treatment efficiencies depended

strongly on the selected AOP method type, whether the properties of target contaminants were physical or chemical, and the operating conditions. Moreover, the knowledge gaps and future research methods are also provided to assess the effects of these technologies in the treatment of petroleum wastewater.

## 2. Methodology

The review provides an overview of the findings from recent studies from 2017 to 2021 which have been applied to different types of AOPs to degrade and remove different compounds from petroleum refinery wastewater. Few articles published from 2012–2015 were also considered as they presented crucial data. The major source of these articles was google-scholar and Scopus databases; the keywords applied for the search were “advanced oxidation”, “petroleum”, “refinery”, “wastewater pollutants”, “Fenton”, “catalyst”, and “review”. The assembled data were introduced in Tables 1–5 and studied in four sections. Information on the characteristics of petroleum refinery wastewater and the environmental impact of petroleum refinery wastewater was presented in Tables 1 and 2, and discussed in Sections 3 and 4, respectively. The fundamentals of AOPs were discussed in Section 5, an overview of the process in petroleum refinery wastewater treatment was represented by Figure 1, and the classification of the AOPs was presented in Table 3. In this section (Section 5) four types of AOPs including H<sub>2</sub>O<sub>2</sub>/UV, Fenton, photo-Fenton, and ozonation AOPs and their applications in petroleum refinery wastewater treatment were discussed. The data relating to each process was presented in Tables 4 and 5, and Figures 2–6 were included to present crucial concepts related to each process (the reaction mechanism, the drawbacks of Fenton, and photo-Fenton processes, solar photoreactor setup, experimental setup of photoreactor, and detailed steps of the mechanism of organic degradation of wastewater contaminants through O<sub>3</sub>/UV) [25,26]. In Section 6, the integrated AOPs were reviewed, and a diagram of the integrated system was presented in Figure 7. Finally, from the analysis of the assembled data, conclusions are presented and recommendations for additional research are provided.

## 3. Characteristics of Petroleum Refinery Wastewater

Petroleum refinery effluent has numerous amounts of complex substances present in it. They were present in the form of oil, gas, wax, grease, metals, minerals, hydrocarbons, etc. Few components present in very low amounts; such components are N, S, O, and a few other metals which have minor importance. Aromatic organic compounds containing solely carbon and hydrogen atoms are colorless, white, or pale-yellow solids. It has been proven that, when it enters the human body, our potential immune system will suppress it. This can cause carcinogenic and mutagenic damage [27].

The constituents present in the produced include oil and gases and different organic and inorganic matters that are complex in nature. The particles implicated are hydrocarbons, dissolved oil, dissolved salts [28], naturally formed radioactive elements, and heavy metals [29]. Furthermore, with gases such as hydrogen sulfides, carbon dioxide composition will be encompassed as dissolved gases. The generation of produced water is strictly controlled by different countries because the components present in it will increase the pollution rate [30]. The concentration of salt present in seawater is lower than compared to the concentration of salt present in the produced water. The percentage of salinity is enhanced due to the concentration of the additional component present in it. Those components are Ca, K, Mg, and dissolved Cl, etc. [31].

The previous survey [31] reveals that the electrical conductivity of the produced water lies in a range from 200  $\mu$ S/cm to 300  $\mu$ S/cm, while the TDS concentration range of produced water lies in a range from 120 g/L to 140 g/L. Some of the major compositions are sodium with a range of (42,720  $\pm$  2093 mg/L), calcium ions (4247  $\pm$  752 mg/L), magnesium ions (727  $\pm$  54 mg/L), potassium ion (805  $\pm$  230 mg/L), strontium ions (257  $\pm$  20 mg/L), chlorine ions (65,800  $\pm$  1600 mg/L), sulphate (1010  $\pm$  9 mg/L), bromide ion (591  $\pm$  16 mg/L) and silicon dioxide (32  $\pm$  2 mg/L) [27]. The concentration of ammonia present

in the PW has a range of  $(655 \pm 77 \text{ mg/L})$  [31]. The value of pH, as well as alkalinity, are  $7.30 \pm 0.21$  and  $2345 \pm 329 \text{ mg/L}$ , respectively, such as  $\text{CaCO}_3$  [32]. Table 1 shows the composition present in the petroleum refinery wastewater [33]. The composition of nitrogen in the produced water coming from the oil platform is 50 v/v%. The summation of all nitrogen compounds in the water is termed total nitrogen; it contains ammonia nitrogen ( $\text{NH}_3\text{-N}$ ), nitrite nitrogen ( $\text{NO}_2\text{-N}$ ), nitrate nitrogen ( $\text{NO}_3\text{-N}$ ), and organically bonded nitrogen [34].

**Table 1.** The compositions present in the petroleum refinery wastewater.

Composition of Each Element	Composition in Petroleum Wastewater	Limitations	Metal Compositions	Components in Petroleum Wastewater	Limitations
pH	4.3–10	6.5–8.5	Ca	18–132,687	100
Density	1014–1140	-	Na	316–134,652	-
TOC	3.4–5960	-	K	8.6–14,649	-
COD	1200	$\leq 50$	Mg	4–18,145	100
BOD	-	$\leq 30$	Fe	$<0.1$ –100	0.3
TSS	1.2–21,820	30	Al	310–410	$\leq 0.2$
TDS	$1 \times 10^3$ – $4 \times 10^5$	1200	B	5.00–95	1
DO	8.2	$<4.0$	Ba	0–22400	1
TPH	2–565	-	Cd	$<0.005$ –0.2	0.005
BTEX	0.39–35	-	Cr	0.02–1.1	$\leq 0.1$
base and neutrals	$<140$	-	Cu	$<0.002$ –1.5	1.3
Cl	80–310,561	1400–190,000	Li	3–50.00	-
Br	0–12,000	150–1149	Mn	$<0.004$ –175	0.05
I	0–500	-	Ni	-	0.3
$\text{HCO}_3$	1.9–7355	-	Pb	0.002–8.8	0.015
$\text{CO}_3$	0–800	-	Sr	0.02–1000	-
$\text{SO}_4$	0.5–7851	$<0.1$ –47	Ti	$<0.01$ –0.7	-
$\text{PO}_4$	0–0.10	-	Zn	0.01–35	7.4
$\text{SO}_3$	$\sim 10$	-	As	$<0.005$ –0.3	0.02
$\text{NO}_3$	0–3.5	-	Hg	$<0.001$ –0.002	0.005
$\text{NO}_2$	0.05	-	Ag	$<0.001$ –0.15	0.1
$\text{NH}_3\text{-N}$	10–300	-	Be	$<0.001$ –0.004	-
Total Polar	9.7–600	-	NORM (pCi/L)	-	-
Higher acids	$<1$ –63	-	Total Ra	0.054–32,400	5
Phenols	till 23	-	U	0.008–2.7	-
VFA	2–4900	-	Th	0.008–0.027	15
Oil & Grease	6.9–210	2.3–60	Pb	1.35–5130	-
m-xylene	0.01–54	-	Po	0.005–0.17	-
MBAS	0.01–54	-	-	-	-
HEM	0.6–2000	0.02	-	-	-
Alkalinity	6.1–200	-	-	-	-

The configuration of these substances and their tenacious character affects the rate of chemical oxygen demand and the level of toxicity. The wastewater encompasses a high level of COD. The presence of these toxic oils considerably disperses the chemical oxidation demand [32]. If the produced water contains a high content of BOD value, it is due to the large content of organic materials present in the drilling fluids. Before discharging a high value of BOD content water into the water bodies, oxidation of the water must be maintained so that only it can resist the wastewater with a larger BOD content [29]. The PW containing the range of the TOC is (0–1500 mg/L). The naturally formed water has a TOC concentration that lies in the range of  $<0.01$ –11,000 mg/L [35]. The World Health

Organization proposes that a fringe of the permissible volume of benzene and toluene in drinking water are 10 and 700 mg/L, respectively, while the permissible proportion of ethylbenzene and xylene is 300 mg/L and 500 mg/L, respectively [27].

The characteristic of the petroleum refinery wastewater fluctuates according to their base. The constitution of the wastewater depends on the final product induced, the undertaking process, and the type of crude oil that is utilized. The produced water is assorted with aromatic and aliphatic hydrocarbons, MTBE, PAHs, phenols, naphthenic acid, sulfides, metal products as well as benzene, toluene, ethylbenzene and xylene (BTEX) that usually possess a high toxicity. In addition, xylene has three more topical isomers named o-xylene, m-xylene, and p-xylene [36].

#### 4. Environmental Impact of Petroleum Refinery Wastewater

Enormous amounts of contaminants were released by petroleum products in the environment [37]. As known, petroleum wastewater is the main of three waste types (wastewater, waste gas, and industrial residue) whose harmful impacts cannot be misjudged [38]. Wastewater discharged by petroleum industries include significant amounts of heavy metals, petroleum hydrocarbons [39], polyaromatic hydrocarbons [40], benzene, toluene, ethylbenzene, xylene (BTEX), phenolic compounds, and other contaminated materials [41]. Some of the major petroleum wastewater contaminants and their environmental impacts are presented in Table 2. Owing to the incompetence of treatment methods, petroleum refinery wastewater is dangerous to the environment and other life systems which could become mutagenic and toxic to human beings [42]. This wastewater can influence various elements of the environment, for example clean water, human health, the different sources of groundwater, air, marine life, crop manufacturing, etc. [43]. An increase in contaminants in the water bodies raises significant concerns, either long-term or short-term, for the ecology and living organisms, which can be severe and chronic [44]. Different studies revealed that petroleum refinery wastewater composites have the ability to biologically build up, which is the main reason to create a method for the separation of pollutants from water before the release [39]. The following problems were created when a huge quantity of petroleum oily wastewater was arbitrarily released into water bodies [7].

Regarding aquatic life where the wastewater was released into the river and oceans, oil and other contaminants create a film on the water surface that lead to a block in the air and sunlight, thus causing a shortage of oxygen for the aquatic organisms and affecting the plants and animals' growth [45]. Furthermore, owing to the existence of heavy oil on the surface of seawater, serious problems were observed, including slow growth of the head of aquatic organisms, unusual neural growth in the embryo of the aquatic organisms, and other issues [46]. Benzene, toluene, ethylbenzene, and xylene (BTEX) are some of the main pollutants that harm aquatic organisms, the nervous system, genotoxicity, and the respiratory system [46], due to their highly carcinogenic nature as distinguished by The U.S. Environmental Protection Agency (USEPA) [42]. Moreover, petroleum refinery wastewater includes a solvable aromatic hydrocarbon, many radioactive substances, and heavy metals which can generate negative impacts on some organisms accountable for water purification and biological treatment [36]. In the case of direct release, pollutants in the wastewater are transported by the food chain through the infected foods, and, hence, human health will be critically affected [47]. Aquatic contamination will also occur, owing to the spread of toxic components between the food chain via the marine ecosystem from the influenced marine environment [48]. Some studies reported that the consumption of the contaminated oil with marine food could produce many toxic consequences on human health, such as skin tumors due to the existence of the contaminated hydrocarbons in the polluted wastewater [49]. Another study presented the effect of wastewater pollutants during the separation processes of oil throughout the marine water [40]. It was found that the co-workers that engaged in certain processes developed a urinary infection due to the presence of a high concentration of volatile organic composites and polycyclic aromatic hydrocarbons which can be absorbed by their body. Furthermore, it was found that

contaminated oil in the wastewater represents a toxic material to certain microorganisms that is accountable for the biological treatment of wastewater [50].

**Table 2.** Some of the main wastewater contaminants mentioned in the work and their environmental impacts.

Contaminant	Environmental Impact	Ref
Phenol	Have harmful effects on the muscles, causing moving problems, pain to the gastrointestinal system, and even death.	Yang et al. (2020)
Methyl-butyl ether	In an aquatic environment, it quickly causes the reduction in dissolved oxygen. Regarding human health, it causes kidney and blood cancers and affects the nerve. The existence in the aquatic environment affects the stability and health of the organisms, leading to a low regenerative rate, and affecting the behavior of the organisms. It also reduces the growth of plants and animals, and, with long time exposure, it can lead to their death.	Gallo et al. (2020)
Benzene	Have harmful impacts on the different types of microorganism (aquatic, soil, etc).	Rabani et al. (2020)
Toluene	Exposure for long periods affects the kidney which can lead to pain in the inner ear. Affects the kidney, nervous system, and the dysfunctions of the liver. In addition, various negative impacts on the neurological system have been stated.	Poyraz et al. (2020)
Ethylbenzene		Wollin et al. (2020)
Xylene		Egendorf et al. (2020)

Phenols are other toxic compounds that generally appear in the wastewater produced from petroleum refinery and can impact the enzymatic processes of marine microorganisms even at small phenol concentrations. As the degradation of the phenolic composite takes a long time, they will gather in the aquatic organisms' tissues and consequently produce biomagnification. The phenolic compounds have been identified to be genetically, physiologically, and haematologically toxic [51]. Thus, the phenolic compounds have been classified by USEPA as a significant contaminant [52]. The phytotoxicity of phenols was experimentally verified on *EU cyclops agilis* by Kottuparambil et al. [53]. The results showed the high toxicity of phenol compounds even in the presence of a small dose of phenols and how this negatively impacts human life [54].

Polycyclic aromatic hydrocarbon (PAHs) compounds are other toxic contaminants that existed in the petroleum industry wastewater and have toxic effects on aquatic organisms. The study reported by Badibostan et al. [55] showed that the presence of specific polycyclic aromatic hydrocarbons, for example chrysene (CHR) compounds and benzo[b]fluoranthene (BbF) with high concentrations, causes serious problems including drinking, inhalation, etc. When its overall concentration exceeded the concentrations of the standards defined by USEPA for toxic chemicals, it negatively impacted human life and health.

Another concern is that, when petroleum oily wastewater used for irrigation, these compounds can have harmful impacts on the soil and make it stronger [56]. This change on soil texture inhibits the breathing of plants and organisms as the soil microorganisms have a high sensitivity to MTBE compared to the microorganisms present in the water. In addition, oily wastewater could have a harmful effect on environmental processes such as nutrient cycles and biodegradation [56]. Consequently, the microorganism's decline rate will decrease, and then the plants and animal growth will be influenced [57].

## 5. Advanced Oxidation Process (AOPs) for Petroleum Refinery Wastewater

### 5.1. Fundamentals/Chemistry of the Advanced Oxidation Process

Advanced oxidation processes (AOPs) are the methods defined through the creation of hydroxyl radicals; the core purpose of the advanced oxidation process is to produce highly reactive free radicals which are extremely sensitive, and to apply non-selective materials to reduce contaminated organic composites that exist in a medium for example wastewater, soil, marine mediums, etc. [58].

Hydroxyl radicals are efficient in eliminating organic chemicals since they are reactive electrophiles [59]. They are powerful oxidizing agents to demolish compounds that cannot be oxidized by the standard oxidant. Hydroxyl radicals have a more rapid oxidation rate compared to  $\text{KMnO}_4$  or  $\text{H}_2\text{O}_2$  [60]. The produced hydroxyl radicals can remove the organic chemicals through different ways such as radical addition, hydrogen extraction, or electron transmission [61]. The creation of hydroxyl radicals is generally enhanced by merging  $\text{O}_3$ ,  $\text{H}_2\text{O}_2$ ,  $\text{TiO}_2$ , UV radiation, ultrasound, and electron-beam irradiation [62].

The hydroxyl radical has great oxidation potential ( $E_0 = 2.8 \text{ V}$ ) [63] and is competent to react with almost all types of organic composites, leading to full mineralization of these composites which form from carbon dioxide ( $\text{CO}_2$ ), inorganic salts, and water, or their transformation into fewer destructive substances [64]. The removal of contaminants and the inhibition of the production of toxic compounds are some of the major advantages of AOPs since traditional techniques of water treatment. For example filtration, adsorption, and flotation are not effective in completely separating the organic pollutants (non-destructive physical separation procedures), which only eliminate the pollutants, transporting them to other stages, and thus producing intense residues [65]. An overview of the AOP in petroleum wastewater treatment is presented in Figure 1.

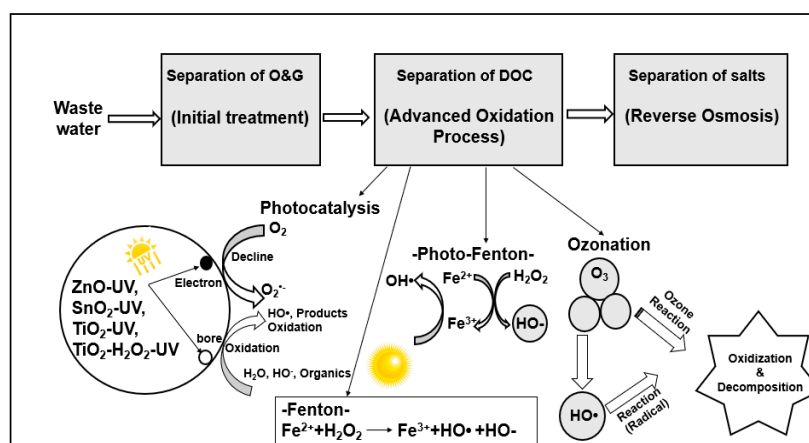
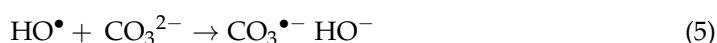
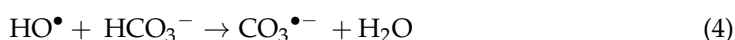


Figure 1. An overview for the AOP in petroleum refinery wastewater treatment.

The main reaction produce hydroxyl radicals ( $\text{HO}\bullet$ ) that attack organic composites in electrophilic position leading to degradation. In addition  $\text{HO}\bullet$  reaction with organic composites (aromatic or unsaturated) that include a  $\pi$  bond result in the formation of the organic radicals (Equation (1)) [66]. This includes hydrogen removal through the reaction of the  $\text{HO}\bullet$  radicals with a saturated aliphatic compound (Equation (2)) and electron transmission by decreasing the  $\text{HO}\bullet$  radical into a hydroxyl anion through an organic

substrate (Equation (3)) [67]. The attack of the HO• radical on organic substrates could be affected by the existence of different chemical types in water (which are created in the mineralization method), for example, bicarbonate and carbonate ions [68]. These ions can react with the HO• radicals (Equations (4) and (5)), and, by consequently vying with the organic substrates via the HO• radicals. HO•, radicals can be created from numerous AOPs, allowing the use of a superior method for every treatment condition.



Following Flouret and his colleagues (2018), the AOP can be classed as homogeneous and heterogeneous [69]. They introduced this categorization in terms of the light type that is utilized in the method. Table 3 shows the categorization of AOPs consistent with these studies. The AOP are costly methods due to the high cost of chemicals applied (e.g., H<sub>2</sub>O<sub>2</sub> and O<sub>3</sub>), also due of electric energy for UV radiation. Hence, they are studied in other treatments of wastewater that cannot be organically handled. An additional substantial part is the weight of contaminants that appear in the wastewater, commonly identified according to the existing amounts of COD. The application of these methods is revealed solely for wastewater that contains COD under 5 g/L, since a greater index of COD inhibiting the treatment would need an extremely higher utilization of chemicals [70]. For high organic wastewaters, pretreatment processes, such as dilution, coagulation, and flocculation, are needed to lessen the initial concentrations [71]. Additionally, AOPs can be utilized for treating the polluted waters containing very small organic contents (in ppb) which include dispersed organic composites that are hard to eliminate. One method of decreasing the AOPs' costs is to utilize them as initial treatment processes to decrease harmfulness, supported by biological treatment. This alternative has demonstrated to be very exciting from an economic perspective and has been examined by numerous studies [72,73].

**Table 3.** Types and categorization of advanced oxidation methods (AOPs).

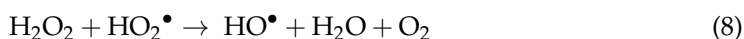
Non-photochemical-Homogeneous Methods	Photochemical-Homogeneous Methods	Non-Photochemical-Heterogeneous Processes	Photochemical-Heterogeneous Processes
<ul style="list-style-type: none"> <li>Ozonation in alkaline media (O<sub>3</sub>/HO<sup>-</sup>)</li> <li>Ozonation with hydrogen peroxide (O<sub>3</sub>/H<sub>2</sub>O<sub>2</sub>)</li> <li>Fenton (Fe<sup>2+</sup> or Fe<sup>3+</sup>/H<sub>2</sub>O<sub>2</sub>)</li> <li>Electro-oxidation</li> <li>Electrohydraulic discharge-ultrasound</li> <li>Wet air oxidation (WAO)</li> <li>Supercritical water oxidation (SCWO)</li> </ul>	<ul style="list-style-type: none"> <li>Photolysis of water in vacuum ultraviolet (VUV)</li> <li>UV/H<sub>2</sub>O<sub>2</sub>tyg,v =</li> <li>UV/O<sub>3</sub></li> <li>UV/O<sub>3</sub>/H<sub>2</sub>O<sub>2</sub></li> <li>Photo-Fenton Fe<sup>2+</sup> or Fe<sup>3+</sup>/H<sub>2</sub>O<sub>2</sub>/UV</li> </ul>	<ul style="list-style-type: none"> <li>Catalytic wet air oxidation (CWAO)</li> </ul>	<ul style="list-style-type: none"> <li>Heterogeneous photocatalysis: /UV, SnO<sub>2</sub>/UV, TiO<sub>2</sub>/UV, TiO<sub>2</sub>/H<sub>2</sub>O<sub>2</sub>/UV</li> </ul>

## 5.2. H<sub>2</sub>O<sub>2</sub>/UV Advanced Oxidation Process and Their Application in Petroleum Refinery Wastewater

Hydrogen peroxide (H<sub>2</sub>O<sub>2</sub>) is a powerful oxidant among other oxidant types with a standard reduction potential = 1.77 V that is used to decrease the small levels of contaminants that exist in wastewaters [74]. However, the specific utilization of H<sub>2</sub>O<sub>2</sub> is not effective in treating more compounds and mutinous substances with a low reaction rate. The application of H<sub>2</sub>O<sub>2</sub> is more successful when it performs in combination with other components or sources of energy that are competent of separating it to produce HO• radicals, which can behave as oxidizing factors [75]. Through UV radiation in wavelengths >300 nm, hydrogen peroxide (H<sub>2</sub>O<sub>2</sub>) can decompose and create HO•, as demonstrated in Equation (6).



H<sub>2</sub>O<sub>2</sub> can also react with HO• and created transitional products in line with the reaction, the method is explained easily by Equations (7)–(11) [76].



The damage on organic composites occurs when HO• and hydroperoxyl (HO<sub>2</sub>•) radicals are created. Nevertheless, the hydroperoxyl radicals have a smaller reduction potential with a value of 1.7 V compared to hydroxyl radicals with a value of 2.8 V; as a result, their production is not attractive to the method. Numerous researchers have indicated that the increase in the first amount of H<sub>2</sub>O<sub>2</sub> enhances the pollutants degradation rate up to the highest value, after which, when they achieve very high H<sub>2</sub>O<sub>2</sub> levels, they start to decrease. Khan and coworkers (2020) ascribe this reduction in the H<sub>2</sub>O<sub>2</sub>/UV process outputs to hydroxyl radicals reacting with additional H<sub>2</sub>O<sub>2</sub> (Equation (7)), rather than reacting by the organic substrates, resulting in the creation of the HO<sub>2</sub>•. The H<sub>2</sub>O<sub>2</sub> photolysis is generally achieved using different mercury vapor lights (low or medium pressure) with great intensity, which decreases the required quantity of H<sub>2</sub>O<sub>2</sub>. Almost 50% of the energy expended is wasted in heat form or in emissions of wavelengths >185 nm, which are noticed by the jacket made of quartz [77].

A cheaper and widely used alternative is the germicide lamp; though, the efficiency is smaller as it radiates in a range from 210 to 240 nm, and H<sub>2</sub>O<sub>2</sub> absorption achieves a peak of 220 nm [78]. The application of the H<sub>2</sub>O<sub>2</sub>/UV process has different advantages that can be ascribed to different facts, for example: the H<sub>2</sub>O<sub>2</sub> reagent is completely solvable in water, there is no restriction of mass transfer, it is an active supply of HO•, and there is no necessity for a removal method after the treatment [79]. The operating pH should be small (pH < 4) to void the impact of separating radical types, mainly ionic types such as bicarbonate and carbonate ions, which results in improving the degradation rate.

The applications of H<sub>2</sub>O<sub>2</sub> was evaluated in the existence and the nonappearance of UV radiation, and in the degradation of petroleum refinery wastewater which is pretreated using different separation processes such as coagulation and flotation, studying total petroleum hydrocarbons (TPH), 1,2-dichloroethane (DCE), dichloromethane (DCM), and MTBE [80]. It was remarked that UV emission did not substantially impact the compound degradation, except for DCM which was highly stable compared to others. Overall, 83% was eliminated with 11.76 nM of H<sub>2</sub>O<sub>2</sub> in the existence of UV radiation. The studies showed sluggish degradation of the TPH, which separated by 69% in the first 8 days of testing. They found that the degradation of MTBE was identical to that of DCM, and that total degradation occurred after 24 h. The application of the H<sub>2</sub>O<sub>2</sub>/UV process for



the purification of oily wastewater from a lubricant production unit was analyzed by Gilpavas et al. (2019). Chromatographic characterizations that were carried out in the study indicated that most of the composites detected in the wastewater were separated with the ending of the treatment, utilizing great amounts of H<sub>2</sub>O<sub>2</sub>. However, a decrease in just 40% of preliminary wastewater COD was achieved, which is equivalent to around 9000 mg/L. This was assigned to the creation of organic acids, generated because of the decomposition of the organic compounds that exist in the wastewater, which are more resistant to photo-degradation with H<sub>2</sub>O<sub>2</sub>. The influence of pH on the process was also evaluated and it was found that, in an acidic condition of pH 3.5, there was a greater decrease in the wastewater COD, in comparison to basic and neutral pH conditions [81]. The degradation of MTBE was investigated by Neisi and coworkers (2018), and the gasoline was evaluated as one of the highly popular pollutants in polluted underground waters. The H<sub>2</sub>O<sub>2</sub>/UV process was evaluated at certain conditions, and the removal percentage of MTBE was found to be more than 98%. A rise in the removal percentage was obtained with an increase in the concentration of H<sub>2</sub>O<sub>2</sub>, after which the percentage began to drop [82]. This result was assigned to the competitive reactions of H<sub>2</sub>O<sub>2</sub> and HO•, presented in Equations (7)–(11). A comparison between some studies applying H<sub>2</sub>O<sub>2</sub> advanced oxidation-based process in the treatment of different types of wastewater was illustrated in Table 4.

**Table 4.** Comparison between recent studies using H<sub>2</sub>O<sub>2</sub> advanced oxidation-based process in wastewater treatment.

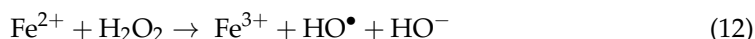
Process	Type of Wastewater (WW)	Conditions	Efficiency	Comments and Details	Ref
TiO <sub>2</sub> /UV	Model: TPH Benzene (Toluene Phenol) Naphthalene	[TiO <sub>2</sub> ] 100 mg/L pH 6.5 for 1 h	COD reduction from 970 mg/L to 65 mg/L = 93% removal at 90 min, 30 °C and pH 3 using 100 mg/L	Higher degradations rates for with TiO <sub>2</sub> /UV = 92%, 98.8%, 91.5%, and 93% for B, T, P and N, respectively.	Ihtisham et al. 2020
H <sub>2</sub> O <sub>2</sub> /UV	Model [Phenol] 100 mg/L	(H <sub>2</sub> O <sub>2</sub> ) 3060 mg/L pH 9	99% phenol removal in 60 min	H <sub>2</sub> O <sub>2</sub> /UV < O <sub>3</sub> /UV 0.081 min <sup>-1</sup> < 0.0881 min <sup>-1</sup>	Alrousan et al. 2020
H <sub>2</sub> O <sub>2</sub> /UV	Oil COD 9000 ± 500 mg/L	(H <sub>2</sub> O <sub>2</sub> ) 3330 mg/L pH 12	40% COD removal in 150 min	Negative impact on COD removal at basic pH	GilPavas et al. 2019
H <sub>2</sub> O <sub>2</sub> /UV	Model: [nonylphenol] 4.41 mg/L	(H <sub>2</sub> O <sub>2</sub> ) 1.7–17 mg/L pH 11	To achieve 90% of degradation [H <sub>2</sub> O <sub>2</sub> ] 1.7 mg/L in 20 min (H <sub>2</sub> O <sub>2</sub> ) 3.4 mg/L in 16 min (H <sub>2</sub> O <sub>2</sub> ) 8.5 mg/L in 12 min	At pH 7 the time needed was 3 times higher in all concentrations studied	Kaur et al. 2020
H <sub>2</sub> O <sub>2</sub> H <sub>2</sub> O <sub>2</sub> /UV	Linear Alkyl Benzene COD 300–350 mg/L	(H <sub>2</sub> O <sub>2</sub> ) 340 mg/L pH 9	H <sub>2</sub> O <sub>2</sub> : 27% COD removal in 180 min H <sub>2</sub> O <sub>2</sub> /UV: 36% COD removal in 180 min	H <sub>2</sub> O <sub>2</sub> (27%) < O <sub>3</sub> /UV, H <sub>2</sub> O <sub>2</sub> /UV (36%) < O <sub>3</sub> , (37%) < H <sub>2</sub> O <sub>2</sub> /O <sub>3</sub> (39%) < H <sub>2</sub> O <sub>2</sub> /O <sub>3</sub> /UV (42%)	Fernandes et al. 2019
H <sub>2</sub> O <sub>2</sub> /UV	Model: MTBE 25 mg/L	(H <sub>2</sub> O <sub>2</sub> ) 34 mg/L pH 12	98% MTBE removal in 60 min	H <sub>2</sub> O <sub>2</sub> /UV (0.126 min <sup>-1</sup> )	Neisi et al. 2018

Table 4 shows a comparison between recent studies for wastewater treatment using H<sub>2</sub>O<sub>2</sub> advanced oxidation-based processes at different conditions. The studies showed the high efficiency of the H<sub>2</sub>O<sub>2</sub>-based advanced oxidation process in the degradation and removal of different wastewater compounds, such as COD, TOC, MTBE, phenol, etc., from different wastewater types. The efficiency was found to be more than 90% for each

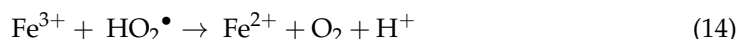
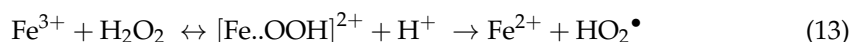
wastewater that either utilized the hydrogen peroxide  $H_2O_2$  alone or added in the existence of ultraviolet (UV) light.

### 5.3. Fenton and Photo-Fenton Advanced Oxidation Processes and Their Application in Petroleum Refinery Wastewater

Fenton's chemical is a mixture of  $H_2O_2$  and ferric ions found by Henry John Horstman Fenton (1854–1929). In 1894, he stated that this mixture had great oxidizing potency in an acid medium [83]. However, the use of Fenton's chemical in oxidation procedures to remove contaminated organic composites was reported by different researchers [84,85]. There is significant disagreement about the mechanism of reaction, including Fenton's reaction. The standard reaction of the Fenton process is taken by Haber and Weiss et al. (1934), as mentioned by Zouanti et al. [86], which contains an aqueous integration of hydrogen peroxide ( $H_2O_2$ ) and ferrous ions ( $Fe^{2+}$ ) in an acidic medium, leading to  $H_2O_2$  breaking into a hydroxyl ion and a hydroxyl radical, and the oxidation from  $Fe^{2+}$  to  $Fe^{3+}$ , as characterized by Equation (12) [87].



The  $Fe^{2+}$  and  $Fe^{3+}$  types exhibited in an easy manner coincide with the  $[Fe(OH)(H_2O)_5]^+$  aqueous compounds, which, combined with  $H_2O_2$ , create the  $[Fe(OH)(H_2O_2)(H_2O)_4]^+$  and  $[Fe(OH)(H_2O)_5]^{2+}$  composites, respectively, as stated by [88]. The  $Fe^{3+}$  created in Equation (12) are able to react with the  $H_2O_2$  that exists in the medium, and can be decreased to  $Fe^{2+}$  once more by producing the hydroperoxyl radical, according to Equation (13). This reaction happens more sluggishly than reaction 12, as described by Kim et al. [89]. The  $Fe^{3+}$  ions also react with the  $HO_2^\bullet$  and are decreased to  $Fe^{2+}$ , as indicated with Equation (14).

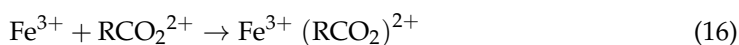


The preliminary rate of degradation employing  $Fe^{+3}$  is significantly smaller than that utilizing  $Fe^{+2}$ , as presented by Yuan et al. [90]. The standard pH in Fenton's reaction observed in several reports is 3 [91,92] and, consequently, can be considered the suitable operational pH. At an extremely low pH (<2.5), the creation of compounds, for example  $[Fe(H_2O)_6]^{2+}$ , occurs. These react more sluggishly with  $H_2O_2$  than  $[Fe(OH)(H_2O)_5]^+$ , generating a smaller volume of hydroxyl radicals and consequently reducing the efficiency of the system [93]. In the case of basic pH conditions, the reaction between the iron and hydroxide ions ( $HO^-$ ) produced the iron hydroxide ( $Fe(OH)_2$  or  $Fe(OH)_3$ ) which does not react with  $H_2O_2$ , thus prohibiting the Fenton reaction. Hence, a change in pH is necessary for wastewater treatment before the addition of Fenton reagents. Previously, it is crucial to determine the ideal correlation between  $H_2O_2$  ions and ferrous ions. Once the ferrous ions were applied with higher concentrations more than hydrogen peroxide ions, the  $HO^\bullet$  created by Equation (12) can react with additional ferrous ions following Equation (15), and then reduce the raid of  $HO^\bullet$  on organic reacted material [94].



Wang et al. (2019) noticed that, while the ratio of  $[Fe^{2+}]/[H_2O_2]$  is 1:2 and has a greater degradation rate, it is generally suggested to utilize a ratio of 1:5, which generates identical findings and needs fewer reagents. In general, only the reaction of the Fenton process is not able to depredate organic composites and mineralize them effectively. The reaction of the Fenton method is efficient up to the instant where each  $Fe^{2+}$  that exists in the reaction is reacted to  $Fe^{3+}$ , hence disrupting the production of hydroxyl radicals and subsequently degrading the organic compound [95]. Wang et al. [89] mentioned that one of the parameters that have a great effect in disturbing the Fenton's reaction under normal

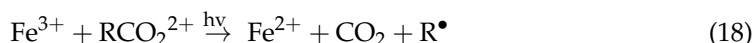
conditions with the degradation products  $\text{Fe}^{3+}$  ions can produce steady organic composites, specifically the organic acids existing in the reaction [91], as revealed by Equation (16).



While Fenton's reaction has been extensively reviewed and has presented great results in the wastewater treatment process, the reaction of Fenton was identified as a strong means to reduce organic composites when UV radiation is applied to the system. This was accomplished in the initial 1990s when used for treating wastewaters that include polluted carbon-based contaminants. It has acted as an initial step for different researchers associated with the use of the photo-Fenton method [96,97]. It has observed that UV irradiation greatly increases the organic contaminants degradation rate from Fenton's chemical, which has the feature of being susceptible to UV-Vis emission for wavelengths over 300 nm. Below these situations, the  $\text{Fe}^{3+}$  compounds photolysis allows the existence of Fenton's reaction and the  $\text{Fe}^{2+}$  to be reused many times if  $\text{H}_2\text{O}_2$  is presented. Clarizia et al. [98] stated that, in a pH range from 2.5 to 5, the ferric compound  $\text{Fe}(\text{OH})^{2+}$  is the main type in the photo-Fenton method, a shortened form of demonstrating the aqueous composite  $\text{Fe}(\text{OH})(\text{H}_2\text{O}_5)^{2+}$ . The photolysis of this compound at wavelengths less than 410 nm is found to be the major  $\text{HO}\cdot$  radical source (Equation (17)) [98]. Additional photoreactive classes also exist in the medium of the reaction, for example  $\text{Fe}_2(\text{OH})_2^{4+}$  and  $\text{Fe}(\text{OH})_2^+$ , which could lead to the creation of hydroxyl radicals [99].



The regeneration of  $\text{Fe}^{2+}$  can also happen with the produced compounds photolysis (Equation (16)) from  $\text{Fe}^{3+}$  and the organic compounds created in the degradation method, as demonstrated by Equation (18) [89].



Hence, the ferrous ions reformed by Equations (17) and (18) can react once again with the  $\text{H}_2\text{O}_2$  in solution (Equation (12)) to produce more hydroxyl radicals, forming a photocatalytic cycle in the  $\text{Fe}^{2+}/\text{Fe}^{3+}$  system. The utilization of radiation considerably lowers the essential number of ferrous ions, in comparison to the dim Fenton reaction (lack of light). The number of ferrous ions applied in the Fenton's reaction must be reduced to attain good efficiency, because adding high concentrations of ferrous ions rises the opacity of the solution, prohibiting the radiation diffusion and the  $\text{Fe}^{2+}$  production when oxidized to  $\text{Fe}^{3+}$ . As a result, the rate of degradation is reduced [100]. It is also found that the elevated intensity of light dispersion and the strong connection between the contaminant and the oxidizing factor act as benefits of the photo-Fenton method because it is a consistent method [101,102]. Figure 2 shows the reaction mechanism for the photo-Fenton process.

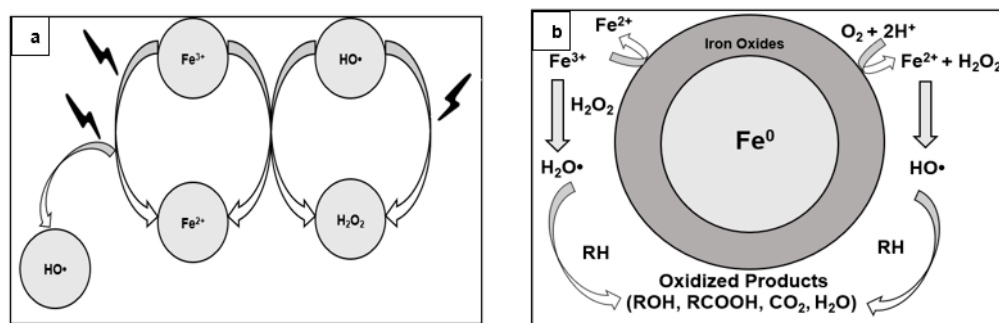
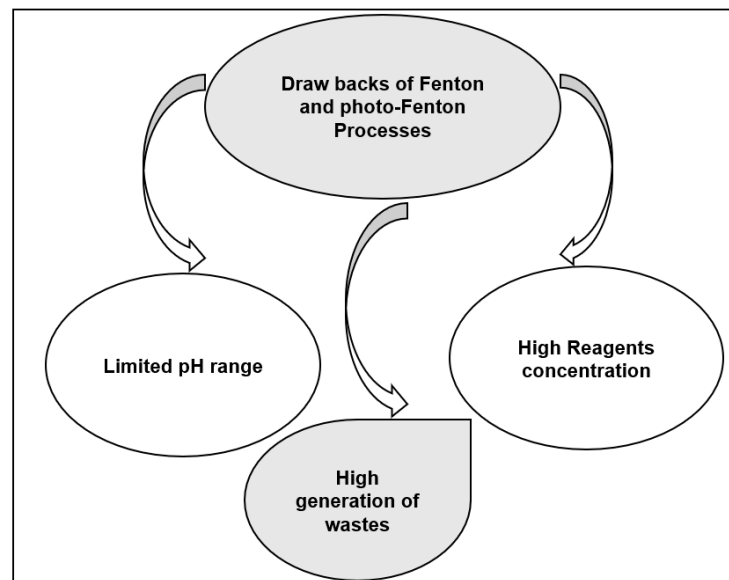


Figure 2. (a) Photo-Fenton, (b) Fenton process reactions mechanism.

The drawbacks of the Fenton and photo-Fenton processes are related to need for pH values which are too small (usually less than 2) and the need to eliminate the iron after reaction [103]. The solution pH in Fenton and photo-Fenton processes should be shifted to protect the catalyst stability, as at pH 6 iron hydroxide is normally generated. For various materials, the proper pH for the Fenton reaction is between 2.8 and 3, and the ideal ratio between catalyst and peroxide is generally 1:5 wt/wt. At an operational pH of >3 (acidic pH), the decomposition rate declines as a result of the reduction in free iron types in the solution, possibly owing to the creation of Fe(II) complexes with the barrier hindering the production of free radicals. At pH greater than 3,  $\text{Fe}^{3+}$  begins precipitating as ferric oxyhydroxides and breaks down the  $\text{H}_2\text{O}_2$  into  $\text{O}_2$  and  $\text{H}_2\text{O}$  [104], consequently decreasing the production of ferrous ions. Moreover, the  $\bullet\text{OH}$  radical oxidation potential is known to reduce with a rise in pH [105]. Nevertheless, at low pH (pH = 2.5), the creation of  $\text{Fe(II)}(\text{H}_2\text{O})^{2+}$  happens, which reacts more slowly with hydrogen peroxide, generating a reduced volume of reactive hydroxyl radicals and consequently decreasing the degradation efficiency [75]. The main drawbacks for Fenton and photo-Fenton processes are summarized in Figure 3.



**Figure 3.** The major drawbacks for Fenton and photo-Fenton processes.

As stated by Rajala et al., [106] iron separation could not be required if it is applied with amounts under the removal range determined by regulation. It is crucial to have the previous familiarity of the original wastewater's physical and chemical features (untreated wastewater). Using this method, since some materials or inorganic ions for example  $\text{Cl}^-$ ,  $(\text{SO}_4)^{2-}$ ,  $[(\text{H}_2\text{PO}_4)^- / (\text{HPO}_4)^{2-}]$  exist in the wastewater or are added as reagents such as  $(\text{FeSO}_4, \text{FeCl}_3, \text{HCl}, \text{H}_2\text{SO}_4)$ , may negatively affect the Fenton and photo-Fenton system reaction mechanism, thus hindering the degradation method [107]. The main reason for this is the scavenging effect of these ion ( $\text{Fe}^{2+}$  or  $\text{Fe}^{3+}$  or any other inorganic ions) to  $\text{OH}\bullet$  radicals. It was highlighted that these reactions with  $\text{OH}\bullet$  could create new radicals such as  $(\text{Cl}\bullet^-, \text{Cl}_2\bullet^-, \text{SO}_4\bullet^-)$ , which are of low oxidation potential [108].

Owing to the existence of  $\text{Cl}\bullet^-$  ions in the reaction, the production of  $\text{Cl}_2\bullet^-$  radical anions can be evaded by monitoring the pH throughout the reaction time at a value of 3, which indicates that the degradation process of organic substrate through the photo-Fenton method aid in the formation of the acid consequently reduces the pH. This happens due to pH reduction (smaller than 2.5) in the existence of  $\text{Cl}\bullet^-$  ions, resulting in more severe production of ferric chloride compounds ( $\text{FeCl}_2^+$  and  $\text{FeCl}_2^+$ ). These components also endure photolysis, thus reducing the volume of  $\text{Fe}(\text{OH})^{+2}$ , which is the major supply of  $\text{OH}\bullet$  in the photo-Fenton method. Furthermore the creation of the  $\text{Cl}_2\bullet^-$  radical anion can

react with  $\text{Fe}^{2+}$  (reacting to  $\text{Fe}^{3+}$  with no production of  $\text{OH}^\bullet$ ) and the organic substrate. One of the major benefits of utilizing the photo-Fenton method in comparison to the other oxidation methods is the application of solar radiation in its reaction process [109]. The existence of oxalate ions  $(\text{C}_2\text{O}_4)^{2-}$  and the  $\text{Fe}^{3+}$  present in the reaction medium can produce the  $[\text{Fe}(\text{C}_2\text{O}_4)]^+$  compound (Equation (19)) with light absorption at wavelengths lower than 570 nm [110,111]. The solar photoreactor setup is shown in Figure 4 by Pourehie and Saïen [111].

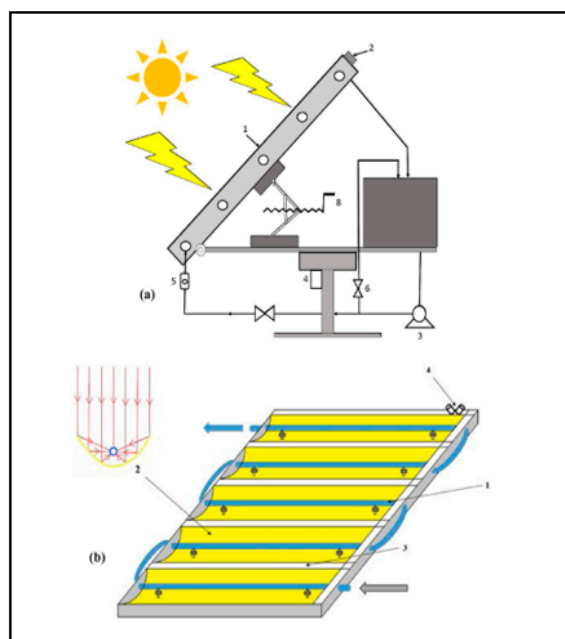
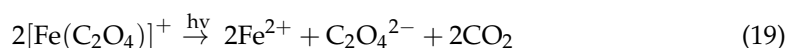


**Figure 4.** (a) The used solar photoreactor setup. (1) the surface of solar reactor, (2) light sensor, (3) recycle pump, (4) electromotor for rotation, (5) flow meter, (6) flow recycle valves, (7) storage tank, (8) and dynamic Jack. (b). The surface of the solar reactor; (1) quartz tubes, (2) parabolic polished aluminum reflector sheets, (3) Wind crossing paths, and (4) light sensor (Reprinted with permission from ref. [111]. Copyright 2020 Elsevier).



The ability to utilize solar radiation represents massive conservation from the energetic perspective, given that there is no necessity to utilize lamps. The progress of pilot plants for treating the wastewater that utilizes solar reactors used to the AOPs has been one of the major aims of study in the field [13,103].

The application of Fenton and photo-Fenton processes in the wastewater treatment process was studied by Giwa et al. [102] who use ferrioxalate as an iron source to analyze and reduce various wastewaters components, including BTEX and pentachlorophenol. Applying the photo-Fenton method has contrasted with additional photodegradation methods. Depending on the utilization of energy, the outcomes revealed that the method was above 30 times more effective than the  $\text{UV}/\text{H}_2\text{O}_2$  and  $\text{UV}/\text{Fe}^{2+}/\text{H}_2\text{O}_2$  methods. Therefore, the authors determined that the method utilizing ferrioxalate needs less electric energy compared to the  $\text{UV}/\text{H}_2\text{O}_2$  process, leading to a decrease in the treatment costs.

The photo-Fenton method was applied to reduce the existing hydrocarbons in the produced wastewater synthesized using gasoline oil to mimic the water generated from oil industries in oil production fields that include dissolved salts with great amounts. It was noticed that the existence of NaCl (salts) prohibit the total degradation of contaminants. This was attained in the assessments without adding any amount of salt to the prepared wastewater [112]. The researchers assigned this impact to  $\text{Fe}^{3+}$  ions that reacted with  $\text{Cl}^-$  ions producing  $\text{FeCl}_2^+$  composites, which, in the existence of UV radiation, can provide an

increase to  $\text{Cl}_2^{\bullet -}$  radicals with smaller oxidation potential compared to  $\text{HO}^{\bullet}$  radicals, thus decreasing the productivity of the method. Fenton and photo-Fenton methods oxidation potential were examined to reduce different contaminants in the solution, including BTX and water polluted with gasoline including ethanol with a percentage of 25%. The degradation of prompt BTX composites was noted, along with the creation of transitional phenolic complexes in the primary reaction times that were degraded with 30 min of reaction. About 75% of total hydrocarbons introduced in gasoline-polluted water were removed and degraded, and the BTX composites were eliminated in the initial reaction mins (when phenolic composites were produced), after which they degraded sluggishly [113].

The impact of the photo-Fenton process in degrading phenol composites was examined by Brillas et al. 2020, which is an extremely popular contaminant in petrochemical production utilizing black light fluorescent lights as a source of UV-A emission. These are not expensive and are more efficient from the energy use perspective in comparison to medium-pressure mercury vapor lights. The effectiveness of black light fluorescent lamps was verified when compared to the degradation of phenol applying dark Fenton and photo-Fenton methods. The rate of degradation was twice as high when applying the photo-Fenton method. The degradation rate of phenol improved when the intensity of the radiation emission source increased, due to the increase in  $\text{Fe}^{2+}$  ion production (Equation (17)) [114]. Thus, this then increased the number of  $\text{HO}^{\bullet}$  radicals that were produced. These studies showed that the analysis of this factor is crucial as it facilitates the construction of the reactor that utilizes lamps as a source of UV radiation, which is essential for continuous wastewater treatment. This cannot be achieved by solar reactors only, which indicates that they are just used in cases of sunlight availability.

The application of the photo-Fenton method for the treatment of wastewater including diesel oil was examined by Hassan and his colleagues (2020). They performed research to enhance the number of chemicals utilized and to attain high degradation rates using a lesser number of chemicals. It was found that, by utilizing a small concentration of 0.1 mM  $\text{Fe}^{2+}$  ion, the rate of degradation of the organic composites existing in the wastewater was 90% classified as total organic carbon (TOC) [115]. The photo-Fenton method needs to be efficient from the commercial approach below these operating conditions, as it does not need successive treatment to eliminate the remaining iron. Besides, the degraded acid that exists in the wastewater from oil processing plants includes emulsified oil and a sequence of small-biodegradability micro contaminants, for example sulfides, phenols, ammonia, and mercaptans using different advanced oxidation process (AOP) methods.

Among the methods studied, Fenton and photo-Fenton achieved the most significant findings. The reaction of the dark Fenton process was applied until reaction stagnation with a separation efficiency for initial dissolved organic carbon (DOC) of only 27%, supported with the photo-Fenton method using UV radiation. The use of both methods together utilized constantly decreased the preliminary amount of DOC with a high percentage (more than 90%). The BTEX contaminants existing in the initial wastewater were eliminated to non-measurable amounts. The studies confirmed that the two methods were effective in eliminating contaminants from wastewater, but by utilizing high amounts of chemicals. They confirm that there is a need for optimizing the processes to decrease the number of chemicals used and thus increasing the efficiency of the process [116].

The productivity of Fenton chemicals in mineralizing organic complexes existing in water polluted with crude oil was also examined. The process was evaluated by observing the  $\text{H}_2\text{O}_2$  using spectrophotometric analysis and via the  $\text{CO}_2$  titrimetric quantification which allowed researchers to determine the level of mineralized TOC. These assessments indicated a 75% decrease in the initial TOC volume of water polluted by petroleum oil [117]. The efficiencies of the Fenton and photo-Fenton methods in the treatment of petroleum wastewater are summarized in Table 5.

Table 5. The efficiencies of Fenton and Photo-Fenton methods in the treatment of petroleum wastewater.

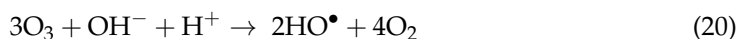
No	Method	Parameter	Removal Efficiency (%)	pH	H <sub>2</sub> O <sub>2</sub> (ppm)	Fe <sup>2+</sup> (ppm)	Ratio of H <sub>2</sub> O <sub>2</sub> :Fe <sup>2+</sup>	Reaction Time (min)	Ref
1	H <sub>2</sub> O <sub>2</sub> /Fe <sup>2+</sup> /solar	TOC	84	2	1	0.08	12.5	300	Aljuboury et al. 2017
2	H <sub>2</sub> O <sub>2</sub> /Fe <sup>2+</sup>	COD/ TOC	56 COD 54 TOC	4.3	9.7	1.1	8.8	120	Edison et al. 2019
3	H <sub>2</sub> O <sub>2</sub> /Fe <sup>2+</sup> /UV	COD	92	3	110	35	3.14	92	Majed et al. 2020
4	H <sub>2</sub> O <sub>2</sub> /Fe <sup>2+</sup> /solar	COD	84	3.2	200	1.5	133	180	Asaithambi et al. 2017
5	H <sub>2</sub> O <sub>2</sub> /Fe <sup>3+</sup>	TOC	90	3	500	250	2	120	Deng et al. 2017
6	H <sub>2</sub> O <sub>2</sub> /Fe <sup>2+</sup> /UV	COD	72	5.6	17.86	1.76	10.14	70	Shokri et al. 2019
7	H <sub>2</sub> O <sub>2</sub> /Fe <sup>3+</sup> /TiO <sub>2</sub>	COD	69.6	3	1600	30	53	60	Hassan 2018
8	H <sub>2</sub> O <sub>2</sub> /Fe <sup>2+</sup> /UV	COD	76.8	3	250	40	6.25	30	Tufaner 2020

Table 5 shows the efficiencies of the Fenton and photo-Fenton process in the treatment of petroleum refinery wastewater and the separation of different contaminants including TOC and COD compounds. The studies showed that, at different conditions including the pH, reaction time, and H<sub>2</sub>O<sub>2</sub> concentration, Fe<sup>+2</sup> concentrations under both processes were effective in eliminating contaminants from the wastewater but utilizing high amounts of reagents.

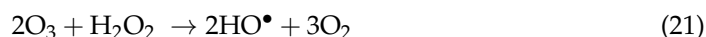
#### 5.4. Ozone Based AOPs and Their Application in Petroleum Wastewater Treatment

The use of ozone (O<sub>3</sub>) has been extensively applied to eliminate undesirable organic pollutants in both purification of drinking water and wastewater treatment [118]. Ozone (O<sub>3</sub>) is a selective oxidant that reacts with electron-rich organic compounds at a high reaction rate constant (kO<sub>3</sub>, pH7 > 105 M<sup>-1</sup> s<sup>-1</sup>) [119,120]. Hydroxyl radical (OH•) produced from the consumption of O<sub>3</sub> is a nonselective oxidant, which quickly reacts with several organic composites at closely controlled rates of diffusion [121].

The creation of radicals, for example the superoxide radical (O<sup>2-</sup>•) and hydroxyl radical (HO•), happens when ozone is combined with water, via a complicated series of reactions. The ozone degeneration rate in water is improved at a greater pH [122]. The reaction integration with HO• and molecular ozone produces the oxidation of the organic compound.



The ozone decomposition cycle can be improved by adding hydrogen peroxide (H<sub>2</sub>O<sub>2</sub>) to cause the creation of HO• [123]. H<sub>2</sub>O<sub>2</sub>, to some extent, separates in water to generate the hydroperoxide ion. These HO<sup>2-</sup> ions react with the O<sub>3</sub>, promptly generating the HO•. In brief, the reactions integration results in the next equation:



Different parameters determine the performance of the process including the contact time, water alkalinity, and ozone concentrations. By presenting hydrogen peroxide (H<sub>2</sub>O<sub>2</sub>) when the highly reactive materials oxidized with O<sub>3</sub>, it improves the degradation rate. The ozonation method using H<sub>2</sub>O<sub>2</sub>/O<sub>3</sub> systems was found to be the greatest proper AOP method in the purification of water in comparison to other technologies of AOPs. Therefore, there is a discipline-verified operation history in the application of H<sub>2</sub>O<sub>2</sub>/O<sub>3</sub> techniques. Another approach to accelerate ozonation is by utilizing catalysts (homogenous or heterogeneous). Research has been conducted with several metal ions, and metal oxides have demonstrated considerable variations in decomposition, but just in certain situations. The amount of ozone in the inlet gas and the ozone process time have been deemed as major parameters to develop the degradation rate. The research of oxidation has been conducted on numerous organic pollutants utilizing TiO<sub>2</sub>, Fe<sub>2</sub>O<sub>3</sub>, Mn<sup>2+</sup>, MnO<sub>2</sub>, Fe<sup>2+</sup>, and Fe<sup>3+</sup>. The system of ozone/catalyst was found to be more efficient for the COD and TOC reduction, and ozone oxidation only at a high pH [124]. In the tests conducted with [125,126], it was noticed that the chemical decomposition is successfully enhanced with the synergistic impact of photocatalytic reactions happening on TiO<sub>2</sub>-photocatalyst. The experimental setup of the photoreactor is shown in Figure 5 [126].



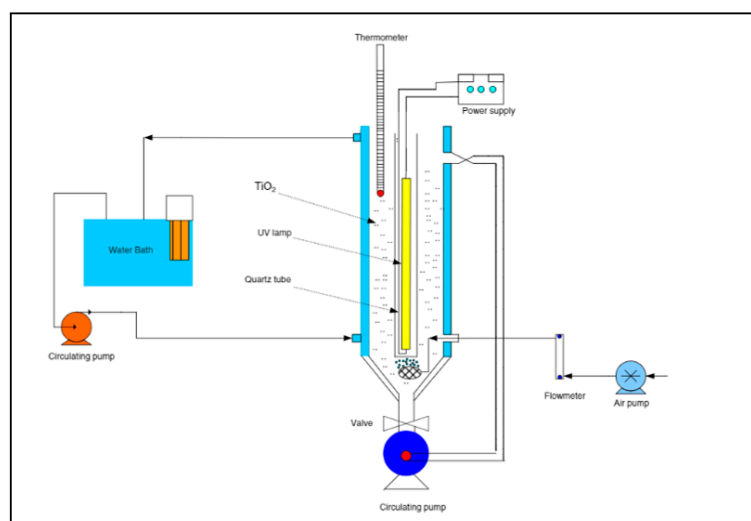
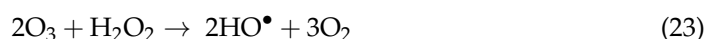
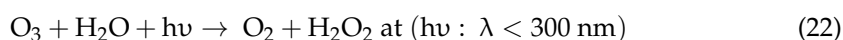


**Figure 5.** The experimental set up of photoreactor (Reprinted with permission from ref. [126]. Copyright 2012 Elsevier).

The ozone process can also be improved through the decomposition of ozone with direct absorption via UV radiation ( $\lambda = 254 \text{ nm}$ ) which produces  $\text{H}_2\text{O}_2$  as a transitional and then decomposes to  $\text{HO}\bullet$  radicals. The reactions shown in Equations (22) and (23) demonstrate the photolysis of ozone to produce  $\text{H}_2\text{O}_2$ , which leads to the creation of a very reactive  $\text{HO}\bullet$  radical [127]. Though numerous oxidation methods can damage and eliminate organic pollutants,  $\text{HO}\bullet$  is the main separation method.



This technique includes all the mechanisms of organic degradation via  $\text{O}_3/\text{UV}$ ,  $\text{H}_2\text{O}_2/\text{O}_3$  and  $\text{H}_2\text{O}_2/\text{UV}$ ,  $\text{O}_3/\text{Fenton}$ , catalytic ozonation ( $\text{O}_3/\text{Metal oxide}$ ), and photocatalytic ozonation, etc. [125]. The detailed steps of the mechanism of organic degradation of wastewater contaminants through  $\text{O}_3/\text{UV}$  are described in Figure 6. It is more efficient to separate organic materials than applying UV or  $\text{O}_3$  separately, and it is an additional effective means of producing  $\text{HO}\bullet$  in comparison to the  $\text{UV}/\text{H}_2\text{O}_2$  technique at the same oxidant dosages [128,129]. However, this procedure is costly and energy-intensive [130]. Moreover, ozone techniques have the possibility to create bromate [131,132]. Inhibiting composites can influence the absorption of UV radiation, therefore decreasing the effectiveness of the method. Nevertheless, this difficulty will be lessened by increasing the ratio between the  $\text{H}_2\text{O}_2$  and  $\text{O}_3$ , decreasing the pH, or increasing the hydroxyl radical amount [133,134]. In addition, it is found that the absorption of UV radiation by  $\text{O}_3$  was affected by the turbidity. The ozone production energy costs are the major operating expenses for this procedure. The existence of carbonate or bicarbonate may behave as hunters of the hydroxyl radical in normal structures which is an additional problem of these methods [135]. The usage of AOPs with ozone has more industrial uses in water treatment in comparison to all other AOPs. The method of ozone has been utilized to handle the petroleum refineries wastewater pollution.

A study conducted by [136] on the biochemical wastewater sewage treatment plant uses a combination of  $\text{O}_3/\text{UV}$  advanced oxidation process. The authors showed that the major parameters affecting the efficiency of the  $\text{UV}/\text{O}_3$  process were the efficient  $\text{O}_3$  distribution means, monitoring of the comparative pressure in the reactor, the ratio of ozone added, and UV radiation intensity. Cruz and his workers named the ozone concentration that consumes reactions with the initiator's composites as the ozone dose line, beyond which the addition of  $\text{H}_2\text{O}_2$  rises the rate of  $\text{HO}\bullet$  production. The authors

noticed that, in the case of  $\text{H}_2\text{O}_2$  addition, ozonation does not have much effect on the exposure of  $\text{HO}\bullet$  until the concentrations become more than the threshold ozone dosages used [137,138]. It was noted that the usage of a homogeneous reactor allows the quick and high formation of the radical species directly in the bulk liquid without any movement and mass transfer limits in comparison to a classical gas–liquid reactor, whereby the oxidation of the contaminants through hydroxyl radicals could be restricted via their transportation from the liquid phase to the interface as these radicals are extensively reactive and do not disperse in the solution [139]. The study carried out by Meshref et al. [140] on the identification and monitoring of the volatile organic compounds (VOCs) presents that the effluent’s wastewater showed 43% and 34% of COD and BOD reduction, respectively, resulting in an effective AOP process for VOCs degradation [141]. It also showed that, at certain ozone concentrations between 0.5–1.5 mg  $\text{O}_3$ /mg dissolved organic carbon, the efficiencies of removing the contaminants increased up to ~14–18% in groundwater, above 6–10% in surface water, and insignificantly in secondary effluent through the  $\text{O}_3/\text{H}_2\text{O}_2$  treatment in comparison to the conventional ozonation method.

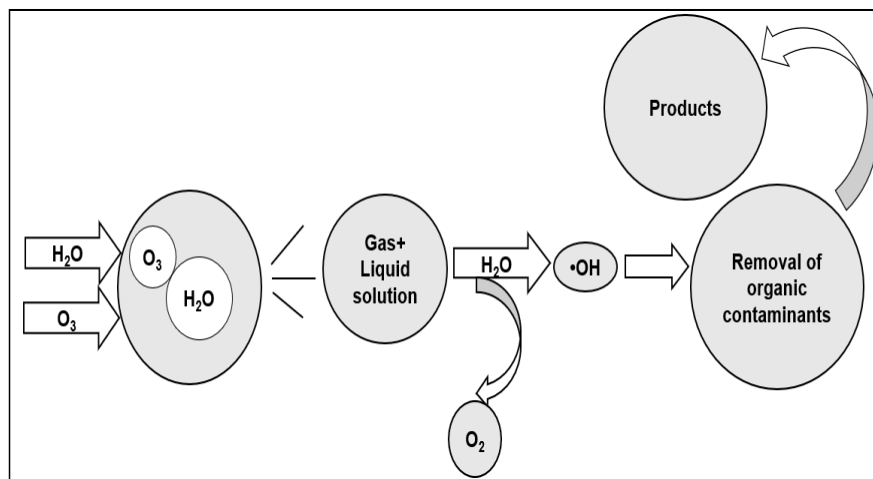


**Figure 6.** The detailed steps of the mechanism of organic degradation through the  $\text{O}_3/\text{UV}$  method.

## 6. Integrated AOP Processes

In recent years, AOP methods have been extensively used for the treatment of petroleum wastewater applying different types of AOP methods. A combination of AOPs methods and additional conventional methods for wastewater treatment have been confirmed to be more efficient for the treatment of contaminated industrial wastewater sources efficiently. The selection means of these methods rely on the waste stream properties, environmental policies, and the cost.

AOPs were integrated with biological methods and other different processes to increase the efficiency of the AOP process in the degradation and separation of contaminants. Biological treatment methods include the decomposition of every residual oil, the degradation of organic composites, the breaking of organic contaminants, the removal of trace metals and nutrients, etc. [4,142]. Various methods of biological treatment have been effective in treating petroleum refinery wastewater. Between them, the activated sludge process (ASP) is the most biological of treatment methods used [143]. Ebrahimi et al. and Jain et al. [31,144] noticed a COD separation effectiveness ranging from 70–80% through the treatment of petroleum refinery wastewater utilizing ASP integrated with the AOP methods. A comparatively greater COD separation efficiency of 96% was achieved by Mirbagheri et al. [145], which was reported for the great synthetic aeration generated in the method. The integration of binary or extra-biological methods or the combination of the biological method with membrane-based AOP techniques were also found to be an efficient method for wastewater treatment. The study carried out by [146] combined an expanded granular sludge bed bioreactor (EGSB-BR) with an ASP-based AOP for petroleum

wastewater treatment, with a COD of 4600–5300 mg/L, which achieved a decrease in COD of 85% after a 62.8 h retention time. An application of biological-AOP was carried out by Razavi et al. [147], utilizing hollow fiber membrane bioreactors (HF-MBR) for the treatment of refinery effluent and attaining a COD separation of 82% after a 36 h retention time. The research reported by El-Naas et al. [148] utilized the anaerobic baffled reactor (ABR) for the treatment of produced water including heavy oil by applying a biological-based advanced oxidation process. The removal efficiency of 65% and 88% were then attained for heavy oil and oil and grease, respectively. The study reported by [149] examined the feasibility of combined electrocoagulation and membrane process. The combination of electrocoagulation and membrane filtration methods was used with integrated intelligent automation and process optimization in the structure of a mobile treatment platform (Figure 7). Up to 95% of oil, TOC, COD, TSS, and turbidity in produced water could be removed. The system could also effectively remove about 90% of ions, including chloride, sulfate, sodium, calcium, manganese, etc.

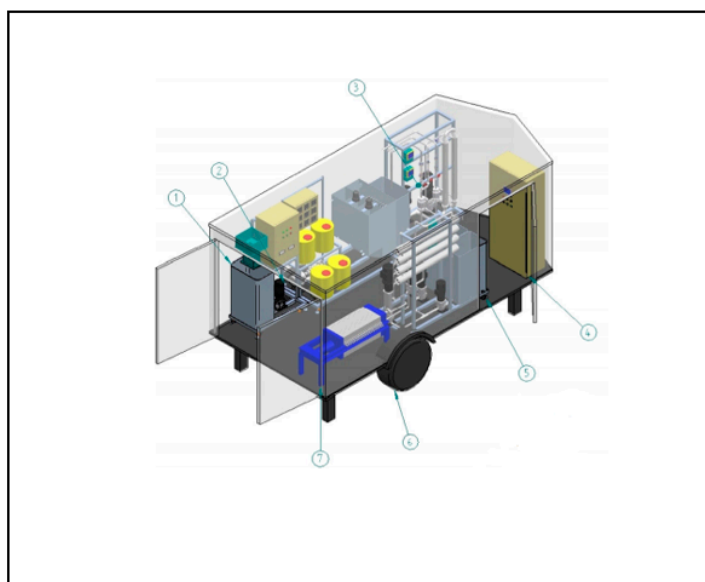


**Figure 7.** The integrated mobile system for oilfield produced water treatment. (1) EC equipment; (2) reaction/sedimentation equipment; (3) UF membrane unit; (4) controller; (5) RO unit; (6) trailer platform; (7) pressure filter (Reprinted with permission from ref. [147]. Copyright 2017 Elsevier).

However, most of these procedures generate a huge quantity of sludge, trained staff, and frequent maintenance. Certain methods also require extremely high hydraulic retention time (HRT), which is an essential drawback to the Bio-AOP techniques.

Another integrated advanced oxidation process was reported by [150]. They joined photo-bioreactors (PBR) with conventional oxic/anoxic methods for the treatment of petrochemical wastewater with an insignificant COD concentration of 312.8 mg/L and attained a separation rate of 71% using an electrocoagulation-based AOP method. A high concentration of petrochemical water with COD values in the range 3600–5300 mg/L was reduced and a separation rate of 97% was achieved in a spouted bed bioreactor (SBBR) with a packed activated carbon treatment (PACT) and an electrocoagulation cell (EC). There are several studies in integrating other AOPs, for example integration of photocatalysis and ultrasound [151], ozonation and ultrasound integration [152], the integration of Fenton, and photo-Fenton processes with ultrasound [153]. Fernandes et al. [151] showed that the integration of photocatalytic and electrochemical processes achieved a high degradation rate compared to the photocatalytic AOP process alone. The major factor in the integration methods to assess the efficiency of the system is the synergetic impact. The synergetic impact is a factor that indicates the development in the degradation of organic compounds below the integrated process. In general, the studies found that the integration of ad-

vanced oxidation technology with other methods is simple, effective, and economic for the treatment of wastewater, except when employing biological methods. The biological process is uncommon due to the creation of hydroxyl radicals throughout the AOPs which can negatively affect the biomass. Furthermore, the existence of  $H_2O_2$  is also toxic to microorganisms. Consequently, it is better to utilize the integrated procedure in the AOP part to improve biodegradability and oxidation in a short time.

AOP-bioremediation is a new type of integrated method applied for industrial wastewater to separate micropollutants. The AOP-bioremediation integrated process concentrates on the treatment of petroleum industrial wastewater including bio-resistant pollutants. The combined two-step process has been studied, partially owing to the capability of AOPs for the degradation of these toxic pollutants to biodegradable compounds [103]. However, the recent literature from the last two years has indicated that the feasible application of the integrated process might be difficult, owing to the variety of potential effluent properties, operating conditions, and design structures. Consequently, the integrated process of AOPs with bioremediation has been recently studied for wastewater treatment [154].

AOP methods were also combined with the membrane (membrane-based AOP) as an innovative technique for the degradation of pollutants in the wastewater. This method is strongly related to the photocatalytic process which utilizes semiconductor catalysts [155,156]. A membrane gives an extra advantage of filtration. [157] This explains the mechanism of the process where the nanoparticle catalysts are inserted and dispersed in the reactor suspension in the form of soluble particles, and where the membrane performs as a barrier for the photocatalyst particles, i.e., the particles are settled inside or on membrane surface. The combination of photocatalyst nanoparticles is predictable to develop the quality of the permeate via the reduction oxidation process which generated active radicals to degrade the pollutants.

## 7. Knowledge Gaps and Future Perspectives

Hydrocarbon existing in petroleum are categorized as important contaminants. The contaminants which are introduced in wastewater of the petroleum industry can be efficiently removed by utilizing various techniques. Studies on the review of new techniques with the least environmental and economic impact showed that it is a research focus field. This review concentrates on reviewing AOP methods applied for petroleum wastewater treatment produced with the activities of the petroleum industry. The wastewater produced by the petroleum industry includes several harmful materials, for example xylene, toluene, ethylbenzene, benzene, phenols, polycyclic aromatic hydrocarbons (PAHs), etc. It is extremely challenging to immediately separate the contaminants through applying a single technique, especially biological treatment, which is deemed as a green method. Therefore, advanced oxidation process treatments in integration with other treatment techniques are needed. It has been described that the combination of different methods could provide greater outcomes more than a single process utilized for oily wastewater treatment. However, understanding the concept of technology combination is still at its initial stages which require to be investigated by scientists. The latest improvements in the process are mainly more costly, and need maintenance and long time. Future techniques require simple operation techniques which are appropriate for the petroleum industry and other different industries. A massive volume of solid and liquid waste is generated, owing to the activities of the petroleum industry. Controlling and treating the produced waste is currently a significant problem in any country. Owing to the increase in wastewater production, appropriate removal, treatment, and recycling are presenting extra problems, as treatment and disposal are extremely expensive. In addition, waste recovery is developing as a focus research field since it presents sustainability of the environment and social possibilities. Several studies are concentrating on the recovery of several supplies produced by human activities, for example energy, bio-products, metals, and oil from wastewater. Significant pollutants are introduced in petroleum industrial wastewaters, which can be considered as resources after recovery. Effective resource recovery and recycle can generate green life, while, on the other hand, it can help in developing economy through decreasing waste and enhance

environmental health and recovery cost. Consequently, there is a necessity to recover and recycle the produced waste from petroleum industry activities in an effective way. Viable treatment methods to generate less contaminated products generate a new approach for the sustainability of the environment and economy. To enhance the development of the petroleum wastewater industry, there is a necessity to create sustainable techniques such as AOP processes. The development of AOP methods can open up new chances for the market and attain effective application of resources.

Moreover, these technologies are favorable and valuable methods where toxic compounds are efficiently degraded and separated from the wastewater. Therefore, these methods were assessed at a pilot scale. Different combination with other types of studied AOP were studied at highly recyclable catalysts to evaluate the treatment efficiency of the wastewater before discharged with no hazardous impacts to the environment. In addition to the future studies on this method at pilot scale treatment unit, the studies must also contain the application of accessible AOPs based on modified catalysts, for example titanium dioxide, with an improvement in the process efficiency in visible light, following that a remarkable decrease in the process costs related to the energy consumption. However, the difference between the catalyst costs (modified catalysts) and energy costs for other types of AOP methods stays a wide-open case. AOP methods give a green, economic, and efficient methodology for the deep degradation of contaminants from petroleum refinery wastewater. Other future research viewpoints would be targeted near the use of some combined methods with AOP methods, such as fluidized-bed Fenton, fixed bed Fenton processes, etc., which study the competence of electro-Fenton processes for treating petroleum wastewater and identify the reaction kinetics and mechanisms that utilize newly developed catalysts as an effort to enhance the total oxidation productivity.

## 8. Conclusions

Petroleum wastewaters can be handled via the oxidation of chemical and biological treatment methods. There are various harmful components introduced in wastewater produced through the petroleum industry activities. An effective treatment approach should be designed to consider the environment and human health. AOP is one of the techniques which is getting a lot of worldwide concern for cleaning petroleum contaminants such as hydrocarbons. Nevertheless, the combination of different methods provide greater findings more than a single procedure utilized for the treatment of wastewater. The present wastewater treatment methods were concentrated to eliminate the contaminants from wastewaters to match the wastewater release criteria. To settle the risks related to the components of petroleum, an appropriate technique that handles the waste and removes those contaminants from wastewater would be a favorable choice. Recent studies related to the application of advanced oxidation processes (AOPs) in petroleum wastewater treatment that use the latest advanced oxidation types either separately or by combination with reverse to wastewater characteristics for generating non-toxic by-products were presented. A highly comprehensive literature review was presented for comparing the different AOP technologies described in this review, and a discussion about their advantages and disadvantages was also highlighted.

**Author Contributions:** Data curation, W.F.E.; Formal analysis, F.A.; Investigation, B.H.H. and A.Z.A.; Methodology, W.F.E. and B.H.H.; Project administration, F.A. All authors have read and agreed to the published version of the manuscript.

**Funding:** This paper was made possible by the grant provided by Qatar University, International Research Collaboration Co-Fund, Grant number IRCC-2020-011. The statements made herein are solely the responsibility of the authors.

**Conflicts of Interest:** The authors declare no conflict of interest.

## Abbreviation

AOP	Advanced oxidation process
BTEX	Benzene, Toluene, Ethylbenzene Xylene
RFCC	Residual Fluid Catalytic Cracking
UV	Ultraviolet
BOD	Biological oxygen demand
COD	Chemical oxygen demand
PAHs	Polycyclic aromatic hydrocarbons
SBBR	Spouted bed bioreactor
PACT	Packed activated carbon
EC	Electrocoagulation cell
ABR	Anaerobic baffled reactor
ASP	Activated Sludge Process
HF-MBR	Hollow fiber membrane bioreactors
PBR	Photo-bioreactors
EGSB-BR	Expanded granular sludge bed bioreactor
VOCs	Volatile Organic Compounds
TOC	Total organic carbon
O <sub>3</sub>	Ozone
OH•	Hydroxyl radical
O <sup>2-</sup> •	Superoxide radical
H <sub>2</sub> O <sub>2</sub>	Hydrogen peroxide
MnO <sub>2</sub>	Manganese dioxide
Fe <sub>2</sub> O <sub>3</sub>	Iron III oxide
TiO <sub>2</sub>	Titanium dioxide
Fe <sup>2+</sup>	Ferrous iron
Fe <sup>3+</sup>	Ferric iron
Mn <sup>2+</sup>	Manganese
Min	Minute
ppm	Part per million
Ref	Reference
DOC	Dissolved Organic Compounds
C <sub>2</sub> O <sub>4</sub> <sup>2-</sup>	Oxalate ions
MTBE	Methyl tert-butyl ether
mg/L	milligram/litter
g/l	gram/litter
TPH	Total petroleum hydrocarbon
Ppb	Parts per billion
E <sub>0</sub>	Oxidation potential
CHR	Chrysene
BbF	Benzo[b]fluoranthene
USEPA	United States Environmental Protection Agency
VFA	Volatile fatty acids
TDS	Total dissolved solids
TSS	Total suspended solids
DO	Dissolved oxygen
HEM	Hexane Extractable Material
MBAS	Methylene Blue Active Substance
API	American Petroleum Institute
O & G	oil and grease
hr	hour

## References

- Chen, Y.-C. Evaluating greenhouse gas emissions and energy recovery from municipal and industrial solid waste using waste-to-energy technology. *J. Clean. Prod.* **2018**, *192*, 262–269. [CrossRef]
- Zhang, X.; He, W.; Ren, L.; Stager, J.; Evans, P.J.; Logan, B.E. COD removal characteristics in air-cathode microbial fuel cells. *Bioresour. Technol.* **2015**, *176*, 23–31. [CrossRef] [PubMed]

3. Varjani, S.; Kumar, G.; Rene, E.R. Developments in biochar application for pesticide remediation: Current knowledge and future research directions. *J. Environ. Manag.* **2019**, *232*, 505–513. [CrossRef]
4. Jafarinejad, S.; Jiang, S.C. Current technologies and future directions for treating petroleum refineries and petrochemical plants (PRPP) wastewaters. *J. Environ. Chem. Eng.* **2019**, *7*, 103326. [CrossRef]
5. Abdulredha, M.M.; Aslina, H.S.; Luqman, C.A. Overview on petroleum emulsions, formation, influence and demulsification treatment techniques. *Arab. J. Chem.* **2020**, *13*, 3403–3428. [CrossRef]
6. Raza, W.; Lee, J.; Raza, N.; Luo, Y.; Kim, K.-H.; Yang, J. Removal of phenolic compounds from industrial waste water based on membrane-based technologies. *J. Ind. Eng. Chem.* **2019**, *71*, 1–18. [CrossRef]
7. Varjani, S.J. Microbial degradation of petroleum hydrocarbons. *Bioresour. Technol.* **2017**, *223*, 277–286. [CrossRef]
8. Jiménez, S.; Andreozzi, M.; Micó, M.M.; Álvarez, M.G.; Contreras, S. Produced water treatment by advanced oxidation processes. *Sci. Total Environ.* **2019**, *666*, 12–21. [CrossRef]
9. Almomani, F.A.; Shawaqfah, M.; Bhosale, R.R.; Kumar, A. Removal of emerging pharmaceuticals from wastewater by ozone-based advanced oxidation processes. *Environ. Prog. Sustain. Energy* **2016**, *35*, 982–995. [CrossRef]
10. Almomani, F.; Bhosale, R.; Kumar, A.; Khraisheh, M. Potential use of solar photocatalytic oxidation in removing emerging pharmaceuticals from wastewater: A pilot plant study. *Solar Energy* **2018**, *172*, 128–140. [CrossRef]
11. Al Mayyahi, A.; Al-Asadi, H.A.A. Advanced oxidation processes (AOPs) for wastewater treatment and reuse: A brief review. *Asian J. Appl. Sci. Technol.* **2018**, *2*, 18–30.
12. Kilic, M.Y.; Abdelraheem, W.H.; He, X.; Kestioglu, K.; Dionysiou, D.D. Photochemical treatment of tyrosol, a model phenolic compound present in olive mill wastewater, by hydroxyl and sulfate radical-based advanced oxidation processes (AOPs). *J. Hazard. Mater.* **2019**, *367*, 734–742. [CrossRef]
13. Garrido-Cardenas, J.A.; Esteban-García, B.; Agüera, A.; Sánchez-Pérez, J.A.; Manzano-Agugliaro, F. Wastewater treatment by advanced oxidation process and their worldwide research trends. *Int. J. Environ. Res. Public Health* **2020**, *17*, 170. [CrossRef]
14. Lei, J.; Alvarado, J.; Li, H.; Zhu, X.; Tian, Y.; Liang, L. The Advanced Oxidation Processes of Oilfield Wastewater: A Review. In Proceedings of the 4th International Conference on Water Resource and Environment (WRE 2018), Kaohsiung City, Taiwan, 17–21 July 2018.
15. Ikehata, K.; Li, Y. Ozone-based processes. In *Advanced Oxidation Processes for Waste Water Treatment*; Elsevier: Amsterdam, The Netherlands, 2018; pp. 115–134.
16. Silva, P.C.; Ferraz, N.P.; Perpetuo, E.A.; Asencios, Y.J.O. Oil produced water treatment using advanced oxidative processes: Heterogeneous-photocatalysis and photo-Fenton. *J. Sediment. Environ.* **2019**, *4*, 99–107. [CrossRef]
17. Gaurav, G.K.; Yadav, D. Probing the excellence of wastewater PAHs removal approaches: A critical review. *J. Contam. Hydrol.* **2020**, *236*, 103715. [CrossRef]
18. Paździor, K.; Bilińska, L.; Ledakowicz, S. A review of the existing and emerging technologies in the combination of AOPs and biological processes in industrial textile wastewater treatment. *Chem. Eng. J.* **2019**, *376*, 120597. [CrossRef]
19. Wang, B.; Zhang, H.; Wang, F.; Xiong, X.; Tian, K.; Sun, Y.; Yu, T. Application of heterogeneous catalytic ozonation for refractory organics in wastewater. *Catalysts* **2019**, *9*, 241. [CrossRef]
20. Chen, D.; Cheng, Y.; Zhou, N.; Chen, P.; Wang, Y.; Li, K.; Huo, S.; Cheng, P.; Peng, P.; Zhang, R. Photocatalytic degradation of organic pollutants using TiO<sub>2</sub>-based photocatalysts: A review. *J. Clean. Prod.* **2020**, *268*, 121725. [CrossRef]
21. Ani, I.; Akpan, U.; Olutoye, M.; Hameed, B. Photocatalytic degradation of pollutants in petroleum refinery wastewater by TiO<sub>2</sub>-and ZnO-based photocatalysts: Recent development. *J. Clean. Prod.* **2018**, *205*, 930–954. [CrossRef]
22. Azizah, A.N.; Widiada, I.N. *Advanced Oxidation Processes (AOPs) for Refinery Wastewater Treatment Contains High Phenol Concentration*; MATEC Web of Conferences, EDP Sciences: Les Ulis, France, 2018; p. 03012.
23. Lofrano, G.; Pedrazzani, R.; Libralato, G.; Carotenuto, M. Advanced oxidation processes for antibiotics removal: A review. *Curr. Org. Chem.* **2017**, *21*, 1054–1067. [CrossRef]
24. De Oliveira, C.P.M.; Viana, M.M.; Amaral, M.C.S. Coupling photocatalytic degradation using a green TiO<sub>2</sub> catalyst to membrane bioreactor for petroleum refinery wastewater reclamation. *J. Water Process. Eng.* **2020**, *34*, 101093. [CrossRef]
25. Al Momani, F.A.; Shawaqfeh, A.T.; Mo'ayyed, S.S. Solar wastewater treatment plant for aqueous solution of pesticide. *Solar Energy* **2007**, *81*, 1213–1218. [CrossRef]
26. Al Momani, F.; Gonzalez, O.; Sans, C.; Esplugas, S. Combining photo-Fenton process with biological sequencing batch reactor for 2, 4-dichlorophenol degradation. *Water Sci. Technol.* **2004**, *49*, 293–298. [CrossRef] [PubMed]
27. Mohammadi, L.; Rahdar, A.; Bazrafshan, E.; Dahmardeh, H.; Susan, M.; Hasan, A.B.; Kyzas, G.Z. Petroleum Hydrocarbon Removal from Wastewaters: A Review. *Processes* **2020**, *8*, 447. [CrossRef]
28. Jiménez, S.; Micó, M.; Arnaldos, M.; Medina, F.; Contreras, S. State of the art of produced water treatment. *Chemosphere* **2018**, *192*, 186–208. [CrossRef]
29. Lusnier, N.; Seyssiecq, I.; Sambusiti, C.; Jacob, M.; Lesage, N.; Roche, N. A comparative study of conventional activated sludge and fixed bed hybrid biological reactor for oilfield produced water treatment: Influence of hydraulic retention time. *Chem. Eng. J.* **2020**, *420*, 127611. [CrossRef]
30. Ye, H.; Liu, B.; Wang, Q.; How, Z.T.; Zhan, Y.; Chelme-Ayala, P.; Guo, S.; El-Din, M.G.; Chen, C. Comprehensive chemical analysis and characterization of heavy oil electric desalting wastewaters in petroleum refineries. *Sci. Total Environ.* **2020**, *724*, 138117. [CrossRef]

31. Jain, M.; Majumder, A.; Ghosal, P.S.; Gupta, A.K. A review on treatment of petroleum refinery and petrochemical plant wastewater: A special emphasis on constructed wetlands. *J. Environ. Manag.* **2020**, *272*, 111057. [CrossRef]
32. Rodriguez, A.Z.; Wang, H.; Hu, L.; Zhang, Y.; Xu, P. Treatment of Produced Water in the Permian Basin for Hydraulic Fracturing: Comparison of Different Coagulation Processes and Innovative Filter Media. *Water* **2020**, *12*, 770. [CrossRef]
33. Olajire, A.A. Recent advances on the treatment technology of oil and gas produced water for sustainable energy industry—Mechanistic aspects and process chemistry perspectives. *Chem. Eng. J. Adv.* **2020**, *4*, 100049. [CrossRef]
34. Sun, Y.; Liu, Y.; Chen, J.; Huang, Y.; Lu, H.; Yuan, W.; Yang, Q.; Hu, J.; Yu, B.; Wang, D. Physical pretreatment of petroleum refinery wastewater instead of chemicals addition for collaborative removal of oil and suspended solids. *J. Clean. Prod.* **2021**, *278*, 123821. [CrossRef]
35. Nanda, S.; Berruti, F. A technical review of bioenergy and resource recovery from municipal solid waste. *J. Hazard. Mater.* **2020**, *403*, 123970. [CrossRef] [PubMed]
36. Bustillo-Lecompte, C.F.; Kakar, D.; Mehrvar, M. Photochemical treatment of benzene, toluene, ethylbenzene, and xylenes (BTEX) in aqueous solutions using advanced oxidation processes: Towards a cleaner production in the petroleum refining and petrochemical industries. *J. Clean. Prod.* **2018**, *186*, 609–617. [CrossRef]
37. Kuppasamy, S.; Maddela, N.R.; Megharaj, M.; Venkateswarlu, K. An Overview of Total Petroleum Hydrocarbons. In *Total Petroleum Hydrocarbons*; Springer: Berlin/Heidelberg, Germany, 2020; pp. 1–27.
38. Thakur, C.; Srivastava, V.C.; Mall, I.D.; Hiwarkar, A.D. Mechanistic Study and Multi-Response Optimization of the Electrochemical Treatment of Petroleum Refinery Wastewater. *CLEAN—Soil Air Water* **2018**, *46*, 1700624. [CrossRef]
39. Al-Hawash, A.B.; Dragh, M.A.; Li, S.; Alhujaily, A.; Abbood, H.A.; Zhang, X.; Ma, F. Principles of microbial degradation of petroleum hydrocarbons in the environment. *Egypt. J. Aquat. Res.* **2018**, *44*, 71–76. [CrossRef]
40. Putatunda, S.; Bhattacharya, S.; Sen, D.; Bhattacharjee, C. A review on the application of different treatment processes for emulsified oily wastewater. *Int. J. Environ. Sci. Technol.* **2019**, *16*, 2525–2536. [CrossRef]
41. Varjani, S.J.; Joshi, R.R.; Kumar, P.S.; Srivastava, V.K.; Kumar, V.; Banerjee, C.; Kumar, R.P. Polycyclic aromatic hydrocarbons from petroleum oil industry activities: Effect on human health and their biodegradation. In *Waste Bioremediation*; Springer: Berlin/Heidelberg, Germany, 2018; pp. 185–199.
42. Varjani, S.J.; Gnansounou, E.; Pandey, A. Comprehensive review on toxicity of persistent organic pollutants from petroleum refinery waste and their degradation by microorganisms. *Chemosphere* **2017**, *188*, 280–291. [CrossRef] [PubMed]
43. Zainab, S.M.; Junaid, M.; Xu, N.; Malik, R.N. Antibiotics and antibiotic resistant genes (ARGs) in groundwater: A global review on dissemination, sources, interactions, environmental and human health risks. *Water Res.* **2020**, *187*, 116455. [CrossRef]
44. Chowdhary, P.; Bharagava, R.N.; Mishra, S.; Khan, N. Role of industries in water scarcity and its adverse effects on environment and human health. In *Environmental Concerns and Sustainable Development*; Springer: Berlin/Heidelberg, Germany, 2020; pp. 235–256.
45. Schweitzer, L.; Noblet, J. Water contamination and pollution. In *Green Chemistry*; Elsevier: Amsterdam, The Netherlands, 2018; pp. 261–290.
46. Armstrong, T.; Khursigara, A.J.; Killen, S.S.; Fearnley, H.; Parsons, K.J.; Esbaugh, A.J. Oil exposure alters social group cohesion in fish. *Sci. Rep.* **2019**, *9*, 1–9.
47. Sharma, S.; Chatterjee, S. Microplastic pollution, a threat to marine ecosystem and human health: A short review. *Environ. Sci. Pollut. Res.* **2017**, *24*, 21530–21547. [CrossRef] [PubMed]
48. Mojiri, A.; Zhou, J.L.; Ohashi, A.; Ozaki, N.; Kindaichi, T. Comprehensive review of polycyclic aromatic hydrocarbons in water sources, their effects and treatments. *Sci. Total Environ.* **2019**, *696*, 133971. [CrossRef] [PubMed]
49. Li, J.; Luo, C.; Song, M.; Dai, Q.; Jiang, L.; Zhang, D.; Zhang, G. Biodegradation of phenanthrene in polycyclic aromatic hydrocarbon-contaminated wastewater revealed by coupling cultivation-dependent and-independent approaches. *Environ. Sci. Technol.* **2017**, *51*, 3391–3401. [CrossRef] [PubMed]
50. Zango, Z.U.; Sambudi, N.S.; Jumbri, K.; Ramli, A.; Abu Bakar, N.H.H.; Saad, B.; Rozaini, M.N.H.; Isiyaka, H.A.; Osman, A.M.; Sulieman, A. An Overview and Evaluation of Highly Porous Adsorbent Materials for Polycyclic Aromatic Hydrocarbons and Phenols Removal from Wastewater. *Water* **2020**, *12*, 2921. [CrossRef]
51. Mustapha, H.I.; van Bruggen, H.J.J.A.; Lens, P.N. Vertical subsurface flow constructed wetlands for the removal of petroleum contaminants from secondary refinery effluent at the Kaduna refining plant (Kaduna, Nigeria). *Environ. Sci. Pollut. Res.* **2018**, *25*, 30451–30462. [CrossRef]
52. Saleem, H.; Rehman, K.; Arslan, M.; Afzal, M. Enhanced degradation of phenol in floating treatment wetlands by plant-bacterial synergism. *Int. J. Phytoremediation* **2018**, *20*, 692–698. [CrossRef]
53. Kottuparambil, S.; Kim, Y.-J.; Choi, H.; Kim, M.-S.; Park, A.; Park, J.; Shin, W.; Han, T. A rapid phenol toxicity test based on photosynthesis and movement of the freshwater flagellate, *Euglena agilis* Carter. *Aquat. Toxicol.* **2014**, *155*, 9–14. [CrossRef] [PubMed]
54. Li, J.; Li, F. Polycyclic aromatic hydrocarbons in the Yellow River estuary: Levels, sources and toxic potency assessment. *Mar. Pollut. Bull.* **2017**, *116*, 479–487. [CrossRef]
55. Badibostan, H.; Feizy, J.; Daraei, B.; Shoeibi, S.; Rajabnejad, S.H.; Asili, J.; Taghizadeh, S.F.; Giesy, J.P.; Karimi, G. Polycyclic aromatic hydrocarbons in infant formulae, follow-on formulae, and baby foods in Iran: An assessment of risk. *Food Chem. Toxicol.* **2019**, *131*, 110640. [CrossRef]



56. Shaikh, S.S.; Abu-Dieyeh, M.H.; Al Naemi, F.A.; Ahmed, T.; Al-Ghouti, M.A. environmental impact of utilization of “produced water” from oil and gas operations in turfgrass systems. *Sci. Rep.* **2020**, *10*, 1–13. [CrossRef]
57. Njoku, L.; Okporuanefe, F.; Ude, E. *Responses of Accessions of Zea Mays to Crude Oil Pollution Using Growth Indices and Enzyme Activities As Markers*; University of Lagos: Lagos, Nigeria, 2018.
58. Sathasivam, M.; Shanmugapriya, S.; Yogeshwaran, V.; Priya, A. Industrial waste water treatment using advanced oxidation process—A review. *Int. J. Eng. Adv. Technol.* **2019**, *8*, 485–488.
59. Cao, J.; Yang, J.; Yue, K.; Wang, Z. Preparation of modified citrus pectin (MCP) using an advanced oxidation process with hydroxyl radicals generated by UV-H<sub>2</sub>O<sub>2</sub>. *Food Hydrocoll.* **2020**, *102*, 105587. [CrossRef]
60. Li, D.; Sun, T.; Wang, L.; Wang, N. Enhanced electro-catalytic generation of hydrogen peroxide and hydroxyl radical for degradation of phenol wastewater using MnO<sub>2</sub>/Nano-Gl Foam-Ni/Pd composite cathode. *Electrochim. Acta* **2018**, *282*, 416–426. [CrossRef]
61. Yang, Y.; Hoffmann, M.R. Synthesis and stabilization of blue-black TiO<sub>2</sub> nanotube arrays for electrochemical oxidant generation and wastewater treatment. *Environ. Sci. Technol.* **2016**, *50*, 11888–11894. [CrossRef] [PubMed]
62. Rostam, A.B.; Taghizadeh, M. Advanced oxidation processes integrated by membrane reactors and bioreactors for various wastewater treatments: A critical review. *J. Environ. Chem. Eng.* **2020**, *8*, 104566. [CrossRef]
63. Qu, R.; Li, C.; Liu, J.; Xiao, R.; Pan, X.; Zeng, X.; Wang, Z.; Wu, J. Hydroxyl radical based photocatalytic degradation of halogenated organic contaminants and paraffin on silica gel. *Environ. Sci. Technol.* **2018**, *52*, 7220–7229. [CrossRef] [PubMed]
64. Ghanbari, F.; Khatebasreh, M.; Mahdavianpour, M.; Lin, K.-Y.A. Oxidative removal of benzotriazole using peroxymonosulfate/ozone/ultrasound: Synergy, optimization, degradation intermediates and utilizing for real wastewater. *Chemosphere* **2020**, *244*, 125326. [CrossRef]
65. Dutta, V.; Sharma, S.; Raizada, P.; Hosseini-Bandegharaei, A.; Gupta, V.K.; Singh, P. Review on augmentation in photocatalytic activity of CoFe<sub>2</sub>O<sub>4</sub> via heterojunction formation for photocatalysis of organic pollutants in water. *J. Saudi Chem. Soc.* **2019**, *23*, 1119–1136.
66. Abdelraheem, W.H.; Nadagouda, M.N.; Dionysiou, D.D. Solar light-assisted remediation of domestic wastewater by NB-TiO<sub>2</sub> nanoparticles for potable reuse. *Appl. Catal. B Environ.* **2020**, *269*, 118807. [CrossRef]
67. Mishra, N.S.; Reddy, R.; Kuila, A.; Rani, A.; Mukherjee, P.; Nawaz, A.; Pichiah, S. A review on advanced oxidation processes for effective water treatment. *Curr. World Environ.* **2017**, *12*, 470. [CrossRef]
68. Tufail, A.; Price, W.E.; Mohseni, M.; Pramanik, B.K.; Hai, F.I. A critical review of advanced oxidation processes for emerging trace organic contaminant degradation: Mechanisms, factors, degradation products, and effluent toxicity. *J. Water Process Eng.* **2020**, *40*, 101778. [CrossRef]
69. Flouret, A.; de Almeida, M.C.; de Oliveira, T.F.; de Sá, F.P. Advanced treatment of phenol by H<sub>2</sub>O<sub>2</sub>/UV/activated carbon coupling: Influence of homogeneous and heterogeneous phase. *Can. J. Chem. Eng.* **2018**, *96*, 1979–1985. [CrossRef]
70. da Silva, J.R.P.; Monteiro, M.A.; de Mendonça Ochs, S.; da Silva Moura, C.; da Fonseca, F.V.; Borges, C.P. Study of effects of pharmaceuticals on the activated sludge process combining advanced oxidation using ultraviolet/hydrogen peroxide to increase their removal and mineralization of wastewater. *J. Environ. Chem. Eng.* **2020**, *9*, 104576. [CrossRef]
71. Enaime, G.; Baçaoui, A.; Yaacoubi, A.; Belaqziz, M.; Wichern, M.; Lübken, M. Phytotoxicity assessment of olive mill wastewater treated by different technologies: Effect on seed germination of maize and tomato. *Environ. Sci. Pollut. Res.* **2020**, *27*, 8034–8045. [CrossRef]
72. Ferreira, L.; Salmerón, I.; Peres, J.; Tavares, P.; Lucas, M.; Malato, S. Advanced Oxidation Processes as sustainable technologies for the reduction of elderberry agro-industrial water impact. *Water Resour. Ind.* **2020**, *24*, 100137. [CrossRef]
73. Rueda-Márquez, J.J.; Levchuk, I.; Manzano, M.; Sillanpää, M. Toxicity Reduction of Industrial and Municipal Wastewater by Advanced Oxidation Processes (Photo-Fenton, UVC/H<sub>2</sub>O<sub>2</sub>, Electro-Fenton and Galvanic Fenton): A Review. *Catalysts* **2020**, *10*, 612. [CrossRef]
74. Rott, E.; Kuch, B.; Lange, C.; Richter, P.; Kugele, A.; Minke, R. Removal of emerging contaminants and estrogenic activity from wastewater treatment plant effluent with UV/chlorine and UV/H<sub>2</sub>O<sub>2</sub> advanced oxidation treatment at pilot scale. *Int. J. Environ. Res. Public Health* **2018**, *15*, 935. [CrossRef]
75. Liu, Y.; Zhao, Y.; Wang, J. Fenton/Fenton-like processes with in-situ production of hydrogen peroxide/hydroxyl radical for degradation of emerging contaminants: Advances and prospects. *J. Hazard. Mater.* **2020**, *404*, 124191. [CrossRef]
76. Hassanshahi, N.; Karimi-Jashni, A. Comparison of photo-Fenton, O<sub>3</sub>/H<sub>2</sub>O<sub>2</sub>/UV and photocatalytic processes for the treatment of gray water. *Ecotoxicol. Environ. Saf.* **2018**, *161*, 683–690. [CrossRef]
77. García, C.A.; Hodaifa, G. Real olive oil mill wastewater treatment by photo-Fenton system using artificial ultraviolet light lamps. *J. Clean. Prod.* **2017**, *162*, 743–753. [CrossRef]
78. Nguyen, T.M.H.; Suwan, P.; Koottatep, T.; Beck, S.E. Application of a novel, continuous-feeding ultraviolet light emitting diode (UV-LED) system to disinfect domestic wastewater for discharge or agricultural reuse. *Water Res.* **2019**, *153*, 53–62. [CrossRef] [PubMed]
79. Dhivakar, D.T. BTEX Compounds Removal from Waste Water by using UV&UV/H<sub>2</sub>O<sub>2</sub> Process. *Int. J. Recent Eng. Sci.* **2018**, *5*, 22–25.
80. Aljouboury, D.; Palaniandy, P.; Abdul Aziz, H.; Feroz, S. Treatment of petroleum wastewater by conventional and new technologies—A review. *Glob. Nest J.* **2017**, *19*, 439–452.

81. GilPavas, E.; Dobrosz-Gómez, I.; Gómez-García, M.-Á. Optimization and toxicity assessment of a combined electrocoagulation, H<sub>2</sub>O<sub>2</sub>/Fe<sup>2+</sup>/UV and activated carbon adsorption for textile wastewater treatment. *Sci. Total Environ.* **2019**, *651*, 551–560. [CrossRef] [PubMed]
82. Neisi, A.; Afshin, S.; Rashtbari, Y.; Babaei, A.A.; Khaniabadi, Y.O.; Asadi, A.; Shirmardi, M.; Vosoughi, M. Efficiency of sequencing batch reactor for removal of organic matter in the effluent of petroleum wastewater. *Data Brief* **2018**, *19*, 2041–2046. [CrossRef]
83. Raji, M.; Mirbagheri, S.A. A global trend of Fenton-based AOPs focused on wastewater treatment: A bibliometric and visualization analysis. *Water Pract. Technol.* **2020**, *16*, 19–34. [CrossRef]
84. Ghime, D.; Ghosh, P. Removal of organic compounds found in the wastewater through electrochemical advanced oxidation processes: A review. *Russ. J. Electrochem.* **2019**, *55*, 591–620. [CrossRef]
85. Ghasemi, H.; Aghabarari, B.; Alizadeh, M.; Khanlarkhani, A.; Abu-Zahra, N. High efficiency decolorization of wastewater by Fenton catalyst: Magnetic iron-copper hybrid oxides. *J. Water Process. Eng.* **2020**, *37*, 101540. [CrossRef]
86. Zouanti, M.; Bezzina, M.; Dhib, R. Experimental study of degradation and biodegradability of oxytetracycline antibiotic in aqueous solution using Fenton process. *Environ. Eng. Res.* **2020**, *25*, 316–323. [CrossRef]
87. Litter, M.I.; Slodowicz, M. An overview on heterogeneous Fenton and photoFenton reactions using zerovalent iron materials. *J. Adv. Oxid. Technol.* **2017**, *20*. [CrossRef]
88. Ushie, E. *Simultaneous Removal of Alkylphenols and Oils in Simulated Produced Water by UV/MW/Fenton-Like Process Using a Novel Surface Functionalised Heterogeneous Pan Catalyst*; De Montfort University: Leicester, UK, 2018.
89. Kim, D.-H.; Lee, D.; Monllor-Satoca, D.; Kim, K.; Lee, W.; Choi, W. Homogeneous photocatalytic Fe<sup>3+</sup>/Fe<sup>2+</sup> redox cycle for simultaneous Cr (VI) reduction and organic pollutant oxidation: Roles of hydroxyl radical and degradation intermediates. *J. Hazard. Mater.* **2019**, *372*, 121–128. [CrossRef] [PubMed]
90. Yuan, D.; Zhang, C.; Tang, S.; Li, X.; Tang, J.; Rao, Y.; Wang, Z.; Zhang, Q. Enhancing CaO<sub>2</sub> fenton-like process by Fe (II)-oxalic acid complexation for organic wastewater treatment. *Water Res.* **2019**, *163*, 114861. [CrossRef] [PubMed]
91. Wang, Y.; Lin, X.; Shao, Z.; Shan, D.; Li, G.; Irini, A. Comparison of Fenton, UV-Fenton and nano-Fe<sub>3</sub>O<sub>4</sub> catalyzed UV-Fenton in degradation of phloroglucinol under neutral and alkaline conditions: Role of complexation of Fe<sup>3+</sup> with hydroxyl group in phloroglucinol. *Chem. Eng. J.* **2017**, *313*, 938–945. [CrossRef]
92. Jiang, Z.; Wang, L.; Lei, J.; Liu, Y.; Zhang, J. Photo-Fenton degradation of phenol by CdS/rGO/Fe<sup>2+</sup> at natural pH with in situ-generated H<sub>2</sub>O<sub>2</sub>. *Appl. Catal. B Environ.* **2019**, *241*, 367–374. [CrossRef]
93. Thakare, Y.D.; Wani, K.S. Treatment of Industrial Waste Water by Fenton Process. *J. Archit. Technol.* **2019**, *XI*, 43–49.
94. Villegas-Guzman, P.; Giannakis, S.; Rtimi, S.; Grandjean, D.; Bensimon, M.; De Alencastro, L.F.; Torres-Palma, R.; Pulgarin, C. A green solar photo-Fenton process for the elimination of bacteria and micropollutants in municipal wastewater treatment using mineral iron and natural organic acids. *Appl. Catal. B Environ.* **2017**, *219*, 538–549. [CrossRef]
95. Wang, B.; Liu, Y.; Zhang, Y.; Shen, F.; Yang, G.; Zhang, X.; Wang, L.; Luo, L.; He, Y.; Deng, S. Degradation process and kinetics study of actual urotropine wastewater by Fenton method. *Desalination Water Treat.* **2019**, *160*, 219–228. [CrossRef]
96. Perini, J.A.L.; Tonetti, A.L.; Vidal, C.; Montagner, C.C.; Nogueira, R.F.P. Simultaneous degradation of ciprofloxacin, amoxicillin, sulfathiazole and sulfamethazine, and disinfection of hospital effluent after biological treatment via photo-Fenton process under ultraviolet germicidal irradiation. *Appl. Catal. B Environ.* **2018**, *224*, 761–771. [CrossRef]
97. Shokri, A. Application of Sono-photo-Fenton process for degradation of phenol derivatives in petrochemical wastewater using full factorial design of experiment. *Int. J. Ind. Chem.* **2018**, *9*, 295–303. [CrossRef]
98. Clarizia, L.; Russo, D.; Di Somma, I.; Marotta, R.; Andreozzi, R. Homogeneous photo-Fenton processes at near neutral pH: A review. *Appl. Catal. B Environ.* **2017**, *209*, 358–371. [CrossRef]
99. Danforth, R.A. *Ultrafast Photochemistry of Aqueous Iron (III) Complexes*. Ph.D. Thesis, College of Letters & Science, Montana State University-Bozeman, Bozeman, MT, USA, 2017.
100. Muramatsu, K.; Tokumura, M.; Wang, Q.; Miyake, Y.; Amagai, T.; Makino, M. Mitigation of the inhibitory effects of co-existing substances on the Fenton process by UV light irradiation. *J. Environ. Sci. Health Part A* **2020**, *55*, 730–738. [CrossRef] [PubMed]
101. Zhang, M.-H.; Dong, H.; Zhao, L.; Wang, D.-x.; Meng, D. A review on Fenton process for organic wastewater treatment based on optimization perspective. *Sci. Total Environ.* **2019**, *670*, 110–121. [CrossRef] [PubMed]
102. Ye, Z.; Sirés, I.; Zhang, H.; Huang, Y.-H. Mineralization of pentachlorophenol by ferrioxalate-assisted solar photo-Fenton process at mild pH. *Chemosphere* **2019**, *217*, 475–482. [CrossRef]
103. Giwa, A.; Yusuf, A.; Balogun, H.A.; Sambudi, N.S.; Bilad, M.R.; Adeyemi, I.; Chakraborty, S.; Curcio, S. Recent advances in advanced oxidation processes for removal of contaminants from water: A comprehensive review. *Process Saf. Environ. Prot.* **2021**, *146*, 220–256. [CrossRef]
104. Matavos-Aramyan, S.; Moussavi, M. Advances in Fenton and Fenton based oxidation processes for industrial effluent contaminants control—a review. *Int. J. Environ. Sci. Nat. Resour.* **2017**, *2*, 1–18.
105. Fernandes, A.; Makoś, P.; Boczkaj, G. Treatment of bitumen post oxidative effluents by sulfate radicals based advanced oxidation processes (S-AOPs) under alkaline pH conditions. *J. Clean. Prod.* **2018**, *195*, 374–384. [CrossRef]
106. Rajala, K.; Grönfors, O.; Hesampour, M.; Mikola, A. Removal of microplastics from secondary wastewater treatment plant effluent by coagulation/flocculation with iron, aluminum and polyamine-based chemicals. *Water Res.* **2020**, *183*, 116045. [CrossRef] [PubMed]

107. Dalari, B.L.S.K.; Giroletti, C.L.; Dalri-Cecato, L.; Domingos, D.G.; Hassemer, M.E.N. Application of heterogeneous photo-fenton process using chitosan beads for textile wastewater treatment. *J. Environ. Chem. Eng.* **2020**, *8*, 103893. [CrossRef]
108. Lumbaque, E.C. *Degradation of Pharmaceuticals in Hospital Wastewater by Solar Photo-Fenton Processes*; UFRGS: Porto Alegre, Brazil, 2020.
109. Nikraves, B.; Shomalnasab, A.; Nayyer, A.; Aghababaei, N.; Zarebi, R.; Ghanbari, F. UV/Chlorine process for dye degradation in aqueous solution: Mechanism, affecting factors and toxicity evaluation for textile wastewater. *J. Environ. Chem. Eng.* **2020**, *8*, 104244. [CrossRef]
110. Amildon, I.; Paniagua, C.E.; Paiva, V.A.; Gonçalves, B.R.; Sousa, R.M.; Machado, A.E.; Trovó, A.G. Degradation and initial mechanism pathway of chloramphenicol by photo-Fenton process at circumneutral pH. *Chem. Eng. J.* **2018**, *339*, 531–538. [CrossRef]
111. Pourehie, O.; Saien, J. Homogeneous solar Fenton and alternative processes in a pilot-scale rotatable reactor for the treatment of petroleum refinery wastewater. *Process Saf. Environ. Prot.* **2020**, *135*, 236–243. [CrossRef]
112. El-Qanni, A. *Development of Sustainable Nanosorbents Based Technology for Hydrocarbons and Organic Pollutants Recovery from Industrial Wastewater*; University of Calgary: Calgary, Alberta, 2017.
113. Radwan, M.; Alalm, M.G.; El-Etriby, H.K. Application of electro-Fenton process for treatment of water contaminated with benzene, toluene, and p-xylene (BTX) using affordable electrodes. *J. Water Process Eng.* **2019**, *31*, 100837. [CrossRef]
114. Brillas, E.; Garcia-Segura, S. Benchmarking recent advances and innovative technology approaches of Fenton, photo-Fenton, electro-Fenton, and related processes: A review on the relevance of phenol as model molecule. *Sep. Purif. Technol.* **2020**, *237*, 116337. [CrossRef]
115. Hassan, A.K.; Hassan, M.M.A.; Hasan, A.F. *Treatment of Iraqi Petroleum Refinery Wastewater by Advanced Oxidation Processes*; Journal of Physics: Conference Series; IOP Publishing: Bristol, UK, 2020; p. 012071.
116. Pintor, A.M.; Vilar, V.J.; Botelho, C.M.; Boaventura, R.A. Oil and grease removal from wastewaters: Sorption treatment as an alternative to state-of-the-art technologies. A critical review. *Chem. Eng. J.* **2016**, *297*, 229–255. [CrossRef]
117. Testolin, R.C.; Mater, L.; Sanches-Simões, E.; Dal Conti-Lampert, A.; Corrêa, A.X.; Groth, M.L.; Oliveira-Carneiro, M.; Radetski, C.M. Comparison of the mineralization and biodegradation efficiency of the Fenton reaction and Ozone in the treatment of crude petroleum-contaminated water. *J. Environ. Chem. Eng.* **2020**, *8*, 104265. [CrossRef]
118. Boczkaj, G.; Fernandes, A.; Makoś, P. Study of different advanced oxidation processes for wastewater treatment from petroleum bitumen production at basic pH. *Ind. Eng. Chem. Res.* **2017**, *56*, 8806–8814. [CrossRef]
119. Cruz Alcalde, A. Contribution to Performance Characterization and Kinetic Modelling of Micropollutants Abatement in Water and Wastewater by Ozone-based Oxidation Processes. Ph.D. Thesis, Universitat de Barcelona, Barcelona, Spain, 2019.
120. Contreras, S.; Rodriguez, M.; Al Momani, F.; Sans, C.; Esplugas, S. Contribution of the ozonation pre-treatment to the biodegradation of aqueous solutions of 2, 4-dichlorophenol. *Water Res.* **2003**, *37*, 3164–3171. [CrossRef]
121. Kim, M.S.; Cha, D.; Lee, K.-M.; Lee, H.-J.; Kim, T.; Lee, C. Modeling of ozone decomposition, oxidant exposures, and the abatement of micropollutants during ozonation processes. *Water Res.* **2020**, *169*, 115230. [CrossRef]
122. Rekhate, C.V.; Srivastava, J. Recent advances in ozone-based advanced oxidation processes for treatment of wastewater—A review. *Chem. Eng. J. Adv.* **2020**, *3*, 100031. [CrossRef]
123. Malvestiti, J.A.; Dantas, R.F. Disinfection of secondary effluents by O<sub>3</sub>, O<sub>3</sub>/H<sub>2</sub>O<sub>2</sub> and UV/H<sub>2</sub>O<sub>2</sub>: Influence of carbonate, nitrate, industrial contaminants and regrowth. *J. Environ. Chem. Eng.* **2018**, *6*, 560–567. [CrossRef]
124. Wen, C.; Wang, H.; Wang, L.; Lou, Z.; Sun, Z.; Zhou, Z. The reduction of waste lubricant oil distillate through the enhancement of organics degradation by ozonation with elevated temperature and stable pH for the zero discharge. *J. Clean. Prod.* **2019**, *240*, 118194. [CrossRef]
125. Krishnan, S.; Rawindran, H.; Sinnathambi, C.; Lim, J. Comparison of various advanced oxidation processes used in remediation of industrial wastewater laden with recalcitrant pollutants. *IOP Conf. Ser. Mater. Sci. Eng.* **2017**, *206*, 012089. [CrossRef]
126. Shahrezaei, F.; Mansouri, Y.; Zinatizadeh, A.A.L.; Akhbari, A. Process modeling and kinetic evaluation of petroleum refinery wastewater treatment in a photocatalytic reactor using TiO<sub>2</sub> nanoparticles. *Powder Technol.* **2012**, *221*, 203–212. [CrossRef]
127. Tao, P.; Yang, C.; Wang, H.; Zhao, Y.; Zhang, X.; Shao, M.; Sun, T. Synergistic effects of ultrasonic-assisted ozonation on the formation of hydrogen peroxide. *J. Environ. Chem. Eng.* **2020**, *9*, 104905. [CrossRef]
128. Liu, Z.; Chys, M.; Yang, Y.; Demeestere, K.; Van Hulle, S. Oxidation of trace organic contaminants (TrOCs) in wastewater effluent with different ozone-based AOPs: Comparison of ozone exposure and •OH formation. *Ind. Eng. Chem. Res.* **2019**, *58*, 8896–8902. [CrossRef]
129. Al Momani, F. Impact of photo-oxidation technology on the aqueous solutions of nitrobenzene: Degradation efficiency and biodegradability enhancement. *J. Photochem. Photobiol. A Chem.* **2006**, *179*, 184–192. [CrossRef]
130. Miklos, D.B.; Remy, C.; Jekel, M.; Linden, K.G.; Drewes, J.E.; Hübner, U. Evaluation of advanced oxidation processes for water and wastewater treatment—A critical review. *Water Res.* **2018**, *139*, 118–131. [CrossRef]
131. Buehlmann, P.H. Balancing Bromate Formation, Organics Oxidation, and Pathogen Inactivation: The Impact of Bromate Suppression Techniques on Ozonation System Performance in Reuse Waters. Ph.D. Thesis, Virginia Tech, Blacksburg, VA, USA, 2019.
132. El-Din, M.G.; Smith, D.W.; Al Momani, F.; Wang, W. Oxidation of resin and fatty acids by ozone: Kinetics and toxicity study. *Water Res.* **2006**, *40*, 392–400. [CrossRef]

133. Tufail, A.; Price, W.E.; Hai, F.I. A critical review on advanced oxidation processes for the removal of trace organic contaminants: A voyage from individual to integrated processes. *Chemosphere* **2020**, *260*, 127460. [CrossRef]
134. Al Momani, F. Degradation of cyanobacteria anatoxin-a by advanced oxidation processes. *Sep. Purif. Technol.* **2007**, *57*, 85–93. [CrossRef]
135. Wei, C.; Zhang, F.; Hu, Y.; Feng, C.; Wu, H. Ozonation in water treatment: The generation, basic properties of ozone and its practical application. *Rev. Chem. Eng.* **2017**, *33*, 49–89. [CrossRef]
136. Yang, S.; Song, Y.; Chang, F.; Wang, K. Evaluation of chemistry and key reactor parameters for industrial water treatment applications of the UV/O<sub>3</sub> process. *Environ. Res.* **2020**, *188*, 109660. [CrossRef]
137. Cruz-Alcalde, A.; Esplugas, S.; Sans, C. Continuous versus single H<sub>2</sub>O<sub>2</sub> addition in peroxone process: Performance improvement and modelling in wastewater effluents. *J. Hazard. Mater.* **2020**, *387*, 121993. [CrossRef]
138. Al Momani, F.A.; Jarrah, N. Treatment and kinetic study of cyanobacterial toxin by ozone. *J. Environ. Sci. Health Part A* **2010**, *45*, 719–731. [CrossRef]
139. Biard, P.-F.; Dang, T.T.; Bocanegra, J.; Couvert, A. Intensification of the O<sub>3</sub>/H<sub>2</sub>O<sub>2</sub> advanced oxidation process using a continuous tubular reactor filled with static mixers: Proof of concept. *Chem. Eng. J.* **2018**, *344*, 574–582. [CrossRef]
140. Meshref, M.N.; Klammerth, N.; Islam, M.S.; McPhedran, K.N.; El-Din, M.G. Understanding the similarities and differences between ozone and peroxone in the degradation of naphthenic acids: Comparative performance for potential treatment. *Chemosphere* **2017**, *180*, 149–159. [CrossRef] [PubMed]
141. Wang, H.; Zhan, J.; Yao, W.; Wang, B.; Deng, S.; Huang, J.; Yu, G.; Wang, Y. Comparison of pharmaceutical abatement in various water matrices by conventional ozonation, peroxone (O<sub>3</sub>/H<sub>2</sub>O<sub>2</sub>), and an electro-peroxone process. *Water Res.* **2018**, *130*, 127–138. [CrossRef]
142. Khatri, I.; Singh, S.; Garg, A. Performance of electro-Fenton process for phenol removal using Iron electrodes and activated carbon. *J. Environ. Chem. Eng.* **2018**, *6*, 7368–7376. [CrossRef]
143. Ahmadi, M.; Jorfi, S.; Kujlu, R.; Ghafari, S.; Soltani, R.D.C.; Haghhighifard, N.J. A novel salt-tolerant bacterial consortium for biodegradation of saline and recalcitrant petrochemical wastewater. *J. Environ. Manag.* **2017**, *191*, 198–208. [CrossRef]
144. Ebrahimi, M.; Kazemi, H.; Mirbagheri, S.; Rockaway, T.D. An optimized biological approach for treatment of petroleum refinery wastewater. *J. Environ. Chem. Eng.* **2016**, *4*, 3401–3408. [CrossRef]
145. Mirbagheri, S.A.; Ebrahimi, M.; Mohammadi, M. Optimization method for the treatment of Tehran petroleum refinery wastewater using activated sludge contact stabilization process. *Desalination Water Treat.* **2014**, *52*, 156–163. [CrossRef]
146. Liang, J.; Mai, W.; Tang, J.; Wei, Y. Highly effective treatment of petrochemical wastewater by a super-sized industrial scale plant with expanded granular sludge bed bioreactor and aerobic activated sludge. *Chem. Eng. J.* **2019**, *360*, 15–23. [CrossRef]
147. Razavi, S.M.R.; Miri, T. A real petroleum refinery wastewater treatment using hollow fiber membrane bioreactor (HF-MBR). *J. Water Process Eng.* **2015**, *8*, 136–141. [CrossRef]
148. El-Naas, M.H.; Alhajja, M.A.; Al-Zuhair, S. Evaluation of a three-step process for the treatment of petroleum refinery wastewater. *J. Environ. Chem. Eng.* **2014**, *2*, 56–62. [CrossRef]
149. An, C.; Huang, G.; Yao, Y.; Zhao, S. Emerging usage of electrocoagulation technology for oil removal from wastewater: A review. *Sci. Total Environ.* **2017**, *579*, 537–556. [CrossRef]
150. Huo, S.; Zhu, F.; Zou, B.; Xu, L.; Cui, F.; You, W. A two-stage system coupling hydrolytic acidification with algal microcosms for treatment of wastewater from the manufacture of acrylonitrile butadiene styrene (ABS) resin. *Biotechnol. Lett.* **2018**, *40*, 689–696. [CrossRef]
151. Fernandes, A.; Gałol, M.; Makoś, P.; Khan, J.A.; Boczkaj, G. Integrated photocatalytic advanced oxidation system (TiO<sub>2</sub>/UV/O<sub>3</sub>/H<sub>2</sub>O<sub>2</sub>) for degradation of volatile organic compounds. *Sep. Purif. Technol.* **2019**, *224*, 1–14. [CrossRef]
152. Dastpak, H.; Pasalari, H.; Jafari, A.J.; Gholami, M.; Farzadkia, M. Improvement of Co-Composting by a combined pretreatment Ozonation/Ultrasonic process in stabilization of raw activated sludge. *Sci. Rep.* **2020**, *10*, 1–7. [CrossRef]
153. Zhai, J.; Ma, H.; Liao, J.; Rahaman, M.; Yang, Z.; Chen, Z. Comparison of Fenton, ultraviolet-Fenton and ultrasonic-Fenton processes on organics and colour removal from pre-treated natural gas produced water. *Int. J. Environ. Sci. Technol.* **2018**, *15*, 2411–2422. [CrossRef]
154. Shah, A.; Shah, M. Characterisation and bioremediation of wastewater: A review exploring bioremediation as a sustainable technique for pharmaceutical wastewater. *Groundw. Sustain. Dev.* **2020**, *11*, 100383. [CrossRef]
155. Horovitz, I.; Avisar, D.; Luster, E.; Lozzi, L.; Luxbacher, T.; Mamane, H. MS2 bacteriophage inactivation using a N-doped TiO<sub>2</sub>-coated photocatalytic membrane reactor: Influence of water-quality parameters. *Chem. Eng. J.* **2018**, *354*, 995–1006. [CrossRef]
156. Yadav, D.N.; Kishore, K.A.; Bethi, B.; Sonawane, S.H.; Bhagawan, D. ZnO nanophotocatalysts coupled with ceramic membrane method for treatment of Rhodamine-B dye waste water. *Environ. Dev. Sustain.* **2018**, *20*, 2065–2078. [CrossRef]
157. Giwa, A.; Yusuf, A.; Dindi, A.; Balogun, H.A. Polygeneration in desalination by photovoltaic thermal systems: A comprehensive review. *Renew. Sustain. Energy Rev.* **2020**, *130*, 109946. [CrossRef]

Review

# Recent Combinations of Electrospinning with Photocatalytic Technology for Treating Polluted Water

He Lv <sup>1</sup>, Yanan Liu <sup>1</sup>, Yubin Bai <sup>1</sup>, Hongpu Shi <sup>1</sup>, Wen Zhou <sup>1</sup>, Yaoning Chen <sup>1</sup>, Yang Liu <sup>2</sup> and Deng-Guang Yu <sup>1,\*</sup> 

<sup>1</sup> School of Materials and Chemistry, University of Shanghai for Science and Technology, 516 Jungong Road, Shanghai 200093, China

<sup>2</sup> School of Chemistry and Chemical Engineering, Shanghai University of Engineering Science, 333 Long Teng Road, Shanghai 201620, China

\* Correspondence: ydg017@usst.edu.cn

**Abstract:** Dyes, antibiotics, heavy metal ions, and bacteria are important sources of water pollution. How to solve these issues has become a problem in the fields of science and technology. People have developed a variety of technologies to treat pollutants in water. Photocatalytic technology came into being. As a simple and environmentally friendly treatment technology, it has been widely studied by the scientific community. Traditional powder photocatalysts cause secondary pollution to the environment and are not conducive to recycling. Therefore, large specific surface area and reusable membrane photocatalysts built by electrospinning technology have become a favorite of today's scientific community. Nanofiber membranes prepared by electrospinning technology have a variety of structures, which can meet the needs of different occasions. This review summarizes and discusses research progress in electrospinning technology, the relationship between the structure and treatment of electrospun fiber membranes, and their impacts on the photocatalytic performance of nanofiber membranes. The performance, challenges, and future development directions of nanofiber membranes with different structures, prepared by different kinds of electrospinning techniques using photocatalysis to treat different pollutants, are reviewed.

**Citation:** Lv, H.; Liu, Y.; Bai, Y.; Shi, H.; Zhou, W.; Chen, Y.; Liu, Y.; Yu, D.-G. Recent Combinations of Electrospinning with Photocatalytic Technology for Treating Polluted Water. *Catalysts* **2023**, *13*, 758. <https://doi.org/10.3390/catal13040758>

Academic Editors: Juan José Rueda-Márquez, Javier Moreno-Andrés and Irina Levchuk

Received: 31 January 2023  
Revised: 4 April 2023  
Accepted: 12 April 2023  
Published: 15 April 2023



**Copyright:** © 2023 by the authors. Licensee MDPI, Basel, Switzerland. This article is an open access article distributed under the terms and conditions of the Creative Commons Attribution (CC BY) license (<https://creativecommons.org/licenses/by/4.0/>).

**Keywords:** electrospinning technology; photocatalytic technology; polluted water; nanofibers; nanostructures; composites

## 1. Introduction

With the development of global industrialization and the rapid growth in population, the problem of environmental pollution has become increasingly prominent. The environment is heavily threatened by poisonous and dangerous contaminants, which pose a severe threat to human existence and growth [1]. Water contamination has become a significant contributor to declining public health. Wastewater from a variety of sources, including landfill leachate, domestic sewage, hospital sewage, industrial, and agricultural sewage discharge, among others, may infiltrate surface water and groundwater environments directly or indirectly [2,3]. How to solve these problems has become a primary consideration for socially sustainable development. Conventional treatment technologies include physical, chemical, and biological technologies [4–6]. However, some pollutants in water have stable chemical properties and strong toxicity, and these treatment technologies can not completely treat them, instead converting them into another form of pollutant [7]. Thus, it is problematic to use these technologies for treatment.

Therefore, photocatalytic technology came into being. Photocatalytic technology [8,9] is the preferred option in water treatment due to its benefits of low energy consumption, gentle reaction conditions, and non-toxicity products. Under certain conditions, pollutants that are difficult to treat by ordinary methods and have strong toxicity can be oxidized by high reactivity hydroxyl radicals ( $\bullet\text{OH}$ ), superoxide radicals ( $\bullet\text{O}_2^-$ ), and holes ( $\text{h}^+$ ),

with oxidation to CO<sub>2</sub>, H<sub>2</sub>O, and other inorganic substances or small molecular substances with low toxicity and easy degradation [10]. There are two conditions for generating a photocatalytic reaction: (1) illumination and excitation from various energy sources; (2) the material contains semiconductor photocatalysts. When a semiconductor photocatalyst is excited by an energy source, electrons on the valence band of the semiconductor are excited to the conduction band, leaving holes on the valence band. The formed electrons and holes react with water molecules and oxygen to generate active radicals, which can react with pollutants in water, ultimately forming non-toxic products, such as water and carbon dioxide [11]. Although photocatalysis has developed rapidly in recent years, few photocatalysts stand out in real-world applications due to their weak photocatalytic efficiency and recycling durability. The majority of photocatalysts are available as powders [12,13]. Powder photocatalysts not only lump readily, losing the activity centers, but are also difficult to separate and recycle from water. Most significantly, if the photocatalyst has not yet fully reacted, the toxicity of the photocatalyst and other pollutants will also be greater. In addition, powdered photocatalysts are prone to aggregation, and may quickly and readily cause health hazards by entering the body through the respiratory system.

In order to overcome the shortcomings of powder photocatalysts, many carriers have been developed to immobilize powder photocatalysts, including photocatalytic membranes [14]. The photocatalytic membranes can improve the recycle photocatalytic rate and reduce the toxicity of powder photocatalysts. Most importantly, loading photocatalysts onto electrospun NF membranes provides new solutions for photocatalytic technology to degrade pollutants in wastewater. Due to the load, large specific surface area, and high porosity of electrospun NFs, they can stabilize the material structure, provide more reactive sites, and improve the separation efficiency of photogenerated carriers. Photocatalytic membranes, such as polyacrylonitrile (PAN) [15], cellulose acetate (CA) [16], and poly(vinylidene fluoride) (PVDF) [17] membranes have been prepared to degrade pollutants. However, traditional photocatalytic membranes are obtained by coating or mixing photocatalysts in the membrane and then pouring [18] or spin coating [19]. Compared to powder photocatalysts, these technologies can severely limit the efficiency of photocatalytic membranes; the photocatalysts coated on the surface of the membranes can exhibit aggregation, which can significantly reduce the photocatalytic efficiency [20]. After several cycles, the photocatalyst on the surface is prone to fall off due to poor adhesion. The photocatalyst doped in the photocatalyst membrane is trapped inside the membrane, resulting in a decrease in the degradation efficiency of the photocatalyst. Membrane carrier materials may age under the action of light and degrade, which can decrease the mechanical stability of the material. Powdered photocatalysts in the membrane are also prone to agglomerate, resulting in pore clogging of the membrane, which not only reduces the separation efficiency of electrons and holes but also reduces the active sites of the photocatalytic reaction. Therefore, it is crucial to develop a new type of photocatalyst. Photocatalytic membranes [21,22] are regarded as a vital avenue for innovation and sustainable development since they are effective and simple to recover. In addition, compared with powder materials, membranes are easier to recover and have a stable structure, suggesting great potential in the treatment of pollutants in water using photocatalytic technology.

Electrospinning technology [23–25] is a simple and convenient technology to prepare membrane materials. Membrane materials prepared by electrospinning technology [26–28] retain the stability of the material structure after treatment. These materials are widely used in various fields, such as environmental remediation, food preservation, drug release, multifunctional materials, hydrogen evolution reaction performance, electronic devices, etc., [1,29–36]. Due to their high surface area and ease of retrieval, which are favorable to the photocatalytic activities required to remove pollutants from water, nanofibrous structures have significant potential for this task. Electrospinning is a potent technique for different morphologies and structure fibers [16,20,31] that are appropriate for use in tissue engineering, biological materials, and air and water filters. The nonwoven nature of the nanofibers (NFs), in particular, makes it easier to remove contaminants from water

effectively. This research area is very active, with an increasing number of scientific articles published each year (Figure 1). In 1997, Martin et al. initially proposed electrospun NFs for the photocatalytic degradation of pollutants [37]. Then, the first research on electrospun NFs for photocatalytic degradation of pollutants appeared in 2003 [38], and research on electrospun NFs has increased year by year (Figure 1). Uniaxial nanofiber (NF) membranes, porous NF membranes, coaxial NF membranes, Janus NF membranes, and multi-fluid electrospun fiber membranes gradually appeared [20]. Uniaxial NFs have the advantage of simple preparation and are widely used for the photocatalytic degradation of pollutants in water. However, due to the difficulties associated with the electrospinning of polymers, solvents, and photocatalysts, the mechanical properties and structure, and the easy combination of  $e^-$  and  $h^+$  of uniaxial NFs, multi-fluid electrospinning came into being. Nanofiber membranes with special structures prepared by multi-fluid electrospinning can solve the above problems. Importantly, electrospun nanofiber membranes with different morphology and structure prepared by electrospinning technology have a good photocatalytic effect. The mechanical properties are also improved compared with uniaxial electrospun fiber membranes. Multi-fluid electrospinning technology [1,16,20,39] can be compatible with polymers with different properties, it can be used to prepare the NF membranes with stronger photocatalytic performance, better mechanical properties, higher secondary recovery. The aim of this review is to introduce progress in research relating to electrospinning technology and the use of different methods to treat electrospun nanofiber membranes, focusing on the influence of the structure and morphology of electrospun nanofiber membranes after treatment on their photocatalytic performance. In addition, this review also considers the impact of electrospun nanofiber membranes on the photocatalytic degradation performance of different pollutants, and discusses the impact, challenges, and future development directions of nanofiber membranes with different structures prepared by different electrospun technologies on photocatalytic performance, and provides guidance for research in this field.

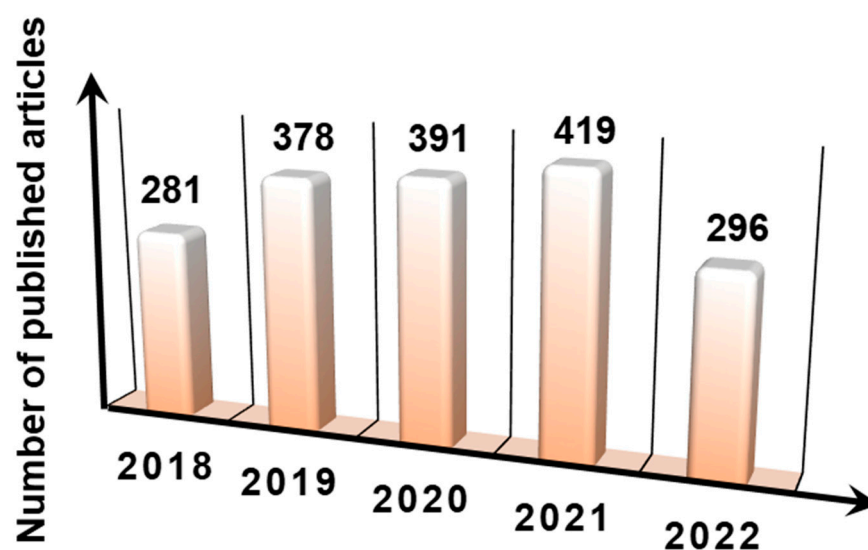


**Figure 1.** According to the Web of Science database, the number of papers published during the past five years. “electrospinning or NFs” and “photocatalysis or photocatalyst” were the keywords used for the Title/Abstract section. (<https://www.webofscience.com>, accessed on 29 January 2023).

## 2. The Most Recent Developments in Electrospinning

### 2.1. The Electrospinning Process

Electrospinning technology, abbreviated as “electrospinning”, is a technology that uses polymer fluids to obtain nano- or micro-fibers by pulling under a strong electric field. The electrospinning process refers to a syringe being filled with the solution, and the formation of a droplet at the tip of the needle under the action of surface pressure. When the voltage is

turned on, the droplets form the shape of a cone as a result of the action of the high-voltage electric field. At the same time, the small droplets are mutually rejected by the surface tension and the surface charge [40]. The direction of these two forces is opposite. When the electric field power and the surface tension are equal, the small liquid droplets reach balance and the half-cone angle is  $49.3^\circ$ , which is the Taylor cone. When the strength of the electric field exceeds the surface tension, the top of the Taylor cone forms a fine flow spray (liquid fiber bundle). In the process of leaving the spraying head, the material passes through a series of unstable stretching, splitting, and refinement phases during the migration of the collecting board. The solvent on the surface of the fiber beam continues to volatilize (or undergoes melt cooling and solidification). Finally, the fiber falls onto the collecting board [40]. The process of electrospinning is shown in Figure 2.

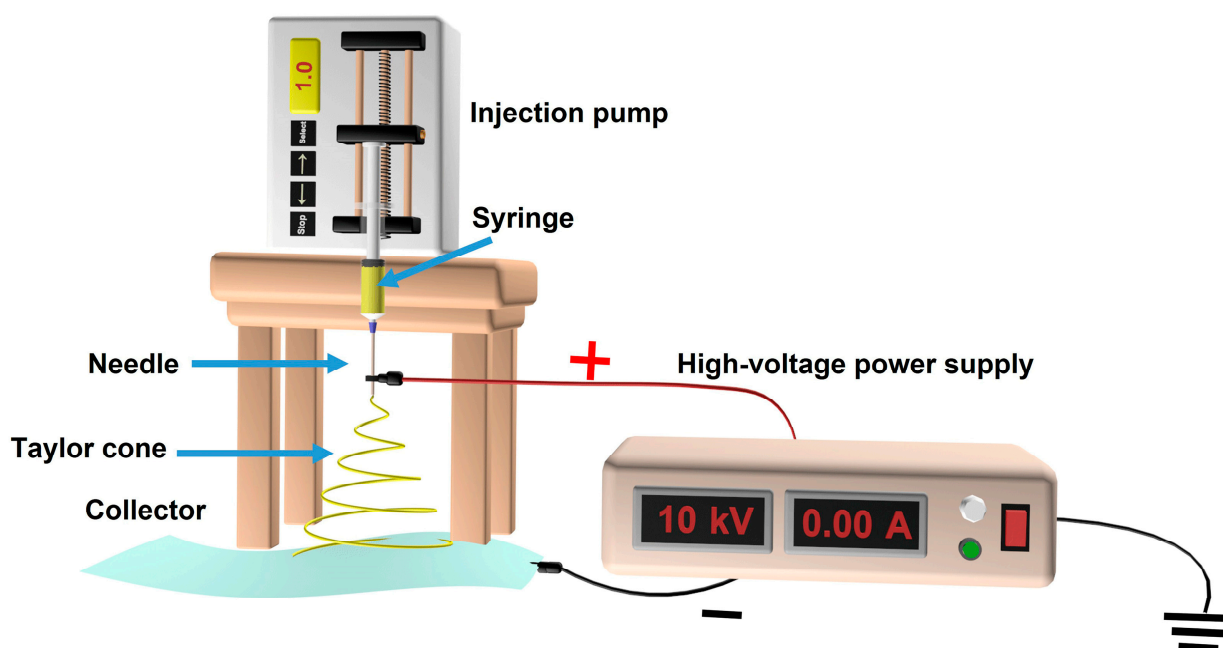


**Figure 2.** Schematic diagram of the electrospinning devices.

## 2.2. The Devices and Processing Parameters of Electrospinning

The devices used in the electrospinning process are divided into the following types: electrostatic generators, syringes, pushing pumps, and receivers [41]. Traditional electrospinning generators are positive poles [23]. Negative high-voltage electrospinning generators have been developed in recent years, which are often used in conjugated electrospinning [42], as shown in Figure 3a. The electrospinning fluid in the two spinnerets can overcome surface tension and viscous forces to spray out, generating numerous NFs with positive and negative charges under the influence of positive and negative high-voltage direct-current (DC) power supplies. At the two nozzles, a significant quantity of positive and negative charges assemble to create an electric field. In Figure 2, the red dot dotted region indicates the direction of the electric field lines. Using conjugated electrospinning, Janus NFs can be easily prepared, but the components of the NFs do not interact with each other at the same time. However, due to the interference of electric charges and other factors in the air, the yield of Janus NFs is relatively low. In addition, alternating current (AC) electrospinning generators [43] (Figure 3b) and low-voltage electrostatic generators [44] (Figure 3c) have gradually appeared. The fibers prepared by AC electrospinning technology are positively charged and react negatively to polarity changes; unlike DC rotation, they do not need opposing electrodes. Under the electric field, the formed fibers are pulled in the opposite direction, the NFs are transferred from the electrode, and are dragged toward the existing fibers by charge effects. Low-voltage electrospinning is relatively safe. However,



its application range is relatively narrow, and it can only prepare some polymers to form fibers easily. Due to the relatively low voltage, the molecular stretching in the fibers is not sufficient and the morphology of fibers varies. The most widely used method involves a high-voltage positive electrostatic generator [45] due to its safety, stability, and yield. A more stable surface charge (+) distribution of the polymer jet can be generated by positive high-voltage electricity, with the charges (−) carried by the receiver. NFs prepared by positive high-voltage electrospinning have a uniform diameter distribution, more diverse morphology, and are produced in greater yield.

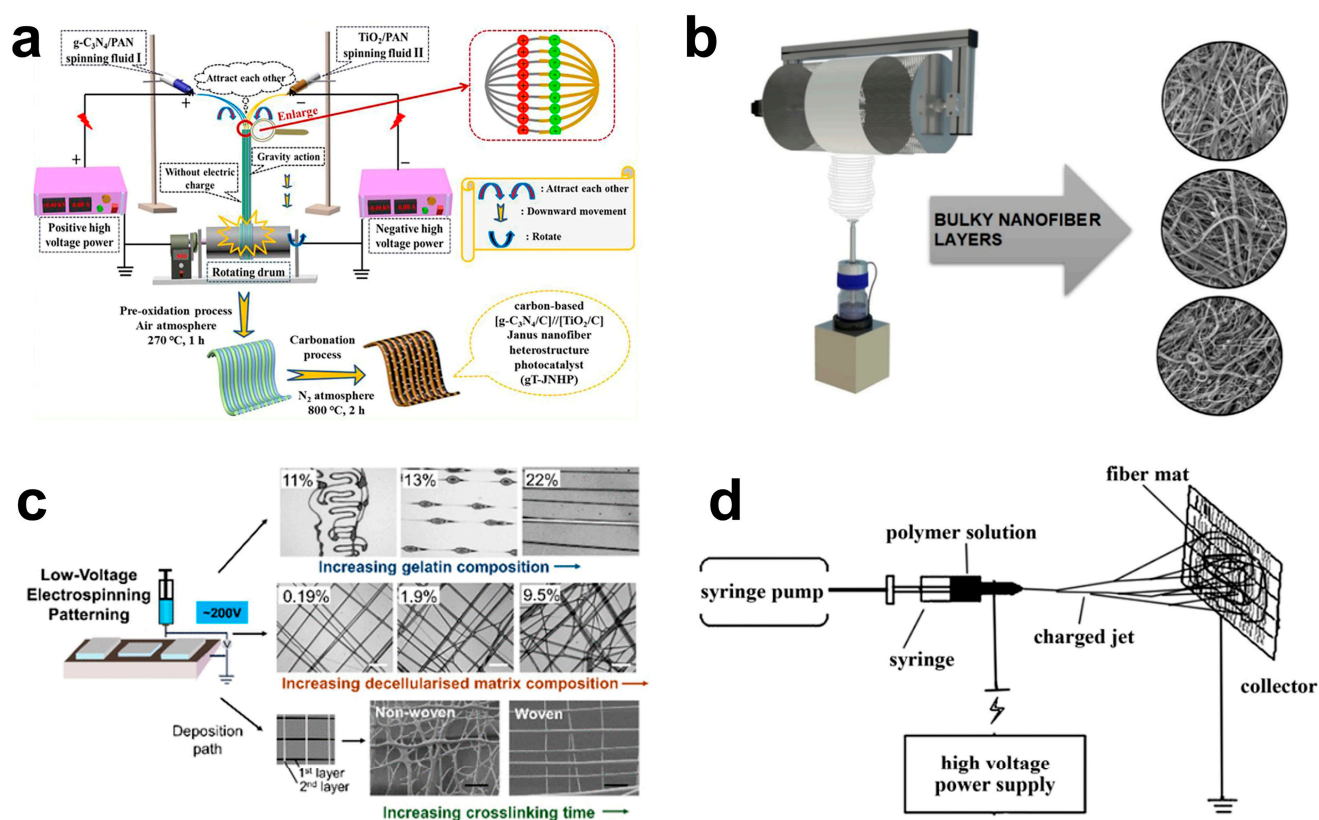


**Figure 3.** Diagram of conjugated electrospinning set-up (a) [42], Copyright 2022, Wiley. Diagram of AC electrospinning set-up (b) [43], Copyright 2019, American Chemical Society. Diagram of low-voltage electrospinning set-up (c) [44]. Diagram of positive high-voltage electrospinning devices set-up (d) [45], Copyright 2011, Elsevier.

The syringe is generally made from plastic. The needles are of two types: stainless-steel needles and plastic needles [43]. The types of receivers are wire mesh and tin foil, which are developed for the roller [42], turntable [46], and liquid-phase receiving devices [47]. Different kinds of receivers greatly enrich the types and performance of NF membranes. The wire mesh, tin foil, and liquid-phase receivers are used to receive the uniform NFs membrane. The orderly aligned nanofiber membrane can be prepared using a roller and turntable. Typically, some NFs that cannot be fully dried are collected using liquid phase technology during the electrospinning process; the obtained nanofiber membranes have better performance.

Factors affecting electrospinning include systemic factors and the electrospinning process parameters.

Systemic factors include the polymer type, solution concentration [48], and solvent type [49]. Polymers selected for the preparation of electrospun NFs were initially mainly polyvinylpyrrolidone (PVP) [50], PAN [51], PVDF [33], methyl polyacrylate (PMMA) [31], polyvinyl alcohol (PVA) [52], polystyrene (PS) [53] or other organic polymers [54] that were easy to spin. Organic polymers have been developed into biocompatible polymers, such

as collagen [55], polylactic acid [56], gelatin [57], chitin [58], chitosan [58], and sodium alginate [59]. Some inorganic materials and non-spinnable materials [39] are also added. Adding polymers which are easy to electrospin into some non-spinnable polymers can enhance the spinnability of NFs [17]. At the same time, different kinds of polymers will undergo phase separation [60]. Compared with NFs prepared by a single kind of polymer, NFs prepared using a variety of polymers will have different morphologies, and their performances will also be improved [17]. In addition, NFs membranes with different morphologies can also be prepared using different solvents, water-soluble polymers, and salts. The principles for selecting polymers are related to the polymer types, the solvent volatility, the compatibility between the solvent and the polymer, and the interaction between the solvent and the polymer molecular chain. Highly volatile solvents and solvents with less interaction with molecular chains can enable preparation of NFs with a smaller diameter. In addition, all electrospinning solutions have spinnable concentrations; the electrospinning solution is sprayed out in the form of droplets or beads below the appropriate concentration. Above this concentration, the concentration is too high, and achieving flow of the electrospinning fluid is difficult, which will hinder the electrospinning process. The types of solvents initially used in electrospinning were mostly single organic solvents. Today, most solvents used are multiple organic solvents, which enable preparation of a variety of NF membranes with different appearances and properties [61,62]. The solvents used for electrospinning are mainly divided into two categories: one category is volatile solvents, such as chloroform and acetone [63,64]; the other category is non-volatile solvents, such as water, ethanol [63,64], and so on. By combining different volatile organic solvents, NF membranes with different morphologies can be prepared. For example, porous NFs can be prepared by mixing acetone and DMF [65]. Because acetone is volatile, holes will appear on the fiber surface; the relatively weak volatility of DMF plays a role in maintaining the fiber morphology. Solvents can also be divided into good solvents and poor solvents according to their solubility. The molecular chain structure of polymers can be stretched in good solvents, while poor solvents are not easy to stretch. The structural differences caused by mixing these two kinds of solvents can easily cause local defects in the polymer, resulting in different morphologies and pore structures on the NFs [66].

The electrospinning process parameters include the electric field strength and receiving distance, which are important parameters affecting the performance of NF membranes [67]. The applied electric field strength generally increases with increase in the electric field strength. At the same time, a high electric field strength enables greater acceleration of the jet. These two factors can cause the electrostatic stress of the jet to increase, increasing the tensile rate, which is conducive to the preparation of finer fibers. If some conductive solutions are added appropriately to the spinning solution to improve the conductivity, finer fibers can be prepared. The relationship between the distance between the needle and the receiver is important: if the spinning distance is too close, the solvent will be too slow to volatilize, and the fibers will tend to bond with each other; if the spinning distance is too large, the filaments will not be easy to collect on the receiver due to weakening of the electric field strength. With increase in the receiving distance, the fiber diameter decreases.

In addition, environmental factors, such as the humidity and temperature, can also affect the morphology of fibers. For example, Liu et al. [68] found that adjusting the relief temperature can affect the polymer's annual and solvent evaporation rate during electrospinning, thereby affecting the diameter and morphology of the fiber. Liu et al. [69] have shown that suitable humidity can enable preparation of NFs with better morphology. As indicated above, many factors can affect the electrospinning process, enabling preparation of NFs with different morphologies and functions. The effects of varying factors, provides a theoretical basis for the preparation of NF membranes with excellent photocatalytic properties.

### 2.3. Types of Nanofibers Prepared by Electrospinning Technology

Prototype of electrospinning technology include uniaxial NF [70], coaxial NF [71,72], and Janus NF [73], as shown in Figure 4. In the 16th century, William Gilbert identified the

electrostatic force in liquids, which underpinned the development of electrospinning [74]. The simplest approach is the uniaxial electrospinning technique, as shown in Figure 2. In uniaxial electrospinning technology, only a single fluid is involved; the compositions of solvents, polymers, and functional particles are relatively simple, without considering the impact of other factors. Uniaxial electrospinning technology is simple, easy to operate, and the prepared membranes have stable structure and high yield, which is beneficial for further surface functionalization, heat treatment, and hydrothermal growth of functional particles.

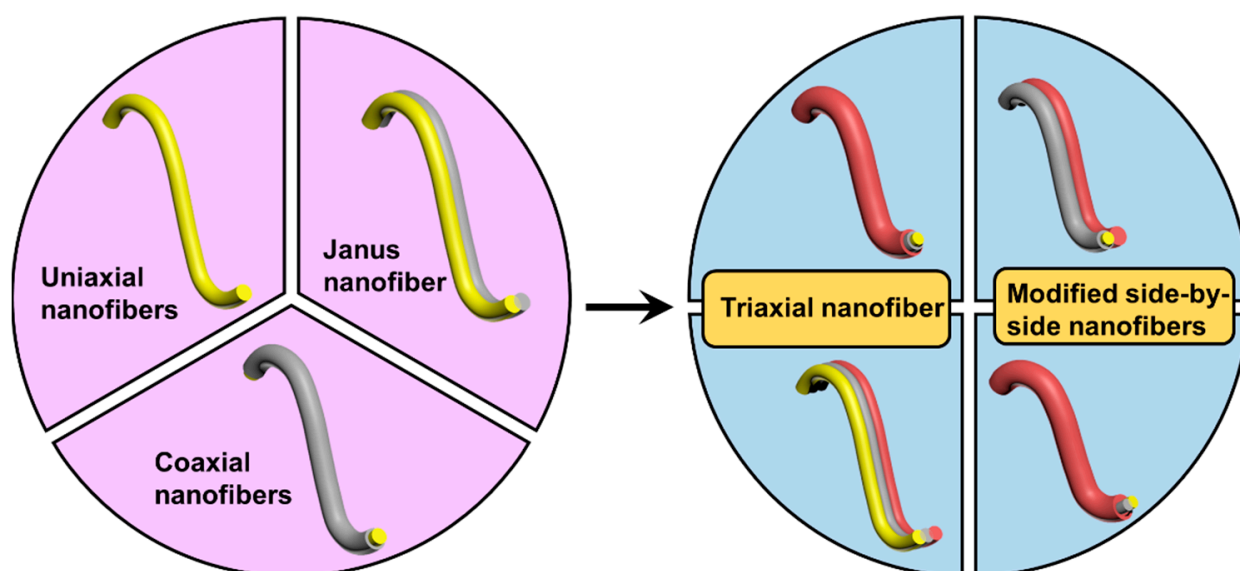


**Figure 4.** Diagram showing recent developments in electrospinning.

In 2003, coaxial electrospinning technology was established to manufacture core–shell nanofibers with varied material properties [75]. Two different kinds of polymers can be combined using coaxial electrospinning technology to create core–shell micro– or nanofibers. The ability of coaxial electrospinning to prepare core–shell structured fibers has attracted increasing attention because it can enhance the properties of the materials for a variety of applications, particularly for environmental purification. The coaxial electrospinning technique is anticipated to be able to prevent the mixing of the polymers that make up the core and the shell. Additionally, this technology offers superior mechanical characteristics, porosity, and hydrophilicity, and minimizes membrane swelling. The synergistic effect created by the two distinct polymers can compensate for the weakness of one of the polymers.

Uniaxial NFs [70] and coaxial NFs have the advantages of simple operation and easy preparation. However, the demands of people have increased with the development of society, so there is a need to introduce particles and polymers with different functions to enhance the performance of NF membranes. However, the addition of some non–spinning polymers and functional particles increases the difficulty of electrospinning. In addition, in order to achieve required multifunctional and mechanical properties, improvements in multi–fluid electrospinning [16,54] were developed. Improved multi–fluid electrospinning includes: (1) Triaxial NF membranes, which can enhance the multifunctional ability of the membrane and divide different functional particles into different areas. The division of functional areas can avoid the adverse effects of different types of particles. It contributes to enhancing the functions of a single function area [75]; (2) Three–level coaxial NF membranes. This structure is developed based on coaxial NFs. After adding the working solution fluid, the electrospinning performance of the polymer and particles can be greatly improved [76]. (3) Modified side–by–side electrospinning NF membranes. These can mainly be divided into two types: one type involves changing the side of the Janus NF into a coaxial NF, with the aim of it dividing the working area [77]; the other type involves adding the working

fluid to the outside of the Janus NF membrane, which can increase the spinnability of the Janus NF.

### 3. Treatment of Membrane

#### 3.1. Modification of Electrospinning Membrane

##### 3.1.1. Surface Modification

In order to improve photocatalytic degradation activity, moderately inert polymer NFs are treated with compounds that have reactive functional groups, such as amines, carboxyls, hydroxyls, or nitriles. Typically, NF materials are submerged in an alkaline liquid to produce hydroxyl or carboxyl groups on their surface so the surface of the NF membrane can be altered to improve the interaction or deposition of photocatalyst particles.

Mohamed et al. [78] studied the photocatalytic degradation performance of a surface-modified PAN NFs/biosilica composite membrane, as depicted in Figure 5a. The PAN NF membrane was prepared by electrospinning technology. As shown in Figure 5b–d, the NF membrane contained porous diatomite and rice husk which were cross-linked. The photocatalytic performances of these membranes for the degradation of malachite green (MG) were compared. The results showed that the photocatalytic degradation efficiency of diatomite and rice straw silica membranes for MG could reach 99% after 15 and 25 min, respectively. The degradation efficiency was highest at pH = 7. Under optimal conditions, the material was able to degrade 98% of MG within 10 min. The prepared NF membrane can be used in a continuous operating mode.

A PAN NF membrane [79] was placed in solution with hydroxylamine hydrochloride and sodium hydroxide to aminate the membrane (AO-PANNM). After that, AO-PANNM was thoroughly washed and dried. The obtained AO-PANNM was put in the solution with copper sulfate and iron chloride to prepare a copper-iron bimetal modified PAN NF membrane (BM-PANNM), as shown in Figure 5e; the NFs became thinner, but their morphologies were intact (Figure 5f,g). BM-PANNM has a superfine fiber diameter (600 nm) and a large surface area ( $5.34 \text{ m}^2 \text{ g}^{-1}$ ). It exhibits significant photocatalytic activity (>99.99%) against Active Blue 19, Active Red 195, and Acid Orange 7 within 60 min, and it has good cycle performance. This kind of modified PAN NF membrane can provide a broader platform for the degradation of dyes by NF materials in the future.

Through surface modification with hydrazine hydrate (HH) and hydroxylamine (HA) (HA-n-PAN, HH-n-PAN), and subsequent coordination with  $\text{Fe}^{3+}$ , a series of Fe-complexed PAN NF membranes (Fe-M-n-PANs) were prepared [80]. They were able to significantly improve the adsorption and photocatalytic degradation properties of azo dyes under visible light in water, as exhibited in Figure 5i–k. The higher removal efficiency was mainly due to the synergistic effect of adsorption and photocatalytic degradation in the presence of  $\text{H}_2\text{O}_2$ . In addition, the removal efficiency was determined by the ratio of HA to HH. The membrane modified with HA and HH simultaneously had higher removal efficiency than the membrane modified with a single solvent, because more active sites can be produced using HA and HH at the same time, accelerating the removal of dyes. Fe-M-n-PANs were found to enable rapid degradation of dye molecules and to free up adsorption sites for the surface to adsorb dye molecules (Figure 5h); the Fe-M-n-PANs had good cycle stability and were able to maintain excellent photocatalytic performance after five cycles. This study provides a new direction for the treatment of industrial wastewater in the future.

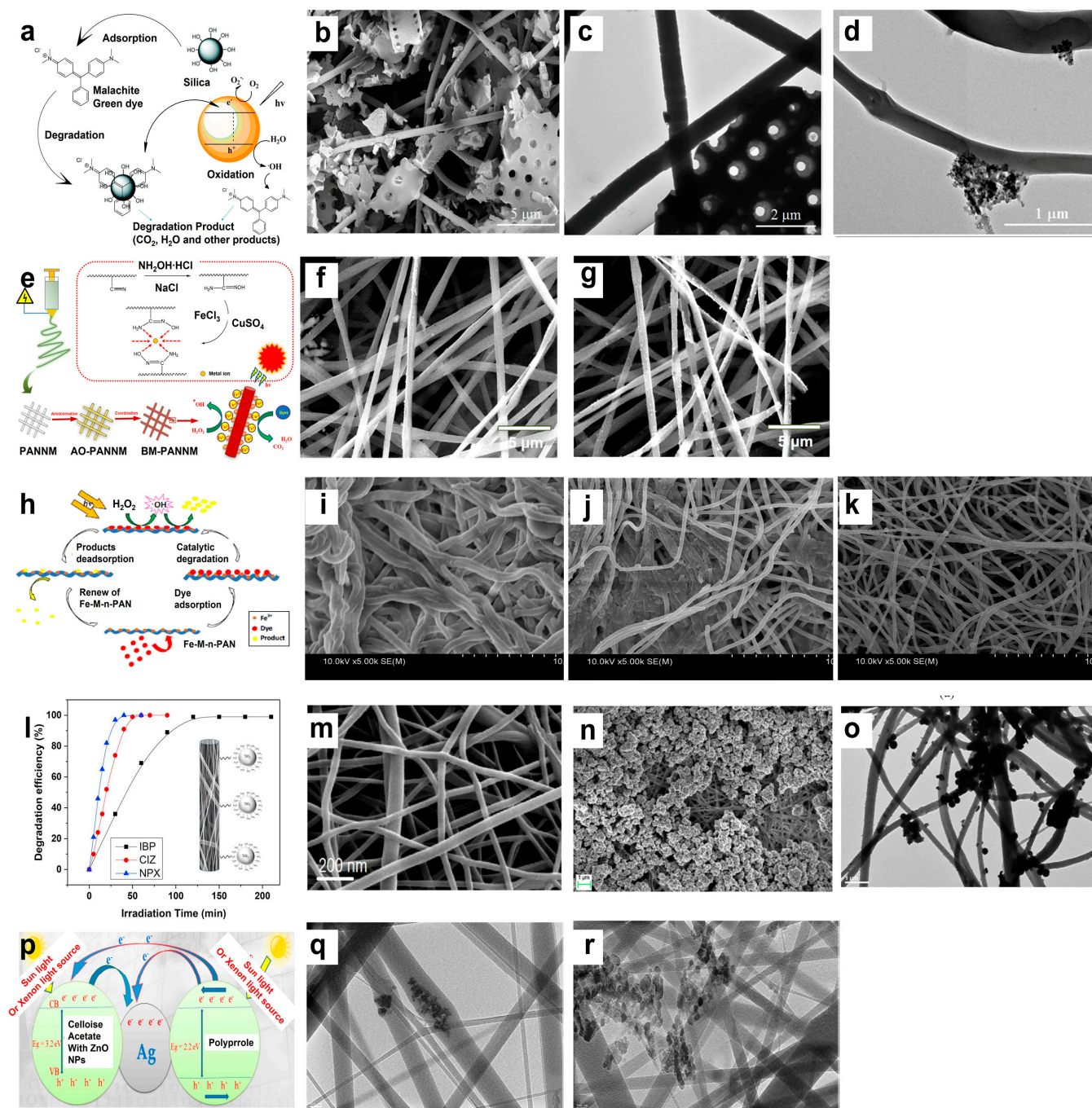


**Figure 5.** MG photodegradation mechanism (a), SEM image (b), TEM images (c,d) of diatomite porous microparticles on the surface of the NFs [78], Copyright 2019, Elsevier. Scheme of the design, processing, and photocatalytic degradation mechanism of BM-PANNM (e), SEM images of PANNM (f), BM-PANNM (g) [79], Copyright 2020, Elsevier. Schematic of removal of azo dyes from water using Fe-M-n-PAN in the presence of  $\text{H}_2\text{O}_2$  (h), FE-SEM images (the plotting scale: 10  $\mu\text{m}$ ) of HA-n-PAN (i), Fe-M-n-PAN (j), HH-n-PAN (k) [80], Copyright 2017, Elsevier. The photocatalytic degradation efficiency of PAN-CNT/ $\text{TiO}_2$ - $\text{NH}_2$  NFs (l), SEM images of PAN-CNT (m), PAN-CNT/ $\text{TiO}_2$ - $\text{NH}_2$  (the plotting scale: 1  $\mu\text{m}$ ) (n), and TEM image of PAN-CNT/ $\text{TiO}_2$ - $\text{NH}_2$  NFs composite (the plotting scale: 1  $\mu\text{m}$ ) (o) [81], Copyright 2019, Elsevier. Diagram of the photocatalytic degradation mechanism of malachite green dye (MG) on ZnO composite NF immobilized with silver (p), TEM images (the plotting scale: 100 nm) of ZnO composite NF before silver immobilization (q), and after silver immobilization (r) [82].

UHeida et al. [81] added modified titanium dioxide ( $\text{TiO}_2$ ) nanoparticles (NPs) to PAN/multi-walled carbon nanotube composite NFs (PAN-MWCNT/ $\text{TiO}_2$ - $\text{NH}_2$ ) and evaluated the photocatalytic degradation performance of PAN-MWCNT/ $\text{TiO}_2$ - $\text{NH}_2$  for ibuprofen, cetirizine, and naproxen. Comparing Figure 5m with Figure 5i, it can be observed that amino-functionalized  $\text{TiO}_2$  NPs were distributed on the surface of PAN-CNT NFs (PAN-MWCNT/ $\text{TiO}_2$ - $\text{NH}_2$ ), and the NFs were cross-linked. Examining the TEM image (Figure 5n), it can be seen that amino-functionalized  $\text{TiO}_2$  NPs were successfully attached to the surface of PAN-CNT NFs. Because the PAN-MWCNT/ $\text{TiO}_2$ - $\text{NH}_2$  composite NF membrane has a large specific surface area, multiple catalytic sites, and good flexibility, it exhibited excellent photodegradation efficiency for ibuprofen, naproxen, and cetirizine. In addition, the effect of the pH value on the photocatalytic degradation efficiency was also studied; it was found that the photocatalytic degradation efficiency was highest at pH = 2–4. The NF membrane has very wide application potential in the highly efficient photocatalytic degradation of pollutants.

A high-efficiency, environment-compatible, and porous silver surface-modified photocatalytic zinc oxide/cellulose acetate/polypyrrole (ZnO/CA/Ppy) hybrid NF membrane [82] was prepared. The effects of the flow rate, applied voltage, and other electrospinning parameters were also studied. Adjusting various electrospinning parameters enabled preparation of a ZnO/CA/Ppy composite NFs with uniform morphology; the distance between the needle tip and collector was 18 cm, the CA polymer concentration was 16%, the electrospinning flow rate was 0.2 mL/h, and the applied voltage was 18 kV. Depositing Ag NPs on the ZnO/CA/Ppy composite NFs enabled production of NFs with a narrower band gap, so the photocatalytic efficiency of composite NFs could be improved (Figure 5p). The results showed that ZnO NPs were uniformly distributed on the NF membrane (Figure 5q), and ZnO/CA/Ppy/Ag composite NFs were formed after Ag NPs were deposited (Figure 5r). The photocatalytic degradation efficiency of the ZnO/CA/Ppy/Ag composite NFs was 30% higher than that of the ZnO/CA/Ppy composite NFs.

### 3.1.2. Pore-Making Treatment

The pore-forming treatment of NF membranes is also an important means to improve photocatalytic performance. Based on NF membranes, many improvements have been achieved using different pore-making technologies, such as post-treatment technology [83], direct technology [84], solvent technology [85], thermal treatment technology [86], etc. The porous structure of MIL-88A/PAN nanoporous membranes is enhanced by porous MIL-88A material [84].  $\text{Ag}_3\text{PO}_4$ /P25 composite bi-polymer NF membrane were synthesized by two different polymers PMMA and PVP through post-treatment [87]. Lv et al. [83] used post-treatment technology to prepare dimethylglyoxime (DMG)/ $\text{TiO}_2$ /PAN NF mats (WS6), as shown in Figure 6. PVP was able to be removed in hot water because of the water solubility of PVP; the surface of the remaining PAN membrane appeared to have vacancies occupied by PVP (Figure 6a). An innovative porous WS6 prepared by electrospinning technology was used to deal with  $\text{Ni}^{2+}$  and methylene blue (MB) mixture pollutant treatment. Due to the capacity of DMG for detecting  $\text{Ni}^{2+}$ , the red and virgulate  $\text{Ni}(\text{DMG})_2$  that formed on the surface of NFs showed that the complex had observable adsorption capacity. The MB degradation efficiency of WS6 was 97% within 60 min, which is the most crucial factor. Most importantly, the  $e^-$  and hole ( $h^+$ ) transmission paths were shortened through the porous structures. These functional NF mats may have potential application in sensing,  $\text{Ni}^{2+}$  adsorption, and the photocatalytic degradation of organic pollutants via the intermediate  $\text{Ni}(\text{DMG})_2$  as a photocatalyst. The enhanced degradation mechanism of WS6 is depicted in Figure 6b. When the heterojunction is built, an electric field is created at the interface between  $\text{Ni}(\text{DMG})_2$  and  $\text{TiO}_2$  to encourage the accelerated flow of  $e^-$  and  $h^+$ . Inside the mat,  $\text{Ni}(\text{DMG})_2$  and  $\text{TiO}_2$  is able to absorb ultraviolet light to produce  $e^-$  and  $h^+$ . The excited  $e^-$  in the CB of  $\text{Ni}(\text{DMG})_2$  leaps onto the CB of  $\text{TiO}_2$ . Under the action of the electric field, some of the  $h^+$  in  $\text{TiO}_2$  migrates to the VB in  $\text{Ni}(\text{DMG})_2$  at the same time. As a result,  $e^-$  and  $h^+$  are separated.  $\bullet\text{O}_2^-$  radicals can be created when the  $e^-$  on CB

reacts with oxygen. Water and the  $h^+$  on VB may combine to create  $\bullet OH$  radicals. These two varieties of radicals can oxidize MB. Small molecules, such as water and  $CO_2$ , can be produced after the degradation of MB molecules. This work successfully integrates the photocatalytic degradation of organic contaminants and metal ion adsorption. Porous NF membranes prepared by post-treatment technology can not only shorten the path of electrons and holes, but also provide more sites for photocatalytic reactions. However, this membrane has the disadvantage of easy recombination of  $e^-$  and  $h^+$  and poor mechanical properties. How to solve this problem should be a future direction of research.

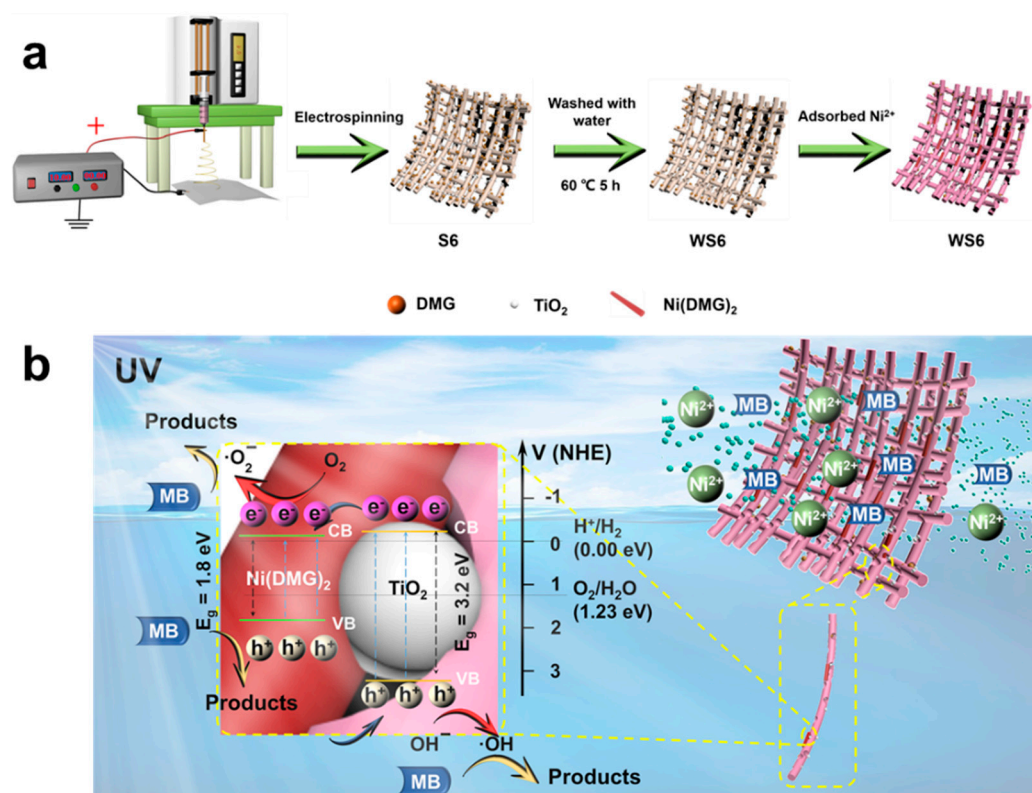


**Figure 6.** Schematic of preparing nanofibrous mats process (a) and photocatalytic degradation of MB on  $Ni(DMG)_2/TiO_2$  nanofibrous mats (b) [83]. Copyright 2022, Elsevier.

### 3.2. Thermal Treatment

Heat treatment [88] of inorganic materials can change their morphology, physical structure and enhance their strength and crystallinity [89,90]. Researchers have paid a lot of attention to the preparation of inorganic NF membranes [91] because of their excellent mechanical and thermal stability [92]. Organic membranes are easily broken down under light in photocatalytic degradation [93]. Heat treatment is carried out to enhance their properties, such as wettability, mechanical capabilities, thermal characteristics, and pore size distribution. Generally, NF membranes are heated through calcination, carbonization, and hydrothermal treatment.

#### 3.2.1. Calcination

The process of heating materials to a high temperature in a controlled atmosphere is referred to as calcination. In order to increase the mechanical and thermal stability of inorganic or ceramic materials, calcination is typically utilized.

Singh et al. [94] used *N, N*-dimethylformamide (DMF), zinc acetate, PAN, and ZnO to prepare porous ZnO NF by uniaxial electrospinning. Figure 7a,b show the morphologies of porous ZnO NFs under different calcination temperatures. Comparing Figure 7a with Figure 7b, the diameter of the fibers is reduced by 80% after calcination at 650 °C, and

the crystallinity and crystal size of the porous ZnO NFs are significantly increased after calcination at high temperatures. The band gap decreases as the crystal size increases, as depicted in Figure 7c. Singh et al. also found that porous ZnO NFs showed good photocatalytic degradation performance for naphthalene and anthracene.

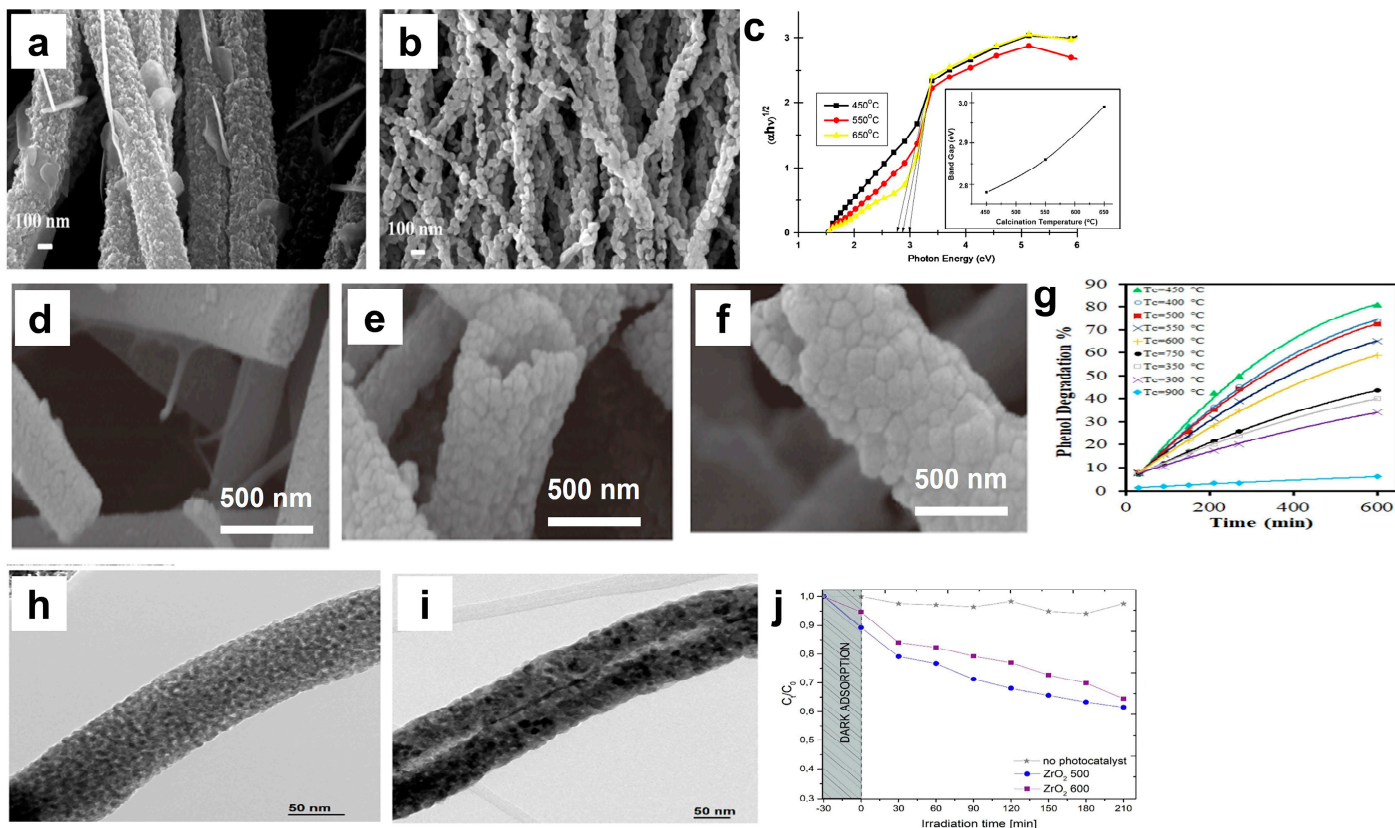


**Figure 7.** SEM images of ZnO NFs treated at 450 °C (a), 650 °C (b); the band gap of ZnO NFs treated at different calcination temperatures (c) [94], Copyright 2013, Elsevier. SEM images of 5% Ag/TiO<sub>2</sub> photocatalytic NFs treated at 450 (d), 600 (e), and 750 °C (f); the photocatalytic degradation of 5% Ag/TiO<sub>2</sub> treated at different calcination temperatures (g) [95], Copyright 2022, Elsevier. TEM images of ZrO<sub>2</sub> 500 (h) and ZrO<sub>2</sub> 600 (i) nanostructure; the photocatalytic degradation of ZrO<sub>2</sub> at 500 and 600 °C (j) [96], Copyright 2023, Elsevier.

Ag/TiO<sub>2</sub> photocatalytic NFs were prepared [95], and the effects of silver content (0.5–15%) and calcination temperature (300–900 °C) on the degradation of phenol were studied. It can be seen from Figure 7d,f that some cracks appeared on the surface of NFs after being treated under high temperatures. With increase in calcination temperature, the fiber diameter decreased from 5 μm to 500 nm, the boundaries of the grains on the surface of the NFs became clearer, and the grains became rougher. The grains shrunk and the boundaries of the grain appeared to crack with increasing calcination temperatures. This may have been due to the continuous decrease in PVP, or the growth and change in the crystal structure of TiO<sub>2</sub> during the calcination process. This study also found that the highest degradation rate of phenol was 82.65% when the calcination temperature was 450 °C.

Zaborowska et al. [96] prepared PVP/EtOH/ZrOCl<sub>2</sub>/DMF one-dimensional zirconia NFs using a uniaxial electrospinning technique. The PVP/ZrOCl<sub>2</sub> composite fiber exhibited a smooth and uniform surface, the average diameter being 324 nm. The average diameters of ZrO<sub>2</sub> (500 °C) and ZrO<sub>2</sub> (600 °C) were 162 and 95 nm, respectively. XRD analysis confirmed the existence of monoclinic and tetragonal phases in ZrO<sub>2</sub> (500 °C) and ZrO<sub>2</sub> (600 °C). The specific surface area of PVP/ZrOCl<sub>2</sub> composite fiber mats calcinated at 500 °C was 53.8 m<sup>2</sup>/g, which was 15 m<sup>2</sup>/g higher than the mats calcinated at 600 °C. The bandgap widths of PVP/ZrOCl<sub>2</sub> composite fiber obtained at 500 °C and 600 °C were 4.9 and 5.6 eV,



respectively. The larger specific surface area and lower band gap of  $ZrO_2$  NFs treated at lower temperatures contributed to enhancing the photocatalytic degradation performance. Compared with the mats calcinated at  $600\text{ }^\circ\text{C}$ , the efficiency of MB degradation was only increased by 3%. The photocatalytic degradation performance of fiber mats was not improved significantly by increasing the calcination temperature, so selecting a suitable temperature is very important for improving photocatalytic performance and making rational use of energy.

### 3.2.2. Carbonization

Carbonization is defined as the heating of materials at high temperatures in nitrogen or other inert gases. By combining electrospinning and carbonization techniques, Song et al. prepared C/TiO<sub>2</sub> NFs [97]. The impact of the carbonization temperature on the electrochemical performance and photocatalytic degradation of MB was investigated. C/TiO<sub>2</sub> NFs prepared at carbonization temperatures at 400, 600, and 900 °C are shown in Figure 8a–c. The diameters of NFs carbonized at various temperatures were uniformly distributed between 280 and 480 nm. The NFs formed network structures and they were continuous and random. The morphologies of the NFs were not appreciably altered by heat treatment. These findings indicated that C/TiO<sub>2</sub> NFs carbonized at 900 °C exhibited the highest capacitance, while C/TiO<sub>2</sub> NFs carbonized at 400 °C had the best photocatalytic activity. The transfer of photogenerated electrons from the conduction band of TiO<sub>2</sub> to carbon was able to improve the separation efficiency of electrons and holes during the photocatalytic process, so the photocatalytic degradation efficiency of C/TiO<sub>2</sub> NFs was increased. This research serves as a guide to the potential for using C/TiO<sub>2</sub> NFs in energy storage technologies and photocatalytic materials in the future.

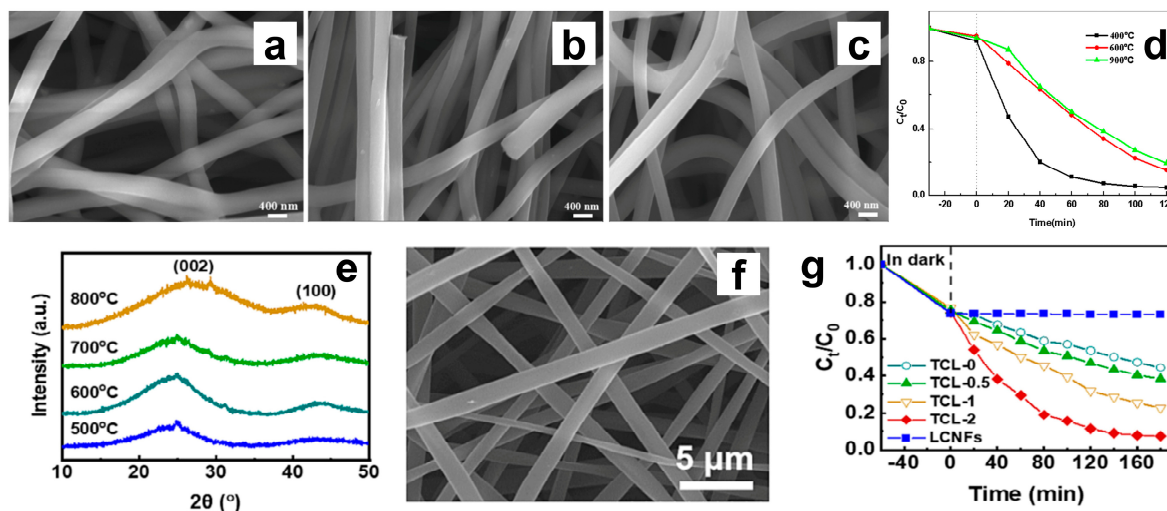


**Figure 8.** SEM images of C/TiO<sub>2</sub> NFs carbonized at 400 °C (a), 600 °C (b), and 900 °C (c); the photocatalytic degradation of C/TiO<sub>2</sub> NFs (d) [97], Copyright 2020, Elsevier. XRD patterns of LCNFs carbonized at different temperatures (e), SEM image of LCNFs obtained at 800 °C (f); the photocatalytic degradation of TCL to rhodamine B (RhB) (g) [98], Copyright 2023, Elsevier.

Zhai et al. [98] loaded TiO<sub>2</sub> and g-C<sub>3</sub>N<sub>4</sub> into lignin-based carbon NFs (LCNFs) and then prepared TiO<sub>2</sub>/g-C<sub>3</sub>N<sub>4</sub>@LCNFs (TCL) through carbonization treatment. The spinnability of lignin solutions, the chemical structure and morphology of LCNFs, TiO<sub>2</sub>/g-C<sub>3</sub>N<sub>4</sub>@LCNFs, and the catalytic degradation performance of RhB were studied. Lignin-based precursor NFs were able to be completely carbonized, and melamine was converted into g-C<sub>3</sub>N<sub>4</sub> at 600 °C (Figure 8e); the SEM image of it is shown in Figure 8f. Under visible light irradiation, the degradation rate of RhB over TiO<sub>2</sub>/g-C<sub>3</sub>N<sub>4</sub>@LCNFs was 92.76% (Figure 8g). The high photodegradation performance of TiO<sub>2</sub>/g-C<sub>3</sub>N<sub>4</sub>@LCNFs can be attributed to the synergistic effect of TiO<sub>2</sub> and g-C<sub>3</sub>N<sub>4</sub>; the synergistic effect can improve

the separation efficiency of electrons and holes. This work opens a new direction for the development of high-efficiency photocatalysts based on biomass-derived fiber materials.

### 3.2.3. Hydrothermal and Solvothermal Technology

Hydrothermal technology refers to the chemical reactions carried out in water at a certain temperature and pressure. Using hydrothermal technology to prepare materials can enrich the structure and functional groups, increase the specific surface area, and improve the performance of materials. Mesoporous  $\text{TiO}_2/\text{In}_2\text{O}_3$  NF was synthesized by electrospinning and hydrothermal technology [99].  $\text{In}_2\text{O}_3$  tightly adheres to the surface of  $\text{TiO}_2$  NFs, and  $\text{TiO}_2/\text{In}_2\text{O}_3$  hybrid NFs are mesoporous, as shown in Figure 9(a1–a3). This study also found that the additional amount of  $\text{In}_2\text{O}_3$  plays an important role in the formation of mesoporous NFs. When the raw material weight of  $\text{In}_2\text{O}_3$  was 53.25 mg (TI–A, Figure 9(a1)), 95.5 mg (TI–B, Figure 9(a2)), and 190.1 mg (TI–D, Figure 9(a3)), the NFs were mesoporous. Compared with  $\text{TiO}_2$  and  $\text{In}_2\text{O}_3$ , the mesoporous  $\text{TiO}_2/\text{In}_2\text{O}_3$  NFs exhibited better photocatalytic degradation ability for RhB degradation, as shown in Figure 9b. The improvement in photocatalytic ability can be mainly attributed to more active sites provided by the mesoporous structures, and the expansion of the light response range provided by type II heterostructures. This work provides a new strategy for efficiently constructing mesoporous heterostructure photocatalysts.

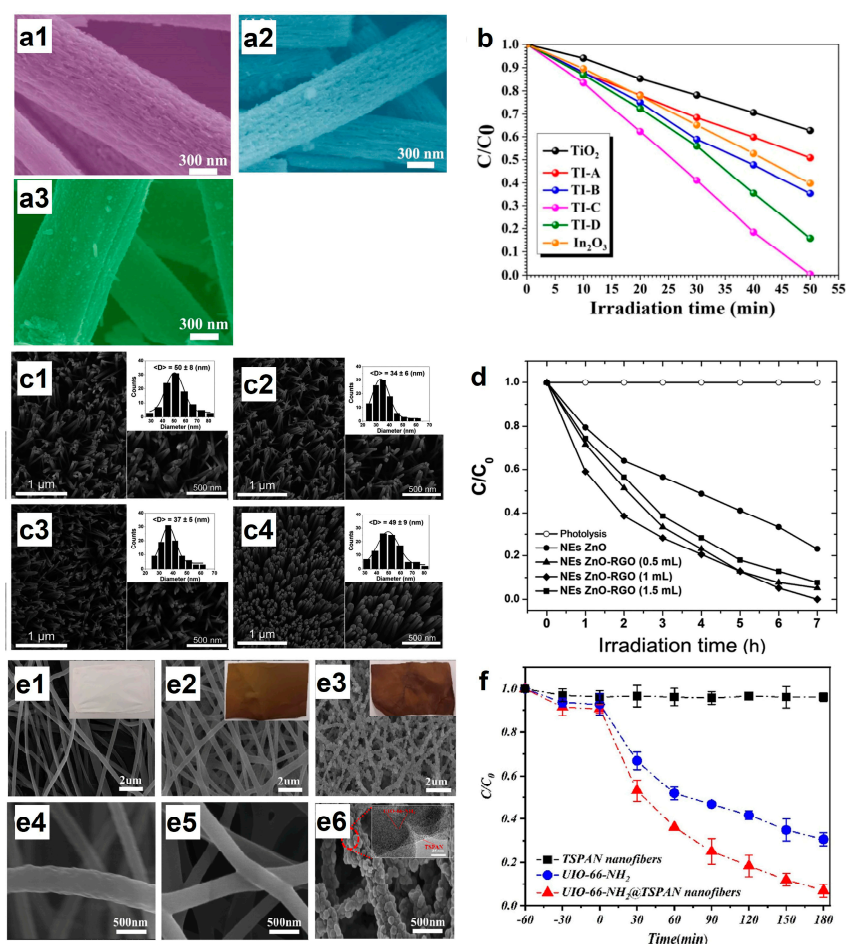


**Figure 9.** SEM images of TI–A (a1), TI–B (a2), and TI–D (a3), photocatalytic RhB degradation profiles (b) [99], Copyright 2021, Elsevier. SEM images of ZnO–RGO seed layers with different amounts of RGO: 0 mL (c1), 0.5 mL (c2), 1.0 mL (c3), and 1.5 mL (c4) in the spinning solutions; the photocatalytic degradation of methyl orange (MO) over ZnO–RGO NRs (d) [100], Copyright 2019, Elsevier. SEM images of electrospun PAN NFs (e1,e4), TSPAN NFs (e2,e5), and UIO–66–NH<sub>2</sub>@TSPAN NFs (e3,e6); the photocatalytic degradation of Cr(VI) over different NFs (f) [101], Copyright 2022, Elsevier.

ZnO and reduced graphene oxide (ZnO–RGO) nanorods were grown on tin fluoride oxide (FTO) glass substrates by electrospinning and hydrothermal techniques [100]. Electrospun NFs containing PVP, zinc acetate, and different amounts of RGO were calcinated at 400 °C for 1 h to prepare a ZnO–RGO precursor layer. Then the precursor layer was used for hydrothermal growth of (ZnO–RGO) nanorods. Figure 9(c1–c4) shows that ZnO grew on the surface of the RGO sheets (the areas surrounded by discontinuous white lines). This may have been due to the fact that there was a strong interaction between ZnO NPs and RGO sheets and that the functional groups on the surface of the modified graphene provided sites for aggregation and nucleation of the host material. The average diameter of ZnO NPs which formed ZnO–RGO nanorods decreased as the amount of RGO increased. This was related to the increment in electrical conductivity of the electrospinning solution by the addition of RGO. ZnO–RGO nanostructures containing 1.0 mL of RGO exhibited the highest photocatalytic activity for the degradation of MO, as depicted in Figure 9d.

Solvothermal technology is a synthesis technology based on hydrothermal technology, which refers to mixtures reacted in a closed system using organic or non-aqueous solvents. It differs from hydrothermal reactions in terms of the solvent. Hydrothermal technology is often only applicable to the preparation and treatment of oxide materials or water-insensitive materials. Compounds such as carbides, fluorides, and novel phosphate materials are not applicable for preparation by hydrothermal technologies, so the development of solvothermal technology has been promoted.

A metal–organic framework (MOF) [1] as a precursor for the synthesis of NF membranes has gained prominence. MOF-based NF membranes have the advantages of a distinctive crossing network connection, an extraordinarily wide surface area, and a porous structure. In the synthesis process of MOFs, solvothermal technologies are generally used because the metal ions in MOF are more sensitive to water. Zhou et al. [101] have successfully grown UIO–66–NH<sub>2</sub> on thermally stabilized electrospun PAN NFs (TSPAN) using solvothermal technologies (UIO–66–NH<sub>2</sub>@TSPAN NFs) to reduce Cr(VI). TSPAN has high stability and abundant nucleation sites, providing active sites for the growth of an MOF. Figure 9(e1,e4) shows SEM images of electrospun PAN NFs before and after thermal oxidation stabilization treatment. It can be observed that the prepared PAN NFs were randomly distributed, with uniform fiber diameter distribution and a smooth surface. The thermally stabilized TSPAN NFs were cross-linked and had a smoother surface, as shown in Figure 9(e2,e5). The SEM images after the growth of UIO–66–NH<sub>2</sub> are shown in Figure 9(e3,e6). It can be seen that the particles were uniformly distributed on the surface of the NF. The spherical UIO–66–NH<sub>2</sub> particles directly nucleated and grew on the TSPAN NFs, illustrating that UIO–66–NH<sub>2</sub> and TSPAN bound tightly. This is because there are acridone rings, naphthyridine rings, and hydrogen–naphthyridine rings in TSPAN NFs, which can act as reaction sites to promote the heterogeneous nucleation of UIO–66–NH<sub>2</sub>. Compared to powdered UIO–66–NH<sub>2</sub>, the photocatalytic reduction efficiency of Cr(VI) on UIO–66NH<sub>2</sub>@TSPAN was improved by 23% (Figure 9f).

## 4. The Application of Photocatalytic Degradation of Pollutants in Wastewater

### 4.1. Photocatalytic Degradation of Dyes

For many industries, including textile, dyeing, papermaking, pulp, tanning and paint, synthetic dyes are essential. Dyes have high water solubility, which makes them challenging to remove and treat. Typically, only 80% of the dye is absorbed by the fabric; the other 20% is desorbed and discharged into the water. Dyes block light from penetrating the water, so that photosynthesis is slowed down and dissolved oxygen levels are reduced, which has an impact on the entire aquatic ecosystem [102]. Furthermore, dyes are poisonous and carcinogenic compounds can enter the entire food chain [103]. It is necessary to remove dyes from wastewater using modern technology. Photocatalysis technology is regarded as an excellent “green strategy” because of its low energy consumption and other environmental advantages. Photocatalysts can produce oxidation species such as •O<sub>2</sub><sup>−</sup> and •OH to degrade pollutants such as dyes in wastewater [104]. The widespread

use of photocatalysts is due to their beneficial traits, such as their quick and thorough decomposition of a variety of organic compounds prevalent in water and wastewater, without generation of persistent by-products, and their ease of scaling up.

The earliest electrospinning NFs photocatalysts to degrade dyes were prepared by uniaxial electrospinning technology [23]. The uniaxial NFs prepared by uniaxial electrospinning technology were the origin of complex structural NFs. As the simplest NF with the simplest structure, uniaxial NFs have the advantages of easy preparation, simple operation, and capacity to load a variety of functional materials. The membrane materials prepared by this technology are widely used for the photocatalytic degradation of pollutants in water [1,38]. In order to improve the photocatalytic performance, Zhou et al. [105] consistently integrated g-C<sub>3</sub>N<sub>4</sub> onto bacterial cellulose (BC) with a 3D NF network. In contrast to the modification of polypyrrole (PPy) in most research, developing carrier materials and reactors can significantly increase the catalytic performance. The prepared PPy@(BC/g-C<sub>3</sub>N<sub>4</sub>) flexible membrane was used under a xenon lamp ( $\lambda > 420$  nm) in the designed reactor. It exhibited strong catalytic performance (64.28%, 2 h), which was 5.27 times higher than BC/g-C<sub>3</sub>N<sub>4</sub>. After 10 cycles, more than 80% of the original catalytic performance was sustained. This research can be also applied to design flexible membrane materials with excellent photocatalytic performance [20]. A positive feature of this study was the loading of the functional materials layer-by-layer onto the BC. In this study, the BC mainly acted as a load carrier. The g-C<sub>3</sub>N<sub>4</sub> was responsible for visible light absorption and photocatalytic degradation for the entire material. The primary function of PPy is conductivity because the essence of photocatalysis degradation is the transfer of e<sup>-</sup> and h<sup>+</sup>. PPy can guide e<sup>-</sup> in time to achieve the purpose of e<sup>-</sup> and h<sup>+</sup> separation. However, the e<sup>-</sup> and h<sup>+</sup> can still be readily combined. How to solve the combination of e<sup>-</sup> and h<sup>+</sup> in the same type of particle is a problem that future research should address.

With the development of electrospinning technology, coaxial electrospinning technology has also emerged, in which the photocatalytic degradation performance of NF membranes prepared using coaxial electrospinning is improved. Coaxial electrospinning technology has two independent parts. By controlling the flow rate of the injection pump, the thickness of the shell layer of the NF can be adjusted, and even NF membranes with hollow structures can be prepared. The mechanical and photocatalytic performance of the NF membrane can be controlled by varying the thickness of the shell layer [106]. Compared with uniaxial NF membranes, NF membranes prepared using coaxial electrospinning technology have greatly improved mechanical properties [38]. Limiting the functional particles in the shell area can save a portion of the functional particles. In addition, using appropriate solvents can expose functional particles to the surface of NF, which can improve photocatalytic performance.

Coaxial electrospinning was used to prepare a new structure with TiO<sub>2</sub> micro-/nanospheres embedded in NFs [106], as illustrated in Figure 10a. The construction technology of the structure and the impacts of the core flow rates on photocatalytic capabilities were explored. Moreover, their photocatalytic performances were compared to those of comparison samples. The TiO<sub>2</sub> micro-/nanospheres were embedded in the NFs with various core and shell-spinning solutions and physical characteristics. The degradation efficiency for MB was 91.56% when the specific surface area of the NFs was 23.852 m<sup>2</sup>/g. There were substantial NF gaps in the innovative construction. The micro-/nanospheres had a large specific surface area and loose structure and were amenable to UV injection to boost the photocatalytic efficiency. In this study, the TiO<sub>2</sub> micro-/nanospheres were firmly fixed in the NF membrane by the coaxial electrospinning technology, which was able to reduce the loss of functional particles in the repeated cycle experiment and contribute to the maintenance of photocatalytic performance. However, the mechanical properties of the membrane may have been greatly weakened after calcination, and there were many functional particles embedded in the membrane. Suitable experimental design is important to improve the photocatalytic performance in the second cycle process, and the mechanical properties of membranes.

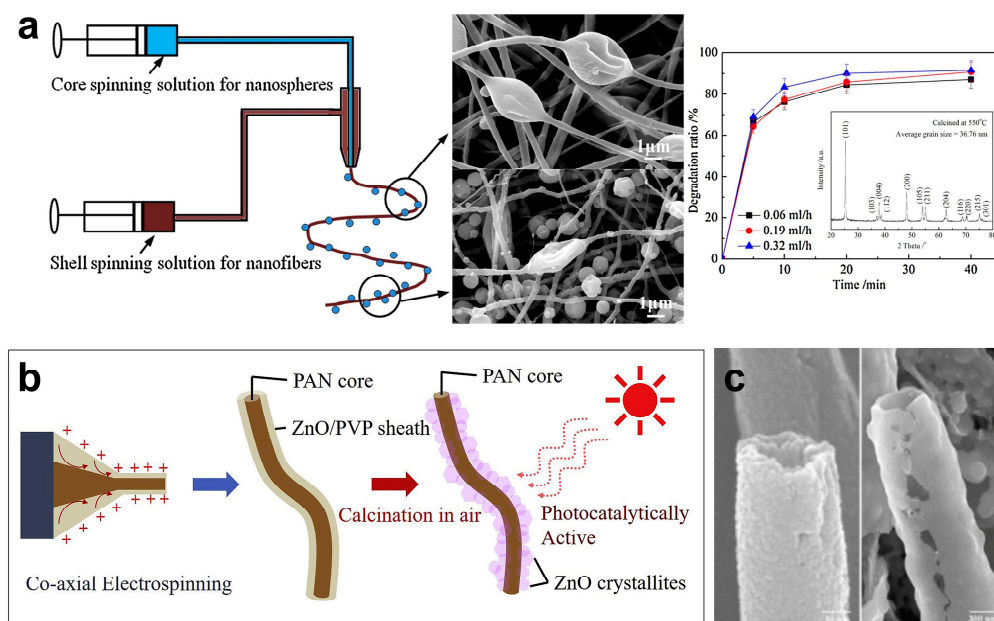


**Figure 10.** Schematic diagram of preparing hollow TiO<sub>2</sub> NFs and SEM image of TiO<sub>2</sub> micro-/nanospheres embedded in NFs and degradation rate of MB (a) [106], Copyright 2016, Elsevier. Schematic diagram of preparing ZnO/PVP coaxial NFs (b) [107], Copyright 2020, Elsevier. SEM image of hollow TiO<sub>2</sub> NFs (c) [108], Copyright 2013, Elsevier.

Large surface areas, prevention of nanoparticle aggregation, and easy separation from wastewater are all provided by NF membrane photocatalysts. In one study, flexible PAN was coated with ZnO photocatalysts in a single-step using sol-gel coaxial electrospinning [107], as shown in Figure 10b. In order to remove the PVP and crystallize the ZnO, a core/sheath structure made of a PAN polymer embedded in a ZnO–PVP mixture was prepared. To identify the ideal parameters for preparing NFs, the PAN and PVP concentrations and viscosities were changed. Thermogravimetric analysis and Fourier transform infrared spectroscopy were used to evaluate the thermal behavior and ideal calcination temperature. The flexibility and photocatalytic activity for the degradation of the MB of the NFs were maintained after several cycles. In this study, ZnO was mainly responsible for photocatalytic degradation. However, ZnO can only absorb ultraviolet light, which seriously limits its practical application. The mechanical properties of NF membranes are improved with the use of coaxial electrospinning technology. However, NF membranes calcinated in air are fragile, which is not conducive to later recovery and treatment.

A simple coaxial electrospinning approach was used to design two kinds of hollow TiO<sub>2</sub> NFs [108]. Titanium sol and a titanium precursor were used for the shell of two kinds of hollow TiO<sub>2</sub> NFs. The two types of hollow TiO<sub>2</sub> NFs shared a similar tubular structure on the nanoscale, although they differed in size and shell thickness. An SEM image of hollow TiO<sub>2</sub> NFs is depicted in Figure 10c. Hollow NFs made from titanium sol showed that the diffusion of the core and shell solutions may have been effectively prevented by a modest amount of water in the core. In order to develop the titanium precursor into the nanostructured TiO<sub>2</sub> wall of the hollow NFs, it was coated on the PVP core NFs as a shell template by coaxial electrospinning. The hollow TiO<sub>2</sub> NFs showed greater photocatalytic activity for the degradation of MB than uniaxial TiO<sub>2</sub> NFs. In this study, TiO<sub>2</sub> hollow NFs were obtained by coaxial electrospinning and high-temperature calcination. The hollow NFs had a large specific surface area and more active sites for photodegradation. Compared with uniaxial NFs, the photocatalytic performance was improved. However, the high-temperature calcination treatment seriously limits its mechanical properties, which makes it difficult to apply in practical environments in the future.

Peng et al. [109] prepared highly uniform SnO<sub>2</sub>/TiO<sub>2</sub> coaxial NFs with an adjustable interior morphology by one-pot step coaxial electrospinning. The core of these NFs was able to be varied from filled solid to peapod-like, and even to hollow tubes, by changing the concentration of the precursor solution. The degradation rate of RhB was  $4.6 \times 10^{-3} \text{ cm}^{-1}$  (Tubular SnO<sub>2</sub>/TiO<sub>2</sub> coaxial NFs). It was discovered that the photocatalytic activity of commercial TiO<sub>2</sub> photocatalysts was lower than that of tubular SnO<sub>2</sub>/TiO<sub>2</sub> coaxial NFs. This finding was explained by the formation of a heterojunction between SnO<sub>2</sub> and TiO<sub>2</sub>; the coaxial structure also an important role. The overall findings suggest that coaxial electrospinning can be used as a unique, simple technology for designing one-dimensional inorganic coaxial nanoscale heterostructures on a large scale. It can also be used for a variety of other purposes. This study ingeniously used oil to prepare coaxial NFs, which provides a direction for the preparation of such NF membranes in the future. However, the oil used in this study has certain limitations. The materials mixed with oil can easily come out of the membrane during catalytic treatment, which can cause secondary pollution to the water. The compatibility of the oil and the outer material in the electrospinning process should also be solved. In addition, looking for other materials to prepare coaxial nanostructures to enhance photocatalytic performance is important.

Janus NF membranes have been prepared by side-by-side electrospinning technology [57]. This technology is similar to coaxial electrospinning technology. Both have two independent parts. The difference between them is that the form of side-by-side electrospinning technology is similar to the p-orbit electronic cloud, with the two parts only having a small amount of contact. The contact point can form a heterojunction. The combination rate efficiency of e<sup>-</sup> and h<sup>+</sup> is greatly depressed and the efficiency of photocatalytic degradation is improved. Side-by-side electrospinning technology can reduce the inappropriate agglomeration between different kinds of particles. The structure of the design material can achieve an ideal photocatalytic effect, which provides a good example for the future photocatalytic treatment of pollutants in water.

(ZnO/PAN/DMF)/(Mn<sub>3</sub>O<sub>4</sub>CeO<sub>2</sub>/PAN/DMF) Janus NFs were electrospun in [110]. The Janus NFs consisted of ZnO NF on one side and Mn<sub>3</sub>O<sub>4</sub>/CeO<sub>2</sub> NF on the other. Using the MB solution, the photocatalytic performance was verified. The as-prepared Janus NFs outperformed conventional NFs (CFs) in terms of photocatalytic performance under UV and visible light. The results also showed that it was feasible to alter their photocatalytic activity under the appropriate light wavelength by varying the ratio of photocatalyst weights on each side of the Janus NF. Water purification, photocatalysis, and other applications can greatly benefit from membranes made of functional Janus NFs prepared using a specifically designed nozzle. ZnO, Mn<sub>3</sub>O<sub>4</sub>, and CeO<sub>2</sub> were used to realize the absorption of materials in different light bands. The Janus heterojunction was formed using an ingenious electrospinning design. Uniaxial and coaxial NFs membrane have the problem of e<sup>-</sup> and h<sup>+</sup> combination, this kind of Janus NFs can solve this problem because different kinds of particles are separated in different parts. However, compared with coaxial NF membranes, the material also has certain defects in mechanical properties.

Through conjugate electrospinning and the subsequent calcination procedure, a [TiO<sub>2</sub>/C]/[Bi<sub>2</sub>WO<sub>6</sub>/C] Janus NF heterojunction photocatalyst (JNHP) was conceived and built [20]. The JNHP with a distinctive Janus structure has two aspects: TiO<sub>2</sub>/C NF responds to ultraviolet light, and Bi<sub>2</sub>WO<sub>6</sub>/C NF responds to visible light, as shown in Figure 11a. JNHP exhibited excellent MB degradation. Under visible light and sunlight irradiation, the MB degradation efficiencies of JNHP were 93.3% (160 min) and 97.9% (140 min), respectively. Compared to TiO<sub>2</sub>/C and Bi<sub>2</sub>WO<sub>6</sub>/C photocatalysts, the photocatalytic activity of JNHP was improved, which primarily resulted from the cooperative effect of novel heterojunctions between TiO<sub>2</sub> and Bi<sub>2</sub>WO<sub>6</sub>, and conductive carbon NF. Additionally, JNHP showed great recyclable stability. The Bi<sub>2</sub>WO<sub>6</sub> nanoparticle (NP) can absorb light to create e<sup>-</sup>-h<sup>+</sup> pairs and excite the e<sup>-</sup> from the Bi<sub>2</sub>WO<sub>6</sub> (VB) to the conductive band (CB) when the surface of the JNHP is exposed to visible light. The e<sup>-</sup> on CB can easily move to the CNF because of the excellent conductivity of CNF. Additionally, it is simple

to transfer the  $h^+$  on the VB of  $Bi_2WO_6$  to the VB of  $TiO_2$ . The  $e^-$  and  $h^+$  are successfully separated and involved in the oxidation reaction because  $TiO_2$  and  $Bi_2WO_6$  can form a heterojunction. The  $h^+$  on the VB of JNHP quickly moves to the surface of JNHP, and  $h^+$  is oxidized with the MB molecule during the photodegradation process of MB. At the same time,  $O_2$  can absorb  $e^-$  by dissolving in water to produce  $\bullet O_2^-$ , which combines with  $H_2O$  to form  $\bullet OH$ . The active oxidation properties of chemicals  $\bullet OH$  and  $\bullet O_2^-$  can destroy MB molecules, as shown in Figure 11b,c. The Janus NF membrane preparation technology in this study is novel, and the proposed Janus NF heterojunction is innovative. In addition, the treatment of NF membranes in  $N_2$  solves the problem of material fragility, which provides an example for the preparation of self-supporting Janus NF heterojunction materials in the future. However, due to the defects of PAN and conjugated electrospinning technology, the material has the disadvantage of a low parallel rate in the preparation process, which leads to the preparation of too few Janus NFs. How to solve this problem is particularly important.

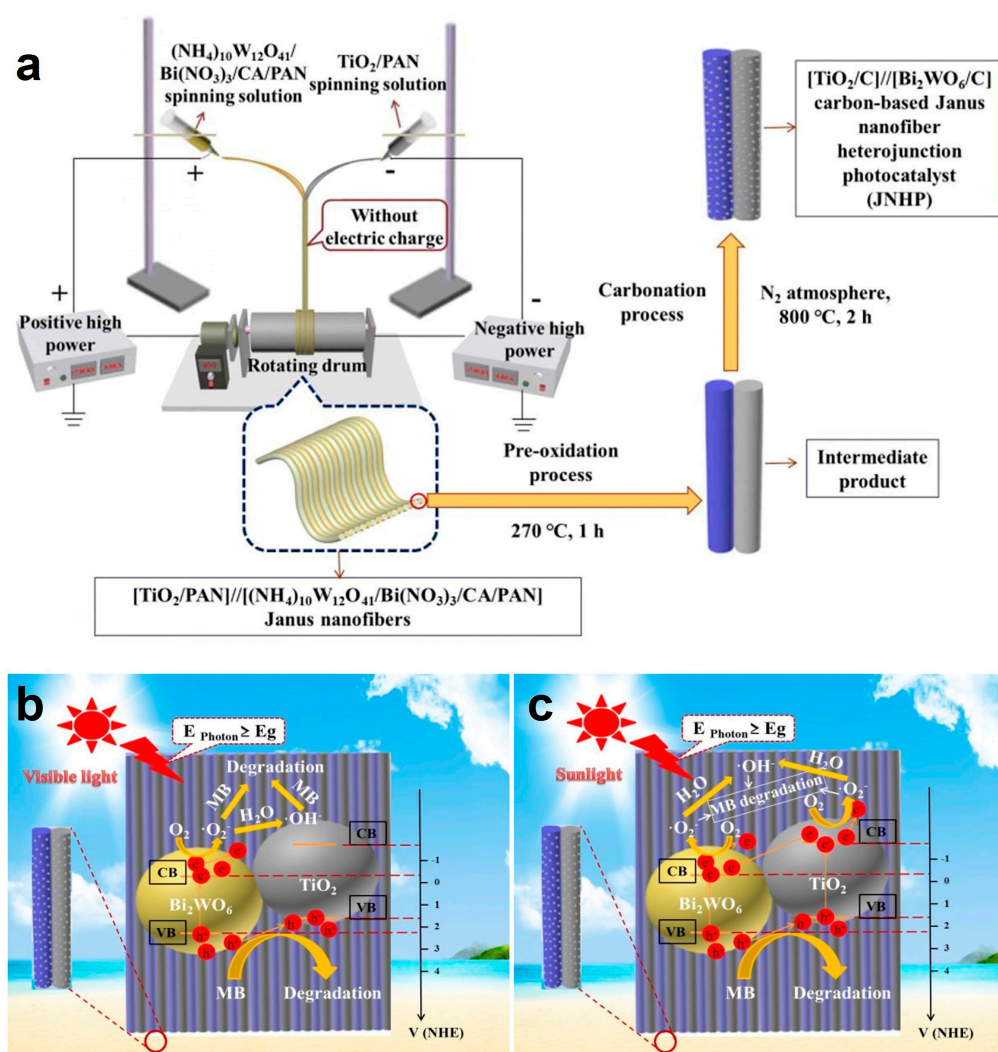


**Figure 11.** Schematic illustration of the preparation procedure of JNHP (a) and photocatalytic degradation mechanism (b,c) [20]. Copyright 2020, Elsevier.

The photocatalytic degradation performance of NF membranes prepared by different electrospinning techniques are shown in Table 1. These membranes show extensive application abilities in the degradation of MB. By comparison, it can be seen that Janus NF membranes have the highest degradation efficiency and the lowest energy consumption, which is related to the special structure of NFs prepared by improved electrospinning

technology. The formed special structure of NFs can improve the separation efficiency of electrons and holes, so the photocatalytic performance can be improved. However, the low mechanical properties, permeability, and high energy consumption of electrospun NF membranes need to be further resolved.

**Table 1.** Photocatalytic degradation performance of NF membranes prepared by different electrospinning techniques.

Photocatalytic Electrospinning Membrane	Technology	Pollutants	Source Light	Photocatalytic Degradation (%)	Degradation Time (min)	References
TiO <sub>2</sub> /g-C <sub>3</sub> N <sub>4</sub> fibers	Uniaxial electrospinning	MB	Xenon lamp (200 nm cutoff)	90%	20 min	[9]
TiO <sub>2</sub> micro-/nano-spheres coaxial NFs	Coaxial electrospinning	MB	UV light 365 nm	91.56%	40 min	[106]
ZnO/PAN/PVP NF	Coaxial electrospinning	MB	UV lamp 15 W	80%	6 h	[107]
TiO <sub>2</sub> hollow NFs	Coaxial electrospinning	MB	mercury lamp (200 W, $\lambda_{\max} = 365$ nm)	99%	50 min	[108]
(ZnO/PAN/DMF)//(Mn <sub>3</sub> O <sub>4</sub> CeO <sub>2</sub> /PAN/DMF) Janus NF	Parallel electrospinning	MB	MR16 lamp (50 W)	100%	2 h	[110]
[TiO <sub>2</sub> /C]/[Bi <sub>2</sub> WO <sub>6</sub> /C] Janus NF	Conjugate electrospinning	MB	Xenon lamp (400 nm cutoff)	100%	140 min	[20]

#### 4.2. Photocatalytic Degradation of Antibiotics

Antibiotics are employed as growth boosters in animal husbandry or to prevent and treat infectious infections in humans, animals, and plants [111]. The majority of antibiotics, along with urine and feces, are expelled into the environment as compounds, and they cannot be completely absorbed by the body [112]. Moreover, the majority of antibiotics are soluble in water, so it is easy to mix them with water in the environment. Antimicrobial pollutants have a considerable impact on antibiotic-resistant bacteria and genes, which can readily encourage the formation of “super bacteria” and constitute a serious threat to human health and environmental stability [113], so the antibiotics must be treated immediately. The photocatalytic degradation technique is outstanding because it can break down antibiotics into non-toxic compounds, water, and carbon dioxide; it is safer and more efficient than other methods.

Electrospinning was used to prepare SiW<sub>12</sub>/CA composite NF membranes. SiW<sub>12</sub> has successfully coupled with CA [114]. According to FT-IR, EDS, and XPS measurements, the Keggin structure of the composite membrane was unchanged. Due to the high porosity and specific surface area of the NF membrane, electrospun CA NFs offer additional contact regions and reaction sites between SiW<sub>12</sub> and tetracycline (TC) during the photodegradation. As a result, the SiW<sub>12</sub>/CA composite NF membrane has higher photocatalytic activity than SiW<sub>12</sub> NPs. In addition, CA additionally supplies electrons to SiW<sub>12</sub> leading to higher degradation efficiency. It can be concluded that CA membranes play various roles in the photodegradation of MO and TC, which involve various photocatalytic pathways and various degradation rates, as shown in Figure 12a. Most importantly, the composite membrane is ideally suited to practical applications and has exceptional reusability. As a result, SiW<sub>12</sub>/CA NF membranes can be extensively employed to remove organic contaminants.



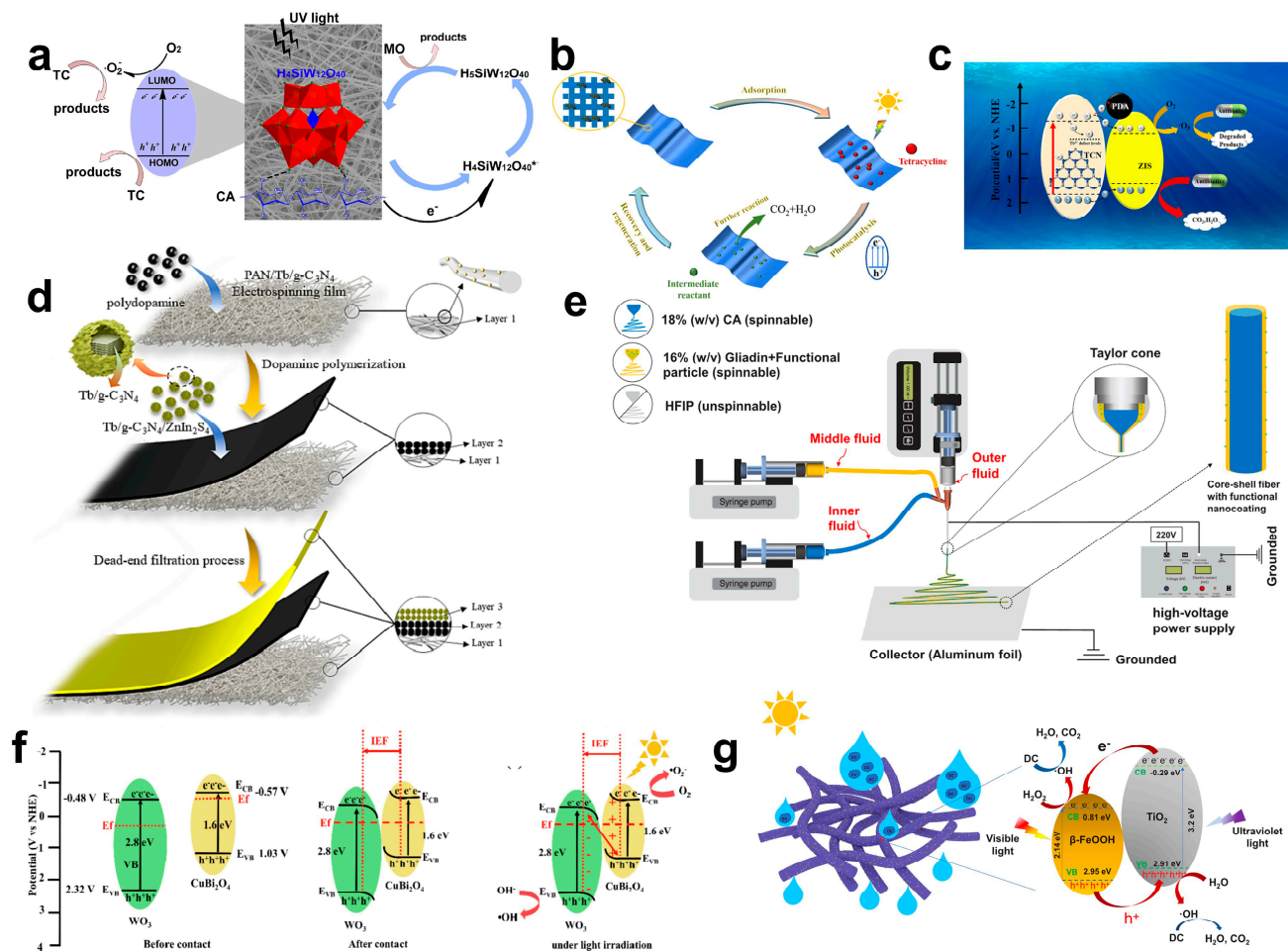


**Figure 12.** Photocatalytic mechanism diagram of SiW<sub>12</sub>/CA nanofibrous membrane for degradation of TC and MO (a) [114], Copyright 2017, Elsevier. Adsorption and photocatalytic regeneration diagram of PAN/BT fiber membrane (b) [115], Copyright 2022, Elsevier. Diagram of the photocatalytic mechanism of PPTZ (c), the synthetic route of PPTZ (d) [116], Copyright 2023, Elsevier. Energy level diagram of CuBi<sub>2</sub>O<sub>4</sub>@WO<sub>3</sub> before and after contact; S-scheme charge transfer diagram (f) [117], Copyright 2023, Elsevier. Schematic diagram of improved triaxial electrospinning technologies and photocatalytic mechanism of β-FeOOH/TiO<sub>2</sub> membrane (e,g) [16], Copyright 2021, Elsevier.

Electrospinning was used to prepare a PAN/Bi<sub>2</sub>MoO<sub>6</sub>/Ti<sub>3</sub>C<sub>2</sub> (PAN/BT) NF membrane [115]. It demonstrated high photocatalytic activity and was able to break down 90.3% of TC under visible light. In Figure 10b, the routes for treating TC are depicted. TC in water is adsorbed by using functional groups on the surface of the membrane. The Bi<sub>2</sub>MoO<sub>6</sub>/Ti<sub>3</sub>C<sub>2</sub> heterojunction in the membrane may efficiently degrade TC in the photocatalytic degradation stage. At the same time, the PAN/BT NF membrane showed a consistent recovery performance, and the degradation efficiency was maintained at 80% after three recoveries. According to this research, the built Bi<sub>2</sub>MoO<sub>6</sub>/Ti<sub>3</sub>C<sub>2</sub> heterojunction can significantly enhance photocatalytic performance. The regeneration capabilities of the electrospun fiber membranes provide a new avenue for investigating the affordable and effective degradation of antibiotics in water.

Membranes are employed as carriers and bulk photocatalysts can be deposited in them. The restriction of low powder recovery can be reduced and recovery performance can be enhanced. The reuse rate and recovery efficiency of photocatalysis powder can also be increased. Wang et al. [116] used electrospinning and coating techniques to create a three-dimensional layered photocatalytic fiber membrane. Figure 12d illustrates the PAN, polydopamine (PDA), and Tb-doped graphitized carbon nitride/ZnIn<sub>2</sub>S<sub>4</sub>

(Tb-g-C<sub>3</sub>N<sub>4</sub>/ZnIn<sub>2</sub>S<sub>4</sub>) (PPTZ) membrane. Under simulated sunlight, the photocatalytic performance of the prepared composite membrane was investigated. Compared with PAN@Tb-g-C<sub>3</sub>N<sub>4</sub> (PT) and PAN@PDA/Tb-g-C<sub>3</sub>N<sub>4</sub> (PPT), the photocatalytic efficiency of PAN@PDA/Tb-g-C<sub>3</sub>N<sub>4</sub>/ZnIn<sub>2</sub>S<sub>4</sub> (PPTZ) was highest. Tylosin (TYL) and TC were degraded by PPTZ, the degradation rates being 2.1 and 2.5 times higher than those of the other samples, respectively. As illustrated in Figure 12c, electrons can be transferred using PDA as the medium from Tb-g-C<sub>3</sub>N<sub>4</sub> to ZnIn<sub>2</sub>S<sub>4</sub>. The construction of heterostructures between Tb-g-C<sub>3</sub>N<sub>4</sub>, ZnIn<sub>2</sub>S<sub>4</sub>, and PDA can boost the separation efficiency of photogenerated carriers, so the photocatalytic activity of PPTZ is outstanding. In addition, the toxicity of the membrane has been studied, and the membrane would not cause secondary pollution in practical applications.

Zhang et al. [117] prepared photoresponsive-optical CuBi<sub>2</sub>O<sub>4</sub>@WO<sub>3</sub> fibers by combining electrospinning technology with post-calcination technology. It has an S-type heterojunction structure, as shown in Figure 12f. The degradation efficiency of TC on CuBi<sub>2</sub>O<sub>4</sub>@WO<sub>3</sub> was 70.42% within 2 h, much higher than for pure CuBi<sub>2</sub>O<sub>4</sub> (30.42%) or pure WO<sub>3</sub> (15.89%). There are three reasons for the increment in photocatalytic activity: 1. An interface of charge transfer and separation is formed between WO<sub>3</sub> NFs and CuBi<sub>2</sub>O<sub>4</sub> NPs; 2. NFs and NPs provide a large number of reactive sites for photocatalytic reactions; 3. The S-heterojunction in CuBi<sub>2</sub>O<sub>4</sub>@WO<sub>3</sub> provides sufficient holes and electrons for WO<sub>3</sub> and CuBi<sub>2</sub>O<sub>4</sub> and provides the prerequisite for the separation of carriers in photocatalytic reactions. This work provides a new way to construct new types of heterostructures to treat antibiotics under visible light irradiation by electrospinning technology.

The NFs prepared from uniaxial and coaxial NFs have functional limitations, such as: 1. Mixing of different kinds of particles may accelerate the recombination of photogenerated carriers; 2. The photocatalytic degradation efficiency cannot meet the demand by adding a single kind of material; 3. If too many functional particles are added, it will be difficult to electrospin during the electrospinning process. Therefore, multi-level electrospinning has emerged. Using heating, calcination, and improved triaxial electrospinning technologies (Figure 12e), Zhao et al. [16] prepared a variety of NPs and NF membranes; doxycycline (DC) was chosen as a pollutant. Under sunlight, the functional NF membrane loaded with β-FeOOH/TiO<sub>2</sub> (1/1, w/w) exhibited the best DC degradation. The ideal concentration of H<sub>2</sub>O<sub>2</sub> was 9 mmol/L, while the ideal pH for degradation was 6. The maximal natural photodegradation efficiency for DC was 90.14% in 5 h. Two semiconductor materials (β-FeOOH and TiO<sub>2</sub>) were responsible for the enhancement of photocatalytic degradation, and their suitable band potentials played key roles in the higher photo-induced carrier separation efficiency. Moreover, electrospun NF membranes can be used as carriers to create multifunctional electrospun membranes, which have enormous potential for use in real-world pollutant photodegradation.

#### 4.3. Photocatalytic Degradation of Heavy Metal Ions

With the expansion of sectors such as electronic manufacturing, electroplating, chemical processing, mechanical manufacturing, and oil refining, heavy metals have become more and more necessary [118]. Through sewage discharge, rainfall corrosion, air deposition, and other pathways, various kinds of heavy metals enter the water. Exposure to significant quantities of heavy metals, which are highly hazardous and carcinogenic compounds, can kill organisms [119]. Heavy metal ions in water cannot be entirely treated using conventional membrane separation, electrolysis, and adsorption technologies. Heavy metal ions can be converted to non-toxic materials by photocatalytic technology, which increases the efficiency and safety when treating heavy metal ions [120].

UiO-66-NH<sub>2</sub> was doped into 4,4,4-(porphyrin-5,10,15,20 tetrayl) tetrakis (benzoic acid) (TCPP) ligand (Zr-TCPP) by one-pot electrospinning technology, and was then coordinated with different amounts of Ag<sup>+</sup> using -NH<sub>2</sub> [121]. Ag NPs were then in situ encapsulated in Zr-TCPP under ultraviolet light (Ag NPs@Zr-TCPP (ZATx)). The effects of pH, Cr(VI) concentration, and the presence of inorganic salts on the photocatalytic degradation efficiency

for Cr(VI) were also studied. The results showed that ZATx exhibited excellent photocatalytic reduction performance for Cr(VI) under acidic conditions with a Cr(VI) concentration of 100 mg/L in the presence of inorganic salts, because of the light absorption ability of TCPP and the electron transfer ability of Ag NPs in the photocatalytic process. In addition, NF membrane filters were also prepared using electrospinning technology. ZATx/PAN still exhibited an excellent photocatalytic degradation effect for Cr(VI). This research not only expands the application of traditional powder photocatalysts in photocatalysis, but also provides insights into the reconstruction strategy of photocatalysts. It also paves the way for the development of efficient photocatalysts with environmental benefits.

A cellulose-based FeOOH@MIL-100 (Fe)/CeP electrospun NF membrane with core-sheath structure and high photocatalytic activity for simultaneous dye degradation and Cr(VI) reduction was prepared [122]. The  $\beta$ -FeOOH@MIL-100 (Fe)/CeP electrospun NF membrane has ultra-high MIL-100 (Fe) (78 wt%) loading rate and super wettability (WCA = 0° in air). Due to the deacetylation of CA and partial solvent leaching of PVP, the immobilization of hydrophilic MIL-100 (Fe) crystals is promoted, which is conducive to the treatment of complex wastewater systems containing oil-water lotion, organic dyes, and heavy metal ions. B-FeOOH@MIL-100 (Fe)/CeP electrospun NF membranes have the following advantages: (1) The electronegativity of the  $\beta$ -FeOOH surface is conducive to the adsorption of Cr(VI); (2)  $\beta$ -FeOOH@MIL-100 (Fe) heterojunctions improve the absorption and utilization of visible light, and promote the separation of electrons and holes; (3) The combination of iron ions (Fe) in  $\beta$ -FeOOH@MIL-100 and visible light forms a photo-Fenton synergistic effect, which promotes the rapid degradation of pollutants. The heterojunction in the core-sheath structure of FeOOH@MIL-100 (Fe)/CeP electrospun NF membrane can not only be used as an adsorbent for dye, but also acts as a photo-Fenton catalyst. It produces a membrane with high pollutant degradation and self-cleaning capabilities, as well as good cycle stability. The degradation efficiency of Cr(VI) by  $\beta$ -FeOOH@MIL-100 (Fe)/CeP electrospun NF membrane was 99.7%.

#### 4.4. Photocatalytic Degradation of Bacteria

The complex existence of various bacteria and viruses in water poses a significant threat to humans and they have become a global problem [123]. Therefore, developing antibacterial strategies is necessary to prevent infection caused by pathogens. Photocatalysis is a technology for treating different bacteria in water [124]. Active free radicals can oxidize and kill most bacteria and pathogens.

PAN and TiO<sub>2</sub> were electrospun into NFs [125], and antibacterial tests were conducted using *E. coli* and *Bacillus*. The results showed that the PAN/TiO<sub>2</sub> NF membrane hindered the growth of these bacteria under visible light; the membrane had a greater impact on the Gram-positive bacterium *Bacillus*. It can be seen from Figure 13(a1,a2) that the PAN/TiO<sub>2</sub> NF membrane has a certain inhibitory effect on the growth of both Gram-positive and negative organisms. There are two reasons for this: 1. Active oxygen generated during the photocatalytic process can kill bacteria; 2. Bacteria that accumulate on the surface of the fiber are eliminated by photocatalysts, especially Gram-positive bacteria. Compared to the control sample (bacteria only), the bacterial density of the PAN-TiO<sub>2</sub> NF membrane decreased slightly under dark conditions. Because the catalytic ions on the PAN/TiO<sub>2</sub> can adsorb bacteria inhibiting bacterial growth.

A Ag<sub>3</sub>PO<sub>4</sub>/P25 NFs membrane was prepared by electrospinning [87], and then a portion of PVP was removed because PVP is water soluble. P25 NFs had no antibacterial activity in the dark (Figure 13(b2)). Ag<sub>3</sub>PO<sub>4</sub>/P25 NFs showed significant antibacterial effects because there were no bacterial cells, as shown in Figure 13(b3). Under the light, the Ag<sub>3</sub>PO<sub>4</sub>/P25 NF membrane can produce more reactive oxygen species (ROS), and the •OH produced by electron-hole pairs can react with cell proteins, membranes, and DNA; finally, the cells will die. In the dark, the oxidized Ag and Ag<sup>+</sup> have bactericidal properties, leading to bacterial inactivation. This work solves the problem of nanoparticle loss in solution and opens a new direction for future research on antibacterial materials.

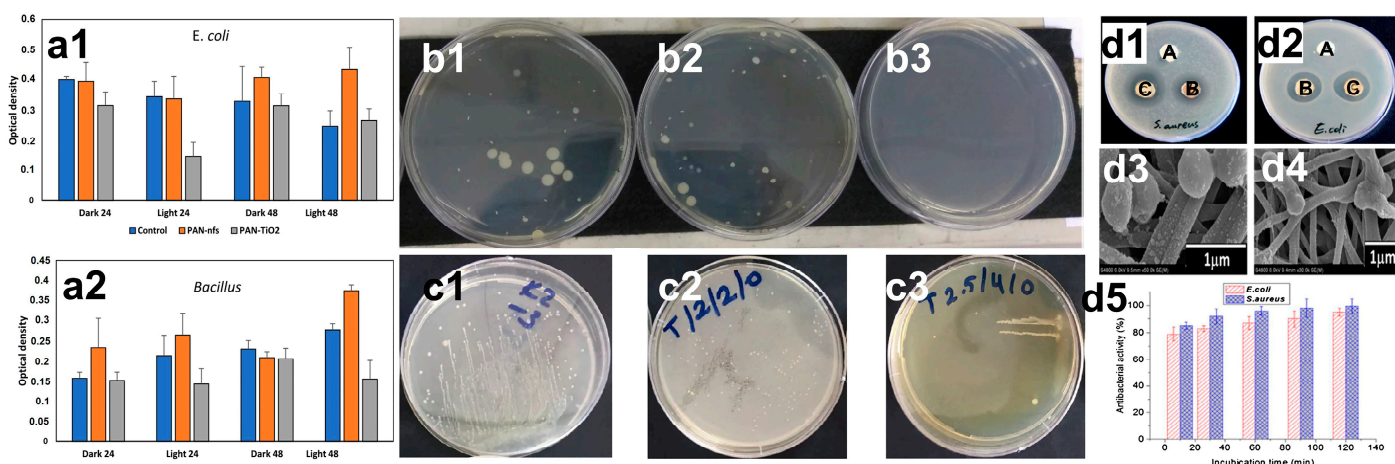


**Figure 13.** The optical density of *E. coli* (a1) and *Bacillus* (a2) under dark and light [125], Copyright 2021, Elsevier. The *E. coli* colonies without NFs (b1), after contact with P25 (b2) and  $\text{Ag}_3\text{PO}_4/\text{P25}$  NFs (b3) [87]. Colony counts images of *E. coli* contact with pure  $\text{TiO}_2$  (c1)  $\text{TiO}_2$  doped with 2% Ag NPs (c2), and  $\text{TiO}_2$  doped with 2.5% Ag NPs (c3) [126], Copyright 2022, American Chemical Society. The inhibition zone of various NF membranes: PAN membrane (A), PAN/Ag membrane (B), and PAN/Ag/ $\text{TiO}_2$  membrane (C) contact with *S. aureus* (d1) and *E. coli* (d2); SEM images of *S. aureus* (d3) and *E. coli* (d4) contact with PAN/Ag/ $\text{TiO}_2$  NF membranes; the bactericidal activity of PAN/Ag/ $\text{TiO}_2$  NF membranes (d5) [127], Copyright 2020, Elsevier.

Ag– $\text{TiO}_2$  nanocomposite membranes [126] with different contents of  $\text{TiO}_2$  and Ag NPs were successfully prepared by the combination of sol–gel and electrospinning technologies. The *E. coli* cells on the membranes after 24 h of incubation are shown in Figure 13(c1–c3). The doping of Ag NPs significantly improved the inhibition rate against *E. coli*. Compared to other membranes, the  $\text{TiO}_2$  nanocomposite membranes doped with 2.5% Ag NPs had higher antibacterial efficiency (99.999%) (Figure 13(c3)). The high bactericidal effect of Ag NP–doped membranes may have been due to the induction of reactive oxygen species (ROS), which were formed by the interaction between silver ions and bacterial cell walls. Ag NPs trigger the formation of free radicals, which can damage bacterial cell membranes. On the other hand, more oxidative stress forms in the cells when the level of ROS increases, leading to cell membrane damage.

Ag/ $\text{TiO}_2$ /PAN composite NFs [127] were prepared by needleless electrospinning. The addition of  $\text{AgNO}_3$  significantly increased the electrical conductivity of the spinning solution. In addition, DMF was used as a reducing agent to form Ag NPs in the electrospinning solution. The antibacterial properties of Ag/ $\text{TiO}_2$ /PAN composite NFs against *E. coli* and *S. aureus* were tested using agar plate technology (Figure 13(d1,d2)). For the pure PAN NF membrane, there were no inhibitory regions against these two bacteria, which is consistent with the non–bactericidal properties of PAN. It is worth noting that inhibition regions were observed for the membranes containing Ag and Ag/ $\text{TiO}_2$ , and the inhibition regions of Ag/ $\text{TiO}_2$  samples were larger than those of the Ag–containing membranes. The results showed that 95% of *E. coli* and 99% of *S. aureus* were killed within 2 h, as shown in Figure 13(d5). The high antibacterial activity was attributed to Ag NPs with large surface areas, which were able to increase the chances of connection between NPs and bacteria to promote antibacterial effects. Moreover, the antibacterial activity of Ag NPs may have been caused by the formation of free radicals and subsequent free radical–induced membrane damage. The irregular shape of pits at the outer membrane of cells was caused by metal depletion. This changed the permeability of the membrane and allowed the release of lipopolysaccharide molecules and membrane proteins. Most importantly, the results suggest that the combination of silver and  $\text{TiO}_2$  can achieve excellent antibacterial properties and have synergistic antibacterial effects against *S. aureus* and *E. coli*.

Potential secondary contamination may result from the partial or incomplete degradation of pollutants. Pollutants must undergo complete photodegradation before finishing treatment and entering the water body, so photocatalytic membranes are essential. The photocatalysts carried by the electrospun fiber membrane allow pollutants to adsorb onto its surface before photodegradation and to complete the destruction of organic pollutants. However, if too many photocatalysts are employed, some of them will detach from the reaction. Moreover, using too many photocatalysts can result in photogenerated carriers recombining too quickly. This can decrease the performance of the photocatalytic system, resulting in secondary pollution. Hence, developing photocatalytic NF membranes for the degradation of diverse pollutants in the future will require enhancing the supporting photocatalyst and electrospinning technology.

## 5. Conclusions and Perspective

NF membranes prepared by electrospinning technology show excellent performance and have important potential applications in the photocatalytic degradation of pollutants in water [101,128–130]. However, the existing electrospinning technology, materials, and industrialization issues limit the photocatalytic efficiency and practical applications [122,131–133]. Multi-fluid electrospinning technology can solve the problem of the low efficiency of electrospinning technology preparation, and further improve the efficiency of the preparation of materials. For example, improvement in tri-axial and parallel electrospinning technology can solve the problem of lower loading function particles and the difficulty of spinning [134–137]. In addition, multi-fluid electrospinning technology can also prepare idealized materials according to actual needs, which is conducive to further practical applications [138–140]. A novel platform can be built to create an increasing number of functional nanostructures for environmental remediation based on the combination of modified coaxial electrospinning and several active substances to address environmental pollutants. The development of novel nanomaterials and associated applications by modified coaxial electrospinning with a non-electrospinnable liquid as the working fluid for the sheath is still in its infancy. Future predictions indicate that there will be an increase in the number of options. With one or more electrospinning fluids, such as tri-axial and parallel electrospinning, non-electrospinning fluids can be processed in a variety of ways. Photocatalysts can be evenly distributed on the surface of polymer NFs using a non-electrospun solution as the sheath working fluid, enhancing photocatalytic performance. Combined with other techniques, modified coaxial electrospinning might further increase its performance.

Finding new photocatalytic particles and improving the photocatalytic efficiency is also a problem that we should face in the future. For example, identifying materials with a lower separation rate of  $e^-$  and  $h^+$ , oxygen vacancy materials [141,142], carbon materials [143,144], doping composite materials [145,146], triboelectric materials [147,148], piezoelectric materials [149,150], etc., will further improve photocatalytic efficiency. Improving the crystal structure and optimizing the material structure can help to solve the problem of the separation efficiency of  $e^-$  and  $h^+$ . In addition, the material can make full use of energy existing in nature, such as water energy, wind energy [149,150], friction energy [147,148], etc., to improve treatment efficiency and reduce the emission of greenhouse gases. A hollow structure, confined structure, porous NFs, and porous photocatalysts should be prepared to reduce  $e^-$ – $h^+$  recombination and increase the active sites for the photocatalytic reaction of materials [151,152]. Moreover, the preparation steps of materials should be further simplified to reduce excessive energy consumption. New suggestions and supports can be proposed for developing novel materials to combine electrospinning and advanced oxidation technologies [153–155], such as synthetic strategies, and taking advantage of polymeric special properties as well as filament-forming properties [156,157].

The issue of industrialization needs to be further investigated and developed. For example, how to achieve large-scale production, how to design experiments in actual water bodies to examine the effects of the influence of light-aging and actual conditions on photocatalytic degradation efficiency, and how to improve the mechanical properties of

materials to reduce the problems of practical application, etc. Determining biological toxicity is also an important step in industrial production. Developing environmentally friendly polymers and photocatalytic particles is an important issue for future research. Given the above problems, combining photocatalytic technology with the structural optimization of electrospinning NFs to treat sewage in the future may not only have the advantages of simple and stable structure and easy recycling, but also greatly improve photocatalytic efficiency. Establishing reasonable structural relationships and using materials for high efficiency, fast, and stronger photocatalytic efficiency, is of great significance for the future economy, humanity, and national construction.

**Author Contributions:** Conceptualization, D.-G.Y. and Y.L. (Yanan Liu); funding acquisition, D.-G.Y.; project administration, D.-G.Y.; writing—original draft, H.L.; writing—review and editing, D.-G.Y., H.L., Y.B., H.S., W.Z., Y.C., Y.L. (Yanan Liu) and Y.L. (Yang Liu). All authors have read and agreed to the published version of the manuscript.

**Funding:** This work was supported by the Natural Science Foundation of Shanghai (No.20ZR1439000).

**Data Availability Statement:** The data supporting the findings of this manuscript are available from the corresponding authors upon reasonable request.

**Conflicts of Interest:** The authors declare no conflict of interest.

## References

- Du, Y.; Yu, D.-G.; Yi, T. Electrospun Nanofibers as Chemosensors for Detecting Environmental Pollutants: A Review. *Chemosensors* **2023**, *11*, 208. [CrossRef]
- Cao, X.; Chen, W.; Zhao, P.; Yang, Y.; Yu, D.-G. Electrospun porous nanofibers: Pore-forming mechanisms and applications for photocatalytic degradation of organic pollutants in wastewater. *Polymers* **2022**, *14*, 3390. [CrossRef] [PubMed]
- Xu, X.; Lv, H.; Zhang, M.; Wang, M.; Zhou, Y.; Liu, Y.; Yu, D.-G. Recent progress in electrospun nanofibers and their applications in heavy metal wastewater treatment. *Front. Chem. Sci. Eng.* **2023**, *17*, 249–275. [CrossRef]
- Jiang, N.; Shang, R.; Heijman, S.G.J.; Rietveld, L.C. High-silica zeolites for adsorption of organic micro-pollutants in water treatment: A review. *Water. Res.* **2018**, *144*, 145–161. [CrossRef] [PubMed]
- Vasilachi, I.C.; Asiminicesei, D.M.; Fertu, D.I.; Gavrilescu, M. Occurrence and fate of emerging pollutants in water environment and options for their removal. *Water* **2021**, *13*, 181. [CrossRef]
- Tan, L.C.; Nancharaiyah, Y.V.; Van Hullebusch, E.D.; Lens, P.N.L. Selenium: Environmental significance, pollution, and biological treatment technologies. *Biotechnol. Adv.* **2016**, *34*, 886–907. [CrossRef]
- Rapti, I.; Boti, V.; Albanis, T.; Konstantinou, I. Photocatalytic degradation of psychiatric pharmaceuticals in hospital WWTP secondary effluents using g-C<sub>3</sub>N<sub>4</sub> and g-C<sub>3</sub>N<sub>4</sub>/MoS<sub>2</sub> catalysts in laboratory-scale pilot. *Catalysts* **2023**, *13*, 252. [CrossRef]
- Li, D.; Xu, K.; Niu, Z.; Zhang, C. Annealing and plasma effects on the structural and photocatalytic properties of TiO<sub>2</sub> fibers produced by electrospinning. *Catalysts* **2022**, *12*, 1441. [CrossRef]
- Bairamis, F.; Konstantinou, I.; Petrakis, D.; Vaimakis, T. Enhanced performance of electrospun nanofibrous TiO<sub>2</sub>/g-C<sub>3</sub>N<sub>4</sub> photocatalyst in photocatalytic degradation of methylene blue. *Catalysts* **2019**, *9*, 880. [CrossRef]
- Nasir, A.M.; Awang, N.; Jaafar, J.; Ismail, A.F.; Othman, M.H.D.; Rahman, A.M.; Aziz, F.; Mat Yajid, M.A. Recent progress on fabrication and application of electrospun nanofibrous photocatalytic membranes for wastewater treatment: A review. *J. Water Process Eng.* **2021**, *40*, 101878. [CrossRef]
- Chen, H.; Huang, M.; Liu, Y.; Meng, L.; Ma, M. Functionalized electrospun nanofiber membranes for water treatment: A review. *Sci. Total Environ.* **2020**, *739*, 139944. [CrossRef]
- Kaneva, N.; Bojinova, A.; Papazova, K. Enhanced removal of organic dyes using co-catalytic Ag-modified ZnO and TiO<sub>2</sub> sol-gel photocatalysts. *Catalysts* **2023**, *13*, 245. [CrossRef]
- Dutta, D.P.; Abraham, S. Composite of  $\alpha$ -FeOOH and mesoporous carbon derived from Indian blackberry seeds as low-cost and recyclable photocatalyst for degradation of ciprofloxacin. *Catalysts* **2023**, *13*, 191. [CrossRef]
- Zhang, H.; Mane, A.U.; Yang, X.; Xia, Z.; Barry, E.F.; Luo, J.; Wan, Y.; Elam, J.W.; Darling, S.B. Visible-light-activated photocatalytic films toward self-cleaning membranes. *Adv. Funct. Mater.* **2020**, *30*, 2002847. [CrossRef]
- Yue, Y.; Hou, K.; Chen, J.; Cheng, W.; Wu, Q.; Han, J.; Jiang, J. Ag/AgBr/AgVO<sub>3</sub> photocatalyst-embedded polyacrylonitrile/polyamide/chitosan nanofiltration membrane for integrated filtration and degradation of rhb. *ACS Appl. Mater. Inter.* **2022**, *14*, 24708–24719. [CrossRef] [PubMed]
- Wang, M.; Ge, R.L.; Zhang, F.; Yu, D.G.; Liu, Z.P.; Li, X.; Shen, H.; Williams, G.R. Electrospun Fibers with Blank Surface and Inner Drug Gradient for Improving Sustained Release. *Biomater. Adv.* **2023**, *2*, 213404. [CrossRef]
- Lee, C.-G.; Javed, H.; Zhang, D.; Kim, J.-H.; Westerhoff, P.; Li, Q.; Alvarez, P.J.J. Porous electrospun fibers embedding TiO<sub>2</sub> for adsorption and photocatalytic degradation of water pollutants. *Environ. Sci. Technol.* **2018**, *52*, 4285–4293. [CrossRef] [PubMed]

18. Joshi, B.N.; Yoon, H.; van Hest, M.F.A.M.; Yoon, S.S. Niobium-doped titania photocatalyst film prepared via a nonaqueous sol-gel method. *J. Am. Ceram. Soc.* **2013**, *96*, 2623–2627. [CrossRef]
19. Wu, W.; Yin, X.; Dai, B.; Kou, J.; Ni, Y.; Lu, C. Water flow driven piezo-photocatalytic flexible films: Bi-piezoelectric integration of ZnO nanorods and PVDF. *Appl. Surf. Sci.* **2020**, *517*, 146119. [CrossRef]
20. Sun, F.; Qi, H.; Xie, Y.; Ma, Q.; He, W.; Xu, D.; Wang, G.; Yu, W.; Wang, T.; Dong, X. Flexible self-supporting bifunctional [TiO<sub>2</sub>/C]/[Bi<sub>2</sub>WO<sub>6</sub>/C] carbon-based Janus nanofiber heterojunction photocatalysts for efficient hydrogen evolution and degradation of organic pollutant. *J. Alloy. Compd.* **2020**, *830*, 154673. [CrossRef]
21. Yao, L.; Sun, C.; Lin, H.; Li, G.; Lian, Z.; Song, R.; Zhuang, S.; Zhang, D. Electrospun Bi-decorated Bi<sub>x</sub>Ti<sub>y</sub>O<sub>z</sub>/TiO<sub>2</sub> flexible carbon nanofibers and their applications on degrading of organic pollutants under solar radiation. *J. Mater. Sci. Technol.* **2023**, *150*, 114–123. [CrossRef]
22. Sharifi Rad, A.; Afshar, A.; Azadeh, M. Antireflection and photocatalytic single layer and double layer ZnO and ZnO–TiO<sub>2</sub> thin films. *Opt. Mater.* **2023**, *136*, 113501. [CrossRef]
23. Yao, L.; Sun, C.; Lin, H.; Li, G.; Lian, Z.; Song, R.; Zhuang, S.; Zhang, D. Enhancement of AFB1 Removal Efficiency via Adsorption/Photocatalysis Synergy Using Surface-Modified Electrospun PCL-g-C<sub>3</sub>N<sub>4</sub>/CQDs Membranes. *Biomolecules* **2023**, *13*, 550. [CrossRef]
24. Li, C.; Yang, J.; He, W.; Xiong, M.; Niu, X.; Li, X.; Yu, D.-G. A review on fabrication and application of tunable hybrid micro–nano array surfaces. *Adv. Mater. Interfaces* **2023**, *10*, 2202160. [CrossRef]
25. Yu, D.-G.; Du, Y.; Chen, J.; Song, W.; Zhou, T. A Correlation Analysis between Undergraduate Students' Safety Behaviors in the Laboratory and Their Learning Efficiencies. *Behav. Sci.* **2023**, *13*, 127. [CrossRef] [PubMed]
26. Kang, S.; Hou, S.; Chen, X.; Yu, D.-G.; Wang, L.; Li, X.; Williams, G.R. Energy-Saving Electrospinning with a Concentric Teflon-Core Rod Spinneret to Create Medicated Nanofibers. *Polymers* **2020**, *12*, 2421. [CrossRef] [PubMed]
27. Liu, H.; Bai, Y.; Huang, C.; Wang, Y.; Ji, Y.; Du, Y.; Xu, L.; Yu, D.-G.; Bligh, S.W. Recent progress of electrospun herbal medicine nanofibers. *Biomolecules* **2023**, *13*, 184. [CrossRef]
28. Zhou, Y.; Wang, M.; Yan, C.; Liu, H.; Yu, D.-G. Advances in the application of electrospun drug-loaded nanofibers in the treatment of oral ulcers. *Biomolecules* **2022**, *12*, 1254. [CrossRef] [PubMed]
29. Huang, X.; Jiang, W.; Zhou, J.; Yu, D.-G.; Liu, H. The applications of ferulic-acid-loaded fibrous films for fruit preservation. *Polymers* **2022**, *14*, 4947. [CrossRef]
30. Wang, Y.; Yu, D.-G.; Liu, Y.; Liu, Y.-N. Progress of electrospun nanofibrous carriers for modifications to drug release profiles. *J. Funct. Biomater.* **2022**, *13*, 289. [CrossRef]
31. Tang, X.; Qi, H.; Yang, L.; Xie, Y.; Ma, Q.; Yu, W.; Dong, X.; Li, D.; Liu, G.; Wang, J. Novel photosensitive dual-anisotropic conductive Janus film endowed with magnetic-luminescent properties and derivative 3D structures. *J. Colloid. Interf. Sci.* **2021**, *601*, 899–914. [CrossRef] [PubMed]
32. Xu, J.; Zhong, M.; Song, N.; Wang, C.; Lu, X. General synthesis of Pt and Ni co-doped porous carbon nanofibers to boost HER performance in both acidic and alkaline solutions. *Chin. Chem. Lett.* **2023**, *34*, 107359. [CrossRef]
33. Bai, Y.; Liu, Y.; Lv, H.; Shi, H.; Zhou, W.; Liu, Y.; Yu, D.-G. Processes of electrospun polyvinylidene fluoride-based nanofibers, their piezoelectric properties, and several fantastic applications. *Polymers* **2022**, *14*, 4311. [CrossRef] [PubMed]
34. Yu, D.-G.; Zhao, P. The key elements for biomolecules to biomaterials and to bioapplications. *Biomolecules* **2022**, *12*, 1234. [CrossRef]
35. Shen, Y.; Yu, X.; Cui, J.; Yu, F.; Liu, M.; Chen, Y.; Wu, J.; Sun, B.; Mo, X. Development of biodegradable polymeric stents for the treatment of cardiovascular diseases. *Biomolecules* **2022**, *12*, 1245. [CrossRef]
36. Xie, D.; Zhou, X.; Xiao, B.; Duan, L.; Zhu, Z. Mucus-penetrating silk fibroin-based nanotherapeutics for efficient treatment of ulcerative colitis. *Biomolecules* **2022**, *12*, 1263. [CrossRef]
37. Lakshmi, B.B.; Dorhout, P.K.; Martin, C.R. Sol-gel template synthesis of semiconductor nanostructures. *Chem. Mater.* **1997**, *9*, 857–862. [CrossRef]
38. He, C.-H.; Gong, J. The preparation of PVA–Pt/TiO<sub>2</sub> composite nanofiber aggregate and the photocatalytic degradation of solid-phase polyvinyl alcohol. *Polym. Degrad. Stabil.* **2003**, *81*, 117–124. [CrossRef]
39. Du, Y.; Yang, Z.; Kang, S.; Yu, D.-G.; Chen, X.; Shao, J. A Sequential Electrospinning of a Coaxial and Blending Process for Creating Double-Layer Hybrid Films to Sense Glucose. *Sensors* **2023**, *23*, 3685. [CrossRef]
40. Yu, D.-G.; Li, Q.; Song, W.; Xu, L.; Zhang, K.; Zhou, T. Advanced technique-based combination of innovation education and safety education in higher education. *J. Chem. Educ.* **2023**, *100*, 507–516. [CrossRef]
41. Song, W.; Tang, Y.; Qian, C.; Kim, B.J.; Liao, Y.; Yu, D.-G. Electrospinning spinneret: A bridge between the visible world and the invisible nanostructures. *Innovation* **2023**, *4*, 100381. [CrossRef] [PubMed]
42. Sun, F.; Qi, H.; Xie, Y.; Xu, D.; Yu, W.; Ma, Q.; Yang, Y.; Yu, H.; Dong, X. Self-standing Janus nanofiber heterostructure photocatalyst with hydrogen production and degradation of methylene blue. *J. Am. Ceram. Soc.* **2022**, *105*, 1428–1441. [CrossRef]
43. Jirkovec, R.; Holec, P.; Hauzerova, S.; Samkova, A.; Kalous, T.; Chvojka, J. Preparation of a composite scaffold from polycaprolactone and hydroxyapatite particles by means of alternating current electrospinning. *ACS Omega* **2021**, *6*, 9234–9242. [CrossRef] [PubMed]
44. Li, Z.; Lei, I.M.; Davoodi, P.; Huleihel, L.; Huang, Y.Y.S. Solution formulation and rheology for fabricating extracellular matrix-derived fibers using low-voltage electrospinning patterning. *ACS Biomater. Sci. Eng.* **2019**, *5*, 3676–3684. [CrossRef]

45. Deng, J.; Kang, X.; Chen, L.; Wang, Y.; Gu, Z.; Lu, Z. A nanofiber functionalized with dithizone by co-electrospinning for lead (II) adsorption from aqueous media. *J. Hazard. Mater.* **2011**, *196*, 187–193. [CrossRef]
46. Yin, J.; Bai, Y.; Lu, J.; Ma, J.; Zhang, Q.; Hong, W.; Jiao, T. Enhanced mechanical performances and high-conductivity of rGO/PEDOT:PSS/PVA composite fiber films via electrospinning strategy. *Colloid. Surf. A* **2022**, *643*, 128791. [CrossRef]
47. Smit, E.; Büttner, U.; Sanderson, R.D. Continuous yarns from electrospun fibers. *Polymer* **2005**, *46*, 2419–2423. [CrossRef]
48. Haghi, A.K.; Akbari, M. Trends in electrospinning of natural nanofibers. *Phys. Status Solidi A* **2007**, *204*, 1830–1834. [CrossRef]
49. Valizadeh, A.; Mussa Farkhani, S. Electrospinning and electrospun nanofibres. *IET Nanobiotechnol.* **2014**, *8*, 83–92. [CrossRef]
50. Han, W.; Wang, L.; Li, Q.; Ma, B.; He, C.; Guo, X.; Nie, J.; Ma, G. A review: Current status and emerging developments on natural polymer-based electrospun fibers. *Macromol. Rapid Comm.* **2022**, *43*, 2200456. [CrossRef]
51. Wang, M.-L.; Yu, D.-G.; Annie Bligh, S.W. Progress in Preparing Electrospun Janus Fibers and Their Applications. *App. Mater. Today* **2023**, *31*, 101766. [CrossRef]
52. Shen, M.; Liu, H.; Pan, T.; Ning, J.; Zhou, D.; Song, G.; Wang, Y.; Cai, S.; Xia, X.; Zhang, G.; et al. Crosslinked PVA electrospinning nanofibrous film as a new platform for the design of K<sup>+</sup> sensor. *Sens. Actuators B-Chem.* **2023**, *380*, 133317. [CrossRef]
53. Yogeswari, C.; Hijas, K.M.; Sabari Girisun, T.C.; Nagalakshmi, R. Synthesis of nanoscale 4-nitroaniline-polystyrene fiber for optical limiting application using electrospinning technique. *Mater. Today Proc.* **2021**, *39*, 1719–1721. [CrossRef]
54. Wang, M.; Hou, J.; Yu, D.-G.; Li, S.; Zhu, J.; Chen, Z. Electrospun tri-layer nanodepots for sustained release of acyclovir. *J. Alloy. Compd.* **2020**, *846*, 156471. [CrossRef]
55. Matthews, J.A.; Wnek, G.E.; Simpson, D.G.; Bowlin, G.L. Electrospinning of collagen nanofibers. *Biomacromolecules* **2002**, *3*, 232–238. [CrossRef]
56. Zhou, H.; Green, T.B.; Joo, Y.L. The thermal effects on electrospinning of polylactic acid melts. *Polymer* **2006**, *47*, 7497–7505. [CrossRef]
57. Xu, H.; Zhang, F.; Wang, M.; Lv, H.; Yu, D.-G.; Liu, X.; Shen, H. Electrospun hierarchical structural films for effective wound healing. *Biomater. Adv.* **2022**, *136*, 212795. [CrossRef] [PubMed]
58. Schiffman, J.D.; Stulga, L.A.; Schauer, C.L. Chitin and chitosan: Transformations due to the electrospinning process. *Polym. Eng. Sci.* **2009**, *49*, 1918–1928. [CrossRef]
59. Fang, D.; Liu, Y.; Jiang, S.; Nie, J.; Ma, G. Effect of intermolecular interaction on electrospinning of sodium alginate. *Carbohydr. Polym.* **2011**, *85*, 276–279. [CrossRef]
60. Rezabeigi, E.; Sta, M.; Swain, M.; McDonald, J.; Demarquette, N.R.; Drew, R.A.L.; Wood-Adams, P.M. Electrospinning of porous polylactic acid fibers during nonsolvent induced phase separation. *J. Appl. Polym. Sci.* **2017**, *134*, 44862. [CrossRef]
61. Zavgorodnya, O.; Shamshina, J.L.; Bonner, J.R.; Rogers, R.D. Electrospinning biopolymers from ionic liquids requires control of different solution properties than volatile organic solvents. *ACS Sustain. Chem. Eng.* **2017**, *5*, 5512–5519. [CrossRef]
62. Chuangchote, S.; Sagawa, T.; Yoshikawa, S. Electrospinning of poly(vinyl pyrrolidone): Effects of solvents on electrospinnability for the fabrication of poly(p-phenylene vinylene) and TiO<sub>2</sub> nanofibers. *J. Appl. Polym. Sci.* **2009**, *114*, 2777–2791. [CrossRef]
63. Alipour, S.M.; Nouri, M.; Mokhtari, J.; Bahrami, S.H. Electrospinning of poly(vinyl alcohol)–water-soluble quaternized chitosan derivative blend. *Carbohydr. Res.* **2009**, *344*, 2496–2501. [CrossRef]
64. Chapman, B.S.; Mishra, S.R.; Tracy, J.B. Direct electrospinning of titania nanofibers with ethanol. *Dalton Trans.* **2019**, *48*, 12822–12827. [CrossRef] [PubMed]
65. Lv, H.; Liu, Y.; Zhao, P.; Bai, Y.; Cui, W.; Shen, S.; Liu, Y.; Wang, Z.; Yu, D.-G. Insight into the superior piezophotocatalytic performance of BaTiO<sub>3</sub>/ZnO Janus nanofibrous heterostructures in the treatment of multi-pollutants from water. *Appl. Catal. B-Environ.* **2023**, *330*, 122623. [CrossRef]
66. Wang, P.; Lv, H.; Cao, X.; Liu, Y.; Yu, D.-G. Recent Progress of the Preparation and Application of Electrospun Porous Nanofibers. *Polymers* **2023**, *15*, 921. [CrossRef]
67. Liu, H.; Dai, Y.; Li, J.; Liu, P.; Zhou, W.; Yu, D.G.; Ge, R. Safe, Fast and Convenient Delivery of Fluidextracts Licorice through Electrospun Core-Shell Nanohybrids. *Front. Bioeng. Biotechnol.* **2023**, *11*, 1172133. [CrossRef]
68. De Vrieze, S.; Van Camp, T.; Nelvig, A.; Hagström, B.; Westbroek, P.; De Clerck, K. The effect of temperature and humidity on electrospinning. *J. Mater. Sci.* **2009**, *44*, 1357–1362. [CrossRef]
69. Pelipenko, J.; Kristl, J.; Janković, B.; Baumgartner, S.; Kocbek, P. The impact of relative humidity during electrospinning on the morphology and mechanical properties of nanofibers. *Int. J. Pharmaceut.* **2013**, *456*, 125–134. [CrossRef]
70. Deitzel, J.M.; Kleinmeyer, J.; Harris, D.; Beck Tan, N.C. The effect of processing variables on the morphology of electrospun nanofibers and textiles. *Polymer* **2001**, *42*, 261–272. [CrossRef]
71. Lv, H.; Guo, S.; Zhang, G.; He, W.; Wu, Y.; Yu, D.-G. Electrospun structural hybrids of acyclovir-polyacrylonitrile at acyclovir for modifying drug release. *Polymers* **2021**, *13*, 4286. [CrossRef] [PubMed]
72. Ge, R.; Ji, Y.; Ding, Y.; Huang, C.; He, H.; Yu, D.-G. Electrospun self-emulsifying core-shell nanofibers for effective delivery of paclitaxel. *Front. Bioeng. Biotechnol.* **2023**, *11*, 1112338. [CrossRef] [PubMed]
73. Bi, F.; Dong, X.; Wang, J.; Liu, G. Tuned magnetism–luminescence bifunctionality simultaneously assembled into flexible Janus nanofiber. *RSC Adv.* **2015**, *5*, 12571–12577. [CrossRef]
74. Tucker, N.; Stanger, J.J.; Staiger, M.P.; Razzaq, H.; Hofman, K. The history of the science and technology of electrospinning from 1600 to 1995. *J. Eng. Fiber. Fabr.* **2012**, *7*, 155892501200702. [CrossRef]



75. Liu, X.; Xie, Y.; Yang, L.; Qi, H.; Ma, Q.; Dong, X.; Li, D.; Liu, G.; Wang, J.; Yu, W. Tricolor flag-shaped nanobelt array and derivant 3D structures display concurrent conductive anisotropy, up-conversion fluorescence and magnetism. *Mater. Des.* **2021**, *211*, 110121. [CrossRef]
76. Feng, Z.; Wang, K.; Liu, Y.; Han, B.; Yu, D.-G. Piezoelectric Enhancement of Piezoceramic Nanoparticle-Doped PVDF/PCL Core-Sheath Fibers. *Nanomaterials* **2023**, *13*, 1243. [CrossRef]
77. Xi, X.; Yu, W.; Li, D.; Ma, Q.; Dong, X.; Wang, J.; Liu, G. Employing novel Janus nanobelts to achieve anisotropic conductive array pellicle functionalized by superparamagnetism and green fluorescence. *J. Mater. Sci.-Mater. El.* **2019**, *30*, 4219–4230. [CrossRef]
78. Mohamed, A.; Ghobara, M.M.; Abdelmaksoud, M.K.; Mohamed, G.G. A novel and highly efficient photocatalytic degradation of malachite green dye via surface modified polyacrylonitrile nanofibers/biogenic silica composite nanofibers. *Sep. Purif. Technol.* **2019**, *210*, 935–942. [CrossRef]
79. Yi, S.; Sun, S.; Zhang, Y.; Zou, Y.; Dai, F.; Si, Y. Scalable fabrication of bimetal modified polyacrylonitrile (PAN) nanofibrous membranes for photocatalytic degradation of dyes. *J. Colloid. Interf. Sci.* **2020**, *559*, 134–142. [CrossRef] [PubMed]
80. Li, F.; Dong, Y.; Kang, W.; Cheng, B.; Cui, G. Enhanced removal of azo dye using modified PAN nanofibrous membrane Fe complexes with adsorption/visible-driven photocatalysis bifunctional roles. *Appl. Surf. Sci.* **2017**, *404*, 206–215. [CrossRef]
81. Uheida, A.; Mohamed, A.; Belaqziz, M.; Nasser, W.S. Photocatalytic degradation of Ibuprofen, Naproxen, and Cetirizine using PAN-MWCNT nanofibers crosslinked TiO<sub>2</sub>-NH<sub>2</sub> nanoparticles under visible light irradiation. *Sep. Purif. Technol.* **2019**, *212*, 110–118. [CrossRef]
82. Elkady, M.F.; Hassan, H.S. Photocatalytic degradation of malachite green dye from aqueous solution using environmentally compatible Ag/ZnO polymeric nanofibers. *Polymers* **2021**, *13*, 2033. [CrossRef] [PubMed]
83. Lv, H.; Zhang, M.; Wang, P.; Xu, X.; Liu, Y.; Yu, D.-G. Ingenious construction of Ni(DMG)<sub>2</sub>/TiO<sub>2</sub>-decorated porous nanofibers for the highly efficient photodegradation of pollutants in water. *Colloids Surf. A* **2022**, *650*, 129561. [CrossRef]
84. Wu, H.; Xu, L.; Jia, J.; Dong, F.; Jia, Y.; Liu, X. In situ electrospun porous MIL-88A/PAN nanofibrous membranes for efficient removal of organic dyes. *Molecules* **2023**, *28*, 760. [CrossRef] [PubMed]
85. Liu, Y.; Wang, M.; Li, Z.; Liu, H.; He, P.; Li, J. Preparation of porous aminopropylsilsesquioxane by a nonhydrolytic sol-gel method in ionic liquid solvent. *Langmuir* **2005**, *21*, 1618–1622. [CrossRef]
86. Dutta, T.; Kim, T.; Vellingiri, K.; Tsang, D.C.W.; Shon, J.R.; Kim, K.-H.; Kumar, S. Recycling and regeneration of carbonaceous and porous materials through thermal or solvent treatment. *Chem. Eng. J.* **2019**, *364*, 514–529. [CrossRef]
87. Habib, Z.; Lee, C.-G.; Li, Q.; Khan, S.J.; Ahmad, N.M.; Jamal, Y.; Huang, X.; Javed, H. Bi-polymer electrospun nanofibers embedding Ag<sub>3</sub>PO<sub>4</sub>/P25 composite for efficient photocatalytic degradation and anti-microbial activity. *Catalysts* **2020**, *10*, 784. [CrossRef]
88. Machida, S.; Katsumata, K.; Yasumori, A. A stable layered inorganic solid at high temperature: Heat treatment of Eu-doped hexacelsian without phase transformation. *J. Solid State Chem.* **2023**, *322*, 123945. [CrossRef]
89. Sun, C.; Dai, L.; He, X.; Liu, F.; Yuan, F.; Gao, Y. Effect of heat treatment on physical, structural, thermal and morphological characteristics of zein in ethanol-water solution. *Food Hydrocolloid.* **2016**, *58*, 11–19. [CrossRef]
90. Sun, C.; Dai, L.; Liu, F.; Gao, Y. Simultaneous treatment of heat and high pressure homogenization of zein in ethanol-water solution: Physical, structural, thermal and morphological characteristics. *Innov. Food Sci. Emerg.* **2016**, *34*, 161–170. [CrossRef]
91. Swanckaert, B.; Geltmeyer, J.; Rabaey, K.; De Buysser, K.; Bonin, L.; De Clerck, K. A review on ion-exchange nanofiber membranes: Properties, structure and application in electrochemical (waste)water treatment. *Sep. Purif. Technol.* **2022**, *287*, 120529. [CrossRef]
92. Kalashnikov, I.S.; Acselrad, O.; Shalkevich, A.; Chumakova, L.D.; Pereira, L.C. Heat treatment and thermal stability of FeMnAlC alloys. *J. Mater. Process. Tech.* **2003**, *136*, 72–79. [CrossRef]
93. Gao, J.; Qiao, L.; Li, L.; Wang, Y. Hemolysis effect and calcium-phosphate precipitation of heat-organic-film treated magnesium. *Trans. Nonferrous Met. Soc. China* **2006**, *16*, 539–544. [CrossRef]
94. Singh, P.; Mondal, K.; Sharma, A. Reusable electrospun mesoporous ZnO nanofiber mats for photocatalytic degradation of polycyclic aromatic hydrocarbon dyes in wastewater. *J. Colloid. Interf. Sci.* **2013**, *394*, 208–215. [CrossRef]
95. Norouzi, M.; Fazeli, A.; Tavakoli, O. Photocatalytic degradation of phenol under visible light using electrospun Ag/TiO<sub>2</sub> as a 2D nano-powder: Optimizing calcination temperature and promoter content. *Adv. Powder Technol.* **2022**, *33*, 103792. [CrossRef]
96. Zaborowska, M.; Smok, W.; Tański, T. Electrospinning synthesis and characterization of zirconia nanofibers annealed at different temperatures. *Appl. Surf. Sci.* **2023**, *615*, 156342. [CrossRef]
97. Song, M.; Cao, H.; Zhu, Y.; Wang, Y.; Zhao, S.; Huang, C.; Zhang, C.; He, X. Electrochemical and photocatalytic properties of electrospun C/TiO<sub>2</sub> nanofibers. *Chem. Phys. Lett.* **2020**, *747*, 137355. [CrossRef]
98. Zhai, G.; Zhou, J.; Xie, M.; Jia, C.; Hu, Z.; Xiang, H.; Zhu, M. Improved photocatalytic property of lignin-derived carbon nanofibers through catalyst synergy. *Int. J. Biol. Macromol.* **2023**, *233*, 123588. [CrossRef] [PubMed]
99. Zhao, Y.; Nie, L.; Yang, H.; Song, K.; Hou, H. Tailored fabrication of TiO<sub>2</sub>/In<sub>2</sub>O<sub>3</sub> hybrid mesoporous nanofibers towards enhanced photocatalytic performance. *Colloids Surf. A* **2021**, *629*, 127455. [CrossRef]
100. Ramos, P.G.; Flores, E.; Luyo, C.; Sánchez, L.A.; Rodríguez, J. Fabrication of ZnO-RGO nanorods by electrospinning assisted hydrothermal method with enhanced photocatalytic activity. *Mater. Today Commun.* **2019**, *19*, 407–412. [CrossRef]
101. Zhou, M.; Zou, W.; Zhu, X.; Ma, H.; Wang, P.; Shang, J.; Luo, P. In situ growth of UIO-66-NH<sub>2</sub> on thermally stabilized electrospun polyacrylonitrile nanofibers for visible-light driven Cr(VI) photocatalytic reduction. *J. Solid State Chem.* **2022**, *307*, 122836. [CrossRef]

102. Sharma, J.; Sharma, S.; Soni, V. Classification and impact of synthetic textile dyes on Aquatic Flora: A review. *Reg. Stud. Mar. Sci.* **2021**, *45*, 101802. [CrossRef]
103. Al-Tohamy, R.; Ali, S.S.; Li, F.; Okasha, K.M.; Mahmoud, Y.A.-G.; Elsamahy, T.; Jiao, H.; Fu, Y.; Sun, J. A critical review on the treatment of dye-containing wastewater: Ecotoxicological and health concerns of textile dyes and possible remediation approaches for environmental safety. *Ecotoxicol. Environ. Saf.* **2022**, *231*, 113160. [CrossRef] [PubMed]
104. Rauf, M.A.; Ashraf, S.S. Fundamental principles and application of heterogeneous photocatalytic degradation of dyes in solution. *Chem. Eng. J.* **2009**, *151*, 10–18. [CrossRef]
105. Zhou, T.; Zhao, L.; Wu, D.; Feng, Q.; Zhao, B. Uniformly assembled polypyrrole-covered bacterial cellulose/g-C<sub>3</sub>N<sub>4</sub> flexible nanofiber membrane for catalytic degradation of tetracycline hydrochloride. *J. Water Process Eng.* **2022**, *47*, 102775. [CrossRef]
106. Tang, Y.; Fu, S.; Zhao, K.; Teng, L.; Xie, G. Fabrication of TiO<sub>2</sub> micro-/nano-spheres embedded in nanofibers by coaxial electrospinning. *Mater. Res. Bull.* **2016**, *78*, 11–15. [CrossRef]
107. Methaapanon, R.; Chutchakul, K.; Pavarajarn, V. Photocatalytic zinc oxide on flexible polyacrylonitrile nanofibers via sol-gel coaxial electrospinning. *Ceram. Int.* **2020**, *46*, 8287–8292. [CrossRef]
108. Chang, W.; Xu, F.; Mu, X.; Ji, L.; Ma, G.; Nie, J. Fabrication of nanostructured hollow TiO<sub>2</sub> nanofibers with enhanced photocatalytic activity by coaxial electrospinning. *Mater. Res. Bull.* **2013**, *48*, 2661–2668. [CrossRef]
109. Peng, X.; Santulli, A.C.; Sutter, E.; Wong, S.S. Fabrication and enhanced photocatalytic activity of inorganic core-shell nanofibers produced by coaxial electrospinning. *Chem. Sci.* **2012**, *3*, 1262–1272. [CrossRef]
110. Ji, S.M.; Tiwari, A.P.; Kim, H.Y. PAN-ZnO//PAN-Mn<sub>3</sub>O<sub>4</sub>/CeO<sub>2</sub> Janus nanofibers: Controlled fabrication and enhanced photocatalytic properties under UV and visible light. *Chem. Phys. Lett.* **2020**, *759*, 138050. [CrossRef]
111. Van, T.T.H.; Yidana, Z.; Smooker, P.M.; Coloe, P.J. Antibiotic use in food animals worldwide, with a focus on Africa: Pluses and minuses. *J. Glob. Antimicrob. Resist.* **2020**, *20*, 170–177. [CrossRef]
112. Park, Y.; Kim, S.; Kim, J.; Khan, S.; Han, C. UV/TiO<sub>2</sub> photocatalysis as an efficient livestock wastewater quaternary treatment for antibiotics removal. *Water* **2022**, *14*, 958. [CrossRef]
113. Yin, H.; Li, G.; Chen, X.; Wang, W.; Wong, P.K.; Zhao, H.; An, T. Accelerated evolution of bacterial antibiotic resistance through early emerged stress responses driven by photocatalytic oxidation. *Appl. Catal. B-Environ.* **2020**, *269*, 118829. [CrossRef]
114. Li, W.; Li, T.; Li, G.; An, L.; Li, F.; Zhang, Z. Electrospun H<sub>4</sub>SiW<sub>12</sub>O<sub>40</sub>/cellulose acetate composite nanofibrous membrane for photocatalytic degradation of tetracycline and methyl orange with different mechanism. *Carbohydr. Polym.* **2017**, *168*, 153–162. [CrossRef] [PubMed]
115. Zhang, J.-J.; Kai, C.-M.; Zhang, F.-J.; Wang, Y.-R. Novel PAN/Bi<sub>2</sub>MoO<sub>6</sub>/Ti<sub>3</sub>C<sub>2</sub> ternary composite membrane via electrospinning with enhanced photocatalytic degradation of tetracycline. *Colloids Surf. A* **2022**, *648*, 129255. [CrossRef]
116. Wang, B.; Cao, Q.; Cheng, M.; Li, G.; Zhang, J.; Jiang, H. Photocatalytic degradation of antibiotics in water by pollution-free photocatalytic films with a three-dimensional layered structure and the reaction mechanism study. *J. Water Process Eng.* **2023**, *52*, 103550. [CrossRef]
117. Zhang, L.; Shen, Q.; Huang, F.; Jiang, L.; Liu, J.; Sheng, J.; Li, Y.; Yang, H. Electrospinning directly synthesis of 0D/1D CuBi<sub>2</sub>O<sub>4</sub>@WO<sub>3</sub> nanofiber photocatalyst with S-scheme heterojunction. *Appl. Surf. Sci.* **2023**, *608*, 155064. [CrossRef]
118. Li, X. Technical solutions for the safe utilization of heavy metal-contaminated farmland in China: A critical review. *Land Degrad. Dev.* **2019**, *30*, 1773–1784. [CrossRef]
119. Mitra, S.; Chakraborty, A.J.; Tareq, A.M.; Emran, T.B.; Nainu, F.; Khusro, A.; Idris, A.M.; Khandaker, M.U.; Osman, H.; Alhumaydhi, F.A.; et al. Impact of heavy metals on the environment and human health: Novel therapeutic insights to counter the toxicity. *J. King Saud. Univ. Sci.* **2022**, *34*, 101865. [CrossRef]
120. Li, Z.; Wang, L.; Qin, L.; Lai, C.; Wang, Z.; Zhou, M.; Xiao, L.; Liu, S.; Zhang, M. Recent advances in the application of water-stable metal-organic frameworks: Adsorption and photocatalytic reduction of heavy metal in water. *Chemosphere* **2021**, *285*, 131432. [CrossRef]
121. Gu, D.; Liu, Y.; Li, X.; Zhu, H.; Cui, Y.; Yang, W.; Hao, J. Porphyrin-based metal-organic frameworks loaded with Ag nanoparticles and their nanofibrous filters for the photocatalytic reduction of Cr(VI). *Appl. Surf. Sci.* **2023**, *614*, 156192. [CrossRef]
122. Lu, W.; Duan, C.; Zhang, Y.; Gao, K.; Dai, L.; Shen, M.; Wang, W.; Wang, J.; Ni, Y. Cellulose-based electrospun nanofiber membrane with core-sheath structure and robust photocatalytic activity for simultaneous and efficient oil emulsions separation, dye degradation and Cr(VI) reduction. *Carbohydr. Polym.* **2021**, *258*, 117676. [CrossRef] [PubMed]
123. Imran, M.; Das, K.R.; Naik, M.M. Co-selection of multi-antibiotic resistance in bacterial pathogens in metal and microplastic contaminated environments: An emerging health threat. *Chemosphere* **2019**, *215*, 846–857. [CrossRef]
124. Baaloudj, O.; Assadi, I.; Nasrallah, N.; El Jerry, A.; Khezami, L.; Assadi, A.A. Simultaneous removal of antibiotics and inactivation of antibiotic-resistant bacteria by photocatalysis: A review. *J. Water Process Eng.* **2021**, *42*, 102089. [CrossRef]
125. Ademola Bode-Aluko, C.; Perea, O.; Kyaw, H.H.; Al-Naamani, L.; Al-Abri, M.Z.; Tay Zar Myint, M.; Rossouw, A.; Fatoba, O.; Petrik, L.; Dobretsov, S. Photocatalytic and antifouling properties of electrospun TiO<sub>2</sub> polyacrylonitrile composite nanofibers under visible light. *Mater. Sci. Eng. B-Adv.* **2021**, *264*, 114913. [CrossRef]
126. Yerli-Soylu, N.; Akturk, A.; Kabak, Ö.; Erol-Taygun, M.; Karbancioglu-Guler, F.; Küçükbayrak, S. TiO<sub>2</sub> nanocomposite ceramics doped with silver nanoparticles for the photocatalytic degradation of methylene blue and antibacterial activity against *Escherichia coli*. *Eng. Sci. Technol.* **2022**, *35*, 101175. [CrossRef]



127. Wang, L.; Ali, J.; Zhang, C.; Mailhot, G.; Pan, G. Simultaneously enhanced photocatalytic and antibacterial activities of TiO<sub>2</sub>/Ag composite nanofibers for wastewater purification. *J. Environ. Chem. Eng.* **2020**, *8*, 102104. [CrossRef]
128. Van-Pham, D.-T.; Thi Yen Nhi, P.; Vu Bao Long, T.; Nguyen, C.-N.; Minh Nhan, L.; Thi Bich Quyen, T.; Thi Cam Tuyen, L.; Truong Ngoc Mai, N.; Van Hong Thien, D. Electrospun Fe-doped TiO<sub>2</sub>/chitosan/PVA nanofibers: Preparation and study on photocatalytic and adsorption properties. *Mater. Lett.* **2022**, *326*, 132930. [CrossRef]
129. Sarkodie, B.; Amesimeku, J.; Frimpong, C.; Howard, E.K.; Feng, Q.; Xu, Z. Photocatalytic degradation of dyes by novel electrospun nanofibers: A review. *Chemosphere* **2023**, *313*, 137654. [CrossRef]
130. Asgari, S.; Mohammadi Ziarani, G.; Badiei, A.; Setayeshmehr, M.; Kiani, M.; Pourjavadi, A. Electrospun Ag-decorated reduced GO-graft-chitosan composite nanofibers with visible light photocatalytic activity for antibacterial performance. *Chemosphere* **2022**, *299*, 134436. [CrossRef]
131. Khademi, D.; Zargazi, M.; Chahkandi, M.; Baghayeri, M. A novel  $\gamma$ -BMO@BMWO Z-Scheme heterojunction for promotion photocatalytic performance: Nanofibers thin film by co-axial-electrospun. *Environ. Res.* **2023**, *219*, 115154. [CrossRef]
132. Qi, W.; Yang, Y.; Du, J.; Yang, J.; Guo, L.; Zhao, L. Highly photocatalytic electrospun Zr/Ag co-doped titanium dioxide nanofibers for degradation of dye. *J. Colloid Interf. Sci.* **2021**, *603*, 594–603. [CrossRef]
133. Pascariu, P.; Cojocaru, C.; Samoila, P.; Olaru, N.; Bele, A.; Airinei, A. Novel electrospun membranes based on PVDF fibers embedding lanthanide doped ZnO for adsorption and photocatalytic degradation of dye organic pollutants. *Mater. Res. Bull.* **2021**, *141*, 111376. [CrossRef]
134. Wang, D.; Yue, Y.; Wang, Q.; Cheng, W.; Han, G. Preparation of cellulose acetate-polyacrylonitrile composite nanofibers by multi-fluid mixing electrospinning method: Morphology, wettability, and mechanical properties. *Appl. Surf. Sci.* **2020**, *510*, 145462. [CrossRef]
135. Zhang, X.; Xie, L.; Wang, X.; Shao, Z.; Kong, B. Electrospinning super-assembly of ultrathin fibers from single- to multi-Taylor cone sites. *Appl. Mater. Today* **2022**, *26*, 101272. [CrossRef]
136. Zhao, T.; Zheng, Y.; Zhang, X.; Teng, D.; Xu, Y.; Zeng, Y. Design of helical groove/hollow nanofibers via tri-fluid electrospinning. *Mater. Des.* **2021**, *205*, 109705. [CrossRef]
137. Li, D.; Yue, G.; Li, S.; Liu, J.; Li, H.; Gao, Y.; Liu, J.; Hou, L.; Liu, X.; Cui, Z.; et al. Fabrication and applications of multi-fluidic electrospinning multi-structure hollow and core-shell nanofibers. *Engineering* **2022**, *13*, 116–127. [CrossRef]
138. Wang, M.; Ge, R.; Zhao, P.; Williams, G.R.; Yu, D.-G.; Bligh, S.W.A. Exploring wettability difference-driven wetting by utilizing electrospun chimeric Janus microfiber comprising cellulose acetate and polyvinylpyrrolidone. *Mater. Des.* **2023**, *226*, 111652. [CrossRef]
139. Huang, H.; Song, Y.; Zhang, Y.; Li, Y.; Li, J.; Lu, X.; Wang, C. Electrospun nanofibers: Current progress and applications in food systems. *J. Agric. Food Chem.* **2022**, *70*, 1391–1409. [CrossRef]
140. Lu, H.; Zhao, Y.; Qin, S.; Zhang, Y.; Liu, J.; Zhang, J.; Feng, C.; Zhao, W. Fluorine substitution tunes the nanofiber chirality of supramolecular hydrogels to promote cell adhesion and proliferation. *Adv. Fiber Mater.* **2023**, *5*, 377–387. [CrossRef]
141. Sun, Z.; Liu, T.; Shen, Q.; Li, H.; Liu, X.; Jia, H.; Xue, J. Synergetic effect of oxygen vacancies coupled with in-situ Bi clusters in Bi<sub>2</sub>WO<sub>6</sub> for enhancing photocatalytic CO<sub>2</sub> reduction. *Appl. Surf. Sci.* **2023**, *616*, 156530. [CrossRef]
142. Guo, N.; Cao, X.; Li, Q.; Han, Y.; Li, H.; Yuan, Y. Oxygen-vacancy-rich Ag/Bi<sub>5</sub>O<sub>7</sub>Br nanosheets enable improved photocatalytic no removal and oxygen evolution under visible light exposure. *Adv. Powder Technol.* **2023**, *34*, 103927. [CrossRef]
143. Reddy, N.R.; Reddy, P.M.; Jyothi, N.; Kumar, A.S.; Jung, J.H.; Joo, S.W. Versatile TiO<sub>2</sub> bandgap modification with metal, non-metal, noble metal, carbon material, and semiconductor for the photoelectrochemical water splitting and photocatalytic dye degradation performance. *J. Alloy Compd.* **2023**, *935*, 167713. [CrossRef]
144. Liu, Q.; Fan, Z.; Yi, X.; Chen, S.; Li, B.; Luo, W. Porous polyimide/carbon quantum dots/ZnS quantum dots material aerogel for efficient visible-light photocatalytic degradation over oxytetracycline. *React. Funct. Polym.* **2022**, *178*, 105330. [CrossRef]
145. Bashir, S.; Jamil, A.; Alazmi, A.; Khan, M.S.; Alsafari, I.A.; Shahid, M. Synergistic effects of doping, composite formation, and nanotechnology to enhance the photocatalytic activities of semiconductive materials. *Opt. Mater.* **2023**, *135*, 113264. [CrossRef]
146. Bashir, S.; Jamil, A.; Amin, R.; Ul-hasan, I.; Alazmi, A.; Shahid, M. Hydrothermally synthesized Gd-doped BiSbO<sub>4</sub> nanoparticles and their graphene-based composite: A novel photocatalytic material. *J. Solid State Chem.* **2022**, *312*, 123217. [CrossRef]
147. Zhang, H.; Yin, F.; Shang, S.; Li, Y.; Qiu, Z.; Lin, Q.; Wei, X.; Li, S.; Kim, N.Y.; Shen, G. A high-performance, biocompatible, and degradable piezoresistive-triboelectric hybrid device for cross-scale human activities monitoring and self-powered smart home system. *Nano Energy* **2022**, *102*, 107687. [CrossRef]
148. Zhao, W.; Zheng, J.; Han, C.; Jun, R.; Lu, Y.; Zhou, K.; Zhai, T.; Wang, H.; Yan, H. MnO<sub>x</sub>-PMMA self-powered triboelectric catalysts based on three-dimensional nanocomposite structures for formaldehyde degradation at room temperature. *Chem. Eng. J.* **2022**, *440*, 135877. [CrossRef]
149. Zhu, Y.; Zhao, W.; Jing, B.; Zhou, J.; Cai, B.; Li, D.; Ao, Z. Density functional theory calculations on 2H-MoS<sub>2</sub> monolayer for HCHO degradation: Piezoelectric-photocatalytic synergy. *Chin. Chem. Lett.* **2023**, *34*, 107816. [CrossRef]
150. Liu, L.; Zhong, S.; Zhang, L.; Liu, B.; Wang, W. Ti doped BiOCl nanowires for piezoelectric photocatalytic degradation of organic pollutants. *Catal. Commun.* **2022**, *170*, 106493. [CrossRef]
151. Song, W.; Zhang, M.; Huang, X.; Chen, B.; Ding, Y.; Zhang, Y.; Yu, D.-G.; Kim, I. Smart l-borneol-loaded hierarchical hollow polymer nanospheres with antipollution and antibacterial capabilities. *Mater. Today Chem.* **2022**, *26*, 101252. [CrossRef]

152. Li, H.; Zhang, Z.; Ren, Z.; Chen, Y.; Huang, J.; Lei, Z.; Qian, X.; Lai, Y.; Zhang, S. A quadruple biomimetic hydrophilic/hydrophobic Janus composite material integrating Cu(OH)<sub>2</sub> micro-needles and embedded bead-on-string nanofiber membrane for efficient fog harvesting. *Chem. Eng. J.* **2023**, *455*, 140863. [CrossRef]
153. Zhao, P.; Li, H.; Bu, W. A forward vision for chemodynamic therapy: Issues and opportunities. *Angew. Chem. Int. Ed.* **2023**, *62*, e202210415. [CrossRef]
154. Meng, Y.; Chen, L.; Chen, Y.; Shi, J.; Zhang, Z.; Wang, Y.; Wu, F.; Jiang, X.; Yang, W.; Zhang, L.; et al. Reactive metal boride nanoparticles trap lipopolysaccharide and peptidoglycan for bacteria-infected wound healing. *Nat. Commun.* **2022**, *13*, 7353. [CrossRef]
155. Wu, Y.; Li, Y.; Lv, G.; Bu, W. Redox dyshomeostasis strategy for tumor therapy based on nanomaterials chemistry. *Chem. Sci.* **2022**, *13*, 2202–2217. [CrossRef] [PubMed]
156. Wang, Q.; Liu, Q.; Gao, J.; He, J.; Zhang, H.; Ding, J. Stereo coverage and overall stiffness of biomaterial arrays underly parts of topography effects on cell adhesion. *ACS Appl. Mater. Inter.* **2023**, *15*, 6142–6155. [CrossRef]
157. Li, C.; Wang, J.; Deng, C.; Wang, R.; Zhang, H. Protocol for atmospheric water harvesting using in situ polymerization honeycomb hygrosopic polymers. *STAR Protoc.* **2022**, *3*, 101780. [CrossRef]

**Disclaimer/Publisher's Note:** The statements, opinions and data contained in all publications are solely those of the individual author(s) and contributor(s) and not of MDPI and/or the editor(s). MDPI and/or the editor(s) disclaim responsibility for any injury to people or property resulting from any ideas, methods, instructions or products referred to in the content.

## Article

# Full-Scale O<sub>3</sub>/Micro-Nano Bubbles System Based Advanced Oxidation as Alternative Tertiary Treatment in WWTP Effluents

Laura Ponce-Robles <sup>1,\*</sup>, Aránzazu Pagán-Muñoz <sup>2</sup>, Andrés Jesús Lara-Guillén <sup>2</sup>, Beatriz Masdemont-Hernández <sup>3</sup>, Teresa Munuera-Pérez <sup>3</sup>, Pedro Antonio Nortes-Tortosa <sup>1</sup> and Juan José Alarcón-Cabañero <sup>1</sup>

<sup>1</sup> Group of Irrigation, Centro de Edafología y Biología Aplicada del Segura (CEBAS-CSIC), 30100 Murcia, Spain

<sup>2</sup> Technology Centre for Energy and Environment (CETENMA), 30353 Murcia, Spain

<sup>3</sup> SISTEMA AZUD, S.A., 30820 Alcantarilla, Spain

\* Correspondence: lponce@cebas.csic.es

**Abstract:** Wastewater treatment plant effluents can be an important source of contamination in agricultural reuse practices, as pharmaceuticals are poorly degraded by conventional treatments and can enter crops, thereby becoming a toxicological risk. Therefore, advanced tertiary treatments are required. Ozone (O<sub>3</sub>) is a promising alternative due to its capacity to degrade pharmaceutical compounds, together with its disinfecting power. However, mass transfer from the gas to the liquid phase can be a limiting step. A novel alternative for increased ozone efficiency is the combination of micro-nano bubbles (MNBs). However, this is still a fairly unknown method, and there are also many uncertainties regarding their implementation in large-scale systems. In this work, a combined O<sub>3</sub>/MNBs full-scale system was installed in a WWTP to evaluate the removal efficiency of 12 pharmaceuticals, including COVID-19-related compounds. The results clearly showed that the use of MNBs had a significantly positive contribution to the effects of ozone, reducing energy costs with respect to conventional O<sub>3</sub> processes. Workflow and ozone production were key factors for optimizing the system, with the highest efficiencies achieved at 2000 L/h and 15.9 gO<sub>3</sub>/h, resulting in high agronomic water quality effluents. A first estimation of the transformation products generated was described, jointly with the energy costs required.

**Keywords:** alternative tertiary treatment; COVID-19; micro-nano bubbles; ozonation; pharmaceuticals

**Citation:** Ponce-Robles, L.; Pagán-Muñoz, A.; Lara-Guillén, A.J.; Masdemont-Hernández, B.; Munuera-Pérez, T.; Nortes-Tortosa, P.A.; Alarcón-Cabañero, J.J. Full-Scale O<sub>3</sub>/Micro-Nano Bubbles System Based Advanced Oxidation as Alternative Tertiary Treatment in WWTP Effluents. *Catalysts* **2023**, *13*, 188. <https://doi.org/10.3390/catal13010188>

Academic Editors: Juan José Rueda-Márquez, Javier Moreno-Andrés and Irina Levchuk

Received: 10 December 2022

Revised: 9 January 2023

Accepted: 10 January 2023

Published: 13 January 2023



**Copyright:** © 2023 by the authors. Licensee MDPI, Basel, Switzerland. This article is an open access article distributed under the terms and conditions of the Creative Commons Attribution (CC BY) license (<https://creativecommons.org/licenses/by/4.0/>).

## 1. Introduction

High levels of pharmaceutical manufacturing, and therefore their widespread use, can contribute to their discharge in concentrations high enough to cause adverse effects in aquatic environments, posing a new global challenge [1]. Specifically, from 2010 to 2022, an increase of more than 35% was detected in the consumption and manufacture of pharmaceuticals, and this is expected to increase by 3–6% in 2025 [2]. This increase is attributed to continuously changing demand, which has been impacted in recent years by critical events, including COVID-19 [3]. The main environmental problem is that most of the pharmaceuticals used both at home and in hospitals are excreted from the body either unchanged or as active metabolites at high concentrations, resulting in their continuous release into wastewater collection systems (mainly through wastewater treatment plants, WWTP) [4,5]. However, conventional WWTPs are not effective in the complete removal of these types of compounds (highly variable removal rates, from 0 to 100%). This has given rise to detection of compounds from different therapeutic groups (antibiotics, analgesics, anti-inflammatories, antiretrovirals, etc.) in aquatic environments in recent years, in both developed and developing countries, with values greater than 100 µg/L observed in some cases [6,7]. These concentrations are usually associated with consumption patterns. As an example, the model developed by Kuroda et al. (2021) showed an increase in the

concentration of chloroquine in domestic wastewater due to its consumption during the COVID-19 pandemic, with predicted values of 857 ng/L [8], while various commonly used pharmaceuticals (diclofenac, naproxen, or ketoprofen) were the most detected in WWTP effluents [9]. Although the information on the effects of many of these compounds on the environment and public health remains scarce, and no strict legal regulations on the release of pharmaceuticals into water bodies have been implemented on a global scale, most of them are considered priority substances, and included in European watch lists ((EU) 2022/1307, (EU) 2020/1161, etc.) [10,11].

Furthermore, the problem becomes aggravated when, in order to deal with water stress, the intention is to valorize WWTP effluents through agricultural reuse practices to promote the use of alternative water resources according to the circular economy action plans [12,13]. However, the reality is that the pharmaceutical compounds contained in these effluents could enter the food chain, which may result in health problems due to their potential accumulation risk (chronic effects) [14,15]. In light of this, the application of recently developed tertiary treatments to produce better water quality is currently attracting the attention of researchers and water managers as an opportunity for its reuse for suitable purposes. The challenge is to remove pharmaceutical compounds and pathogens that could have negative effects on human health, animal health, or the environment. In addition, the emergence of new, increasingly restrictive reuse policies (such as the new (EU) 2020/741 on minimum requirements for water reuse, to be implemented at the European level from June 2023) makes investing money in appropriate treatments a short-term necessity, as well as the development of efficient treatments to meet these legal requirements with assumable energy, costs, or other resources [16].

Ozone-based processes are an attractive option that could be implemented as a tertiary treatment in WWTP as ozone, as a result of its strong oxidizing power (2.07 V), is reported to be an effective disinfectant, and an agent capable of degrading pharmaceuticals using two mechanisms: (a) direct electrophilic attack by molecular ozone; and (b) indirect attack by hydroxyl radicals ( $\bullet\text{OH}$ ), produced through the ozone decomposition process. It is this path that makes ozonation to be considered part of the classification of advanced oxidation processes (AOPs) [17]. The main advantage of ozone over other AOPs, such as Fenton or photo-Fenton processes, is the fact that the addition of complex chemical reagents (i.e., iron salts or chelating agents) are not needed to carry out the reaction [18].

However, the ozone mass transfer process from the gas to the liquid phase can be a limiting step, resulting in a low-efficiency process. Therefore, ozone coupling with other technologies ( $\text{O}_3/\text{H}_2\text{O}_2$ ,  $\text{O}_3/\text{UV}$ ,  $\text{O}_3/\text{ultrasound}$ ,  $\text{O}_3/\text{electrolysis-ozonation}$ , or catalytic ozonation) has been studied in recent years [19–22]. In fact, this process seems to be the bottleneck that is hampering the definitive implementation of this technique, given the large investments needed in ozone generation systems.

One innovative technique for enhancing mass transfer and increasing ozone solubility in water is the combination of  $\text{O}_3$  with micro-nano bubbles (MNBs) [23]. Their tiny size (with diameters ranging from tens of nanometers to several tens of micrometers) and specific properties have captured the attention of researchers recently. Specifically, MNBs have been shown to have a significantly lower rising velocity than larger bubbles, and their negatively charged surface prevents coalescence, so they may persist in water for longer periods [24]. MNBs also have an internal pressure and a specific surface that favors mass transfer, increasing ozone dissolution. In addition, the effective generation of  $\bullet\text{OH}$  radicals by the collapse of  $\text{O}_3/\text{MNBs}$  under a broad pH band can contribute to the oxidation of organic molecules [25–27], increasing the effectiveness with respect to conventional  $\text{O}_3$  processes. As an example, Azuma et al., 2019, reported an increase in the rates of pharmaceutical compound removal between 8% and 34% when a combined  $\text{O}_3/\text{MNBs}$  treatment was used, as compared with  $\text{O}_3$  alone. Thus, the degradation rates of compounds such as acetaminophen glucuronide, bortezomib acid, or loxoprofen, increased from 19% to 32%, 48% to 88%, and 48% to 82%, respectively, while less persistent compounds such as carbamazepine or acetaminophen were completely removed [28].

However, despite all these promising advantages, most studies have been conducted at the laboratory scale and under controlled conditions, or even using distilled or simulated water as a model. Therefore, studies on the benefits of using O<sub>3</sub>/MNBs systems using real wastewater are limited, and even more so, the application of this technology on a large scale. Consequently, factors such as design parameters for large-scale reactors, their operation, process control, or associated costs are not yet sufficiently studied. In addition, there is limited evidence on the benefits for disinfection purposes. Another uncertainty comes from the lack of knowledge about the transformation products (TPs) related to the process of degradation of pharmaceuticals that could be generated in this type of system and their impact on the environment.

This work aims to evaluate the combined use of MNBs/O<sub>3</sub> in a large-scale regeneration system to obtain water of high agronomic quality. Pharmaceutical removal efficiency, including COVID-19-related compounds, along with disinfection, as well as transformation products generated and cost evaluation, will be key aspects in system optimization and evaluation.

## 2. Results and Discussion

### 2.1. Pharmaceuticals Removal Efficiency

The results provided evidence of the influence of the workflow on pharmaceutical removal percentages, showing higher efficiencies working at 2000 L/h and 500 L/h as compared to the intermediate flow rate (1200 L/h) (see Figure 1). This phenomenon can be due to two different issues: the dilution carried out and, therefore, the final concentration of ozone, and the reaction with molecular ozone. At a high workflow, more turbulence is generated in the wastewater, so the MNBs collide with each other and with O<sub>3</sub> molecules, increasing the concentration of reactive species (mainly •OH radicals) capable of reacting and breaking down pharmaceuticals [29]. Since •OH has a higher oxidation potential than O<sub>3</sub>, the pharmaceuticals oxidation process will increase with respect to a lower workflow [30]. On the other hand, at low working flows, the O<sub>3</sub>-MNBs/pharmaceuticals ratio is higher, meaning a higher ozone concentration which increases the oxidizing species, favoring the removal of pharmaceuticals [31].

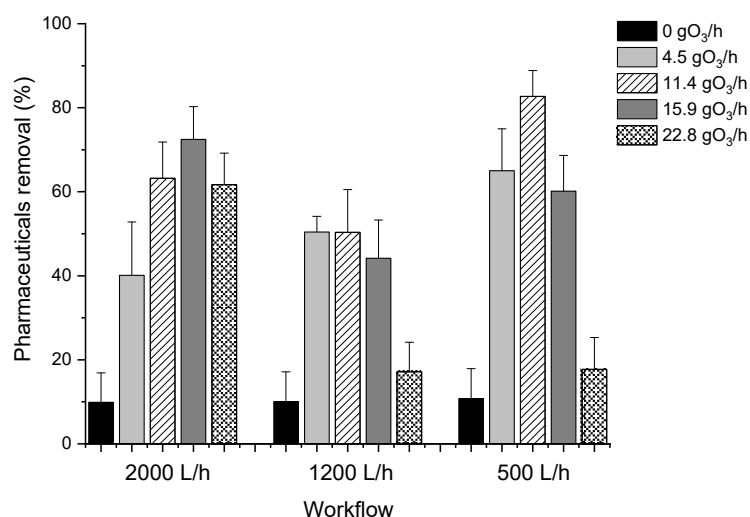


**Figure 1.** Influence of inlet ozone concentration and flow rate in pharmaceuticals removal.

A clear relationship was also observed between the pharmaceutical removal percentages and ozone production, according to Dawood et al., 2021 [29]. In particular, an increase in the ozone dose applied was related to an increase in pharmaceuticals removal, reaching maximum values of  $72.5 \pm 7.8\%$  working with  $15.9 \text{ gO}_3/\text{h}$ ,  $50.3 \pm 10.2\%$  working with  $11.4 \text{ gO}_3/\text{h}$  and  $82.7 \pm 6.2\%$  working with  $11.4 \text{ gO}_3/\text{h}$ , when 2000 L/h, 1200 L/h, and 500 L/h workflow were tested, respectively. However, a decrease in removal efficiency was observed in all cases when working at maximum ozone production values ( $22.8 \text{ gO}_3/\text{h}$ ).

These effects may be related to ozone solubility. In general, the increase in ozone concentration promotes the transfer of ozone from the gas phase to the liquid phase up to the solubility limit. At this point, there is no transfer of a greater supply of ozone to the liquid phase, so the efficiency of pharmaceutical removal remains constant or even decreases, according to Joseph et al. (2021) [32]. This was tested experimentally by measuring dissolved oxygen (indigo method). In all cases, the dissolved ozone percentage increased as the inlet ozone concentration increased, reaching a maximum value of 82.0% working with 15.9 gO<sub>3</sub>/h, a dissolved ozone percentage similar to those reported by Kokkoli et al. (2021) [33]. From that point on, this percentage remained constant and even decreased, thus corroborating our hypothesis.

On the other hand, it should be noted that, in the absence of ozone, an average removal of 10% of pharmaceuticals was observed, regardless of the workflow used, suggesting the ability of MNBs to enhance the efficiency of the process. These results are consistent with the experiments by Bui et al. (2020) [34]. These authors reported that the electrostatic attraction between MNBs and organic matter (due to the opposite surface charge between molecules), along with reactive species that can be generated by the collapse of the MNBs, lead to a decrease in organic matter in wastewater.

The percentages obtained from Figure 1 were also related to the ozone consumed in the process. The results (Figure 2) showed that the highest ozone consumption occurred at 500 L/h, followed by 1200 L/h and 2000 L/h, respectively. This allowed us to corroborate the hypotheses and justify the results presented above. In this sense, at high flows, indirect O<sub>3</sub> reactions would predominate, due to the presence of a greater number of radical species (<sup>•</sup>OH), due to the reactivity of the MNBs (molecular collision). However, at low flows, direct O<sub>3</sub> reactions may predominate. In both cases, the reactivity would be greater than at intermediate flows, where the contact time between molecules is lower, and there is not enough flow to make collisions between molecules too effective, so there would be a balance between direct and indirect reactions, limiting them both. On the other hand, a decrease in ozone consumption was observed at the highest ozone generation rate, verifying that this concentration reaches the O<sub>3</sub> solubility limit.

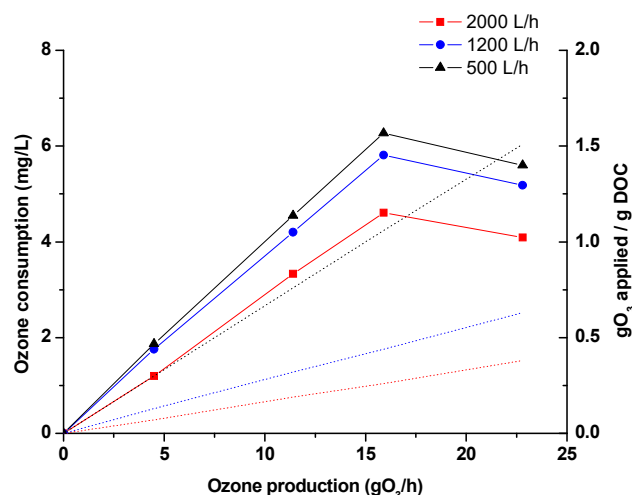


**Figure 2.** Ozone consumption (straight line) and applied normalized ozone (dash line) under experimental conditions.

On the other hand, the specific ozone dose applied, normalized to the dissolved organic carbon (DOC) of effluents, showed values between 0 to 0.38 gO<sub>3</sub>/gDOC, 0 to 0.63 gO<sub>3</sub>/gDOC, and 0 to 1.51 gO<sub>3</sub>/gDOC when flowrates of 2000 L/h, 1200 L/h, and 500 L/h were used, respectively. In all cases, the values of gO<sub>3</sub> applied/g DOC working at 2000 L/h were much lower than those reported in the literature for conventional O<sub>3</sub> reactions in large-scale systems. Specifically, Hollender et al. (2009) studied the removal of 24 pharmaceuticals in wastewater with O<sub>3</sub> at full scale. The results showed that a dose of



0.47 gO<sub>3</sub>/gDOC was needed to remove compounds of greater reactivity (including CBZ or SMX), while higher doses were needed for slow-reacting compounds [35]. The same removal of compounds under conventional O<sub>3</sub> reactions was studied by Antoniou et al. (2013) [36], demonstrating that a dose between 0.55 gO<sub>3</sub>/gDOC to 0.77 gO<sub>3</sub>/gDOC was necessary to reach a 90% removal of highly reactive compounds while for slow-reacting compounds (such as NPX) a specific ozone dose > 1 g O<sub>3</sub>/gDOC was necessary. Therefore, the positive impact of the use of MNBs in O<sub>3</sub> reactions is demonstrated, decreasing the gO<sub>3</sub>/gDOC to be applied as compared to conventional ozonation reactions, which could also have an impact on cost reduction.

According to these results, and considering that the treated water is intended to be reused for agriculture irrigation, with disinfection crucial for optimization, an evaluation of disinfection based on *E. coli* removal during the process under the selected operational conditions was performed. The results (Figure 3) showed that the reduction in *E. coli* bacteria was significantly affected by ozone dosage and workflow, as was the case for pharmaceutical removal, with the mechanisms being the same. A combination of direct (involving O<sub>3</sub> molecules) and indirect (involving free •OH) reactions are involved in pharmaceuticals removal and *E. coli* inactivation processes under selected wastewaters due to their pH value (~pH 7), and this reactivity is further enhanced by the presence and behavior of MNBs under particular conditions [37–39]. Therefore, the study of the operating conditions for each specific system is essential for achieving the highest removal efficiency.

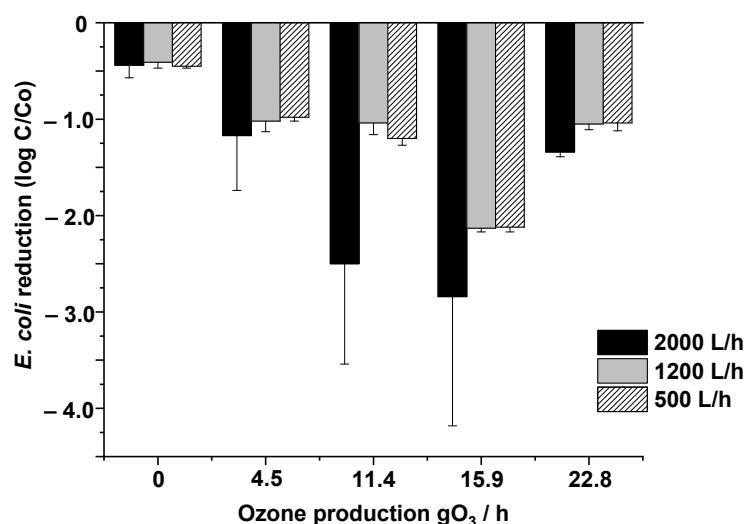


**Figure 3.** Influence of inlet ozone concentration and flow rate on *E. coli* removal.

Considering that the initial abundance of *E. coli* in the inlet wastewater was  $2.3 \times 10^4 \pm 1.1 \times 10^4$  CFU/100 mL (see Table S1), 15.9 gO<sub>3</sub>/h of ozone production was the only condition able to inactivate *E. Coli* values below LOD, showing reduction values of up to 4-log, while lower removal efficiencies were obtained for the other conditions tested. In all cases, the best removal efficiencies were observed using the 2000 L/h workflow, due to increased reactivity as a result of the collisions between molecules, while the use of air MNBs managed to remove an average of 0.5 log, demonstrating that the hydroxyl radicals alone, generated by the collapse of the MNBs, have a disinfectant activity, according to Sumikura et al., 2007 [40]. In this work, the authors reported a 24.5% removal of *E. coli* in wastewater using micro-air bubbles, while this percentage increased progressively when increasing amounts of ozone were added.

Therefore, considering the combination of the efficient disposal of pharmaceuticals and disinfection requirements for agricultural reuse, 2000 L/h and 15.9 gO<sub>3</sub>/h were considered optimal conditions for continued work in the large-scale system.

## 2.2. Prediction of the Pharmaceutical Removal from Physico-Chemical Properties

Despite the high efficiencies in pharmaceutical removal obtained under the different operational conditions studied, not all compounds behaved in the same way in the O<sub>3</sub>/MNBs system. Specifically, of the 12 pharmaceuticals analyzed, 6 of them showed high removal percentages, reaching, in all cases, values higher than 80% (TRZ, TCL, AMX, CBZ, ACT, and SMX), 4 of them (KTP, NPX, DCF, and ERY) showed moderate efficiencies (between 57.62% and 77.34%), while the remaining 2 (HLP and CHL) had low removal efficiencies (approximately 22.50%, see Figure 4). This may be related to the structure and functional groups of the pharmaceuticals to be degraded and, therefore, to the reactivity of these groups with O<sub>3</sub> and •OH radicals in an aqueous solution, and may result in oxidation processes, cycloadditions, or mainly electrophilic substitution reactions according to Beltran et al., 2003 [41]. Specifically, the presence of electron-rich functional groups has been reported to react with O<sub>3</sub> molecules by electrophilic substitution via electron transfer, increasing removal percentages [42]. These groups include C=C bonds (mainly found in CBZ), nitrogen-containing compounds (mainly found in TRZ, TCL, or SMX), or organosulfur compounds such as AMX. However, electron-withdrawing functional groups, such as fluoro, chloro, or carboxyl groups (found in DCF, CHL, or HLP) reduce electronic density from pharmaceuticals inhibiting electrophilic substitution reactions, resulting in a shielding effect [36]. In this perspective, and in order to simplify and predict the pharmaceutical removal efficiency in O<sub>3</sub>/MNBs systems, the removal percentages obtained were directly associated with the ionic capacity of the pharmaceuticals, following the trend: cationic compounds > dipolar ions > neutral compounds > anionic compounds. Thus, cationic, dipolar ions, and neutral compounds would be considered as high removal rate compounds, while the anionic compounds would be considered as compounds with moderate removal percentages. However, CHL and HPL, despite being cationic compounds, showed the lowest removal rates (22.5 ± 2.6% and 22.5 ± 3.1%, respectively). This behavior could be associated with the presence of electron-withdrawing functional groups (mainly fluoro and chloro in their structure, limiting their removal [43]). On the other hand, another exception to this behavior was the case of ERY. Despite being a neutral compound, its low reactivity was due to the scarcity of its C=C bond and other electron-rich functional groups in their structure, which limited its reactivity. In this sense, knowing the polarity and chemical structure of the pharmaceuticals to be degraded by O<sub>3</sub>/MNBs reactions could be crucial for predicting the removal efficiency of selected compounds in real systems.

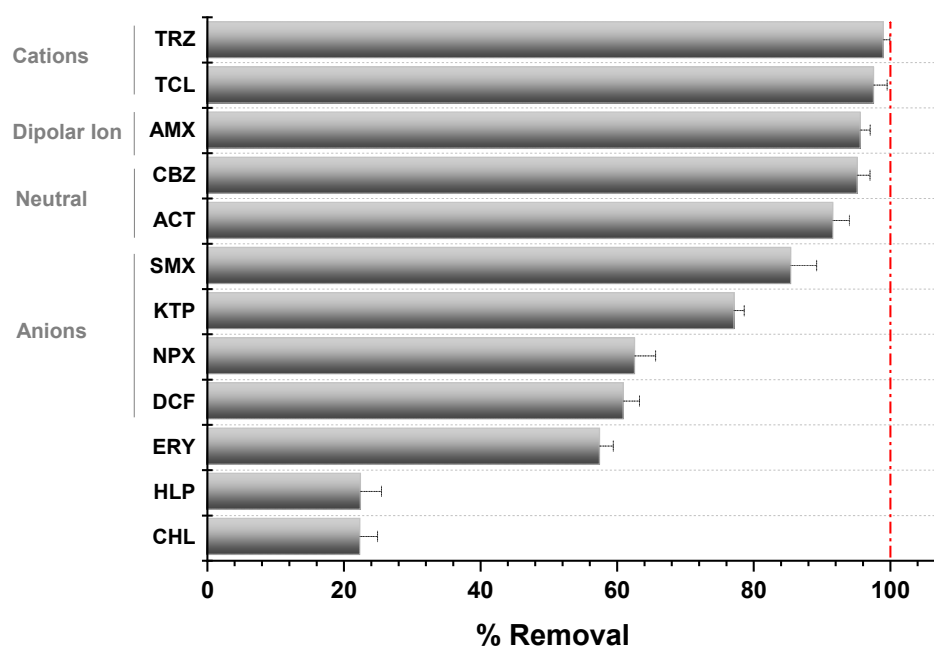


Figure 4. Influence of ionic capacity in pharmaceuticals removal.

### 2.3. Transformation Products Generated in the Process

One aspect to consider for the implementation of  $O_3$ /MNBs-based systems on a large scale is related to the TPs that can be generated due to the degradation of pharmaceutical compounds during the process due to  $\bullet OH$  radical reactivity [44]. Although the generation of TPs in ozonation-based processes ( $O_3$ ,  $O_3/H_2O_2$ , etc.) and their potential effect on the environment have been studied for many years [45], to our knowledge, there are no studies yet that have considered the TPs generated in  $O_3$ /MNBs processes. In this light, a study was conducted to evaluate whether the TPs generated in  $O_3$ /MNBs processes are consistent with those reported in the literature for other  $O_3$ -based processes [46–55].

Of the 104 TPs considered in the suspect list, only 9 chromatographic peaks were detected as positive, following the settings described in Section 2.3. After grouping retention time signals, only five remained, which originated from CBZ (three TPs (TPC10, TPC4, and TPC13) at retention times of 6.54, 8.67, and 9.45 min, respectively), DCF (1 by-product at a retention time of 9.08 min, TPD6), and NPX (1 by-product at a retention time of 10.83 min, TPN1), with the proposed structure previously reported in the literature (see Table S2). For all selected chromatographic peaks, score values were 100% and the mass error was  $<5$  ppm. For more information, see Table S3.

Significant differences were observed according to the different workflows. In particular, TPC4 (carbamazepine by-product) was the largest by-product area and was detected only at the 2000 L/h (see Figure 5). It formed from  $4.5 \text{ gO}_3/\text{h}$  and the peak area increased following the ozone production, while a small decrease was detected at  $22.8 \text{ gO}_3/\text{h}$ , following a pattern similar to the pharmaceutical's behaviour. Although several authors have found this by-product of carbamazepine in ozonation reactions, and some of them have reported it as one of the most persistent TPs [56,57], it was Kråkström et al. (2020) [51] who first associated this mass to a specific structure (2,2'-azanediyldibenzaldehyde) using NMR. The authors reported that this by-product was formed via radical reactions from the intermediate product N, N-bis(2-formylphenyl) urea, continuing to react with  $\bullet OH$  radicals forming other intermediates, confirming their quick reactivity under higher flow rates.

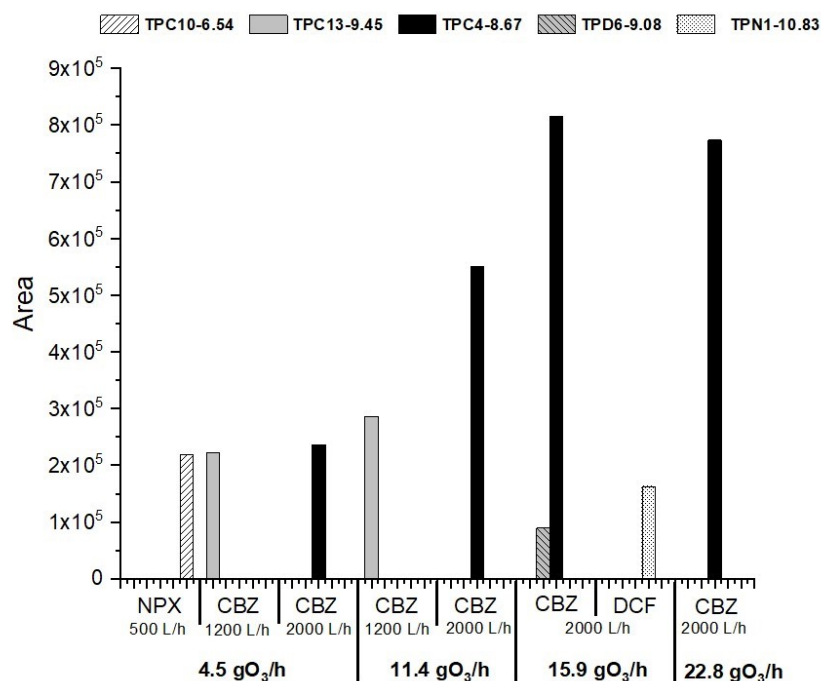


**Figure 5.** TPs obtained according to the selected suspect list under different operational conditions.

On the other hand, TPC10 was detected in the 1200 L/h workflow under 4.5 and  $11.4 \text{ gO}_3/\text{h}$  ozone productions, while at higher production values, it was not detected, probably due to its reactivity under the  $O_3$ /MNBs system. Although it is difficult to predict

their origin, these TPs could be hydroxylated derivatives formed from other carbamazepine TPs, according to Kråkström et al. (2020) [51]. Other TPs, such as TPN1, TPC13, or TPD6 were found on a spot basis in the samples, which shows that, although they can be formed in O<sub>3</sub>-MNBs, their persistence is lower than the other TPs found.

However, despite the preliminary results obtained, the appearance of other TPs cannot be ruled out if the concentrations of the starting pharmaceuticals were higher, as many studies reported in the literature were carried out with concentrations close to 1000 µg/L, five times higher than the concentration tested in this study.

#### 2.4. Agronomic Quality of System Effluents under Optimal Operation Conditions

In order to determine whether the effluents from the proposed and optimized full-scale O<sub>3</sub>/MNBs system would be suitable for agricultural use, the most recent EU directive (EU, 2020/741) on minimum requirements for water reuse was chosen as a reference [15]. Particularly, this directive stipulates four different “classes of reclaimed water quality” (A, B, C, and D) based on permitted agricultural use and irrigation method, with class A being the most restrictive. With this aim, the system with real effluents (non-spiked wastewater) under optimal operating conditions (2000 L/h and 15.9 gO<sub>3</sub>/h) was monitored working in continuous mode for 6 months (2 monthly samples).

A significant reduction in the different physico-chemical parameters was detected in all O<sub>3</sub>/MNBs effluents analyzed. Specifically, turbidity, BOD<sub>5</sub>, and TSS values decreased by  $45.0 \pm 10.5\%$ ,  $33.3 \pm 15.2\%$ , and  $15.1 \pm 2.0\%$ , respectively, showing in all cases values below the most restrictive limits included the EU regulation (class A) (BOD<sub>5</sub> ≤ 10 mg/L; TSS ≤ 10 mg/L and turbidity ≤ 5 NTU). On the other hand, an increase of approximately 9% in transmittance values was detected in the system effluents, from  $53.7 \pm 4.6\%$  to  $62.4 \pm 3.3\%$ , while the pH and ion content remained practically constant, with pH values of  $7.4 \pm 2.1$  and sodium adsorption ratio values of less than 6 meq/L, with the limit regulated for agricultural practices being 6 meq/L according to Spanish Royal Decree 1620/2007 [58].

Regarding the pharmaceuticals, all the samples entering the system showed low concentrations of all analyzed compounds, with average values between 0.03 µg/L and 0.08 µg/L, mainly because the WWTP used for the study was located in a rural area with an agricultural perspective, so the concentration of pharmaceuticals that reached this WWTP was relatively low throughout the year. In spite of this, all the samples treated using the O<sub>3</sub>/MNBs system showed a total removal of pharmaceuticals, with values, in all cases below the analytical detection limits.

As for the disinfection purposes, the effluents showed a significant reduction in *E. coli* (between 3-log to 4-log), with concentrations in all cases below the European regulation on minimum quality requirements established for this bacterium (<10 CFU/100 mL), the value marked for “the point of compliance” in “class A” reuse. Recently, several authors have demonstrated the potential of O<sub>3</sub>/MNBs combination for wastewater disinfection. Specifically, Furuichi et al. (2013) reported the inactivation of Gram-positive and Gram-negative bacteria, including *E. coli*, when a combination 1.5 mg/L of dissolved ozone and MNBs were used as the water treatment obtained removal percentages higher than 99.99% (from  $1.6 \times 10^9$  CFU/mL to <10 CFU/mL) [59], while Cruz et al., 2017 [60], analyzed the inactivation of fecal and total coliforms in domestic wastewaters from Peru, demonstrating the reduction of more than 99% for both indicators.

However, despite the promising results, studies evaluating the efficiency of O<sub>3</sub>/MNBs systems in the inactivation of highly persistent microorganisms are limited. Under this perspective, an additional study based on the removal efficiency of *Clostridium perfringens* spores as protozoa indicator was carried out. This indicator was selected due to their recent introduction in EU 2020/741 and their resistance to complete removal in conventional tertiary treatments (including chlorine, UV-C light, or even conventional ozonation) as compared with other parasites [61–63]. The results showed an average removal percentage of  $75 \pm 10\%$  during continuous work under optimal conditions (from  $800 \pm 141$  CFU/100 mL in the O<sub>3</sub>/MNBs inlet wastewater). However, water quality changes in *Clostridium perfringens*

spores removal were detected during storage of treated water, reaching 90% to 99% removal efficiencies after 24–72 h. This may be related to the persistence of MNBs in water, lengthening the activity of ozone and radical species in the solution, thus prolonging the antimicrobial activity [64]. These changes in water quality during storage have been reported by other authors. Chuajedton et al., 2016 [65] studied the use of a lab-scale O<sub>3</sub>/MNBs system for the inactivation of *E. coli* in fresh-cut pineapple. The authors obtained the highest *E. coli* removal values (between 4–5 log reduction) after 2 days of storage. On the other hand, Seki et al., 2017, studied the microbicidal effects of O<sub>3</sub>/MNBs after long-term storage. The results confirmed the ozone retention capacity in the MNBs, and their antimicrobial activity, removing resistant microorganisms even after long storage seasons under suitable conditions [66].

### 2.5. Cost Assessment Approach

Since the removal of pharmaceutical compounds under advanced tertiary treatments (including O<sub>3</sub>/MNBs) are reported as energy-intensive processes, the energy requirement is one of the most important factors to consider from an economic point of view [67,68]. Under this perspective, an estimation of the economic cost of the process based on electrical energy consumption is presented. The analysis was performed according to figures of merit related to •OH-involved processes described by the International Union of Pure and Applied Chemistry (IUPAC) [69]. Following the marked recommendations, the electrical energy per order factor (E<sub>EO</sub>) was calculated. This factor describes the electric energy (kWh) per unit of volume (m<sup>3</sup> of wastewater) required to degrade a pharmaceutical compound by one order of magnitude. E<sub>EO</sub> can be calculated with the following equation:

$$E_{EO} = \frac{P}{F \times \log(C_i/C_f)} \quad (1)$$

where P is the rated power (kWh) of the oxidation system, F is the flow rate (m<sup>3</sup>) and C<sub>i</sub> and C<sub>f</sub> are the initial and final concentrations of the pharmaceutical compounds [70]. The energy consumption of pumping, ozone generation, and MNBs formation was found to be about 6.1 kWh. Considering that E<sub>EO</sub> values are directly related to the pharmaceutical removal efficiency (log C<sub>i</sub>/C<sub>f</sub>), two different groups were considered: group 1 (99% average removal efficiencies, such as some cations) and group 2 (90% average removal efficiencies, mainly dipolar ions or some neutral compounds). The calculated E<sub>EO</sub> values were 1.80 kWh/m<sup>3</sup>/order for group 1 and 3.05 kWh/m<sup>3</sup>/order for group 2, for the O<sub>3</sub>/MNBs process. To our knowledge, this is the first time that the costs associated with a large-scale O<sub>3</sub>/MNBs process have been calculated, and these results confirm that the energy costs are directly associated with the physico-chemical properties of the compounds to be degraded. Therefore, in WWTP where group 1 compounds predominate, costs would be lower as compared to other WWTP having compounds of higher persistence. The calculated E<sub>EO</sub> values were analogous to those predicted by Miklos et al. (2018) and Joseph et al. (2021) [32,71] for the implementation of large-scale ozonation systems. However, it would be necessary to specifically know the energy requirements that were considered for these predictions (such as pumping), as well as redesign the location of the tertiary step in the treatment line under the criteria of energy optimization. At any rate, E<sub>EO</sub> values were in line with those predicted by the same authors for other advanced oxidation processes. Specifically, the authors suggested an average energy consumption for conventional large-scale ozonation processes of 1 kWh/m<sup>3</sup>/order, while higher values (between 2.6 (photo-Fenton) to 38.1 kWh/m<sup>3</sup>/order (eAOP)) were suggested for the degradation of specific pollutants with AOPs technologies. On the other hand, studies reported higher E<sub>EO</sub> values for UV-based photocatalysis (335 kWh/m<sup>3</sup>/order), ultrasound (2616 kWh/m<sup>3</sup>/order), or microwave-based AOPs (543 kWh/m<sup>3</sup>/order), so the use of large-scale O<sub>3</sub>/MNBs could have great energy benefits over other technologies. However, despite these approaches, there is a great lack of knowledge about the energy costs required in O<sub>3</sub>/MNBs large-scale systems, as E<sub>EO</sub> values are mostly dependent on experimental conditions (pH, physico-chemical properties of the water to be treated, etc.), mainly due to the competition between direct and

indirect ozonation reactions. In spite of this, the advantages of using  $O_3$ /MNBs systems are promising. Azuma et al. reported that the combination of  $O_3$ /MNBs could reduce energy costs as compared to conventional  $O_3$  treatments due to the higher consumption of  $O_3$  during the reaction and its rapid diffusion into the liquid phase [28].

On the other hand, it is important to note that the estimated  $E_{EO}$  values reported generally do not reflect the additional energy demand required for the production of chemicals or catalysts used in processes, so these factors should be included in the  $E_{EO}$  calculation [72]. As such, when evaluating the overall costs, e.g., when calculating capital expenditures (CapEx) and operational expenditures (OpEx), other costs such as chemicals and material cost, control, and maintenance expenses should be included and determined. Nevertheless,  $E_{EO}$  is a good starting point for comparing the energy requirement of ozone for pharmaceutical removal.

### 3. Materials and Methods

#### 3.1. System Design

The combined  $O_3$ /MNBs full-scale system (Figure 6a) was a non-commercial system specifically designed by SISTEMA AZUD, S. A. for these tests. It was installed in a conventional WWTP located in Murcia Region (Spain) (latitude  $37^{\circ}47'48''$  N, longitude  $0^{\circ}57'36''$  W). Specifically, this WWTP receives domestic and industrial effluents from three municipalities (Roldán, Lo Ferro, and Balsicas) and has a maximum treatment capacity of  $2,007,500\text{ m}^3/\text{year}$  of wastewater. The water line consists of a primary treatment, followed by an activated sludge secondary treatment with extended aeration and sedimentation, and a final tertiary treatment based on coagulation–flocculation, sand filter, and disinfection using UV radiation. WWTP effluents are commonly used for agricultural irrigation.

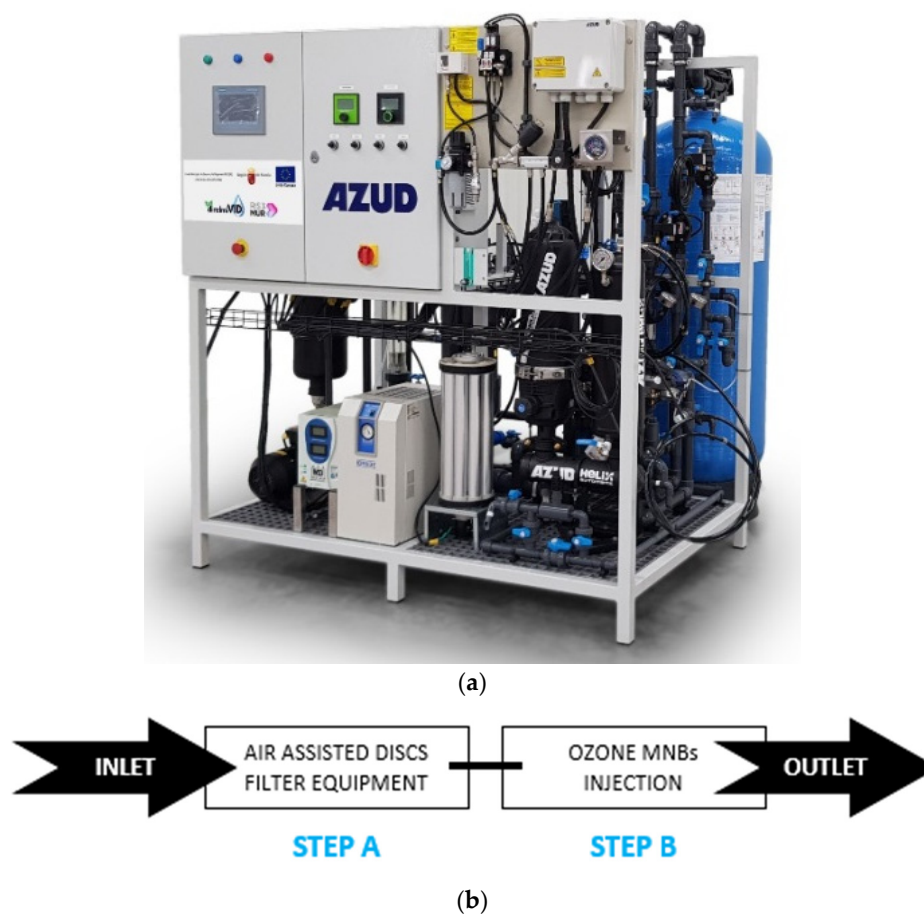


Figure 6. (a)  $O_3$ /MNBs system design; (b) system treatment line steps.

The designed system was connected to the WWTP secondary clarifier, bypassing the WWTP's conventional tertiary treatment. The physico-chemical characterization of inlet wastewater is reported in Table S1. The system consists of a modular and compact system with combinable steps, automation for monitoring operational parameters, and remote control. The workflow range during operation is 500 L/h to 2000 L/h.

The experimental treatment line is based on two different stages arranged in series (Figure 6b). Both stages treat the entire treatment flow, so there is no shunt in which the treated flow can be diluted.

**Step A:** The first stage is an air-assisted disc filtering equipment AZUD HELIX AUTOMATIC<sup>®</sup>. Specifically, the experimental module is based on a mono stage equipment, AZUD HELIX AUTOMATIC FT201/2VX AA DLP (Sistema AZUD, S.A., Murcia, Spain), provided by a filtration grade limit of 50 µm. The disc filter technology was selected because it allows deep filtration that removes all particles larger than the filtration grade and a high percentage of smaller ones, regardless of geometry or nature, protecting the next step, according to Ponce-Robles et al., 2020 [73]. In addition, this experimental module includes an automatic washing system that combines water and compressed air, which allows working at low pressure (even during the counter-washing process), reducing the hydraulic interaction of the system during cleaning, optimizing water and energy consumption, and achieving total disk recovery [73].

**Step B.** The second stage is based on ozone micro-nano bubbles (MNBs) injection. This step consists of two combined systems: (i) ozone generation system; (ii) ozone mass transfer system based on MNB technology. The ozone generator system is fed by on-site-treated atmospheric air. The air treatment line is composed of an air dryer, a particle filter, and an oxygen concentrator. The percentage of oxygen in the air after this treatment can be increased up to 90%. The ozone generation system, which uses corona discharge technology, is fed at 5 lpm of this oxygen-concentrated air to produce a maximum of 22,800 mgO<sub>3</sub>/h. Likewise, the generation can be regulated between 0–100%. The ozone mass transfer system consists of a non-commercial prototype composed of an MNBs bubble injector which is simultaneously fed by the ozone generator and filtered water. This system is based on a gas–liquid mixing pump that absorbs the gas phase by negative pressure on the suction inlet and has a high-speed rotary impeller to stir liquid and gas phases.

An optional ozonization tank is located at the outlet of the O<sub>3</sub>/MNBs system to study the behavior in water after an established period. The volume of this tank is 5.000 L.

### 3.2. Pharmaceutical Compounds Included in the Study

A total of 12 pharmaceutical compounds were selected as a case study considering different aspects: (i) Cover pharmaceuticals from different therapeutic groups (analgesics, antibacterial, anticonvulsants, antimalarials, anti-inflammatories, antipsychotics, antidepressants); (ii) Study of persistent or bio-recalcitrant compounds commonly found in worldwide WWTP effluents, such as acetaminophen (ACT), amoxicillin (AMX), carbamazepine (CBZ), diclofenac (DCF), erythromycin (ERY), ketoprofen (KTP), naproxen (NPX), sulfamethoxazole (SMX), or tetracycline (TCL) [4]; (iii) Study of pharmaceuticals included in the list of trial drugs for the diagnosis and treatment of COVID-19, and so, considered essential for the management of sanitary emergence, such as chloroquine (CHL) [74], trazodone (TRZ), [75] or haloperidol (HLP), (included in the Resolution from 19 June 2020, of the Spanish Agency for Medicines and Medical Devices, on urgent prevention, containment, and coordination measures to address the health crisis caused by COVID-19) [76].

Pure standards (>98%) of selected compounds were purchased from Sigma–Aldrich<sup>®</sup> (Steinheim, Germany). Individual stock standard solutions and work solutions used in both analytical and experimental viewpoints were prepared in methanol or MilliQ water and stored at −20 °C. The physico-chemical properties of all selected compounds are reported in Table 1 [77,78].

**Table 1.** Physico-chemical properties of selected pharmaceuticals.

	Drug Type	Formula	Molecular Weight (g/mol)	Log Kow	pKa
Acetaminophen (ACT)	Analgesic	C <sub>9</sub> H <sub>9</sub> NO <sub>2</sub>	151.16	3.06	8.9
Amoxicillin (AMX)	Antibacterial	C <sub>16</sub> H <sub>19</sub> N <sub>3</sub> O <sub>5</sub> S	365.4	0.87	2.6
Carbamazepine (CBZ)	Anticonvulsant	C <sub>15</sub> H <sub>12</sub> N <sub>2</sub> O	236.3	2.45	15.9, −3.8
Chloroquine (CHL)	Antimalarial	C <sub>18</sub> H <sub>26</sub> ClN <sub>3</sub>	319.9	4.63	10.1
Diclofenac (DCF)	Anti-inflammatory	C <sub>14</sub> H <sub>11</sub> C <sub>12</sub> NO <sub>2</sub>	296.1	4.51	3.9
Erythromycin (ERY)	Antibacterial	C <sub>37</sub> H <sub>67</sub> NO <sub>13</sub>	733.9	3.06	8.8
Haloperidol (HLP)	Antipsychotic	C <sub>21</sub> H <sub>23</sub> ClFNO <sub>2</sub>	375.9	4.30	8.65
Ketoprofen (KTP)	Anti-inflammatory	C <sub>16</sub> H <sub>14</sub> O <sub>3</sub>	254.3	-	3.98
Naproxen (NPX)	Anti-inflammatory	C <sub>14</sub> H <sub>14</sub> O <sub>3</sub>	230.26	3.18	4.18
Sulfamethoxazole (SMX)	Anticonvulsant	C <sub>10</sub> H <sub>11</sub> N <sub>3</sub> O <sub>3</sub> S	253.28	0.89	pKa1 = 1.6 pKa2 = 5.7
Tetracycline (TCL)	Antibacterial	C <sub>22</sub> H <sub>24</sub> N <sub>2</sub> O <sub>8</sub>	444.4	−1.37	7.68, 3.3
Trazodone (TRZ)	Antidepressant	C <sub>19</sub> H <sub>22</sub> ClN <sub>5</sub> O	371.9	3.21	6.79

Data from PubChem (<https://pubchem.ncbi.nlm.nih.gov/> (accessed on 1 December 2022)) and network of reference laboratories, research centers, and related organizations for monitoring of emerging environmental substances (<https://www.norman-network.net/> (accessed on 1 December 2022)).

### 3.3. Analytical Determinations

Total suspended solids (TSS), electrical conductivity (EC), pH, turbidity, dissolved organic carbon (COD), 5-day biological demand (BOD<sub>5</sub>), total nitrogen (TN), and chemical oxygen demand (COD) analyses were carried out following Standard Methods (APHA, 2012) [79].

The dissolved ozone in the system was determined using the indigo method according to the standard methods (APHA-AWWA-WEF, 1992) procedure. The analysis was performed using potassium indigo tri-sulfonate (Sigma–Aldrich<sup>®</sup>, Steinheim, Germany) and an ultraviolet-visible (UV-vis) spectrophotometer set at 600 nm [80].

*Escherichia coli* measurements were determined by the standard membrane filtration method, according to ISO 9308-1:2014 [81]. The detection limit was set at 1 CFU/ 100 mL (Colony Forming Unit per 100 mL), according to the Class A maximum value (10 CFU of *E. coli*/100 mL) set by the new European Regulation on minimum requirements for water reuse ((EU) 2020/741). *Clostridium perfringens* spores were analyzed through an external ENAC-certified reference laboratory (IPROMA S.L) located in Castellón, Spain, following the standard membrane filtration method established in the UNE-EN ISO 14189:2007 [82], based on selective cultivation on TSCF agar at 44 ± 1 °C for 21 ± 3 h and subsequent colony identification by acid phosphatase reaction. The limit of detection was set at 1 CFU/100 mL.

A liquid chromatography-quadrupole time-of-flight mass spectrometry (UPLC-QqTOF-MS) system was used for targeted and non-targeted analysis (pharmaceuticals and TPs). The LC separation was achieved using an ACQUITY I-Class UPLC system (Waters Corporation, Milford, MA, USA) coupled with an ACQUITY BEH C18 (100 mm × 2.1 mm, 1.7 µm) column, according to Martínez-Alcalá et al., 2017 [83]. The LC system was connected to a Bruker Daltonics, maXis q-TOF mass spectrometer equipped with an electrospray ion source (Bruker Daltonics, Bremen, Germany). The system worked via a TOF-MS survey scan (resolving power ≥ 55,000 FWHM). The targeted and non-targeted substances were



identified and reported from accurate-mass scan data using the software Target Analysis (1.3) and Data Analysis (4.2) from Bruker. For more information, see general information S1. Before injection into the chromatographic system, samples were filtered using a 0.22  $\mu\text{m}$  PTFE filter (Millipore). The detection limit (DL) for the selected compounds was adjusted to 5  $\mu\text{g/L}$  with an associated error for each concentration level < 10%, using matrix calibration curves. An additional sample pre-concentration step was performed in real samples containing pharmaceutical compounds below limits set using solid phase extraction (SPE), allowing for a decrease in the detection limit by two orders of magnitude (detailed SPE procedure is described in general information S2).

For TP analysis, the literature research focused on previously reported TPs under  $\text{O}_3$  wastewater treatments. The suspect list developed contained 104 TPs (see Table S2), and included transformation products of TRZ, TCL, AMX, CBZ, SMX, KTP, NPX, DCF, and ERY, while TPs of other compounds such as ACT, HPL, CHL, or TRZ were excluded since relevant  $\text{O}_3$  TPs were not found in the literature [46–55].

Only chromatographic peaks with an absolute intensity threshold of 1000 counts per second (cps) and an exact mass matching the values reported in the literature were considered tentative candidates. Finally, only candidates with an intensity response 10 times higher than the analyzed blanks [84] and showing score values close to 100% (intrinsic statistical parameter of the chromatographic peak quality indicator system) were considered positive.

### 3.4. Experimental Procedure and Sampling

All experiments were performed in the full-scale system in continuous mode at ambient temperature ( $18.0 \pm 5.0$  °C) and natural wastewater pH ( $7.4 \pm 0.2$ ).

Different percentages of ozone generation, together with flow rate effects on pharmaceutical removal efficiency, were studied to analyze different operating conditions and optimize the proposed system. With this aim, three working flows (i) 2000 L/h; (ii) 1200 L/h and (iii) 500 L/h of inlet treated wastewater, and 5 different percentages of ozone production, adjustable in the ozone generator (i) 0%, corresponding only to the injection of purified atmospheric air; (ii) 25%; (iii) 50%; (iv) 75%; (v) 100% were studied. These production percentages are related to (i) 0.0; (ii) 4.5; (iii) 11.4; (iv) 15.9; (v) 22.8  $\text{gO}_3/\text{h}$  of ozone produced, respectively. To ensure a constant ozone production rate throughout the experiment, all samples were collected 15 min after ozone generator activation and MNBs injection. All optimization experiments were performed using real secondary effluents spiked with 200  $\mu\text{g/L}$  of selected pharmaceuticals. For this, required volumes of a stock solution containing pharmaceutical compounds were added to real wastewater into an external reaction tank connected directly to the system, as pharmaceuticals are commonly found in real wastewater in the  $\text{ng/g}$  range [4]. This initial concentration was chosen as it is sufficiently high to obtain degradation values with available analytical techniques and low enough to simulate real environmental conditions. The experiments were conducted in triplicate to ensure repeatability, and the averaged data are presented below. All samples were collected in 1-L amber glass bottles and taken directly to the laboratory for further analysis (stored at 4 °C in the dark and analyzed within 24 h).

Once the optimization phase was completed, the efficiency of the system was monitored under real-world conditions (real unfortified water) following the same sampling and analysis protocols. Finally, an evaluation of the TPs likely to be generated in the system was carried out, as well as a detailed study of the associated costs.

## 4. Conclusions and Future Perspectives

This work clearly demonstrates the feasibility of implementing  $\text{O}_3$ /MNBS systems as a tertiary treatment in conventional WWTPs for agronomical purposes. After optimization, the workflow of 2000 L/h and ozone production of 15.9  $\text{gO}_3/\text{h}$  showed the best results, with pharmaceutical removal percentages of  $72.46 \pm 7.8\%$  and a significant *E. Coli* reduction between 3-log and 4-log.

The presence of MNBs favored the efficiency of the system, improving the direct (involving O<sub>3</sub> molecules) and indirect (involving free •OH) oxidation mechanisms. However, in low workflows, the direct reaction predominates, while in high workflows, the indirect reaction predominates, due to the reactivity of the MNBs (molecular collision).

As for pharmaceutical removal percentages, three ranges can be considered: removal efficiencies higher than 85.68% (cationic, dipolar ions, and neutral compounds), moderate removal efficiencies, between 57.62% and 77.34% (anionic compounds), and low removal efficiencies of 22.50% (pharmaceuticals that contain mainly choro and fluor groups in their structure). In this sense, knowing the polarity and chemical structure of the pharmaceuticals to be degraded by O<sub>3</sub>/MNBs reactions could be crucial for predicting the removal efficiency of the selected compounds in real systems.

The energy consumption required was also associated with the structure of the pharmaceutical compounds. Therefore, in WWTPs where cationic groups predominate, the costs would be lower as compared to other WWTPs that are more persistent.

The effluents generated in the system showed high agronomic quality, complying with the standards set in the European regulation for wastewater reuse. In addition, quality changes were detected during storage, increasing disinfection after 24–72 h, due to the persistence of the MNBs. This is promising, as proper storage could help not only to improve water quality, but also to reduce costs, as less ozone and therefore less energy may be needed.

Although this work has made a first estimation of the TPs generated in the O<sub>3</sub>/MNBs processes, more knowledge is needed to better assess the risks associated with the implementation of these large-scale systems, as the TPs generated in hydroxy-radical reactions in some cases may be even more toxic than the starting compounds. Finally, despite the promising results found on the implementation of O<sub>3</sub>/MNBs systems on a large scale, the impacts of their use at the agronomic level are still largely unknown, from the point of view of plant growth, effects on fertilizers, etc., so these aspects need to be examined further.

**Supplementary Materials:** The following supporting information can be downloaded at: <https://www.mdpi.com/article/10.3390/catal13010188/s1>, General Information S1: UPLC-QqTOF-MS analysis for water samples; General Information S2: Solid-phase extraction (SPE) protocol; Table S1: Inlet wastewater characterization; Table S2: Suspect list developed under literature research; Table S3: Transformation products detected under experimental conditions.

**Author Contributions:** Conceptualization, methodology, software, validation, formal analysis, investigation, resources and data curation, L.P.-R., A.P.-M. and B.M.-H.; writing—original draft preparation, writing—review and editing, L.P.-R.; visualization, supervision, project administration and funding acquisition, A.J.L.-G., P.A.N.-T., J.J.A.-C. and T.M.-P. All authors have read and agreed to the published version of the manuscript.

**Funding:** The work included in this article was funded by: (i) the strategic project Ris3MUR DIRELMIVID (Total investment: €600,000, EXP: 2120SAE00078), funded by the Consejería de Empresa, Industria y Portavocía, within the framework of the European Regional Development Fund 2014–2020, and (ii) by the strategic project Operational Group Subalma, within the framework of the National Rural Development Program 2014–2020, convened in 2020 by the Spanish Agrarian Guarantee Fund O.A. (FEGA). Total investment €568,758.11 (EAFRD (80%) and by MAPA (20%)). (EXP: O0000226e2000044888).

**Conflicts of Interest:** The authors declare that they have no known competing financial interest or personal relationships that could have appeared to influence the work reported in this paper.

## References

1. Hejna, M.; Kapuścińska, D.; Aksmann, A. Pharmaceuticals in the aquatic environment: A review on eco-toxicology and the remediation potential of algae. *Int. J. Environ. Res. Public Health* **2022**, *19*, 7717. [CrossRef]
2. Aitken, M.; Kleinrock, M.; Munoz, E. *Global Medicine Spending and Usage Trends: Outlook to 2025*; IQVIA Institute for Human Data Science: Parsippany, NJ, USA, 2021.
3. Ayati, N.; Saiyarsarai, P.; Nikfar, S. Short and long-term impacts of COVID-19 on the pharmaceutical sector. *DARU J. Pharm. Sci.* **2020**, *28*, 799–805. [CrossRef]

4. Tran, N.H.; Reinhard, M.; Gin, K.Y.H. Occurrence and fate of emerging contaminants in municipal wastewater treatment plants from different geographical regions—a review. *Water Res.* **2018**, *133*, 182–207. [CrossRef]
5. Lindim, C.; Van Gils, J.; Georgieva, D.; Mekenyan, O.; Cousins, I.T. Evaluation of human pharmaceutical emissions and concentrations in Swedish river basins. *Sci. Total Environ.* **2016**, *572*, 508–519. [CrossRef] [PubMed]
6. Fekadu, S.; Alemayehu, E.; Dewil, R.; Van der Bruggen, B. Pharmaceuticals in freshwater aquatic environments: A comparison of the African and European challenge. *Sci. Total Environ.* **2018**, *654*, 324–337. [CrossRef] [PubMed]
7. Shraim, A.; Diab, A.; Alsuhaime, A.; Niazy, E.; Metwally, M.; Amad, M.; Sioud, S.; Dawoud, A. Analysis of some pharmaceuticals in municipal wastewater of Almadinah Almunawarah. *Arab. J. Chem.* **2017**, *10*, S719–S729. [CrossRef]
8. Kuroda, K.; Li, C.; Dhangar, K.; Kumar, M. Predicted occurrence, ecotoxicological risk and environmentally acquired resistance of antiviral drugs associated with COVID-19 in environmental waters. *Sci. Total Environ.* **2021**, *776*, 145740. [CrossRef]
9. Verlicchi, P.; Al Aukidy, M.; Zambello, E. Occurrence of pharmaceutical compounds in urban wastewater: Removal, mass load and environmental risk after a secondary treatment—A review. *Sci. Total Environ.* **2012**, *429*, 123–155. [CrossRef] [PubMed]
10. European Union. Decision (EU) 2022/1307 of 22 July 2022 establishing a watch list of substances for Union-wide monitoring in the field of water policy pursuant to Directive 2008/105/EC of the European Parliament and of the Council. *Off. J. Eur. Union* **2022**, *197*, 117–120. Available online: <https://eur-lex.europa.eu/legal-content/ES/TXT/?uri=CELEX:32022D1307> (accessed on 16 November 2022).
11. European Union. Decision (EU) 2020/1161 of 4 August 2020 establishing a watch list of substances for Union-wide monitoring in the field of water policy pursuant to Directive 2008/105/EC of the European Parliament and of the Council. *Off. J. Eur. Communities* **2020**, *257*, 32–35. Available online: <https://eur-lex.europa.eu/legal-content/ES/TXT/?uri=CELEX%3A32020D1161> (accessed on 16 November 2022).
12. Gilardoni, A. (Ed.) *The Italian Water Industry: Cases of Excellence. Circular Economy and WWTPs: Water Reuse and Biogas Production Chapter*; Springer: Berlin/Heidelberg, Germany, 2018.
13. Smol, M.; Koneczna, R. Economic Indicators in Water and Wastewater Sector Contributing to a Circular Economy (CE). *Resources* **2021**, *10*, 129. [CrossRef]
14. Carter, L.J.; Chefetz, B.; Abdeen, Z.; Boxall, A.B. Emerging investigator series: Towards a framework for establishing the impacts of pharmaceuticals in wastewater irrigation systems on agro-ecosystems and human health. *Environ. Sci. Process. Impacts* **2019**, *21*, 605–622. [CrossRef]
15. Ponce-Robles, L.; Benelhadj, L.; García-García, A.J.; Pedrero-Salcedo, F.; Nortes-Tortosa, P.A.; Albacete, J.; Alarcón, J.J. Risk assessment for uptake and accumulation of pharmaceuticals by baby leaf lettuce irrigated with reclaimed water under commercial agricultural activities. *J. Environ. Manag.* **2022**, *324*, 116321. [CrossRef]
16. European Union. Regulation (EU) 2020/741 of the European Parliament and of the Council of 25 May 2020 on minimum requirements for water reuse. *Off. J. Eur. Union* **2022**, *177*, 32–55. Available online: <https://eur-lex.europa.eu/legal-content/EN/TXT/PDF/?uri=CELEX:32020R0741&from=EN> (accessed on 17 November 2022).
17. Wang, J.L.; Xu, L.J. Advanced oxidation processes for wastewater treatment: Formation of hydroxyl radical and application. *Crit. Rev. Environ. Sci. Technol.* **2012**, *42*, 251–325. [CrossRef]
18. Maniakova, G.; Salmerón, I.; Aliste, M.; Polo-López, M.I.; Oller, I.; Malato, S.; Rizzo, L. Solar photo-Fenton at circumneutral pH using Fe (III)-EDDS compared to ozonation for tertiary treatment of urban wastewater: Contaminants of emerging concern removal and toxicity assessment. *Chem. Eng. J.* **2022**, *431*, 133474. [CrossRef]
19. Ribeiro, A.R.; Nunes, O.C.; Pereira, M.F.; Silva, A.M. An overview on the advanced oxidation processes applied for the treatment of water pollutants defined in the recently launched Directive 2013/39/EU. *Environ. Int.* **2015**, *75*, 33–51. [CrossRef] [PubMed]
20. Osawa, R.A.; Barrocas, B.T.; Monteiro, O.C.; Oliveira, M.C.; Florencio, M.H. Photocatalytic degradation of amitriptyline, trazodone and venlafaxine using modified cobalt-titanate nanowires under UV-Vis radiation: Transformation products and in silico toxicity. *Chem. Eng. J.* **2019**, *373*, 1338–1347. [CrossRef]
21. Yu, D.; Wang, L.; Yang, T.; Yang, G.; Wang, D.; Ni, H.; Wu, M. Tuning Lewis acidity of iron-based metal-organic frameworks for enhanced catalytic ozonation. *Chem. Eng. J.* **2021**, *404*, 127075. [CrossRef]
22. Hu, Q.; Zhang, M.; Xu, L.; Wang, S.; Yang, T.; Wu, M.; Lu, W.; Li, Y.; Yu, D. Unraveling timescale-dependent Fe-MOFs crystal evolution for catalytic ozonation reactivity modulation. *J. Hazard. Mater.* **2022**, *431*, 128575. [CrossRef]
23. Fan, W.; An, W.G.; Huo, M.X.; Yang, W.; Zhu, S.Y.; Lin, S.S. Solubilization and stabilization for prolonged reactivity of ozone using micro-nano bubbles and ozone-saturated solvent: A promising enhancement for ozonation. *Sep. Purif. Technol.* **2020**, *238*, 116484. [CrossRef]
24. Hu, L.; Xia, Z. Application of ozone micro-nano-bubbles to groundwater remediation. *J. Hazard. Mater.* **2018**, *342*, 446–453. [CrossRef] [PubMed]
25. Takahashi, M.  $\zeta$  potential of microbubbles in aqueous solutions: Electrical properties of the gas—Water interface. *J. Phys. Chem. B* **2005**, *109*, 21858–21864. [CrossRef] [PubMed]
26. Gurung, A.; Dahl, O.; Jansson, K. The fundamental phenomena of nanobubbles and their behavior in wastewater treatment technologies. *Geosyst. Eng.* **2016**, *19*, 133–142. [CrossRef]
27. Nam, G.; Mohamed, M.M.; Jung, J. Enhanced degradation of benzo [a] pyrene and toxicity reduction by microbubble ozonation. *Environ. Technol.* **2021**, *42*, 1853–1860. [CrossRef] [PubMed]

28. Azuma, T.; Otomo, K.; Kunitou, M.; Shimizu, M.; Hosomaru, K.; Mikata, S.; Mino, Y.; Hayashi, T. Removal of pharmaceuticals in water by introduction of ozonated microbubbles. *Sep. Purif. Technol.* **2019**, *212*, 483–489. [CrossRef]
29. Dawood, F.K.; Abdulrazzaq, N.N. Direct Oxidation of Antibiotics from Aqueous Solution by Ozonation with Microbubbles. *J. Phys. Conf. Ser.* **2021**, *1973*, 012157. [CrossRef]
30. Zheng, T.; Zhang, T.; Wang, Q.; Tian, Y.; Shi, Z.; Smale, N.; Xu, B. Advanced treatment of acrylic fiber manufacturing wastewater with a combined microbubble-ozonation/ultraviolet irradiation process. *RSC Adv.* **2015**, *5*, 77601–77609. [CrossRef]
31. Tsuge, H. *Characteristics of microbubbles. Micro- and Nanobubbles Fundamentals and Applications*; Jenny Stanford Publishing: Dubai, United Arab Emirates, 2014; Volume 2, pp. 978–981.
32. Joseph, C.G.; Farm, Y.Y.; Taufiq-Yap, Y.H.; Pang, C.K.; Nga, J.L.; Puma, G.L. Ozonation treatment processes for the remediation of detergent wastewater: A comprehensive review. *J. Environ. Chem. Eng.* **2021**, *9*, 106099. [CrossRef]
33. Kokkoli, A.; Agerholm, N.; Andersen, H.R.; Kaarsholm, K.M. Synergy between ozonation and GAC filtration for chlorinated ethenes-contaminated groundwater treatment. *J. Water Process Eng.* **2021**, *44*, 102356. [CrossRef]
34. Bui, T.T.; Han, M. Decolorization of dark green Rit dye using positively charged nanobubbles technologies. *Sep. Purif. Technol.* **2020**, *233*, 116034. [CrossRef]
35. Hollender, J.; Zimmermann, S.G.; Koepke, S.; Krauss, M.; McArdell, C.S.; Ort, C.; Singer, H.; von Gunten, U.; Siegrist, H. Elimination of organic micropollutants in a municipal wastewater treatment plant upgraded with a full-scale post-ozonation followed by sand filtration. *Environ. Sci. Technol.* **2009**, *43*, 7862–7869. [CrossRef] [PubMed]
36. Antoniou, M.G.; Hey, G.; Vega, S.R.; Spiliotopoulou, A.; Fick, J.; Tysklind, M.; la Cour Jansen, J.; Andersen, H.R. Required ozone doses for removing pharmaceuticals from wastewater effluents. *Sci. Total Environ.* **2013**, *456*, 42–49. [CrossRef] [PubMed]
37. Seridou, P.; Kalogerakis, N. Disinfection applications of ozone micro-and nanobubbles. *Environ. Sci. Nano* **2021**, *8*, 3493–3510. [CrossRef]
38. Gardoni, D.; Vailati, A.; Canziani, R. Decay of ozone in water: A review. *Ozone Sci. Eng.* **2012**, *34*, 233–242. [CrossRef]
39. Rodsong, P.; Tirawanichakul, S.; Tirawanichakul, Y. Disinfection of E. coli and Removal of Pesticide Residues on Fresh Chili by Micro-bubble Plasma Ozonation. *Plasma Phys. Membr. Technol.* **2021**, *9*, 1–16.
40. Sumikura, M.; Hidaka, M.; Murakami, H.; Nobutomo, Y.; Murakami, T. Ozone micro-bubble disinfection method for wastewater reuse system. *Water Sci. Technol.* **2007**, *56*, 53–61. [CrossRef]
41. Beltran, F.J. *Ozone Reaction Kinetics for Water and Wastewater Systems*; CRC Press: Boca Raton, FL, USA, 2003.
42. Lim, S.; Shi, J.L.; von Gunten, U.; McCurry, D.L. Ozonation of organic compounds in water and wastewater: A critical review. *Water Res.* **2022**, *213*, 118053. [CrossRef] [PubMed]
43. Xia, Z.; Hu, L. Treatment of organics contaminated wastewater by ozone micro-nano-bubbles. *Water* **2018**, *11*, 55. [CrossRef]
44. Tang, K.; Spiliotopoulou, A.; Chhetri, R.K.; Ooi, G.T.; Kaarsholm, K.M.; Sundmark, K.; Florian, B.; Kragelund, C.; Bester, K.; Andersen, H.R. Removal of pharmaceuticals, toxicity and natural fluorescence through the ozonation of biologically-treated hospital wastewater, with further polishing via a suspended biofilm. *Chem. Eng. J.* **2019**, *359*, 321–330. [CrossRef]
45. Tay, K.S.; Madehi, N. Ozonation of ofloxacin in water: By-products, degradation pathway and ecotoxicity assessment. *Sci. Total Environ.* **2015**, *520*, 23–31. [CrossRef]
46. Kidak, R.; Doğan, Ş. Medium-high frequency ultrasound and ozone based advanced oxidation for amoxicillin removal in water. *Ultrason. Sonochem.* **2018**, *40*, 131–139. [CrossRef] [PubMed]
47. Luiz, D.B.; Genena, A.K.; Virmond, E.; José, H.J.; Moreira, R.F.; Gebhardt, W.; Schröder, H.F. Identification of degradation products of erythromycin A arising from ozone and advanced oxidation process treatment. *Water Environ. Res.* **2010**, *82*, 797–805. [CrossRef] [PubMed]
48. Feng, L.; Watts, M.J.; Yeh, D.; Esposito, G.; van Hullebusch, E.D. The efficacy of ozone/BAC treatment on non-steroidal anti-inflammatory drug removal from drinking water and surface water. *Ozone Sci. Eng.* **2015**, *37*, 343–356. [CrossRef]
49. Gulde, R.; Rutsch, M.; Clerc, B.; Schollée, J.E.; von Gunten, U.; McArdell, C.S. Formation of transformation products during ozonation of secondary wastewater effluent and their fate in post-treatment: From laboratory-to full-scale. *Water Res.* **2021**, *200*, 117200. [CrossRef]
50. Hübner, U.; Seiwert, B.; Reemtsma, T.; Jekel, M. Ozonation products of carbamazepine and their removal from secondary effluents by soil aquifer treatment—indications from column experiments. *Water Res.* **2014**, *49*, 34–43. [CrossRef]
51. Kråkström, M.; Saeid, S.; Tolvanen, P.; Kumar, N.; Salmi, T.; Kronberg, L.; Eklund, P. Ozonation of carbamazepine and its main transformation products: Product determination and reaction mechanisms. *Environ. Sci. Pollut. Res.* **2020**, *27*, 23258–23269. [CrossRef] [PubMed]
52. Sein, M.M.; Zedda, M.; Tuerk, J.; Schmidt, T.C.; Golloch, A.; Von Sonntag, C. Oxidation of diclofenac with ozone in aqueous solution. *Environ. Sci. Technol.* **2008**, *42*, 6656–6662. [CrossRef] [PubMed]
53. Alharbi, S.K.; Ansari, A.J.; Nghiem, L.D.; Price, W.E. New transformation products from ozonation and photolysis of diclofenac in the aqueous phase. *Process Saf. Environ. Prot.* **2022**, *157*, 106–114. [CrossRef]
54. Rodayan, A.; Roy, R.; Yargeau, V. Oxidation products of sulfamethoxazole in ozonated secondary effluent. *J. Hazard. Mater.* **2010**, *177*, 237–243. [CrossRef]
55. Khan, M.H.; Bae, H.; Jung, J.Y. Tetracycline degradation by ozonation in the aqueous phase: Proposed degradation intermediates and pathway. *J. Hazard. Mater.* **2010**, *181*, 659–665. [CrossRef]
56. Andreozzi, R.; Marotta, R.; Pinto, G.; Pollio, A. Carbamazepine in water: Persistence in the environment, ozonation treatment and preliminary assessment on algal toxicity. *Water Res.* **2002**, *36*, 2869–2877. [CrossRef] [PubMed]





57. Gebhardt, W.; Schröder, H.F. Liquid chromatography–(tandem) mass spectrometry for the follow-up of the elimination of persistent pharmaceuticals during wastewater treatment applying biological wastewater treatment and advanced oxidation. *J. Chromatogr. A* **2007**, *1160*, 34–43. [CrossRef] [PubMed]
58. BOE 2007 Royal Decree 1620/2007, 294, 50639–50661. Available online: <https://www.boe.es/buscar/doc.php?id=BOE-A-2007-21092> (accessed on 30 November 2022).
59. Furuichi, A.; Arakawa, S.; Mano, Y.; Morita, I.; Tachikawa, N.; Yamada, Y.; Kasugai, S. Comparative analysis of efficacy of ozone nano bubble water (NBW3) with established antimicrobials. Bactericidal efficacy and cellular response. An in vitro study. *J. Oral Tissue Eng.* **2013**, *10*, 131–141.
60. Cruz, R.; Flores, J.V. Reduction of coliforms presents in domestic residual waters by air-ozone micro-nanobubbles in Carhuaz city, Perú. *J. Nanotechnol.* **2017**, *1*, 9–17. [CrossRef]
61. Vivar, M.; Fuentes, M.; Torres, J.; Rodrigo, M.J. Solar disinfection as a direct tertiary treatment of a wastewater plant using a photochemical-photovoltaic hybrid system. *J. Water Process Eng.* **2021**, *42*, 102196. [CrossRef]
62. Rojas-Valencia, M.N. Research on ozone application as disinfectant and action mechanisms on wastewater microorganisms. *Virus* **2011**, *3*, 4.
63. Ternes, T.A.; Stüber, J.; Herrmann, N.; McDowell, D.; Ried, A.; Kampmann, M.; Teiser, B. Ozonation: A tool for removal of pharmaceuticals, contrast media and musk fragrances from wastewater? *Water Res.* **2003**, *37*, 1976–1982. [CrossRef] [PubMed]
64. Chuajedton, A.; Uthaibutra, J.; Pengphol, S.; Whangchai, K. Inactivation of Escherichia coli O157: H7 by treatment with different temperatures of micro-bubbles ozone containing water. *Int. Food Res. J.* **2017**, *24*, 1006–1010.
65. Chuajedton, A.; Aoyagi, H.; Uthaibutra, J.; Whangchai, K. Effect of Micro-bubbles Ozone for Inactivation of Escherichia coli O157: H7 on Fresh-cut Pineapple cv. Phu Lae. *Asian J. Appl. Sci.* **2016**, *4*, 1.
66. Seki, M.; Ishikawa, T.; Terada, H.; Nashimoto, M. Microbicidal effects of stored aqueous ozone solution generated by nano-bubble technology. *Vivo* **2017**, *31*, 579–583.
67. Mehrjouei, M.; Müller, S.; Möller, D. Catalytic and photocatalytic ozonation of tert-butyl alcohol in water by means of falling film reactor: Kinetic and cost–effectiveness study. *Chem. Eng. J.* **2014**, *248*, 184–190. [CrossRef]
68. Bolton, J.R.; Bircher, K.G.; Tumas, W.; Tolman, C.A. Figures-of-merit for the technical development and application of advanced oxidation technologies for both electric-and solar-driven systems (IUPAC Technical Report). *Pure Appl. Chem.* **2001**, *73*, 627–637. [CrossRef]
69. Liu, Z.; Demeestere, K.; Van Hulle, S. Comparison and performance assessment of ozone-based AOPs in view of trace organic contaminants abatement in water and wastewater: A review. *J. Environ. Chem. Eng.* **2021**, *9*, 105599. [CrossRef]
70. Daneshvar, N.; Aleboyyeh, A.; Khataee, A.R. The evaluation of electrical energy per order (EEo) for photooxidative decolorization of four textile dye solutions by the kinetic model. *Chemosphere* **2005**, *59*, 761–767. [CrossRef]
71. Miklos, D.B.; Remy, C.; Jekel, M.; Linden, K.G.; Drewes, J.E.; Hübner, U. Evaluation of advanced oxidation processes for water and wastewater treatment—A critical review. *Water Res.* **2018**, *139*, 118–131. [CrossRef]
72. Priyadarshini, M.; Das, I.; Ghangrekar, M.M.; Blaney, L. Advanced oxidation processes: Performance, advantages, and scale-up of emerging technologies. *J. Environ. Manag.* **2022**, *316*, 115295. [CrossRef]
73. Ponce-Robles, L.; Masdemont-Hernández, B.; Munuera-Pérez, T.; Pagán-Muñoz, A.; Lara-Guillén, A.J.; García-García, A.J.; Pedrero-Salcedo, F.; Nortes-Tortosa, P.A.; Alarcón-Cabañero, J.J. WWTP effluent quality improvement for agricultural reuse using an autonomous prototype. *Water* **2020**, *12*, 2240. [CrossRef]
74. Race, M.; Ferraro, A.; Galdiero, E.; Guida, M.; Núñez-Delgado, A.; Pirozzi, F.; Siciliano, A.; Fabbicino, M. Current emerging SARS-CoV-2 pandemic: Potential direct/indirect negative impacts of virus persistence and related therapeutic drugs on the aquatic compartments. *Environ. Res.* **2020**, *188*, 109808. [CrossRef]
75. Stingl, J.C. Antidepressant drug treatment protecting from COVID-19: One more piece in the repurposing puzzle. *BJPsych Open* **2022**, *8*, e20. [CrossRef]
76. Resolution of 19 June 2020, of the Spanish Agency for Medicines and Medical Devices, Establishing the List of Medicines Considered Essential in the Management of the Health Crisis Caused by COVID-19, Pursuant to Article 19.1 of Royal Decree-Law 21/2020 of 9 June, on Urgent Prevention, Containment and Coordination Measures to Address the Health Crisis Caused by COVID-19. Available online: <https://www.boe.es/boe/dias/2020/06/20/pdfs/BOE-A-2020-6474.pdf> (accessed on 17 November 2022).
77. PubChem, National Library of Medicine. Available online: <https://pubchem.ncbi.nlm.nih.gov/> (accessed on 17 November 2022).
78. Network of Reference Laboratories, Research Centres and Related Organisations for Monitoring of Emerging Environmental Substances. Available online: <https://www.norman-network.net> (accessed on 17 November 2022).
79. Baird, R.B.; Eaton, A.D.; Clesceri, L.S. *Standard Methods for the Examination of Water and Wastewater*; Rice, E.W., Ed.; American Public Health Association: Washington, DC, USA, 2012; Volume 10.
80. Wef, A.A. *Standard Methods for the Examination of Water and Wastewater*, 18th ed.; American Public Health Association: Washington, DC, USA, 1992.
81. *ISO 9308-1: 2014*; International Standards Organisation 9308-1-Water Quality-Determination and Counting of Escherichia Coli and Coliform Bacteria-Part 1: Membrane Filtration Method for Low Bacterial Ground Water. Turkish Standards Institute: Ankara, Turkey, 2014.

82. ISO 14189; Water Quality—Enumeration of Clostridium Perfringens—Method Using Membrane Filtration. International Standards Organisation (ISO): Geneva, Switzerland, 2013.
83. Martínez-Alcalá, I.; Guillén-Navarro, J.M.; Fernández-López, C. Pharmaceutical biological degradation, sorption and mass balance determination in a conventional activated-sludge wastewater treatment plant from Murcia, Spain. *Chem. Eng. J.* **2017**, *316*, 332–340. [CrossRef]
84. Cantwell, H. *Blanks in Method Validation—Supplement to Eurachem Guide the Fitness for Purpose of Analytical Methods*; Eurachem: Middlesex, UK, 2019.

**Disclaimer/Publisher’s Note:** The statements, opinions and data contained in all publications are solely those of the individual author(s) and contributor(s) and not of MDPI and/or the editor(s). MDPI and/or the editor(s) disclaim responsibility for any injury to people or property resulting from any ideas, methods, instructions or products referred to in the content.

## Article

# Photocatalytic Removal of Thiamethoxam and Flonicamid Pesticides Present in Agro-Industrial Water Effluents

Michalis K. Arfanis <sup>1</sup>, George V. Theodorakopoulos <sup>1,2</sup>, Christos Anagnostopoulos <sup>3</sup>, Irene Georgaki <sup>3</sup>, Evangelos Karanasios <sup>3</sup>, George Em. Romanos <sup>1</sup>, Emilia Markellou <sup>3</sup> and Polycarpos Falaras <sup>1,\*</sup>

<sup>1</sup> Institute of Nanoscience and Nanotechnology, National Center of Scientific Research “Demokritos”, Agia Paraskevi, 15310 Athens, Greece

<sup>2</sup> Inorganic and Analytical Chemistry Laboratory, School of Chemical Engineering, National Technical University of Athens, Zografou Campus, 9 Iroon Polytechniou Str., Zografou, 15772 Athens, Greece

<sup>3</sup> Benaki Phytopathological Institute, 8 St. Delta Str., 14561 Kifissia, Greece

\* Correspondence: p.falaras@inn.demokritos.gr; Tel.: +30-2106503644

**Abstract:** Pesticide residues, when present in agricultural wastewater, constitute a potential risk for the environment and human health. Hence, focused actions for their abatement are of high priority for both the industrial sectors and national authorities. This work evaluates the effectiveness of the photocatalytic process to decompose two frequently detected pesticides in the water effluents of the fruit industry: thiamethoxam—a neonicotinoid compound and flonicamid—a pyridine derivative. Their photocatalytic degradation and mineralization were evaluated in a lab-scale photocatalytic batch reactor under UV-A illumination with the commercial photocatalyst Evonik P25 TiO<sub>2</sub> by employing different experimental conditions. The complete degradation of thiamethoxam was achieved after 90 min, when the medium was adjusted to natural or alkaline pH. Flonicamid was proven to be a more recalcitrant substance and the removal efficiency reached ~50% at the same conditions, although the degradation overpassed 75% in the acidic pH medium. Overall, the pesticides’ degradation follows the photocatalytic reduction pathways, where positive charged holes and hydroxyl radicals dominate as reactive species, with complete mineralization taking place after 4 h, regardless of the pH medium. Moreover, it was deduced that the pesticides’ degradation kinetics followed the Langmuir-Hinshelwood (L-H) model, and the apparent rate constant, the initial degradation rate, as well as the L-H model parameters, were determined for both pesticides.

**Keywords:** thiamethoxam; flonicamid; insecticides; photocatalytic degradation; titanium dioxide; scavengers; solution pH

**Citation:** Arfanis, M.K.; Theodorakopoulos, G.V.; Anagnostopoulos, C.; Georgaki, I.; Karanasios, E.; Romanos, G.E.; Markellou, E.; Falaras, P. Photocatalytic Removal of Thiamethoxam and Flonicamid Pesticides Present in Agro-Industrial Water Effluents. *Catalysts* **2023**, *13*, 516. <https://doi.org/10.3390/catal13030516>

Academic Editors: Juan José Rueda-Márquez, Javier Moreno-Andrés and Irina Levchuk

Received: 3 February 2023  
Revised: 28 February 2023  
Accepted: 1 March 2023  
Published: 3 March 2023



**Copyright:** © 2023 by the authors. Licensee MDPI, Basel, Switzerland. This article is an open access article distributed under the terms and conditions of the Creative Commons Attribution (CC BY) license (<https://creativecommons.org/licenses/by/4.0/>).

## 1. Introduction

At present, agricultural industry activities encompass the utilization of a plethora of pesticides, such as fungicides, herbicides and insecticides. Even if the pesticide usage improves the quality, and augments the productivity of, cereals, top fruits and vegetables, it also induces potentially harmful effects for the aquatic environment and human health [1]. Certain pesticides are recalcitrant organic molecules, non-biodegradable and resistant in removal by means of conventional wastewater treatment methods, eventually accumulating in soil and groundwater. Regarding the European legislations and watchlists [2,3], the impact and the hazards of the pesticides on environment and human health are constantly monitored and the database of the permitted pesticides is frequently updated.

As an example of a commonly detected substance in groundwater, thiamethoxam (TMX) an insecticide based on the natural toxin of neonicotinoid and was considered to be an environmentally benign compound when it was first introduced in crop protection [4]. This insecticide helps to deactivate the nervous system of several pests, such as whiteflies, aphids and micro-lepidoptera, thus protecting a wide range of crops, such as top fruits, vegetables, legumes, potatoes, barley, cotton and sunflowers [5,6]. However, TMX, as a

highly soluble and recalcitrant molecule, may gradually accumulate in aquatic environments and soil [7]. More recently, many countries have begun to face problems with bee populations due to TMX usage, implying its direct negative impact on the environment and food chain [4,8]. Toxicity examination revealed that TMX and its intermediates produced during disinfection processes could harm algae and bacteria [9]. At present, TMX is non-approved in the European Union (EU) [2], while the Environmental Protection Agency (EPA) of the United States of America (USA) frequently reconsiders the ecological risk assessments and regulations for crops in consecutive publishable guidance, entitled “Thiamethoxam; Pesticide Tolerance”.

On the other hand, many alternative and efficient pesticides with lower toxicity towards mammals, birds and fishes have been developed for agricultural use. For example, flonicamid (FND), a biodegradable pyridine carboxamide compound, is used in wheat, potatoes and citrus, acting against aphids, whiteflies and sucking insects through the inhibition of pests’ feeding activity, without raising serious ecological and health concerns [10,11]. However, even if there is no unacceptable risk for humans, FND can be present in surface and groundwater, tea leaves and their extractions, or be poisonous for beneficial insects via contaminated honeydew [12–14]. The continuous discharge of FND in the environment could create potential risks for the agro-products consumption in the future; therefore, appropriate methods for detecting FND in human serum and urine in low quantities ( $\sim$ ng/L) have been already established [15,16].

Depending on the stability of pesticide residues, chemical substances remaining in the soil may reach the surface or groundwater. Although the EU has a strict regulatory framework for the authorization and waste management of pesticide residues, the development of novel removal techniques is essential as implementation tools. Conventional wastewater treatment methods, involving adsorption [17], chemical coagulation [18], membrane filtration [19], ion exchange resins [20] or other chemical systems [21], are costly and inefficient for their abatement [22]. Among the proposed solutions, advanced oxidation technologies (AOPs) based on heterogeneous photocatalysis with titania ( $\text{TiO}_2$ ) are very promising treatment methods [23]. Titania is a non-toxic, low-cost and earth-abundant semiconductor, endowed with the capacity to treat water contaminated with pollutants by forming highly reactive and non-selective radical species under UV-A illumination [24,25]. Titania is a well-studied photocatalyst, which has been established as an appropriate candidate to be incorporated into pilot wastewater treatment plants of municipal, industrial or agro-industrial influents, aiming to eliminate a variety of organic pollutants, including pesticides, antibiotics, etc. [26–28].

In this work, the photocatalytic degradation of TMX and FND insecticides was investigated in order to evaluate the ability of titania, under a variety of experimental conditions, to decline these highly water-soluble pesticides and to avoid their leaching to the environment. To the best of our knowledge, this is the first time that such an extensive analysis on the photocatalytic performance of  $\text{TiO}_2$  against TMX and FND has been implemented alongside an elaboration of the effects of pesticide dosage, solution pH and quenchers present during the photocatalytic process. The obtained results on these water contaminants are currently employed in the development and optimization of an innovative hybrid photocatalytic nanofiltration reactor prototype unit (PNFR), with the capability to recycle  $15 \text{ m}^3$ /day of real agro-wastewater [29].

## 2. Results

### 2.1. Photocatalytic Degradation and Reaction Kinetics of Pesticides

To begin, the kinetics of pesticides adsorption and photolysis were determined. In the absence of UV-A light (dark conditions), both the TMX and FND presented negligible adsorption onto the catalyst, even after 90 min. Considering these preliminary results, it was concluded that even 30 min of stirring under dark conditions was sufficient to reach an adsorption/desorption equilibrium. Subsequently, the molecules’ photostability was also corroborated under UV-A illumination for a period of 90 min and it was found that



the pesticides' concentrations did not alter significantly in the absence of photocatalyst P25 (UV photolysis). In summary, the adsorption and photolysis effects should be considered as negligible during the photocatalytic processes; thus, no interferences with the interpretations of the photocatalysis results were expected.

The effect of the initial concentration on the photocatalytic performance of the commercial P25 for both pesticides was studied and the order of the photocatalytic degradation reaction was determined from experimental tests at concentrations of 1, 5, 10 and 20 ppm. Hence, the photocatalytic degradation kinetics of the polar and water soluble TMX and FND were examined, and the relevant results are presented in Figure 1. It has often been noticed that the rate of the heterogeneous photocatalytic degradation of dyes and pesticides follows the Langmuir-Hinshelwood (L-H) model [30], as described in detail in the supplementary information (SI). In brief, the calculated parameters derived from the L-H model are: the apparent rate constant ( $k_{app}$ ,  $\text{min}^{-1}$ ), the initial degradation rate ( $r_{r,0}$ ,  $\text{mg}\cdot\text{L}^{-1}\cdot\text{min}^{-1}$ ), the reaction rate constant ( $k_r$ ,  $\text{mg}\cdot\text{L}^{-1}\cdot\text{min}^{-1}$ ) and the adsorption constant of the reactant ( $K_{LH}$ ,  $\text{L}\cdot\text{mg}^{-1}$ ).

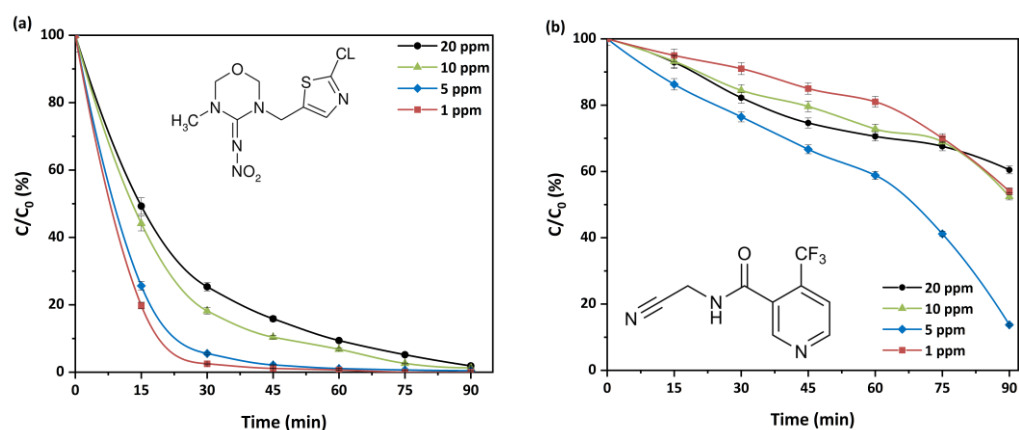


**Figure 1.** Degradation kinetics of photocatalytic degradation of (a) thiamethoxam (TMX) and (b) flonicamid (FND) using titania P25 at the studied concentrations (UV-A irradiation, 0.1 g/L  $\text{TiO}_2$ , natural pH, 25 °C).

A plot of the  $\ln(C_0/C)$  versus time for the examined initial concentrations is displayed in Figure S1a,b and the linear regression slope is equal to the  $k_{app}$  rate constant. The  $k_{app}$  and  $r_{r,0}$  values corresponding to these initial concentrations are summarized in Table 1 for both pesticides. As observed in Figure S1c, for both pesticides, the initial degradation rate increases with the increasing initial concentration, even at highly concentrated solutions, proving the excellent photocatalytic efficiency of the photocatalyst without having any sign of a saturated and finite performance.

**Table 1.** Apparent pseudo first-order rate constants and initial reaction rates calculated for the different initial concentrations of TMX and FND. The presented half-life reaction times for both pesticides have been calculated at the examined initial concentrations.

Thiamethoxam					Flonicamid			
$C_0$ ( $\text{mg}\cdot\text{L}^{-1}$ )	$K_{app}$ ( $\text{min}^{-1}$ )	$r_{r,0}$ ( $\text{mg}\cdot\text{L}^{-1}\cdot\text{min}^{-1}$ )	$t_{1/2}$ (min)	$t_{1/2}'$ (min)	$K_{app}$ ( $\text{min}^{-1}$ )	$r_{r,0}$ ( $\text{mg}\cdot\text{L}^{-1}\cdot\text{min}^{-1}$ )	$t_{1/2}$ (min)	$t_{1/2}'$ (min)
1.0	0.0998	0.091	6.81	6.95	0.0035	0.004	217.46	198.61
5.0	0.0848	0.397	8.56	8.17	0.0089	0.046	252.21	77.53
10.0	0.0479	0.368	11.10	14.48	0.0052	0.054	295.64	132.03
20.0	0.0399	0.849	16.47	17.38	0.0061	0.120	379.89	114.00

The  $k_r$  and  $K_{LH}$  values for TMX, calculated from the slope and intercept of the linear regression, were  $1.0504\text{ mg}\cdot\text{L}^{-1}\cdot\text{min}^{-1}$  and  $0.1042\text{ L}\cdot\text{mg}^{-1}$ , respectively, with a coefficient of

determination of  $R^2 = 0.992$ . As the initial adsorption rates of TMX in the dark could not be calculated from the experimental data due to the negligible adsorption, it can be concluded that the initial TMX photodegradation rates are much faster than the adsorption rates under dark conditions. In this context, the experimental results with TMX could only be reconciled with the Langmuir-Hinshelwood model by assuming light-induced changes of the photocatalyst surface, which may have a significant effect on the adsorption of the probe molecule. Similarly, the  $k_r$  and  $K_{LH}$  of FND were calculated to be  $0.0576 \text{ mg}\cdot\text{L}^{-1}\cdot\text{min}^{-1}$  and  $0.0577 \text{ L}\cdot\text{mg}^{-1}$ , respectively, with a coefficient of determination of  $R^2 = 0.99$ , using the parameters in Table 1, which are in accordance with first-order kinetics. In the case of the TMX, the rate constant was presented to be 18 times higher than that of the FND, verifying the more recalcitrant nature of the FND pesticide. Moreover, the titania photocatalyst showed a higher tendency of adsorbing the TMX more strongly compared to the FND, as the  $K_{LH}$  was almost double ( $0.1042$  and  $0.0577 \text{ L}\cdot\text{mg}^{-1}$ , respectively). Finally, the similar trend for the  $K_{LH}$  of the FND with the respective to the TMX concludes that the assumption of light-induced changes on the surface properties of the photocatalyst is valid and that this asset has a significant effect on the adsorption of the pesticide molecule during irradiation.

As observed in Figure 1a,b, the data points of all the experimental runs for both pesticides were well fitted, employing an exponential decay model for the TMX, although for the FND, a more linear decay was observed. In addition, the neonicotinoid TMX presented high photodegradation rates, reaching complete removal after 60 min for the diluted solutions (1 and 5 ppm) and 90 min for the more concentrated ones, with no toxic by-product residuals in the solution. As expected, the FND was more resistant to photocatalysis, reaching removal efficiencies  $\sim 48\%$  after the photocatalytic experiments, with the exception of the concentration of 5 ppm [31].

Furthermore, the half-life time of the reaction was calculated for the reaction rate of a pseudo-first order kinetics approximation, as it a valuable parameter in order to estimate the reaction rate [32]. In particular, at the half-life time  $t_{1/2}$  of the reaction, where the concentration is half of the initial ( $C = 0.5\cdot C_0$ ), this time is calculated by the following equation:

$$t_{1/2} = 0.5\cdot C_0/k_r + \ln 2/k_r\cdot K_{LH} \quad (1)$$

In addition, for reactions exhibiting pseudo first-order kinetics, the half-life time based on the  $k_{app}$  can be derived from the following equation:

$$t_{1/2}' = \ln 2/k_{app} \quad (2)$$

When Equation (1) is true, the estimated values of the half-life time for different initial concentrations would be the same as those obtained from the observation (Equation (2)) [33]. The values of  $t_{1/2}$  and  $t_{1/2}'$  are summarized in Table 1, including the results obtained for both of the studied pesticides. As observed in this table, the half time of the TMX is much shorter compared to the corresponding values of the FND, implying that the TMX degradation has a faster rate. In addition, the evaluation of these values presented a difference between  $t_{1/2}$  and  $t_{1/2}'$ , which became significant with a rise in the initial pollutant concentration. This trend, which was smoother in the case of the TMX solution, could be elucidated by the intermediates' formation [32,33], which could be adsorbed competitively on the photocatalyst, leading to the retardation of the kinetics. Hence, this effect becomes more prominent as the initial concentration of the pesticides increases, causing the generation of more intermediates, which in turn leads to the decline in the pesticides' degradation. Overall, the L-H model satisfactorily approves the TMX degradation, while the model cannot respond accurately to the degradation of the recalcitrant FND pesticide, especially in higher concentrations.

Figure 2 shows the photocatalytic degradation percentage and total organic carbon concentration (TOC) removal for the TMX (10 ppm) and FND (10 ppm) pollutants, following the UV-A irradiation of aqueous solutions for 90 min, in the presence of titania P25. Thus, the degree of their mineralization was determined, and the effectiveness of

the photocatalytic process was comparatively evaluated. It can be seen that after 90 min under UV-A irradiation, the carbon content percentage drops to 76% and 53.5% for the TMX and FND, respectively. This means that 24% of the TMX was mineralized after 90 min irradiation time, although the degradation for TMX was almost complete, probably due to the presence of intermediate organic products. Thus, the observed delay in the mineralization process with respect to the corresponding photocatalytic degradation degree is expected, as the recalcitrant parent compounds should be first converted to intermediate fragments, which undergo a progressive transformation leading to CO<sub>2</sub> and inorganic species as final products, until the complete removal of the organic load after ~4.5 h (Figure S2). Moreover, the degradation of the FND parent closely follows its direct mineralization in contrast to the TMX parent, while for both pesticides, mineralization presents a linear dependence with time (Figure S2). However, despite the presence of organic matter in the photocatalytically treated pesticide solutions indicated by the TOC analysis, no toxic by-products were detected, with the exception of traces (<0.0004 ppm) of clothianidin and 4-(Trifluoromethyl)nicotinoyl glycine degradation products of the TMX and FND, respectively [10,34]. Even if the analytical examination by HPLC-MS was limited only to expected toxic by-products of FND and TMX, these results clearly demonstrate the ability of the TiO<sub>2</sub> photocatalyst to degrade hazardous contaminants and its potential use in wastewater purification technologies.

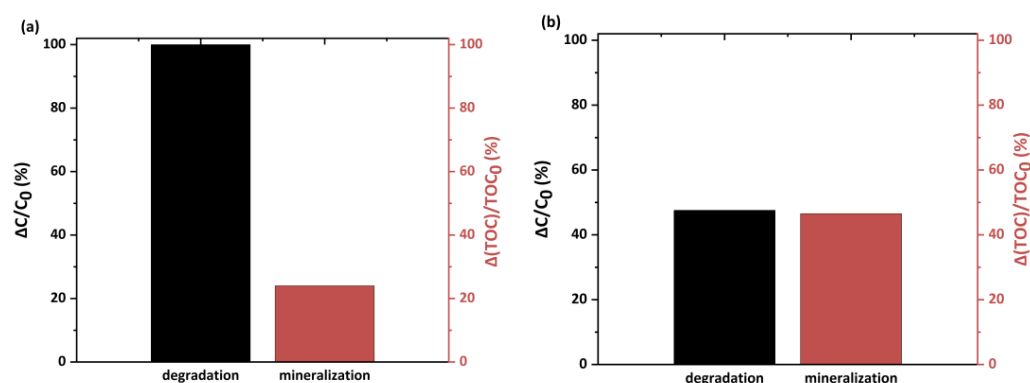


**Figure 2.** Photocatalytic degradation and TOC removal of TMX (a) and FND (b) using titania P25 (UV-A irradiation for 90 min, 10 ppm pesticides concentration, 0.1 g/L TiO<sub>2</sub>, natural pH, 25 °C).

## 2.2. Effect of Solution pH

As the pH of real water varies relatively to the climate conditions and the type of effluents, the affinity between the organic molecules and the surface of the photocatalyst is highly correlated with the pH of the water matrix. In this work, we have considered that it is extremely important to conduct a thorough investigation of the effect of the pH on the photodegradation kinetics of TMX and FND. Regarding the catalyst, TiO<sub>2</sub> is a chemically stable semiconductor exhibiting a point of zero charge close to 6.2, meaning that it can be positively charged below pH = 6.2, or negatively above this value [35]. On the contrary, the pesticides could only be charged negatively if polarization occurs, while there are some studies reporting that the half-life of TMX is reduced in a strong alkaline environment [7,36]. The experiments were performed at a concentration of 10 ppm for both pesticides, whereas the pH was selectively adjusted by the addition of HCl (0.1 M) and NaOH (0.1 M). It should be noted that the choice of 10 ppm allows for the tracking and examination of the degradation alterations with time, regardless of the kinetics enhancement or hindering with pH adjustment. Moreover, the pH values of the starting TMX and FND solutions were 5 and 7, respectively. Therefore, the respective experiments were performed with no addition of HCl or NaOH.

Starting with TMX, the adsorption experiments in the dark showed that there are not any substantial alterations of the TiO<sub>2</sub> adsorption capacity with the pH (Figure 3a). Despite the changes in the TiO<sub>2</sub> surface charge, this behavior was expected, as TMX has

no dissociation constant ( $pK_a$ ) [6]. Indeed, the TMX concentration was the same after the adsorption-desorption equilibrium, independently of the pH value (not shown), denoting that the changes in the photocatalytic degradation rate (with pH) should only be attributed to the variation in the active species concentration in the solution. As shown in Figure 3a, the photodegradation of TMX was similar for the experiments performed at pH = 7 and pH = 5 (the initial pH value of the 10 ppm solution), reaching almost 100% removal after 90 min under UV-A illumination. The reaction kinetics were decreased at pH = 9, although the TMX concentration was eventually zeroed. The increase in the  $OH^-$  concentration in the alkaline solution shifts the reaction equilibria to the products, thus favoring the generation of hydroxyl radicals onto the photocatalyst and promoting a higher photo-quantum yield and protonation level of the excited pesticide molecules, as proposed by Liang et al. [37]. On the other hand, the acidic environment (pH = 3) hampered the removal efficiency significantly, which did not surpass the value of 40%. Yang et al. proposed, as a possible explanation, the protonation of TMX (the contained sulfur and nitrogen atoms can be protonated under these conditions); therefore, coulombic repulsion forces occur among the molecule and the positively charged titania (catalyst's surface), and the photocatalytic activity is reduced [7].

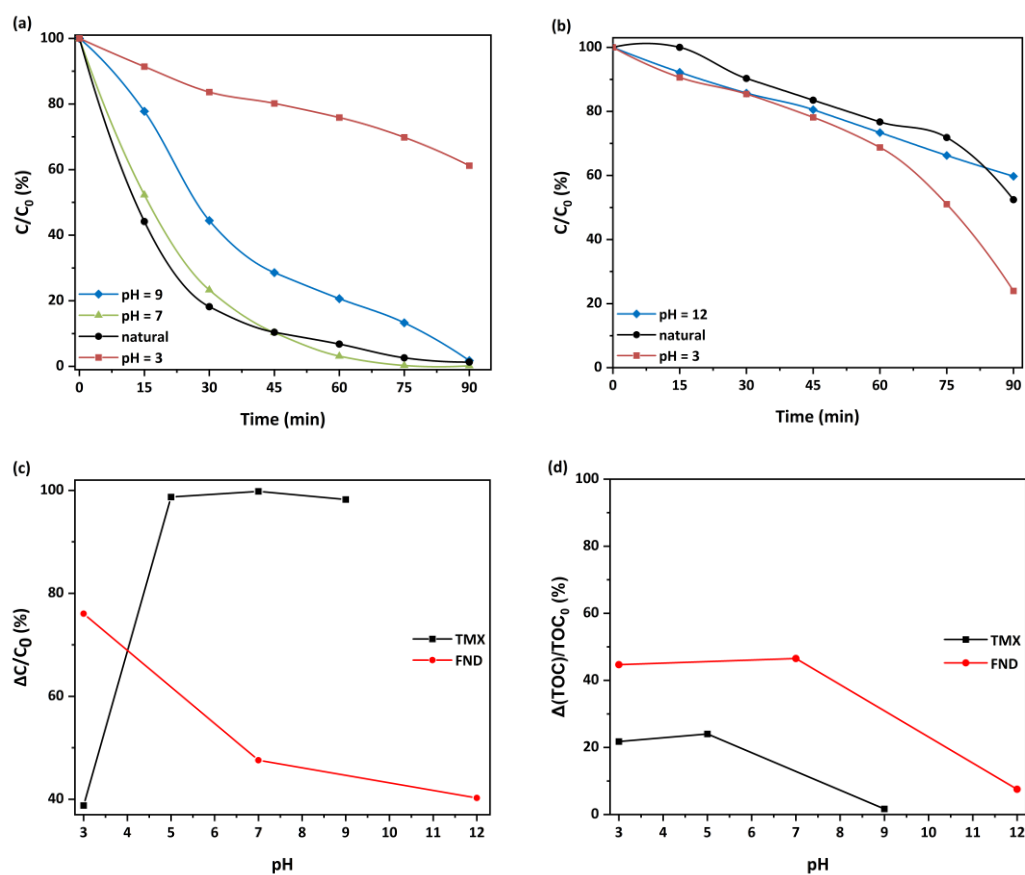


**Figure 3.** Effect of solution pH on the photocatalytic removal of (a) thiamethoxam (TMX) and (b) flonicamid (FND); (c) Comparative representation of medium pH effect on photocatalytic efficiency; and (d) total mineralization for both pesticides after 90 min UV-A irradiation.

Concerning the removal of FND from the solutions of varied pH (Figure 3b), the pesticide  $pK_a$  value is close to 11 [38], so its polarization above that limit could affect the photocatalytic reaction. Nevertheless, when the pH was fixed to 12, the photocatalytic efficiency was not altered significantly compared to the performance of the initial solution (pH = 7). In general, both the FND and titania surface are negatively charged in such a medium, so the electrostatic repulsion forces generated among them are expected to restrict

the photocatalytic process. It is possible that the excess of  $\text{OH}^-$  anions in the solution generated a high number of  $\bullet\text{OH}$  reactive radicals, which compensated the negative effect of electrostatic repulsion and, thus, the photocatalytic effect remained intact. Surprisingly, the acidification of the solution improved the FND degradation, reaching ~80% removal, although the FND molecule was not polarized and the sorption abilities of the positively charged  $\text{TiO}_2$  remained insignificant (not shown). In this context, a possible reason for the achieved enhancement of the photocatalytic activity could be related to the easiest and faster dissociation of water molecules into hydroxyl radicals and the higher oxidation potential of the generated hydroxyl radicals at a lower pH in comparison to that at a higher pH [39].

As a result, the pH control can be considered to be a very important parameter for the pesticides' removal and its effect was clarified in each case (Figure 3c). The natural pH (pH = 5) fits the neonicotinoid pesticide better, whereas the solution acidification decreases the degradation rate. Instead, the FND degradation rate was noticeably improved in the acidic environment (Figure 3c), surpassing the photocatalytic efficiencies in the natural and alkaline media. Nevertheless, it should be also considered that the pH does not only affect the degradation of the target molecules during photocatalysis, but also the photodecomposition of their by-products (Figure 3d). The determination of the TMX and FND mineralization efficiencies in the acidic medium demonstrated that the mineralization was not altered compared to the initial pH at the same time intervals. Regardless of the observed photodegradation rates of the parent pesticides and the competitive phenomena among the initial compound and their by-products, the photogenerated reactive species can still attack and reduce the organic load. In contrast, the solution's pH adjustment to alkaline totally hindered the mineralization of the pesticides; even if the P25 photocatalyst broke up the target molecules to intermediate fragments, these fragments were not degraded further. It is possible that repulsion occurs between the organic substances and titania surface under the applied conditions; therefore, the species' activity might be impeded.

### 2.3. Effect of Additives as Quenchers

In addition to the pH variations, the photocatalytic processes could be either intensified or deteriorated by the presence of other additives in the contaminants' solutions. The addition of inorganic anions increases the removal efficiency of the catalysts if the anions act as oxidation agents, leading to an improved separation of the photogenerated charged carriers and prolonged holes lifetime, or if they are able to generate extra reactive oxidative species in the solution [7]. On the other hand, if the inorganic anions are accumulated on the photocatalysts' surface or if they quench the reactive species, then the  $\text{TiO}_2$  is deactivated, and the efficiency attenuates [7]. When metal ions are added, photocatalysis could be more effective as metals act as an electron sink and/or additional catalyst, although hindering effects cannot be excluded [6]. The insertion of organic additives is more complex for the ROS photoactivity because competitive phenomena occur among the target pollutants and the additives [40].

To better understand the photocatalytic degradation mechanism, radical trap experiments were performed, employing the appropriate additives as quenchers [41], with high affinity in relation to the photocatalytic reactive species, such as isopropanol (IPA), potassium iodide (KI), benzoquinone (BZQ) and potassium bromate ( $\text{KBrO}_3$ ). The obtained results (Figure 4a,c) reveal that both photocatalytic oxidation and reduction pathways can be equally considered as the reaction mechanism of TMX degradation. In particular, the addition of IPA, which is the scavenger consuming hydroxyl radicals, has the most negative effect during the photocatalytic degradation of TMX. On the other hand, KI (potassium iodide) mostly interacts with photogenerated holes, which are the charge carriers responsible for the photo-oxidation of the adsorbed water and the concomitant production of the hydroxyl radicals. It is thus reasonable that KI also has a significant negative impact on the pesticide photodegradation efficiency. Similarly, the photocatalytic degradation of TMX was adversely affected when BZQ was used as a superoxide radical quencher, implying that the superoxide radicals were also participating in the process. In contrast, the use of

KBrO<sub>3</sub> as an electron scavenger led to slightly improved photocatalytic degradation. This tendency has also been observed in the literature by Mir and co-workers [6], who proposed that KBrO<sub>3</sub> enhances the e<sup>-</sup>/h<sup>+</sup> charge carriers' separation by acting as an electron acceptor. In fact, the excess of positive charged holes could now either degrade the TMX directly or generate the necessary hydroxyl radicals, leading to the enhanced photocatalytic oxidation efficiency of TMX under these conditions.

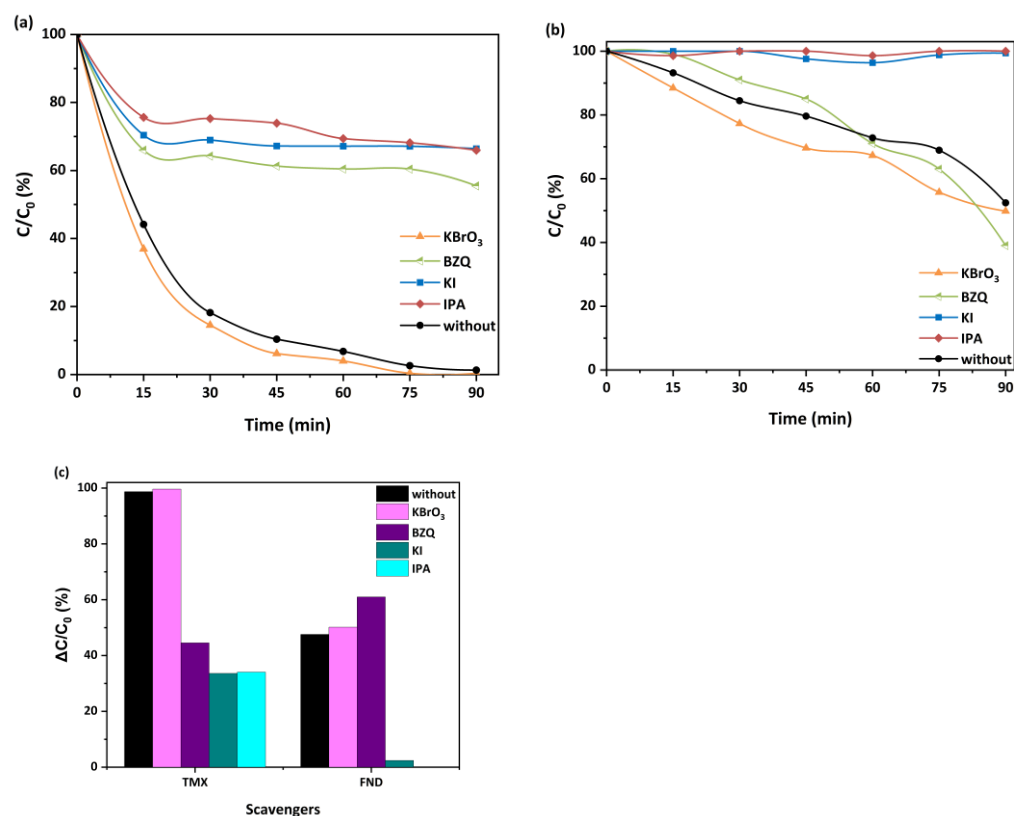


**Figure 4.** Radical trap experiments of (a) thiamethoxam (TMX); and (b) flonicamid (FND) in the presence of appropriate scavengers: IPA for  $\bullet\text{OH}$  quenching, KI for  $\text{h}^+$ , BZQ for  $\text{O}_2^{\bullet-}$  and KBrO<sub>3</sub> for  $\text{e}^-$ ; (c) Scavengers' effect on the photocatalytic degradation performance for both pesticides.

Thereafter, the main degradation mechanism for the FND was also elucidated through trap experiments (Figure 4b,c). The results showed a clear dependence of the pesticide removal under the photocatalytic oxidation pathways, while the trapping of the reductive species increased the photocatalytic efficiency. Specifically, the addition of IPA and KI entirely hindered the photocatalytic processes against the pesticide, clearly demonstrating that the FND degradation could not occur in the absence of hydroxyl radicals and holes, respectively. On the other hand, the removal rate of the FND in the presence KBrO<sub>3</sub> (electron acceptor) was enhanced with time. This observation indicates that the photogenerated electrons, which negatively affected the photocatalytic degradation pathways, were now quenched by the respective scavenger and could not participate in the recombination processes. Thus, the observed FND behavior arises from rather limited electron-hole recombination and the main reactive species are holes and/or hydroxyl radicals, which are both able to oxidize the FND pollutant.

### 3. Discussion

Photocatalytic experiments were also performed in the presence of both pesticides to access the potential of the titania photocatalyst in more realistic conditions. The results of the photocatalytic degradation and carbon removal (TOC) for the mixture (5 ppm of TMX and 5 ppm of FND) after 90 min are shown in Figure 5, and their comparison with

those of Figure 1a,b indicates that the photocatalytic kinetics and removal percentage in the mixture is almost identical to the performance achieved in the single pollutant experiments. Indeed, the excellent photocatalytic efficiency of the titania catalyst toward TMX was preserved. Regarding the FND, the photocatalytic degradation reaction remains relatively slow and proceeds with a significantly low rate, until the acceleration after 60 min, as observed in the aforementioned isolated experiments. Furthermore, the TOC analysis enabled the calculation of the mineralization degree of the pesticide mixture. As such, the mineralization efficiency in the mixture is compared to the average of the mineralization efficiencies achieved in the single solute experiments. In this context, a first observation reveals that the mixture mineralization proceeds at a slower rate compared to the respective degradation rates. In particular, the carbon removal efficiency of the mixture reached up to approximately 31%, which adequately coincides with the theoretical efficiency of 35%, as produced by averaging the efficiencies achieved in the single solute experiments (dashed line in Figure 5).

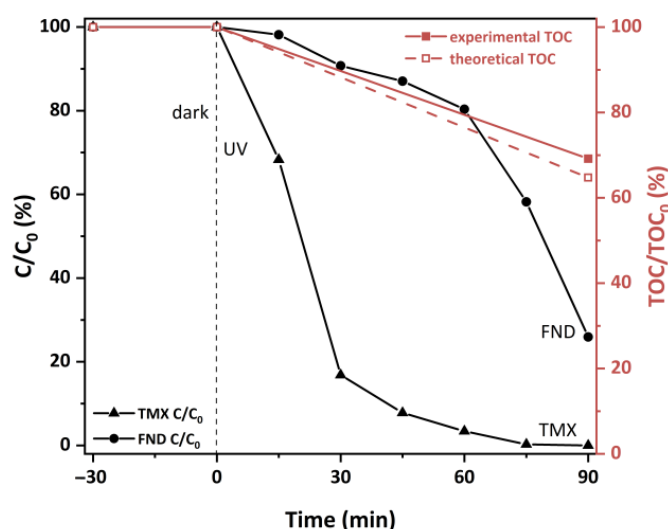


**Figure 5.** Kinetics of photocatalytic degradation and TOC removal of TMX and FND mixture (comparison with theoretical TOC removal of each pesticide individually) using titania P25 (UV-A irradiation, 5 ppm TMX and 5 ppm FND concentrations, 0.1 g/L  $\text{TiO}_2$ , natural pH, 25 °C).

The overall results confirm that the photocatalytic degradation of TMX and FND pesticides with P25 titania is feasible and can be effectively applied, regardless of the experimental conditions. The degradation and mineralization results of the TMX are in accordance with the literature data, where larger amounts of  $\text{TiO}_2$  photocatalyst were used and where the photocatalysis was also combined with other advanced oxidation techniques [4,5,42]. The performance of Degussa P25  $\text{TiO}_2$  was compared with various photocatalysts in the form of slurry or immobilized on substrate from the literature reports and is presented in Table 2. Notably, for almost similar reaction conditions, the photocatalytic efficiency of Degussa P25 (with low light intensity) is approximately of the same level than that reported in the literature. Apparently, the photocatalytic conditions (catalyst loading, pH, light intensity) have a significant impact on the efficiency of a photocatalyst. Among them, light intensity constitutes a decisive factor as it plays a significant role in photocatalytic degradation, determining the number of generated electron-hole pairs. However, the absence of a common roadmap during the investigation of the photocatalytic process makes the comparison between the literature works rather difficult.

**Table 2.** Photocatalytic performance of Degussa P25 TiO<sub>2</sub> photocatalyst against TMX and FND compared to other photocatalysts reported in literature.

Photocatalyst	Catalyst Amount (g/L)	Pesticide/Concentration (ppm)	Light Intensity (mW/cm <sup>2</sup> )	Removal Efficiency (%)	Reference
CuO	1	FND/75 ppm (pH = 2)	High-pressure mercury UVA lamp (125 W), n/a	52.73% (COD), 2 h	[11]
ZnO	0.75	FND/75 ppm (pH = 2)	High-pressure mercury UVA lamp (125 W), n/a	60.58% (COD), 2 h	[11]
ZnO	2	TMX/~110 ppm (natural pH)	1.75	77%, 2 h	[22]
TiO <sub>2</sub> onto glass slides	0.24 (~10 mg on each slide)	TMX/100 ppm (pH n/a)	42	90.1%, 2 h	[4]
ZnO	0.2	TMX/0.1 ppm (pH = 7.1)	8.5	97%, 2 h	[43]
g-C <sub>3</sub> N <sub>4</sub> -TiO <sub>2</sub> @LMPET	4.3 (130 mg PET fiber mat)	TMX/5.8 ppm (pH = 1)	Q-sun Xe-1 test chamber (solar irradiation), n/a	>97%, 3 h	[44]
TiO <sub>2</sub>	0.1	TMX/10 ppm (natural pH)	0.5	~99%, 1.5 h	This work
TiO <sub>2</sub>	0.1	FND/10 ppm (natural pH)	0.5	~48%, 1.5 h	This work

In the case of FND, this is the first instance of a full examination, whereas the available studies to date mainly confirm the molecule's recalcitrant nature with COD techniques [11,27,45]. In summary, the reported photocatalytic results of the pesticides removal (both isolated and mixture) are very promising, rendering TiO<sub>2</sub> materials as excellent candidates for scale-up applications, targeting their integration in existing wastewater treatment units. In this context, dynamic experiments under continuous flow in lab-scale are in progress in order to prove their applicability in an upscaled hybrid photocatalytic nanofiltration membrane reactor (PNFR) and their feasibility for agricultural wastewater purification processes in the fruit industrial sector [46,47].

#### 4. Materials and Methods

The commercial titania Evonik Aeroxide P25 was selected as the model photocatalyst for the photocatalytic removal of pesticides from the water matrix. The experiments were carried out in open vessel glass vials in batch-mode, using 10 mL of aqueous solutions of thiamethoxam (TMX, analytical standard, Sigma-Aldrich, St. Louis, MO, USA) or flonicamid (FND, analytical standard, Sigma-Aldrich, St. Louis, MO, USA). Depending on the experiment, the pesticide concentration varied between 1 and 20 ppm, while 1 mg of P25 (0.1 g/L) was suspended in the aforementioned solutions. In brief, the photodegradation process of the pesticides with P25 was accomplished under UV-A irradiation, inside a lab-made photoreactor. The pesticide concentration and total organic carbon (TOC, BioTector B3500, Hach, Loveland, CO, USA) were calculated using analytical methods (LC-MS/MS, Varian model 1200 L, Agilent Technologies, Foster City, CA, USA) and a TOC analyzer, respectively, and then the respective photocatalytic and mineralization efficiencies were estimated. The effect of the solution's pH was evaluated, and trap experiments through the addition of the appropriate additives were also conducted to expose the photocatalytic degradation mechanism. The photocatalytic experimental procedures concerning the effect of the additives [25,41] and solution's pH, as well as the analytical procedure and evaluation [48,49], are described in detail in the supplementary information (SI).

#### 5. Conclusions

In this study, the photodegradation of the thiamethoxam and flonicamid pesticides accumulated and frequently detected in the wastewater of the fruit industry, was achieved. In particular, TMX was totally removed from the solution after 90 min of UV-A illumination and an approximately 86% removal was achieved for the more recalcitrant FND pesticide (depending on the solution concentration) in the presence of the commercial titania photocatalyst Aeroxide P25. The observed degradation was accompanied by sufficient pollutant mineralization, while no toxic by-products were detected during the photocatalysis. In this extensive examination, the effect of the solution acidity and pollutant concentration on the photocatalytic efficiency were evaluated. Furthermore, the photocatalytic oxidation pathways were recognized as the main degradation mechanism for both the TMX and FND, where the photogenerated hydroxyl radicals were the most reactive species. These



results verify the highly photocatalytic performance of TiO<sub>2</sub> materials against pesticide pollutants with different physicochemical properties under various experimental conditions and promote their potential use in scale-up applications.

**Supplementary Materials:** The following supporting information can be downloaded at: <https://www.mdpi.com/article/10.3390/catal13030516/s1>, Table S1: Chromatography parameters with time for the pesticides' detection. Table S2: Chromatography parameters with time for the detection of FND metabolites. Table S3: Overview of the LCMS-MS parameters for the analytes investigated. Figure S1: Degradation kinetics of photocatalytic degradation of (a) Linear transform  $\ln(C_0/C) = f(t)$  of thiamethoxam (TMX) and (b) flonicamid (FND) using titania P25 at the studied concentrations (UV-A irradiation, 0.1 g/L TiO<sub>2</sub>, natural pH, 25 °C); Effect of the concentration on the initial degradation rate of both pesticides (c). Figure S2: Total mineralization efficiency of thiamethoxam (TMX) and flonicamid (FND) during the photocatalytic process (UV-A irradiation, 0.1 g/L P25 TiO<sub>2</sub>, natural pH, 25 °C). Refs. [25,41,48,49] are cited in the Supplementary Material file.

**Author Contributions:** Conceptualization, G.E.R. and P.F.; Investigation, writing—original draft preparation, G.V.T. and M.K.A.; Validation, methodology, G.V.T., M.K.A., C.A., E.K. and I.G.; Project administration, E.M.; Resources, E.M. and P.F.; Supervision, writing—review and editing, G.E.R. and P.F. All authors have read and agreed to the published version of the manuscript.

**Funding:** This work was funded by the EC, Environment Program (EU: H2020 LIFE17 ENV/GR/000387 PureAgroH2O Project). The Green Fund is co-financing actions of the partner NCSR "Demokritos" in the frame of the implementation of the LIFE PureAgroH2O project.

**Data Availability Statement:** Not applicable.

**Acknowledgments:** P.F. acknowledges funding of this work by Prince Sultan Bin Abdulaziz International Prize for Water (PSIPW)-Alternative Water Resources Prize 2014.

**Conflicts of Interest:** The authors declare no conflict of interest. The funders had no role in the design of the study; in the collection, analyses, or interpretation of data; in the writing of the manuscript; or in the decision to publish the results.

## References

- Díez, A.; Sanromán, M.; Pazos, M. New approaches on the agrochemicals degradation by UV oxidation processes. *J. Chem. Eng.* **2019**, *376*, 120026. [CrossRef]
- Regulation (EC) No 1107/2009 of the European Parliament and of the Council of 21 October 2009. Available online: <https://eur-lex.europa.eu/LexUriServ/LexUriServ.do?uri=OJ:L:2009:309:0001:0050:en:PDF> (accessed on 24 February 2023).
- Commission Implementing Decision (EU) 2018/840 of 5 June 2018. Available online: <https://eur-lex.europa.eu/legal-content/EN/TXT/PDF/?uri=CELEX:32018D0840> (accessed on 24 February 2023).
- Žabar, R.; Komel, T.; Fabjan, J.; Kralj, M.; Trebše, P. Photocatalytic degradation with immobilised TiO<sub>2</sub> of three selected neonicotinoid insecticides: Imidacloprid, thiamethoxam and clothianidin. *Chemosphere* **2012**, *89*, 293–301. [CrossRef]
- Banić, N.; Šojić, D.; Krstić, J.; Abramović, B. Photodegradation of Neonicotinoid Active Ingredients and Their Commercial Formulations in Water by Different Advanced Oxidation Processes. *Wat. Air Soil Pollut.* **2014**, *225*, 1954. [CrossRef]
- Mir, N.; Khan, A.; Muneer, M.; Vijayalakshmi, S. Photocatalytic degradation of a widely used insecticide Thiamethoxam in aqueous suspension of TiO<sub>2</sub>: Adsorption, kinetics, product analysis and toxicity assessment. *Sci. Total Environ.* **2013**, *458–460*, 388–398. [CrossRef] [PubMed]
- Yang, H.; Liu, H.; Hu, Z.; Liang, J.; Pang, H.; Yi, B. Consideration on degradation kinetics and mechanism of thiamethoxam by reactive oxidative species (ROs) during photocatalytic process. *J. Chem. Eng.* **2014**, *245*, 24–33. [CrossRef]
- Serrano, E.; Munoz, M.; de Pedro, Z.; Casas, J. Fast oxidation of the neonicotinoid pesticides listed in the EU Decision 2018/840 from aqueous solutions. *Sep. Purif. Technol.* **2020**, *235*, 116168. [CrossRef]
- Šojic, D.; Despotovic, V.; Orcic, D.; Szabó, E.; Arany, E.; Armakovic, S.; Illés, E.; Gajda-Schranz, K.; Dombi, A.; Alapi, T.; et al. Degradation of thiamethoxam and metoprolol by UV, O<sub>3</sub> and UV/O<sub>3</sub> hybrid processes: Kinetics, degradation intermediates and toxicity. *J. Hydrol.* **2012**, *472–473*, 314–327. [CrossRef]
- Zhao, Y.; Guo, L.; Wang, L.; Jiang, N.; Chen, K.; Dai, Y. Biodegradation of the pyridine carboxamide insecticide flonicamid by Microvirga flocculans and characterization of two novel amidases involved. *Ecotox. Environ. Saf.* **2021**, *220*, 112384. [CrossRef]
- Ayare, S.; Gogate, P. Sonochemical, Photocatalytic and sonophotocatalytic oxidation of flonicamid pesticide solution using different catalysts. *Chem. Eng. Process.* **2020**, *154*, 108040. [CrossRef]
- Hao, C.; Morse, D.; Zhao, X.; Sui, L. Liquid chromatography/tandem mass spectrometry analysis of neonicotinoids in environmental water. *Rapid Commun. Mass Spectrom.* **2015**, *29*, 2225–2232. [CrossRef]

13. Li, H.; Zhong, Q.; Wang, X.; Luo, F.; Zhou, L.; Sun, H.; Yang, M.; Lou, Z.; Chen, Z.; Zhang, X. The degradation and metabolism of chlorflazuron and flonicamid in tea: A risk assessment from tea garden to cup. *Sci. Total Environ.* **2021**, *754*, 142070. [CrossRef]
14. Calvo-Agudo, M.; Gonzalez-Cabrera, J.; Sadutto, D.; Pico, Y.; Urbaneja, A.; Dicke, M.; Tena, A. IPM-recommended insecticides harm beneficial insects through contaminated honeydew. *Environ. Pollut.* **2020**, *267*, 115581. [CrossRef]
15. Zhang, Q.; Wang, X.; Li, Z.; Jin, H.; Lu, Z.; Yu, C.; Huang, Y.; Zhao, M. Simultaneous determination of nine neonicotinoids in human urine using isotope-dilution ultra-performance liquid chromatography-tandem mass spectrometry. *Environ. Pollut.* **2018**, *240*, 647–652. [CrossRef]
16. Yamamuro, T.; Ohta, H.; Aoyama, M.; Watanabe, D. Simultaneous determination of neonicotinoid insecticides in human serum and urine using diatomaceous earth-assisted extraction and liquid chromatography-tandem mass spectrometry. *J. Chromatogr. B* **2014**, *969*, 85–94. [CrossRef] [PubMed]
17. Yuan, M.; Liu, X.; Li, C.; Yu, J.; Zhang, B.; Ma, Y. A higher efficiency removal of neonicotinoid insecticides by modified cellulose-based complex particle. *Int. J. Bio. Macromol.* **2019**, *126*, 857–866. [CrossRef]
18. Alexander, J.; Hai, F.; Al-Aboud, T. Chemical coagulation-based processes for trace organic contaminant removal: Current state and future potential. *J. Environ. Manag.* **2012**, *111*, 195–207. [CrossRef]
19. Zhang, Y.; Lu, H.; Wang, B.; Zhang, Z.; Lin, X.; Chen, Z. Removal of imidacloprid and acetamiprid from tea infusions by microfiltration membrane. *Int. J. Food Sci. Technol.* **2015**, *50*, 1397–1404. [CrossRef]
20. Humbert, H.; Gallard, H.; Suty, H.; Croué, J. Natural organic matter (NOM) and pesticides removal using a combination of ion exchange resin and powdered activated carbon (PAC). *Water Res.* **2008**, *42*, 1635–1643. [CrossRef] [PubMed]
21. de Urzedo, A.; Nascentes, C.; Augusti, R. Degradation of the insecticides thiamethoxam and imidacloprid in aqueous solution as promoted by an innovative Fe/Fe<sub>3</sub>O<sub>4</sub> composite. *J. Braz. Chem. Soc.* **2009**, *20*, 51–56. [CrossRef]
22. Banic, N.; Abramovic, B.; Šojica, D.; Krstic, J.; Fincur, N.; Bockovic, I. Efficiency of neonicotinoids photocatalytic degradation by using annular slurry reactor. *J. Chem. Eng.* **2016**, *286*, 184–190. [CrossRef]
23. Athanasekou, C.; Likodimos, V.; Falaras, P. Recent developments of TiO<sub>2</sub> photocatalysis involving advanced oxidation and reduction reactions in water. *J. Environ. Chem. Eng.* **2018**, *6*, 7386–7394. [CrossRef]
24. Arfanis, M.; Athanasekou, C.; Sakellis, E.; Boukos, N.; Ioannidis, N.; Likodimos, V.; Sygellou, L.; Bouroushian, M.; Kontos, A.; Falaras, P. Photocatalytic properties of copper—Modified core-shell titania Nanocomposites. *J. Photochem. Photobiol. A* **2019**, *370*, 145–155. [CrossRef]
25. Arfanis, M.; Adamou, P.; Moustakas, N.; Triantis, T.; Kontos, A.; Falaras, P. Photocatalytic degradation of salicylic acid and caffeine emerging contaminants using titania nanotubes. *J. Chem. Eng.* **2017**, *310*, 525–536. [CrossRef]
26. Moles, S.; Mosteo, R.; Gómez, J.; Szpunar, J.; Gozzo, S.; Castillo, J.; Ormad, M. Towards the Removal of Antibiotics Detected in Wastewaters in the POCTEFA Territory: Occurrence and TiO<sub>2</sub> Photocatalytic Pilot-Scale Plant Performance. *Water* **2020**, *12*, 1453. [CrossRef]
27. Mahy, J.; Wolfs, C.; Mertes, A.; Vreuls, C.; Drot, S.; Smeets, S.; Dircks, S.; Boegers, A.; Tuerkd, J.; Lambert, S. Advanced photocatalytic oxidation processes for micropollutant elimination from municipal and industrial water. *J. Environ. Manag.* **2019**, *250*, 109561. [CrossRef] [PubMed]
28. Fenoll, J.; Garrido, I.; Flores, P.; Hellín, P.; Vela, N.; Navarro, G.; García-García, J.; Navarro, S. Implementation of a new modular facility to detoxify agro-wastewater polluted with neonicotinoid insecticides in farms by solar photocatalysis. *Energy* **2019**, *175*, 722–729. [CrossRef]
29. Athanasiou, D.; Romanos, G.; Falaras, P. Design and optimization of a photocatalytic reactor for water purification combining optical fiber and membrane technologies. *J. Chem. Eng.* **2016**, *305*, 92–103. [CrossRef]
30. Papageorgiou, S.; Katsaros, F.; Favvas, E.; Romanos, G.; Athanasekou, C.; Beltsios, K.; Tziaila, O.; Falaras, P. Alginate fibers as photocatalyst immobilizing agents applied in hybrid photocatalytic/ultrafiltration water treatment processes. *Water Res.* **2012**, *46*, 1858–1872. [CrossRef]
31. Garrido, I.; Pastor-Belda, M.; Campillo, N.; Viñas, P.; Yañez, M.; Vela, N.; Navarro, S.; Fenoll, J. Photooxidation of insecticide residues by ZnO and TiO<sub>2</sub> coated magnetic nanoparticles under natural sunlight. *J. Photochem. Photobiol. A* **2019**, *372*, 245–253. [CrossRef]
32. Guettaï, N.; Amar, H. Photocatalytic oxidation of methyl orange in presence of titanium dioxide in aqueous suspension. Part II: Kinetics study. *Desalination* **2005**, *185*, 439–448. [CrossRef]
33. Chan, Y.; Chen, J.; Lu, M. Intermediate inhibition in the heterogeneous UV-catalysis using a TiO<sub>2</sub> suspension system. *Chemosphere* **2001**, *45*, 29–35. [CrossRef] [PubMed]
34. Wang, Y.; Li, X.; Shen, J.; Lang, H.; Dong, S.; Zhang, L.; Fang, H.; Yu, Y. Uptake, translocation, and metabolism of thiamethoxam in soil by leek plants. *Environ. Res.* **2022**, *211*, 113084. [CrossRef]
35. Suttiponparnit, K.; Jiang, J.; Sahu, M.; Suvachittanont, S.; Charinpanitkul, T.; Biswas, P. Role of surface area, primary particle size, and crystal phase on titanium dioxide nanoparticle dispersion properties. *Nanoscale Res. Lett.* **2011**, *6*, 1–8. [CrossRef]
36. Karmakar, R.; Singh, S.; Kulshrestha, G. Kinetics and mechanism of the hydrolysis of thiamethoxam. *J. Environ. Sci. Health B* **2009**, *44*, 435–441. [CrossRef]
37. Liang, R.; Tang, F.; Wang, J.; Yue, Y. Photo-degradation dynamics of five neonicotinoids: Bamboo vinegar as a synergistic agent for improved functional duration. *PLoS ONE* **2019**, *14*, e0223708. [CrossRef]

38. MacBean, C. *The e-Pesticide Manual*, 15th ed.; Version 5.0.1; British Crop Protection Council. Flonicamid: Surrey, UK, 2010; p. 158062-67-0.
39. Gole, V.; Gogate, P. Degradation of brilliant green dye using combined treatment strategies based on different irradiations. *Sep. Purif. Technol.* **2014**, *133*, 212–220. [CrossRef]
40. Ibrahim, I.; Belessiotis, G.; Antoniadou, M.; Kaltzoglou, A.; Sakellis, E.; Katsaros, F.; Sygellou, L.; Arfanis, M.; Salama, T.; Falaras, P. Silver decorated TiO<sub>2</sub>/g-C<sub>3</sub>N<sub>4</sub> bifunctional nanocomposites for photocatalytic elimination of water pollutants under UV and artificial solar light. *Results Eng.* **2022**, *14*, 100470. [CrossRef]
41. Palominos, R.; Mondaca, M.; Giraldo, A.; Penuela, G.; Perez-Moya, M.; Mansilla, H. Photocatalytic oxidation of the antibiotic tetracycline on TiO<sub>2</sub> and ZnO suspensions. *Catal. Today* **2009**, *144*, 100–105. [CrossRef]
42. Li, S.; Cao, X.; Liu, L.; Ma, X. Degradation of thiamethoxam in water by the synergy effect between the plasma discharge and the TiO<sub>2</sub> photocatalysis. *Desalin. Water Treat.* **2015**, *53*, 3018–3025. [CrossRef]
43. Fenoll, J.; Garrido, I.; Hellín, P.; Flores, P.; Navarro, S. Photodegradation of neonicotinoid insecticides in water by semiconductor oxides. *Environ. Sci. Pollut. Res.* **2015**, *22*, 15055–15066. [CrossRef]
44. Chen, Y.; Lu, W.; Shen, H.; Gu, Y.; Xu, T.; Zhu, Z.; Wang, G.; Chen, W. Solar-driven efficient degradation of emerging contaminants by g-C<sub>3</sub>N<sub>4</sub> shielding polyester fiber/TiO<sub>2</sub> composites. *Appl. Catal. B-Environ.* **2019**, *258*, 117960. [CrossRef]
45. Aliste, M.; Lucas, G.; Vela, N.; Garrido, I.; Fenoll, J.; Navarro, S. Solar-driven photocatalytic treatment as sustainable strategy to remove pesticide residues from leaching water. *Environ. Sci. Pollut. Res.* **2020**, *27*, 7222–7233. [CrossRef] [PubMed]
46. Athanasekou, C.; Moustakas, N.; Morales-Torres, S.; Pastrana-Martínez, L.; Figueiredo, J.; Faria, J.; Silva, A.; Dona-Rodríguez, J.M.; Romanos, G.; Falaras, P. Ceramic photocatalytic membranes for water filtration under UV and visible light. *Appl. Catal. B-Environ.* **2015**, *178*, 12–19. [CrossRef]
47. Theodorakopoulos, G.; Arfanis, M.; Pérez, J.S.; Agüera, A.; Aponte, F.X.C.; Markellou, E.; Romanos, G.; Falaras, P. Novel pilot-scale photocatalytic nanofiltration reactor for agricultural wastewater treatment. *Membranes* **2023**, *13*, 202. [CrossRef] [PubMed]
48. Anagnostopoulos, C.; Miliadis, G.; Liapis, K.; Aplada-Sarlis, P. A multiresidue method for analysis of 56 pesticides in peaches using liquid chromatography with tandem mass spectrometry detection. *Hell. Plan. Prot. J.* **2009**, *2*, 75–90.
49. EURL-SRM 2015, Analysis of Flonicamid-Metabolites TFNA and TFNG Using Acidified QuEChERS Method. Version 2. Available online: [https://www.eurl-pesticides.eu/userfiles/file//EurISRM/EurISRM\\_meth\\_FlonicamidMetabolites.pdf](https://www.eurl-pesticides.eu/userfiles/file//EurISRM/EurISRM_meth_FlonicamidMetabolites.pdf) (accessed on 24 February 2023).

**Disclaimer/Publisher’s Note:** The statements, opinions and data contained in all publications are solely those of the individual author(s) and contributor(s) and not of MDPI and/or the editor(s). MDPI and/or the editor(s) disclaim responsibility for any injury to people or property resulting from any ideas, methods, instructions or products referred to in the content.

Article

# Enhancement of Iron-Based Photo-Driven Processes by the Presence of Catechol Moieties

Javier Moreno-Andrés <sup>\*,†</sup> , Iván Vallés, Paula García-Negueroles, Lucas Santos-Juanes and Antonio Arques <sup>\*</sup>

Grupo de Procesos de Oxidación Avanzada, Departamento de Ingeniería Textil y Papelera, Campus de Alcoy, Universitat Politècnica de València, 03801 Alcoy, Spain; ivvalfer@epsa.upv.es (I.V.); paugarne@txp.upv.es (P.G.-N.); lusanju1@txp.upv.es (L.S.-J.)

<sup>\*</sup> Correspondence: javier.moreno@uca.es (J.M.-A.); aarques@txp.upv.es (A.A.)

<sup>†</sup> Present address: Department of Environmental Technologies, Faculty of Marine and Environmental Sciences, INMAR—Marine Research Institute, CEIMAR—International Campus of Excellence of the Sea, University of Cadiz, Campus Universitario de Puerto Real, 11510 Cádiz, Spain.

**Abstract:** Photo-induced Advanced Oxidation Processes (AOPs) using  $\text{H}_2\text{O}_2$  or  $\text{S}_2\text{O}_8^{2-}$  as radical precursors were assessed for the abatement of six different contaminants of emerging concern (CECs). In order to increase the efficiency of these AOPs at a wider pH range, the catechol organic functional compound was studied as a potential assistant in photo-driven iron-based processes. Different salinity regimes were also studied (in terms of  $\text{Cl}^-$  concentration), namely low salt water ( $1 \text{ g}\cdot\text{L}^{-1}$ ) or a salt–water ( $30 \text{ g}\cdot\text{L}^{-1}$ ) matrix. Results obtained revealed that the presence of catechol could efficiently assist the photo-Fenton system and partly promote the photo-induced  $\text{S}_2\text{O}_8^{2-}$  system, which was highly dependent on salinity. Regarding the behavior of individual CECs, the photo-Fenton reaction was able to enhance the degradation of all six CECs, meanwhile the  $\text{S}_2\text{O}_8^{2-}$ -based process showed a moderate enhancement for acetaminophen, amoxicillin or clofibrac acid. Finally, a response-surface methodology was employed to determine the effect of pH and catechol concentration on the different photo-driven processes. Catechol was removed during the degradation process. According to the results obtained, the presence of catechol in organic macromolecules can bring some advantages in water treatment for either freshwater (wastewater) or seawater (maritime or aquaculture industry).

**Keywords:** phenolic moieties; photo-Fenton; persulfate; emerging contaminants; Fe-binding ligands; iron chelates

**Citation:** Moreno-Andrés, J.; Vallés, I.; García-Negueroles, P.; Santos-Juanes, L.; Arques, A. Enhancement of Iron-Based Photo-Driven Processes by the Presence of Catechol Moieties. *Catalysts* **2021**, *11*, 372. <https://doi.org/10.3390/catal11030372>

Academic Editor: Detlef W. Bahnemann

Received: 12 February 2021

Accepted: 8 March 2021

Published: 12 March 2021

**Publisher's Note:** MDPI stays neutral with regard to jurisdictional claims in published maps and institutional affiliations.



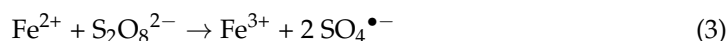
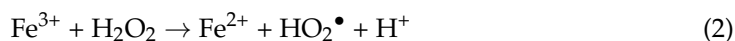
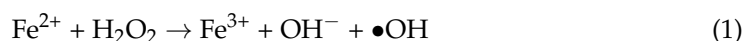
**Copyright:** © 2021 by the authors. Licensee MDPI, Basel, Switzerland. This article is an open access article distributed under the terms and conditions of the Creative Commons Attribution (CC BY) license (<https://creativecommons.org/licenses/by/4.0/>).

## 1. Introduction

Fenton-based processes are among the most promising Advanced Oxidation Processes (AOPs) for water detoxification and, specifically, for the abatement of Contaminants of Emerging Concern (CECs), for which conventional treatment methods are poorly effective [1]. These processes are based on the Haber–Weiss reaction, where iron salts catalyze the decomposition of  $\text{H}_2\text{O}_2$  into highly oxidizing hydroxyl radicals and/or other reactive oxygen species [2–5], briefly described by Equations (1) and (2) (Equation (1):  $k = 63 \text{ M}^{-1}\cdot\text{s}^{-1}$ ; Equation (2):  $k = 0.01\text{--}0.001 \text{ M}^{-1}\cdot\text{s}^{-1}$ ). It may occur naturally in aquatic ecosystems [6–8] but they can also be applied in engineered water systems [1,9]. Iron ions can also activate persulfate salts (Equation (3);  $k = 12\text{--}27 \text{ M}^{-1}\cdot\text{s}^{-1}$ ) to produce sulfate radicals, which are also powerful oxidants but with higher selectivity and longer life-time (half-life: 30–40  $\mu\text{s}$ ) in comparison with  $\bullet\text{OH}$  (half-life:  $10^{-3} \mu\text{s}$ ) [10].

Iron speciation plays a significant role in Fenton chemistry, but iron deactivation also occurs at pH above 3, which limits the applicability of these iron-based processes in mildly acidic or basic medium [4]. Accordingly, research on strategies to enhance the regeneration of ferrous iron in both Fenton and persulfate-based systems are now receiving increasing attention. For instance, the use of organic ligands able to form photoactive compounds with Fe(III) has been examined, using different substances for this purpose

such as oxalate, citrate, EDTA or EDDS [9,11,12]. Since they have to be added to the solution, their biodegradability and/or potential toxicity are key factors for their use in water treatment systems. Hence, searching for naturally occurring substances to be used as chemical auxiliaries for photo-Fenton processes has received scientific interest.



The use of iron for living organisms is essential for growth but its low solubility at physiological pH also limits its availability [13]. In this sense, most of the Fe available in aquatic ecosystems is found complexed by organic Fe-binding ligands [8,14]. These organic chelates, which are known as the Fe ligand pool, can be released by microorganisms, or generated as transformation products of natural organic matter. For instance, an interesting source of iron ligands is siderophore production by microorganisms [14]. They are defined as iron chelates produced mainly by bacterial cells, which facilitate uptake of iron into the microorganisms. Siderophores are typically classified in the basis of their chemical nature and functional groups; among them can be found catecholates (also so-called phenolates), which are present in several bacterial and cyanobacterial species [13,15,16]. These functional groups are considered a major contributor to the stability of metal-siderophore complexes.

Another interesting source of iron ligands are humic-like substances, which have been shown to be efficient for the enhancement of photo-Fenton processes (Table 1) [17–19]. Interestingly, a recent study suggests that iron chelated by humic substances is the major reservoir of Fe-complexed in oceans [20]. Humic substances are complex organic macromolecules with some specific functional groups, such as carboxylic, carbonyl or catechol moieties [21,22]. These functional groups have been employed as simplified model compounds to simulate the effect of humic-like substances in different processes such as sorption [22] or photo-oxidation of As(III) [21].

The catechol organic functional compound presents moderate binding capacity with Fe (III) ( $\text{Log } K_1 = 20.01$ ) [15,23] and high photo-reactivity as a free ligand [24]. This UV photo-reactivity of the Fe (III) complex is important since leads to oxidation of the ligand and reduction of Fe (III) to Fe (II) generally through Equation (4), thus could introduce Fe (II) again into the Fenton cycle. It has been proposed that once catechol is bound to Fe (III), the metal is reduced to Fe (II) [25–27], while the ligand is oxidized to a quinone (via semiquinone). Quinone-intermediates can regenerate themselves (mainly by reaction with  $\text{HO}_2\bullet$  species, which are abundant in Fenton-based processes) and might result in a catalytic redox cycle [25,26,28]. However, most of studies have been focused on catechol as target pollutant, as it is an intermediate of phenol degradation [10,29–31], but very few have investigated on the enhancement of Fenton-based process by the catechol Fe-complexes [25,26,28,32].



In this scenario, the main goal of this study is to investigate catechol as a possible assistant in photo-driven iron-based processes for water treatment, namely the photo-Fenton process, i.e.,  $\text{H}_2\text{O}_2$ -based, or persulfate (PDS;  $\text{S}_2\text{O}_8^{2-}$ -based) process. This is interesting in two ways: (i) the possibility of using catechol as auxiliary for iron-based AOPs and (ii) to be employed as a surrogate to better understand the behavior of complex macromolecules such as humic-like substances (HLS) where catechol moieties can act as active sites for iron complexation and to drive photo-Fenton-like reactions.

Six different contaminants of emerging concern (CECs) were used as target contaminants, namely acetamiprid (insecticide), amoxicillin (antibiotic), acetaminophen (analgesic), caffeine (stimulating agent), clofibrac acid (metabolite of clofibrate, also employed as herbicide) and carbamazepine (psychiatric drug). They were selected according to: (i) their presence in different effluents from diverse origin, such as aquaculture, urban wastewater,

shipping, membrane rejection [33–38], (ii) their detection in natural waters [38–40] but also (iii) their inclusion on the European monitoring list, i.e., the Watch List of Substances (Decision 2018/840/EU), in which amoxicillin and acetamiprid are included.

**Table 1.** Previous studies that make use of Humic-like Substances for the enhancement of Photo-Fenton processes. OMW-HLS: Olive Mill Waste humic like substances. SBO: Soluble Bio-Organic substances.

Humic Like Substances	Concentration of HLS Tested	Operational Variables pH/H <sub>2</sub> O <sub>2</sub>	Target Compounds	Improvement	References
OMW-HLS	10 mg L <sup>-1</sup> 30 mg L <sup>-1</sup> 60 mg L <sup>-1</sup>	pH 5 [H <sub>2</sub> O <sub>2</sub> ] = 60 mg L <sup>-1</sup>	Caffeine	Removal of 95% of initial amount at 10 min with 10 mg L <sup>-1</sup> of HLS vs. 45% removal without these substances.	García-Ballesteros et al., 2018 [18]
	30 mg L <sup>-1</sup>	pH 5 [H <sub>2</sub> O <sub>2</sub> ] = 60 mg L <sup>-1</sup>	Caffeine	Removal of 100% of initial amount at 90 min. vs. 60% removal without these substances.	García-Negueroles et al., 2019 [17]
SBO from urban wastes	10 mg L <sup>-1</sup>	pH 5.2 [H <sub>2</sub> O <sub>2</sub> ] = 75 mg L <sup>-1</sup>	Acetaminophen, amoxicillin, caffeine, acetamiprid, carbamazepine and clofibrac acid.	Removal of 100% of initial amount of 4 pollutants at t <sub>30w</sub> = 30 min vs. 80 min (t <sub>30w</sub> ) needed in absence of these substances.	Gomis et al., 2014 [41]

In order to address the water matrix, different salinity regimes were studied, namely low salt water (LSW) or a salt–water (SW) matrix, so as to represent fresh and saline water effluents. To gain further insight into the action mode of both H<sub>2</sub>O<sub>2</sub> and PDS systems, scavenging tests were performed with the tested CECs splitting into two groups, in accordance with their different reactivity with sulfate or hydroxyl radicals. Finally, a response surface methodology based on Doehlert design was employed to determine the effect of pH and catechol concentration on the different photo-driven processes. Accordingly, the main hypothesis is that catechol can accelerate photo-driven iron-based processes in a wide pH and salinity range. Their potential use can entail biomimetics and some advantages in water treatment for either fresh water (wastewater) or saline water (maritime or aquaculture industry).

## 2. Results and Discussion

### 2.1. Effect of Catechol in Photo-Fenton and Persulfate-Based Systems

A first series of experiments was devoted to assessing the role of catechol in both photo-induced processes, i.e., a H<sub>2</sub>O<sub>2</sub>-based (Fenton) and a persulfate-based system at pH = 5. Time resolved data of the cumulative concentration of the Σ CECs were obtained (Figure 1A). Figure 1A compares photo-Fenton processes without and with catechol, in both low and high salinity matrices but also including a control experiment in the absence of chlorides, i.e., distilled water (DW). A very strong enhancement of the process can be observed as the concentration of CECs was negligible after 15 min of irradiation when catechol (CAT) was present, while significant amounts remained even after 60 min (ca. 20% in SW and 10% in LSW) in the absence of CAT. This fact might be attributed to the formation of a complex between iron and CAT that prevents inactivation of the catalytic role of iron at mild pH.

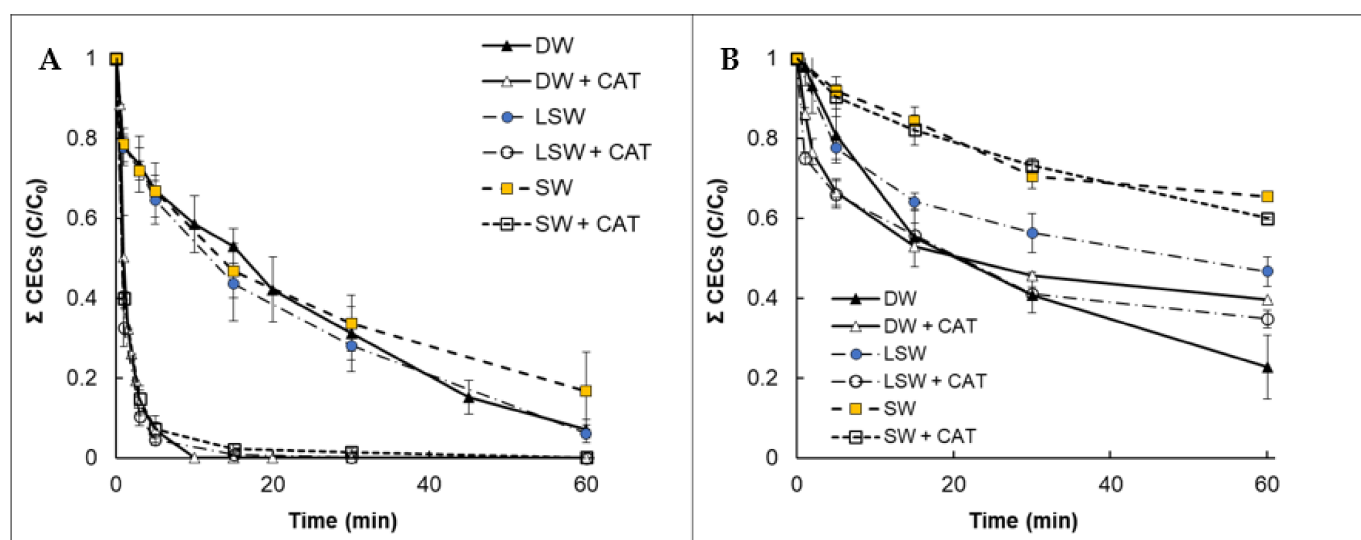


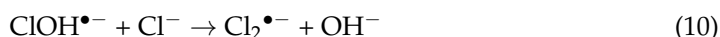
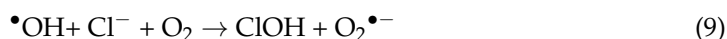
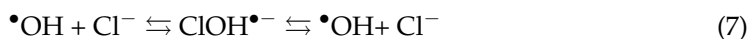
**Figure 1.** Degradation profiles of sum of the total concentration of contaminants of emerging concern (CECs) in Distilled Water (DW), low salt water (LSW), and salt-water (SW) matrix matrices under (A) a photo-Fenton system (Fe(III)/H<sub>2</sub>O<sub>2</sub>) in the presence and absence of catechol (CAT). (B) Fe(III)/persulfate (PDS) system in the presence and absence of catechol (CAT). Experimental conditions: ([Fe(III)] = 5 mg·L<sup>-1</sup>, [H<sub>2</sub>O<sub>2</sub>] or [S<sub>2</sub>O<sub>8</sub><sup>2-</sup>] = 146 mg·L<sup>-1</sup>, [CAT] = 13 mg·L<sup>-1</sup>; pH<sub>0</sub> = 5).

By comparison with previous studies, similar trends have been observed when Humic-like Substances (HLS) are used as auxiliaries of the photo-Fenton reaction (Table 1). For instance, García-Ballesteros et al. 2018 [18] and García-Negueroles et al. 2019 [17] concluded that the degradation of caffeine (in a photo-Fenton system at pH = 5) was increased by the addition of different HLS in the range of 10–60 mg·L<sup>-1</sup>. Moreover, Gomis et al. 2014 [41], tested soluble bio-based substances (with the presence of phenolic carbon, phenoxy and carboxylic functional groups), obtaining an enhancement of the photo-Fenton reaction at pH 5.2. Thus, if catechol (and in general phenolic moieties) can be assumed to be among the active sites of these HLS it might be proposed as a simplified model compound to simulate the effect of HLS on oxidation processes [21,22].

Following the same approach as with the photo-Fenton reaction, the ability of iron to activate PDS was assessed under irradiation (Figure 1B). As has been mentioned in the Introduction, PDS can be activated by Fe<sup>2+</sup> (Equation (3)) but also by irradiation (S<sub>2</sub>O<sub>8</sub><sup>2-</sup> + hν → SO<sub>4</sub><sup>•-</sup>), so these two activation factors are expected sources of radical production [42]. Additionally, irradiation can also photo-reduce the ferric iron-complexes into ferrous iron (Equation (4)). Thus, the presence of CAT in PDS system is expected to assist the formation of Fe<sup>2+</sup> through photoreduction of Fe(III)–CAT complexes. The degradation profiles of the ΣCECs according to the irradiation time are depicted in Figure 1B, where a series of experiments were performed with the presence of CAT at pH = 5 and compared with the results obtained in the absence of catechol. In both DW and LSW, a slight improvement can be perceived when catechol is present in the solution. For instance, in LSW, the Σ CECs reaches degradation of 53.4% and 65.3% with and without catechol in solution, respectively. In contrast, the PDS-based process was scarcely efficient in SW, either with or without CAT in solution.

High salinity (in terms of Cl<sup>-</sup> concentration) generally seems to decrease the efficiency of both processes, which is especially remarkable in the PDS-based system. In the presence of chlorides, Fe(III) can yield to Fe(Cl)<sub>2</sub><sup>2+</sup> and FeCl<sub>2</sub><sup>+</sup> complexes, which are highly photo-active and can promote the iron reduction into Fe(II) and chloride radicals (Equations (5) and (6)) [43,44]. This fact might explain the slight improvement of the photo-Fenton process in LSW. On the other hand, chlorides also present a scavenging effect with •OH radicals (Equations (7)–(10)) [44,45]. The generation of these chloride radicals (less reactive and with higher selectivity) might be the reason for which a slowing down of the photo-Fenton process is observed as salinity increases, as observed in SW. However, the

presence of catechol in solution, could successfully assist the photo-Fenton process, since similar results were obtained in DW, LSW and SW matrices (Figure 1A).



Similarly, sulfate radicals can also interact with chlorides in solution, giving as a result less reactive radicals such as  $\text{Cl}^\bullet$ ,  $\text{Cl}_2^{\bullet-}$  (Equations (11) and (12)). In fact, it is worth noticing that  $\text{Cl}^-$  oxidation is more favored by  $\text{SO}_4^{\bullet-}$  than  $\bullet\text{OH}$  [46,47]. This might explain the poor performance of the system in high salinity matrix for the PDS system (Figure 1B). Additionally, it is known that both sulfate and chloride radicals can selectively react with specific compounds [46,48–50]. In this regard, some insights by assessing individual CECs will be addressing in the next sub-section.



## 2.2. Some Insights by Assessing Individual Behavior of the Different CECs

To gain further insight into the action mode of both  $\text{H}_2\text{O}_2$  and  $\text{S}_2\text{O}_8^{2-}$  radical precursors, the tested CECs were classified into two groups in accordance to their different reactivity with sulfate or hydroxyl radicals [48,50–52]. Thus, group I includes those compounds that exhibit higher reactivity with  $\bullet\text{OH}$ , rather than  $\text{SO}_4^{\bullet-}$  (i.e., carbamazepine, caffeine and acetamiprid), with  $k_{\bullet\text{OH}} \approx 6 \times 10^9 \text{ M}^{-1}\cdot\text{s}^{-1}$ ;  $k_{\text{SO}_4^{\bullet-}} \approx 1\text{--}3 \times 10^9 \text{ M}^{-1}\cdot\text{s}^{-1}$ . Group II includes the compounds that could have more affinity for reaction with  $\text{SO}_4^{\bullet-}$  (i.e., clofibric acid, amoxicillin and acetaminophen), with  $k_{\text{SO}_4^{\bullet-}} \approx 2\text{--}7 \times 10^9 \text{ M}^{-1}\cdot\text{s}^{-1}$ .

Degradation curves can be divided into both groups: Figure 2-upper (group I) and Figure 2-lower (group II). Although similar results and trends are observed among groups I and II in the photo-Fenton process, some differences can be found in the PDS system. Here, lower degradation rates can be observed for those compounds belonging to group I, with similar trends in DW, LSW and SW matrices (Figure 2-upper). Interestingly, these results match with recent studies that make use of similar target pollutants [53]. On the contrary, degradation rates of group II compounds notably increase in the three aqueous solutions (Figure 2-down).

In general,  $\bullet\text{OH}$  has a high oxidation potential (ca. 2.8 V), and that of sulfate radical is 2.43 V [54]. This makes  $\text{SO}_4^{\bullet-}$  show higher selectivity towards some substances, giving in general fast reactions towards aromatic rings that are activated for electrophilic attack. It is the case of acetaminophen, clofibric acid and amoxicillin, with electro-donating groups directly attached to the ring. On the other hand, the pyridinic group of acetamiprid or the imidazole moiety of caffeine are reluctant to attack electrophilically, this explaining the bad performance of the sulfate radical towards these compounds.

Accordingly, in the case of group II compounds, the addition of CAT can promote the efficiency of the PDS-based system in both LSW and SW, which means that the time to reach 50% of degradation is reduced by approximately half in the presence of CAT in solution. On the other hand, the selectivity of primary sulfate radicals can limit the process to specific contaminants, since no effect has been observed in compounds of group I. In consequence, the limited efficiency of PDS system has been obtained (Section 2.1) when the sum of whole contaminants is studied.



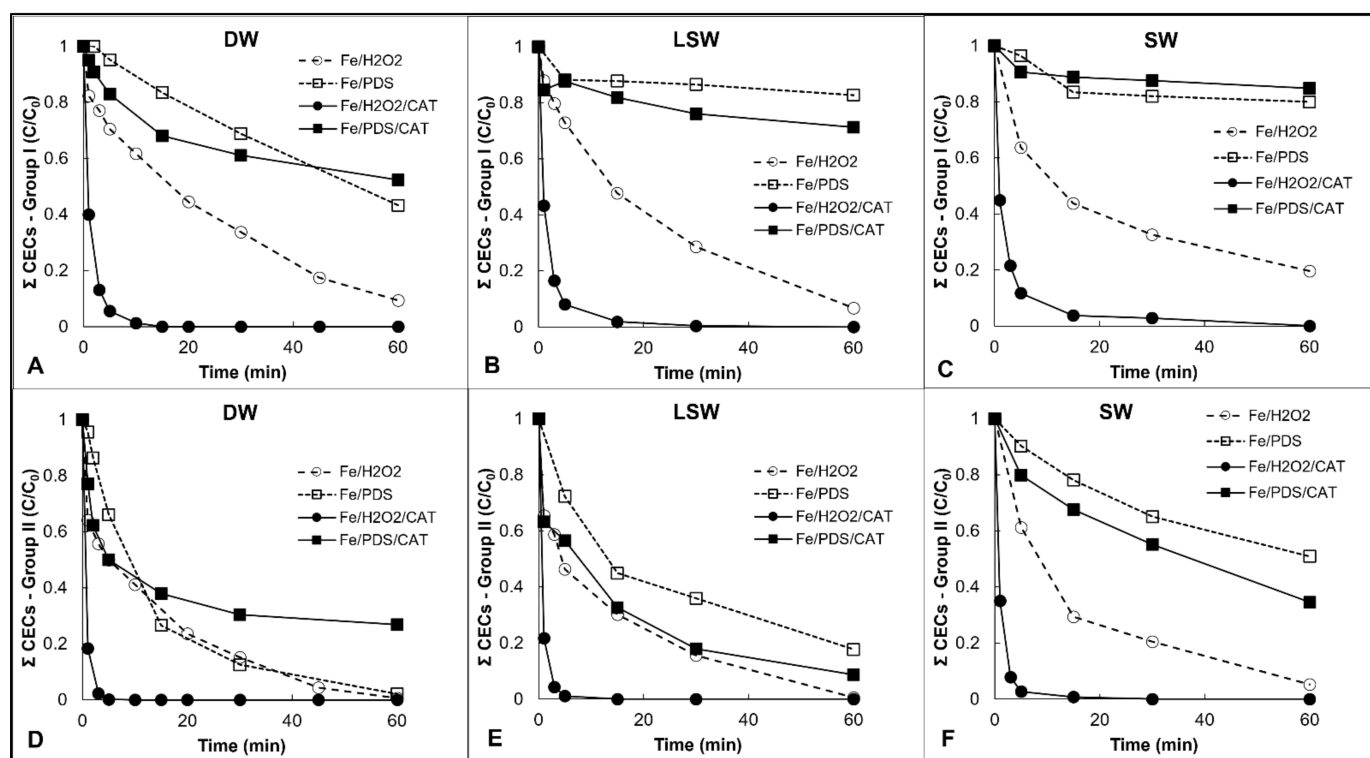


**Figure 2.** Degradation profiles of the sum of CECs in a photo-Fenton system ( $\text{Fe}/\text{H}_2\text{O}_2$ ) and irradiated  $\text{Fe}/\text{PDS}$  system with the presence/absence of catechol (CAT) in DW (A,D) LSW (B,E) and SW (C,F). CECs have been split into Group I (Upper): Carbamazepine, Caffeine and Acetamidiprid; and Group II (Down): Clofibric acid, Amoxicillin and Acetaminophen. Standard Deviation of each experimental point is always  $\text{S.D.} < 0.05$ . Experimental conditions:  $[\text{Fe(III)}] = 5 \text{ mg}\cdot\text{L}^{-1}$ ,  $[\text{H}_2\text{O}_2]$  or  $[\text{PDS}] = 146.16 \text{ mg}\cdot\text{L}^{-1}$ ,  $[\text{CAT}] = 13 \text{ mg}\cdot\text{L}^{-1}$ ,  $\text{pH}_0 = 5$ .

Scavenging experiments were also performed to consider the involvement of different radical species. 2-Propanol ( $k_{\bullet\text{OH}-2\text{-Prop}} = 1.9 \times 10^9 \text{ M}^{-1}\cdot\text{s}^{-1}$ ;  $k_{\text{SO}_4^{\bullet-}-2\text{-Prop}} = 6.9 \times 10^7 \text{ M}^{-1}\cdot\text{s}^{-1}$ ), and tert-butanol (t-BuOH) ( $k_{\bullet\text{OH}-\text{t-BuOH}} = 6 \times 10^8 \text{ M}^{-1}\cdot\text{s}^{-1}$ ;  $k_{\text{SO}_4^{\bullet-}-\text{t-BuOH}} = 8.4 \times 10^5 \text{ M}^{-1}\cdot\text{s}^{-1}$ ) were used as radical probes, considering that 2-propanol can effectively quench both  $\bullet\text{OH}$  and  $\text{SO}_4^{\bullet-}$ , while t-BuOH selectively reacts with  $\bullet\text{OH}$  [55,56]. The same approach has been performed successfully in previous studies [42]. Accordingly, the results obtained are depicted in Figure 3, where the presence of scavengers was assessed in SW matrix at operational conditions of  $[\text{Fe(III)}] = 5 \text{ mg}\cdot\text{L}^{-1}$ ,  $[\text{CAT}] = 13 \text{ mg}\cdot\text{L}^{-1}$ ,  $\text{pH}_0 = 5$ .

For compounds of group I, a similar degradation rate was obtained for the PDS system in the presence of both scavengers (Figure 3A). However, in the photo-Fenton system, a clear inhibition in the presence of 2-propanol is observed (Figure 3B), which suggests a major role in degradation for hydroxyl radicals. On the other hand, for compounds of group II, slight inhibition is observed in the PDS system, majorly attributed to  $\text{SO}_4^{\bullet-}$ , but also to  $\bullet\text{OH}$  derived from the photolysis of iron-aqua complexes (Figure 3C). In the photo-Fenton system, the degradation of CECs is notably inhibited (28%), although at a minor rate than group I compounds (56%).

Those results support that  $\bullet\text{OH}$  radicals play a major role in CECs degradation of both group I and group II compounds. Furthermore, they also suggest that the role of  $\text{SO}_4^{\bullet-}$  in CECs degradation is slightly higher for group II, and almost negligible in compounds of group I, supporting the selectivity of these  $\text{SO}_4^{\bullet-}$  towards specific compounds. It is also noteworthy that, despite the presence of scavengers, the CECs degradation is remarkable, especially for those pollutants of group II. Thus, the involvement of other reactive species is expected. Taking into account the high  $\text{Cl}^-$  concentration, probably  $\text{Cl}^\bullet$  and  $\text{Cl}_2^{\bullet-}$  radicals are also taking part in the degradation process, due to the rapidly oxidation of  $\text{Cl}^-$  in the presence of  $\text{SO}_4^{\bullet-}$  ( $k_{\text{SO}_4^{\bullet-}-\text{Cl}^-} = 3\text{--}6.6 \times 10^8 \text{ M}^{-1}\cdot\text{s}^{-1}$ ) and  $\bullet\text{OH}$

( $k_{\bullet\text{OH}-\text{Cl}_2^-} = 3\text{--}4.3 \times 10^9 \text{ M}^{-1}\cdot\text{s}^{-1}$ ), especially suitable for the production of  $\text{Cl}_2^{\bullet-}$  [56,57]. Additionally, the high reactivity of  $\text{Cl}_2^{\bullet-}$  radicals with compounds of group II, such as acetaminophen ( $k_{\text{Cl}_2^{\bullet-}} = 4.32 \times 10^8 \text{ M}^{-1}\cdot\text{s}^{-1}$ ) in front of compounds of group I, such as carbamazepine ( $k_{\text{Cl}_2^{\bullet-}} = 0.43 \times 10^8 \text{ M}^{-1}\cdot\text{s}^{-1}$ ) supports the results obtained [49].

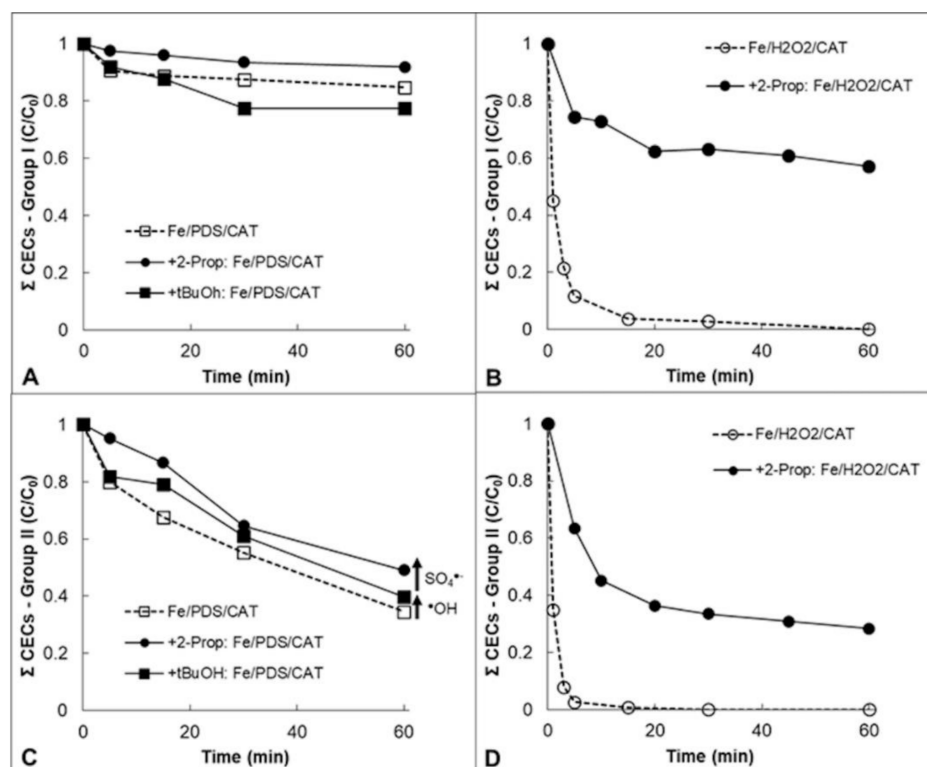


**Figure 3.** Degradation profiles of the sum of CECs in an irradiated Fe/PDS/CAT system (A,C) and photo-Fenton system (Fe/H<sub>2</sub>O<sub>2</sub>/CAT) (B,D) with the presence of scavengers in SW. CECs have been split into Group I (A,B): Carbamazepine, Caffeine and Acetamidrid; and Group II (C,D): Clofibrac acid, Amoxicillin and Acetaminophen. Experimental conditions: [Fe(III)] = 5 mg·L<sup>-1</sup>, [H<sub>2</sub>O<sub>2</sub>]/[PDS] = 146.16 mg·L<sup>-1</sup>, [CAT] = 13 mg·L<sup>-1</sup>, pH<sub>0</sub> = 5.

### 2.3. Effect of Operational Factors and Reagents Consumption

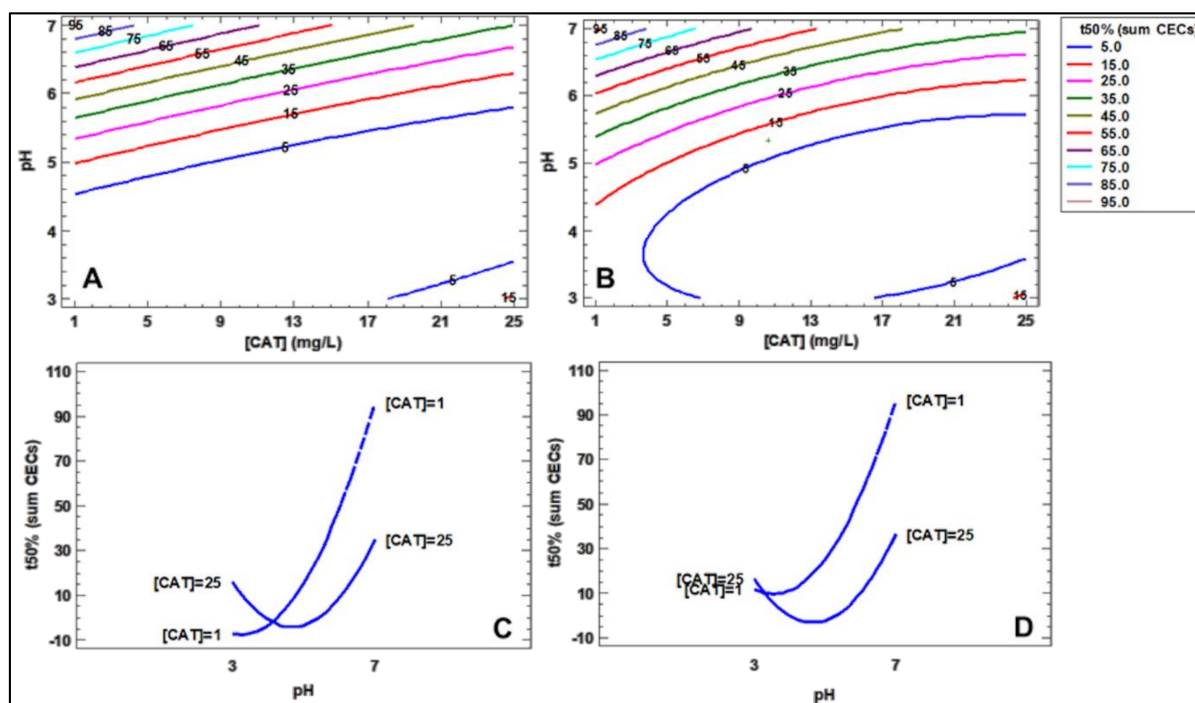
In order to study how pH and [CAT] influences in the different photo-induced systems (Fenton-based and PDS-based), a two-variable Doehlert matrix design was employed (see Table 2 for experimental points). The time required for the removal of 50% of the CECs ( $t_{50\%}$ ) was estimated from the plot of  $\Sigma$  CECs vs. irradiation time. A detailed discussion on this parameter can be found elsewhere [19].

#### 2.3.1. Photo-Fenton System

Based on the results obtained in the different experimental runs, a bidimensional quadratic response-surface model was obtained. Good agreement between experimental and calculated data was supported by  $R^2$  values ( $R^2_{\text{LSW}} = 0.92$ ,  $R^2_{\text{SW}} = 0.97$ ). Model equations can be found in Supplementary Material, Equation (S1). In order to visualize the effect of the studied operational variables, bi-dimensional contour plots, together with the interaction effect plot are represented in Figure 4. 3D contour plots are represented in Figure S1.

**Table 2.** Experimental points used in the Doehlert matrix and associated response, which is based on the time required to degrade the sum of CECs to 50% of its initial concentration ( $t_{50\%}$ ).

Number of Experiments	Coded Values		Operational Variables		$t_{50\%}$ ( $\Sigma$ CECs), (min)		
	$X_1$ (5 Levels)	$X_2$ (3 Levels)	[CAT] ( $\text{mg}\cdot\text{L}^{-1}$ )	pH	Fe(III)/ $\text{H}_2\text{O}_2$		Fe(III)/ $\text{S}_2\text{O}_8^{2-}$
					LSW	SW	LSW
1	0	0	13	5	0.67	0.82	18.99
2	1.0	0	25	5	2.48	0.85	83.31
3	0.5	0.817	19	7	40.31	40.49	90.16
4	-1.0	0.000	1	5	9.66	22.22	34.95
5	-0.5	-0.817	7	3	0.41	8.01	18.90
6	0.5	-0.817	19	3	0.39	4.16	88.96
7	-0.5	0.817	7	7	82.39	76.61	43.69
8	0.0	0.000	13	5	0.80	0.87	19.86
9	0.0	0.000	13	5	0.76	0.82	19.08

**Figure 4.** Surface response obtained for the  $\Sigma$  CECs in LSW (Left: A,C) and SW (Right: B,D) in a photo-Fenton system with the presence of catechol (CAT) as an assistant (Fe(III)/ $\text{H}_2\text{O}_2$ /CAT). Contour plots of  $t_{50\%}$  (A,B) and the interaction effect plot (C,D) are plotted by means of CAT concentration and pH. Experimental conditions:  $[\text{Fe(III)}] = 5 \text{ mg}\cdot\text{L}^{-1}$ ,  $[\text{H}_2\text{O}_2] = 146.16 \text{ mg}\cdot\text{L}^{-1}$ .

For LSW, there is a trend mainly controlled by the pH, in which the  $t_{50\%}$  increases as the pH does, in particular at  $\text{pH} > 5$ . However, some interaction among pH and [CAT] can be found. For instance, a  $t_{50\%}$  of 35 min can be obtained at [CAT] of  $1 \text{ mg}\cdot\text{L}^{-1}$  and  $\text{pH} \approx 5.5$ ; the same  $t_{50\%}$  of 35 min is reached at  $\text{pH} 7$  when the  $[\text{CAT}] = 25 \text{ mg}\cdot\text{L}^{-1}$  (Figure 4A). So, it suggests an enhancement of the photo-Fenton process by the addition of catechol. Interestingly, at low pH, a slight detrimental effect of [CAT] is denoted. This can be more easily seen in the interaction effect plot (Figure 4C), where contrary effect is observed at  $\text{pH} = 3$  and at  $\text{pH} = 7$ . In other words, the presence of catechol clearly assists the photo-Fenton reaction in the range of near-neutral pH, however it might be a hindrance at low pH, where the photo-Fenton system is known to be highly efficient by itself, hence CAT can compete with the CECs for the reactive species. Thus, it is in agreement with the associated ANOVA table (Table S1) and Pareto charts obtained within the analysis, which

gives significance ( $p < 0.05$ ) for pH and its quadratic variable, not for [CAT]. It suggests that the effect of pH is so pronounced and could mask the effects of the [CAT] for some pH conditions.

On the other hand, for the SW matrix, significance ( $p < 0.05$ ) was obtained for pH,  $\text{pH}^2$ , [CAT] and the interaction of them both (Equation (S2)), which means that these two operational factors significantly influence the  $t_{50\%}$  values at 95% of the confidence level. The effect of salinity (in terms of  $\text{Cl}^-$  concentration) generally seems to decrease the efficiency of the photo-Fenton process at low pH. In fact, the fixed 5 min. line for the  $t_{50\%}$  is stretched in comparison with LSW (Figure 4B). However, similar trends were observed as with LSW (Figure 2). In addition, the similar trends observed in both water matrices at  $\text{pH} > 5$  can be explained according to Equations (5)–(8), where the scavenging effect of  $\bullet\text{OH}$  radicals by chlorides can be overwhelmed at neutral–basic conditions, since  $\text{HOCl}^{\bullet-}$  can revert back to  $\text{Cl}^-$  and  $\bullet\text{OH}$  [44,45]. Thus, the presence of catechol in SW matrix could help to avoid the negative effect provoked mainly by pH rather than salinity.

The [CAT] and  $\text{H}_2\text{O}_2$  concentrations were also monitored during the experiments. Catechol achieved  $>90\%$  degradation within the first minutes of reaction in all cases. It implies a fast degradation of this compound within the process, which is in agreement with other studies [26,28], and evidence of the fast photo-oxidation of this ligand [24]. However, this is not a drawback, as the efficiency of the process is kept until the complete removal of the CECs, as observed in Figure 1A. This might imply that byproducts formed from CAT are also good auxiliaries to drive the photo-Fenton reaction at mild pH.

Regarding  $\text{H}_2\text{O}_2$  consumption (Figure S2), some differences between LSW and SW can be found at pH 3 and 7, but similar consumption rates were obtained in both matrices at pH 5. These differences can be associated to the efficiency of  $\text{H}_2\text{O}_2$  utilization by the photo-Fenton system and supports the  $t_{50\%}$  values obtained for the  $\Sigma$  CECs degradation. It has been reported that CAT–Fe(III) complexes become more stable as the pH increases, so it implies a slow  $\text{H}_2\text{O}_2$  consumption due to the slow photo-reduction of Fe(III) and slow pH decrease during oxidation [26,32,58]. On the other hand, in SW matrices, a worst performance can be also ascertained, especially at  $\text{pH} = 3$  that could be due to competitive degradation of catechol with CECs. In addition, it might imply low mineralization yields in SW despite the faster removal of the different CECs [59]. Further studies are recommended in this regard.

### 2.3.2. Photo-Induced Iron Activation of Persulfate

In order to gain further insight into the effect of the pH and [CAT] as operational variables, a quadratic response-surface model was obtained for LSW. Thus, the influence of pH and [CAT] variables was investigated using  $t_{50\%}$  as variable response. A bi-dimensional contour plot, together with the interaction effect plot, are represented in Figure 5. The obtained  $R^2_{\text{LSW}}$  was 0.91, the model equation was defined on Supplementary Material, Equation (S3). 3D contour plots are represented in Figure S3.

Plots were different when compared with  $\text{H}_2\text{O}_2$ , as only the [CAT] variable gains significance ( $p < 0.05$ ). A minimum for  $t_{50\%}$  was observed at pH between 4 and 5;  $[\text{CAT}] = 5\text{--}10 \text{ mg L}^{-1}$  which means that those were the optimal conditions within the studied region. This indicates that the mechanism of PDS is clearly different to the Fenton-like process, which also support the results obtained in previous sections. Furthermore,  $t_{50\%}$  values are systematically higher for Fe/PDS than for Fe/ $\text{H}_2\text{O}_2$ , indicating the lower efficiency of PDS. However, too high concentrations of CAT are detrimental (Figure 5), as this organic can compete with the pollutants for the reactive species. Even so, an improvement has been obtained in LSW with the presence of CAT ( $\text{pH} = 5$ ;  $[\text{CAT}]_0 = 13 \text{ mg}\cdot\text{L}^{-1}$ ), able to short  $t_{50\%}$  values at 68%.

Finally, regarding the degradation of CAT itself, it was very fast in most cases, reaching degradation  $>90\%$  within the first minutes of reaction, with some exceptions when  $[\text{CAT}]_0 = 19 \text{ mg}\cdot\text{L}^{-1}$  (degradation rates of 80% and 95% in 15 min at pH 7 and pH 3, respectively). PDS was also monitored during the reactions, and a higher consumption in the

presence of CAT was observed (Figure S4A–C); this might indicate that CAT activates iron to catalyze PDS decomposition. On the contrary, experiments conducted in SW resulted in a lower consumption of PDS when compared with LSW, resulting in similar PDS consumption rates with the presence or absence of CAT (Figure S4D, SW). This suggests that high salinity supposes a major hinderance for the Fe/PDS process, even in the presence of CAT, in sharp contrast with the Fe/H<sub>2</sub>O<sub>2</sub> system.

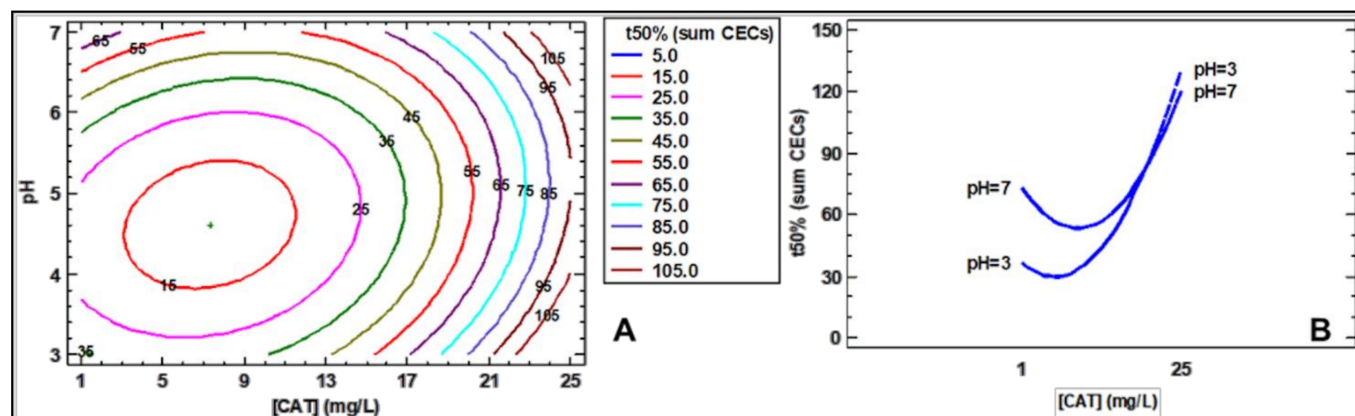


**Figure 5.** Surface response obtained for the  $\Sigma$  CECs in LSW in an irradiated Fe/PDS system with the presence of catechol (CAT) as assistant. Contour plots of  $t_{50\%}$  are plotted by means of CAT concentration and pH (A) as the interaction effect plot (B). Experimental conditions:  $[\text{Fe(III)}] = 5 \text{ mg}\cdot\text{L}^{-1}$ ,  $[\text{S}_2\text{O}_8^{2-}] = 146.16 \text{ mg}\cdot\text{L}^{-1}$ .

### 3. Materials and Methods

#### 3.1. Reagents

High purity (>98%) Acetamidrid, Acetaminophen, Caffeine, Amoxicillin, Clofibric Acid and Carbamazepine were supplied by Sigma-Aldrich (Madrid, Spain). Catechol, was used as high purity grade reagent ( $\geq 95.0\%$ , Sigma-Aldrich).

Fenton-based reactions were performed with iron (III) chloride ( $\text{FeCl}_3\cdot 6\text{H}_2\text{O}$ ), and hydrogen peroxide (30% *w/w*) purchased from PanReac (Barcelona, Spain). Persulfate-based process were performed with potassium peroxodisulphate, PDS ( $\text{K}_2\text{S}_2\text{O}_8$ ), 99.0%-PanReac. When necessary, pH adjustments were performed with sodium hydroxide and sulfuric acid (PanReac). Water employed in all solutions was of Milli-Q grade. Salinity was modified by adding NaCl, 99% (Panreac) to Milli-Q water. Scavenging tests, were performed with analytical grade 2-propanol and tert-butanol (Sigma-Aldrich). Methanol, formic acid and acetonitrile were HPLC grade and purchased from PanReac.

#### 3.2. Target Solution and Water Matrices

The target solution consisted in a mixture of six different CECs, namely acetamidrid, amoxicillin, acetaminophen, caffeine, clofibric acid and carbamazepine. The initial concentration of each was fixed at  $5 \text{ mg}\cdot\text{L}^{-1}$ , which is slightly above the concentration commonly found in ecosystems, but it was chosen to ensure good kinetic data to compare the different processes and reactions.

Two different water matrices were used as aqueous solutions: low salt-water, LSW and salt-water, SW, which was prepared by adding  $1 \text{ g}\cdot\text{L}^{-1}$  or  $30 \text{ g}\cdot\text{L}^{-1}$  of NaCl respectively, to distilled water (Milli-Q grade) so as to represent fresh and saline water effluents. Additional tests were also performed in distilled water as control experiments. Initial pH of the solutions was 5.35 (S.D.  $\pm 0.12$ ) and 4.93 (S.D.  $\pm 0.34$ ), conductivity was determined as 1.68 (S.D.  $\pm 0.07$ ) and 30.7 (S.D.  $\pm 0.96$ )  $\text{mS}\cdot\text{cm}^{-1}$  for LSW and SW, respectively. The temperature was kept at ca. 30 °C during the whole experimentation.

### 3.3. Experimental Set-up

All the experiments were performed in 250-mL cylindrical open glass reactors. A solar simulator (Oriel Instruments, Model 81160 equipped with a 300-W xenon lamp, Oriel Corp. Stratford, CT, USA) was employed as the irradiation source. Specific glass filters for cutting off the transmission of wavelengths  $\lambda < 300$  nm was used. The UVA irradiance (315–400 nm) was  $32 \text{ W}\cdot\text{m}^{-2}$  [60]. Control experiments showed that direct photolysis of the pollutants was negligible under the employed conditions.

All systems were tested with  $5 \text{ mg}\cdot\text{L}^{-1}$  of iron, according to previous studies [19,32]. Hydrogen peroxide was added at  $146.16 \text{ mg}\cdot\text{L}^{-1}$ , which is the stoichiometric amount to mineralize the mixture of CECs. It is considered as a useful procedure commonly employed (i) to normalize the amount of  $\text{H}_2\text{O}_2$  added to the reaction medium, and (ii) to ensure that the process is not stopped because of the exhaustion of  $\text{H}_2\text{O}_2$  [19]. The same mass amount of  $\text{S}_2\text{O}_8^{2-}$  was selected for comparative purposes. Main operational factors, such as pH and the initial concentration of catechol ( $[\text{CAT}]_0$ ) were varied to assess photo-driven processes.

The same experimental procedure was followed for all tested systems: CECs were prepared in the different aqueous matrices (LSW and SW). Then, reagents were added when required by the experimentation in the following order: (i) catechol, (ii) iron, (iii)  $\text{H}_2\text{O}_2$  or  $\text{S}_2\text{O}_8^{2-}$ . It is important to note that when required, the pH was adjusted to the desired value by dropwise addition of either  $0.1 \text{ mmol L}^{-1}$  NaOH or  $0.1 \text{ mmol L}^{-1}$   $\text{H}_2\text{SO}_4$  before  $\text{H}_2\text{O}_2/\text{S}_2\text{O}_8^{2-}$  addition. Irradiance was then started, and the experiment was carried out for up to two hours. Samples were periodically taken from the solution to determine the concentration of CECs, catechol, consumption of oxidant, dissolved iron and pH. Those submitted to HPLC analysis were diluted 1:0.4 with methanol to quench the excess of oxidant.

### 3.4. Analytical Measurements

The concentration of each CEC was determined by HPLC (Hitachi Chromaster chromatograph; VWR) with a Chromaster System Manager (v1.1). A Prevail Hichrom column (C18-Select;  $250 \times 4.6 \text{ mm}$ ;  $5 \mu\text{m}$ ) was employed as the stationary phase. The mobile phase consisted of a binary mixture of acetonitrile (A) and a 10 mM aqueous solution of formic acid (B). The linear gradient was operated from 10% A to 90% A in 25 min. Re-equilibration time was 7 min. A flow rate of  $1 \text{ mL}\cdot\text{min}^{-1}$  was used. The wavelength used for the quantification of the CECs was 225 nm. The same procedure was used for monitoring catechol.

$\text{H}_2\text{O}_2$  measurements were performed through peroxide tests (colorimetric test strips method, 0.5–25 and 1–100 mg/L  $\text{H}_2\text{O}_2$  Merckoquant–Merck, Madrid, Spain). In parallel, the PDS and  $\text{H}_2\text{O}_2$  concentrations were measured in all of the experiments spectrophotometrically (UH5300—Hitachi Spectrophotometer) with a iodometric titration and the metavanadate method, respectively [59,61]. pH and conductivity were determined by the VWR pHenomenal MU61002.

### 3.5. Data Treatment

Time resolved data of the cumulative concentration of the  $\Sigma$  CECs were obtained and degradation curves were represented according to the irradiation exposure time. Through these curves, the time required to degrade the CECs mixture to 50% of its initial concentration ( $t_{50\%}$ ) can be obtained as variable response through linear interpolation.

A response surface methodology based on Doehlert design was employed as a chemometric tool. This is a convenient methodology to investigate the effect of operational variables [62]. In this study, the efficiency of photo-driven processes was explored in two salinities, i.e., low saltwater ( $[\text{Cl}^-] = 1 \text{ g}\cdot\text{L}^{-1}$ , LSW) and saltwater ( $[\text{Cl}^-] = 30 \text{ g}\cdot\text{L}^{-1}$ , SW), and two oxidants ( $\text{H}_2\text{O}_2$ ,  $\text{S}_2\text{O}_8^{2-}$ ). An experimental domain was defined by considering two different operational factors i.e., pH which was studied at three levels between 3 and 7 and catechol, concentration of which was varied between 1 and  $25 \text{ mg}\cdot\text{L}^{-1}$  at 5 levels.

According to the experimental design, the number of experiments required is given by  $N = k^2 + k + C_0$ , where  $k$  is the number of analyzed variables (2 in this study) plus two replicates of the central level,  $C_0$ . Experimental conditions of all experiments can be found in Table 2. The irradiation time required to degrade the sum of the pollutant's concentration to 50% of its initial value ( $t_{50\%}$ ) was used as the response.

Statistical analysis and response surface model fitting by means of the least squares method was obtained with Statgraphics® Centurion 18 (Version 18.1.12-Statpoints Technologies, Inc., The Plains, VA, USA).

#### 4. Conclusions

According to the results obtained, catechol was shown to be a worthy assistant for the photo-Fenton process, in both LSW and SW, since promising times for degrading different CECs were obtained, i.e.,  $t_{50\%}$  values are reached in less than 60 min with  $[CAT] > 7 \text{ mg}\cdot\text{L}^{-1}$  in all pH ranges tested. Best operational ranges are estimated around pH 5 and  $[CAT] = 10\text{--}15 \text{ mg}\cdot\text{L}^{-1}$ . The enhancement of the process is clearly stronger in the case of highly saline waters, which is the matrix where the performance is worse. On the other hand, in the PDS system, the  $[CAT]$  have a significant influence on the  $\Sigma$  CECs degradation, rather than the pH, highlighting that  $[CAT] > 15 \text{ mg}\cdot\text{L}^{-1}$  implies adverse effects on CECs degradation. The PDS-based system was strongly dependent on salinity conditions and nature of CECs. It is important to highlight that catechol compound is efficiently eliminated in both systems within the degradation process.

The good performance of the CAT-based photo-Fenton reaction in SW is of great interest, as it opens the door to a niche application of these processes, namely the treatment of seawater effluents, such as fish-farms or ballast waters. Moreover, the use of persulfate-based processes might be of interest for the group of pollutants that show scarce selectivity between hydroxyl radical and other less reactive species.

It is noteworthy indicating that phenolic moieties can be found in humic substances, that have been demonstrated to enhance the photo-Fenton reaction at mild pH, although its structure is too complex to perform an accurate mechanistic study. If catechol (and in general phenolic moieties) can be assumed to be among the active sites of these macromolecules, they can be proposed as models to gain further insight into the role of humic substances in the photo-oxidation of xenobiotics. Hence, further research to study the role of other aromatics moieties (e.g., phenolic acids) might be of interest in the future, but also research on the involvement of transient reactive species by means of photophysical measurements.

**Supplementary Materials:** The following are available online at <https://www.mdpi.com/2073-4344/11/3/372/s1>, Equations (S1)–(S3): Response surface models obtained; Figure S1: 3D estimated response surface obtained for the  $\Sigma$  CECs in LSW and SW in the photo-Fenton system with the presence of catechol (CAT) as assistant (Fe(III)/H<sub>2</sub>O<sub>2</sub>/CAT); Figure S2: H<sub>2</sub>O<sub>2</sub> consumption for the photo-Fenton system at different operational conditions in the different studied water matrices; Figure S3: 3D estimated response surface obtained for the  $\Sigma$ CECs in LSW with the presence of catechol (CAT) as assistant (Fe(III)/PDS/CAT); Figure S4: PDS consumption for the irradiated Fe(III)/PDS/CAT system at different operational conditions in LSW and SW; Table S1-S3: Analysis of variance (ANOVA).

**Author Contributions:** Conceptualization, J.M.-A. and A.A.; methodology, J.M.-A., L.S.-J. and A.A.; validation, J.M.-A., L.S.-J. and A.A.; formal analysis, J.M.-A., P.G.-N.; investigation, J.M.-A., I.V. and P.G.-N.; resources, A.A.; data curation, J.M.-A., I.V. and P.G.-N.; writing—original draft preparation, J.M.-A. and A.A.; writing—review and editing, J.M.-A., L.S.-J., P.G.-N. and A.A.; visualization, J.M.-A. and A.A.; supervision, A.A.; project administration, A.A.; funding acquisition, J.M.-A. and A.A. All authors have read and agreed to the published version of the manuscript.

**Funding:** This research was funded by Spanish Ministry of Science, Innovation and Universities, AEI and FEDER for funding under the CalypSol Project (Ref: RTI2018-097997-B-C31) and the co-funding by the 2014–2020 ERDF Operational Programme and by the Department of Economy, Knowledge, Business and University of the Regional Government of Andalusia (Spain). Ref.: FEDER-UCA18-108023. J. Moreno-Andrés is grateful to Generalitat Valenciana (Spain) (APOSTD/2019/207) and the financial support from the European Social Fund (ESF).

**Conflicts of Interest:** The authors declare no conflict of interest.

## References

- Rizzo, L.; Malato, S.; Antakyali, D.; Beretsou, V.G.; Đolić, M.B.; Gernjak, W.; Heath, E.; Ivancev-Tumbas, I.; Karaolia, P.; Lado Ribeiro, A.R.; et al. Consolidated vs. new advanced treatment methods for the removal of contaminants of emerging concern from urban wastewater. *Sci. Total Environ.* **2019**, *655*, 986–1008. [CrossRef]
- Fenton, H.J.H. Oxidation of tartaric acid in presence of iron. *J. Chem. Soc. Trans.* **1894**, *65*, 899–910. [CrossRef]
- Haber, F.; Weiss, J. The catalytic decomposition of hydrogen peroxide by iron salts. *Proc. R. Soc. Lond. Ser. A Math. Phys. Sci.* **1934**, *147*, 332–351. [CrossRef]
- Pignatello, J.J.; Oliveros, E.; MacKay, A. Advanced oxidation processes for organic contaminant destruction based on the fenton reaction and related chemistry. *Crit. Rev. Environ. Sci. Technol.* **2006**, *36*, 1–84. [CrossRef]
- Barb, W.G.; Baxendale, J.H.; George, P.; Hargrave, K.R. Reactions of ferrous and ferric ions with hydrogen peroxide. Part II.—The ferric ion reaction. *Trans. Faraday Soc.* **1951**, *47*, 591–616. [CrossRef]
- Gligorovski, S.; Strekowski, R.; Barbati, S.; Vione, D. Environmental Implications of Hydroxyl Radicals ( $\bullet\text{OH}$ ). *Chem. Rev.* **2015**, *115*, 13051–13092. [CrossRef]
- Pérez-Almeida, N.; González, A.G.; Santana-Casiano, J.M.; González-Dávila, M. Iron and copper redox interactions in UV-seawater: A kinetic model approach. *Chem. Geol.* **2019**, *506*, 149–161. [CrossRef]
- Lueder, U.; Jørgensen, B.B.; Kappler, A.; Schmidt, C. Photochemistry of iron in aquatic environments. *Environ. Sci. Process. Impacts* **2020**, *22*, 12–24. [CrossRef]
- Giannakis, S.; López, M.I.P.; Spuhler, D.; Pérez, J.A.S.; Ibáñez, P.F.; Pulgarin, C. Solar disinfection is an augmentable, in situ-generated photo-Fenton reaction—Part 2: A review of the applications for drinking water and wastewater disinfection. *Appl. Catal. B Environ.* **2016**, *198*, 431–446. [CrossRef]
- Olmez-Hanci, T.; Arslan-Alaton, I. Comparison of sulfate and hydroxyl radical based advanced oxidation of phenol. *Chem. Eng. J.* **2013**, *224*, 10–16. [CrossRef]
- Clarizia, L.; Russo, D.; Di Somma, I.; Marotta, R.; Andreozzi, R. Homogeneous photo-Fenton processes at near neutral pH: A review. *Appl. Catal. B Environ.* **2017**, *209*, 358–371. [CrossRef]
- Dong, H.; Qiang, Z.; Hu, J.; Sans, C. Accelerated degradation of iopamidol in iron activated persulfate systems: Roles of complexing agents. *Chem. Eng. J.* **2017**, *316*, 288–295. [CrossRef]
- Sandy, M.; Butler, A. Microbial iron acquisition: Marine and terrestrial siderophores. *Chem. Rev.* **2009**, *109*, 4580–4595. [CrossRef]
- Gledhill, M.; Buck, K.N. The organic complexation of iron in the marine environment: A review. *Front. Microbiol.* **2012**, *3*, 1–17. [CrossRef] [PubMed]
- Avdeef, A.; Sofen, S.R.; Bregante, T.L.; Raymond, K.N. Coordination chemistry of microbial iron transport compounds. 9.1 Stability constants for catechol models of enterobactin. *J. Am. Chem. Soc.* **1978**, *100*, 5362–5370. [CrossRef]
- Årstøl, E.; Hohmann-Marriott, M.F. Cyanobacterial siderophores—Physiology, structure, biosynthesis, and applications. *Mar. Drugs* **2019**, *17*, 281. [CrossRef]
- García-Negueroles, P.; García-Ballesteros, S.; Amat, A.M.; Laurenti, E.; Arques, A.; Santos-Juanes, L. Unveiling the dependence between hydroxyl radical generation and performance of fenton systems with complexed iron. *ACS Omega* **2019**, *4*, 21698–21703. [CrossRef] [PubMed]
- García-Ballesteros, S.; Grimalt, J.; Berto, S.; Minella, M.; Laurenti, E.; Vicente, R.; López-Pérez, M.F.; Amat, A.M.; Bianco Prevot, A.; Arques, A. New route for valorization of oil mill wastes: Isolation of humic-like substances to be employed in solar-driven processes for pollutants removal. *ACS Omega* **2018**, *3*, 13073–13080. [CrossRef] [PubMed]
- Gomis, J.; Carlos, L.; Bianco Prevot, A.; Teixeira, A.C.S.C.; Mora, M.; Amat, A.M.; Vicente, R.; Arques, A. Bio-based substances from urban waste as auxiliaries for solar photo-Fenton treatment under mild conditions: Optimization of operational variables. *Catal. Today* **2015**, *240*, 39–45. [CrossRef]
- Whitby, H.; Planquette, H.; Cassar, N.; Bucciarelli, E.; Osburn, C.L.; Janssen, D.J.; Cullen, J.T.; González, A.G.; Völker, C.; Sarthou, G. A call for refining the role of humic-like substances in the oceanic iron cycle. *Sci. Rep.* **2020**, *10*, 6144. [CrossRef] [PubMed]
- Huang, X.; Peng, Y.; Xu, J.; Wu, F.; Mailhot, G. Iron(III)-induced photooxidation of arsenite in the presence of carboxylic acids and phenols as model compounds of natural organic matter. *Chemosphere* **2021**, *263*, 128142. [CrossRef]
- Xu, S.; Zhao, J.; Yu, Q.; Qiu, X.; Sasaki, K. Understanding how specific functional groups in humic acid affect the sorption mechanisms of different calcinated layered double hydroxides. *Chem. Eng. J.* **2020**, *392*, 123633. [CrossRef]
- Perron, N.R.; Wang, H.C.; Deguire, S.N.; Jenkins, M.; Lawson, M.; Brumaghim, J.L. Kinetics of iron oxidation upon polyphenol binding. *Dalt. Trans.* **2010**, *39*, 9982–9987. [CrossRef]



24. Barbeau, K.; Rue, E.L.; Trick, C.G.; Bruland, K.W.; Butler, A. Photochemical reactivity of siderophores produced by marine heterotrophic bacteria and cyanobacteria based on characteristic Fe(III) binding groups. *Limnol. Oceanogr.* **2003**, *48*, 1069–1078. [CrossRef]
25. Chen, F.; Ma, W.; He, J.; Zhao, J. Fenton degradation of malachite green catalyzed by aromatic additives. *J. Phys. Chem. A* **2002**, *106*, 9485–9490. [CrossRef]
26. Xiao, J.; Wang, C.; Liu, H. Fenton-like degradation of dimethyl phthalate enhanced by quinone species. *J. Hazard. Mater.* **2020**, *382*, 121007. [CrossRef]
27. Santana-Casiano, J.M.; González-Dávila, M.; González, A.G.; Millero, F.J. Fe(III) reduction in the presence of Catechol in seawater. *Aquat. Geochem.* **2010**, *16*, 467–482. [CrossRef]
28. Zanta, C.L.P.S.; Friedrich, L.C.; Machulek, A.; Higa, K.M.; Quina, F.H. Surfactant degradation by a catechol-driven Fenton reaction. *J. Hazard. Mater.* **2010**, *178*, 258–263. [CrossRef] [PubMed]
29. Nichela, D.A.; Donadelli, J.A.; Caram, B.F.; Haddou, M.; Rodriguez Nieto, F.J.; Oliveros, E.; García Einschlag, F.S. Iron cycling during the autocatalytic decomposition of benzoic acid derivatives by Fenton-like and photo-Fenton techniques. *Appl. Catal. B Environ.* **2015**, *170–171*, 312–321. [CrossRef]
30. Calza, P.; Campra, L.; Pelizzetti, E.; Minero, C. Role of H<sub>2</sub>O<sub>2</sub> in the photo-transformation of phenol in artificial and natural seawater. *Sci. Total Environ.* **2012**, *431*, 84–91. [CrossRef] [PubMed]
31. Lofrano, G.; Rizzo, L.; Grassi, M.; Belgiorio, V. Advanced oxidation of catechol: A comparison among photocatalysis, Fenton and photo-Fenton processes. *Desalination* **2009**, *249*, 878–883. [CrossRef]
32. Xiao, J.; Wang, C.; Lyu, S.; Liu, H.; Jiang, C.; Lei, Y. Enhancement of Fenton degradation by catechol in a wide initial pH range. *Sep. Purif. Technol.* **2016**, *169*, 202–209. [CrossRef]
33. Lulijwa, R.; Rupia, E.J.; Alfaro, A.C. Antibiotic use in aquaculture, policies and regulation, health and environmental risks: A review of the top 15 major producers. *Rev. Aquac.* **2019**, *2000*, 1–24. [CrossRef]
34. Ganiyu, S.O.; Van Hullebusch, E.D.; Cretin, M.; Esposito, G.; Oturan, M.A. Coupling of membrane filtration and advanced oxidation processes for removal of pharmaceutical residues: A critical review. *Sep. Purif. Technol.* **2015**, *156*, 891–914. [CrossRef]
35. García-Vaquero, N.; Lee, E.; Jiménez Castañeda, R.; Cho, J.; López-Ramírez, J.A. Comparison of drinking water pollutant removal using a nanofiltration pilot plant powered by renewable energy and a conventional treatment facility. *Desalination* **2014**, *347*, 94–102. [CrossRef]
36. Vicente-Cera, I.; Moreno-Andrés, J.; Amaya-Vías, D.; Biel-Maeso, M.; Pintado-Herrera, M.G.; Lara-Martín, P.A.; Acevedo-Merino, A.; López-Ramírez, J.A.; Nebot, E. Chemical and microbiological characterization of cruise vessel wastewater discharges under repair conditions. *Ecotoxicol. Environ. Saf.* **2019**, *169*, 68–75. [CrossRef]
37. Carra, I.; Sánchez Pérez, J.A.; Malato, S.; Autin, O.; Jefferson, B.; Jarvis, P. Performance of different advanced oxidation processes for tertiary wastewater treatment to remove the pesticide acetamiprid. *J. Chem. Technol. Biotechnol.* **2016**, *91*, 72–81. [CrossRef]
38. Gavrilescu, M.; Demnerová, K.; Aamand, J.; Agathos, S.; Fava, F. Emerging pollutants in the environment: Present and future challenges in biomonitoring, ecological risks and bioremediation. *N. Biotechnol.* **2015**, *32*, 147–156. [CrossRef]
39. Álvarez-Muñoz, D.; Llorca, M.; Blasco, J.; Barceló, D. *Chapter 1—Contaminants in the Marine Environment*; Blasco, J., Chapman, P.M., Campana, O., Hampel, M., Eds.; Academic Press: Cambridge, MA, USA, 2016; pp. 1–34, ISBN 9780128033715. [CrossRef]
40. Lara-Martín, P.A.; Chiaia-Hernández, A.C.; Biel-Maeso, M.; Baena-Nogueras, R.M.; Hollender, J. Tracing urban wastewater contaminants into the atlantic ocean by nontarget screening. *Environ. Sci. Technol.* **2020**, *54*, 3996–4005. [CrossRef]
41. Gomis, J.; Bianco Prevot, A.; Montoneri, E.; González, M.C.; Amat, A.M.; Mártire, D.O.; Arques, A.; Carlos, L. Waste sourced bio-based substances for solar-driven wastewater remediation: Photodegradation of emerging pollutants. *Chem. Eng. J.* **2014**, *235*, 236–243. [CrossRef]
42. Wu, Y.; Monfort, O.; Dong, W.; Brigante, M.; Mailhot, G. Enhancement of iron-mediated activation of persulfate using catechin: From generation of reactive species to atenolol degradation in water. *Sci. Total Environ.* **2019**, *697*. [CrossRef]
43. Kiwi, J.; Lopez, A.; Nadtochenko, V. Mechanism and kinetics of the OH-radical intervention during Fenton oxidation in the presence of a significant amount of radical scavenger (Cl<sup>-</sup>). *Environ. Sci. Technol.* **2000**, *34*, 2162–2168. [CrossRef]
44. Rommozzi, E.; Giannakis, S.; Giovannetti, R.; Vione, D.; Pulgarin, C. Detrimental vs. beneficial influence of ions during solar (SODIS) and photo-Fenton disinfection of *E. coli* in water: (bi)carbonate, chloride, nitrate and nitrite effects. *Appl. Catal. B Environ.* **2020**, *270*, 118877. [CrossRef]
45. Machulek Amilcar, J.; Moraes Jose, E.F.; Vautier-Giongo, C.; Silverio Cristina, A.; Friedrich Leidi, C.; Nascimento Claudio, A.O.; Gonzalez Monica, C.; Quina Frank, H. Abatement of the inhibitory effect of chloride anions on the photo-Fenton process. *Environ. Sci. Technol.* **2007**, *41*, 8459–8463. [CrossRef]
46. Yang, Y.; Pignatello, J.J.; Ma, J.; Mitch, W.A. Comparison of halide impacts on the efficiency of contaminant degradation by sulfate and hydroxyl radical-based advanced oxidation processes (AOPs). *Environ. Sci. Technol.* **2014**, *48*, 2344–2351. [CrossRef]
47. Moreno-Andrés, J.; Farinango, G.; Romero-Martínez, L.; Acevedo-Merino, A.; Nebot, E. Application of persulfate salts for enhancing UV disinfection in marine waters. *Water Res.* **2019**, *163*, 114866. [CrossRef] [PubMed]
48. Nihemaiti, M.; Miklos, D.B.; Hübner, U.; Linden, K.G.; Drewes, J.E.; Croué, J.P. Removal of trace organic chemicals in wastewater effluent by UV/H<sub>2</sub>O<sub>2</sub> and UV/PDS. *Water Res.* **2018**, *145*, 487–497. [CrossRef] [PubMed]
49. Lei, Y.; Cheng, S.; Luo, N.; Yang, X.; An, T. Rate constants and mechanisms of the reactions of Cl<sup>•</sup> and Cl<sub>2</sub><sup>•-</sup> with Trace Organic Contaminants. *Environ. Sci. Technol.* **2019**, *53*, 11170–11182. [CrossRef]

50. Ye, T.; Wei, Z.; Spinney, R.; Tang, C.J.; Luo, S.; Xiao, R.; Dionysiou, D.D. Chemical structure-based predictive model for the oxidation of trace organic contaminants by sulfate radical. *Water Res.* **2017**, *116*, 106–115. [CrossRef] [PubMed]
51. Lu, X.; Shao, Y.; Gao, N.; Chen, J.; Deng, H.; Chu, W.; An, N.; Peng, F. Investigation of clofibric acid removal by UV/persulfate and UV/chlorine processes: Kinetics and formation of disinfection byproducts during subsequent chlor(am)ination. *Chem. Eng. J.* **2018**, *331*, 364–371. [CrossRef]
52. Li, B.; Ma, X.; Deng, J.; Li, Q.; Chen, W.; Li, G.; Chen, G.; Wang, J. Comparison of acetaminophen degradation in UV-LED-based advance oxidation processes: Reaction kinetics, radicals contribution, degradation pathways and acute toxicity assessment. *Sci. Total Environ.* **2020**, *723*, 137993. [CrossRef]
53. Deemter, D.; Oller, I.; Amat, A.M.; Malato, S. Effect of salinity on preconcentration of contaminants of emerging concern by nanofiltration: Application of solar photo-Fenton as a tertiary treatment. *Sci. Total Environ.* **2020**, *756*, 143593. [CrossRef] [PubMed]
54. Neta, P.; Madhavan, V.; Zemel, H.; Fessenden, R.W. Rate Constants and Mechanism of Reaction of sulfate radical anion with Aromatic Compounds. *J. Am. Chem. Soc.* **1977**, *99*, 163–164. [CrossRef]
55. Buxton, G.V.; Greenstock, C.L.; Helman, W.P.; Ross, A.B. Critical Review of rate constants for reactions of hydrated electrons, hydrogen atoms and hydroxyl radicals (OH/O<sup>-</sup>) in Aqueous Solution. *J. Phys. Chem. Ref. Data* **1988**, *17*, 513–886. [CrossRef]
56. Neta, P.; Huie, R.E.; Ross, A.B. Rate Constants for Reactions of Inorganic Radicals in Aqueous Solution. *J. Phys. Chem. Ref. Data* **1988**, *17*, 1027–1284. [CrossRef]
57. Wang, L.; Zhang, Q.; Chen, B.; Bu, Y.; Chen, Y.; Ma, J.; Rosario-Ortiz, F.L.; Zhu, R. Some issues limiting photo(cata)lysis application in water pollutant control: A critical review from chemistry perspectives. *Water Res.* **2020**, *174*, 115605. [CrossRef] [PubMed]
58. Nichela, D.; Haddou, M.; Benoit-Marquié, F.; Maurette, M.T.; Oliveros, E.; García Einschlag, F.S. Degradation kinetics of hydroxy and hydroxynitro derivatives of benzoic acid by fenton-like and photo-fenton techniques: A comparative study. *Appl. Catal. B Environ.* **2010**, *98*, 171–179. [CrossRef]
59. Sciscenko, I.; Garcia-Ballesteros, S.; Sabater, C.; Castillo, M.A.; Escudero-Oñate, C.; Oller, I.; Arques, A. Monitoring photolysis and (solar photo)-Fenton of enrofloxacin by a methodology involving EEM-PARAFAC and bioassays: Role of pH and water matrix. *Sci. Total Environ.* **2020**, *719*, 137331. [CrossRef]
60. Santos-Juanes, L.; García Einschlag, F.S.; Amat, A.M.; Arques, A. Combining ZVI reduction with photo-Fenton process for the removal of persistent pollutants. *Chem. Eng. J.* **2017**, *310*, 484–490. [CrossRef]
61. Liang, C.; Huang, C.F.; Mohanty, N.; Kurakalva, R.M. A rapid spectrophotometric determination of persulfate anion in ISCO. *Chemosphere* **2008**, *73*, 1540–1543. [CrossRef] [PubMed]
62. Ferreira, S.L.C.; Dos Santos, W.N.L.; Quintella, C.M.; Neto, B.B.; Bosque-Sendra, J.M. Doehlert matrix: A chemometric tool for analytical chemistry—Review. *Talanta* **2004**, *63*, 1061–1067. [CrossRef] [PubMed]

Article

# Peroxymonosulfate Activation by Different Synthesized CuFe-MOFs: Application for Dye, Drugs, and Pathogen Removal

Antia Fdez-Sanromán, Bárbara Lomba-Fernández, Marta Pazos, Emilio Rosales and Angeles Sanromán \* 

CINTECX, Department of Chemical Engineering, Universidade de Vigo, 36310 Vigo, Spain; antia.fernandez.sanroman@uvigo.gal (A.F.-S.); barbara.lomba.fernandez@uvigo.gal (B.L.-F.); mcurras@uvigo.gal (M.P.); emiliorv@uvigo.gal (E.R.)

\* Correspondence: sanroman@uvigo.gal

**Abstract:** In this study, three CuFe-MOFs were successfully synthesized by a solvothermal process by changing the ratio of solvents, salts, or temperature. These MOFs named CuFe(BDC-NH<sub>2</sub>)<sub>R</sub>, CuFe(BDC-NH<sub>2</sub>)<sub>S</sub>, and CuFe(BDC-NH<sub>2</sub>)<sub>D</sub> showed rod-shaped, spindle-like, and diamond-like structures, respectively. The CuFe(BDC-NH<sub>2</sub>)<sub>D</sub> and CuFe(BDC-NH<sub>2</sub>)<sub>S</sub> were found to exhibit an improved PMS activation for Rhodamine B removal attaining levels around 92%. Their effective removal capability was investigated as a function of the pH, catalyst dosage, and the effect of the application of UV radiation. The best degradation system was photo-assisted activation of PMS when CuFe(BDC-NH<sub>2</sub>)<sub>D</sub> and CuFe(BDC-NH<sub>2</sub>)<sub>S</sub> were used. Under these conditions, the degradation of a mixture of antibiotic and anti-inflammatory drugs (sulfamethoxazole and antipyrine) was evaluated with the results revealing the total degradation of both drugs after 1 h. A higher antibacterial activity was attained with the system CuFe(BDC-NH<sub>2</sub>)<sub>R</sub>/PMS due to the high copper content with respect to the others.

**Keywords:** CuFe-MOFs; PMS activation; dye removal; drug degradation; antibacterial activity

**Citation:** Fdez-Sanromán, A.; Lomba-Fernández, B.; Pazos, M.; Rosales, E.; Sanromán, A. Peroxymonosulfate Activation by Different Synthesized CuFe-MOFs: Application for Dye, Drugs, and Pathogen Removal. *Catalysts* **2023**, *13*, 820. <https://doi.org/10.3390/catal13050820>

Academic Editors: Juan José Rueda-Márquez, Javier Moreno-Andrés and Irina Levchuk

Received: 21 March 2023

Revised: 23 April 2023

Accepted: 25 April 2023

Published: 29 April 2023



**Copyright:** © 2023 by the authors. Licensee MDPI, Basel, Switzerland. This article is an open access article distributed under the terms and conditions of the Creative Commons Attribution (CC BY) license (<https://creativecommons.org/licenses/by/4.0/>).

## 1. Introduction

In recent years, sulfate radicals-based advanced oxidation processes (SR-AOPs) or peroxymonosulfate (PMS) activation using catalysts have drawn notable attention in wastewater treatment due to their high efficiency and cost-effectiveness. Such a process does not require external energy and offers several operational advantages, including its application at a wide range of pHs [1,2]. There are several pathways by which the O–O bond of PMS may be disrupted, including heating, ultrasound, light, and transition metals. Among them, transition metal-based material activation using Co, Cu, Fe, or Mn seems to be the most usual method [3–6].

Several studies have demonstrated the high degradation capability of sulfate radicals generated in SR-AOPs when used to remove organic contaminants such as dyes, phenolic and pharmaceuticals compounds, pesticides, and pathogens [7,8]. However, to improve its application several drawbacks must be overcome. Among these factors is the difficulty of recovering and recycling the catalyst in a homogeneous process, which is one reason why heterogeneous catalysts are preferred for PMS activation. The main advantages of these heterogeneous catalysts are as follows: (i) reusability and easiness for the separation from the reaction system; (ii) minimum release of metal catalyst that could be considered as a secondary pollutant; (iii) ability to operate in extreme conditions; (iv) higher effectiveness at a low economical cost [9–11]. Among the heterogeneous catalysts, metal–organic frameworks (MOFs) have drawn great interest because of their high surface area, enormous framework flexibility, and huge structural variety, which facilitate the development of tailored properties materials, as well as tunable pore sizes and catalytic activities [12,13]. By combining metallic ions with organic linkers, MOFs are synthesized producing crystalline

porous structures with periodic structures coordinated with inorganic metal nodes and organic bridge ligands. They are capable of serving as heterogeneous catalysts as they possess exposed metal sites in functional pores. Thus, their application in this field has received considerable attention in recent years [14,15].

According to the literature, many MOFs exhibit excellent catalytic properties for PMS activation due to the abundance of oxygen vacancies (as active sites), synergistic mechanisms, and high efficiency [16]. Considering that MOFs are composed of both organic and inorganic components, there is a greater degree of freedom when selecting the starting materials. The versatility of MOFs is attributed to their ability to interact with metal ions and organic ligands in a variety of ways. Furthermore, a variety of conditions can be used to achieve the desired reaction. The presence of two or more metals in a matter can improve their catalytic activity. Mixed metals usually have high stability and low leaching compared to single metals [17].

In this context, recent research has been conducted on the design and synthesis of bimetallic–organic frameworks that take advantage of the synergistic effects of metals. As compared to single-metal MOFs, these MOFs are likely to provide higher activity, stability, and surface area [18]. Bimetallic CuCo-MOFs were synthesized, and it was determined that the introduction of another metal ion into MOFs could significantly enhance the catalytic performance [19,20]. A bimetallic MOF containing Fe and Co showed improved catalytic activity as compared to a monometallic MOF containing a single metal. However, it was also reported that the process could be strongly affected by the shape of the FeCo MOF nanocrystals [21]. Thus, MOFs such as MIL-88B-Fe and MIL-101-Fe, with identical chemical compositions but different exposed facets or shapes, exhibited different activity, MIL-88B-Fe being around five times higher than that of MIL-101-Fe [22]. Similarly, Liao et al. [23] determined that the morphology of MIL-88A-Fe greatly affects its catalytic performance. By a solvent-mediated method, they synthesized several shape-controlled MIL-88A-Fe nanocrystals with different oriented facets and confirmed that the nucleation rate of the MOF defines the morphology or particle size. They synthesized three MIL-88A-Fe with different morphologies such as rod-shaped (100–300 nm length), spindle-like, and diamond-like structures showing different catalytic behaviors.

The catalytic performance is significantly influenced by the composition, structure, and properties of MOFs. For this reason, in this study, different methods were evaluated to synthesize bimetallic CuFe-MOFs and to determine their influence on the synthesis conditions (temperature and solvent compositions) on the catalytic performance for the activation of PMS. Thus, three CuFe-MOFs were prepared by the solvothermal process: two of them using water-free solvents and different salts at 150 °C, CuFe(BDC-NH<sub>2</sub>)<sub>S</sub> and CuFe(BDC-NH<sub>2</sub>)<sub>D</sub>, respectively, and the other one in an aqueous solvent at 90 °C, CuFe(BDC-NH<sub>2</sub>)<sub>R</sub>. The catalytic performance of these bimetallic MOFs was assessed for the removal of dyes, drugs, and pathogens.

## 2. Results

### 2.1. Preliminary Catalytic Performance

Based on the literature, Cu-MOF is becoming a promising alternative transition metal-based heterogeneous PMS activator [24]. However, the use of bimetallic MOFs could provide synergistic effects to increase their catalytic activity. Thus, a comparative study among the Cu(BDC-NH<sub>2</sub>)<sub>R</sub> and CuFe(BDC-NH<sub>2</sub>)<sub>R</sub> catalysts, synthesized in the presence of water as described in Section 3, was performed to determine the possible synergistic effects between metals.

The catalytic activity of these two MOFs towards PMS was evaluated by determining the removal rates of Rhodamine B. These tests were conducted operating at natural pH with 0.25 g/L of catalysts and 1 mM of PMS and compared with PMS alone. Around 16% of Rhodamine B was removed in 60 min by direct oxidation of PMS. However, this level was improved in the presence of Cu(BDC-NH<sub>2</sub>)<sub>R</sub> and CuFe(BDC-NH<sub>2</sub>)<sub>R</sub>, attaining removal levels of Rhodamine B around 20% and 45%, respectively. These results demonstrated the

superiority of bimetallic  $\text{CuFe}(\text{BDC-NH}_2)_\text{R}$  over  $\text{Cu}(\text{BDC-NH}_2)_\text{R}$ , which is in accordance with other studies that had reported the synergistic effect in bimetallic catalysts for PMS activation [25]. Based on these results, other synthesis procedures of bimetallic  $\text{CuFe}(\text{BDC-NH}_2)$  were undertaken to determine their effect on the degradation of Rhodamine B.

The adsorption capabilities of the three different  $\text{CuFe-MOFs}$ , ( $\text{CuFe}(\text{BDC-NH}_2)_\text{R}$ ,  $\text{CuFe}(\text{BDC-NH}_2)_\text{S}$ , and  $\text{CuFe}(\text{BDC-NH}_2)_\text{D}$ ) for dye removal were evaluated before catalytic oxidation. As shown in Figure 1, in the presence of catalysts alone, Rhodamine B was rapidly removed within the first five minutes with an adsorption/desorption equilibrium being reached after 60 min. It was observed that  $\text{CuFe}(\text{BDC-NH}_2)_\text{D}$  exhibited the greatest efficiency in the adsorption of Rhodamine B. There was rapid adsorption of Rhodamine B, with nearly 50% of Rhodamine B being adsorbed within 60 min. Then, to determine the ability of these bimetallic-MOFs to activate PMS, Rhodamine B was degraded in the presence of PMS. The performance of all Rhodamine B degradation assays was significantly improved when catalysts and PMS were present simultaneously. Thus,  $\text{CuFe}(\text{BDC-NH}_2)_\text{S}$  and  $\text{CuFe}(\text{BDC-NH}_2)_\text{D}$  achieved the highest removal efficiency with removal percentages of Rhodamine B higher than 90%. For an in-depth understanding of the degradation process, Rhodamine B degradation data were assessed by using three kinetic models (zero-order, pseudo-first-order, and pseudo-second-order). According to the results, Rhodamine B degradation follows a pseudo-first-order kinetic. It is also clear that  $\text{CuFe}(\text{BDC-NH}_2)_\text{S}$  and  $\text{CuFe}(\text{BDC-NH}_2)_\text{D}$  have elevated  $k$  values ( $0.0650$  and  $0.0637 \text{ min}^{-1}$ , respectively), seven times higher than that of  $\text{CuFe}(\text{BDC-NH}_2)_\text{R}$  ( $0.0091 \text{ min}^{-1}$ ). Consequently, the MOF synthesized in an aqueous media at  $90^\circ\text{C}$  showed different catalytic activities (Table 1).

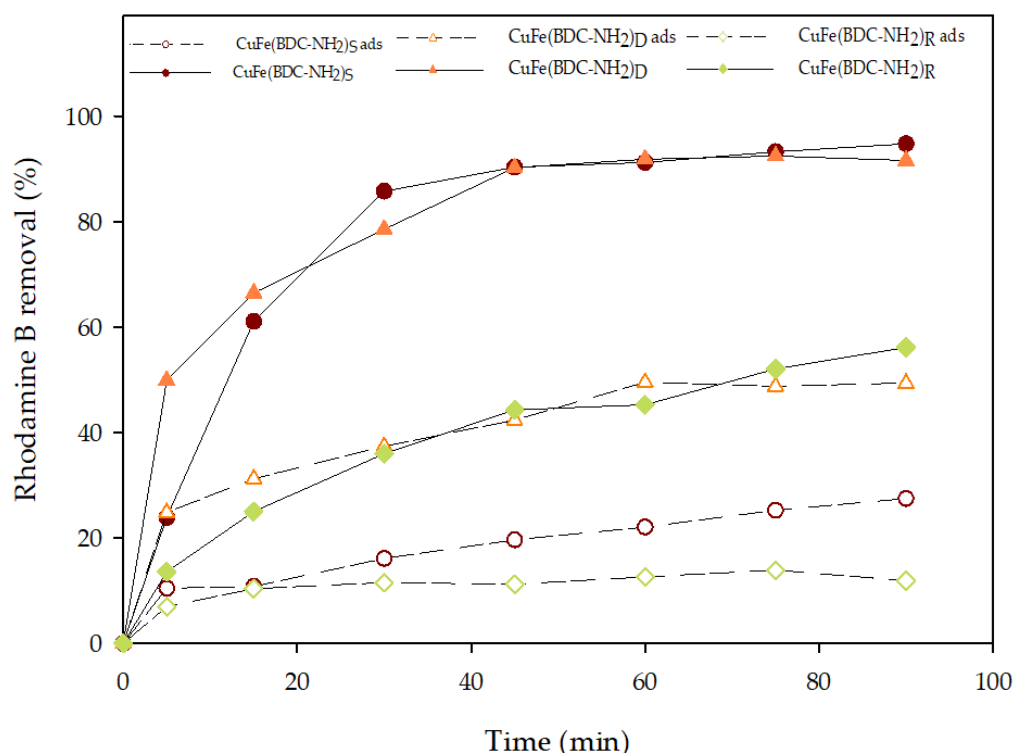
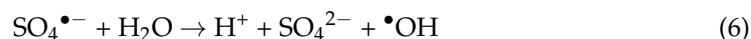
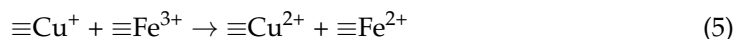
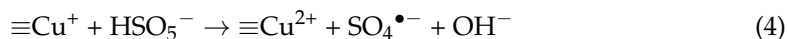
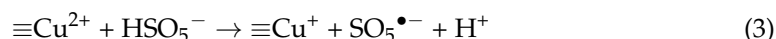
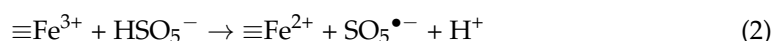
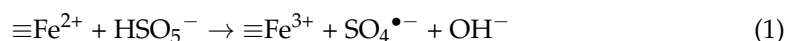


**Figure 1.** Profiles of Rhodamine B by PMS activation and adsorption using the different synthesized  $\text{CuFe-MOFs}$ . Adsorption and PMS assays were performed at natural pH, with a catalyst concentration of  $0.25 \text{ g/L}$  and a PMS concentration of  $1 \text{ mM}$ .

**Table 1.** Pseudo-first-order kinetic parameters and Rhodamine B removal after 60 min.

	Catalyst Dosage (g/L)	k (min <sup>-1</sup> )	R <sup>2</sup>	Rhodamine B Removal at 60 min (%)
CuFe(BDC-NH <sub>2</sub> ) <sub>S</sub>	0.125	0.0316	0.9936	82.52
	0.25	0.0650	0.997	93.22
	0.50	0.0717	0.9735	90.66
CuFe(BDC-NH <sub>2</sub> ) <sub>D</sub>	0.125	0.0112	0.9877	52.47
	0.25	0.0637	0.9709	91.80
	0.50	0.0841	0.9567	94.36
CuFe(BDC-NH <sub>2</sub> ) <sub>R</sub>	0.125	0.0067	0.9896	38.02
	0.25	0.0091	0.9869	45.24
	0.50	0.0215	0.9634	49.89

In these heterogeneous catalytic systems, the reaction between the metal ions Cu and Fe and oxidant PMS occurs in both solutions and catalyst surface. The CuFe-MOF can easily adsorb the pollutants and PMS molecules, and subsequently, with reactions taking place at the catalyst surface generate sulfate and hydroxyl radicals (Equations (1)–(7)).



These reactions explain the synergistic effect observed between Cu<sup>2+</sup> and Fe<sup>3+</sup>, as the generated Cu<sup>+</sup> could undergo disproportionation readily, then the electron transfer from Cu<sup>+</sup> to Fe<sup>3+</sup> produces Fe<sup>2+</sup> which is thermodynamically more stable, increasing the generation of sulfate radical from PMS.

In order to determine the contribution of sulfate and hydroxyl radicals, preliminary experiments were performed with excessive masking agents. As is known, methanol has a distinct masking effect on both radicals, but tertbutyl-alcohol only acts on hydroxyl radical [26]. The results indicated the inhibition of dye removal after their addition. However, the inhibiting effect of methanol was stronger than tertbutyl-alcohol. This fact demonstrated that the sulfate radical plays a major role compared to the hydroxyl radical.

## 2.2. Characterization

The SEM images (Figure 2) depicted the surface structure of the prepared bimetallic CuFe-MOFs, pointing to different types of morphology. CuFe(BDC-NH<sub>2</sub>)<sub>D</sub> showed a diamond-like structure (Figure 2c) that is similar to that observed in other MOFs, which suggested that the amine-functionalized organic ligand would be conducive to forming a regular structure [27]. However, for CuFe(BDC-NH<sub>2</sub>)<sub>S</sub>, two types of morphology, octahedron and spindle-shaped structures, were detected (Figure 2b). If water was used in the

synthesis procedure, a rod-like morphology was observed (Figure 2a) [28]. In addition, the presence of Cu and Fe elements was corroborated by EDS analysis. It was detected that the amount of Cu in the  $\text{CuFe}(\text{BDC-NH}_2)_\text{S}$  and  $\text{CuFe}(\text{BDC-NH}_2)_\text{D}$  samples was lower than the amount used in their preparation. As was concluded by Khosravi et al. [29], this fact could be due to the observed tendency of carboxylate groups to form strong bonds with iron. However, in the presence of water, the elemental mapping proved the existence of a similar percentage of Fe and Cu elements. In addition, the temperature in the synthesis of  $\text{CuFe}(\text{BDC-NH}_2)_\text{S}$  and  $\text{CuFe}(\text{BDC-NH}_2)_\text{D}$  was  $150\text{ }^\circ\text{C}$  which increased the crystal growth rate and size of the MOF [30].

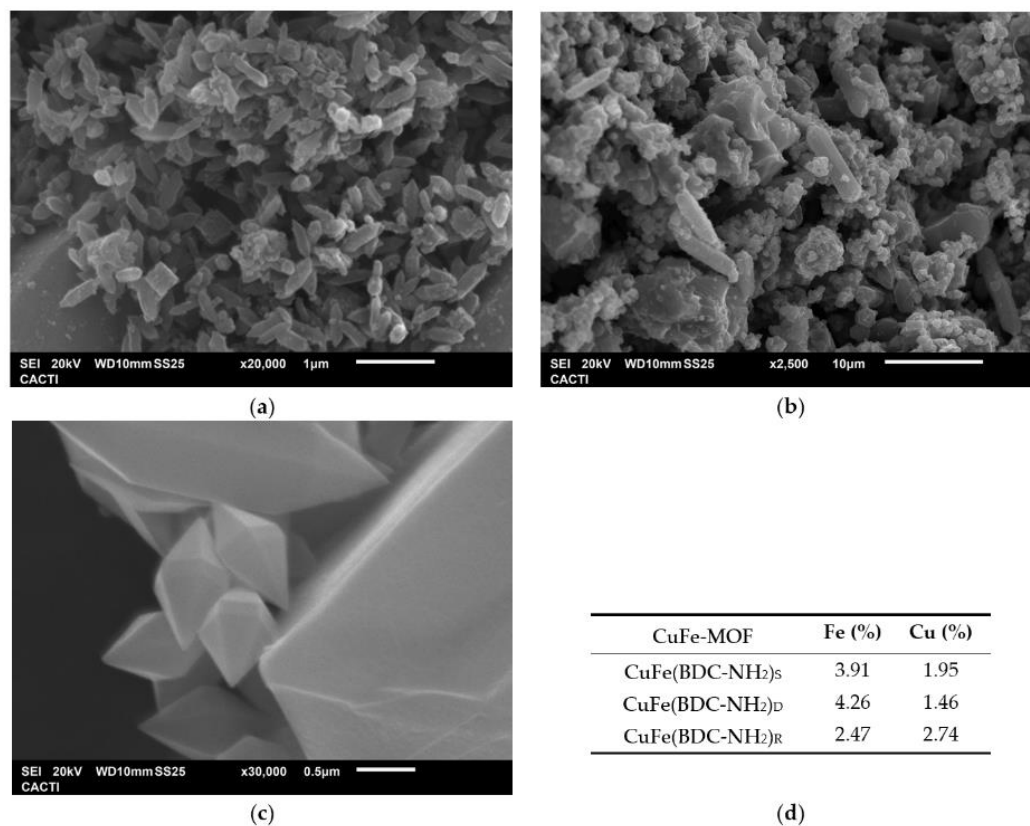


**Figure 2.** SEM images of different CuFe-MOFs: (a)  $\text{CuFe}(\text{BDC-NH}_2)_\text{R}$ ; (b)  $\text{CuFe}(\text{BDC-NH}_2)_\text{S}$ ; and (c)  $\text{CuFe}(\text{BDC-NH}_2)_\text{D}$ . (d) Percentage of Fe and Cu from the EDS analysis.

After analyzing the morphology of the three synthesized MOFs, FTIR and XRD techniques were used to determine the crystalline structure and detect the functional groups of the CuFe-MOFs which could be responsible for the different behavior in the reaction patterns.

First, XRD analysis was carried out to determine whether the MOFs had different crystal lattices. First, it was possible to confirm the differences between CuFe-MOFs due to the Fe/Cu ratio. These differences between the three CuFe-MOFs were investigated by analyzing Fe-MOF-NH<sub>2</sub> and Cu-MOF-NH<sub>2</sub> in the literature. In Figure 3a, the peaks of the three synthesized CuFe-MOFs are shown. Since  $\text{CuFe}(\text{BDC-NH}_2)_\text{R}$  has a Fe/Cu = 1 ratio, it makes the identification of the copper and iron peaks easier. As shown in Figure 3a, the peaks found in  $\text{CuFe}(\text{BDC-NH}_2)_\text{R}$  are intense reflections in  $2\theta = 9.2^\circ, 10.3^\circ, 11.8^\circ,$  and  $16.6^\circ$  and weak reflections in  $2\theta = 13.2^\circ, 18.1^\circ, 18.5^\circ, 20.8^\circ, 24.7^\circ,$  and  $33.7^\circ$ . From the work of Zhong et al. [31], who synthesized a Cu-MOF, and Abdel-Azim et al. [32] a Cu-MOF-NH<sub>2</sub>, it has been possible to associate the peaks with the  $2\theta$  values of  $11.8^\circ, 18.1^\circ,$  and  $24.7^\circ$ . In addition, a small peak at  $2\theta = 33.7^\circ$  was noted. Considering the Fe/Cu ratios of each CuFe-MOFs, it is logical that the intensity and appearance of these peaks are higher in  $\text{CuFe}(\text{BDC-NH}_2)_\text{R}$  than in  $\text{CuFe}(\text{BDC-NH}_2)_\text{D}$ . In fact, in  $\text{CuFe}(\text{BDC-NH}_2)_\text{D}$ ,

the  $33.7^\circ$  peak was not detected and the  $24.7^\circ$  peak had a low intensity. This fact may be due to the low copper content (1.46% Cu) compared to  $\text{CuFe}(\text{BDC-NH}_2)_\text{S}$  (1.95% Cu) and  $\text{CuFe}(\text{BDC-NH}_2)_\text{R}$  (2.74% Cu). However, although  $\text{CuFe}(\text{BDC-NH}_2)_\text{S}$  has a slight increase in copper content, compared to  $\text{CuFe}(\text{BDC-NH}_2)_\text{D}$ , all the aforementioned copper peaks were detected except the  $2\theta = 11.8^\circ$ .

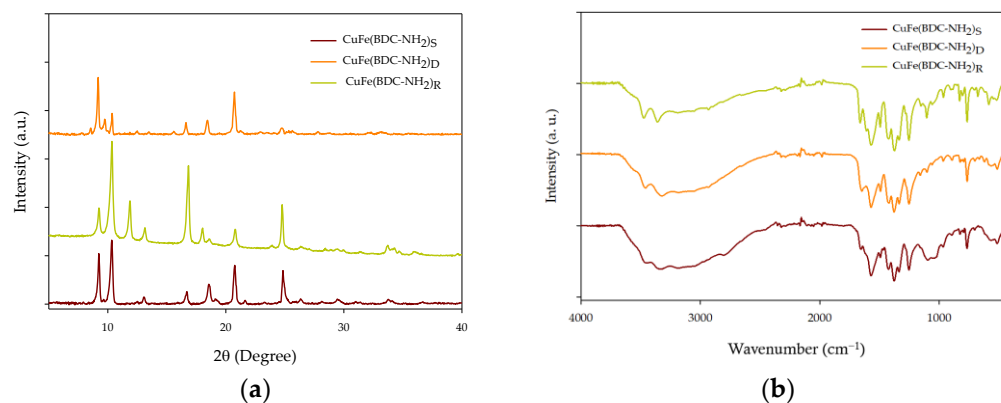


**Figure 3.** CuFe-MOF characterization: (a) XRD patterns of different CuFe-MOFs and (b) FTIR spectra of different CuFe-MOFs.

As for the peaks corresponding to iron, they were associated, by difference, with the peaks of  $2\theta = 9.2^\circ$ ,  $10.3^\circ$ ,  $13.2^\circ$ ,  $16.6^\circ$ ,  $18.6^\circ$ , and  $20.8^\circ$ . These peaks have also been found in other works such as that of Zango et al. [33], who synthesized MIL-88(Fe),  $\text{NH}_2\text{-MIL-88(Fe)}$ , and mixed-MIL-88(Fe). It should be noted that a peak with a value of  $2\theta = 9.8^\circ$  has only been detected in  $\text{CuFe}(\text{BDC-NH}_2)_\text{D}$  and  $\text{CuFe}(\text{BDC-NH}_2)_\text{S}$ . This can be related to crystal formation as both have been synthesized at the same temperature, but with different metal salts.

Figure 3b shows the FTIR analysis of these CuFe-MOFs in the range of  $4000$  to  $400\text{ cm}^{-1}$ . From these FTIR spectra, the bonds that ensure MOF formation and that it is bimetallic are highlighted. Based on the results, it has been possible to confirm in the three CuFe-MOFs the  $516\text{ cm}^{-1}$  bond, which is associated with the tension in the Fe–O bond [34], and the  $1066\text{ cm}^{-1}$  bond, which corresponds to the stretching in the C–O–Cu bond. Additionally, an intense band at  $1570\text{ cm}^{-1}$  can be seen in all three CuFe-MOFs and this corresponds to the asymmetric tension of  $\text{COO}^-$ , a group of the  $\text{NH}_2\text{-BDC}$  ligand. However, as a doublet appears at  $1425\text{ cm}^{-1}$  and another at  $1377\text{ cm}^{-1}$ , it seems that the symmetric tension mode of this group has unfolded. This may be due to the ligand acting as a bridge, allowing binding to two metals. In addition, it was observed that at  $3500\text{ cm}^{-1}$  and  $3200\text{ cm}^{-1}$ , N–H peaks are visible due to amine group stretching [33]. In summary, all the peaks discussed above indicate that the CuFe-MOFs were synthesized successfully.

The differences observed in the chemical and morphological characterization could explain the different behavior of the synthesized CuFe-MOF in the previous assays of Section 2.1. Based on the obtained results, the following experiments were performed using the CuFe-MOFs by the three synthesis methods. The main objective was to determine the best PMS activator for their application in the degradation of pollutants such as dyes, drugs, or pathogens.

### 2.3. Rhodamine B Removal

#### 2.3.1. Effect of pH

In PMS activation by CuFe-MOFs, different reaction conditions may lead to different activation pathways and result in the formation of different reactive oxidants. Consequently, acidic pH levels support the dominance of sulfate radicals, whereas alkaline pH levels shift the reactions towards more production of hydroxyl radicals. This is due to the substantial presence of hydroxide ions under alkaline conditions [35,36]. For this reason, in this study,



the behavior of the degradation process was evaluated at pH 3, 9, and natural. As shown in Figure 4, for each CuFe-MOF similar profiles were obtained operating at the selected pHs.

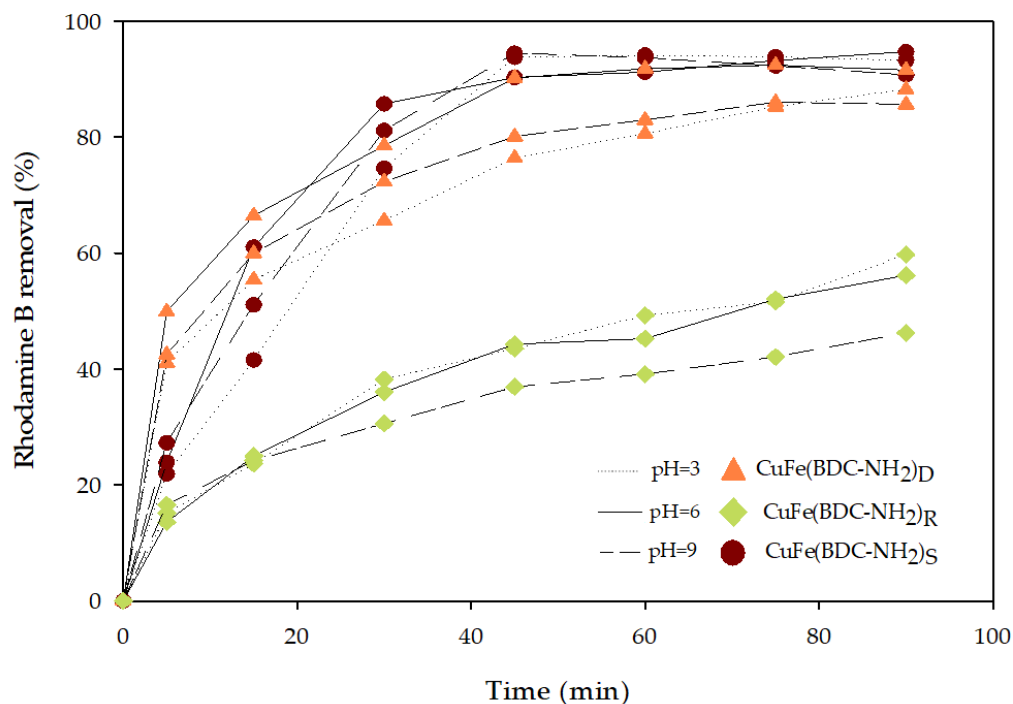


**Figure 4.** Profiles of Rhodamine B removal by PMS activation using the three synthesized CuFe-MOFs operating at different pHs.

These results describing the dominant role of sulfate radicals are in accordance with previous studies [37,38] where it was observed that the value of fenuron pesticide or dye removal decreased when the initial pH was increased. The slight differences in Rhodamine B removal could be due to the evolution of the system of CuFe-MOF/PMS in this pH range in which the final pH of the system achieved a similar value of around pH 3. This fact could be explained due to the oxidation of sulfate radicals and their transformation to hydroxyl radicals (Equation (6)), contributing to the production of hydrogen ions and reducing the pH to acid values in which the production of sulfate radicals is boosted [27,39]. As was determined by Li et al. [38], by the CuFe-MOF/PMS system, acidic conditions are preferred for the removal of methyl blue as under strongly alkaline conditions it was detected that the ferrous iron ions form iron sludge with lost catalytic performance.

Based on the attained results and that reported in the literature, it was confirmed that at acid and natural pH ranges, the generated sulfate radicals are similar. Thus, the operation at natural pH was selected as it is then not required to alter the pH of the water, reducing the cost of the process.

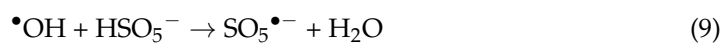
### 2.3.2. Effect of Catalyst Dosage

In this study, different catalyst dosages (0.125–0.5 g/L) were studied to determine their influence on Rhodamine B removal (Table 1). According to the results, Rhodamine B removal rates increased substantially when the catalyst dosages of the three synthesized CuFe-MOFs were increased. The best results were attained using 0.5 g/L of CuFe(BDC-NH<sub>2</sub>)<sub>D</sub> and with dye removal ranging from 52% for 0.125 g/L to 94% for 0.5 g/L after 60 min. The kinetic parameters of the degradation were calculated, and the pseudo-first-order model fitted well to the Rhodamine B removal with all R<sup>2</sup> values exceeding 0.95 (Table 1). It can be also observed from the table that as catalyst dosage increased from 0.125 to 0.5 g/L, the rate constant for Rhodamine B removal also increased.

Based on these results, the removal of Rhodamine B in this system showed a strong dependency on catalyst dosage as this increases the number of active sites for oxidizing PMS and also accelerates the generation of reactive oxygen species. However, it is important to highlight that a significant effect was detected when the catalyst (CuFe(BDC-NH<sub>2</sub>)<sub>D</sub> or CuFe(BDC-NH<sub>2</sub>)<sub>R</sub>) concentration increased from 0.125 to 0.25 g/L, with a slight increase when the dosage reached 0.5 g/L or decrease in the case of CuFe(BDC-NH<sub>2</sub>)<sub>S</sub>. Accordingly, in terms of economics and removal effects, it was decided to operate the next experiments at 0.25 g/L because the low concentration dosage enabled a reduction of process costs. These results are in accordance with previous studies reported in the literature [40]. When MOFs with small catalyst particles are used as catalysts, it may be advantageous to increase their surface area. It is expected that the effectiveness of the whole system will be greatly increased if more surface-active sites are provided for PMS activation, which is a typical heterogeneous reaction process. Nevertheless, if the quantity of active sites exceeds the required amount, the opposite effect could be detected [40].

### 2.3.3. Effect of PMS Concentration

The oxidant concentration is another factor that influences the behavior of the system and that needs to be assessed. In Figure 5, the Rhodamine B degradation profiles show that the removal efficiency of the dye improved with the increase of PMS concentration until a value of 1 mM was attained. Even though the PMS alone can reach a maximum dye degradation value of 24.52% at 1 mM after 90 min, the removal rate is lower than the ones obtained in the presence of CuFe-MOFs (Figure 5a). This degradation level was increased when CuFe(BDC-NH<sub>2</sub>)<sub>R</sub> was added, doubling their removal levels (Figure 5b). Near total Rhodamine B removal was achieved when CuFe(BDC-NH<sub>2</sub>)<sub>S</sub>/PMS (1 mM) and CuFe(BDC-NH<sub>2</sub>)<sub>D</sub>/PMS (1 mM) systems were evaluated (Figure 5c,d). However, in the presence of CuFe(BDC-NH<sub>2</sub>)<sub>S</sub> and CuFe(BDC-NH<sub>2</sub>)<sub>D</sub>, Rhodamine B removal at 0.5 mM and 1 mM differed only by 11–13%. For this reason, the use of higher concentrations is not recommended as excessive PMS concentration could produce free radical self-quenching instead of promoting Rhodamine B degradation [41]. Similarly, Li et al. [42,43] in the perfluorooctane sulfonate degradation determined that a continued increase in PMS concentration brought low removal efficiency and low rate kinetic constants, which was mainly ascribed to the scavenging reaction between PMS and the generated radicals (Equations (8) and (9)) [44]. Despite the fact that increasing the PMS concentration enhances Rhodamine B degradation efficiency, 1 mM was thought to be a suitable concentration and was used in the following assays.



### 2.3.4. Rhodamine B Removal by Photo-Assisted Activation of PMS over CuFe-MOFs

As aforementioned, PMS can be activated and decomposed to sulfate radicals by using different methods such as UV light according to Equation (10). According to the literature, processes with two or more activators for the decomposition of PMS molecules and the generation of sulfate radicals are more effective than ones with one activator [1,45,46].



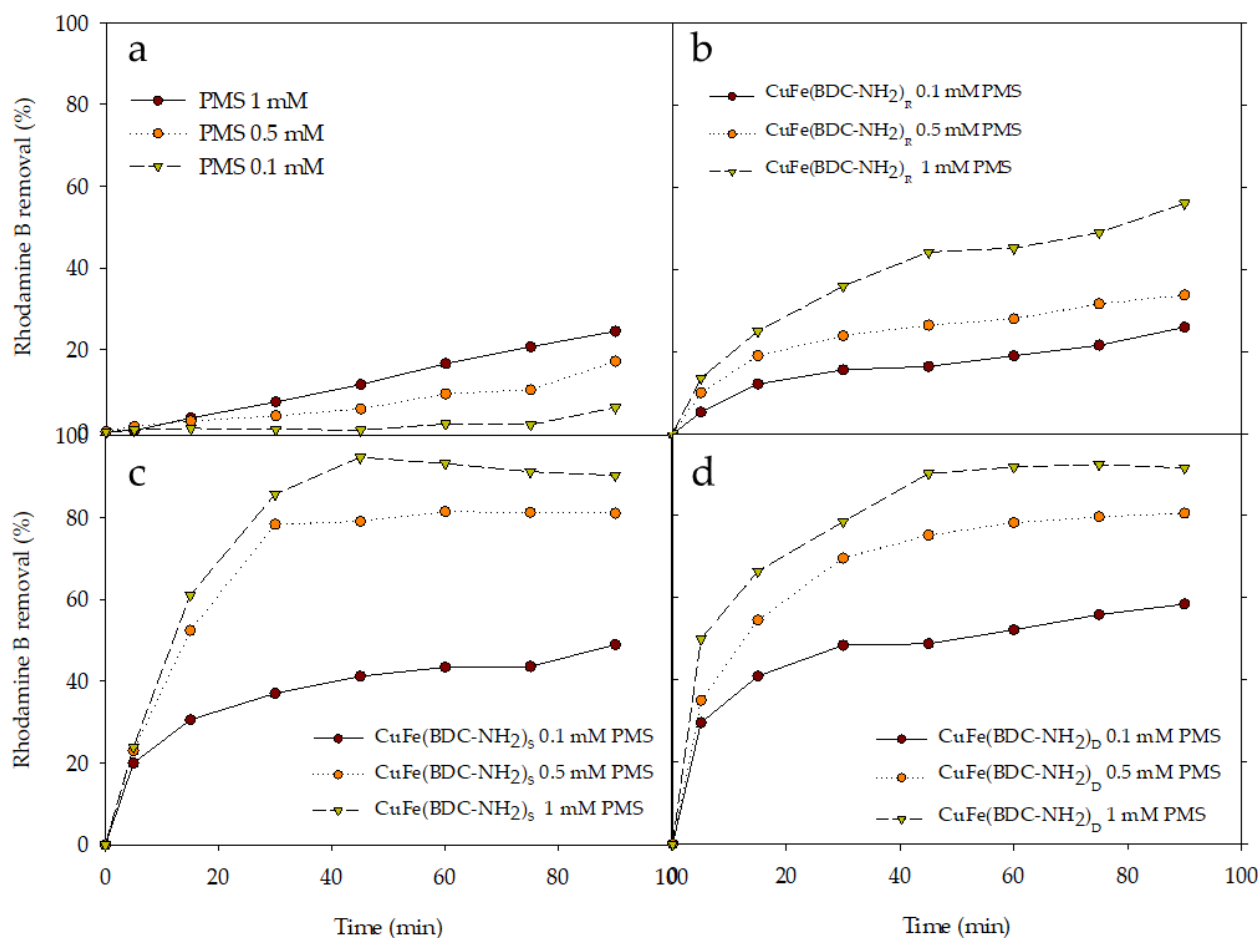


**Figure 5.** Effect of PMS concentration on profiles of Rhodamine B by different CuFe-MOFs/PMS systems: (a) without CuFe-MOF, only PMS; (b)  $\text{CuFe}(\text{BDC-NH}_2)_R$ ; (c)  $\text{CuFe}(\text{BDC-NH}_2)_S$ , and (d)  $\text{CuFe}(\text{BDC-NH}_2)_D$  with PMS concentrations.

Thus, Hassani et al. [47] determined the synergistic role of photocatalytic activation of PMS by UV-LED irradiation over  $\text{CoFe}_2\text{O}_4$ -rGO nanocomposite towards effective Bisphenol A degradation. The coupling catalyst and UV-LED increased the Bisphenol A degradation rate via a sum of mechanisms for the generation of oxidative agents, mainly,  $\text{SO}_4^{\bullet-}$  and  $\bullet\text{OH}$  radicals.

Inspired by these previous studies, we evaluated the PMS activation under low-intensity light irradiation in the presence of the synthesized CuFe-MOFs [48,49]. In Figure 6 the effect of UV irradiation on Rhodamine B degradation was examined using PMS activated by the different evaluated CuFe-MOFs. UV irradiation alone and in combination with PMS did not appear to be effective in dye removal during the testing period. The main bottleneck in relation to UV activation of PMS is low utilization efficiency due to the poor UV penetration and rapid disruption by pollutants and impurities contained in the water matrix since the UV irradiation is in accordance with the transmittance of the treated effluent. Therefore, the UV light activation of PMS systems might not be suitable for effluents with low transmittance [17]. Similarly, the systems UV/CuFe-MOFs showed similar behavior to the adsorption process (Figure 1).

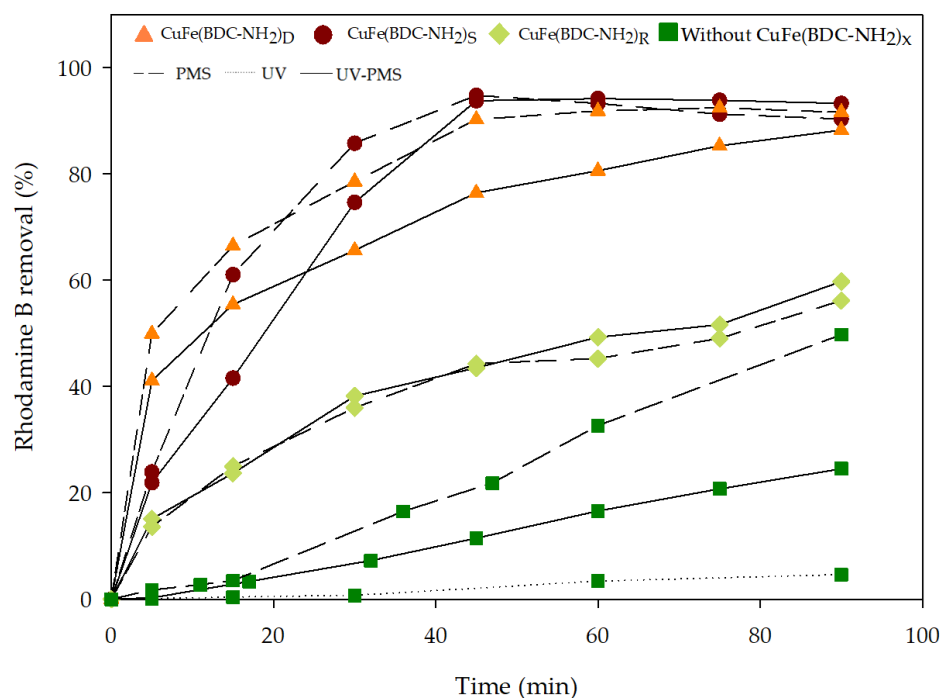
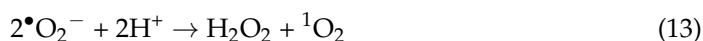
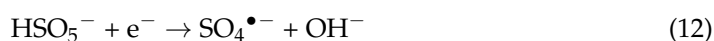


**Figure 6.** Comparison among several processes such as UV/PMS, PMS, UV alone separately and in combination with the three synthesized CuFe-MOFs in the Rhodamine B removal. As a reference, the working conditions for the experiment were natural pH, 0.25 g/L catalyst dose, and 1 mM PMS concentration.

Nevertheless, when the UV was added to the PMS/CuFe-MOFs system, Rhodamine B degradation kinetics were significantly faster than without UV irradiation. A complete degradation of the dye was achieved in the presence of CuFe(BDC-NH<sub>2</sub>)<sub>S</sub> or CuFe(BDC-NH<sub>2</sub>)<sub>D</sub> after 45 min. The corresponding rate constants for the systems with CuFe(BDC-NH<sub>2</sub>)<sub>S</sub> or CuFe(BDC-NH<sub>2</sub>)<sub>D</sub> were 0.0941 and 0.191 min<sup>-1</sup>, respectively. These values were much higher than the rate constant of the test with CuFe(BDC-NH<sub>2</sub>)<sub>R</sub> (0.03 min<sup>-1</sup>). The increase in the kinetics of the reaction is the result of UV radiation facilitating the generation of sulfate radicals and other species and by the effect of the UV irradiation exciting the electron/holes pairs of the CuFe-MOF [50,51].

Similar results were reported by Karim et al. [52] who reported that the introduction of UV irradiation for catalyst-based PMS/PS activation accelerated the transfer of e<sup>-</sup> and enhanced the production of radicals in the system. The reactive species generated under photocatalytic irradiations and enhanced charge transfer assisted in the activation of PMS to generate SO<sub>4</sub><sup>•-</sup> in the solution. Thus, the HSO<sub>5</sub><sup>-</sup> and dissolved oxygen would obtain an e<sup>-</sup> to generate several radicals and hydrogen peroxide, such as described in Equations (11)–(13), with the following generation of reactive oxidation species that increase the dye degradation rate. In addition, the UV light could accelerate the degradation rate via the indirect formation of free radicals by the regeneration of the metal ions Cu and Fe [51,53,54].



In order to evaluate the cost/commercial value of a product, its recovery and reuse is an important factor to consider. Based on the previously obtained results, the reusability of both CuFe-MOFs (CuFe(BDC-NH<sub>2</sub>)<sub>S</sub> or CuFe(BDC-NH<sub>2</sub>)<sub>D</sub>) for PMS activation is crucial for their application for long-term continuous degradation processes. Thus, the UV/[CuFe(BDC-NH<sub>2</sub>)<sub>S</sub> or CuFe(BDC-NH<sub>2</sub>)<sub>D</sub>]/PMS systems were evaluated in seven successive cycles. It was determined that only a slight decrease in the removal efficiency was observed after six cycles, similar to other studies using MOFs as activators for sulfate radical generation [55]. Both CuFe-MOFs showed higher catalytic activity after each run, suggesting high stability. Thus, the proposed system presented good behavior and usability for the removal of the pollutants with low iron and copper leaching (lower than 5%). This behavior was comparable to that reported in the literature in which the mixed metals usually have high stability and low leaching compared to single metals [17].

According to previous studies, the enhancement in catalytic activity of both CuFe-MOFs across successive runs could be explained by the action of the oxidant on the heterogeneous catalyst, generating more defects that increase the contact surface [55]. In addition, the literature reported that bi-metallic, and multi-metallic catalysts have higher stability in comparison with mono-metallic catalysts due to the strong interactions between the metallic species [56]. Thus, the obtained results confirm the applicability of these CuFe-MOFs and open the door of opportunity to use these systems in the continuous treatment of polluted effluents in the future.

#### 2.4. Drug Removal

As expected, the synthesized CuFe-MOFs showed remarkable catalytic activity to induce the oxidation process with sulfate radical generated from PMS to efficiently remove Rhodamine B. This study might open an avenue to study the multiple applications of these MOFs in the degradation of other pollutants such as drugs and pathogens. Nowadays, drugs such as antibiotics have been extensively used in human healthcare and livestock production. However, they are poorly metabolized in animals and human bodies. A great number of consumed drugs are eliminated through excretion and eventually released into our water environment [57]. Their residues left in the water can constitute a potential risk for the ecological environment through inducing antibiotic-resistant bacteria, antibiotic resistance, and toxicity effects on living organisms [58,59]. Due to the large amounts of drugs that have been detected in aquatic ecosystems, their degradation is an urgent task that must be performed by an effective technique [60].

Antibiotic and analgesic drugs such as sulfamethoxazole (SMX) or antipyrine (ANT) are widely used currently in human medicine and detected worldwide in effluents near discharge points of plants for wastewater treatment. It has been revealed that these organic compounds cannot be eliminated by conventional treatments [61]. For this reason, in this study, a mixture of SMX and ANT were selected as target pollutants in the developed treatment systems. The application of these CuFe-MOFs in different degradation systems operating in all cases at natural pH, MOF concentration of 0.25 g/L, and PMS concentration of 1 mM was assessed (Figure 7). Although the typical drug concentrations in the wastewater range from 0.1 to 200 µg/L, in these tests, an initial concentration of 10 mg/L of each drug was used to perform the kinetic studies by conventional analytical techniques with adequate reliability.

As can be observed from Figure 7, similar results were obtained showing the same tendency that was found for Rhodamine B as target pollutant. UV/PMS system can degrade SMX and ANT, reaching 20% of pollutant removal after 30 min. It seems that a low number of radicals are generated from PMS under light irradiation at the beginning of the reaction. In the case of UV/CuFe-MOF, it was highlighted that CuFe(BDC-NH<sub>2</sub>)<sub>D</sub> exhibited a very fast initial degradation of SMX and ANT. This fact could be due to adsorption, the predominant mechanism that, regrettably, stops after the first minutes of treatment. The high SMX and ANT degradation levels of the systems UV/[CuFe(BDC-NH<sub>2</sub>)<sub>S</sub> or CuFe(BDC-NH<sub>2</sub>)<sub>D</sub>]/PMS could be attributed to the redox cycles of both metallic species

that are made available for the activation of PMS to generate the radicals mentioned above to oxidize SMX and ANT under UV [62].

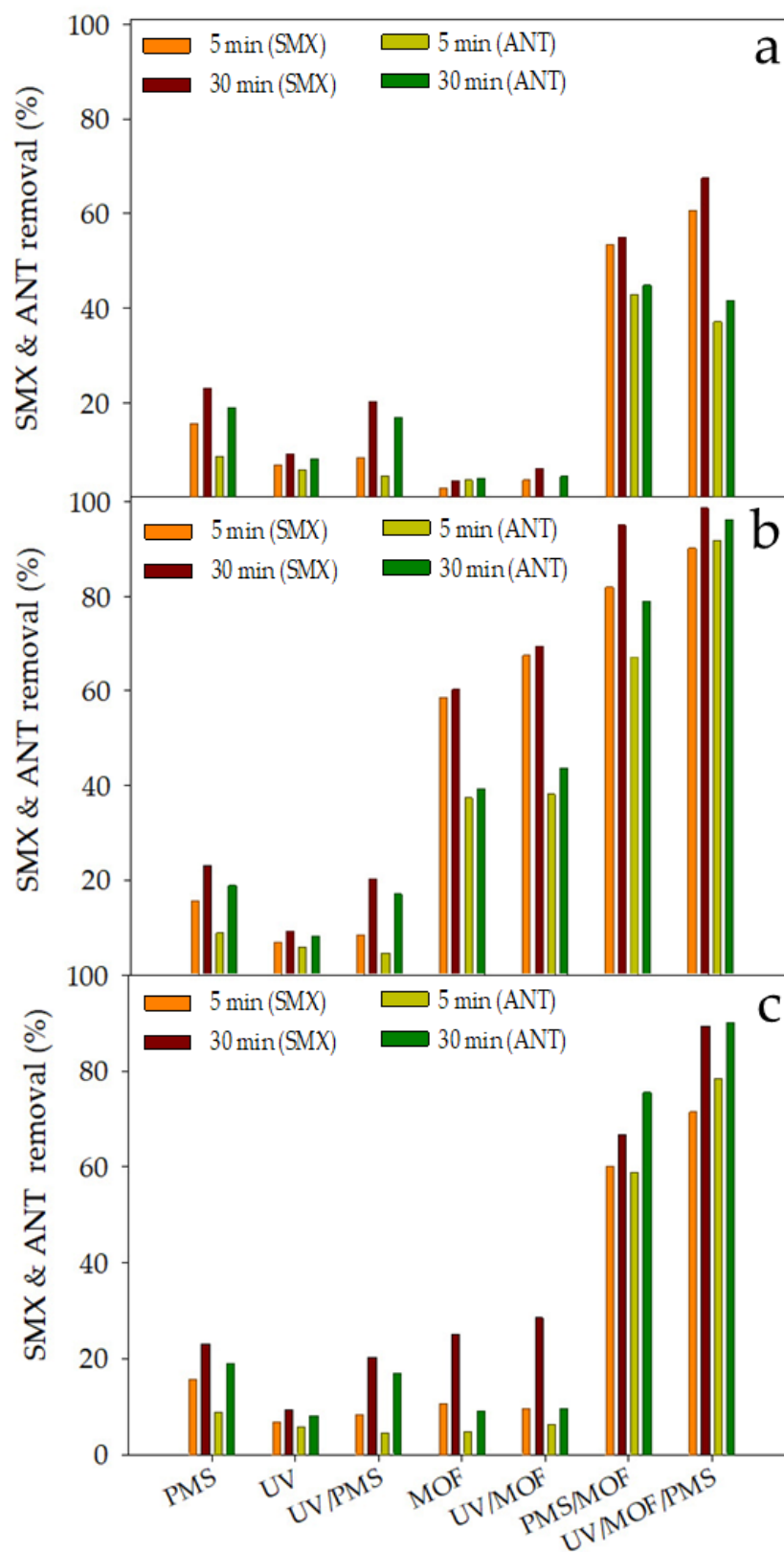


**Figure 7.** Concentration of SMX and ANT with different systems using CuFe-MOFs: (a) CuFe(BDC-NH<sub>2</sub>)<sub>R</sub>; (b) CuFe(BDC-NH<sub>2</sub>)<sub>D</sub>; (c) CuFe(BDC-NH<sub>2</sub>)<sub>S</sub> at different times.

Near complete degradation was obtained for SMX and ANT after 90 min by the photo-assisted system followed by CuFe-MOF/PMS with lower levels for the control systems. In these experiments, the carboxylic acids were detected at 30, 60, and 90 min to prove the generation of degradation products. It was highlighted by the formation of several compounds such as oxalic, succinic, formic, malonic, and acetic acid. The obtained results of short-chain carboxylic acids and the generation of intermediates that correspond to peaks detected by measurement on high-performance liquid chromatography (HPLC), not identified or quantified, are indicative of the generation of reaction products [63]. In Figure 8, the intermediates detected with the systems UV/[CuFe(BDC-NH<sub>2</sub>)<sub>R</sub>, CuFe(BDC-NH<sub>2</sub>)<sub>S</sub>, CuFe(BDC-NH<sub>2</sub>)<sub>D</sub>]/PMS are presented as HPLC area.

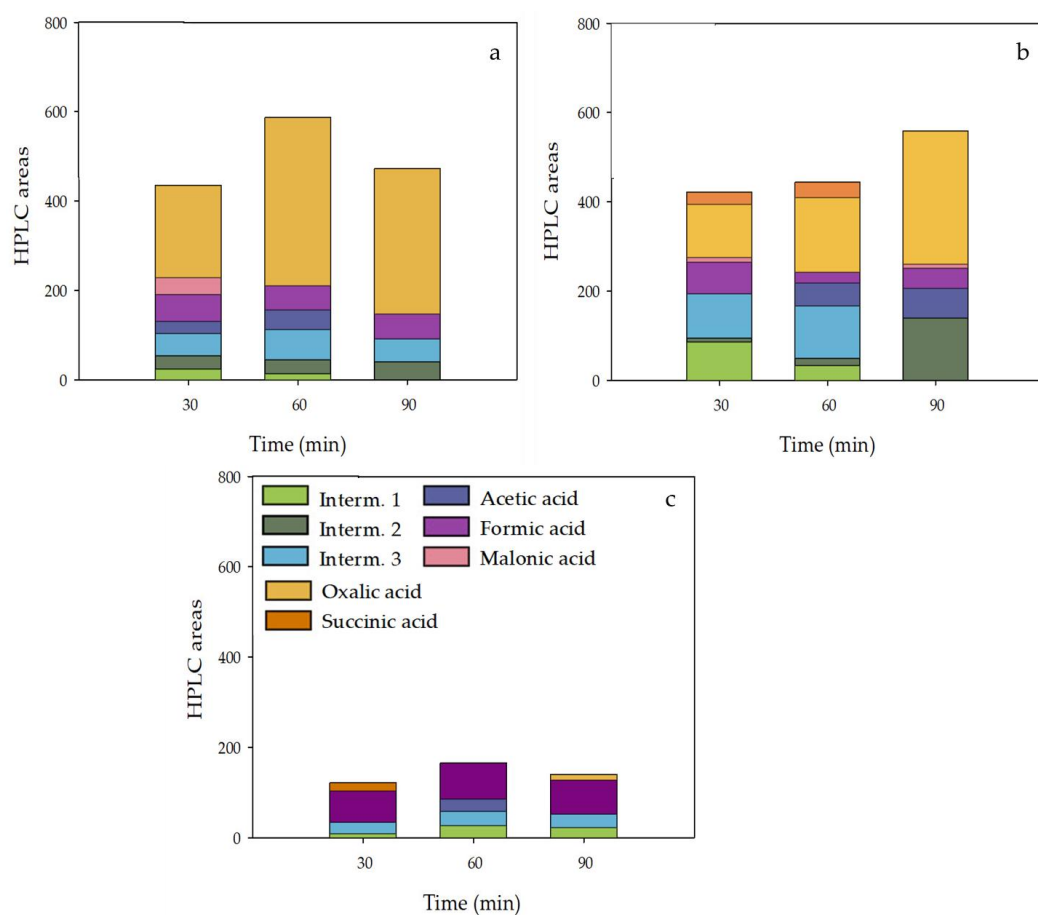


**Figure 8.** Bar graphs with the identified carboxylic acids and several detected intermediates in terms of HPLC area in the degradation of SMX and ANT using UV/PMS with different CuFe-MOFs: (a) CuFe(BDC-NH<sub>2</sub>)<sub>R</sub>; (b) CuFe(BDC-NH<sub>2</sub>)<sub>S</sub>; (c) CuFe(BDC-NH<sub>2</sub>)<sub>D</sub>—in this last figure the common legends of all detected intermediates are shown.

As shown in Figure 8c, the amount of compounds measured during the treatment of SMX and ANT in the system UV/CuFe(BDC-NH<sub>2</sub>)<sub>D</sub>/PMS is lower than the other catalysts. This fact is indicative of the higher degradation action of this system that aligns with the results shown in Figure 7. Furthermore, formic acid, the shortest carboxylic acid, constitutes a high percentage of the carboxylic acids. However, the other systems showed a lower degradation rate, and they are rather resistant to degradation with higher intermediates that are accumulated in the solution (Figure 8a,b).

### 2.5. Antibacterial Capability

Copper-containing compounds display high efficiency and extensive spectrum activity against pathogens through mechanisms such as reactive oxygen species production and penetration of bacterial cell walls [64]. The antibacterial capability of the system of synthesized CuFe-MOFs and PMS was determined by the colony-forming unit assay as described in Section 3. In this study, *Escherichia coli* (*E. coli*) was selected as the model bacteria based on previous studies of our group [8,65]. Due to PMS alone at a concentration of 1 mM removing colonies, its concentration was reduced to 0.1 mM. Figure 9 depicted a comparative antibacterial activity of PMS without activator and in the presence of the different PMS activator CuFe-MOFs by the number of colonies at 5, 15, 30, and 60 min. In this case, the best results were obtained when CuFe(BDC-NH<sub>2</sub>)<sub>R</sub> was used and the increased incubation time significantly reduced the number of colony-forming units (CFU) reaching total disinfection after 1 h. These results suggested that CuFe(BDC-NH<sub>2</sub>)<sub>R</sub> showed potential as antibacterial material with respect to the others. In the presence of CuFe(BDC-NH<sub>2</sub>)<sub>S</sub> and CuFe(BDC-NH<sub>2</sub>)<sub>D</sub> the CFU reduction was lower than 50% after 1 h. This fact could be explained by the composition of each CuFe-MOF (Table 1) where CuFe(BDC-NH<sub>2</sub>)<sub>R</sub> presented the highest percentage of Cu. Other studies have proved that Cu is a proficient disruptor of the bacterial cell envelope and the killing effect increased when the Cu concentration was increased [66,67]. Thus, a double benefit of the use of CuFe(BDC-NH<sub>2</sub>)<sub>R</sub> was detected, with the capacity to generate sulfate radicals and with a structure that contributes to bacterial disinfection strategy.

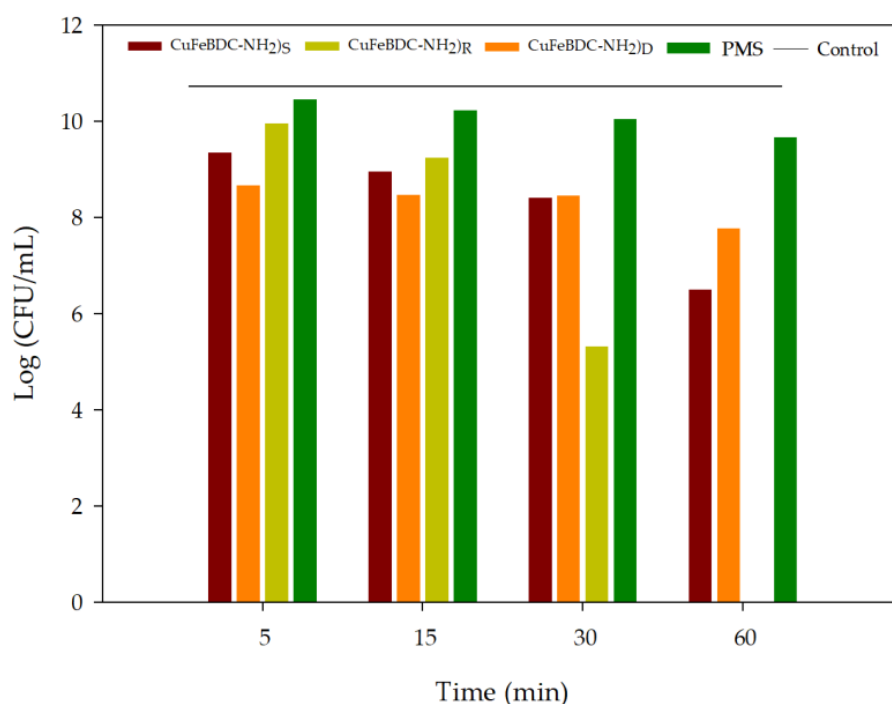


**Figure 9.** Comparative antibacterial activity of different CuFe-MOFs/PMS systems: CuFe(BDC-NH<sub>2</sub>)<sub>R</sub>; CuFe(BDC-NH<sub>2</sub>)<sub>S</sub>; CuFe(BDC-NH<sub>2</sub>)<sub>D</sub>. Experimental conditions: concentration of PMS (0.1 mM), catalyst dosage (0.25 g/L), dark and room temperature.

## 3. Materials and Methods

### 3.1. Chemicals and Microorganisms

The reagents used for the synthesis of the three bimetallics were dimethylformamide (DMF), 2-aminoterephthalic acid (NH<sub>2</sub>BDC), ethanol, iron (II) sulfate heptahydrate (FeSO<sub>4</sub>·7H<sub>2</sub>O), copper (II) acetate (Cu(CH<sub>3</sub>COO)<sub>2</sub>·H<sub>2</sub>O), copper (II) chloride hexahydrate (CuCl<sub>2</sub>·6H<sub>2</sub>O), and iron (III) chloride hexahydrate (FeCl<sub>3</sub>·6H<sub>2</sub>O). All the chemicals mentioned were purchased from Sigma-Aldrich (Madrid, Spain).



As for the reagents utilized for the antibacterial test with *E. coli* culture, meat peptone broth (MPB) culture medium was prepared, including 10 g/L of peptone, 5 g/L of meat extract, and 5 g/L of sodium chloride. MPB culture medium was used as liquid and solid medium. For the microorganism, the strain *E. coli* CECT 102 was used, provided by the Spanish Type Culture Collection.

Several model pollutants were used to determine degradation ability. The dye Rhodamine B, ANT, and SMX, all reagents, and the PMS ( $2\text{KHSO}_5 \cdot \text{KHSO}_4 \cdot \text{K}_2\text{SO}_4$ ) were supplied also by Sigma-Aldrich.

All experimental solutions were prepared using ultrapure deionized water.

### 3.2. Synthesis of the Bimetallic $\text{CuFe}(\text{BDC-NH}_2)_x$

The catalysts were prepared through a solvothermal method and subsequent thermal treatment. Considering the slight differences among these catalysts, the following synthesis procedure is provided here:

- $\text{CuFe}(\text{BDC-NH}_2)_R$ : The procedure of this synthesis was adapted, with slight modifications, from the study of Fu et al. [68]. In this case, 0.724 g of  $\text{NH}_2\text{BDC}$  was added to 32 mL of DMF. When  $\text{NH}_2\text{BDC}$  was completely dissolved, 0.4 g of  $\text{Cu}(\text{CH}_3\text{COO})_2 \cdot \text{H}_2\text{O}$  and 0.556 g of  $\text{FeSO}_4 \cdot 7\text{H}_2\text{O}$ , were added simultaneously with 4 mL of ethanol and 4 mL of ultrapure water. The mixture was dissolved completely after 30 min and transferred to a 100-mL Teflon-lined autoclaved reactor, which was kept in an oven at 90 °C for 24 h. The obtained solid was washed with ethanol and dried overnight at 80 °C. The monometallic  $\text{Cu}(\text{BDC-NH}_2)_R$  was synthesized analogously using only 0.4 g of  $\text{Cu}(\text{CH}_3\text{COO})_2 \cdot \text{H}_2\text{O}$  as precursor.
- $\text{CuFe}(\text{BDC-NH}_2)_D$ : For this catalyst, the synthesis was carried out as described in the work of Khosravi et al. [29]. Briefly, 0.362 g of  $\text{NH}_2\text{BDC}$  was mixed in 14 mL of DMF for 15 min. Meanwhile, 0.341 g  $\text{CuCl}_2 \cdot 6\text{H}_2\text{O}$  and 0.541 g  $\text{FeCl}_3 \cdot 6\text{H}_2\text{O}$  were stirred in 14 mL of DMF. Subsequently, both dilutions were mixed, and 2 mL of ethanol added and shaken vigorously for 30 min, followed by 20 min in ultrasound. Once finished, it was transferred to a 100-mL Teflon-lined autoclaved reactor, which was kept in an oven at 150 °C for 24 h. Subsequently, the obtained solid was washed and filtered with DMF and ethanol and dried overnight at 80 °C.
- $\text{CuFe}(\text{BDC-NH}_2)_S$ : The previous procedure was followed, the only difference being the salts used which were 0.4 g of  $\text{Cu}(\text{CH}_3\text{COO})_2 \cdot \text{H}_2\text{O}$  and 0.556 g of  $\text{FeSO}_4 \cdot 7\text{H}_2\text{O}$ .

### 3.3. Culture Conditions

According to Fdez-Sanromán et al. [8], similar steps were taken to activate and disinfect *E. coli* CECT 102. In summary, the *E. coli* CECT 102 inoculum was transferred into a 250 mL Erlenmeyer flask, with 50 mL of MPB medium. Then, it was grown for 20 h at 180 rpm and 37 °C under darkness. For all disinfection experiments, this culture was used as an inoculum (1% v/v inoculum). The culture was incubated until the stationary phase (approx. 20 h) and then centrifuged at 8000 rpm for 15 min (Sigma Laboratory Centrifuges, 3K18, Osterode am Harz, Germany). As a result of this procedure, a minimum concentration of  $10^{10}$  CFU per mL was assured. Subsequently, it was resuspended in 5 mL of sterile saline solution at 0.9% w/w. For the *E. coli* experiments, all materials and solutions mentioned were sterilized in an autoclave Presoclave II (J.P. Selecta<sup>®</sup>, Barcelona, Spain). Each cycle lasted 20 min at 121 °C and 1 bar pressure.

### 3.4. Experimental Set-Up

#### 3.4.1. Pollutant Degradation

The catalytic performance was evaluated by the decrease of Rhodamine B concentration and further confirmed using a mixture of two pharmaceuticals, ANT and SMX. In both cases, the catalytic activity was evaluated using several AOPs such as Fenton-like, photocatalysis and photo-PMS. In all of them, the heterogeneous degradation experiments were performed in a 0.1 L individual cylindrical cell with an operating volume of 0.05 L

and containing Rhodamine B solution (10 mg/L) or the pharmaceutical mixture solution (10 mg/L of each drug).

Concerning the Rhodamine B assays, the experiment was developed under magnetic stirring at 300 rpm at a determined initial pH (natural, 3, and 9). This pH was adjusted by adding 1 M sodium hydroxide or sulfuric acid ( $\text{H}_2\text{SO}_4$ ). The PMS concentration values were from 1 to 0.1 mM and the catalyst dosage was from 0.125 to 0.5 g/L. The assays involving light irradiation, such as photolysis, photocatalysis, and photo-PMS, were developed using as a light source a UV-A LED lamp (30 W) operating at 365 nm. Sample aliquots of 1 mL were withdrawn at predetermined time intervals and the residual Rhodamine B concentration was measured with a UV-Vis spectrophotometer (Thermo Fisher Genesys M-150, Waltham, MA, USA) at 554 nm. The removal of ANT and SMX was performed by using different AOPs at the best conditions of initial pH, PMS concentration, and catalyst dosage, which were obtained from Rhodamine B experiments. To analyze the sample by HPLC, aliquots of 1 mL were withdrawn at predetermined times and filtered through 0.22  $\mu\text{m}$  PTFE filters. All the results are the average of duplicated assays, and the standard deviations were below 5%.

### 3.4.2. Disinfection Experiment

As mentioned previously, the disinfection process was followed by Fdez-Sanromán et al. [8]. As a first step, 0.5 mL of *E. coli* CECT 102 inoculum was transferred to a 250 mL Erlenmeyer flask, containing 50 mL of MPB medium. This was incubated for 20 h at 180 rpm, at 37 °C, in the dark. In order to obtain a concentrated culture of *E. coli*, that was incubated until the stationary phase (approx. 20 h), it was centrifuged at 8000 rpm for 15 min (Sigma Laboratory Centrifuges, 3K18, Osterode am Harz, Germany).

After that, *E. coli* CECT 102 inactivation experiments were carried out to determine the concentration of the three catalysts (0.25 g/L),  $\text{CuFe}(\text{BDC-NH}_2)_\text{R}$ ,  $\text{CuFe}(\text{BDC-NH}_2)_\text{S}$ , and  $\text{CuFe}(\text{BDC-NH}_2)_\text{D}$  for a concentration of PMS (0.1 mM). The disinfection experiment was accomplished by adding 1 mL of concentrated *E. coli* culture to 99 mL of synthetic water [8] and a mixture of catalyst and PMS. During the experiment, the mixture was kept in an incubator at 80 rpm, 25 °C, and in the dark and samples were taken at 5, 15, 30, and 60 min to follow the disinfection process. At those times, the bacteria concentration was assessed by the standard plate counting method through a serial 10-fold dilution.

## 3.5. Analytical Methods

### 3.5.1. Determination of ANT and SMX

The concentrations of ANT and SMX were monitored by HPLC using an Agilent instrument equipped (Agilent 1260, Santa Clara, CA, USA) with a diode array detector at two wavelengths: 242 nm for ANT and 263 nm for SMX. ZORBAX Eclipse XDB-C8 column (Agilent, Santa Clara, CA, USA) (dimensions of 4.6  $\times$  150 mm; 5  $\mu\text{m}$ ) was used to carry out the chromatographic separation. The eluent was a mixture consisting of acetonitrile and 1.5% acetic acid aqueous solution (10/90%). The mobile phase flow rate was at 1 mL/min and the injection volume was 10  $\mu\text{L}$ .

For carboxylic acids measurement, the same analytical equipment was employed. The chromatographic separation was carried out at room temperature on a Rezex ROA-Organic Acid  $\text{H}^+$  column, supplied by Phenomenex (Torrance, CA, USA). The mobile phase used was  $\text{H}_2\text{SO}_4$  (0.05 M) at a flow rate of 0.5 mL/min. The carboxylic acids were detected at 210 nm with an injection volume of 20  $\mu\text{L}$ .

### 3.5.2. Disinfection Efficiency

The disinfection process efficiency was measured by the logarithmic of the CFU/mL. Through a serial 10-fold dilution, the bacteria's concentrations were assessed using the standard plate counting method. After dilutions were performed in buffered peptone water (15 g/L), aliquots for each dilution were spread onto MPB plates and incubated at 37 °C for

24 h. Afterwards, colonies were counted. For the mean counts (of triplicate samples) in CFU/mL, the coefficient of variation was always less than 15%.

### 3.5.3. Characterization of CuFe-MOFs

Characterization of the catalyst's surface was accomplished by scanning electron microscopy and energy dispersive spectrometry (SEM/EDS) using a JEOL JSM6010LA with EDS Oxford AZtecOne SEM (C.A.C.T.I., University of Vigo, Vigo, Spain). For the crystallographic analysis of CuFe-MOFs, the X-ray diffraction (XRD) was made on a Siemens D5000 diffractometer (C.A.C.T.I., University of Vigo, Vigo, Spain). Fourier transform infrared spectroscopy (FTIR) analyses, Nicolet 6700, Thermo Fisher Scientific Inc. (C.A.C.T.I., University of Vigo, Vigo, Spain) were used to analyze the CuFe-MOF bonds and functional groups.

## 4. Conclusions

In this study, three different bimetallic CuFe-MOFs were assessed and applied for PMS activation. Initially, these heterogeneous bimetallic MOFs were investigated for the removal of Rhodamine B and it was confirmed that the bimetallic catalyst improved the performance of the Cu-MOF. The effects of variables such as pH, catalyst, and PMS dosage were ascertained, and the best conditions were determined for each CuFe-MOF. Their behavior was affected by the Fe/Cu ratio which was found through characterization. It was detected that the MOF with the higher Fe/Cu ratio had better results in the degradation of Rhodamine B and drugs (SMX and ANT). However, for disinfection, the best results were obtained when the Cu content of MOF was increased. In addition, it was proved that the combination system PMS/CuFeMOF/UV is the best system as the radiation improved the generation of radicals. As a result, Rhodamine B and two drugs, namely SMX and ANT, were degraded more efficiently.

The high stability over several cycles and the wide range of applications of these CuFe-MOFs proved the feasibility of the proposed system for application in the environmental field. Thus, these results confirm the applicability of CuFe-MOFs and open the door of opportunity to use these systems for the continuous treatment of polluted effluents in the future.

**Author Contributions:** Conceptualization, A.S. and A.F.-S.; methodology, A.S. and E.R.; formal analysis, A.F.-S. and B.L.-F.; investigation, A.F.-S. and B.L.-F.; resources, M.P. and A.S.; data curation, A.F.-S. and B.L.-F.; writing—original draft preparation, A.F.-S. and B.L.-F.; writing—review and editing, A.F.-S. and A.S.; visualization, A.F.-S., B.L.-F. and A.S.; supervision, A.S. and E.R.; project administration, A.S.; funding acquisition, M.P. and A.S. All authors have read and agreed to the published version of the manuscript.

**Funding:** This research was funded through the join 2019–2020 Biodiversa & Water JPI joint call for research proposals, under the BiodivRestore ERA-Net COFUND programme with the Project PCI2022-132941 funded by MCIN/AEI/10.13039/501100011033 and PID2020-113667GBI00, funded by MCIN/AEI/10.13039/501100011033 and Xunta de Galicia, and the European Regional Development Fund (ED431C 2021-43).

**Data Availability Statement:** Not applicable.

**Acknowledgments:** Antía Fdez-Sanromán thanks Ministerio de Ciencia e Innovación (PRE2021-098540) for her predoctoral fellowships.

**Conflicts of Interest:** The authors declare no conflict of interest.

## References

1. Arellano, M.; Sanromán, M.A.; Pazos, M. Electro-Assisted Activation of Peroxymonosulfate by Iron-Based Minerals for the Degradation of 1-Butyl-1-Methylpyrrolidinium Chloride. *Sep. Purif. Technol.* **2019**, *208*, 34–41. [CrossRef]
2. Nguyen, A.Q.K.; Ahn, Y.Y.; Shin, G.; Cho, Y.; Lim, J.; Kim, K.; Kim, J. Degradation of Organic Compounds through Both Radical and Nonradical Activation of Peroxymonosulfate Using CoWO<sub>4</sub> Catalysts. *Appl. Catal. B Environ.* **2023**, *324*, 122266. [CrossRef]
3. Bouzayani, B.; Rosales, E.; Pazos, M.; Elaoud, S.C.; Sanromán, M.A. Homogeneous and Heterogeneous Peroxymonosulfate Activation by Transition Metals for the Degradation of Industrial Leather Dye. *J. Clean. Prod.* **2019**, *228*, 222–230. [CrossRef]

4. Hammad, M.; Angel, S.; Al-Kamal, A.K.; Asghar, A.; Amin, A.S.; Kräenbring, M.A.; Wiedemann, H.T.A.; Vinayakumar, V.; Ali, M.Y.; Fortugno, P.; et al. Synthesis of novel LaCoO<sub>3</sub>/graphene catalysts as highly efficient peroxymonosulfate activator for the degradation of organic pollutants. *Chem. Eng. J.* **2023**, *454*, 139900. [CrossRef]
5. Dung, N.T.; Thuy, B.M.; Son, L.T.; Ngan, L.V.; Thao, V.D.; Takahashi, M.; Maenosono, S.; Thu, T.V. Mechanistic Insights into Efficient Peroxymonosulfate Activation by NiCo Layered Double Hydroxides. *Environ. Res.* **2023**, *217*, 114488. [CrossRef]
6. Ni, T.; Yang, Z.; Zhang, H.; Zhou, L.; Guo, W.; Pan, L.; Yang, Z.; Chang, K.; Ge, C.; Liu, D. Peroxymonosulfate activation by Co<sub>3</sub>O<sub>4</sub>/SnO<sub>2</sub> for efficient degradation of ofloxacin under visible light. *J. Colloid Interface Sci.* **2022**, *615*, 650–662. [CrossRef]
7. Wang, J.; Wang, S. Activation of persulfate (PS) and peroxymonosulfate (PMS) and application for the degradation of emerging contaminants. *Chem. Eng. J.* **2018**, *334*, 1502–1517. [CrossRef]
8. Fdez-Sanromán, A.; Pazos, M.; Sanroman, A. Peroxymonosulphate Activation by Basolite® F-300 for Escherichia coli Disinfection and Antipyrine Degradation. *Int. J. Environ. Res. Public Health* **2022**, *19*, 6852. [CrossRef] [PubMed]
9. Escudero-Curiel, S.; Pazos, M.; Sanromán, A. Sustainable regeneration of a honeycomb carbon aerogel used as a high-capacity adsorbent for Fluoxetine removal. *J. Mol. Liq.* **2022**, *357*, 119079. [CrossRef]
10. Ghanbari, F.; Moradi, M. Application of peroxymonosulfate and its activation methods for degradation of environmental organic pollutants: Review. *Chem. Eng. J.* **2017**, *310*, 41–62. [CrossRef]
11. Oh, W.D.; Dong, Z.; Lim, T.T. Generation of sulfate radical through heterogeneous catalysis for organic contaminants removal: Current development, challenges and prospects. *Appl. Catal. B Environ.* **2016**, *194*, 169–201. [CrossRef]
12. Joseph, J.; Iftekhar, S.; Srivastava, V.; Fallah, Z.; Zare, E.N.; Sillanpää, M. Iron-based metal-organic framework: Synthesis, structure and current technologies for water reclamation with deep insight into framework integrity. *Chemosphere* **2021**, *284*, 131171. [CrossRef] [PubMed]
13. Fdez-Sanromán, A.; Rosales, E.; Pazos, M.; Sanroman, A. Metal–Organic Frameworks as Powerful Heterogeneous Catalysts in Advanced Oxidation Processes for Wastewater Treatment. *Appl. Sci.* **2022**, *12*, 8240. [CrossRef]
14. Yuan, S.; Feng, L.; Wang, K.; Pang, J.; Bosch, M.; Lollar, C.; Sun, Y.; Qin, J.; Yang, X.; Zhang, P.; et al. Stable Metal–Organic Frameworks: Design, Synthesis, and Applications. *Adv. Mater.* **2018**, *30*, 1704303. [CrossRef] [PubMed]
15. Khalil, I.E.; Fonseca, J.; Reithofer, M.R.; Eder, T.; Chin, J.M. Tackling Orientation of Metal–Organic Frameworks (MOFs): The Quest to Enhance MOF Performance. *Coord. Chem. Rev.* **2023**, *481*, 215043. [CrossRef]
16. Huang, D.; Zhang, G.; Yi, J.; Cheng, M.; Lai, C.; Xu, P.; Zhang, C.; Liu, Y.; Zhou, C.; Xue, W.; et al. Progress and Challenges of Metal–Organic Frameworks-Based Materials for SR-AOPs Applications in Water Treatment. *Chemosphere* **2021**, *263*, 127672. [CrossRef] [PubMed]
17. Hassani, A.; Scaria, J.; Ghanbari, F.; Nidheesh, P.V. Sulfate Radicals-Based Advanced Oxidation Processes for the Degradation of Pharmaceuticals and Personal Care Products: A Review on Relevant Activation Mechanisms, Performance, and Perspectives. *Environ. Res.* **2023**, *217*, 114789. [CrossRef] [PubMed]
18. Yang, S.; Qiu, X.; Jin, P.; Dzakpasu, M.; Wang, X.C.; Zhang, Q.; Zhang, L.; Yang, L.; Ding, D.; Wang, W.; et al. MOF-templated synthesis of CoFe<sub>2</sub>O<sub>4</sub> nanocrystals and its coupling with peroxymonosulfate for degradation of bisphenol A. *Chem. Eng. J.* **2018**, *353*, 329–339. [CrossRef]
19. Li, H.; Yang, Z.; Lu, S.; Su, L.; Wang, C.; Huang, J.; Zhou, J.; Tang, J.; Huang, M. Nano-porous bimetallic CuCo-MOF-74 with coordinatively unsaturated metal sites for peroxymonosulfate activation to eliminate organic pollutants: Performance and mechanism. *Chemosphere* **2021**, *273*, 129643. [CrossRef]
20. Li, H.; Yao, Y.; Chen, J.; Wang, C.; Huang, J.; Du, J.; Xu, S.; Tang, J.; Zhao, H.; Huang, M. Heterogeneous activation of peroxymonosulfate by bimetallic MOFs for efficient degradation of phenanthrene: Synthesis, performance, kinetics, and mechanisms. *Sep. Purif. Technol.* **2021**, *259*, 118217. [CrossRef]
21. Liu, J.; Li, X.; Liu, B.; Zhao, C.; Kuang, Z.; Hu, R.; Liu, B.; Ao, Z.; Wang, J. Shape-Controlled Synthesis of Metal–Organic Frameworks with Adjustable Fenton-Like Catalytic Activity. *ACS Appl. Mater. Interfaces* **2018**, *10*, 38051–38056. [CrossRef] [PubMed]
22. Gao, C.; Chen, S.; Quan, X.; Yu, H.; Zhang, Y. Enhanced Fenton-like catalysis by iron-based metal organic frameworks for degradation of organic pollutants. *J. Catal.* **2017**, *356*, 125–132. [CrossRef]
23. Liao, X.; Wang, F.; Wang, F.; Cai, Y.; Yao, Y.; Teng, B.T.; Hao, Q.; Shuxiang, L. Synthesis of (100) surface oriented MIL-88A-Fe with rod-like structure and its enhanced fenton-like performance for phenol removal. *Appl. Catal. B Environ.* **2019**, *259*, 118064. [CrossRef]
24. Bai, Y.; Nie, G.; He, Y.; Li, C.; Wang, X.; Ye, L. Cu-MOF for effectively organic pollutants degradation and E. coli inactivation via catalytic activation of peroxymonosulfate. *J. Taiwan Inst. Chem. Eng.* **2022**, *132*, 104154. [CrossRef]
25. Zhou, X.; Luo, C.; Luo, M.; Wang, Q.; Wang, J.; Liao, Z.; Chen, Z.; Chen, Z. Understanding the synergetic effect from foreign metals in bimetallic oxides for PMS activation: A common strategy to increase the stoichiometric efficiency of oxidants. *Chem. Eng. J.* **2020**, *381*, 122587. [CrossRef]
26. Liu, S.; Lai, C.; Li, B.; Zhang, C.; Zhang, M.; Huang, D.; Qin, L.; Yi, H.; Liu, X.; Huang, F.; et al. Role of Radical and Non-Radical Pathway in Activating Persulfate for Degradation of p-Nitrophenol by Sulfur-Doped Ordered Mesoporous Carbon. *Chem. Eng. J.* **2020**, *384*, 123304. [CrossRef]


27. Liu, C.; Wang, Y.; Zhang, Y.; Li, R.; Meng, W.; Song, Z.; Qi, F.; Xu, B.; Chu, W.; Yuan, D.; et al. Enhancement of Fe@porous Carbon to Be an Efficient Mediator for Peroxymonosulfate Activation for Oxidation of Organic Contaminants: Incorporation NH<sub>2</sub>-Group into Structure of Its MOF Precursor. *Chem. Eng. J.* **2018**, *354*, 835–848. [CrossRef]
28. Peng, Y.; Zhao, M.; Chen, B.; Zhang, Z.; Huang, Y.; Dai, F. Hybridization of MOFs and COFs: A New Strategy for Construction of MOF@COF Core–Shell Hybrid Materials. *Adv. Mater.* **2018**, *30*, 1705454. [CrossRef] [PubMed]
29. Khosravi, F.; Gholinejad, M.; Sansano, J.M.; Luque, R. Bimetallic Fe–Cu Metal Organic Frameworks for Room Temperature Catalysis. *Appl. Organomet. Chem.* **2022**, *36*, e6749. [CrossRef]
30. Usman, K.A.S.; Maina, J.W.; Seyedin, S.; Conato, M.T.; Payawan, L.M.; Dumée, L.F.; Razal, J.M. Downsizing Metal–Organic Frameworks by Bottom-up and Top-down Methods. *NPG Asia Mater.* **2020**, *12*, 58. [CrossRef]
31. Zhong, M.; Zhang, S.; Dong, A.; Sui, Z.; Feng, L.; Chen, Q. Cu-MOF/Au–Pd Composite Catalyst: Preparation and Catalytic Performance Evaluation. *J. Mater. Sci.* **2020**, *55*, 10388–10398. [CrossRef]
32. Abdel-Azim, S.; Aman, D.; Van Steen, E.; El Salam, H.A. Visible-Light Responsive Cu–MOF–NH<sub>2</sub> for Highly Efficient Aerobic Photocatalytic Oxidation of Benzyl Alcohol. *Kinet. Catal.* **2021**, *62*, S9–S20. [CrossRef]
33. Zango, Z.U.; Jumbri, K.; Sambudi, N.S.; Hanif Abu Bakar, N.H.; Fathihah Abdullah, N.A.; Basheer, C.; Saad, B. Removal of Anthracene in Water by MIL-88(Fe), NH<sub>2</sub>-MIL-88(Fe), and Mixed-MIL-88(Fe) Metal–Organic Frameworks. *RSC Adv.* **2019**, *9*, 41490–41501. [CrossRef] [PubMed]
34. Li, Y.; Wang, Q.; Ding, Z.; Wan, D.; Nie, X.; Zhong, C. A Functionalized Magnetic Graphene-Based MOFs Platform as the Heterogeneous Mimic Enzyme Sensor for Glucose Detection. *Catal. Lett.* **2022**, *152*, 2375–2385. [CrossRef]
35. Guan, Y.H.; Ma, J.; Li, X.C.; Fang, J.Y.; Chen, L.W. Influence of PH on the Formation of Sulfate and Hydroxyl Radicals in the UV/Peroxymonosulfate System. *Environ. Sci. Technol.* **2011**, *45*, 9308–9314. [CrossRef]
36. Ding, Y.; Fu, L.; Peng, X.; Lei, M.; Wang, C.; Jiang, J. Copper Catalysts for Radical and Nonradical Persulfate Based Advanced Oxidation Processes: Certainties and Uncertainties. *Chem. Eng. J.* **2022**, *427*, 131776. [CrossRef]
37. Hayat, W.; Liu, Z.H.; Wan, Y.P.; Zhang, Y. The Analysis of Efficiency of Activated Peroxymonosulfate for Fenuron Degradation in Water. *Environ. Technol. Innov.* **2022**, *26*, 102352. [CrossRef]
38. Li, H.; Xu, C.; Li, N.; Rao, T.; Zhou, Z.; Zhou, Q.; Wang, C.; Xu, S.; Tang, J. Synthesis of Bimetallic FeCu-MOF and Its Performance as Catalyst of Peroxymonosulfate for Degradation of Methylene Blue. *Materials* **2022**, *15*, 7252. [CrossRef]
39. Zhang, Y.; Wei, J.; Xing, L.; Li, J.; Xu, M.; Pan, G.; Li, J. Superoxide Radical Mediated Persulfate Activation by Nitrogen Doped Bimetallic MOF (FeCo/N-MOF) for Efficient Tetracycline Degradation. *Sep. Purif. Technol.* **2022**, *282*, 120124. [CrossRef]
40. Wang, K.; Yang, Y.; Zhang, T.C.; Liang, Y.; Wang, Q. Degradation of Methylene Blue with Magnetic Co-Doped Fe<sub>3</sub>O<sub>4</sub>@FeOOH Nanocomposites as Heterogeneous Catalysts of Peroxymonosulfate. *RSC Adv.* **2019**, *9*, 17664–17673. [CrossRef]
41. Tang, W.; Zhang, Y.; Guo, H.; Liu, Y. Heterogeneous Activation of Peroxymonosulfate for Bisphenol AF Degradation with BiOI<sub>0.5</sub>Cl<sub>0.5</sub>. *RSC Adv.* **2019**, *9*, 14060–14071. [CrossRef] [PubMed]
42. Li, M.; Jin, Y.T.; Yan, J.F.; Liu, Z.; Feng, N.X.; Han, W.; Huang, L.W.; Li, Q.K.; Yeung, K.L.; Zhou, S.Q.; et al. Exploration of Perfluorooctane Sulfonate Degradation Properties and Mechanism via Electron-Transfer Dominated Radical Process. *Water Res.* **2022**, *215*, 118259. [CrossRef] [PubMed]
43. Li, M.; Jin, Y.T.; Cao, D.Y.; Yang, L.L.; Yan, J.F.; Zhang, Z.X.; Liu, Z.; Huang, L.W.; Zhou, S.Q.; Cheng, J.L.; et al. Efficient Decomposition of Perfluorooctane Sulfonate by Electrochemical Activation of Peroxymonosulfate in Aqueous Solution: Efficacy, Reaction Mechanism, Active Sites, and Application Potential. *Water Res.* **2022**, *221*, 118778. [CrossRef] [PubMed]
44. Li, X.; Liu, X.; Lin, C.; Zhang, H.; Zhou, Z.; Fan, G.; Ma, J. Cobalt Ferrite Nanoparticles Supported on Drinking Water Treatment Residuals: An Efficient Magnetic Heterogeneous Catalyst to Activate Peroxymonosulfate for the Degradation of Atrazine. *Chem. Eng. J.* **2019**, *367*, 208–218. [CrossRef]
45. Noorisepehr, M.; Ghadirinejad, K.; Kakavandi, B.; Ramazanpour Esfahani, A.; Asadi, A. Photo-Assisted Catalytic Degradation of Acetaminophen Using Peroxymonosulfate Decomposed by Magnetic Carbon Heterojunction Catalyst. *Chemosphere* **2019**, *232*, 140–151. [CrossRef]
46. Chen, W.S.; Huang, C.P. Mineralization of Aniline in Aqueous Solution by Electrochemical Activation of Persulfate. *Chemosphere* **2015**, *125*, 175–181. [CrossRef]
47. Hassani, A.; Eghbali, P.; Mahdipour, F.; Waclawek, S.; Lin, K.Y.A.; Ghanbari, F. Insights into the Synergistic Role of Photocatalytic Activation of Peroxymonosulfate by UVA-LED Irradiation over CoFe<sub>2</sub>O<sub>4</sub>-RGO Nanocomposite towards Effective Bisphenol A Degradation: Performance, Mineralization, and Activation Mechanism. *Chem. Eng. J.* **2023**, *453*, 139556. [CrossRef]
48. Shen, Y.; Martín de Vidales, M.J.; Espíndola, J.C.; Gómez-Herrero, A.; Dos santos-García, A.J. Paracetamol Degradation by Photo-Assisted Activation of Peroxymonosulfate over Zn<sub>x</sub>Ni<sub>1-x</sub>Fe<sub>2</sub>O<sub>4</sub>@BiOBr Heterojunctions. *J. Environ. Chem. Eng.* **2021**, *9*, 106797. [CrossRef]
49. Lin, K.A.; Chang, H. Zeolitic Imidazole Framework-67 (ZIF-67) as a Heterogeneous Catalyst to Activate Peroxymonosulfate for Degradation of Rhodamine B in Water. *J. Taiwan Inst. Chem. Eng.* **2015**, *53*, 40–45. [CrossRef]
50. Bandala, E.R.; Peláez, M.A.; Dionysiou, D.D.; Gelover, S.; Garcia, J.; Macías, D. Degradation of 2,4-Dichlorophenoxyacetic Acid (2,4-D) Using Cobalt-Peroxymonosulfate in Fenton-like Process. *J. Photochem. Photobiol. A Chem.* **2007**, *186*, 357–363. [CrossRef]
51. He, J.; Yang, J.; Jiang, F.; Liu, P.; Zhu, M. Photo-Assisted Peroxymonosulfate Activation via 2D/2D Heterostructure of Ti<sub>3</sub>C<sub>2</sub>/g-C<sub>3</sub>N<sub>4</sub> for Degradation of Diclofenac. *Chemosphere* **2020**, *258*, 127339. [CrossRef]

52. Karim, A.V.; Hassani, A.; Eghbali, P.; Nidheesh, P.V. Nanostructured Modified Layered Double Hydroxides (LDHs)-Based Catalysts: A Review on Synthesis, Characterization, and Applications in Water Remediation by Advanced Oxidation Processes. *Curr. Opin. Solid State Mater. Sci.* **2022**, *26*, 100965. [CrossRef]
53. Liu, Y.; Guo, H.; Zhang, Y.; Cheng, X.; Zhou, P.; Wang, J.; Li, W. Fe@C Carbonized Resin for Peroxymonosulfate Activation and Bisphenol S Degradation. *Environ. Pollut.* **2019**, *252*, 1042–1050. [CrossRef]
54. Kohantorabi, M.; Moussavi, G.; Giannakis, S. A Review of the Innovations in Metal- and Carbon-Based Catalysts Explored for Heterogeneous Peroxymonosulfate (PMS) Activation, with Focus on Radical vs. Non-Radical Degradation Pathways of Organic Contaminants. *Chem. Eng. J.* **2021**, *411*, 127957. [CrossRef]
55. Khalil, Z.A.; Baalbaki, A.; Bejjani, A.; Ghauch, A. MIL88-A as a Mediator for the Degradation of Sulfamethoxazole in PS Systems: Implication of Solar Irradiation for Process Improvement. *Environ. Sci. Adv.* **2022**, *1*, 797–813. [CrossRef]
56. Yang, Q.; Choi, H.; Al-Abed, S.R.; Dionysiou, D.D. Iron-Cobalt Mixed Oxide Nanocatalysts: Heterogeneous Peroxymonosulfate Activation, Cobalt Leaching, and Ferromagnetic Properties for Environmental Applications. *Appl. Catal. B Environ.* **2009**, *88*, 462–469. [CrossRef]
57. Huang, F.; An, Z.; Moran, M.J.; Liu, F. Recognition of Typical Antibiotic Residues in Environmental Media Related to Groundwater in China (2009–2019). *J. Hazard. Mater.* **2020**, *399*, 122813. [CrossRef]
58. Yan, W.; Xiao, Y.; Yan, W.; Ding, R.; Wang, S.; Zhao, F. The Effect of Bioelectrochemical Systems on Antibiotics Removal and Antibiotic Resistance Genes: A Review. *Chem. Eng. J.* **2019**, *358*, 1421–1437. [CrossRef]
59. Liu, D.; Li, H.; Gao, R.; Zhao, Q.; Yang, Z.; Gao, X.; Wang, Z.; Zhang, F.; Wu, W. Enhanced Visible Light Photoelectrocatalytic Degradation of Tetracycline Hydrochloride by I and P Co-Doped TiO<sub>2</sub> Photoelectrode. *J. Hazard. Mater.* **2021**, *406*, 124309. [CrossRef] [PubMed]
60. dos Santos, A.J.; Kronka, M.S.; Fortunato, G.V.; Lanza, M.R.V. Recent Advances in Electrochemical Water Technologies for the Treatment of Antibiotics: A Short Review. *Curr. Opin. Electrochem.* **2021**, *26*, 100674. [CrossRef]
61. Peralta-Hernández, J.M.; Brillas, E. A Critical Review over the Removal of Paracetamol (Acetaminophen) from Synthetic Waters and Real Wastewaters by Direct, Hybrid Catalytic, and Sequential Ozonation Processes. *Chemosphere* **2023**, *313*, 137411. [CrossRef]
62. Zhu, L.; Shi, Z.; Deng, L. Enhanced Heterogeneous Degradation of Sulfamethoxazole via Peroxymonosulfate Activation with Novel Magnetic MnFe<sub>2</sub>O<sub>4</sub>/GCNS Nanocomposite. *Colloids Surf. A Physicochem. Eng. Asp.* **2021**, *621*, 126531. [CrossRef]
63. Poza-Nogueiras, V.; Moratalla, A.; Pazos, M.; Sanroman, A.; Sáez, C.; Rodrigo, M.A. Exploring the Pressurized Heterogeneous Electro-Fenton Process and Modelling the System. *Chem. Eng. J.* **2022**, *431*, 133280. [CrossRef]
64. Yu, Y.-P.; Pan, M.-M.; Jiang, M.; Yu, X.; Xu, L. Facile Synthesis of Self-Assembled Three-Dimensional Flower-like Cu-MOF and Its Pyrolytic Derivative Cu-N-C450 for Diverse Applications. *J. Environ. Chem. Eng.* **2023**, *11*, 109400. [CrossRef]
65. Blanco-Canella, P.; Lama, G.; Sanromán, M.A.; Pazos, M. Disinfection through Advance Oxidation Processes: Optimization and Application on Real Wastewater Matrices. *Toxics* **2022**, *10*, 512. [CrossRef] [PubMed]
66. Nightingale, P.; Miruszenko, L.; Shillam, R.; Christian, P.; Elliott, T.S.J. Role of Copper in Reducing Hospital Environment. *J. Hosp. Infect.* **2010**, *74*, 72–77. [CrossRef]
67. Chakraborty, D.; Musib, D.; Saha, R.; Das, A.; Raza, M.K.; Ramu, V.; Chongdar, S.; Sarkar, K.; Bhaumik, A. Highly Stable Tetradentate Phosphonate-Based Green Fluorescent Cu-MOF for Anticancer Therapy and Antibacterial Activity. *Mater. Today Chem.* **2022**, *24*, 100882. [CrossRef]
68. Fu, A.; Liu, Z.; Sun, Z. Cu/Fe Oxide Integrated on Graphite Felt for Degradation of Sulfamethoxazole in the Heterogeneous Electro-Fenton Process under near-Neutral Conditions. *Chemosphere* **2022**, *297*, 134257. [CrossRef] [PubMed]

**Disclaimer/Publisher’s Note:** The statements, opinions and data contained in all publications are solely those of the individual author(s) and contributor(s) and not of MDPI and/or the editor(s). MDPI and/or the editor(s) disclaim responsibility for any injury to people or property resulting from any ideas, methods, instructions or products referred to in the content.

## Article

# Synthesis of Green Magnetite/Carbonized Coffee Composite from Natural Pyrite for Effective Decontamination of Congo Red Dye: Steric, Synergetic, Oxidation, and Ecotoxicity Studies

Marwa H. Shemy<sup>1,2</sup>, Sarah I. Othman<sup>3,\*</sup>, Haifa E. Alfassam<sup>3</sup>, Maha A. Al-Waili<sup>3</sup>, Haifa A. Alqhtani<sup>3</sup>, Ahmed A. Allam<sup>4</sup> and Mostafa R. Abukhadra<sup>2,5,\*</sup> 

<sup>1</sup> Chemistry Department, Faculty of Science, Beni-Suef University, Beni-Suef 65211, Egypt

<sup>2</sup> Materials Technologies and Their Applications Lab, Geology Department, Faculty of Science, Beni-Suef University, Beni-Suef City 65211, Egypt

<sup>3</sup> Biology Department, College of Science, Princess Nourah bint Abdulrahman University, Riyadh 11564, Saudi Arabia

<sup>4</sup> Zoology Department, Faculty of Science, Beni-Suef University, Beni-Suef 65211, Egypt

<sup>5</sup> Geology Department, Faculty of Science, Beni-Suef University, Beni-Suef 65211, Egypt

\* Correspondence: sialothman@pnu.edu.sa (S.I.O.); abukhadra89@science.bsu.edu.eg (M.R.A.)

**Abstract:** Green magnetite/carbonized spent coffee (MG/CFC) composite was synthesized from natural pyrite and characterized as an adsorbent and catalyst in photo-Fenton's oxidation system of Congo red dye (C.R). The absorption behavior was illustrated based on the steric and energetic parameters of the advanced Monolayer equilibrium model of one energetic site ( $R^2 > 0.99$ ). The structure exhibits 855 mg/g as effective site density which induces its C.R saturation adsorption capacity to 436.1 mg/g. The change in the number of absorbed C.R per site with temperature ( $n = 1.53$  (293) to 0.51 (313 K)) suggests changes in the mechanism from multimolecular (up to 2 molecules per site) to multianchorage (one molecule per more than one site) processes. The energetic studies ( $\Delta E = 6.2\text{--}8.2$  kJ/mol) validate the physical uptake of C.R by MG/CFC which might be included van der Waals forces, electrostatic attractions, and hydrogen bonding. As a catalyst, MG/CFC exhibits significant activity during the photo-Fenton's oxidation of C.R under visible light. The complete oxidation of C.R was detected after 105 min (5 mg/L), 120 min (10 mg/L), 135 min (15 mg/L), 180 min (20 mg/L), and 240 min (25 mg/L) using MG/CFC at 0.2 g/L dosage and 0.1 mL of  $H_2O_2$ . Increasing the dosage up to 0.5 g/L reduce the complete oxidation interval of C.R (5 mg/L) down to 30 min while the complete mineralization was detected after 120 min. The acute and chronic toxicities of the treated samples demonstrate significant safe products of no toxic effects on aquatic organisms as compared to the parent C.R solution.

**Citation:** Shemy, M.H.; Othman, S.I.; Alfassam, H.E.; Al-Waili, M.A.; Alqhtani, H.A.; Allam, A.A.; Abukhadra, M.R. Synthesis of Green Magnetite/Carbonized Coffee Composite from Natural Pyrite for Effective Decontamination of Congo Red Dye: Steric, Synergetic, Oxidation, and Ecotoxicity Studies. *Catalysts* **2023**, *13*, 264. <https://doi.org/10.3390/catal13020264>

Academic Editors: Juan José Rueda-Márquez, Javier Moreno-Andrés and Irina Levchuk

Received: 25 December 2022

Revised: 16 January 2023

Accepted: 20 January 2023

Published: 24 January 2023



**Copyright:** © 2023 by the authors. Licensee MDPI, Basel, Switzerland. This article is an open access article distributed under the terms and conditions of the Creative Commons Attribution (CC BY) license (<https://creativecommons.org/licenses/by/4.0/>).

**Keywords:** pyrite; coffee; magnetite; composite; adsorption; photo-Fenton's oxidation

## 1. Introduction

The high-income industries in developing countries and the related discharges are the essential reason for the water pollution threats and their toxic impacts on various forms of life. The textile, printing, plastic, and paper industries involve the consumption of huge quantities of pigments and dyes [1,2]. Dyes that are vital aromatic compounds have been widely used. Its annual production has been reported  $7 \times 10^5$  tons [3,4]. 10% to 15% of the annually produced synthetic dyes are disposed of into water bodies as untreated, non-degradable industrial wastewater causing adverse effects on all life forms [5–7]. Among the synthetic dyes, Congo red (CR) is an anionic toxic dye that is of a sodium salt of amine-4-sulfonic acid benzidindiazo-bis-1-navatella and is widely used in the textile industry [8–10]. The leakage of Congo red into the water resources is of several environmental drawbacks. This includes the depletion of dissolved oxygen and the destruction of the photosynthesis

system. Additionally, such hazardous chemical compounds cause suffocation of the aquatic organisms such as fauna and flora [2,11–13]. From a health point of view, CR dye is of carcinogenic, allergenic, mutagenic, and cytotoxic effects [2,10,14].

Therefore, the interested researcher as well as the responsible authorities suggested several physical and chemical techniques to decline the concentrations of the synthetic dyes. This includes advanced oxidation, adsorption, membrane separation, biological degradation, and nano-filtration. The adsorption technique is a simple, cheap, available, and very effective method in the decontamination of both organic and inorganic contaminants [10,15,16]. The reported advanced oxidation techniques involved photocatalytic, Sonocatalytic, Fenton's, and photo Fenton's oxidation were addressed as very promising methods during the remediation of the dyes [17,18]. The photo Fenton oxidation reactions can be divided into homogenous reactions and heterogeneous reactions [6,19]. The homogenous reactions that involve the interaction between hydrogen peroxide and dissolved ferrous iron ions are simple and inexpensive processes [6,20]. However, there are practical difficulties to scale up the reactions for commercial remediation of dyes and other organic compounds [20,21]. This is related to the consumption of huge amounts of iron, the formation of ferric hydroxide sludge as a byproduct, and the tight range of PH [20]. Therefore, the heterogeneous reactions were recommended as they can be applied within a wide pH range, of low iron consumption, excellent efficiency, and significant recyclability [19].

The Zerovalent iron, as well as the other iron-based green synthesized nanomaterials, is an environmentally friendly structure that was applied widely as adsorbents and heterogeneous catalysts [22]. The previous studies demonstrate the effective applications of such materials to remove the organic contaminants either by adsorption or by photo-Fenton's oxidation processes. This was assigned essentially to their significant surface area, reactivity, adsorption capacity, and band gap energy in addition to the existence of bisphenol caps which enhance their affinities for the common organic pollutants [23–26]. Green synthesized magnetite nanoparticles ( $\text{Fe}_3\text{O}_4$ ) were assessed as potential adsorbents and heterogeneous catalysts of promising Physio-chemical properties and can be separated effectively from the treated solutions using an external magnet [27,28]. The synthesis of magnetite/carbon composites was introduced as stable and effective hybrid structures of enhanced electrostatic attractive forces and significant quantities of active functional groups (carboxyl groups) [27,28].

One of the main technical problems that face the synthesis of green iron oxide nanoparticles is the starting precursors. Unfortunately, most of the introduced studies about the synthesis of green iron oxide involved iron-bearing chemical salts as raw materials which raise the cost of fabrication cost [22]. Utilizing natural raw materials in the synthesis of green iron oxide will reduce the production cost and can result in significant changes in the morphological and surficial properties. Pyrite is one of the most famous natural iron sulfide minerals ( $\text{FeS}_2$ ) that is of low economic value either as mining raw products or as by-products during the separation and beneficiation of precious metals [29,30]. Moreover, it is classified as an acid-generating mineral and its weathering results in toxic and hazardous acids that affected negatively the ecosystems and biodiversity in the mining sites including the highly toxic acid drainage wastewater in the mining sites [31]. Framboidal pyrite is a known form of pyrite that was classified in several literatures as a sedimentary mineral of biogenic origin and of considerable geological reserve [30,32–34]. Considering the chemical composition, reactivity, and textural properties of framboidal pyrite, it can be applied effectively in the synthesis of novel and advanced forms of green iron oxide nanoparticles of enhanced physiochemical properties.

Therefore, the current study aims to synthesize and characterization of low-cost magnetite/carbon green nanocomposite (MG/CFC) utilizing framboidal pyrite mining solid wastes as the iron-bearing precursor and commercial coffee as a precursor of carbon and the greed oxidizing reagent. The obtained structure was assessed as a potential adsorbent and heterogeneous catalyst for effective photo Fenton's oxidation of Congo red dye. The adsorption behavior was illustrated based on the advanced equilibrium properties



including the steric and energetic properties. The oxidation studies were assessed based on the main experimental parameters, kinetic properties, oxidizing radicals, synergetic effect, and suggested mechanism. This represents advanced recycling processes of pyrite solid waste and spent coffee powder in an innovative eco-friendly, simple, and low-cost hybrid structure of enhanced adsorption and catalytic properties during the decontamination applications of Congo red dye from the aqueous environment by photo-Fenton's oxidation system in the presence of commercial visible light source.

## 2. Results and Discussion

### 2.1. Characterization of the MG/CFC Catalyst

The XRD pattern of the synthetic Mg/CFC structure was compared to the used raw pyrite to confirm the transformation processes (Figure 1). The studied raw precursor exhibits the typical pattern of pyrite mineral with its characteristic peaks (Ref. No. 01-076-0963) (Figure 1A). The transformation of pyrite into Mg/CFC was confirmed by the remarkable changes in the obtained patterns and the identified phases. The patterns show the characteristic peaks of iron oxide (magnetite) (Ref. No. 01-076-0956; JCPDS. card No. 089-096) in addition to the broad peak of the amorphous carbon that is related to the coffee-based carbon substrate (Figure 1B). Such results confirm the formation of the composite between the precipitated green magnetite and the carbon-based coffee. Moreover, the detection of the iron phase as iron oxide reflects the extensive oxidation of the early-formed zero-valent iron into iron oxide [22,35].

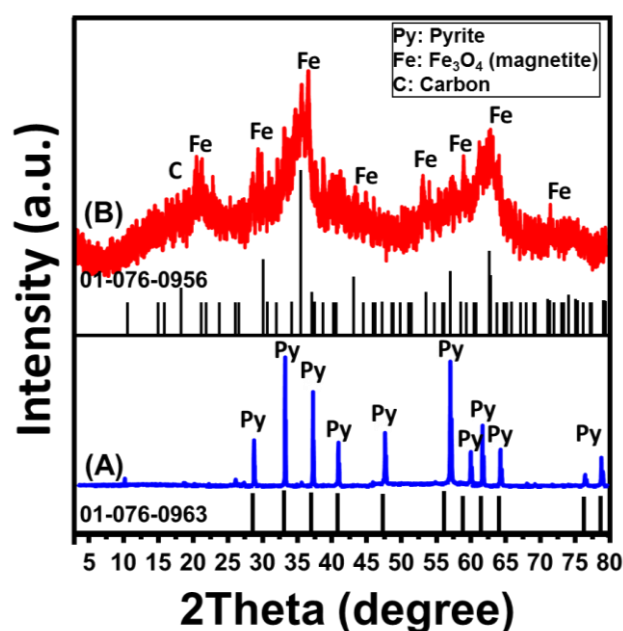


**Figure 1.** XRD pattern of the used raw pyrite (A) and the synthetic MG/CFC green nanocomposite (B).

This was supported significantly by the obtained SEM images of the synthetic structure (Figure 2). The surface of carbonized coffee particles exhibits irregular and wormy-like morphologies with numerous pores which give them significant surface area as carrier or substrate for the loaded green magnetite nanoparticles (Figure 2A). The synthesized green iron oxide appeared as bunches or clusters of numerous spherical nanoparticles related the precipitated Fe<sub>3</sub>O<sub>4</sub> nanoparticles that exhibit random distribution over the surface of carbonized coffee grains (Figure 2B–E). This significant alteration and formation of green magnetite/carbon composite (MG/CFC) was confirmed also based on the EDX findings of both pyrite precursors and the synthetic product (Figure 2F). The elemental EDX composition of the raw pyrite reflected its common composition of two essential elements which are Fe (66.72%) and S (33.25%) (Figure 2F). After the synthesis of the green

magnetite/carbon composite (MG/CFC), the EDX spectrum demonstrates the complete removal of S from the composition and the existence of Fe and O as the components of magnetite and C as the representative element of the carbonized coffee particles (Figure 2F).

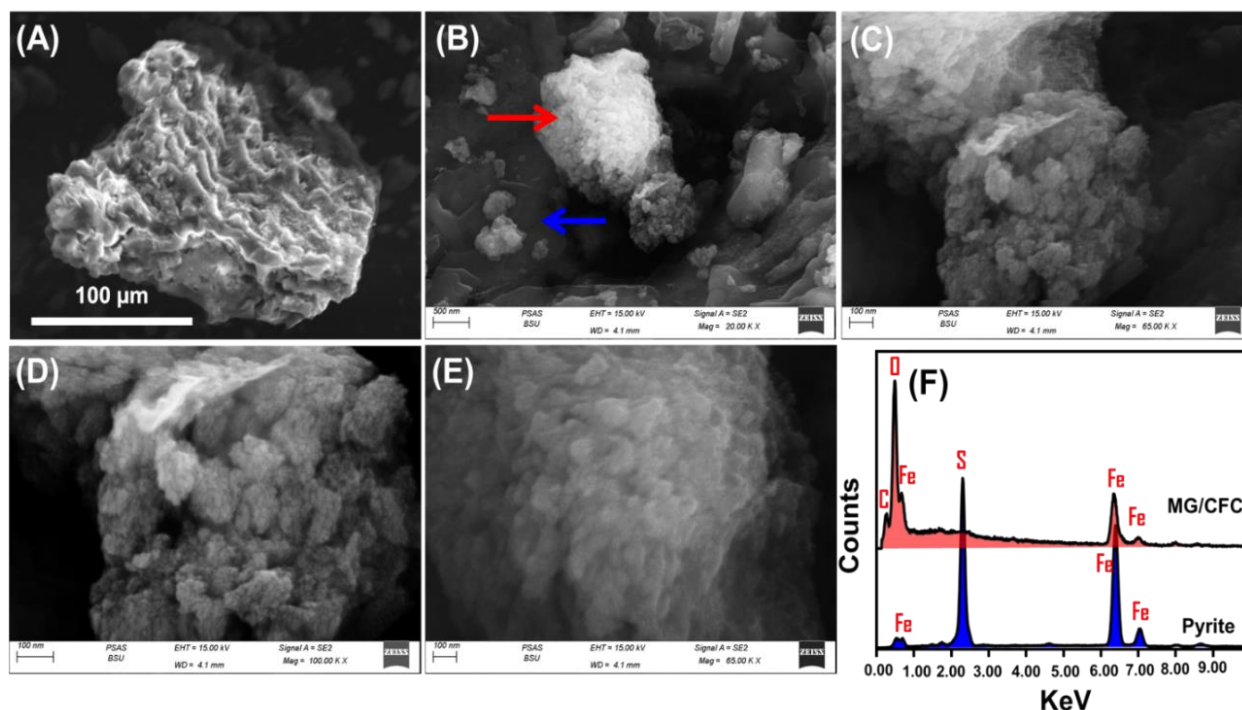


**Figure 2.** SEM images of the carbonized coffee grains (A), the synthetic green magnetite nano particles over the surface of carbonized coffee (B–E), and the EDX spectra of pyrite and the prepared MG/CFC composite (F).

Regarding the FT-IR spectra of pyrite, synthetic MG/CFC, and spent MG/CFC after the adsorption of C.R molecules, the observed spectra are in agreement with the chemical analysis (Figure 3). The spectrum of pyrite validates the existence of its main chemical groups such as Fe-O-OH ( $1087\text{ cm}^{-1}$ ), Fe-S ( $666.63\text{ cm}^{-1}$ ) and S-S ( $608.43\text{ cm}^{-1}$ ) in addition to other bands related to the -OH stretching ( $3300\text{ cm}^{-1}$ ) and vibration ( $556\text{ cm}^{-1}$ ) of adsorbed water molecules or the weathering effects on the pyrite structure (Figure 3A) [36–38]. Regarding the spectrum of green magnetite/carbonized coffee structure, the identification bands of iron oxide were recognized at  $456.4\text{ cm}^{-1}$  and  $611\text{ cm}^{-1}$  which validates the Fe-O bonding (Figure 3B) [39,40]. The chemical groups of the carbonized coffee substrates were signified around  $3184\text{ cm}^{-1}$  (O-H groups related to phenols, alcohols, or carboxylic acid),  $2921.4\text{ cm}^{-1}$  (C-H of methylene (-CH<sub>2</sub>-) and methyl groups (-CH<sub>3</sub>)),  $2859\text{ cm}^{-1}$  (C-H of cellulose backbone),  $1638.9\text{ cm}^{-1}$  (carbonyl groups that are related to the polyphenolic compounds of coffee),  $1409.5\text{ cm}^{-1}$  (-CH<sub>2</sub> and -CH<sub>3</sub> bending),  $1112.9\text{ cm}^{-1}$  (C-O and C-C of cellulose), and  $801\text{--}888.4\text{ cm}^{-1}$  (N-CH<sub>3</sub>) (Figure 3B) [40–42]. The identified chemical groups demonstrate the expected valuable role for the carbonized coffee either as a substrate for magnetite as catalysts during the photo Fenton's oxidation of C.R dye or as an integrated component in the hybrid adsorbent. Regarding the spectrum of the spent MG/CFC after the adsorption of C.R dye, it shows an observable reduction in the intensities of the absorption bands of the essential chemical groups in addition to slight shifting (Figure 3C). This validates a significant effect for most of the chemical groups of both magnetite and carbonized coffee during the uptake of the C.R dye.

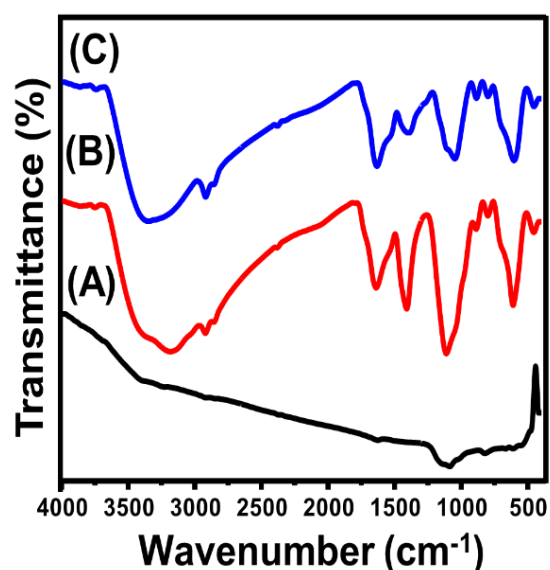


**Figure 3.** FT-IR spectra of the raw pyrite (A), the synthetic green magnetite nano particles over the surface of carbonized coffee (MG/CFC) (B), and spent MG/CFC after the adsorption of C.R molecules (C).

## 2.2. Adsorption Studies

### 2.2.1. Effect of pH

The pH value of the aqueous solutions during the uptakes processes of C.R. by MG/CFC is an essential factor that controls the dominance of the surficial charges as well as the dye molecules in the system. The pH (2–8) as an experimental variable was studied and the other effective variables were preserved at constant values [solid dosage: 0.2 g/L; volume: 100 mL; contact interval: 24 h; concentration: 50 mg/L; temperature: 293 K] during the performed experiments (Figure 4A). The experimentally detected C.R adsorption results signify the noticeable decline in the determined capacity of MG/CFC from pH 2 (143.3 mg/g) until pH 7 (94.6 mg/g) (Figure 4A). The high pH environments induce the generation of the negatively charged hydroxyl ions on the surface of MG/CFC as a result of the de-protonation of its chemical groups in the basic conditions [43]. The negatively charges C.R molecules are remarkably electrostatically repulsed by such deprotonated groups. The recognized behavior in terms of the studied pH validates is in agreement with the determined  $\text{pH}_{\text{ZPC}}$ . The determined  $\text{pH}_{\text{ZPC}}$  of MG/CFC is 4.6 and reveals the high occupation of the MG/CFC surface with numerous negative charges during the uptake of C.R. at  $\text{pH} > 4.6$  and positive charges at  $\text{pH} < 4.6$ .

### 2.2.2. Equilibrium Studies

#### Effect of C.R Concentrations

The investigation of the MG/CFC adsorption capacity in the existence of different C.R concentrations (50–350 mg/L) allows the experimental detection of the equilibrium behavior and actual saturation or maximum capacity of the MG/CFC structure. The other effective variables were preserved at constant values [solid dosage: 0.2 g/L; volume: 100 mL; contact interval: 24 h; pH: 2]. The temperature influence was followed from 293 K to 313 K (Figure 5B). The adsorption of C.R by MG/CFC structure is markedly enhanced when the tested C.R starting concentrations are high (Figure 4B). This enhancement effect is ascribed to an expected increase in the mobility or diffusion speed as well as the driving forces of the dissolved C.R molecules, which can prompt their interactions and collision rates with the essential and effective uptake sites on the MG/CFC surface [44]. The increment in the experimental C.R uptake efficiency is distinguished up to 250 mg/L during the three evaluated equilibriums tests which were performed at 293 K, 303 K, and 313 K (Figure 4B). Therefore, this concentration (250 mg/L) can be categorized as the experimental

C.R equilibrium concentration in the presence of MG/CFC as an adsorbent. The available active receptors that are present on the MG/CFC particles attain their saturation states and fully occupied with the C.R molecules. Therefore, the MG/CFC attains its maximum capacity as an adsorbent for C.R (331 mg/g (293 K), 351.3 mg/g (303 K), and 360.4 mg/g (313 K)) (Figure 4B).

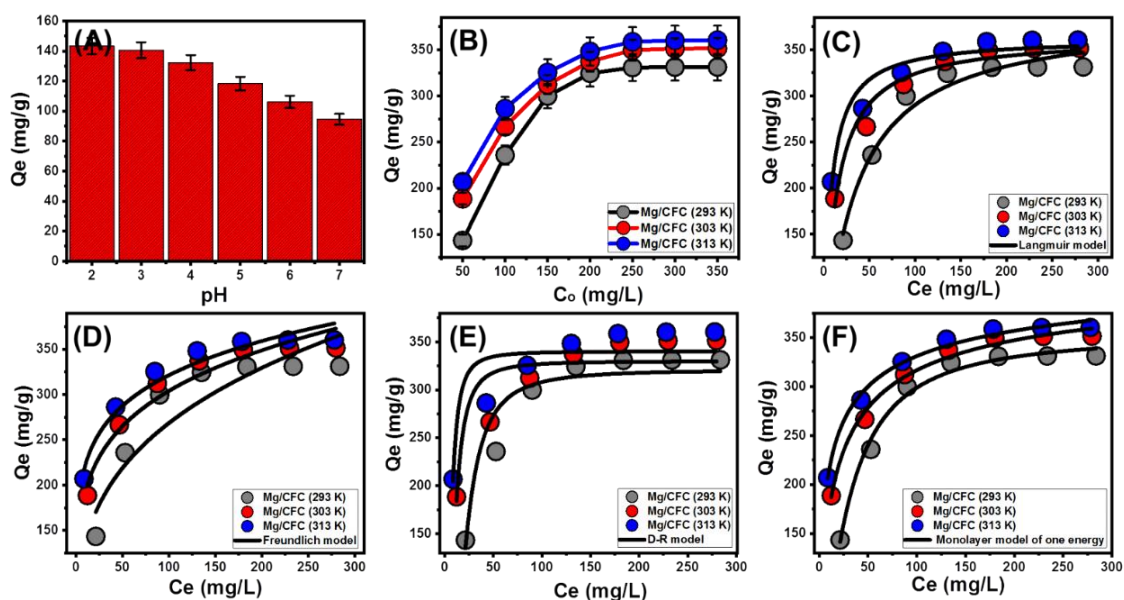


**Figure 4.** Effect of pH on the adsorption of C.R by Mg/CFC [dosage: 0.2 g/L; contact interval: 24 h; concentration: 50 mg/L; temperature: 293 K] (A), adsorption properties of Mg/CFC at different concentrations of C.R [dosage: 0.2 g/L; contact interval: 24 h; pH: 2] (B), fitting of the C.R adsorption data with Langmuir isotherm (C), fitting of the C.R adsorption data with Freundlich isotherm (D), fitting of the C.R adsorption data with D-R isotherm (E), and fitting of the C.R adsorption data with advanced monolayer model with one energy (F).

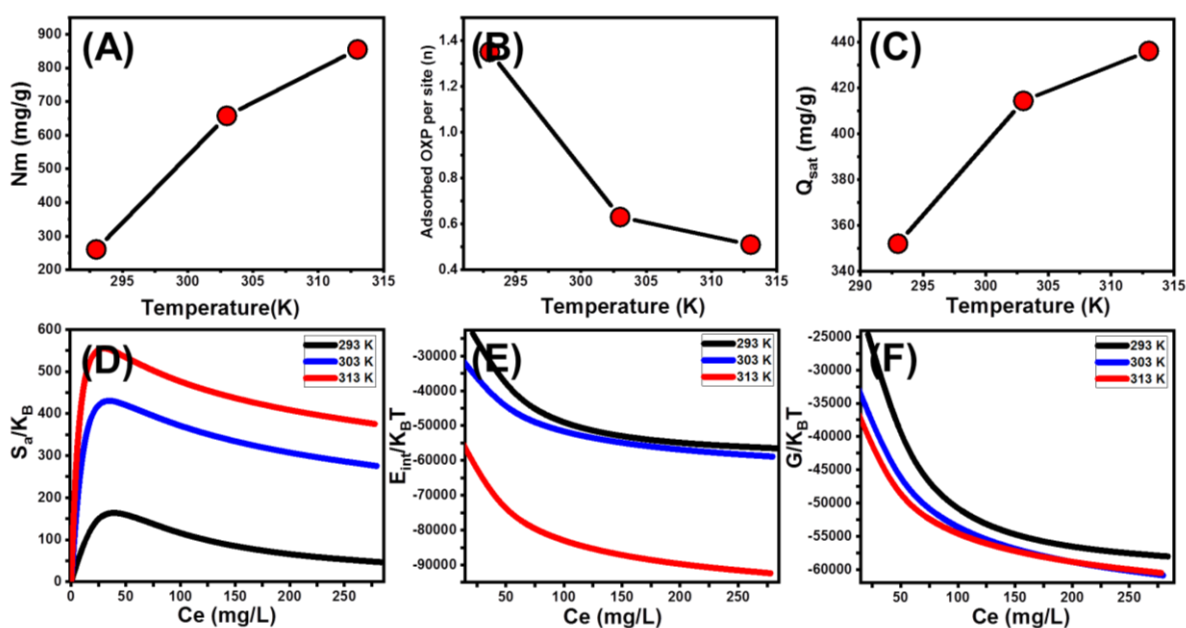


**Figure 5.** The change in (A) the number of adsorbed C.R molecules per each active site of MG/CFC, (B) the occupied active sites density by C.R molecules, (C) the entropy properties of the C.R adsorption reactions by MG/CFC, (D) internal energy of the C.R adsorption reactions by MG/CFC (E), and enthalpy of the C.R adsorption reactions by MG/CFC (F).

### Classic Isotherm Models

The equilibrium properties of the occurred C.R adsorption reactions by MG/CFC carriers were illustrated considering the common assumptions of Langmuir (Figure 4C), Freundlich (Figure 4D), and Dubinin–Radushkevich (D-R) (Figure 4E) models. This was accomplished based on the non-linear fitting degrees with the illustrative equations of these models considering the values of correlation coefficient ( $R^2$ ) as well as Chi-squared ( $\chi^2$ ) (Table 1; Figure 4C,E). Based on the recognized values of the fitting parameters, the C.R uptake process by MG/CFC exhibits the equilibrium properties of the Langmuir isotherm rather than the Freundlich model. This involved a homogenous C.R uptake process by the distributed active receptors throughout the surface of MG/CFC [45,46]. Furthermore, the obtaining of the RL parameter at values less than 1 demonstrates the favorable adsorption of C.R by MG/CFC as an adsorbent. Moreover, the Langmuir fitting parameters suggested theoretically the suitability of MG/CFC to adsorb up to 362.7 mg/g (293 K), 364.8 mg/g (303 K), and 388 mg/g (313 K) as maximum C.R adsorption capacities.

Regarding the investigated D-R model, its isotherm properties can signify strongly the energetic heterogeneity of MG/CFC as an adsorbent of C.R. regarding its homogenous or heterogeneous surface [47]. Moreover, the determination of the Gaussian energy ( $E$ ) as obtained theoretical parameter of the D-R model illustrate significantly the nature of the dominant adsorption processes either of chemical or physical properties. The physically controlled uptake systems exhibit Gaussian energy  $< 8$  KJ/mol while the chemically controlled system display values  $> 16$  KJ/mol. The systems that show Gaussian energy values of 8 to 16 KJ/mol validate the dominant impact of weak chemical mechanisms or complex processes [46,47]. The Gaussian energies of C.R uptake by MG/CFC are 1.73 kJ/mol (293 K), 3.61 kJ/mol (303 K), and 5.43 kJ/mol (313 K) (Table 1). These values reflect the operation of physical mechanisms during the C.R uptake process by MG/CFC.

**Table 1.** The estimated mathematical parameters of the studied classic and advanced equilibrium models.

Parameters of the Classic Isotherm Models				
		293 K	303 K	313 K
Langmuir model	$Q_{\max}$ (mg/g)	362.7	364.8	388.07
	$b$ (L/mg)	0.14	0.079	0.029
	$R^2$	0.95	0.97	0.98
	$\chi^2$	0.53	0.49	0.58
MG/CFC Freundlich model	$1/n$	0.16	0.19	0.29
	$k_F$ (mg/g)	153.5	122	68.9
	$R^2$	0.95	0.95	0.88
	$\chi^2$	0.67	0.81	3.6
D-R model	$\beta$ (mol <sup>2</sup> /KJ <sup>2</sup> )	0.0166	0.0384	0.0169
	$Q_m$ (mg/g)	321	330.1	340.2
	$R^2$	0.92	0.85	0.85
	$\chi^2$	1.96	2.8	2.3
	$E$ (KJ/mol)	1.73	3.61	5.43
Steric and energetic parameters of the advanced isotherm model				
MG/CFC	$R^2$	0.99	0.99	0.99
	$\chi^2$	0.29	0.17	0.12
	$n$	1.53	0.63	0.51
	$N_m$ (mg/g)	260.6	657.7	855.1
	$Q_{\text{Sat}}$ (mg/g)	351.8	414.3	436.1
	$C_{1/2}$ (mg/L)	28.8	17.3	10.79
	$\Delta E$ (kJ/mol)	8.2	7.3	6.2

### Advanced Isotherm Models

The advanced isotherm studies [monolayer model of one energy site] were performed to present more mechanistic significances based on the equilibrium assumptions of the statistical physics theory. This model was assessed considering the best values of RMSE and  $R^2$  which were obtained during the fitting processes (Figure 5F; Table 1). All the steric mathematical parameters of this model [ $n$  (number of adsorbed C.R molecules per site),  $N_m$  (density of the active sites), and  $Q_{sat}$  (the saturation capacity of MG/CFC as an adsorbent of C.R)], and energetic parameters [ $\Delta E$  (uptake energy of C.R),  $S_a$  (entropy),  $G$  (enthalpy), and  $E_{int}$  (internal energy)] (Table 1).

### Steric Parameters

The obtained number of the adsorbed C.R molecules per each active site ( $n$  parameter) of MG/CFC reveals the type of the operating adsorption mechanisms as well as the orientation (horizontal or vertical) of the uptake molecules (Figure 5A; Table 1). The adsorption systems that exhibit  $n$  value lower than 1 validate horizontal uptake of the dissolved ions via multi-docking and multianchorage mechanisms (one C.R. molecule might be adsorbed by more than one receptor or a fraction of molecule can be adsorbed per single site). Conversely, the systems which display  $n$  value of more than 1 ( $n > 1$ ) validate vertical uptake of the C.R molecules by multiple molecular mechanisms (several C.R might be adsorbed by one receptor) [46,48]. The determined values of  $n_{C,R}$  during the uptake of C.R by MG/CFC are 1.35 (293 K), 0.63 (303 K), and 0.51 (313 K) (Figure 5A; Table 1). Therefore, the C.R uptake process by MG/CFC at low-temperature conditions (293 K) involves the uptake up to two molecules by multimolecular mechanisms in a vertical orientation. At the high-temperature conditions (303 K and 313 K), each active site on the surface of MG/CFC can adsorb a fraction of the C.R molecule or each C.R molecule can be adsorbed by more than one site in horizontal orientation involving multianchorage mechanism [49]. The considerable declination in the  $n_{C,R}$  in terms of the temperature value reflects a significant reduction in the aggregation behavior of the C.R molecules during their uptake in addition to the predicted increment in the active uptake sites (Figure 5A; Table 1). The increase in the uptake sites might be related to the impact of temperature in inducing the diffusion rates of the C.R molecules to be in contact with additional sites in the internal structure of MG/CFC.

The recognized  $N_{m,C,R}$  values demonstrate strong enhancement in the quantities of the present active sites of MG/CFC or the occupied active sites density with temperature (260.6 mg/g (293 K), 657.7 mg/g (303 K), and 855.1 mg/g (313 K)) (Figure 5B; Table 1). These values are in agreement with the signified behavior of the  $n_{C,R}$  parameter and the impact of the temperature on the dominance of the active sites. The high-temperature conditions are of positive activation influence on the active sites of MG/CFC either by the exposure of additional active sites or more energetic site groups [49,50]. The increase in the uptake temperature is associated with a decrease in the viscosity of the C.R. solution. Therefore, the dissolved C.R molecules exhibit a significant increase in their mobility and their diffusion rates to be in contact with additional active sites. Such increment in the  $N_{m,C,R}$  values induce the adsorption capacity of MG/CFC especially at its saturation state ( $Q_{sat}$ ) that increased by 351.8 mg/g (293 K), 414.3 mg/g (303 K), and 436.1 mg/g (313 K) (Figure 6C; Table 1).

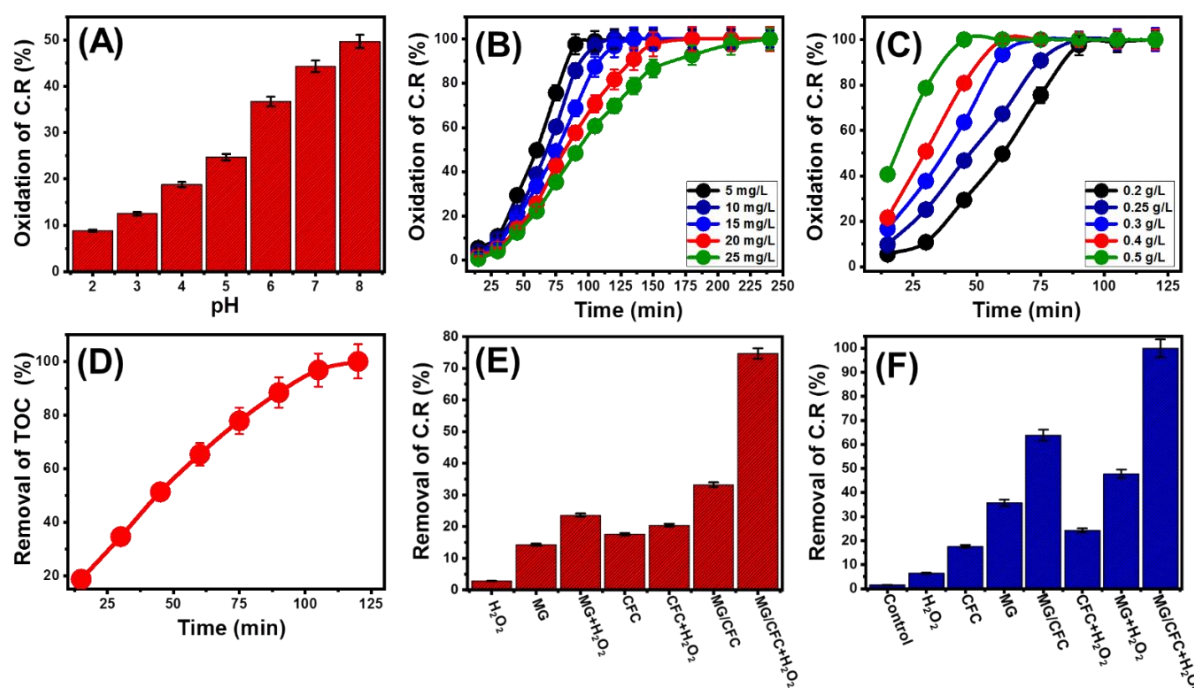


**Figure 6.** Shows (A) effect of pH on the oxidation of C.R. by MG/CFC [solid dosage: 0.2 g/L; interval: 60 min; concentration: 5 mg/L; temperature: 313 K; 0.1 mL H<sub>2</sub>O<sub>2</sub>], (B) oxidation behaviors of different concentrations of C.R. by MG/CFC [solid dosage: 0.2 g/L; temperature: 313 K; Fenton reagent: 0.1 mL H<sub>2</sub>O<sub>2</sub>], (C) effect of the MG/CFC dosages on the oxidation percentages of C.R. [C.R. concentration: 5 mg/L; temperature: 313 K; Fenton reagent: 0.1 mL H<sub>2</sub>O<sub>2</sub>], (D) the reduction in the TOC content during the oxidation of C.R. [C.R. concentration: 5 mg/L; dosage: 0.5 g/L; temperature: 313 K; Fenton reagent: 0.1 mL H<sub>2</sub>O<sub>2</sub>], (E) the synergetic effect of the integration processes between the components of the catalysts and hydrogen peroxide on the removal of C.R. in the dark by adsorption and Fenton reactions [dosage: 0.5 g/L; test interval: 60 min; temperature: 313 K; and C.R. concentration: 5 mg/L], and (F) the synergetic effect of the integration processes, visible light, and hydrogen peroxide on the removal of C.R. by photocatalytic and photo-Fenton's oxidation processes [dosage: 0.5 g/L; test interval: 60 min; temperature: 313 K; and C.R. concentration: 5 mg/L].

## Energetic Properties

### Adsorption energy

The adsorption energy of C.R. by MG/CFC ( $\Delta E$ ) can signify the nature of the operated uptake mechanism (physical ( $\Delta E \leq 40$  kJ/mol) or chemical ( $\Delta E > 80$  kJ/mol)). The physical processes might involve coordination exchange ( $\Delta E = 40$  kJ/mol), hydrogen bonding ( $\Delta E < 30$  kJ/mol), van der Waals forces ( $\Delta E = 4$  to 10 kJ/mol), dipole forces ( $\Delta E = 2$  to 29 kJ/mol), and hydrophobic bonds ( $\Delta E = 5$  kJ/mol) [50,51]. The  $\Delta E$  of the MG/CFC adsorption system was calculated according to Equation (1) considering the solubility of C.R. dye and its concentration at the half saturation state of MG/CFC [49].

$$\Delta E = RT \ln\left(\frac{S}{C}\right) \quad (1)$$

The theoretically determined  $\Delta E$  values of the C.R. uptake process by MG/CFC are 8.2 kJ/mol (293 K), 7.3 kJ/mol (303 K), and 6.2 kJ/mol (313 K) (Table 1). These values validate the uptake of C.R. by MG/CFC according to physical mechanisms which might be involved dipole bond forces, van der Waals forces, and hydrogen bonding in addition to the electrostatic attraction. Furthermore, the positive signs of these values validate the endothermic properties of the C.R. adsorption reactions by MG/CFC.

### Thermodynamic functions

The illustration of the entropy ( $S_a$ ) properties significantly validate the order and disorder properties of the surface of MG/CFC as an adsorbent of C.R dye at its different studied concentrations and uptake temperature values. The values were obtained theoretically from Equation (2) considering the steric parameters of the assessed advanced model [52].

$$\frac{S_a}{K_B} = N_m \left\{ \ln \left( 1 + \left( \frac{C}{C_{1/2}} \right)^n \right) - n \left( \frac{C}{C_{1/2}} \right)^n \frac{\ln \left( \frac{C}{C_{1/2}} \right)}{1 + \left( \frac{C}{C_{1/2}} \right)^n} \right\} \quad (2)$$

The obtained  $S_a$  values show remarkable declination at significant rates in the existence of high C.R concentrations validating a decrease in the disorder properties of MG/CFC and considerable docking of the C.R molecules on the free effective sites in the existence of low dye concentrations (Figure 5D) [49,53]. The equilibrium C.R concentrations which are the corresponding values of the highest  $S_a$  values (21.3 mg/L (293 K), 12.3 mg/L (303 K), and 8.6 mg/L (313 K)) are close to the previously estimated concentrations at half saturation states of MG/CFC (Figure 5D). Consequently, no more C.R molecules can be docked again by the active sites of MG/CFC beyond these concentrations. Moreover, this reflects a significant declination in the diffusion behavior and freedom degrees of C.R molecules as well as the free active sites of MG/CFC [54].

The other thermodynamic functions including the internal energy ( $E_{int}$ ) and free enthalpy ( $G$ ) were obtained theoretically according to Equations (3) and (4), respectively, depending on the estimated steric parameters and the translation partition ( $Z_v$ ) value [52].

$$\frac{E_{int}}{K_B T} = n N_m \left[ \left( \frac{\left( \frac{C}{C_{1/2}} \right)^n \ln \left( \frac{C}{Z_v} \right)}{1 + \left( \frac{C}{C_{1/2}} \right)^n} \right) - \left( \frac{n \ln \left( \frac{C}{C_{1/2}} \right) \left( \frac{C}{C_{1/2}} \right)^n}{1 + \left( \frac{C}{C_{1/2}} \right)^n} \right) \right] \quad (3)$$

$$\frac{G}{K_B T} = n N_m \frac{\ln \left( \frac{C}{Z_v} \right)}{1 + \left( \frac{C_{1/2}}{C} \right)^n} \quad (4)$$

The adsorption of C.R by MG/CFC exhibits negatively signed  $E_{int}$  values with considerable increment with evaluated temperature from 293 to 313 K (Figure 6E). This suggests spontaneous and exothermic uptake of C.R by MG/CFC structure which is supported by the negatively signed values of enthalpy ( $G$ ) which also increase in terms of the uptake temperature (Figure 5F).

### 2.3. Photo-Fenton Oxidation of C.R

#### 2.3.1. Effect of Oxidation Parameters

##### Effect of pH

The oxidation efficiency of C.R dye by MG/CFC as an applied heterogeneous catalyst in terms of the adjusted pH was followed up to pH 8 after attending the adsorption/desorption equilibrium state. The essential effective variables were preserved at constant values [solid dosage: 0.2 g/L; volume: 100 mL; contact interval: 60 min; concentration: 5 mg/L; temperature: 313 K; Fenton reagent: 0.1 mL  $H_2O_2$ ] during the performed experiments (Figure 6A). The recognized oxidation results demonstrate reversible behavior considering the obtained results during the C.R adsorption tests. The oxidation percentages of C.R by MG/CFC exhibit considerable enhancement at the high pH conditions as the percentages increased from 8.8% (pH 2) to 45% (pH 8) (Figure 6A). This difference in the behavior might be assigned to the significant inducing effect of the alkaline environments on the generated hydroxyl groups that are the essential initiators of the main oxidizing species during their oxidation into hydroxyl radicals [31]. The generation of such hydroxyl groups is assigned to the notable de-protonation of the functional groups of MG/CFC [6].



Additionally, the expected uptake of C.R at very high quantities on the surface of MG/CFC at the acidic condition reduces the interaction chances between the light photons and the catalytic sites of MG/CFC as well as the Fenton's reagent which reduces the catalytic performance of MG/CFC.

#### Effect of C.R Concentrations at Different Oxidation Intervals

The catalytic properties of MG/CFC in terms of the tested oxidation interval (15–240 min) and the C.R concentrations (5–25 mg/L) were followed considering the main variables at constant values [solid dosage: 0.2 g/L; volume: 100 mL; temperature: 313 K; Fenton reagent: 0.1 mL H<sub>2</sub>O<sub>2</sub>] during the performed experiments. The MG/CFC structure as heterogeneous catalysts in photo Fenton, oxidation systems of C.R displayed noteworthy oxidation properties within considerable treatment intervals (Figure 6B). The MG/CFC structure achieved complete oxidation for 5 mg/L, 10 mg/L, 15 mg/L, 20 mg/L, and 25 mg/L of C.R after 105 min, 120 min, 135 min, 180 min, and 240 min, respectively (Figure 6B). The marked declines in the oxidation activity of MG/CFC with the increase in the C.R concentration might be assigned to the high accumulation of the adsorbed C.R molecules as a layer on the surface of the catalyst. Such a thick adsorbed layer in addition to the weak penetration properties of light at the high C.R concentrations in the solutions weakens the interaction efficiency between the surface of MG/CFC and the incorporated Fenton reagent as well as the light photons [55]. This negatively affects the generation efficiency of the effective oxidizing species and in turn, the actual rate of the occurred Fenton oxidation reactions. Such weakening in the oxidation rates is notable in terms of the expansion in the oxidation interval until the establishment of the equilibration state at which the system shows a neglected or nearly fixed oxidation rate. This oxidation behavior is assigned to the continuous diminution of the generated oxidizing species during the performed C.R degradation processes over time until occurring the complete the consumption after a certain interval [56].

#### Effect of Catalyst Dosage at Different Oxidation Intervals

The oxidation rates in terms of the MG/CFC dosages were followed from 0.2 g/L until 0.5 g/L as an essential parameter to induce the photo Fenton's oxidation efficiencies of certain concentrations as well as the required oxidation interval which was followed from 5 min until 120 min (Figure 6C). The main variables were selected at constant values [C.R concentration: 5 mg/L; volume: 100 mL; temperature: 313 K; Fenton reagent: 0.1 mL H<sub>2</sub>O<sub>2</sub>] during the performed experiments. The high dosages of MG/CFC validate notable enhancement in the C.R oxidation rate causing remarkable declination in the required interval to achieve the complete oxidation of the test C.R concentrations. The incorporation of MG/CFC as catalysts at systematic dosages of 0.2 g/L, 0.3 g/L, 0.4 g/L, and 0.5 g/L resulted in complete oxidation of 5 mg/L of C.R after 105 min, 75 min, 60 min, and 45 min, respectively (Figure 6C). This behavior was reported widely in literature and signifies the extensive increase in the quantities of the active catalytic sites as well as the exposure surface. This provides a significant increase in the interaction interface between C.R molecules and the surface of MG/CFC as well as the quantities of generated oxidizing species in the system [57,58].

#### 2.3.2. Mineralization Efficiency

The mineralization properties of the oxidized C.R molecules in the existence of MG/CFC as heterogeneous catalysts in photo Fenton's oxidation system were followed to confirm the complete conversion of the dye into safe end products. The mineralization degree was evaluated by detecting the concentrations of the TOC content in the treated C.R solutions at the best experimentally studied oxidation conditions [C.R concentration: 5 mg/L; volume: 100 mL; MG/CFC dosage: 0.5 g/L; temperature: 313 K; Fenton reagent: 0.1 mL H<sub>2</sub>O<sub>2</sub>] within oxidation interval from 5 min until 120 min. However, the complete oxidation or de-colorization of C.R was detected after 45 min, and the complete mineraliza-

tion was detected after 120 min achieving a 100% removal percentage of TOC (Figure 6D). Therefore, the papered MG/CFC structure is a highly effective environmental catalyst that can be applied for complete photo-Fenton's oxidation of C.R molecules into safe and end products. The notable differences between the required intervals for the complete de-colorization of C.R molecules and their complete mineralization reflects the formation of intermediate compounds during the progressive oxidation of the dye.

### 2.3.3. Synergetic Properties of Oxidation System

The influence of the integrated components either the carbonized spent coffee (CFC) or the pyrite-based green magnetite (MG) on the performance of the studied MG/CFC composite either as an adsorbent or as a heterogeneous catalyst was inspected considering the following conditions:

- $\text{H}_2\text{O}_2$  (0.1 mL) without catalyst and a light source (Figure 6E)
- CFC, MG, and MG/CFC without  $\text{H}_2\text{O}_2$  or a light source as a separated test (adsorption) (Figure 6E)
- $\text{H}_2\text{O}_2$  + catalyst (CFC, MG, and MG/CFC) without the light source (Fenton's oxidation) (Figure 6E)
- visible light source without catalyst or  $\text{H}_2\text{O}_2$  (Figure 6F)
- visible light source+  $\text{H}_2\text{O}_2$  (0.1 mL) (Figure 6F)
- visible light source+ catalyst (CFC, MG, and MG/CFC) (photocatalytic oxidation) (Figure 6F)
- visible light source+ catalyst (CFC, MG, and MG/CFC) + $\text{H}_2\text{O}_2$  (photo-Fenton's oxidation) (Figure 6F)

The experiments were accomplished based on certain values for the following variables: MG/CFC dosage: 0.5 g/L; volume: 100 mL; test interval: 60 min; temperature: 313 K; and C.R concentration: 5 mg/L. The direct effect of the visible light source exhibited a neglected oxidation impact on the C.R molecules (1.6%) while the tests which were performed using only  $\text{H}_2\text{O}_2$  (0.1 mL) had a slightly greater oxidation effect than the detected effect of the light source (2.8%) under the same experimental conditions. The combination between the light source and  $\text{H}_2\text{O}_2$  (0.1 mL) enhances the oxidation efficiency of C.R to 6.4%. The incorporation of carbonized spent coffee (CFC), green magnetite (MG), and their composite (MG/CFC) without  $\text{H}_2\text{O}_2$  and light source resulted in adsorption removal percentages of 17.6%, 14.3%, and 33.2%, respectively. This demonstrates the value impact of the integration processes between them on the C.R uptake properties either by introducing additional active chemical groups adsorption sites) or by enhancing the surface area.

The incorporation of CFC, MG, and MG/CFC in the presence of  $\text{H}_2\text{O}_2$  (0.1 mL) without the light source (Fenton's oxidation system) demonstrates notable Fenton's oxidation activities of MG and MG/CFC and no oxidation activity for CFC considering the oxidation percentage of the incorporated  $\text{H}_2\text{O}_2$ . The determined C.R removal percentages are 20.4%, 23.6%, and 74.4% in the existence of CFC, MG, and MG/CFC, respectively. Similar behavior was detected during the incorporation of them in the presence of the light source without  $\text{H}_2\text{O}_2$  (photocatalytic oxidation system). The removal percentages of C.R increased to 35.7% and 63.8% using MG and MG/CFC, respectively, as compared to the achieved results by adsorption. The fixed removal percentage of C.R (17.6%) either by adsorption or photocatalytic processes using CFC demonstrates the photocatalytic activities of MG and MG/CFC as compared to CFC. The combination between developed catalysts (MG and MG/CFC),  $\text{H}_2\text{O}_2$  (0.1 mL), and the light source (photo-Fenton's oxidation system) appear to be of enhanced oxidation effects on the dissolved C.R molecules as the removal percentages upgraded to 50.8% (MG), and 100% (MG/CFC). Therefore, the incorporation of MG/CFC as a green and low-cost catalyst in a photo-Fenton oxidation system toward the dissolved C.R dye is recommended strongly instead of separated photocatalytic or Fenton-oxidation systems.

### 2.3.4. Kinetic and Quantum Yield Studies

The kinetic properties of the occurred photo-Fenton's oxidation of C.R dye by MG/CFC were illustrated considering the common assumptions of first-order (Equation (5)) (Figure 7A,B) and second-order (Equation (6)) (Figure 7C,D) kinetics. The values of  $R^2$ , as well as  $\chi^2$ , were considered to estimate the linear regression fitting degrees between the results and the studied models [57].

$$C_t = C_0 e^{-k_1 t} \quad (5)$$

$$\frac{1}{C_t} = \frac{1}{C_0} + k_2 t \quad (6)$$

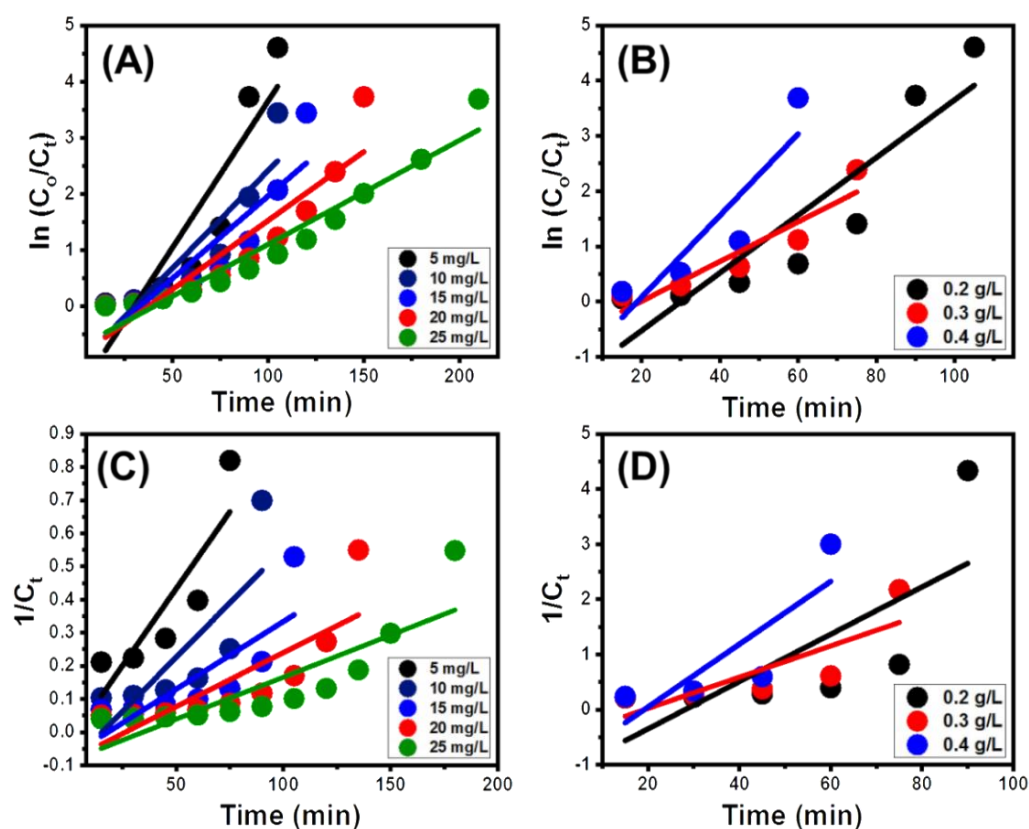


**Figure 7.** Fitting of the C.R photo-Fenton's oxidation results using MG/CFC with First order (A,B) and Second order (C,D) kinetic models.

The recognized fitting degrees validate the occurrence of the C.R oxidation processes by MG/CFC according to the kinetic behaviors of the First-order model either in terms of the C.R concentration or the applied dosages of MG/CFC. This kinetic behavior demonstrates the controlling effect of one of the assessed experimental variables (MG/CFC dosage, C.R concentration, and oxidation duration) on the efficiency of the MG/CFC-based photo-Fenton's oxidation system of C.R dye. The reported cases that show agreement with the two kinetic assumptions at the same time reveal the possible cooperation of more than one oxidation mechanism or more than one of the generated oxidizing radicals. The obtained kinetic rate constants of the evaluated models exhibit marked increment and declination in terms of the increase in the MG/CFC dosages and C.R concentrations, respectively, which are in significant agreement with the reported experimental behaviors (Table 2).

**Table 2.** The estimated correlation coefficient, kinetic rate constants, and quantum yield values.

		First Order		Second Order		Quantum Yield ( $\phi$ )
		R <sup>2</sup>	K <sub>1</sub>	R <sup>2</sup>	K <sub>2</sub>	
Dosage	0.2 g/L	0.83	0.052	0.75	0.0092	$5.34 \times 10^{-8}$
	0.3 g/L	0.87	0.0652	0.66	0.0428	$6.73 \times 10^{-8}$
	0.4 g/L	0.81	0.0739	0.70	0.0569	$7.63 \times 10^{-8}$
Concentration	5 mg/L	0.83	0.052	0.75	0.0092	$5.34 \times 10^{-8}$
	10 mg/L	0.80	0.034	0.63	0.0065	$3.51 \times 10^{-8}$
	15 mg/L	0.81	0.029	0.63	0.0040	$2.99 \times 10^{-8}$
	20 mg/L	0.84	0.024	0.66	0.0032	$2.47 \times 10^{-8}$
	25 mg/L	0.93	0.018	0.72	0.0025	$1.859 \times 10^{-8}$

The apparent values of the quantum yield ( $\phi$ ) of the performed oxidation experiments were obtained based on the rate constant of the fitting processes with the first-order kinetic model ( $k_1$ ), molar absorptivity ( $\epsilon_\lambda$  ( $\text{cm}^{-1} \text{M}^{-1}$ )), the intensity of the light source ( $I_{o,\lambda}$  (Einstein  $\text{I}^{-1} \text{S}^{-1}$ )), and the cell length ( $\ell$  (cm)) (Equation (7)). The  $\phi$  values validate the quantities of the charge carriers that can provide the best oxidation effects on the C.R molecule per the absorbed light photon [6,59]. Therefore, their estimated values can reflect the performances of the studied photo-Fenton's oxidation system in terms of the experimental variables. These values reflect notable agreement with the experimental studies and demonstrate the enhancement effect of the MG/CFC dosages on the photo-Fenton's oxidation of C.R dye (Table 2).

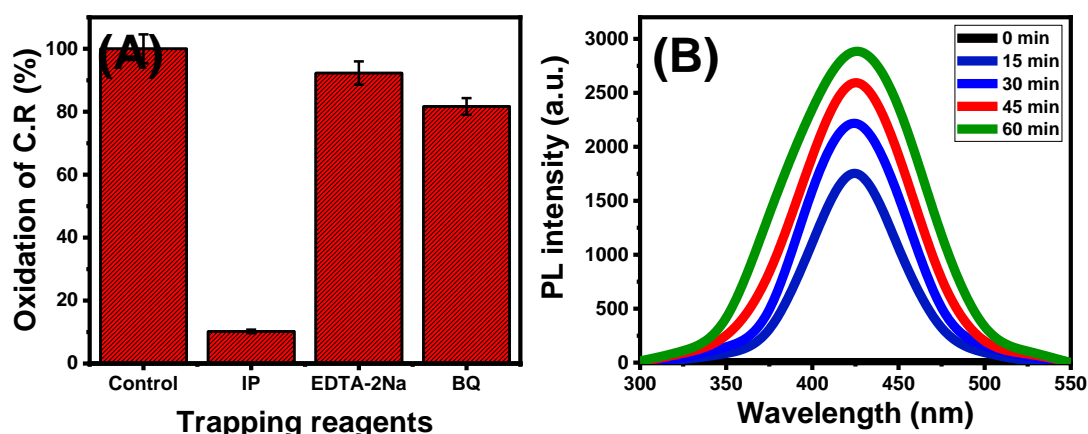
$$\phi = \frac{K_1}{2.303 \times I_{o,\lambda} \times \epsilon_\lambda \times \ell} \quad (7)$$

### 2.3.5. Suggested Oxidation Mechanism

#### Effective Oxidizing Species

The essential and effective oxidizing species were detected to follow the occurred oxidation mechanism as well as the pathway. This was accomplished based on the common trapping tests in the presence of isopropanol, 1-4 benzoquinone, and EDTA-2Na as effective scavenging or trapping chemical reagents of the hydroxyl ( $\text{OH}^\bullet$ ), superoxide ( $\text{O}_2^{\bullet-}$ ), and electron-hole pairs ( $h^+$ ) oxidizing species, respectively. The test was completed at the best experimentally studied oxidation conditions [C.R concentration: 5 mg/L; volume: 100 mL; MG/CFC dosage: 0.5 g/L; oxidation interval: 60 min; temperature: 313 K; Fenton reagent: 0.1 mL  $\text{H}_2\text{O}_2$ ] in the existence of 1 mmol of the scavenging reagents. The decolorization percentages of C.R declined notable from 100% to 10.2% (isopropanol), 81.7% (1-4 benzoquinone), and 92.3% (EDTA-2Na) (Figure 8A). Therefore, the dominant oxidizing species during the Photo-Fenton's oxidation of C.R by MG/CFC are the hydroxyl radicals followed by considerable impact for the generated superoxide radicals ( $\text{O}_2^{\bullet-}$ ).

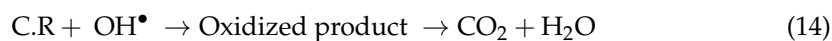
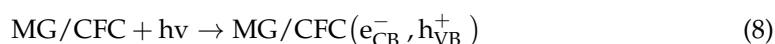
The probe molecule tests using terephthalic acid ( $5 \times 10^{-4} \text{M}$ ) were applied to follow the produced hydroxyl radicals. The terephthalic acid ( $5 \times 10^{-4} \text{M}$ ) probe and NaOH ( $2 \times 10^{-3} \text{M}$ ) were mixed with the C.R solution in the MG/CFC-based photo-Fenton's oxidation system. The quantities of hydroxyterephthalic acid which were produced during the oxidation of terephthalic acid were used as indicators of the generated quantities of oxidizing  $\text{OH}^\bullet$  species. This was followed based on the changes in the intensities of the measured photoluminescence spectroscopy (PL) spectra using a fluorescence spectrophotometer (Figure 8B). The notable intensification in the measured PL spectrum in terms of the gradual increase in the oxidation duration supports the previous experimental finding about the controlling impact of the  $\text{OH}^\bullet$  species during the performed photo-Fenton's oxidation processes of C.R by MG/CFC (Figure 8B).



**Figure 8.** The results of the oxidizing species scavenging tests during the oxidation of C.R by MG/CFC (A) and the changes in the intensities of the PL spectra at different oxidation intervals (B).

#### General Oxidation Mechanism

The Photo-Fenton's oxidation of C.R molecules by MG/CFC involved complex effects of photocatalytic and Fenton's oxidation processes (Figure 9). Both of the operating processes started with effective adsorption of the C.R molecules on the surface of MG/CFC and parallel generation of the main oxidizing species. The photocatalytic process involved the excitation of the outer electrons of MG/CFC by the photons of the used visible light source, which typically causes the significant generation of electron-hole pairs ( $h^+$ ) (Figure 9) [60,61]. The migrated electrons during this process interact with the present oxygen ions forming new oxidizing species (superoxide radicals ( $O_2^{\bullet-}$ )) [60]. The direct interaction between the formed electron-hole pairs ( $h^+$ ) and the water molecules cause significant water splitting processes producing  $OH^{\bullet}$  oxidizing species [62]. The formed oxidizing species are of oxidation and degradation effect on the organic structure of C.R molecules as presented in Equations (8)–(14) [63].



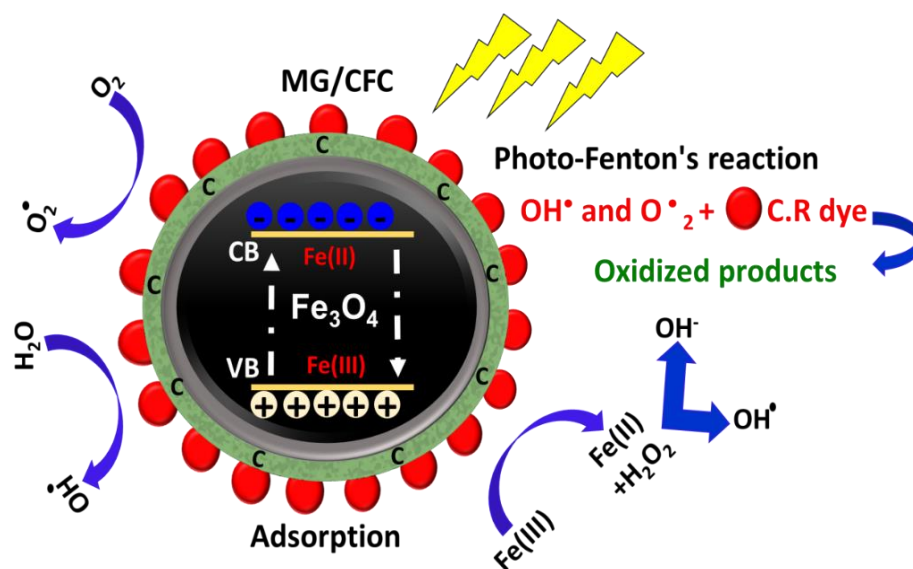
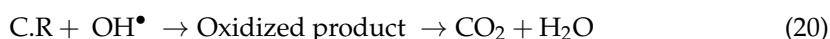
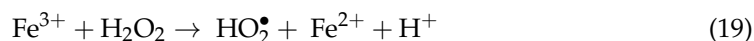
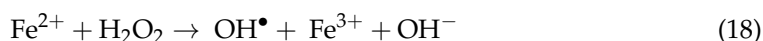
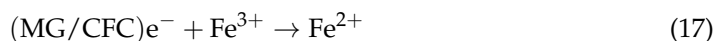
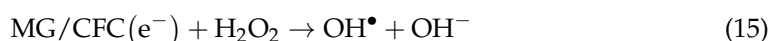


**Figure 9.** Schematic diagram for the suggested photocatalytic and photo-Fenton's oxidation of C.R. by MG/CFC.

For the Fenton oxidation processes, the migrated electrons interact with the incorporated hydrogen peroxide molecules which are associated with the photolysis effect. The photolysis of the hydrogen peroxide results in the formation of free hydroxyl groups  $\text{OH}^-$  in the solutions which in turn oxidize immediately into  $\text{OH}^\bullet$  species during their interaction with the electron-hole pairs ( $h^+$ ) [6]. As a cooperative process, the interaction effect of the migrated electrons on the supported green magnetite causes a significant chemical reduction of its ferric ions (Fe (III)) into ferrous ions (Fe (II)) that oxidize again by the hydrogen peroxide (Figure 9) [6]. The oxidation reaction results in the formation of ferric ions Fe (III) and more  $\text{OH}^\bullet$  species as oxidizing radicals (Figure 9). The  $\text{OH}^\bullet$  species induce the re-formation of the ferrous ions (Fe (II)) by a series of Fenton-like reactions which occurred in a regenerative and continuous process. The formed  $\text{OH}^\bullet$  species during all the mentioned processes exhibit direct oxidizing effects on the organic structure of C.R. (Equations (15)–(20)) (Figure 9).



#### 2.4. Recyclability

The stability and reusability of MG/CFC as the used catalyst or as an adsorbent were studied to assess the suitability of the product to be escalated for realistic and commercial applications. After the performed oxidation test of C.R., the incorporated MG/CFC fractions were re-extracted by filtration using Whitman filter paper. The extracted spent MG/CFC fractions were washed for 5 runs and each run consumed 10 min and then were rinsed by NaOH (0.01 M) for about 5 min. The rinsed MG/CFC fractions were washed again with distilled water and dried at 343 K for 12 h to be applied in an additional oxidation test. The reusability studies were performed for the MG/CFC fractions which were incorporated at the best experimentally conditions [oxidation interval: 60 min; C.R. concentration: 5 mg/L;

volume: 100 mL; MG/CFC dosage: 0.5 g/L; temperature: 293 K; Fenton reagent: 0.1 mL H<sub>2</sub>O<sub>2</sub>]. The same regeneration steps were performed for the incorporated MG/CFC during the adsorption tests and the reusability experiments were conducted at the same conditions but without H<sub>2</sub>O<sub>2</sub> or light source. The determined C.R oxidation percentages demonstrate the significant stability and reusability values of MG/CFC as a heterogeneous catalyst. The determined C.R oxidation percentages during the reusability runs are 100% (Run1), 98.7% (Run2), 96.4% (Run3), 93.2% (Run4), and 87.4% (Run5) (Figure S1). The measured C.R adsorption removal percentages during the reusability runs are 33.2% (Run1), 31.6% (Run2), 27.4% (Run3), 22.8% (Run4), and 16.3% (Run5) (Figure S1). The previously detected results either by adsorption or photo-Fenton's oxidation can be enhanced strongly either by using higher dosages of MG/CFC or by expanding the oxidation intervals.

### 2.5. Ecotoxicity Properties

The acute and chronic toxicities of the C.R polluted solution at different oxidation intervals towards both Fish and green algae were assessed according to the criteria of Chinese hazard evaluation (HJ/T1542004) and European Union classification. The increment in the values of acute and chronic toxicity (mg/L) demonstrated declination in the ecological risk and vice versa. This was assessed considering the treated C.R samples at the best experimentally conditions [oxidation interval: 60 min; C.R concentration: 5 mg/L; volume: 100 mL; MG/CFC dosage: 0.5 g/L; temperature: 293 K; Fenton reagent: 0.1 mL H<sub>2</sub>O<sub>2</sub>]. The recognized results validate notable increases in the measured acute and chronic toxicity values with increasing the photo-Fenton's oxidation intervals in the existence of MG/CFC catalysts as compared to the untreated C.R solution as control sample (Table 3). This displays the environmental value to apply the synthetic structure (MG/CFC) in low cost, effective, and ecological safe oxidation of synthetic dyes.

**Table 3.** Acute toxicity and chronic toxicity of C.R and the tread samples at different oxidation intervals using MG/CFC.

Compound	Fish (LC <sub>50</sub> )	Green Algae (EC <sub>50</sub> )	Fish (ChV)	Green Algae (ChV)
C.R control	0.534	0.311	0.077	0.812
30 min	87.8	71.4	3.86	6.4
60 min	486.9	213.6	211.3	153.7
90 min	4754.4	566.2	1341.6	387.4
120 min	10320.2	924.3	1672.8	934.5

For acute toxicity; LC<sub>50</sub> or EC<sub>50</sub> <1 (highly toxic), 10 < LC<sub>50</sub> or EC<sub>50</sub> <100 (harmful), and LC<sub>50</sub> or EC<sub>50</sub> >100 (Not harmful); For chronic toxicity; ChV < 0.1 (highly toxic), 1 < ChV <10 (harmful), and ChV >10 (Not harmful).

### 2.6. Comparison Study

The value of the synthetic MG/CFC as promising low-cost and effective adsorbents and heterogeneous catalysts during the removal of C.R dye was compared with synthetic structures in the literature (Table 4). The obtained results validate higher adsorption properties of MG/CFC than several studied adsorbents as well as the raw pyrite sample. Moreover, the recognized catalytic activity of MG/CFC towards the effective oxidation of C.R dye validates its higher efficiency than several studied materials as well as the raw pyrite considering the essential factors [oxidation percentage, tested volume, C.R concentration, light source, and oxidation duration]. Considering such enhanced technical advantages as well as the commercial value of MG/CFC, which is realized through the facile synthesis, low cost, and use of extensively available precursors, MG/CFC can be used more effectively in the practical and realistic applications, compared to several types of the reported expensive catalysts.

**Table 4.** Comparison between the adsorption and catalytic activities of MG/CFC and other studied materials in literature.

Catalysts	Dosage	Conc.,	Light Source	Oxidation (%)	References
Ni-TiO <sub>2</sub>	0.02 g/L	10 mg/L	450 W Xe lamp	180 min, ca. 92.3%	[17]
CuO NPs	0.01 g/L	5 × 10 <sup>-5</sup> M	100 W electric bulb	120 min, ca. 91%	[64]
BE/CH@Co <sub>3</sub> O <sub>4</sub>	0.02 g/L	25 mg/L	visible light source	240 min, ca. 98.8%	[65]
ZBiSe-NPs	0.225 g/L	40 mg/L	UV-1602 double beam	120 min, ca. 99.6%	[66]
CoMoO <sub>4</sub> /PDS	0.8 g/L	100 mg/L	500 W xenon lamp, PDS (0.5 mmol/L)	35 min, ca. 96.9%	[67]
SnO <sub>2</sub> -Fe <sub>3</sub> O <sub>4</sub>	0.03 g/L	18 mg/L	14 W UV lamp	90 min, ca. 50.76%	[68]
TiO <sub>2</sub> -CoFe <sub>2</sub> O <sub>4</sub>	0.08 g/L	100 mg/L	150 W metal Halide lamp	250 min, ca. 97%	[69]
MG/CFC	0.5 g/L	5 mg/L	metal Halide lamp, 0.1 mL H <sub>2</sub> O <sub>2</sub>	45 min, ca. 100%	This study
MG/CFC	0.2 g/L	5 mg/L	metal Halide lamp, 0.1 mL H <sub>2</sub> O <sub>2</sub>	105 min, ca. 100%	This study
MG/CFC	0.2 g/L	10 mg/L	metal Halide lamp, 0.1 mL H <sub>2</sub> O <sub>2</sub>	120 min, ca. 100%	This study
MG/CFC	0.2 g/L	20 mg/L	metal Halide lamp, 0.1 mL H <sub>2</sub> O <sub>2</sub>	180 min, ca. 100%	This study

Adsorption		
Adsorbents	Adsorption capacity (mg/g)	References
MNPs@NiFe LDH	79.6	[70]
Zn-MOF	355.16	[71]
Fe <sub>3</sub> O <sub>4</sub> -OPBC-2 NCs	299.82	[72]
Fe <sub>3</sub> O <sub>4</sub> - OPBC-1 NCs	317.33	[73]
polyacrolein (PA-1)	140.8	[72]
Pyrite	123.4	This study
MG/CFC	436.1	This study

### 3. Methodology

#### 3.1. Materials

Natural framboidal pyrite was delivered from Central Metallurgical and Development Institute as raw material to be used as a precursor during the synthesis process. Nitric acid solution (69% AR/ACS) was obtained from Loba Chemie Pvt Ltd.; India was used to dissolve the pyrite samples. Synthetic Congo red dye (benzidinediazo-bis-1-naphthylamine-4-sulfonic acid (C<sub>32</sub>H<sub>22</sub>N<sub>6</sub>Na<sub>2</sub>O<sub>6</sub>S<sub>2</sub>)) was used as a source of the dye pollutants (Sigma Aldrich; Egypt). Hydrogen peroxide (30%; PIOCHEM, Egypt) was used during the Fenton's and photo-Fenton's oxidation. Nitric acid solution and sodium hydroxide pellets were used as pH modifiers.

#### 3.2. Synthesis of MG/CFC Green Nanocomposite

The raw pyrite sample was ground extensively to be within the size range from 25 µm up to 100 µm. 50 g of the ground pyrite was dissolved within 100 mL of nitric acid at 313 K for 48 h. The spent coffee extract was prepared by boiling 10 g of the coffee powder within 100 mL of distilled water for 10 min. After that, 100 mL of the coffee extract containing the coffee residuals was mixed with 200 mL of the pyrite aqueous solution (pyrite/nitric acid). After a certain mixing period, the pH was adjusted to about pH 10 and left for 24 h at room conditions to confirm the successful precipitation of the iron nanoparticles. After that, the obtained products were washed with distilled water for several runs and dried at 333 K for 48 h. Finally, the product was carbonized at 573 K at digital electric muffle furnace for 24 h to produce a hybrid product of coffee-based MG/CFC green composite (Figure 10).



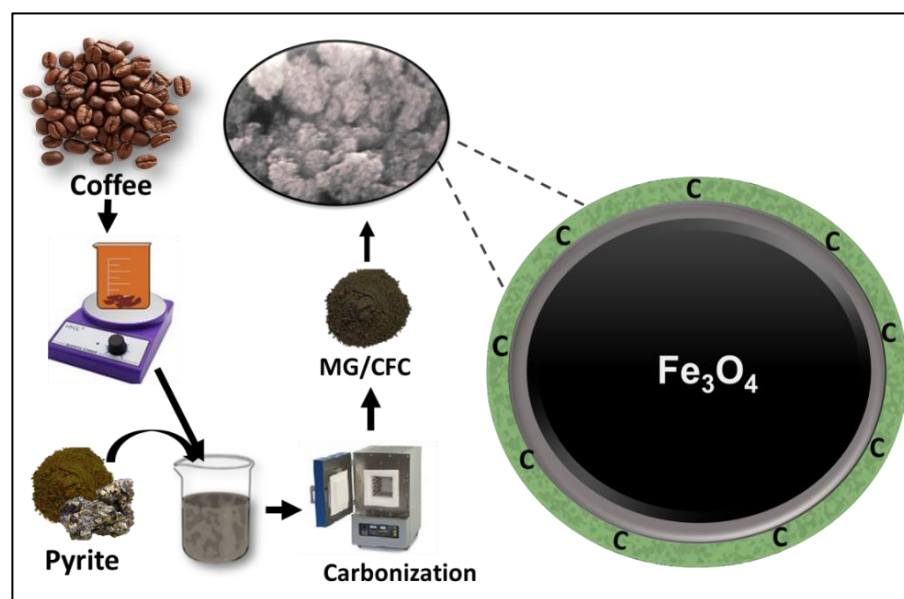


**Figure 10.** Schematic diagram for the synthesis of MG/CFC green composite from pyrite and coffee.

### 3.3. Characterization

The crystal structures of the prepared products were investigated using an X-ray diffractometer (PANalytical-Empyrean type). The used X-ray is Cu-K $\alpha$  X-ray and the producing source is Cu anode which is provided with 40 mA as operation current and 40 kV as determination voltage. The SEM morphological images of the prepared structures were performed utilizing the Scanning-Electron Microscope (Gemini, Zeiss-Ultra 55) after coating the particles with thin film of gold. Meanwhile, the TEM images of the internal structure were addressed using Transmission Electron Microscope (JEOL-JEM, 2100). The chemical composition of the structure and the essential chemical functional groups were inspected using a dispersive X-ray system (EDX) and FT-IR spectrometer (FTIR–8400S) in the transmission mode, respectively. During the FT-IR investigation, the modified samples were milled with KBr powder and then the mixtures were compressed utilizing a hydraulic press into pellets which were fixed in the sample holder of the FT-IR spectrometer. The microstructural features as the surface area and porosity were determined considering BET and BJH methods, respectively, using a Beckman Coulter surface area analyzer (SA3100 type) after degassing step for 15 h at 105 °C and the measuring temperature were adjusted at 77 K.

### 3.4. Batch Adsorption Studies of C.R Dye

The adsorption of C.R dye by MG/CFC was completed in batch forms considering the common adsorption parameters of pH (2–8) and concentration (50 mg/L–350 mg/L) considering the temperature at different values (303–323 K). This was performed considering the other factors at certain values (100 mL for the dye volume, 24 h for the adsorption duration, and 0.2 g/L for the MG/CFC dosage). The tests were conducted in triplicate forms considering the average results during the determination of C.R uptake capacity with a standard deviation of less than 5.6%. The adsorption capacities were estimated based on Equation (21) by measuring the residual C.R concentrations in the treated samples using a UV-vis spectrophotometer at a wavelength number of 520 nm.

$$Q_e \text{ (mg/g)} = \frac{(C_o - C_e)V}{m} \quad (21)$$

The  $Q_e$  (mg/g),  $C_e$  (mg/L),  $C_o$  (mg/L),  $m$  (mg), and  $V$  (mL) symbols are the actual C.R adsorption capacity, rest concentration, started dye concentration, MG/CFC quantity, and dye volume, respectively. The equilibrium properties of the C.R uptake processes were

followed based on the common isotherm models considering the correlation coefficient ( $R^2$ ) (Equation (22)) and chi-square ( $\chi^2$ ) (Equation (23)) for the classic isotherm models. For the classic models based on the statistical physics theory (Table 5), the fitting degrees were considered according to the values of  $R^2$  and root mean square error (RMSE) (Equation (24)). This occurred based on the values utilizing the values of  $Q_{e,exp}$  (experimental uptake capacity) and  $Q_{e,cal}$  (theoretical uptake capacity),  $m'$  (the recognized results), and  $p$  (experimental variables).

$$R^2 = 1 - \frac{\sum (Q_{e,exp} - Q_{e,cal})^2}{\sum (Q_{e,exp} - Q_{e,mean})^2} \quad (22)$$

$$\chi^2 = \sum \frac{(Q_{e,exp} - Q_{e,cal})^2}{Q_{e,cal}} \quad (23)$$

$$RMSE = \sqrt{\frac{\sum_{i=1}^m (Q_{e,cal} - Q_{e,exp})^2}{m' - p}} \quad (24)$$

**Table 5.** Nonlinear equations of kinetic, classic isotherm, and advanced isotherm models.

Classic Isotherm Models		
Model	Equation	Parameters
Langmuir	$Q_e = \frac{Q_{max} b C_e}{(1 + b C_e)}$	$C_e$ is the rest ions concentrations (mg/L), $Q_{max}$ is the maximum adsorption capacity (mg/g), and $b$ is Langmuir constant (L/mg)
Freundlich	$Q_e = K_f C_e^{1/n}$	$K_f$ (mg/g) is the constant of Freundlich model related to the adsorption capacity and $n$ is the constant of Freundlich model related to the adsorption intensities
Dubinin–Radushkevich	$Q_e = Q_m e^{-\beta \epsilon^2}$	$\beta$ ( $\text{mol}^2/\text{KJ}^2$ ) is the D-R constant, $\epsilon$ ( $\text{KJ}^2/\text{mol}^2$ ) is the polanyiil potential, and $Q_m$ is the adsorption capacity (mg/g)
Advanced isotherm models		
Model	Equation	Parameters
Monolayer model with one energy site (Model 1)	$Q = n N_o = \frac{n N_M}{1 + (\frac{C}{C_1/2})^n}$	$Q$ is the adsorbed quantities in mg/g $n$ is the number of adsorbed ion per site
Monolayer model with two energy sites (Model 2)	$Q = \frac{n_1 N_{1M}}{1 + (\frac{C}{C_1})^{n_1}} + \frac{n_2 N_{2M}}{1 + (\frac{C}{C_2})^{n_2}}$	$N_m$ is the density of the effective receptor sites (mg/g) $Q_o$ is the adsorption capacity at the saturation state in mg/g
Double layer model with one energy site (Model 3)	$Q = Q_o \frac{(\frac{C}{C_1/2})^n + 2(\frac{C}{C_1/2})^{2n}}{1 + (\frac{C}{C_1/2})^n + (\frac{C}{C_1/2})^{2n}}$	$C_1/2$ is the concentration of the ions at half saturation stage in mg/L $C_1$ and $C_2$ are the concentrations of the ions at the half saturation stage for the first active sites and the second active sites, respectively
Double layer model with two energy sites (Model 3)	$Q = Q_o \frac{(\frac{C}{C_1})^n + 2(\frac{C}{C_2})^{2n}}{1 + (\frac{C}{C_1})^n + (\frac{C}{C_2})^{2n}}$	$n_1$ and $n_2$ are the adsorbed ions per site for the first active sites and the second active sites, respectively

### 3.5. Photo-Fenton's Oxidation of C.R Dye

The catalytic properties of MG/CFC as a heterogeneous catalyst during the photo-Fenton oxidation of the C.R molecules were evaluated in the existence of hydrogen peroxide (0.5 mL) as Fenton's reagent and visible light source. All these tests were considered after attending the adsorption/desorption equilibrium state and then the catalyst was mixed with the C.R solutions (50 mL) at pH 7 considering the C.R concentration (5–25 mg/L), MG/CFC dosages (0.2–0.5 g), and oxidation interval (30 min–360 min). This was conducted at a fixed volume of 50 mL, at pH 7, and a fixed volume of  $\text{H}_2\text{O}_2$  (0.5 mL) as a Fenton reagent. The used light source is a Metal halide lamp of 400 W power, 490 nm average wavelength, and 18.7 mW/cm<sup>2</sup> incident light intensity. All the performed C.R oxidation tests were repeated for three runs and the average result of the tests were considered during all the explanation with a standard deviation of less than 4.3%. The oxidation percentages of C.R utilizing MG/CF were determined according to Equation (5) while the mineralization

degree was followed based on the reduction in the TOC content in the solutions using TOC-VCPH (Shimadzu, Japan).

$$R., \% = \frac{(C_o - C_e) \times 100}{C_o} \quad (25)$$

### 3.6. Ecotoxicity Studies

The ecotoxicity properties of C.R polluted water before and after the treatment steps toward the aquatic organisms (green algae and fish) was followed using with Ecological Structure Activity Relationship (ECOSAR) predictive program either the chronic toxicity or the acute toxicity. Both the chronic and acute toxicities were determined in terms of EC50, LC50, and ChV (mg/L). The LC50 value reflects the concentrations of the pollutant that can cause inhabitation for 50% of fish after 96 h as exposure time while EC50 reflects the required concentration to inhibit the growth of green algae by 50% and ChV reflects the chronic toxicities effects of the C.R pollutants.

## 4. Conclusions

Magnetite/carbonized coffee (MG/CFC) composite was synthesized successfully from pyrite and applied in effective decontamination of C.R dye by adsorption and photo-Fenton's oxidation process. MG/CFC achieved 436.1 mg/g adsorption capacity of C.R and the adsorption process was controlled by physical processes based on the energetic studies ( $\Delta E = 6.2\text{--}8.2$  kJ/mol). The steric studies reflect the saturation of MG/CFC with 855 mg/g active site density and each C.R molecule can be adsorbed by more than one site by multianchorage process at the best temperature (313 K). As a catalyst, it shows notable activity during the visible light-based photo-Fenton's oxidation of C.R (5 mg/L) achieving complete degradation after 30 min and complete mineralization after 120 min using 0.5 g/L of MG/CFC and 0.1 mL of  $H_2O_2$ . The acute and chronic toxicities of the treated samples reflect their safe effects on aquatic organisms (fish and green algae) as compared to the parent C.R solution.

**Supplementary Materials:** The following supporting information can be downloaded at: <https://www.mdpi.com/article/10.3390/catal13020264/s1>, Figure S1: the recyclability properties of MG/CFC as an adsorbent and catalyst during the photo-Fenton's oxidation of C.R.

**Author Contributions:** Conceptualization, S.I.O., M.R.A., A.A.A. and M.H.S.; methodology, M.H.S., S.I.O., H.E.A. and M.R.A.; software, M.H.S., H.E.A. and M.A.A.-W.; validation, M.R.A., M.A.A.-W., H.A.A. and S.I.O.; formal analysis, M.H.S., H.E.A. and A.A.A.; writing—review and editing, H.E.A., M.R.A., H.A.A., M.H.S., A.A.A. and M.A.A.-W.; investigation, S.I.O., A.A.A. and M.R.A.; resources, M.R.A., M.H.S., M.A.A.-W., H.A.A. and S.I.O.; data curation, M.H.S., H.E.A. and M.R.A.; writing—original draft preparation, M.R.A., H.A.A., M.H.S., M.A.A.-W., A.A.A., H.E.A. and S.I.O.; visualization, M.R.A., A.A.A. and S.I.O.; supervision, A.A.A. and M.R.A.; project administration, S.I.O.; funding acquisition, S.I.O.; All authors have read and agreed to the published version of the manuscript.

**Funding:** This research was funded by [Deanship of Scientific Research at Princess Nourah bint Abdulrahman University], Research Groups Program Grant no. [(RGP-1440-0002)(4)].

**Data Availability Statement:** Data are available upon reasonable, by the Corresponding Authors.

**Acknowledgments:** This work was funded by the Deanship of Scientific Research at Princess Nourah bint Abdulrahman University, through the Research Groups Program Grant no. (RGP-1440-0002)(4).

**Conflicts of Interest:** The authors declare no conflict of interest.

## References

- Bilińska, L.; Blus, K.; Gmurek, M.; Ledakowicz, S. Coupling of electrocoagulation and ozone treatment for textile wastewater reuse. *Chem. Eng. J.* **2018**, *358*, 992–1001.
- Kishor, R.; Purchase, D.; Saratale, G.D.; Ferreira, L.F.R.; Hussain, C.M.; Mulla, S.I.; Bharagava, R.N. Degradation mechanism and toxicity reduction of methyl orange dye by a newly isolated bacterium *Pseudomonas aeruginosa* MZ520730. *J. Water Process. Eng.* **2021**, *43*, 102300. [CrossRef]
- Wekoye, J.N.; Wanyonyi, W.C.; Wangila, P.T.; Tonui, M.K. Kinetic and equilibrium studies of Congo red dye adsorption on cabbage waste powder. *Environ. Chem. Ecotoxicol.* **2020**, *2*, 24–31. [CrossRef]
- Masalvad, S.K.S.; Sakare, P.K. Application of photo Fenton process for treatment of textile Congo-red dye solution. *Mater. Today Proc.* **2020**, *46*, 5291–5297. [CrossRef]
- Abukhadra, M.R.; El-Meligy, M.A.; El-Sherbeeny, A.M. Evaluation and characterization of Egyptian ferruginous kaolinite as adsorbent and heterogeneous catalyst for effective removal of safranin-O cationic dye from water. *Arab. J. Geosci.* **2020**, *13*, 169. [CrossRef]
- Adly, E.R.; Shaban, M.S.; El-Sherbeeny, A.M.; Al Zoubi, W.; Abukhadra, M.R. Enhanced Congo Red Adsorption and Photo-Fenton Oxidation over an Iron-Impeded Geopolymer from Ferruginous Kaolinite: Steric, Energetic, Oxidation, and Synergetic Studies. *ACS Omega* **2022**, *7*, 31218–31232. [CrossRef]
- Navia-Mendoza, J.M.; Filho, O.A.E.; Zambrano-Intriago, L.A.; Maddela, N.R.; Duarte, M.M.M.B.; Quiroz-Fernández, L.S.; Baquerizo-Crespo, R.J.; Rodríguez-Díaz, J.M. Advances in the application of nanocatalysts in photocatalytic processes for the treatment of food dyes: A review. *Sustainability* **2021**, *13*, 11676. [CrossRef]
- Harja, M.; Buema, G.; Bucur, D. Recent advances in removal of Congo Red dye by adsorption using an industrial waste. *Sci. Rep.* **2022**, *12*, 1–18. [CrossRef]
- Han, M.; Wang, S.; Chen, X.; Liu, H.; Gao, H.; Zhao, X.; Wang, F.; Yang, H.; Yi, Z.; Fang, L. Spinel  $\text{CuB}_2\text{O}_4$  (B = Fe, Cr, and Al) oxides for selective adsorption of Congo red and photocatalytic removal of antibiotics. *ACS Appl. Nano Mater.* **2022**, *5*, 11194–11207. [CrossRef]
- Al-Salihi, S.; Jasim, A.M.; Fidalgo, M.M.; Xing, Y. Removal of Congo red dyes from aqueous solutions by porous  $\gamma$ -alumina nanoshells. *Chemosphere* **2021**, *286*, 131769. [CrossRef]
- Kumar, N.; Narayanasamy, S. Toxicological assessment and adsorptive removal of lead (Pb) and Congo red (CR) from water by synthesized iron oxide/activated carbon ( $\text{Fe}_3\text{O}_4/\text{AC}$ ) nanocomposite. *Chemosphere* **2022**, *294*, 133758.
- Kang, X.; Cheng, Y.; Wen, Y.; Qi, J.; Li, X. Bio-inspired co-deposited preparation of GO composite loose nanofiltration membrane for dye contaminated wastewater sustainable treatment. *J. Hazard. Mater.* **2020**, *400*, 123121. [CrossRef] [PubMed]
- Singh, G.; Dwivedi, S.K. Biosorptive and Biodegradative Mechanistic Approach for the Decolorization of Congo Red Dye by *Aspergillus* Species. *Bull. Environ. Contam. Toxicol.* **2021**, *108*, 457–467. [CrossRef]
- Kaur, H.; Jaryal, N. Utilization of biogenic tea waste silver nanoparticles for the reduction of organic dyes. *Mater. Res. Express* **2018**, *5*, 055402. [CrossRef]
- Chen, X.; Huang, Z.; Luo, S.-Y.; Zong, M.-H.; Lou, W.-Y. Multi-functional magnetic hydrogels based on *Millettia speciosa* Champ residue cellulose and Chitosan: Highly efficient and reusable adsorbent for Congo red and  $\text{Cu}^{2+}$  removal. *Chem. Eng. J.* **2021**, *423*, 130198. [CrossRef]
- Mudhoo, A.; Sillanpää, M. Magnetic nanoadsorbents for micropollutant removal in real water treatment: A review. *Environ. Chem. Lett.* **2021**, *19*, 4393–4413. [CrossRef]
- Indira, K.; Shanmugam, S.; Hari, A.; Vasantharaj, S.; Sathiyavimal, S.; Brindhadevi, K.; El Askary, A.; Elfasakhany, A.; Pugazhendhi, A. Photocatalytic degradation of congo red dye using nickel–titanium dioxide nanoflakes synthesized by *Mukia madrasapatna* leaf extract. *Environ. Res.* **2021**, *202*, 111647. [CrossRef] [PubMed]
- do Nascimento, G.E.; de Freitas, R.A.; Rodríguez-Díaz, J.M.; da Silva, P.M.; Napoleão, T.H.; Duarte, M.M.M.B. Degradation of the residual textile mixture cetyltrimethylammonium bromide/remazol yellow gold RNL-150%/reactive blue BF-5G: Evaluation photo-peroxidation and photo-Fenton processes in LED and UV-C photoreactors. *Environ. Sci. Pollut. Res.* **2021**, *28*, 64630–64641. [CrossRef]
- Gorozabel-Mendoza, M.L.; Filho, O.A.E.; Zambrano-Intriago, L.A.; Baquerizo-Crespo, R.J.; Giler-Molina, J.M.; Rodríguez-Díaz, J.M. Degradation of Blue 1 and Yellow 6 Dyes in Binary Mixture Using Photo-Fenton/Sunlight System: Optimization by Factorial Designs. *Water Air Soil Pollut.* **2021**, *232*, 1–10. [CrossRef]
- Tan, X.; Li, H.; Li, X.; Sun, W.; Jin, C.; Chen, L.; Wei, H.; Sun, C. A novel isophorone wastewater treatment technology-wet electrocatalytic oxidation and its degradation mechanism study. *J. Hazard. Mater.* **2020**, *389*, 122035. [CrossRef]
- Shaban, M.; Abukhadra, M.R.; Ibrahim, S.S.; Shahien, M. Photocatalytic degradation and photo-Fenton oxidation of Congo red dye pollutants in water using natural chromite—Response surface optimization. *Appl. Water Sci.* **2017**, *7*, 4743–4756. [CrossRef]
- Abukhadra, M.R.; Saad, I.; Othman, S.I.; Katowah, D.F.; Ajarem, J.S.; Alqarni, S.A.; Allam, A.A.; Al Zoubi, W.; Ko, Y.G. Characterization of  $\text{Fe}^0$ @ Chitosan/Cellulose structure as effective green adsorbent for methyl Parathion, malachite Green, and levofloxacin Removal: Experimental and theoretical studies. *J. Mol. Liq.* **2022**, *368*, 120730. [CrossRef]
- Wu, J.; Wang, B.; Cagnetta, G.; Huang, J.; Wang, Y.; Deng, S.; Yu, G. Nanoscale zero valent iron-activated persulfate coupled with Fenton oxidation process for typical pharmaceuticals and personal care products degradation. *Sep. Purif. Technol.* **2020**, *239*, 116534. [CrossRef]

24. Pasinszki, T.; Krebsz, M. Synthesis and application of zero-valent iron nanoparticles in water treatment, environmental remediation, catalysis, and their biological effects. *Nanomaterials* **2020**, *10*, 917. [CrossRef] [PubMed]
25. Ye, W.; Lu, J.; Ye, J.; Zhou, Y. The effects and mechanisms of zero-valent iron on anaerobic digestion of solid waste: A mini-review. *J. Clean. Prod.* **2020**, *278*, 123567. [CrossRef]
26. Tang, H.; Wang, J.; Zhang, S.; Pang, H.; Wang, X.; Chen, Z.; Li, M.; Song, G.; Qiu, M.; Yu, S. Recent advances in nanoscale zero-valent iron-based materials: Characteristics, environmental remediation and challenges. *J. Clean. Prod.* **2021**, *319*, 128641. [CrossRef]
27. Paz, C.B.; Araújo, R.S.; Oton, L.F.; Oliveira, A.C.; Soares, J.M.; Medeiros, S.N.; Rodríguez-Castellón, E.; Rodríguez-Aguado, E. Acid red 66 dye removal from aqueous solution by Fe/C-based composites: Adsorption, kinetics and thermodynamic studies. *Materials* **2020**, *13*, 1107. [CrossRef]
28. Ahmed, S.F.; Mofijur, M.; Rafa, N.; Chowdhury, A.T.; Chowdhury, S.; Nahrin, M.; Islam, A.S.; Ong, H.C. Green approaches in synthesising nanomaterials for environmental nanobioremediation: Technological advancements, applications, benefits and challenges. *Environ. Res.* **2021**, *204*, 111967. [CrossRef]
29. He, P.; Zhu, J.; Chen, Y.; Chen, F.; Zhu, J.; Liu, M.; Zhang, K.; Gan, M. Pyrite-activated persulfate for simultaneous 2, 4-DCP oxidation and Cr (VI) reduction. *Chem. Eng. J.* **2020**, *406*, 126758. [CrossRef]
30. Li, W.; Yang, S.; Wang, W.; Liu, Q.; He, J.; Li, B.; Cai, Z.; Chen, N.; Fang, H.; Sun, S. Simultaneous removal of Cr (VI) and acid orange 7 from water in pyrite-persulfate system. *Environ. Res.* **2020**, *189*, 109876. [CrossRef]
31. Wang, C.; Sun, R.; Huang, R.; Cao, Y. A novel strategy for enhancing heterogeneous Fenton degradation of dye wastewater using natural pyrite: Kinetics and mechanism. *Chemosphere* **2021**, *272*, 129883. [CrossRef] [PubMed]
32. Rickard, D. How long does it take a pyrite framboid to form? *Earth Planet. Sci. Lett.* **2019**, *513*, 64–68. [CrossRef]
33. Zhao, J.; Liang, J.; Long, X.; Li, J.; Xiang, Q.; Zhang, J.; Hao, J. Genesis and evolution of framboidal pyrite and its implications for the ore-forming process of Carlin-style gold deposits, southwestern China. *Ore Geol. Rev.* **2018**, *102*, 426–436. [CrossRef]
34. Du, M.; Kuang, H.; Zhang, Y.; Zeng, X.; Yi, C.; Hussain, I.; Hung, S.; Zhao, S. Enhancement of ball-milling on pyrite/zero-valent iron for persulfate activation on imidacloprid removal in aqueous solution: A mechanistic study. *J. Environ. Chem. Eng.* **2021**, *9*, 105647. [CrossRef]
35. Liu, A.; Liu, J.; Pan, B.; Zhang, W.X. Formation of lepidocrocite ( $\gamma$ -FeOOH) from oxidation of nanoscale zero-valent iron (nZVI) in oxygenated water. *RSC Adv.* **2014**, *4*, 57377–57382. [CrossRef]
36. Rahimi, F.; van der Hoek, J.P.; Royer, S.; Javid, A.; Mashayekh-Salehi, A.; Sani, M.J. Pyrite nanoparticles derived from mine waste as efficient catalyst for the activation of persulfates for degradation of tetracycline. *J. Water Process. Eng.* **2020**, *40*, 101808. [CrossRef]
37. Khabbaz, M.; Entezari, M. Simple and versatile one-step synthesis of FeS<sub>2</sub> nanoparticles by ultrasonic irradiation. *J. Colloid Interface Sci.* **2016**, *470*, 204–210. [CrossRef]
38. Gong, B.; Li, D.; Niu, Z.; Liu, Y.; Dang, Z. Inhibition of pyrite oxidation using PropS-SH/sepiolite composite coatings for the source control of acid mine drainage. *Environ. Sci. Pollut. Res.* **2020**, *28*, 11090–11105. [CrossRef]
39. Silva, C.A.; Silva, R.L.; Figueiredo, A.T.D.; Alves, V.N. Magnetic solid-phase microextraction for lead detection in aqueous samples using magnetite nanoparticles. *J. Braz. Chem. Soc.* **2020**, *31*, 109–115. [CrossRef]
40. Azizi, A. Green synthesis of Fe<sub>3</sub>O<sub>4</sub> nanoparticles and its application in preparation of Fe<sub>3</sub>O<sub>4</sub>/cellulose magnetic nanocomposite: A suitable proposal for drug delivery systems. *J. Inorg. Organomet. Polym. Mater.* **2020**, *30*, 3552–3561. [CrossRef]
41. Eslami, S.; Ebrahimzadeh, M.A.; Biparva, P. Green synthesis of safe zero valent iron nanoparticles by Myrtus communis leaf extract as an effective agent for reducing excessive iron in iron-overloaded mice, a thalassemia model. *RSC Adv.* **2018**, *8*, 26144–26155. [CrossRef] [PubMed]
42. Hao, L.; Wang, P.; Valiyaveetil, S. Successive extraction of As (V), Cu (II) and P (V) ions from water using spent coffee powder as renewable bioadsorbents. *Sci. Rep.* **2017**, *7*, 1–12. [CrossRef] [PubMed]
43. Tran, T.N.; Do, Q.C.; Kim, D.; Kim, J.; Kang, S. Urchin-like structured magnetic hydroxyapatite for the selective separation of cerium ions from aqueous solutions. *J. Hazard. Mater.* **2022**, *430*, 128488. [CrossRef]
44. Abdel Salam, M.; Mokhtar, M.; Albukhari, S.M.; Baamer, D.F.; Palmisano, L.; Jaremko, M.; Abukhadra, M.R. Synthesis and Characterization of Green ZnO@ polyaniline/Bentonite Tripartite Structure (G. Zn@ PN/BE) as Adsorbent for As (V) Ions: Integration, Steric, and Energetic Properties. *Polymers* **2022**, *14*, 2329. [CrossRef]
45. Albukhari, S.M.; Salam, M.A.; Abukhadra, M.R. Effective retention of inorganic Selenium ions (Se (VI) and Se (IV)) using novel sodalite structures from muscovite; characterization and mechanism. *J. Taiwan Inst. Chem. Eng.* **2021**, *120*, 116–126. [CrossRef]
46. Sayed, I.R.; Farhan, A.M.; AlHammadi, A.A.; El-Sayed, M.I.; El-Gaied, I.M.A.; El-Sherbeeney, A.M.; Al Zoubi, W.; Ko, Y.G.; Abukhadra, M.R. Synthesis of novel nanoporous zinc phosphate/hydroxyapatite nano-rods (ZPh/HPA<sub>NRS</sub>) core/shell for enhanced adsorption of Ni<sup>2+</sup> and Co<sup>2+</sup> ions: Characterization and application. *J. Mol. Liq.* **2022**, *360*, 119527. [CrossRef]
47. Dawodu, F.A.; Akpomie, G.K.; Abuh, M.A. Equilibrium Isotherm Studies on the Batch Sorption of Copper (II) ions from Aqueous Solution onto Nsu Clay. *Int. J. Sci. Eng. Res.* **2012**, *3*, 1–7.
48. Amrhar, O.; El Gana, L.; Mobarak, M. Calculation of adsorption isotherms by statistical physics models: A review. *Environ. Chem. Lett.* **2021**, *19*, 4519–4547. [CrossRef]
49. Dhaouadi, F.; Sellaoui, L.; Badawi, M.; Reynel-Ávila, H.E.; Mendoza-Castillo, D.I.; Jaime-Leal, J.E. Statistical physics interpretation of the adsorption mechanism of Pb<sup>2+</sup>, Cd<sup>2+</sup> and Ni<sup>2+</sup> on chicken feathers. *J. Mol. Liq.* **2020**, *319*, 114168. [CrossRef]

50. Ali, R.A.; Mobarak, M.; Badawy, A.M.; Lima, E.C.; Seliem, M.K.; Ramadan, H. New insights into the surface oxidation role in enhancing Congo red dye uptake by Egyptian ilmenite ore: Experiments and physicochemical interpretations. *Surf. Interfaces* **2021**, *26*, 101316. [CrossRef]
51. Ashraf, M.-T.; AlHammadi, A.A.; El-Sherbeeney, A.M.; Alhammadi, S.; Al Zoubi, W.; Ko, Y.G.; Abukhadra, M.R. Synthesis of cellulose fibers/Zelite-A nanocomposite as an environmental adsorbent for organic and inorganic selenium ions; Characterization and advanced equilibrium studies. *J. Mol. Liq.* **2022**, *360*, 119573. [CrossRef]
52. Dhaouadi, F.; Sellaoui, L.; Reynel-Ávila, H.E.; Landín-Sandoval, V.; Mendoza-Castillo, D.I.; Jaime-Leal, J.E.; Lima, E.C.; Bonilla-Petriciolet, A.; Lamine, A.B. Adsorption mechanism of  $Zn^{2+}$ ,  $Ni^{2+}$ ,  $Cd^{2+}$ , and  $Cu^{2+}$  ions by carbon-based adsorbents: Interpretation of the adsorption isotherms via physical modelling. *Environ. Sci. Pollut. Res.* **2021**, *28*, 30943–30954. [CrossRef] [PubMed]
53. Sellaoui, L.; Ali, J.; Badawi, M.; Bonilla-Petriciolet, A.; Chen, Z. Understanding the adsorption mechanism of  $Ag^+$  and  $Hg^{2+}$  on functionalized layered double hydroxide via statistical physics modeling. *Appl. Clay Sci.* **2020**, *198*, 105828. [CrossRef]
54. Sellaoui, L.; Guedidi, H.; SarraWjihi, S.; Reinert, L.; Knani, S.; Duclaux, L.; Ben Lamine, A. Experimental and theoretical studies of adsorption of ibuprofen on raw and two chemically modified activated carbons: New physicochemical interpretations. *RSC Adv.* **2016**, *6*, 12363–12373. [CrossRef]
55. Abdullah, R.R.; Shabeed, K.M.; Alzubaydi, A.B.; Alsahy, Q.F. Novel photocatalytic polyether sulphone ultrafiltration (UF) membrane reinforced with oxygen-deficient Tungsten Oxide (WO<sub>2</sub>. 89) for Congo red dye removal. *Chem. Eng. Res. Des.* **2022**, *177*, 526–540. [CrossRef]
56. Wang, Y.; Tian, Q.; Yang, G.; Li, X.; Du, W.; Leong, Y.K.; Chang, J.-S. Enhanced chlortetracycline removal by iron oxide modified spent coffee grounds biochar and persulfate system. *Chemosphere* **2022**, *301*, 134654. [CrossRef]
57. Salam, M.A.; AbuKhadra, M.R.; Mohamed, A.S. Effective oxidation of methyl parathion pesticide in water over recycled glass based-MCM-41 decorated by green Co<sub>3</sub>O<sub>4</sub> nanoparticles. *Environ. Pollut.* **2020**, *259*, 113874. [CrossRef]
58. Saad, A.M.; Abukhadra, M.R.; Ahmed, S.A.-K.; Elzanaty, A.M.; Mady, A.H.; Betiha, M.A.; Shim, J.-J.; Rabie, A.M. Photocatalytic degradation of malachite green dye using chitosan supported ZnO and Ce-ZnO nano-flowers under visible light. *J. Environ. Manag.* **2020**, *258*, 110043. [CrossRef]
59. Abukhadra, M.R.; AlHammadi, A.A.; Khim, J.S.; Ajarem, J.S.; Allam, A.A. Enhanced decontamination of Levofloxacin residuals from water using recycled glass based a green zinc oxide/mesoporous silica nanocomposite; adsorption and advanced oxidation studies. *J. Clean. Prod.* **2022**, *356*, 131836. [CrossRef]
60. Zhang, Y.; Zhang, B.-T.; Teng, Y.; Zhao, J.; Sun, X. Heterogeneous activation of persulfate by carbon nanofiber supported Fe<sub>3</sub>O<sub>4</sub>@carbon composites for efficient ibuprofen degradation. *J. Hazard. Mater.* **2020**, *401*, 123428. [CrossRef]
61. Yang, X.; Wang, J.; El-Sherbeeney, A.M.; AlHammadi, A.A.; Park, W.-H.; Abukhadra, M.R. Insight into the adsorption and oxidation activity of a ZnO/piezoelectric quartz core-shell for enhanced decontamination of ibuprofen: Steric, energetic, and oxidation studies. *Chem. Eng. J.* **2021**, *431*, 134312. [CrossRef]
62. Fard, S.G.; Haghghi, M.; Shabani, M. Facile one-pot ultrasound-assisted solvothermal fabrication of ball-flowerlike nanostructured (BiOBr) x (Bi<sub>7</sub>O<sub>9</sub>I<sub>3</sub>) 1-x solid-solution for high active photodegradation of antibiotic levofloxacin under sun-light. *Appl. Catal. B Environ.* **2019**, *248*, 320–331. [CrossRef]
63. Sun, Q.; Hu, X.; Zheng, S.; Zhang, J.; Sheng, J. Effect of calcination on structure and photocatalytic property of N-TiO<sub>2</sub>/g-C<sub>3</sub>N<sub>4</sub>@diatomite hybrid photocatalyst for improving reduction of Cr (VI). *Environ. Pollut.* **2019**, *245*, 53–62. [CrossRef] [PubMed]
64. Alsamhary, K.; Al-Enazi, N.M.; Alhomaidi, E.; Alwakeel, S. Spirulina platensis mediated biosynthesis of CuO Nps and photocatalytic degradation of toxic azo dye Congo red and kinetic studies. *Environ. Res.* **2022**, *207*, 112172. [CrossRef] [PubMed]
65. Abukhadra, M.R.; Adlii, A.; Bakry, B.M. Green fabrication of bentonite/chitosan@cobalt oxide composite (BE/CH@Co) of enhanced adsorption and advanced oxidation removal of Congo red dye and Cr (VI) from water. *Int. J. Biol. Macromol.* **2019**, *126*, 402–413. [CrossRef]
66. Khan, S.; Khan, A.; Ali, N.; Ahmad, S.; Ahmad, W.; Malik, S. Degradation of Congo red dye using ternary metal selenide-chitosan microspheres as robust and reusable catalysts. *Environ. Technol. Innov.* **2021**, *22*, 101402. [CrossRef]
67. Zhou, H.; Qiu, Y.; Yang, C.; Zang, J.; Song, Z.; Yang, T.; Li, J.; Fan, Y.; Dang, F.; Wang, W. Efficient Degradation of Congo Red in Water by UV-Vis Driven CoMoO<sub>4</sub>/PDS Photo-Fenton System. *Molecules* **2022**, *27*, 8642. [CrossRef]
68. Said, M.; Rizki, W.T.; Asri, W.R.; Desnelli, D.; Rachmat, A.; Hariani, P.L. SnO<sub>2</sub>-Fe<sub>3</sub>O<sub>4</sub> nanocomposites for the photodegradation of the Congo red dye. *Heliyon* **2022**, *8*, e09204. [CrossRef]
69. Rohilla, S. Rietveld refinement and structural characterization of TiO<sub>2</sub>/CoFe<sub>2</sub>O<sub>4</sub> nanocomposites. In *IOP Conference Series: Materials Science and Engineering*; IOP Publishing: Bristol, UK, 2020; Volume 872, p. 012171.
70. Taher, T.; Putra, R.; Palapa, N.R.; Lesbani, A. Preparation of magnetite-nanoparticle-decorated NiFe layered double hydroxide and its adsorption performance for congo red dye removal. *Chem. Phys. Lett.* **2021**, *777*, 138712. [CrossRef]
71. Gao, L.; Gao, T.; Zhang, Y.; Hu, T. A bifunctional 3D porous Zn-MOF: Fluorescence recognition of Fe<sup>3+</sup> and adsorption of congo red/methyl orange dyes in aqueous medium. *Dye Pigment.* **2021**, *197*, 109945. [CrossRef]

72. Munagapati, V.S.; Wen, H.-Y.; Gollakota, A.R.; Wen, J.-C.; Shu, C.-M.; Lin, K.-Y.A.; Tian, Z.; Wen, J.-H.; Reddy, G.M.; Zyryanov, G.V. Magnetic Fe<sub>3</sub>O<sub>4</sub> nanoparticles loaded papaya (*Carica papaya* L.) seed powder as an effective and recyclable adsorbent material for the separation of anionic azo dye (Congo Red) from liquid phase: Evaluation of adsorption properties. *J. Mol. Liq.* **2021**, *345*, 118255. [CrossRef]
73. Prajapati, A.K.; Mondal, M.K. Green synthesis of Fe<sub>3</sub>O<sub>4</sub>-onion peel biochar nanocomposites for adsorption of Cr(VI), methylene blue and congo red dye from aqueous solutions. *J. Mol. Liq.* **2022**, *349*, 118161. [CrossRef]

**Disclaimer/Publisher's Note:** The statements, opinions and data contained in all publications are solely those of the individual author(s) and contributor(s) and not of MDPI and/or the editor(s). MDPI and/or the editor(s) disclaim responsibility for any injury to people or property resulting from any ideas, methods, instructions or products referred to in the content.

## Article

# Detection and Degradation Studies of Nile Blue Sulphate Using Electrochemical and UV-Vis Spectroscopic Techniques

Muhammad Nadir Saleem<sup>1</sup>, Afzal Shah<sup>1,\*</sup> , Naimat Ullah<sup>1</sup>, Jan Nisar<sup>2</sup>  and Faiza Jan Iftikhar<sup>3</sup><sup>1</sup> Department of Chemistry, Quaid-i-Azam University, Islamabad 45320, Pakistan<sup>2</sup> National Centre of Excellence in Physical Chemistry, University of Peshawar, Peshawar 25120, Pakistan<sup>3</sup> NUTECH School of Applied Science & Humanities, National University of Technology, Islamabad 44000, Pakistan

\* Correspondence: afzals\_qau@yahoo.com or afzalshah@qau.edu.pk

**Abstract:** An efficient and reliable electrochemical sensing platform based on COOH-fMWCNTs modified GCE (COOH-fMWCNTs/GCE) was designed for the detection of nanomolar concentration of Nile Blue Sulphate (NBS). In comparison to the bare GCE, the electrochemical sensing scaffold considerably enhanced the peak current response of NBS dye as confirmed from the results of voltammetric investigations. The electrochemical approach of detecting NBS in the droplet of its solution dried over the surface of modified electrode validated, the role of modifier in enhancing the sensing response. Under optimized conditions, the designed electrochemical platform demonstrated a wide linearity range (0.03–10  $\mu\text{M}$ ) for NBS, with LOD of 1.21 nM. Moreover, COOH-fMWCNTs/GCE was found reproducible and stable as confirmed by repeatability and inter-day durability tests. The selectivity of the designed sensing matrix was ensured by anti-interference tests. The photocatalytic degradation of NBS dye was carried out by using TiO<sub>2</sub> nanoparticles as photocatalyst in the presence of H<sub>2</sub>O<sub>2</sub>. UV-visible spectroscopic studies revealed 95% photocatalytic degradation of NBS following a pseudo-first-order kinetics with a rate constant of 0.028 min<sup>-1</sup>. These findings were supported electrochemically by monitoring the photocatalytically degraded dye at the designed sensing platform. The color variation and final decolorization of the selected dye in water served as a visual indicator of the degradation process. To conclude, the designed sensing platform immobilized with COOH-fMWCNTs imparted improved selectivity and sensitivity to detect and to, monitor the photocatalytic degradation of NBS.

**Keywords:** acid functionalized MWCNTs; limit of detection; electrochemical sensor; TiO<sub>2</sub> nanoparticles; photocatalysis

**Citation:** Saleem, M.N.; Shah, A.; Ullah, N.; Nisar, J.; Iftikhar, F.J. Detection and Degradation Studies of Nile Blue Sulphate Using Electrochemical and UV-Vis Spectroscopic Techniques. *Catalysts* **2023**, *13*, 141. <https://doi.org/10.3390/catal13010141>

Academic Editors: Juan José Rueda-Márquez, Javier Moreno-Andrés and Irina Levchuk

Received: 11 November 2022

Revised: 1 January 2023

Accepted: 4 January 2023

Published: 7 January 2023



**Copyright:** © 2023 by the authors. Licensee MDPI, Basel, Switzerland. This article is an open access article distributed under the terms and conditions of the Creative Commons Attribution (CC BY) license (<https://creativecommons.org/licenses/by/4.0/>).

## 1. Introduction

The population of the world is continuously soaring. As a result of this increase, the world is confronting environmental problems along with concomitant health, security, and food issues [1–6]. Environmental pollution is one of the major threats to the world. Developing countries are affected the most; they use 80% of the polluted water for cultivation and fertilization purposes. Although industrial development has created innovation and convenience in human life, it has also resulted in harmful health effects and environmental pollution. Since the industrial revolution, pollution has reached an alarming level affecting both developed and developing countries and hence has become a universal challenge that has gripped the world's attention [7–9].

Almost 80 million tonnes of dyes are produced annually worldwide by industries that dump a significant amount of it into waterbodies as wastewater that disturbs the stability of the ecosystems. Approximately 10–15% of the total dye produced in any industry is lost to water during its manufacturing and dyeing stages, and owing to their high solubility and persistent nature, it is challenging to remove them from water. Even



though these dyes are released in water in trace amounts, they are still very harmful to humans (even less than 1 ppm) and other aquatic life [10,11]. When released in water, dyes adversely affect the photosynthetic process of aquatic life. Additionally, dyes also have mutagenic and teratogenic effects on fish species. Their hazardous effects include cancers, allergies, and renal complexities. Hence, there is globally a dire need to develop inexpensive and green methods to remove such pollutants from water and make water reusable [12]. Numerous methods have been proposed for treating dye-contaminated wastewater, including adsorption, incineration, foam flotation, physicochemical methods, and biochemical techniques [13,14]. However, since most of the organic dyes are non-biodegradable and thermally stable, they render these conventional methods ineffective. Thus in the present research work, NBS is sought to be removed from wastewater through the photocatalytic degradation process because it is effective, inexpensive, simple, and rapid compared to other methods [8].

Several semiconductors, including titania, vanadium pentoxide, zinc oxide, ferric oxide, cadmium oxide, cadmium sulfide, and alumina, have been used as photocatalysts for the degradation of different colored organic pollutants such as dyes. Among these,  $\text{TiO}_2$  is the most commonly employed photocatalyst. The current research work focuses on light-assisted catalytic degradation of Nile Blue Sulphate (NBS) dye using  $\text{TiO}_2$  nanoparticles as it possesses very high mechanical strength, nontoxicity, chemical, and thermal stability [15]. However, owing to its band gap of 3.2 eV, the recombination of the electron-hole pair and absorption in the UV region limits its utility. To hinder the recombination of generated electron-hole pair,  $\text{H}_2\text{O}_2$  was used for enhancing the practical utility of  $\text{TiO}_2$  nanoparticles by abstracting the photogenerated electron and avoiding its recombination with the hole. Different free radicals like  $\bullet\text{OH}$ ,  $\bullet\text{O}^{2-}$  /  $\bullet\text{OOH}$  (reactive oxygen species) are generated from  $\text{H}_2\text{O}_2$  at the surface of the catalyst that enhance the  $\text{TiO}_2$  capability of degrading the organic dye molecule in wastewater [16].

But before even its removal, its detection is important. Various techniques, including chromatography, mass spectroscopy, capillary electrophoresis, spectrophotometry, and voltammetry, have been utilized to detect NBS dye. The pre-existing methods, such as chromatography and surface-enhanced Raman spectroscopy are expensive, time-consuming, require calibration, and extensive sample preparation. Industrial effluents are rich in different components which hinder the detection of lower concentrations of NBS using the above mentioned techniques. Electrochemical techniques are preferred owing to their simplicity, reliability and fast responsiveness, yet the structure of NBS is complex offering steric hindrances which impart it with orientational restrictions, making it difficult to be detected using electrochemical techniques [17]. Interestingly the orientational restrictions can be avoided by using a smart approach of skipping the diffusion step by drop casting the analyte on the surface of the modified electrode and detecting it electrochemically. Hence, in this work, a voltammetric method for the detection of NBS was employed owing to its sensitivity, reliability, potential selectivity, and ease of operation compared to all other methods. The electrochemical detection method is based on the principle of sensitivity of the electrode's surface towards the targeted analyte. Thus, an electrochemical sensor was designed by immobilizing the COOH-fMWCNTs at the surface of the glassy carbon electrode (GCE) to impart sensitivity for detecting trace-level concentrations of the selected analyte. CNTs are used as electrode modifiers because of their high surface-to-volume ratio, chemical stability, electrical, and thermal properties which make them the best choice for modifying the electrode surface [18,19]. The surface of CNTs is susceptible to analytes' adsorption, which leads to the formation of the most efficient sensors [20,21].

In this study, a COOH-fMWCNTs modified glassy carbon electrode is developed for ultra-sensitive and selective detection of NBS using square wave voltammetry (SWV), electrochemical impedance spectroscopy (EIS), and cyclic voltammetry (CV). The designed electrochemical sensor is also utilized for voltammetric monitoring of the photocatalytic degradation of NBS along with spectroscopic study. The COOH-fMWCNTs-based recognition layer has been employed for the first time in the current study for the detection

of NBS. A smart unconventional approach was adopted to improve the sensing ability of the designed sensing platform, wherein a drop of dye was cast on the surface of the modified electrode, which enhanced the ease of orientation of analyte molecules towards the surface of the electrode as witnessed by better resolution of peak and enhancement in peak current value as compared to the conventional approach of dye detection in solution. The approach also offers a very small amount of target analyte to be used which makes the diffusion of bulky dye molecules toward the electrode surface expedient. Thus the approach is promising for dye detection in water for abatement of dyes in wastewater and allows the water to be purified.

## 2. Results and Discussion

### 2.1. Electrochemical Characterization

EIS is a non-destructive and effective technique that was employed to reveal the interfacial properties and extent to which the electrode's surface was modified by using Nyquist plot. EIS was performed in an electrochemical cell consisting of 5 mM potassium ferricyanide ( $K_3[Fe(CN)_6]$ ) and 0.1 M potassium chloride (KCl) solution as a supporting electrolyte. Nyquist plots of bare and modified GCEs are depicted in Figure 1a. The Nyquist plot consists of two parts, a semicircle part at higher frequencies that reveals the charge transfer resistance ( $R_{ct}$ ). At the same time, the diffusional limited process is characterized in the second linear part of the Nyquist plots at lower frequencies [22].  $R_{ct}$  can be calculated via the diameter of a semicircle in Nyquist plots at higher frequencies [23,24]. The decrease in  $R_{ct}$  causes enhanced electrical properties which are lower for COOH-*f*MWCNTs/GCE in comparison to MWCNT/GCE and bare GCE. This is attributed to increased surface area that affords more binding sites for the analyte at the modified electrode and hence improved conductivity. Furthermore, the heterogeneous rate constant  $k$  was calculated (Table S1) by using equation ( $k = RT/(nF)^2C_0AR_{ct}$ ) for bare, MWCNTs, and COOH-*f*MWCNTs modified GCE [25–27].

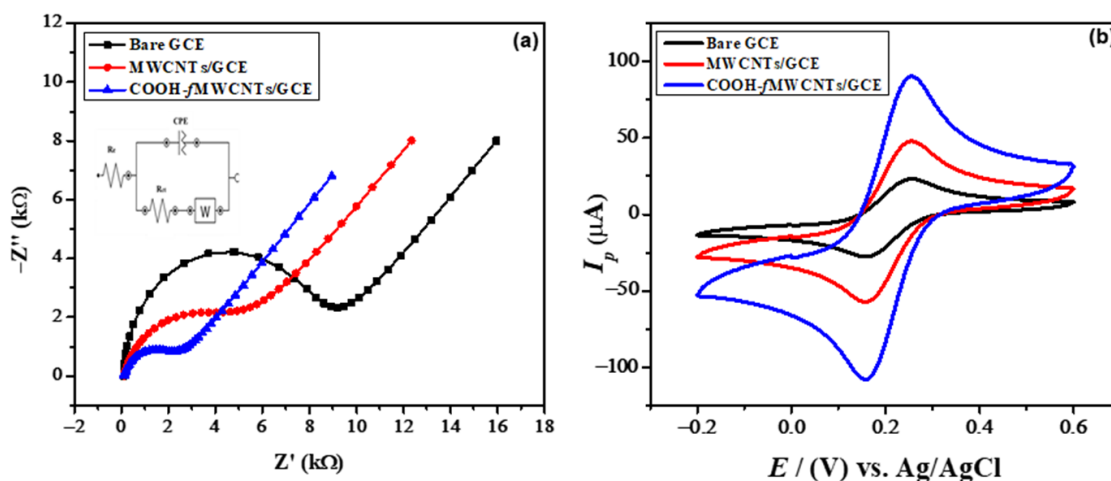


**Figure 1.** (a) Nyquist plots using data obtained at bare and modified GCE in a solution of 5 mM  $K_3[Fe(CN)_6]$  as a redox probe and 0.1 M KCl as a supporting electrolyte. (b) Cyclic voltammograms at the bare and modified GCE in 5 mM  $K_3[Fe(CN)_6]$  as redox probe and 0.1 M KCl as supporting electrolyte at a scan rate of 100 mV s<sup>-1</sup>.

As shown in Table S1, low charge transfer resistance values and higher values of heterogeneous rate constant indicate excellent conductivity and superior electrochemical kinetics for COOH-*f*MWCNTs modified GCE compared to others in solution of  $K_3[Fe(CN)_6]$  and KCl [28,29]. The EIS parameters in Table S1 were obtained from Randles equivalent circuit.

CV was used to investigate the working proficiency of the designed sensing platform by comparing the peak current responses of bare and modified GCE in 5 mM  $K_3[Fe(CN)_6]$  and 0.1 M KCl. The electroactive surface area of the electrode strongly affects

the peak current response [30]. This was determined using the Randles-Sevcik equation ( $I_p = 2.69 \times 10^5 n^{3/2} AD^{1/2} \nu^{1/2} C$ ) where  $D$  represents diffusion coefficient,  $C$  the concentration of analyte and the rest of the symbols stand for their usual notation [31]. Figure 1b illustrates the current responses of bare, MWCNTs, and COOH-fMWCNTs modified GCEs.

Considering  $D = 7.6 \times 10^{-6} \text{ cm}^2\text{s}^{-1}$ ,  $n = 1$ , and  $C = 5 \text{ mM}$  for  $\text{K}_3[\text{Fe}(\text{CN})_6]$ , the calculated electroactive surface area of the bare, MWCNTs modified and COOH-fMWCNTs modified GCE is enlisted in Table S2 and demonstrate that the sensing platform based on COOH-fMWCNTs has the greatest electroactive surface area ( $0.08 \text{ cm}^2$ ) compared to the bare GCE and MWCNTs/GCE. Owing to its greater surface area, the COOH-fMWCNTs-based sensing platform exhibits enhanced peak current response as seen in Figure 1b. The COOH-fMWCNTs sensing platform owing to its increased surface area has several active sites available for binding with the analyte, thus facilitating the electron transfer process and corroborating the results of EIS in Figure 1a. These results show good agreement with EIS results, which indicate the successful modification of GCE for obtaining a selective and sensitive electrochemical platform for detecting NBS in water.

Additionally the “double layer capacitor” on real cells often behaves like a CPE (ref to Figure 1a inset), and not as an ideal capacitor due to surface inhomogeneities of the interface between the modified electrode and electrolyte. These inhomogeneities may include surface roughness, “leaky” capacitor, non-uniform current distribution, etc. that account for the non-ideal behaviour of the double layer. The impedance of the CPE is given as

$$\frac{1}{Z_{CPE}} = Q(i\omega)^n \quad (1)$$

where  $Q$  is a prefactor for CPE with units of capacitance,  $i$  is an imaginary number and  $n$  represents the exponent of CPE ranging in value from 0–1 and is used to indicate the surface roughness of the electrolyte-electrode interface [32]. When  $n = 0$  the CPE represents resistance and when  $n = 1$  the behaviour is that of an ideal capacitor.

Furthermore, if the value of  $n$  is 1 or close to 1, it means the interface surface is homogenous and smooth [33]. As the value of  $n$  decreases, the surface inhomogeneity increases that pertains to increased roughness of the surface. As seen in Table S1, the value of  $n$  is decreasing as the surface of GCE is modified with MWCNT and COOH-fMWCNTs due to increase in surface roughness. Thus, creation of more active sites leads to increased preconcentration of the analyte. This corroborates well with results of NBS (see Figure 2a) showing enhanced signals on GCE modified with COOH-fMWCNTs due to more active sites and consequent increase in electroactive surface area as presented in Table S2.

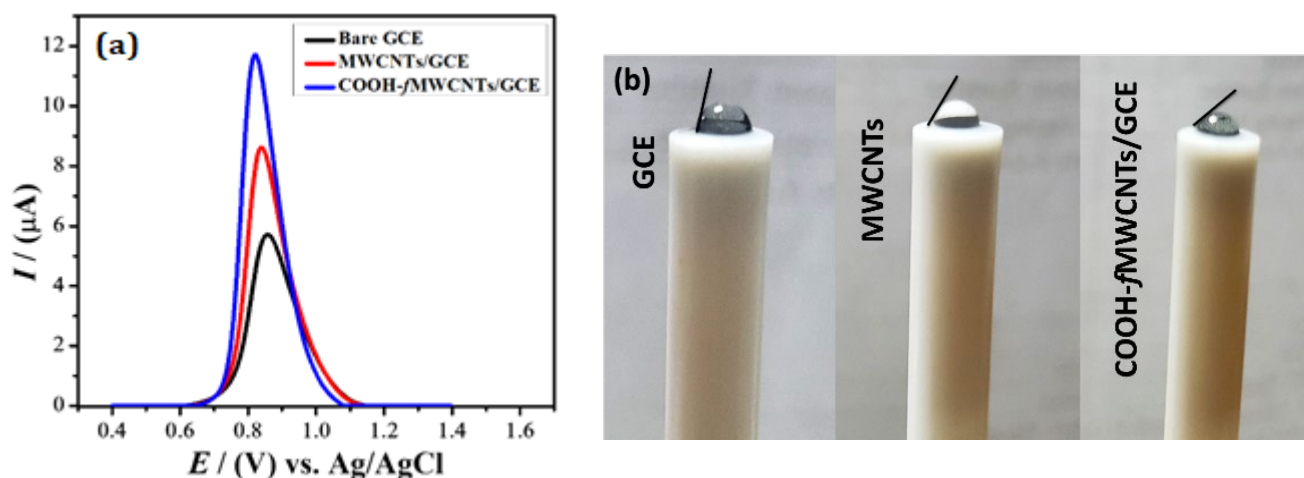


**Figure 2.** (a) SWVs response of  $10 \mu\text{M}$  NBS at bare GCE, MWCNTs/GCE, and COOH-fMWCNTs/GCE in PBS of pH 6.0. (b) Picture recorded after 30 s placement of the same volume of water droplet on bare GCE, MWCNTs/GCE and COOH-fMWCNTs/GCE.

## 2.2. Square Wave Voltammetric Analysis of NBS

Compared to CV, SWV is much more sensitive and can remarkably differentiate between the faradaic and non-Faradaic current [34]. It is a reliable electroanalytical technique that produces results with enhanced resolution. Therefore, in the present work, SWV was employed for the electrochemical sensing of NBS. The intensity of peak current response of NBS at bare and modified GCE was investigated in PBS of pH 6.0 at a scan rate of  $100 \text{ mV s}^{-1}$  keeping frequency and pulse amplitude 20 Hz and 20 mV, respectively. The oxidation peak of NBS was obtained at 0.86 and 0.84 V at bare and MWCNTs modified GCE respectively. After modification with COOH-fMWCNTs, it was shifted to a lower potential of 0.82 V. This negative shift in the potential shows the electrocatalytic behavior of the sensing platform. The peak current of NBS was also enhanced to  $8.63 \mu\text{A}$  and  $11.7 \mu\text{A}$  at MWCNTs and COOH-fMWCNTs respectively, as presented in Figure 2a [35,36]. The current value for COOH-fMWCNTs/GCE is almost twice that of the bare which supports our proposition of availability of more active sites for interaction of analyte. The surface features of the electrodes were distinguished from contact angle analysis as shown in Figure 2b. The contact angle (angle measured in liquid) of the water droplet on bare GCE with a value of  $80^\circ$  shows a slight hydrophilic character of the GCE surface. The hydrophilicity of GCE was increased when modified with MWCNTs as demonstrated by the  $60^\circ$  contact angle of the water droplet. Modification of the GCE surface with COOH-fMWCNTs led to additional enhancement in hydrophilicity as witnessed by further reduction in contact angle ( $45^\circ$ ) of water droplet. Hence, analyte in the droplet of aqueous solution placed at the GCE surface modified with COOH-fMWCNTs should have closer accessibility to the electrode due to more hydrophilic nature of the surface. This behaviour is consistent with the most intense oxidation signal of the NBS at COOH-fMWCNTs/GCE as obvious from observation of Figure 2a which is a direct consequence of maximum surface coverage.

This enhancement in peak current in SWV response is in good agreement with EIS and CV findings, and this is because of the increase in the electrode's electroactive surface area by using COOH-fMWCNTs, as a modifier. Here, the modifier acts as a bridge between the analyte and the transducer (GCE) to facilitate electron transfer. Thus, the NBS transfers electrons through COOH-fMWCNTs to GCE for boosting the oxidation current via the electron hopping mechanism. Moreover, the boosted surface area results in enhanced interaction between the dye molecules and modifier that leads to increased preconcentration of dye molecules near the electrode surface. The preconcentration of the dye molecule at the modified electrode surface may also be the reason for peak current enhancement [35,37].

## 2.3. Effect of Various Scan Rates

The nature of the reaction, whether diffusion-controlled or surface-controlled, was investigated by obtaining cyclic voltammograms of NBS at different scan rates ranging from  $25 \text{ mV s}^{-1}$  to  $150 \text{ mV s}^{-1}$  on the modified electrode. Figure S1 illustrates that with the increase in scan rate, anodic peak potential shifted towards a higher potential [38]. According to reported work [39], if the slope of the plot between the  $\log I_p$  vs.  $\log v$  is equal to 0.5, then the electrochemical process is suggested to be diffusion controlled. In contrast, if the slope is equal to 1, then the process should be adsorption controlled. In the plot depicted in Figure S2, the slope was found to be 0.764, which suggested the involvement of both diffusion as well as adsorption control processes [40]. The  $R^2$  value of the plot of  $I_p$  vs.  $v$  is higher (Figure S3) than the  $R^2$  value of the plot between  $I_p$  vs.  $v^{1/2}$  (Figure S4), depicting that the adsorption process is more dominant as compared to the diffusion-controlled process [38].

## 2.4. Optimization of Experimental Parameters

To achieve further enhanced signals of NBS at the COOH-fMWCNTs/GCE, several parameters such as supporting electrolyte, pH, deposition potential, and deposition time were optimized by employing the SWV technique.

The choice of supporting electrolyte is one of the crucial steps in electrochemical analysis because it controls the decrease in the Ohmic drop or IR drop effect [30]. The supporting electrolyte strongly affects the peak shape, current, and its position. Hence, to obtain enhanced anodic peak current response, the SWV of the targeted analyte using COOH-fMWCNTs modified GCE was performed in a variety of electrolytes such as PBS, acetate buffer, Britton Robinson Buffer, NaOH, KOH, HCl, H<sub>2</sub>SO<sub>4</sub>, and CH<sub>3</sub>COOH. A well-defined peak shape with a maximum peak current was observed in PBS compared to other supporting electrolytes depicted in Figures 3 and S5. Therefore, PBS was selected as an appropriate electrolyte and was used for further electrochemical investigations [41].

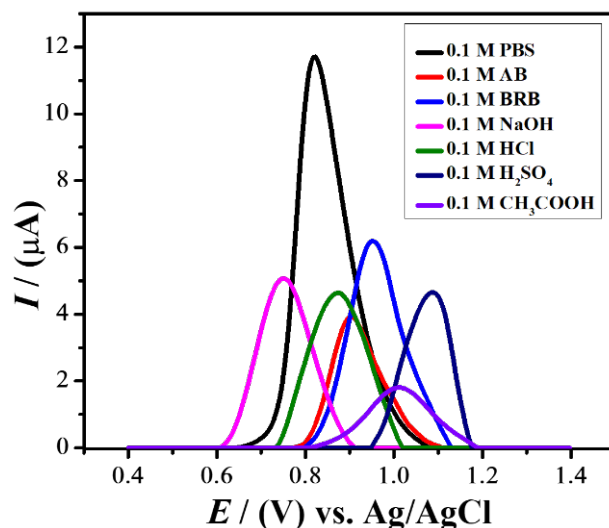


**Figure 3.** Anodic peak current response of 10  $\mu\text{M}$  NBS in various supporting electrolytes using COOH-fMWCNTs modified GCE.

The pH of the electrolytic solution also affects the peak current, peak shape, and peak potential as the response of many functional moieties is pH-dependent. Several voltammograms were recorded at different pH ranges from 3 to 10 to obtain a well-defined peak with the maximum anodic peak current response of the targeted analyte. It was found as depicted in Figure 4a that PBS of pH 6.0 showed maximum peak current response. Therefore, 0.1 M PBS of pH 6.0 was utilized for further studies.

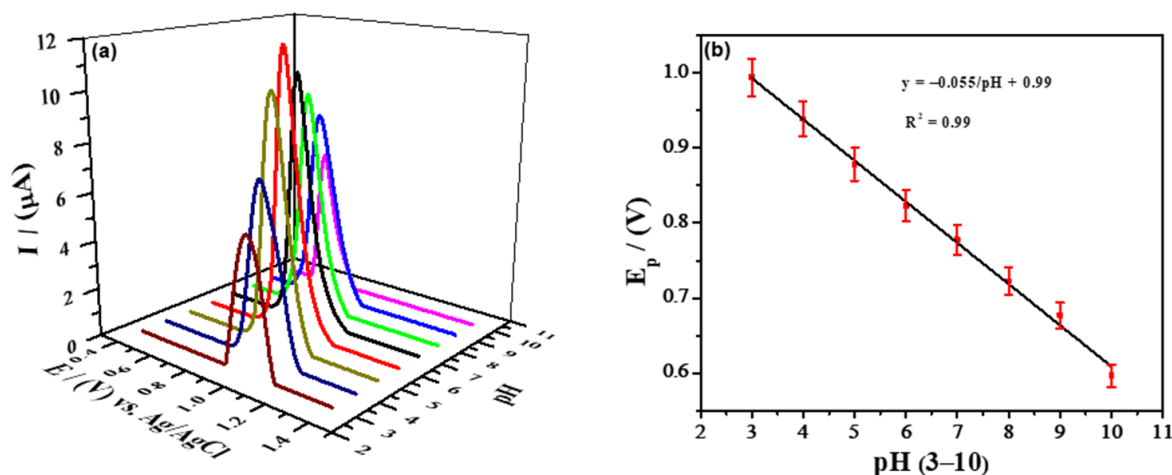


**Figure 4.** (a) SWVs showing the influence of pH on the oxidation response of NBS in PBS solution of pH 3–10 using COOH-fMWCNTs/GCE. (b) The plot of  $E_p$  vs. pH of NBS using 0.1 M PBS as a supporting electrolyte.

As the pH of 0.1 M PBS supporting electrolyte varied from 3 to 10, peak potential shifted toward less potential. This shift in the peak potential by varying pH showed the involvement of protons during the electron transfer reaction of the targeted analyte which can be calculated by the using equation ( $\Delta E_p / \Delta pH = 2.303 mRT / nF$ ). Considering the calibration plot depicted in Figure 4b, the value of the slope for the NBS was calculated to be 55 mV/pH, which is in close agreement with the Nernstian theoretical value (58 mV/pH), indicating the involvement of an equal number of protons and electrons in the redox process.

To investigate the impact of accumulation potential on peak current, it was varied ranging from  $-0.4$  V to  $0.2$  V. Figure S6 illustrated that the anodic peak current intensity increased with the increment in the deposition potential up to  $-0.2$  V. As the deposition potential increases, the number of active sites on the modified GCE increases, which results in maximum interactions between modifier and analyte moieties. Figure S7 revealed that at  $-0.2$  V deposition potential, maximum peak current was recorded, while the peak current decreased with a further increase in deposition potential because of active site saturation at the GCE. Thus,  $-0.2$  V deposition potential was opted as the optimized potential for further electrochemical investigations.

Various voltammetric responses of the designed sensing platform were recorded at different accumulation times ranging from 5 s to 35 s at a deposition potential of  $-0.2$  V in PBS of pH 6.0 as the supporting electrolyte to investigate the influence of accumulation time on anodic peak current intensity. The maximum oxidative peak current response was observed in 20 s, as illustrated in Figures S8 and S9. Dye molecules are bulky in size, and they need some time to orient properly to get oxidized at the surface of modified GCE, yet orientation at the surface COOH-fMWCNTs/GCE is optimum at 20 s by having close accessibility to the electrode when drop casted instead of being in solution. This is evidenced by a maximum peak current response. The saturation of dye molecules and hence interference to properly orient NBS at the surface of the electrode result in plummeting of peak current at higher deposition times.

### 2.5. Analytical Characterization

SWV was used to calculate the detection and quantification limit for NBS dye using COOH-fMWCNTs modified GCE under optimized conditions, i.e., 0.1 M PBS supporting electrolyte of pH 6.0, 20 s deposition time, and  $-0.2$  V deposition potential. In light of IUPAC guidelines, the LOD was investigated by incorporating the value of the standard deviation of the blank solution [42]. The results shown in Figure 5a, depict that peak current decreases linearly with a decrease in the analyte concentration. Figure 5b shows the corresponding linear calibration curves obtained as a result of variation in the analyte's peak current vs. concentration of the analyte ranging from  $0.03 \mu\text{M}$  to  $10 \mu\text{M}$ . The plot is divided into two linear segments which suggest that two types of LODs can be determined. The first linear segment ranges from  $10 \mu\text{M}$  to  $1 \mu\text{M}$  which is towards the higher concentration end and the LOD for this concentration range was found to be 16.9 nM. The comparatively higher LOD is suggestive of the slow mobility of NBS towards the modified GCE and hence the corresponding peak current is lower with increased resistance to charge transfer. This may also indicate the presence of dimers and trimers at higher concentrations. The second linear segment ranges from the lowest concentration of  $0.9 \mu\text{M}$  to  $0.03 \mu\text{M}$  and the LOD was found to be 1.21 nM; this region marks very minute dye concentrations, wherein the dye completely solubilizes and is present in the form of its simplest unit i.e., monomers. Both LODs from two regions show detection in the nanomolar range, however, the lowest concentration range is the most preferred one for measuring LOD for its analytical performance. LOQ was also determined using the equation ( $\text{LOQ} = \frac{10\sigma}{m}$ ) and was found to be 4.06 nM. Here  $\sigma$  represents the standard deviation of the electrodes without any modifier at the GCE and  $m$  represents the slope of the graph.

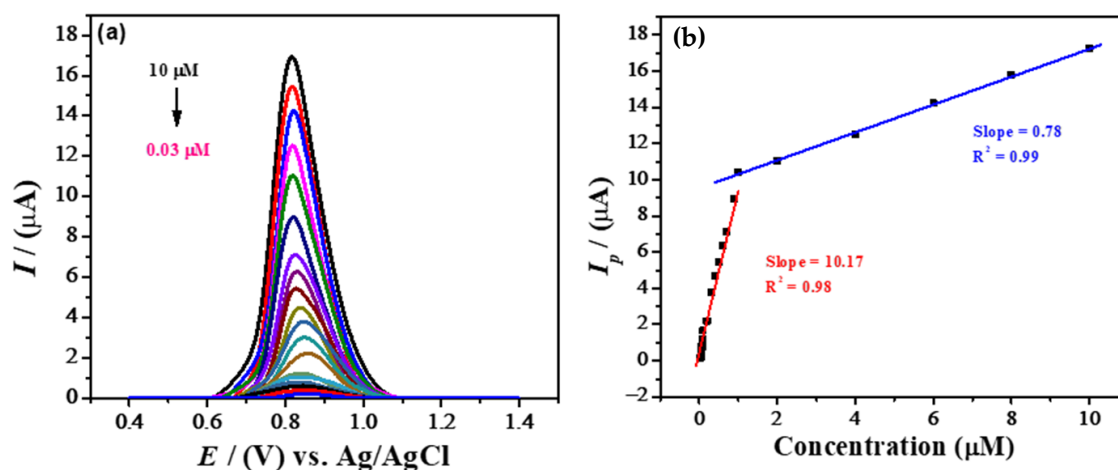


**Figure 5.** (a) Square wave voltammograms of various concentrations of NBS ranging from 0.03  $\mu\text{M}$  to 10  $\mu\text{M}$  under pre-optimized conditions. (b) The calibration plot of NBS concentrations ranging from 0.03  $\mu\text{M}$  to 10  $\mu\text{M}$  under optimized conditions with two distinct regions.

A comparison of previously reported sensors for detecting NBS is given in Table 1. The lowest detection limit of COOH-*f*MWCNTs modified GCE revealed that this is a better sensing platform than previously reported analytical detection tools for NBS detection.

**Table 1.** Assessment of the performance of the designed and reported sensors.

Sr.No	Modifying Material	Method	LOD (nM)	Reference
1	Nanocages of Ni	SERS	5	[43]
2	Gold nanostars	SERS	5	[44]
3	Ag and silica	LC/SERS	157	[45]
4	COOH- <i>f</i> MWCNTs	SWV	1.21	This work

### 2.6. Validity of the Designed Sensor

SWV analysis was carried out to evaluate the reproducibility and repeatability of the designed sensor to investigate its validity for detection of NBS. To examine the reproducibility of the designed sensing platform, five different COOH-*f*MWCNTs modified GCE electrodes were prepared, and their voltammograms were recorded under pre-optimized conditions. The observations suggest that the designed electrochemical sensor had good reproducibility. No noticeable changes were observed in the anodic peak response with %age RSD less than 2% for the developed sensor for NBS, as illustrated in Figure 6a which show the robustness of the as obtained results.

To examine the designed electrochemical sensor's repeatability, different peak current responses from the same modified electrode were recorded for up to 24 h at different time intervals. Figure 6b shows no considerable deviation in peak current at different time intervals as compared to the freshly prepared electrode. These results suggest that the designed sensor had intra-day stability. Due to the poor solubility of modifiers in water, the designed sensing platform not only showed stability but also prevented the leaching of modifiers from the electrode surface as indicated by the response of anodic peak currents. The intensity of the peak current remains almost the same which affirms the applicability of the proposed sensing matrix.

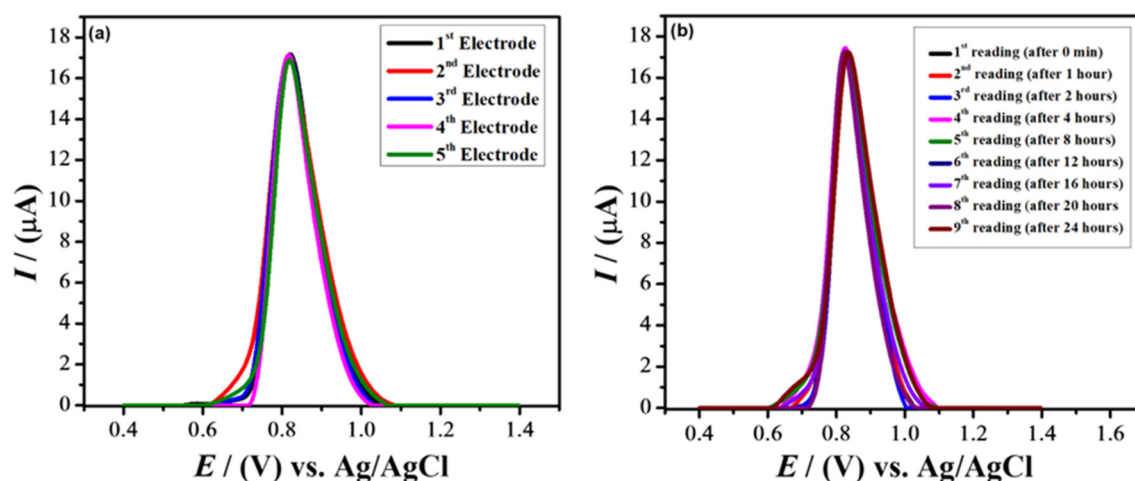


**Figure 6.** (a) SWVs of NBS showing the reproducibility of the designed sensor. (b) SWVs of NBS showing repeatability of the designed sensor.

### 2.7. Study of Effects of Interferents for Validation of Designed Sensor

The influence of interferents on the voltammetric response of the designed electrochemical sensor was investigated to demonstrate the selectivity and sensitivity of the designed sensing platform. It is very likely that wastewater contains several other metal ions and toxic dyes along with NBS dye in real situations. A 0.1 mM solution of different dyes and metal ions was introduced separately as interferents in the solution of NBS to determine their influence on the analyte's peak current response. These interferents include: Erichrome black T (EBT), Orange II dyes, and  $\text{Ba}^{3+}$ ,  $\text{Co}^{3+}$ ,  $\text{Ni}^{3+}$ ,  $\text{Cu}^{3+}$ ,  $\text{Zn}^{2+}$ ,  $\text{Na}^{1+}$ , and  $\text{K}^{1+}$  metals ions. The results suggested that interferents had no considerable impact or had an insignificant effect on the anodic peak current response of the sensor. This is because of the strong binding affinity of the analyte with the modifier. The anodic peak response of the designed sensor in the presence of interfering agents is depicted in Figure 7a. Some other signals, along with the NBS signal, can also be seen, which indicate that this sensor can also be used to detect other dyes and this potential-based selectivity is the beauty of electrochemical sensors. The redox potentials of metallic ions investigated are different from the targeted analyte. However, interfering effects depend not only on the redox potential but also on the interaction of metallic ions with the recognition layer. The analyte's signal was not disturbed by the metallic ions added as interfering agents. This indicates that the designed sensing platform possesses an anti-interfering ability for the tested ions. The bar graph in Figure 7b shows that the %age RSD value for the designed sensor was 1.77% which confirms the validity of the sensor. An RSD value of less than 3% is desirable for confirming the robustness of the proposed sensor.

### 2.8. Photocatalytic Degradation Studies by Designed Electrochemical Sensor

The designed sensing platform was employed to investigate the photocatalytic degradation of the NBS dye. A stock solution of 10  $\mu\text{M}$  NBS was prepared and stirred for 30 min. 50 mL of 10  $\mu\text{M}$  NBS solution was taken in a 100 mL beaker to which 0.1 mg of  $\text{TiO}_2$  as a photocatalyst, and 1 mL of  $\text{H}_2\text{O}_2$  as an oxidizing agent were added. The solution was stirred for 5 min in the presence of sunlight and the aliquot was withdrawn after regular intervals which was investigated for degradation of NBS by sunlight in the presence of  $\text{H}_2\text{O}_2$  by using two methods: electrochemical analysis by the as-prepared COOH-fMWCNTs/GCE sensor and UV-visible spectrophotometry. Thus, after withdrawing from the reaction mixture, the drop of 10  $\mu\text{M}$  of NBS was cast on COOH-fMWCNTs modified GCE, and its voltammogram was recorded in PBS of pH = 6. This was repeated after an interval of 5 min followed every time by an electrochemical investigation of the remaining dye in the droplet. These recorded voltammograms, which were subjected to



photocatalysis before, are depicted in Figure 8a. A decrease in peak current response in the voltammograms indicated that the concentration of dye molecules is decreasing over time suggesting its photocatalytic degradation. The peak current reaches the lowest value indicating that the maximum dye content has deteriorated. The effect of irradiation time on NBS dye photocatalytic degradation was investigated, and percentage degradation was found to be 95% after 100 min of keeping the dye solution under direct sunlight which is evident from Figure S10. The photocatalytic degradation kinetics of NBS was investigated by SWV and the obtained data was fitted in the first-order rate equation. The degradation rate constant with a value of  $0.028 \text{ min}^{-1}$  was obtained from the slope of the plot depicted in Figure 8b.

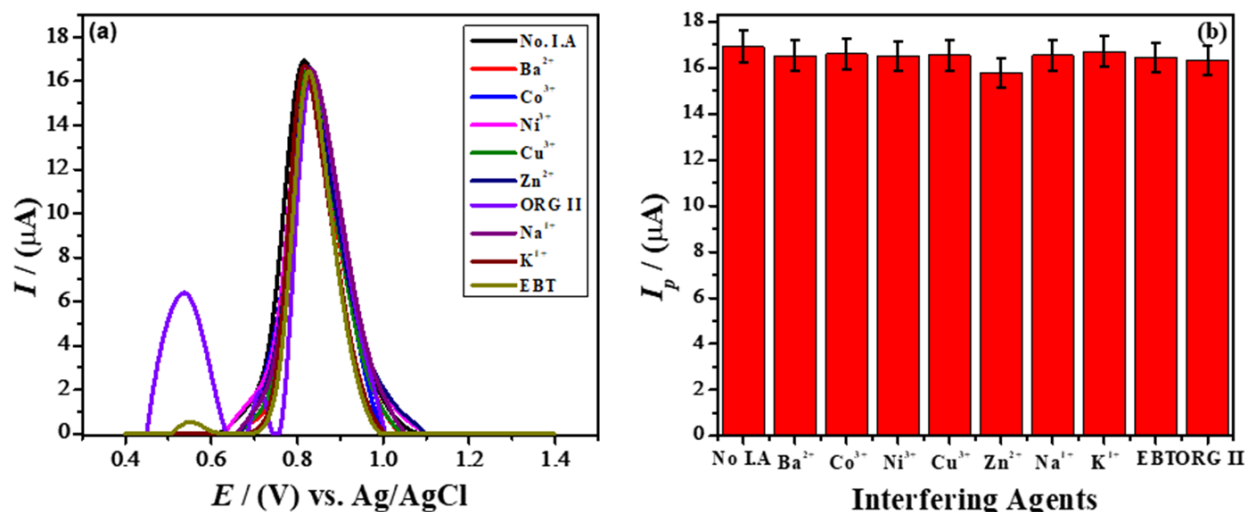


**Figure 7.** (a) SWVs of  $10 \mu\text{M}$  NBS in the presence of different interfering agents using COOH-fMWCNTs/GCE. (b) Bar graph of the peak current of NBS at the designed sensor in the presence of interfering species.

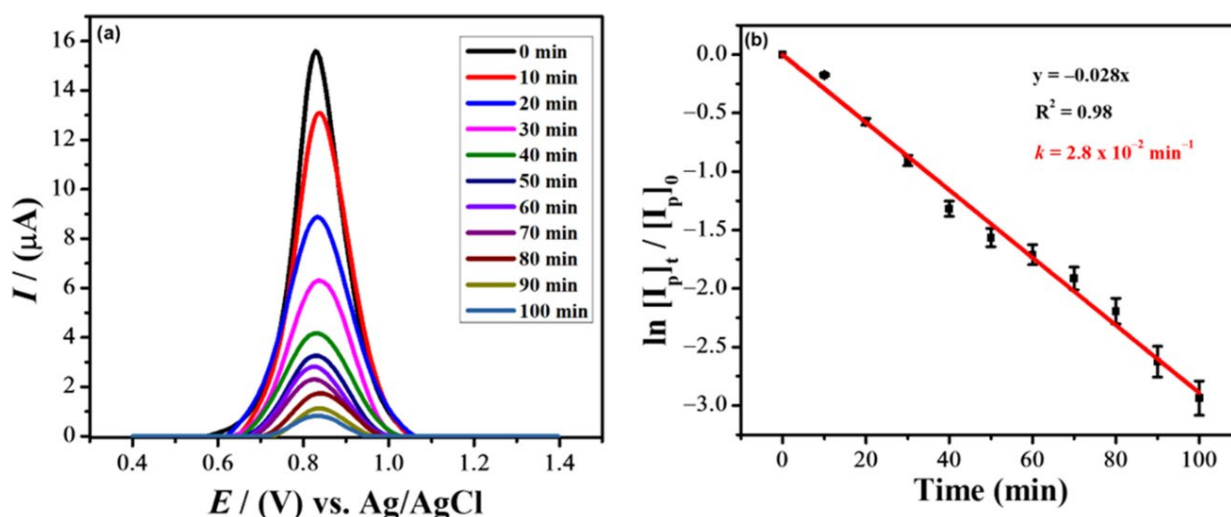


**Figure 8.** (a) The SWV of NBS at different time intervals recorded by using COOH-fMWCNTs/GCE under optimized conditions. (b) Effect of irradiation time on NBS photocatalytic degradation under direct sunlight.

### 2.9. Spectroscopic Studies of NBS Photocatalytic Degradation

A UV-visible spectrophotometer was also used for studying the photocatalytic degradation of NBS. The  $\text{TiO}_2$  nanoparticles and  $\text{H}_2\text{O}_2$  were used as photocatalysts and oxidizing agents respectively, as discussed previously in Section 2.8. The corresponding absorption

spectra at different time intervals are depicted in Figure 9a. The dye molecule's color is because of the conjugation system in the structure. Electron-hole pair generation occurred as the photocatalyst was exposed to sunlight. The generation of electron-hole pair and hydroxyl radical leads to dye degradation by breaking up the conjugation system in the dye molecule. It is evident from UV-visible spectra that over the time, the photocatalytic degradation process increased as the dye molecule was degraded in the presence of sunlight. The presence of  $H_2O_2$  facilitates the production of hydroxyl radicals which leads to the mineralization of the organic molecule.

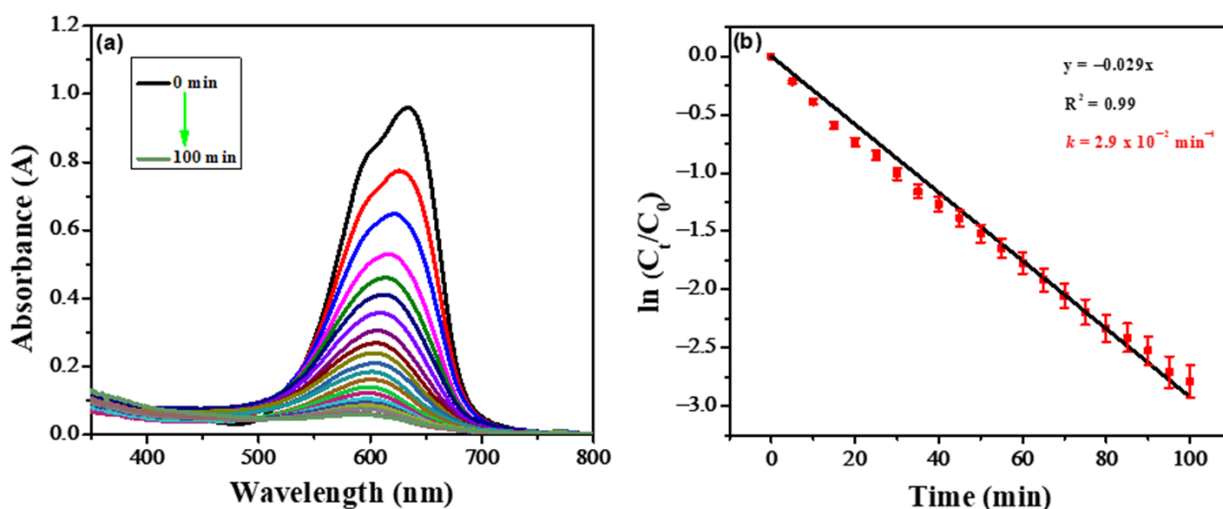
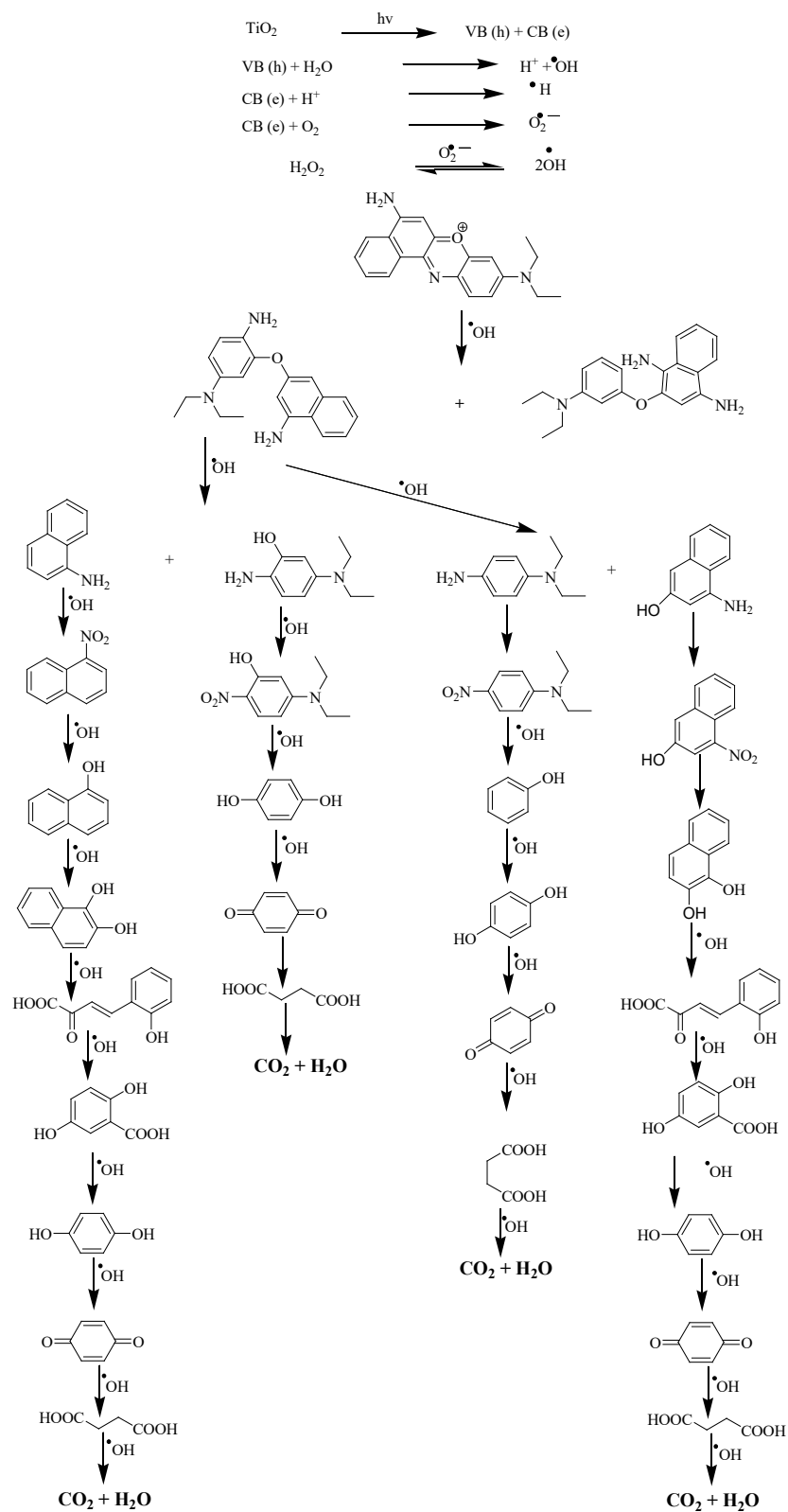


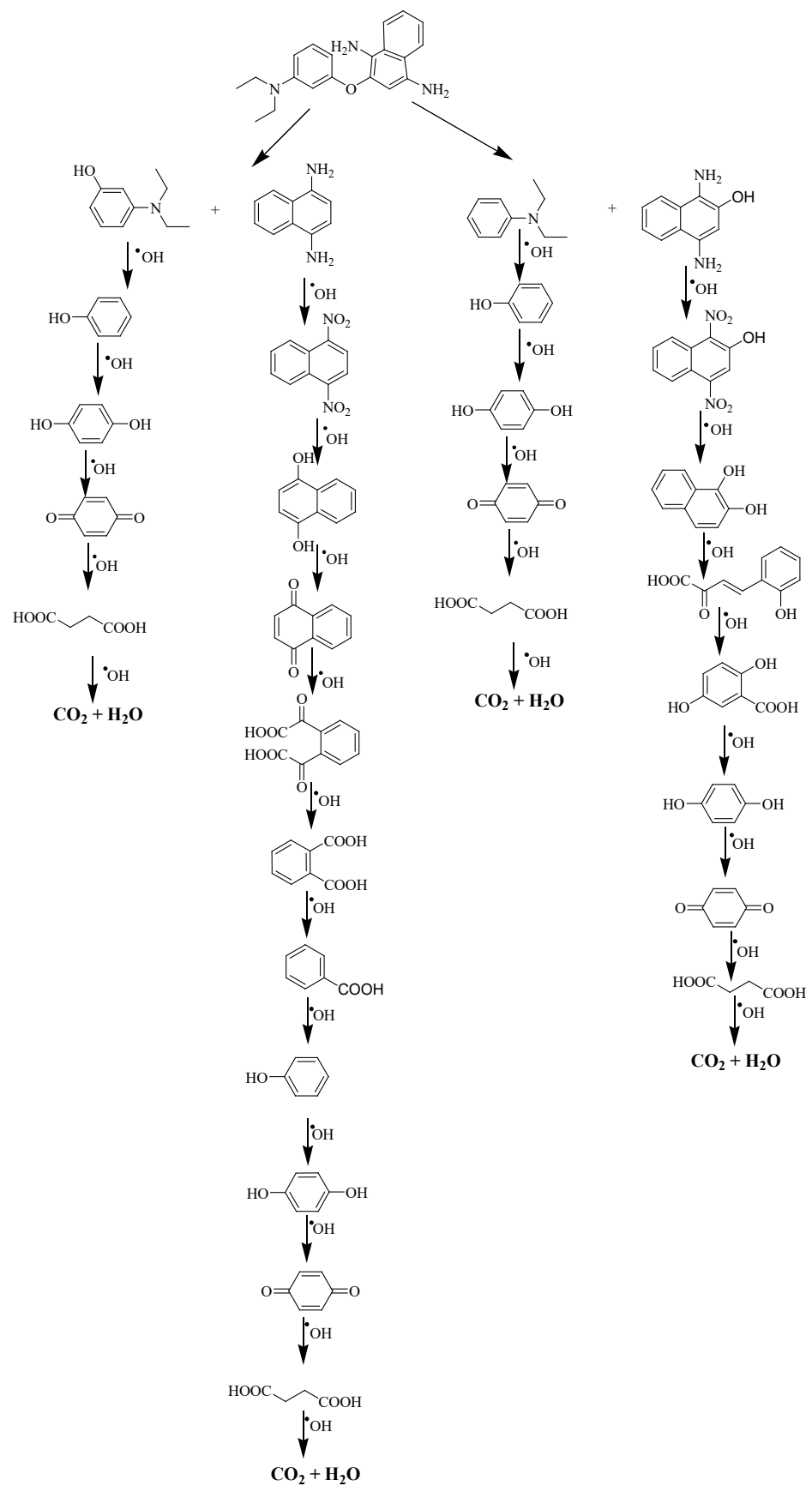
**Figure 9.** (a) UV-Vis spectra of the photocatalytic degradation of NBS at different time intervals. (b) The photocatalytic degradation kinetics of NBS using UV-visible spectroscopic data.

It is evident from Figure S11 that the dye content is photocatalytically degraded to 95%. Furthermore, recovery of  $TiO_2$  and its multiple usage performance were explored with the same concentration of dye i.e.,  $10 \mu\text{M}$  NBS solution. During the process the catalyst was removed by filtering it out from the dye solution and then replacing the supernatant with fresh solution of dye. This solution was then subjected to UV-Vis spectroscopy to investigate the effectiveness of the catalyst. Figures S11–S13 show recovery and reusability of  $TiO_2$  for the degradation of NBS for three cycles where a decrease in photocatalytic degradation efficiency from 95% (cycle-1: Figure S11) to 93% (cycle 2: Figure S12b) to 92% (cycle-3: Figure S13b) is evident. The slight change in %age degradation shows an insignificant change in the catalytic activity which shows good stability of the catalyst against the photocatalytic degradation of the dye. The slight decrease in the photocatalytic degradation efficiency can however be attributed to the decrease in pore size and pore volume due to adsorption and clogging of the pores by dye and its degraded products. The pore size is an important factor that contributes towards performance of the catalyst [46,47]. Thus, a small decrease in its catalytic activity points to reusability of the catalyst in applications where this factor becomes important.

The proposed degradation mechanism as depicted in Scheme 1 of NBS shows attack of hydroxyl free radicals generated by  $TiO_2$  and  $H_2O_2$  at a double bond present in the ring, hence, with the breakdown of conjugation of the ring, the color variation from being intense to dull, was observed (Figure 10). Scheme 1 is the proposed mechanism, based upon the obtained electrochemical and UV-Vis spectroscopic data and also in the light of reported literature, of the degradation of NBS and other dyes using methods other than our developed method [36,48,49]. The final product is the mineralization of the NBS to  $CO_2$  and  $H_2O$ .



Scheme 1. Cont.



Scheme 1. Proposed mechanism for the degradation of NBS.

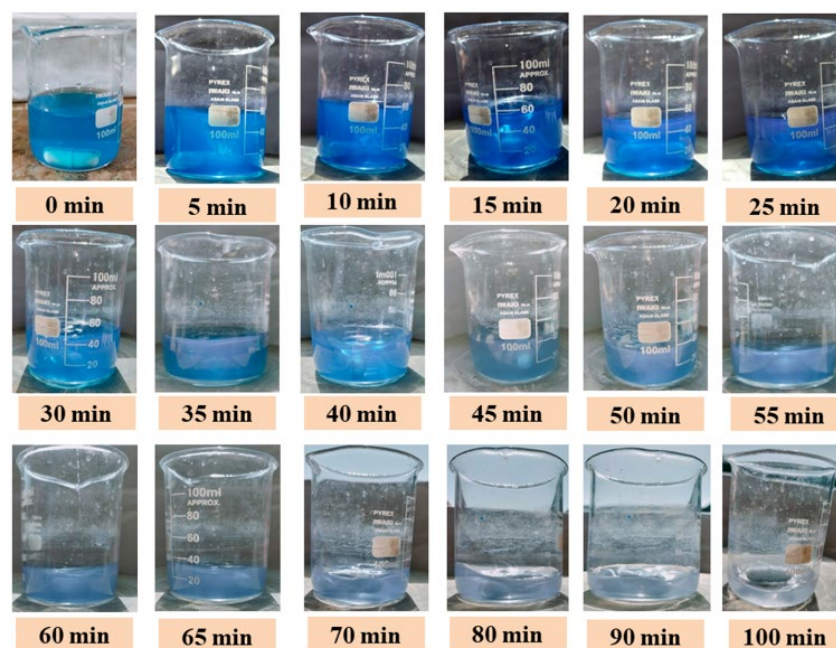


Figure 10. Naked eye evidence of the decolorization of NBS dye.

Using spectroscopic results, the percent degradation of NBS was calculated using the following equation.

$$\% \text{ge degradation} = \frac{\text{maximum absorbance (t = 0)} - \text{absorbance at time t}}{\text{maximum absorbance (t = 0)}} \times 100 \quad (2)$$

The spectroscopic data were also used to explore the kinetics of the photocatalytic degradation process [50–52]. The reaction order and rate were confirmed from the plot between  $\ln [C_t/C_0]$  as a function of time, as shown in Figure 9b. The rate of reaction ( $k$ ) was calculated from the equation i.e.,  $\ln \frac{C_t}{C_0} = -kt$ . Where  $C_t$  is the absorption at time  $t$ ,  $C_0$  is the absorption at zero time, and  $k$  is the rate constant. The straight line of the plot between  $\ln [C_t/C_0]$  as a function of time exhibited that the reaction follows first-order kinetics. The rate of reaction calculated from spectroscopic data is  $0.029 \text{ min}^{-1}$ . The order of reaction and rate of reaction calculated from electrochemical and spectroscopic data are in good agreement revealing that the designed sensor is also efficient for monitoring photocatalytic degradation of NBS.

### 3. Experimental

#### 3.1. Reagents and Materials

All chemicals of analytical grade purity were used as received from Sigma Aldrich (St. Louis, MO, USA). NBS dye was used as an analyte while COOH-functionalized MWCNTs as an electrode modifier.  $\text{TiO}_2$  was utilized for the photocatalytic degradation of NBS. Dimethylformamide (DMF) was used as a solvent to prepare COOH-*f*MWCNTs suspension. Analytical grade reagents  $\text{NaH}_2\text{PO}_4 \cdot \text{H}_2\text{O}$  and  $\text{Na}_2\text{HPO}_4 \cdot 2\text{H}_2\text{O}$  were used to prepare phosphate buffer saline (PBS) as a supporting electrolyte. Additionally, PBS, acetate buffer, Britton Robinson Buffer, NaOH, KOH, HCl,  $\text{H}_2\text{SO}_4$ , and  $\text{CH}_3\text{COOH}$  were used as supporting electrolytes for the optimization of the modified electrode. Thus, all solutions of various electrolytes were prepared by using doubly distilled water with analytical grade reagents.

#### 3.2. Instrumentation

The fabricated sensing platform was electrochemically characterized by executing CV, SWV, and EIS on a Metrohm Autolab (Utrecht, The Netherlands) equipped with NOVA 1.11

software. It comprises a three-cell assembly with GCE as the working electrode, Ag/AgCl (3 M KCl) as the reference electrode, and Pt as the counter electrode. Spectroscopic studies of NBS were carried out at Shimadzu UV-1700 spectrophotometer, Japan working in 200–800 nm range.

### 3.3. Working Electrode Modification

Before subjecting GCE to modification, it was physiochemically treated to achieve a high O/C ratio at its surface. A physically cleaned GCE surface was obtained by rubbing it in a fashion of digit 8 on a nylon buffing pad containing alumina slurry (1  $\mu$ M). Then, the electrode was ultrasonicated in a 1:1 mixture of HNO<sub>3</sub> and ethanol for five minutes, followed by rinsing with a jet of distilled water to remove the undesired moieties from the electrode's surface [53]. The physically cleaned working electrode was then subjected to electrochemical cleaning by taking several CV scans of bare GCE in a supporting electrolyte [41,54,55]. GCE was modified by immobilizing a 5  $\mu$ L drop of a modifier concentration at the pre-cleaned surface. After casting the modifier on the surface of the working electrode, it was left for drying followed by washing away any loosely bound molecules and then allowing it to dry. Finally, a 10  $\mu$ L drop of the analyte (NBS) was applied to the modified electrode. This as-prepared electrode designated as COOH-fMWCNTs/GCE was further applied for electroanalytical measurements.

### 3.4. Experimental Procedure

0.1 mM stock solution of NBS dye was prepared using distilled water which was further diluted to prepare a solution of 10  $\mu$ M concentration using the same solvent. The inks of electrode modifiers MWCNTs and COOH-fMWCNTs with a concentration of 1 mg/mL were prepared individually in DMF and subjected to ultrasonication for 1 h. Once the surface of GCE was dried after modification, a 10  $\mu$ L drop of analyte was cast on the surface of the pre-modified working electrode. The modified electrode was then placed in the electrochemical cell containing the supporting electrolyte, and the sensing ability of the designed sensing platform was analyzed by recording square wave voltammograms. Different experimental parameters were optimized using the same procedure. The surface behavior of the working electrode was investigated using EIS. Electrochemical techniques, such as SWV and CV facilitated different analysis of the sensing platform. The limit of detection (LOD) and limit of quantification (LOQ) were calculated using data obtained by SWV responses. SWV and UV-visible spectroscopy was employed for photocatalytic degradation studies of NBS dye. The solution of 10  $\mu$ M of NBS was kept in direct sunlight for 100 min. After subjecting the solution of NBS to sunlight, 5  $\mu$ L of the sample of the dye was withdrawn at regular intervals which was drop casted at the modified electrode for its electroanalysis in PBS under set optimized conditions. Here recorded voltammograms provided information about the degree of degradation indicated by a decrease in peak current value after the aliquot was taken after every 5 min. The same procedure of withdrawing the photocatalyzed sample was conducted for recording its UV-visible spectra. The voltammetric and spectroscopic responses facilitated the determination of the percentage degradation, reaction order, and reaction rate for NBS photocatalytic degradation. All experimental work was done at an ambient temperature of 298 K (25 °C  $\pm$  1).

## 4. Conclusions

The toxicity of dyes is a threat to life in water and on land. Thus, in order to address abatement of the dyes and overcome issues pertaining to environmental degradation, the current work presents the development of a sensor for the nanomolar detection of Nile Blue Sulphate (NBS) dye. Moreover, it presents employing photocatalyst for the photocatalytic degradation of NBS followed by analytical methods for monitoring the extent and degradation kinetics. Acid-functionalized MWCNTs were immobilized on the surface of the GCE to fabricate an efficient electrochemical sensing platform. Various

experimental parameters such as accumulation potential, accumulation time, supporting electrolyte, and pH of solution were optimized to obtain intense signal of the target analyte at the designed probe. Peak current versus concentration plot was found to have a wide linear range with LOD value of 1.21 nM under optimized experimental conditions for NBS. After detection, photocatalytic degradation experiments for NBS were conducted using TiO<sub>2</sub> nanoparticles in the presence of hydrogen peroxide. The designed sensing platform was then employed for monitoring the photocatalytic degradation of the dye supported with spectroscopic studies. The results obtained from both electrochemical and spectroscopic techniques revealed that the photocatalytic degradation follows pseudo-first-order kinetics. The obtained results suggest that the developed method is promising for the purification of dye contaminated wastewater.

**Supplementary Materials:** The following supporting information can be downloaded at: <https://www.mdpi.com/article/10.3390/catal13010141/s1>, Table S1. Parameters evaluated from EIS experiments conducted on various electrodes; Table S2. Electroactive surface areas of bare and modified electrodes; Figure S1. Influence of scan rate on the anodic peak current of the NBS in supporting electrolyte of PBS of pH 6.0; Figure S2. Calibration plot between the log peak current vs. log scan rate of NBS oxidation; Figure S3. A plot of  $I_p$  vs.  $v$  of NBS oxidation; Figure S4. A plot of  $I_p$  vs.  $v^{1/2}$  of NBS oxidation; Figure S5. Bar graph of the oxidation peak current of NBS vs. various supporting electrolytes; Figure S6. Effect of accumulation potential on the peak current of 10  $\mu$ M NBS in PBS of pH 6.0 using COOH-fMWCNTs/GCE; Figure S7. A plot of  $I_p$  vs. deposition potential; Figure S8. Peak current response of 10  $\mu$ M NBS at different deposition times; Figure S9. Plot between peak current vs. deposition time of NBS oxidation; Figure S10. Kinetic study of NBS photocatalytic degradation using SWV data; Figure S11. Percentage degradation of NBS using UV-visible Spectroscopic data; Figure S12. (a) UV-Vis spectra of the photodegradation of NBS at different time intervals after recovery of photocatalyst for the first time. (b) %age degradation of NBS at different time intervals after recovery of photocatalyst for the first time; Figure S13. (a) UV-Vis spectra of the photodegradation of NBS at different time intervals after recovery of photocatalyst for the second time. (b) %age degradation of NBS at different time intervals after recovery of photocatalyst for the second time.

**Author Contributions:** Conceptualization, A.S.; methodology, A.S.; software, J.N.; validation, M.N.S. and N.U.; formal analysis, F.J.I. and A.S.; investigation, M.N.S.; resources, J.N. and A.S.; writing—original draft preparation, M.N.S.; writing—review and editing, A.S.; supervision, A.S.; project administration, A.S. and J.N. All authors have read and agreed to the published version of the manuscript.

**Funding:** This research received no external funding.

**Data Availability Statement:** Data are contained within the article and in the provided Supplementary Materials.

**Acknowledgments:** We acknowledge the support of Quaid-i-Azam University, Islamabad, Pakistan and Higher Education Commission of Pakistan.

**Conflicts of Interest:** The Authors declare no Competing Financial or Non-Financial Interest.

## References

1. Tahir, M.B.; Nawaz, T.; Nabi, G.; Sagir, M.; Khan, M.I.; Malik, N. Role of nanophotocatalysts for the treatment of hazardous organic and inorganic pollutants in wastewater. *Int. J. Environ. Anal. Chem.* **2022**, *102*, 491–515. [CrossRef]
2. Abd Elaty, I.; Kuriqi, A.; Shahawy, A.E. Environmental rethinking of wastewater drains to manage environmental pollution and alleviate water scarcity. *Nat. Hazards* **2022**, *110*, 2353–2380. [CrossRef]
3. Basu, N.; Abass, K.; Dietz, R.; Krüemmel, E.; Rautio, A.; Weihe, P. The impact of mercury contamination on human health in the Arctic: A state of the science review. *Sci. Total Environ.* **2022**, *831*, 154793. [CrossRef]
4. Naidu, R.; Biswas, B.; Willett, I.R.; Cribb, J.; Singh, B.K.; Nathanail, C.P.; Coulon, F.; Semple, K.T.; Jones, K.C.; Barclay, A. Chemical pollution: A growing peril and potential catastrophic risk to humanity. *Environ. Int.* **2021**, *156*, 106616. [CrossRef]
5. Liu, X.; Yang, H.; Diao, Y.; He, Q.; Lu, C.; Singh, A.; Kumar, A.; Liu, J.; Lan, Q. Recent advances in the electrochemical applications of Ni-based metal organic frameworks (Ni-MOFs) and their derivatives. *Chemosphere* **2022**, *307*, 135729. [CrossRef]
6. Zheng, M.; Chen, J.; Zhang, L.; Cheng, Y.; Lu, C.; Liu, Y.; Singh, A.; Trivedi, M.; Kumar, A.; Liu, J. Metal Organic Framework as an Efficient Adsorbent for Drugs from Wastewater. *Mater. Today Commun.* **2022**, *31*, 103514. [CrossRef]

7. Khan, M.A.; Ghouri, A.M. Environmental pollution: Its effects on life and its remedies. *Res. World J. Arts Sci. Commer.* **2011**, *2*, 276–285.
8. Pereira, J.C. Environmental issues and international relations, a new global (dis) order—the role of International Relations in promoting a concerted international system. *Rev. Bras. Política Int.* **2015**, *58*, 191–209. [CrossRef]
9. Khan, U.; Niaz, A.; Shah, A.; Zaman, M.I.; Zia, M.A.; Iftikhar, F.J.; Nisar, J.; Ahmed, M.N.; Akhter, M.S.; Shah, A.H. Thiamine-functionalized silver nanoparticles for the highly selective and sensitive colorimetric detection of  $Hg^{2+}$  ions. *New J. Chem.* **2018**, *42*, 528–534. [CrossRef]
10. Sutar, S.; Patil, P.; Jadhav, J. Recent advances in biochar technology for textile dyes wastewater remediation: A review. *Environ. Res.* **2022**, *209*, 112841. [CrossRef]
11. Malik, V.; Saya, L.; Gautam, D.; Sachdeva, S.; Dheer, N.; Arya, D.K.; Gambhir, G.; Hooda, S. Review on adsorptive removal of metal ions and dyes from wastewater using tamarind-based bio-composites. *Polym. Bull.* **2022**, *79*, 9267–9302. [CrossRef]
12. Dutta, S.; Gupta, B.; Srivastava, S.K.; Gupta, A.K. Recent advances on the removal of dyes from wastewater using various adsorbents: A critical review. *Mater. Adv.* **2021**, *2*, 4497–4531. [CrossRef]
13. Mani, S.; Bharagava, R.N. Exposure to crystal violet, its toxic, genotoxic and carcinogenic effects on environment and its degradation and detoxification for environmental safety. *Rev. Environ. Contam. Toxicol.* **2016**, *237*, 71–104.
14. Vyavahare, G.; Sutar, S.; Gurav, R.; Patil, R.; Patil, D.; Jadhav, J. Application of biochar for the treatment of textile dyes and wastewaters. In *Biochar and Its Application in Bioremediation*; Springer: Berlin/Heidelberg, Germany, 2021; pp. 169–191.
15. Karthikeyan, C.; Arunachalam, P.; Ramachandran, K.; Al-Mayouf, A.M.; Karuppuchamy, S. Recent advances in semiconductor metal oxides with enhanced methods for solar photocatalytic applications. *J. Alloys Compd.* **2020**, *828*, 154281. [CrossRef]
16. Wu, Z.; Guo, K.; Cao, S.; Yao, W.; Piao, L. Synergetic catalysis enhancement between  $H_2O_2$  and  $TiO_2$  with single-electron-trapped oxygen vacancy. *Nano Res.* **2020**, *13*, 551–556. [CrossRef]
17. Castro, M.; Pereira, F.; Aller, A.; Littlejohn, D. Raman spectrometry as a screening tool for solvent-extracted azo dyes from polyester based textile fibers. *Polym. Test.* **2020**, *91*, 106765. [CrossRef]
18. Metters, J.P.; Banks, C.E. Electrochemical utilisation of chemical vapour deposition grown carbon nanotubes as sensors. *Vacuum* **2012**, *86*, 507–519. [CrossRef]
19. Norizan, M.N.; Moklis, M.H.; Demon, S.Z.N.; Halim, N.A.; Samsuri, A.; Mohamad, I.S.; Knight, V.F.; Abdullah, N. Carbon nanotubes: Functionalisation and their application in chemical sensors. *RSC Adv.* **2020**, *10*, 43704–43732. [CrossRef]
20. Yaghoubi, A.; Ramazani, A. Synthesis of amino-functionalized carbon nanotubes and their applications. *Curr. Org. Chem.* **2018**, *22*, 1505–1522. [CrossRef]
21. Zhu, G.; Hu, N.; Guo, M.; Liu, Y.; Ran, Q.; Zhao, H. A simple and efficient electrochemical sensor for determination of gallic acid based on multi-walled carbon nanotubes with carboxyl functionalization. *Mater. Res. Innov.* **2022**, *26*, 389–396. [CrossRef]
22. Kaur, B.; Srivastava, R.; Satpati, B. Silver nanoparticle decorated polyaniline–zeolite nanocomposite material based non-enzymatic electrochemical sensor for nanomolar detection of lindane. *RSC Adv.* **2015**, *5*, 57657–57665. [CrossRef]
23. Gowda, J.I.; Nandibewoor, S.T. Electrochemical behavior of paclitaxel and its determination at glassy carbon electrode. *Asian J. Pharm. Sci.* **2014**, *9*, 42–49. [CrossRef]
24. Kurbanoglu, S.; Ozkan, S.A.; Merkoci, A. Nanomaterials-based enzyme electrochemical biosensors operating through inhibition for biosensing applications. *Biosens. Bioelectron.* **2017**, *89*, 886–898. [CrossRef]
25. Nandini, S.; Nalini, S.; Sanetuntikul, J.; Shanmugam, S.; Niranjana, P.; Melo, J.S.; Suresh, G.S. Development of a simple bioelectrode for the electrochemical detection of hydrogen peroxide using *Pichia pastoris* catalase immobilized on gold nanoparticle nanotubes and polythiophene hybrid. *Analyst* **2014**, *139*, 5800–5812. [CrossRef]
26. Rastogi, P.K.; Ganesan, V.; Krishnamoorthi, S. Palladium nanoparticles incorporated polymer-silica nanocomposite based electrochemical sensing platform for nitrobenzene detection. *Electrochim. Acta* **2014**, *147*, 442–450. [CrossRef]
27. Gupta, R.; Rastogi, P.K.; Ganesan, V.; Yadav, D.K.; Sonkar, P.K. Gold nanoparticles decorated mesoporous silica microspheres: A proficient electrochemical sensing scaffold for hydrazine and nitrobenzene. *Sens. Actuators B Chem.* **2017**, *239*, 970–978. [CrossRef]
28. Kokab, T.; Shah, A.; Iftikhar, F.J.; Nisar, J.; Akhter, M.S.; Khan, S.B. Amino acid-fabricated glassy carbon electrode for efficient simultaneous sensing of zinc (II), cadmium (II), copper (II), and mercury (II) ions. *ACS Omega* **2019**, *4*, 22057–22068. [CrossRef]
29. Shah, A.; Akhtar, M.; Aftab, S.; Shah, A.H.; Kraatz, H.S. Gold copper alloy nanoparticles (Au-Cu NPs) modified electrode as an enhanced electrochemical sensing platform for the detection of persistent toxic organic pollutants. *Electrochim. Acta* **2017**, *241*, 281–290. [CrossRef]
30. Kokab, T.; Manzoor, A.; Aftab, S.; Aslam, F.; Iftikhar, F.J.; Siddiqi, H.M.; Shah, A. A reliable sensing platform based on tribenzamide for sensitive and selective detection of Pb (II) ions. *Inorg. Chem. Commun.* **2022**, *138*, 109261. [CrossRef]
31. Shah, A.; Ullah, A.; Rauf, A.; Rehman, Z.U.; Shujah, S.; Shah, S.M.; Waseem, A. Detailed electrochemical probing of a biologically active isoquinoline. *J. Electrochem. Soc.* **2013**, *160*, 597. [CrossRef]
32. Abouzari, M.S.; Berkemeier, F.; Schmitz, G.; Wilmer, D. On the physical interpretation of constant phase elements. *Solid State Ionics* **2009**, *180*, 922–927. [CrossRef]
33. Haque, J.; Verma, C.; Srivastava, V.; Quraishi, M.; Ebenso, E.E. Experimental and quantum chemical studies of functionalized tetrahydropyridines as corrosion inhibitors for mild steel in 1 M hydrochloric acid. *Results Phys.* **2018**, *9*, 1481–1493. [CrossRef]
34. Kassa, A.; Amare, M. Poly (4-amino-3-hydroxynaphthalene-1-sulfonic acid) modified glassy carbon electrode for square wave voltammetric determination of amoxicillin in four tablet brands. *BMC Chem.* **2021**, *15*, 10. [CrossRef]



35. Shah, A. A novel electrochemical nanosensor for the simultaneous sensing of two toxic food dyes. *ACS Omega* **2020**, *5*, 6187–6193. [CrossRef] [PubMed]
36. Hayat, M.; Shah, A.; Nisar, J.; Shah, I.; Haleem, A.; Ashiq, M.N. A novel electrochemical sensing platform for the sensitive detection and degradation monitoring of methylene blue. *Catalysts* **2022**, *12*, 306. [CrossRef]
37. Hakeem, M.K.; Shah, A.; Nisar, J.; Iftikhar, F.J.; Khan, S.B.; Shah, I. Electrochemical sensing platform for the detection and degradation studies of Metanil Yellow. *J. Electrochem. Soc.* **2022**, *169*, 056503. [CrossRef]
38. Kokab, T.; Shah, A.; Khan, M.A.; Nisar, J.; Ashiq, M.N. Electrochemical sensing platform for the simultaneous femtomolar detection of amlodipine and atorvastatin drugs. *RSC Adv.* **2021**, *11*, 27135–27151. [CrossRef] [PubMed]
39. Wang, J.; Yang, B.; Wang, H.; Yang, P.; Du, Y. Highly sensitive electrochemical determination of Sunset Yellow based on gold nanoparticles/graphene electrode. *Anal. Chim. Acta* **2015**, *893*, 41–48. [CrossRef]
40. Mo, Z.; Zhang, Y.; Zhao, F.; Xiao, F.; Guo, G.; Zeng, B. Sensitive voltammetric determination of Sudan I in food samples by using gemini surfactant ionic liquid multiwalled carbon nanotube composite film modified glassy carbon electrodes. *Food Chem.* **2010**, *121*, 233–237. [CrossRef]
41. Kokab, T.; Shah, A.; Khan, M.A.; Arshad, M.; Nisar, J.; Ashiq, M.N.; Zia, M.A. Simultaneous femtomolar detection of paracetamol, diclofenac, and orphenadrine using a carbon nanotube/zinc oxide nanoparticle-based electrochemical sensor. *ACS Appl. Nano Mater.* **2021**, *4*, 4699–4712. [CrossRef]
42. Wang, H.; Guo, X.; Fu, S.; Yang, T.; Wen, Y.; Yang, H. Optimized core shell Au@ Ag nanoparticles for label free Raman determination of trace Rhodamine B with cancer risk in food product. *Food Chem.* **2015**, *188*, 137–142. [CrossRef] [PubMed]
43. Chandu, B.; Bharati, M.S.S.; Albrycht, P.; Rao, S.V. Fabrication of nanocages on nickel using femtosecond laser ablation and trace level detection of Malachite Green and Nile Blue dyes using surface enhanced Raman spectroscopic technique. *Opt. Laser Technol.* **2020**, *131*, 106454. [CrossRef]
44. Moram, S.S.B.; Byram, C.; Soma, V.R. Gold nanoparticle and nanostar loaded paper based SERS substrates for sensing nanogram level picric acid with a portable Raman spectrometer. *Bull. Mater. Sci.* **2020**, *43*, 53. [CrossRef]
45. Somsen, G.; Coulter, S.; Gooijer, C.; Velthorst, N.; Brinkman, U.T. Coupling of column liquid chromatography and surface enhanced resonance Raman spectroscopy via a thin layer chromatographic plate. *Anal. Chim. Acta* **1997**, *349*, 189–197. [CrossRef]
46. Drisko, G.L.; Cao, L.; Kimling, M.C.; Harrison, S.; Luca, V.; Caruso, R.A. Pore size and volume effects on the incorporation of polymer into macro and mesoporous zirconium titanium oxide membranes. *ACS Appl. Mater. Interfaces* **2009**, *1*, 2893–2901. [CrossRef] [PubMed]
47. Teixeira, S.; Martins, P.; Lanceros-Mendez, S.; Kuhn, K.; Cuniberti, G. Reusability of photocatalytic TiO<sub>2</sub> and ZnO nanoparticles immobilized in poly (vinylidene difluoride)-co-trifluoroethylene. *Appl. Surf. Sci.* **2016**, *384*, 497–504. [CrossRef]
48. Kushwaha, R.; Garg, S.; Bajpai, S.; Giri, A.S. Degradation of Nile blue sulphate dye onto iron oxide nanoparticles: Kinetic study, identification of reaction intermediates, and proposed mechanistic pathways. *Asia-Pac. J. Chem. Eng.* **2018**, *13*, 2200. [CrossRef]
49. Irfan, M.; Shah, A.; Iftikhar, F.J.; Hayat, M.; Ashiq, M.N.; Shah, I. Electrochemical sensing platform based on functionalized multi-walled carbon nanotubes and metal oxide for the detection and degradation studies of orange II dye. *ACS Omega* **2022**, *7*, 32302–32312. [CrossRef]
50. Yahya, R.; Shah, A.; Kokab, T.; Ullah, N.; Hakeem, M.K.; Hayat, M.; Haleem, A.; Shah, I. Electrochemical Sensor for detection and degradation studies of ethyl violet dye. *ACS Omega* **2022**, *7*, 34154–34165. [CrossRef] [PubMed]
51. Rao, C.; Zhou, L.; Pan, Y.; Lu, C.; Qin, X.; Sakiyama, H.; Muddassir, M.; Liu, J. The extra-large calixarene-based MOFs derived hierarchical composites for photocatalysis of dye: Facile syntheses and contribution of carbon species. *J. Alloys Compd.* **2022**, *897*, 163178. [CrossRef]
52. Wang, J.; Rao, C.; Lu, L.; Zhang, S.; Muddassir, M.; Liu, J. Efficient photocatalytic degradation of methyl violet using two new 3D MOFs directed by different carboxylate spacers. *CrystEngComm* **2021**, *23*, 741–747. [CrossRef]
53. Mosmann, T. Rapid colorimetric assay for cellular growth and survival: Application to proliferation and cytotoxicity assays. *J. Immunol. Methods* **1983**, *65*, 55–63. [CrossRef] [PubMed]
54. Shah, A.; Shah, A.H.; Parveen, N.; Rehman, Z.; Khan, S.Z.; Rana, U.A.; Khan, S.U.D.; Nisar, J.; Lashin, A.; Qureshi, R. Synthesis and electrochemical investigations of piperazines. *Electrochim. Acta* **2016**, *220*, 705–711. [CrossRef]
55. Kokab, T.; Manzoor, A.; Shah, A.; Siddiqi, H.M.; Nisar, J.; Ashiq, M.N.; Shah, A.H. Development of tribenzamide functionalized electrochemical sensor for femtomolar level sensing of multiple inorganic water pollutants. *Electrochim. Acta* **2020**, *353*, 136569. [CrossRef]

**Disclaimer/Publisher’s Note:** The statements, opinions and data contained in all publications are solely those of the individual author(s) and contributor(s) and not of MDPI and/or the editor(s). MDPI and/or the editor(s) disclaim responsibility for any injury to people or property resulting from any ideas, methods, instructions or products referred to in the content.

Article

# Photocatalytic and Sonocatalytic Degradation of EDTA and Rhodamine B over $\text{Ti}^0$ and $\text{Ti@TiO}_2$ Nanoparticles

Sara El Hakim, Tony Chave and Sergey I. Nikitenko \*

ICSM, Univ Montpellier, UMR 5257, CEA-CNRS-UM-ENSCM, Marcoule, F-30207 Bagnols sur Cèze, France; Sara.ELHAKIM2@cea.fr (S.E.H.); tony.chave@cea.fr (T.C.)

\* Correspondence: sergei.nikitenko@cea.fr; Tel.: +33-04-66-33-92-51

**Abstract:** Herein, we report a comparative study of photocatalytic (Xe-lamp) and sonocatalytic (345 kHz power ultrasound) degradation of Ethylenediaminetetraacetic acid (EDTA) and Rhodamine B (RhB) in the presence of  $\text{Ti}^0$  and  $\text{Ti@TiO}_2$  core-shell nanoparticles (NPs).  $\text{Ti@TiO}_2$  NPs have been obtained by sonohydrothermal treatment (20 kHz, 200 °C) of commercially available  $\text{Ti}^0$  NPs in pure water. The obtained material is composed of quasi-spherical  $\text{Ti}^0$  particles (30–150 nm) coated by 5–15 nm crystals of anatase. In contrast to pristine  $\text{TiO}_2$ , the  $\text{Ti@TiO}_2$  NPs exhibit the extend photo response from UV to NIR light region due to the light absorption by nonplasmonic Ti core. EDTA can be oxidized effectively by photocatalysis in the presence of  $\text{Ti@TiO}_2$  NPs. By contrast, air passivated  $\text{Ti}^0$  nanoparticles was found to be inactive in the photocatalytic process for both EDTA and RhB. Photocatalytic degradation of EDTA over  $\text{Ti@TiO}_2$  NPs exhibits strong photothermal effect, which has been attributed to the higher yield of oxidizing radicals produced by light at higher bulk temperature. The efficiency of RhB photocatalytic degradation depends strongly on RhB concentration. At  $[\text{RhB}] \geq 1 \times 10^{-3}$  M, its photocatalytic degradation is not feasible due to a strong self-absorption. At lower concentrations, RhB photocatalytic degradation is observed, but at lower efficiency compared to EDTA. We found that the efficient sonochemical degradation of RhB does not require the presence of any catalysts. For both processes, EDTA and RhB, sonochemical and photocatalytic processes are more effective in the presence of Ar/ $\text{O}_2$  gas mixture compared to pure Ar. The obtained results suggest that the choice of the optimal technology for organic pollutants degradation can be determined by their optical and complexing properties.

**Citation:** El Hakim, S.; Chave, T.; Nikitenko, S.I. Photocatalytic and Sonocatalytic Degradation of EDTA and Rhodamine B over  $\text{Ti}^0$  and  $\text{Ti@TiO}_2$  Nanoparticles. *Catalysts* **2021**, *11*, 928. <https://doi.org/10.3390/catal11080928>

Academic Editors: Juan José Rueda-Márquez, Javier Moreno-Andrés and Irina Levchuk

Received: 24 June 2021

Accepted: 24 July 2021

Published: 30 July 2021

**Publisher's Note:** MDPI stays neutral with regard to jurisdictional claims in published maps and institutional affiliations.



**Copyright:** © 2021 by the authors. Licensee MDPI, Basel, Switzerland. This article is an open access article distributed under the terms and conditions of the Creative Commons Attribution (CC BY) license (<https://creativecommons.org/licenses/by/4.0/>).

**Keywords:** organic pollutants; rhodamine B; EDTA; photocatalysis; photothermal; sonocatalysis; environmental remediation; titanium; nanoparticles

## 1. Introduction

Within the progressive increase in the level of wastewater contamination, more efforts are directed towards finding promising methods for the removal of organic substances, such as dyes, chlorinated organics, antibiotics, complexing agents and other pollutants from wastewater [1,2]. Among the most common water contaminants are organic dyes. For instance, Rhodamine B (RhB) poses a major threat to human health, aquatic life and environmental safety. It is widely used in industry and its uncontrolled disposal into the environment can cause serious health problems, including major irritation to skin eyes and respiratory tract. Conventional wastewater treatment methods like ion exchange, ozonation, membrane separation, biological treatments and adsorption suffered from certain limitation concerning the high cost compared to their slow kinetics and low performance [3]. In addition, strong complexing reagents, like EDTA, are also of environmental concern since their release increases the mobility of heavy metals and radionuclides in groundwater [4]. EDTA removal throughout conventional aerobic biodegradation is hardly accessed [5] and hydrothermal thermolysis is energy consumable [6]. For such reasons, advanced oxidation processes (AOPs) have attracted a lot of attention, among which

ultrasound-based degradation and photocatalysis seem quite promising [7,8]. Ultrasound technology has proven to be an efficient treatment method for toxic waste removal, either when used alone or in combination with other oxidation methods [9]. In some cases, organic waste decomposition under the action of ultrasound (US) is almost 10,000 times faster than the conventional natural aerobic oxidation [10]. Once liquids are subjected to US in the frequency range of ca. 20 kHz–1 MHz, microbubbles are formed in solution, they grow and eventually collapse releasing a large amount of energy inside, and around, the cavitation bubble [11]. The energy released from so-called the cavitation process is sufficient to split water vapor molecules, allowing the in situ production of hydroxyl radicals ( $\text{OH}^\cdot$ ) [12]. The combination of US with catalysts, referred as sonocatalysis, often allows to enhance the efficiency of US treatment, but the mechanism of sonocatalysis is not fully understood and may differ depending on the catalyst [13].

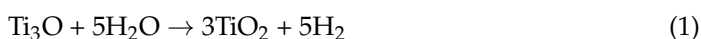
Photocatalysis also emerged as a powerful AOPs towards the degradation of organic pollutants. This process originates from charge separation induced in catalytic materials by photon absorption. The electrons ( $e^-$ ) and holes ( $h^+$ ) generated on the surface of catalysts upon photoexcitation can react with water and oxygen to form radicals, such as  $\text{OH}^\cdot$  and  $\text{O}_2^-$ . These radical species have a strong oxidative/reductive potential providing breaking down organic pollutants [14]. Several studies have reported the kinetics and mechanisms of EDTA photocatalytic degradation on a typical semiconducting photocatalyst P25  $\text{TiO}_2$  loaded by metallic nanoparticles (NPs) or doped by cations or anions for better catalytic performance [15]. Despite significant efforts, preparation of  $\text{TiO}_2$ -based photocatalysts highly efficient under visible light is still a challenge. Other works reported the enhanced photocatalytic degradation of RhB using CdS NPs as a catalyst [3]. However, high toxicity does not allow its application in environmental remediation [16].

In general, photocatalysis and sonocatalysis are often considered as competing technologies. However, the comparative studies of these techniques are scarce in the literature. The aim of this work is to probe sonocatalysis driven by 345 kHz power US and photocatalysis under Xe lamp white light irradiation, as a simulator of the sunlight, for the degradation of RhB and EDTA molecules in aqueous solutions. Herein, air passivated titanium ( $\text{Ti}^0$ ) and  $\text{Ti@TiO}_2$  core-shell NPs were investigated as catalysts in selected systems. Very recently, sonocatalytic degradation of EDTA over these catalysts has been reported [17]. It was found that the combination of 345 kHz US with the metallic  $\text{Ti}^0$  NPs enhances the degradation of EDTA ( $C_0 = 5 \times 10^{-3}$  M) under Ar/20%  $\text{O}_2$  atmosphere, and the presence of  $\text{TiO}_2$  anatase NPs on the surface of the  $\text{Ti}^0$  reduces slightly its efficiency towards EDTA degradation. The suggested mechanism of EDTA sonocatalytic degradation involves the sonochemical oxidation of EDTA molecules by  $\text{OH}^\cdot/\text{HO}_2$  radicals in solution and EDTA oxidation at the surface of  $\text{Ti}^0$  NPs in the presence of  $\text{O}_2$  activated by the cavitation event [17]. These results are being compared herein with those of the photocatalytic EDTA degradation results. Moreover, a detailed comparison between the photocatalytic and sonocatalytic RhB degradation mechanism is presented.

## 2. Results and Discussion

### 2.1. Structural, Chemical and Optical Properties of $\text{Ti}^0$ and $\text{Ti@TiO}_2$ NPs

TEM images show a quasi-spherical morphology of air-passivated  $\text{Ti}^0$  particles with an average size of around 30–150 nm without any crystals at the surface (Figure 1a). SHT treatment leads to the formation of nanocrystalline shell composed of 10–20 nm  $\text{TiO}_2$  particles (Figure 1d). The oxide layer, detected by EDX/STEM on the surface of initial  $\text{Ti}^0$  NPs, contributes to the presence of metastable  $\text{Ti}_3\text{O}$  suboxide (Figure 1b), which has been proven upon Rietveld refinement of powder XRD data (Figure 1c, Table 1). On the other hand, the oxide layer on the surface of SHT treated  $\text{Ti}^0$  NPs corresponds mainly to  $\text{TiO}_2$  anatase (Figure 1d,e). Based on the phase composition shown in Table 1, we related the formation of  $\text{TiO}_2$  to the oxidation of both  $\text{Ti}_3\text{O}$  (Equation (1)), and  $\text{Ti}^0$  (Equation (2)):



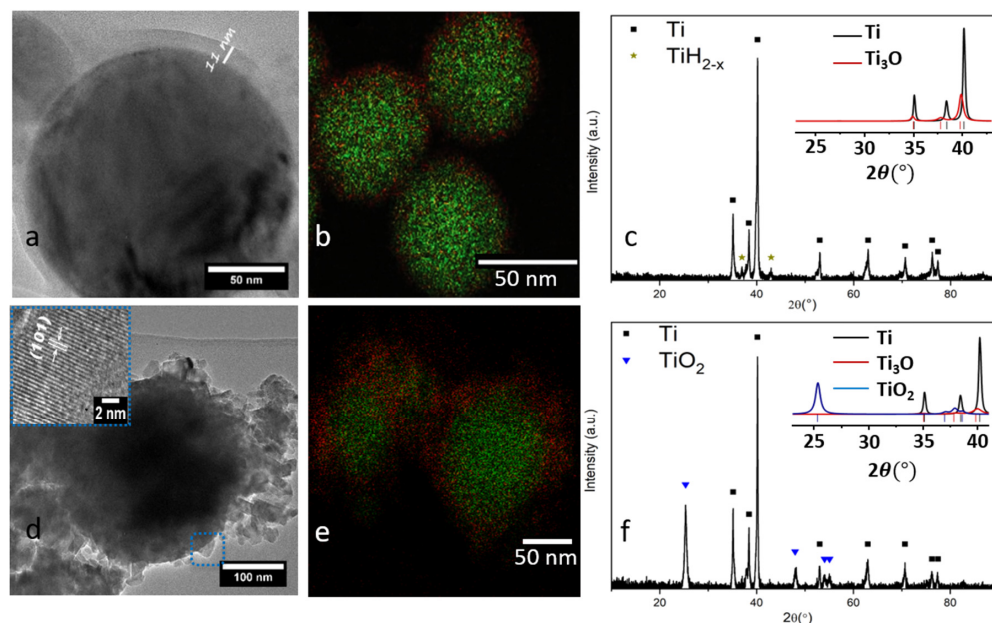


**Figure 1.** TEM images, STEM/EDX mapping and XRD diffraction patterns of air passivated Ti<sup>0</sup> NPs (a–c) and Ti@TiO<sub>2</sub> NPs (d–f). Green dots—Ti, red dots—O.

**Table 1.** Variation in the composition of air passivated Ti<sup>0</sup> NPs and Ti@TiO<sub>2</sub> obtained from the Rietveld refinement of their XRD patterns [18].

Samples	mol. %		
	Ti	Ti <sub>3</sub> O	TiO <sub>2</sub>
Air passivated Ti <sup>0</sup>	86	14	-
Ti@TiO <sub>2</sub>	62	3	35

Recently, it has been reported [18] that the XPS spectrum of air passivated Ti NPs exhibits the presence of Ti<sup>0</sup> and lower oxidation states of titanium (TiO, Ti<sub>x</sub>O<sub>y</sub> and Ti<sub>2</sub>O<sub>3</sub>) at the particle surface in agreement with the XRD analysis revealed the presence of titanium suboxide in Ti<sup>0</sup> NPs. SHT treatment causes disappearance of Ti<sup>0</sup>, TiO, Ti<sub>x</sub>O<sub>y</sub> and Ti<sub>2</sub>O<sub>3</sub> peaks, and the experimental XPS spectrum of Ti@TiO<sub>2</sub> NPs can be fitted by defect-free TiO<sub>2</sub> spectrum, indicating effective coating of metallic titanium core.

As also reported in our previous work [18], diffuse reflectance spectra for both Ti<sup>0</sup> and Ti@TiO<sub>2</sub> NPs exhibit a broad band in the UV-NIR spectral range corresponding to the interband transitions of metallic Ti<sup>0</sup>. The presence of TiO<sub>2</sub> on the surface of the metallic NPs promotes the formation of a characteristic absorption peak around 298 nm. In addition, recent EIS study indicated a faster charge transfer at the interface of the particle and electrolyte for Ti@TiO<sub>2</sub> compared to Ti<sup>0</sup> NPs. In general, the presence of TiO<sub>2</sub> enhances the charge transfer in such materials, which explains the higher photocatalytic activity of Ti@TiO<sub>2</sub> NPs compared to that of Ti<sup>0</sup> NPs [18].

## 2.2. EDTA Study

### 2.2.1. Kinetics of Photocatalytic EDTA Degradation

Degradation of EDTA under the white light of Xe lamp was studied in the presence of both air passivated Ti<sup>0</sup> and Ti@TiO<sub>2</sub> NPs under two different gas atmospheres Ar and Ar/20% O<sub>2</sub>. The kinetics of EDTA photocatalytic degradation tends to vary based on the choice of the catalyst, gas atmosphere and bulk temperature. Regardless of the chosen experimental conditions, all kinetic curves related to the photocatalytic degradation of

5 mM EDTA solution are fitted with the zero-order kinetic model. We have chosen this model in agreement to the previous study of EDTA photocatalytic degradation in the presence of  $\text{TiO}_2$  upon which the profiles for the time course of EDTA degradation at different concentrations were linear in the range of 3 to 5 mM [15].

The significant degradation of EDTA in the presence of  $\text{Ti@TiO}_2$  NPs was proven possible only when operating under  $\text{Ar}/20\% \text{O}_2$  atmosphere (Figure 2a). Using Ar leads to a very low change in EDTA concentration throughout the 4 h of light treatment (Figure S1). Therefore, oxygen is a crucial factor for the efficient photocatalytic EDTA degradation process. The rate of photocatalytic EDTA degradation tends to increase within the increase of the reaction temperature:  $3.6 \pm 0.9 \mu\text{mol L}^{-1}\cdot\text{min}^{-1}$  at  $40^\circ\text{C}$ ,  $5.8 \pm 0.3 \mu\text{mol}\cdot\text{L}^{-1}\cdot\text{min}^{-1}$  at  $60^\circ\text{C}$  and  $12 \pm 0.1 \mu\text{mol}\cdot\text{L}^{-1}\cdot\text{min}^{-1}$  at  $80^\circ\text{C}$ . On the other hand, the rate of EDTA oxidation recorded with  $\text{Ti}^0$  NPs (Figure S2a) at  $60^\circ\text{C}$  in  $\text{Ar}/20\% \text{O}_2$  ( $1.62 \pm 0.3 \mu\text{mol}\cdot\text{L}^{-1}\cdot\text{min}^{-1}$ ) is approximately 4 times smaller than that recorded with  $\text{Ti@TiO}_2$  in the presence of  $\text{Ar}/20\% \text{O}_2$ . It is noteworthy that the photothermal effect in the process of EDTA degradation is somewhat similar to what was observed for the photocatalytic  $\text{H}_2$  production with  $\text{Ti@TiO}_2$  photocatalyst [18]. In contrast to EDTA degradation, the kinetics of TOC removal (Figure 2b) shows only a small decrease of  $\leq 5\%$ , indicating accumulation of intermediate products during EDTA photocatalytic degradation.

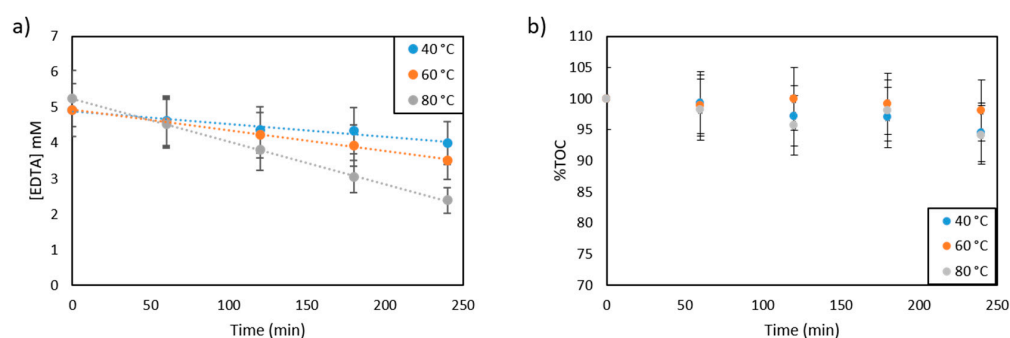


**Figure 2.** Kinetic curves of EDTA evolution and (a) TOC abatement curves (b) during photolysis of 5 mM initial EDTA solutions under  $\text{Ar}/20\% \text{O}_2$  atmosphere at 3 different temperatures in the presence of  $\text{Ti@TiO}_2$  NPs (catalyst concentration  $0.12 \text{ g}\cdot\text{L}^{-1}$ ,  $V = 65 \text{ mL}$ ,  $P_{\text{light}} = 9.5 \text{ W}$ ).

The stability of  $\text{Ti@TiO}_2$  catalyst was evaluated by measurements of Ti ionic species in solution after the photocatalytic experiment using ICP-OES analysis. Table 2 shows the high stability of  $\text{Ti@TiO}_2$  catalyst in the entire temperature range studied.

**Table 2.** Concentration and percentage of Ti species leached into treated EDTA solution after 4 h of Xe light irradiation with  $\text{Ti@TiO}_2$  catalyst in  $\text{Ar}/\text{O}_2$  atmosphere.

Temperature ( $^\circ\text{C}$ )	[Ti] ( $\text{mg}\cdot\text{L}^{-1}$ )	%Ti ( $\pm 5\%$ )
40	0.26	0.27
60	0.32	0.33
80	0.4	0.41

### 2.2.2. Gaseous Products Formation upon Photocatalytic EDTA Degradation

The photocatalytic degradation of EDTA in the presence of  $\text{Ti@TiO}_2$  NPs and  $\text{Ar}/\text{O}_2$  gas mixture is accompanied only by  $\text{CO}_2$  release (Figure S3) and hydrogen formation is not observed in this case. In pure Ar, some  $\text{CO}_2$  and  $\text{H}_2$  are formed in almost equal amounts (Figure S4). No significant release of  $\text{CO}_2$  gas is observed when using  $\text{Ti}^0$  NPs as the photocatalyst in  $\text{Ar}/\text{O}_2$ , which agrees with the low EDTA degradation rate (Figure S2b). As shown in Figure 3, the calculated  $\text{CO}_2$  yields increases ca. 2 times when the bulk temperature increases from  $40$  to  $80^\circ\text{C}$  confirming photothermal effect in studied system. The percentage of  $\text{CO}_2$  released within the temperature range  $40$  to  $80^\circ\text{C}$  are

estimated from TOC curves (Figure 2b) to be between 2 to 5.8% of the initial EDTA content while that calculated from the CO<sub>2</sub> emission curves (Figure S3) is between 3.2 to 6%. It is worth noting that the pH increases from 4.6 to 5.8, 5.9 and 6.2 at 40, 60, and 80 °C, respectively during 4 h of photocatalytic process. As for sonochemical and sonocatalytic EDTA degradation, the increase of pH can be related to the reaction of reducing superoxide anion O<sub>2</sub><sup>•−</sup> (Equation (9)) with EDTA yielding tertiary iminium Schiff bases, which rapidly hydrolyses into aldehydes and strongly basic secondary amines [19]. Formation of H<sub>2</sub> in pure Ar most likely can be attributed to the photocatalytic water splitting with EDTA as an electron hole scavenger. In the presence of O<sub>2</sub>, hydrogen atom produces oxidative HO<sub>2</sub><sup>•</sup> radical as it will be discussed below.

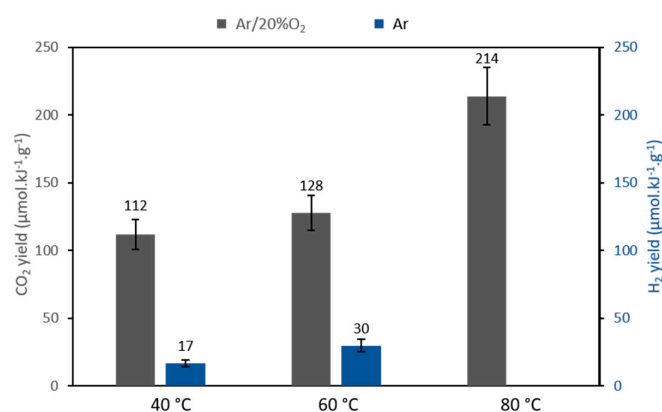


**Figure 3.** Yields of CO<sub>2</sub> for Ar/20% O<sub>2</sub> atmosphere (grey) and H<sub>2</sub> for Ar atmosphere (blue) yields obtained upon photocatalytic degradation of 5 mM EDTA solution over Ti@TiO<sub>2</sub> catalyst under Ar/20% O<sub>2</sub> and Ar at different temperatures (catalyst concentration 0.12 g·L<sup>-1</sup>, V = 65 mL, P<sub>Xe</sub> = 9.5 W).

### 2.2.3. Effect of Temperature

Arrhenius plot for EDTA photocatalytic degradation is shown in Figure 4. The apparent activation energy  $E_{act}$  equal to  $28 \pm 8$  kJ·mol<sup>-1</sup> is quite similar to that of other photocatalytic processes studied with Ti@TiO<sub>2</sub> NPs, and assigned to the diffusion of chemical species at the catalyst surface, rather than to the activation of the chemical bonds [20]. On the other hand, sonocatalytic EDTA degradation with the same catalyst shows very low temperature effect ( $E_{act} = 5.0 \pm 1.2$  kJ·mol<sup>-1</sup>) [18], indicating essential difference in the reaction mechanisms of photocatalytic and sonocatalytic processes.

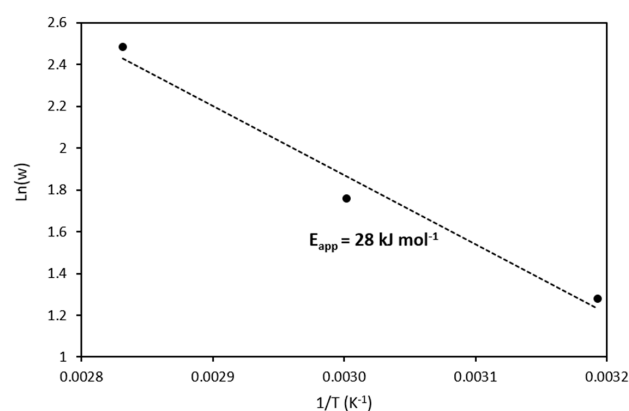


**Figure 4.** Arrhenius plot for the photocatalytic EDTA degradation in the presence of Ti@TiO<sub>2</sub> NPs under Ar/O<sub>2</sub> atmosphere, W is an EDTA degradation rate assuming zero-order kinetics.

### 2.2.4. Comparison of Sonocatalytic and Photocatalytic EDTA Degradation

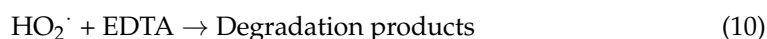
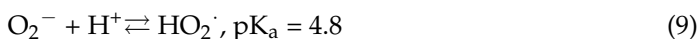
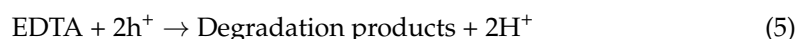
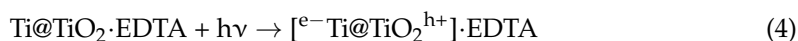
In this section, we compare the photocatalytic EDTA degradation studied in this work in the presence of Ar/O<sub>2</sub> gas mixture and the sonocatalytic EDTA degradation

reported recently at similar conditions [17]. The overall efficiency of photocatalysis and sonocatalysis can be evaluated upon comparing the yield of EDTA degradation,  $Y$ , using the following equation:  $Y = M \cdot P^{-1} \cdot m^{-1}$ , where  $M$  is the amount of degraded EDTA ( $\mu\text{mol}$ ),  $P$  is the energy consumption (kJ), and  $m$  is the mass of catalyst (g). From the calculations summarized in Table 3, one can conclude that photocatalysis over  $\text{Ti@TiO}_2$  NPs is much more efficient towards EDTA degradation than sonocatalysis with  $\text{Ti@TiO}_2$  and  $\text{Ti}^0$  NPs. On the other hand,  $\text{Ti}^0$  NPs show better sonocatalytic performance compared to that of photocatalysis.

**Table 3.** Calculated yields of EDTA degradation using  $\text{Ti@TiO}_2$  and  $\text{Ti}^0$  NPs at 40 °C under Ar/20%  $\text{O}_2$  atmosphere in two different processes. Time of treatment was 4 h for each system.

Process	Catalyst	M ( $\mu\text{mol}$ )	P (kJ)	m (g)	Y ( $\mu\text{mol} \cdot \text{kJ}^{-1} \cdot \text{g}^{-1}$ )
Photocatalysis	$\text{Ti@TiO}_2$	60	118	$7.8 \times 10^{-3}$	65
	$\text{Ti}^0$	<1	118	$7.8 \times 10^{-3}$	<1
Sonocatalysis [17]	$\text{Ti@TiO}_2$	354	720	0.4	1.5
	$\text{Ti}^0$	780	720	0.4	2.7

The mechanism of EDTA sonocatalytic degradation with  $\text{Ti}^0$  and  $\text{Ti@TiO}_2$  NPs reported previously involves the degradation of EDTA by hydroxyl ( $\text{OH}^\cdot$ ), hydroperoxyl ( $\text{HO}_2^\cdot$ ) and superoxide ( $\text{O}_2^{\cdot-}$ ) radicals in solution and bubble/solution interface or by the catalytic degradation of EDTA at the surface of the catalyst (Ti or  $\text{Ti@TiO}_2$ ) by oxygen activated initially by the power US at the surface of titanium [17]. It was reported that sonocatalytic EDTA degradation yields several intermediate products shown in Figure S5a [21]. On the other hand, photocatalytic EDTA degradation process is initiated upon photon absorption by  $\text{Ti@TiO}_2$  NPs in a similar manner reported previously for the photo-thermal production of  $\text{H}_2$  using the same catalyst [18]. The photocatalytic mechanism can be expressed by Equations (3)–(10):



After the electron-hole separation step (Equation (4)), the photogenerated hole ( $h^+$ ) can oxidize EDTA molecules directly into the degradation products (Equation (5)) or it can initially convert  $\text{H}_2\text{O}$  molecules into hydroxyl radicals ( $\text{OH}^\cdot$ ), which in return, oxidize EDTA molecules [22]. In the presence of  $\text{O}_2$  adsorbed at the surface of catalyst, the photo-generated electrons would yield superoxide anion-radicals ( $\text{O}_2^{\cdot-}$  Equation (8)), which in return, can react with EDTA [23]. On the other hand, scavenging of  $e^-$  would increase the yield of electron holes leading to the enhancement of EDTA photocatalytic degradation. It is worth noting that superoxide anion-radical can be converted to  $\text{HO}_2^\cdot$  radical (Equation 9), which can oxidize EDTA (Equation (10)). Furthermore, the reaction of  $\text{O}_2^{\cdot-}$  with EDTA gives tertiary iminium Schiff-bases which rapidly hydrolyses into aldehydes and strongly basic secondary amines [19]. This process can explain the increase of pH during EDTA photocatalytic degradation similar to that reported for sonocatalytic process [17]. Some similarity should be mentioned in the composition of intermediates for both processes, those are iminodiacetic acid, formic acid, oxalic acid, glycolic acid and acetic

acid [15,21]. The principal schemes of intermediate products formation are shown in Figure S5. Recent studies highlighted a crucial role of photogenerated  $h^+$ ,  $OH^\cdot$  and  $O_2^-$  species [24,25] for efficient photocatalytic degradation of organic pollutants in agreement with the proposed mechanism.

The photothermal effect of EDTA degradation is a major finding of this work. In a previous research, the photothermal effect in the process of  $H_2$  production over  $Ti@TiO_2$  photocatalyst has been attributed to the diffusion of intermediates formed after hole scavenger degradation [18,20]. Alternatively, the improved photocatalytic degradation of EDTA at higher temperatures in  $Ar/O_2$  atmosphere can also be related to the higher concentration of  $OH^\cdot$  and  $HO_2^\cdot$  radicals produced. To verify this assumption, we studied the formation of  $H_2O_2$  during photocatalytic treatment of aqueous solutions saturated with  $Ar$  or  $Ar/O_2$  over  $Ti@TiO_2$  NPs at different temperatures.  $H_2O_2$  is a stable product of  $OH^\cdot$  and  $HO_2^\cdot$  radicals recombination and can be quantified in situ as  $TiO(O_2)$  complex [26]. To assess  $TiO(O_2)$  measurements, photocatalytic experiments were performed using 0.02 M  $TiOSO_4/0.25$  M  $H_2SO_4$  solutions and  $Ti@TiO_2$  photocatalyst in the absence of EDTA. After irradiation with Xe lamp, the samples have been withdrawn and analysed spectrophotometrically after removal of catalytic particles with PTFE filter. As shown in Figure 5, the amount of  $H_2O_2$  produced in the presence of  $Ar$  atmosphere is much lower than that produced in the presence of  $Ar/O_2$  at 40 °C in agreement with kinetics of EDTA photodegradation. Moreover, the initial rate of  $H_2O_2$  formation in  $Ar/O_2$  at 60 °C is ca. 2 times higher than that produced at 40 °C. This observation clearly indicates that the observed photothermal effect is related to the improvement of photogenerated radical production with the increase of bulk temperature. In addition, Figure 5 reveals a plateau of  $H_2O_2$  concentration reaching upon photolysis. Perhaps this is because of  $Ti@TiO_2$  NPs photocorrosion in acid medium. Figure S6 demonstrates the increase of titanium in 0.25 M  $H_2SO_4$  solution upon irradiation with Xe lamp, and the rate of metallic titanium core dissolution increases with temperature. Dissolution of titanium metal in  $H_2SO_4$  leads to the formation of  $Ti(III)$ , which is rapidly oxidized by  $H_2O_2$ . Superposition of  $H_2O_2$  formation and consumption yields, finally, its steady-state concentration. It is worth noting that in the absence of light  $Ti@TiO_2$  NPs are quite stable in 0.25 M  $H_2SO_4$  solution.

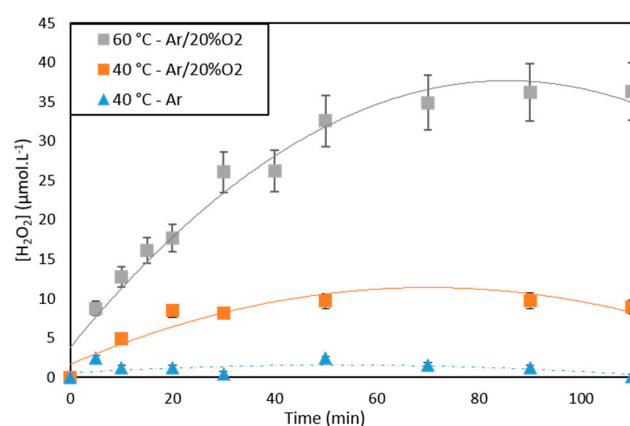


**Figure 5.**  $H_2O_2$  concentration produced during photocatalytic experiments with 0.02 M  $TiOSO_4/0.25$  M  $H_2SO_4$  solutions over  $Ti@TiO_2$  NPs at different temperatures (catalyst concentration  $2\text{ g L}^{-1}$ ,  $V = 65\text{ mL}$ ). Concentration of  $TiO(O_2)$  complex equal to that of formed  $H_2O_2$  was monitored at 410 nm ( $\epsilon = 626\text{ cm}^{-1}\cdot\text{M}^{-1}$ ) [26].

### 2.2.5. Rhodamine B Degradation RhB Sonochemical Degradation

To evaluate the effect of 345 kHz power US on the kinetics of RhB degradation, a set of experiments have been carried out taking into account the initial concentration of RhB, the nature of the saturating gas, and the nature of catalyst.



At  $(\text{RhB})_0 \leq 0.2 \text{ mM}$ , only 15–20 min of ultrasonic treatment was sufficient for the total removal of RhB as it can be seen from the Figure S7a–d. On the other hand, at  $(\text{RhB}) = 1 \text{ mM}$  (500 ppm), RhB degradation is observed over a longer time scale and follows zero-order kinetics (Figure 6). In fact, the kinetics of RhB removal is not influenced by  $\text{Ti}^0$  or  $\text{Ti@TiO}_2$  NPs (Figure 6 and Figure S8), indicating the absence of sonocatalytic effect in this system in contrast to EDTA sonochemical degradation [17].

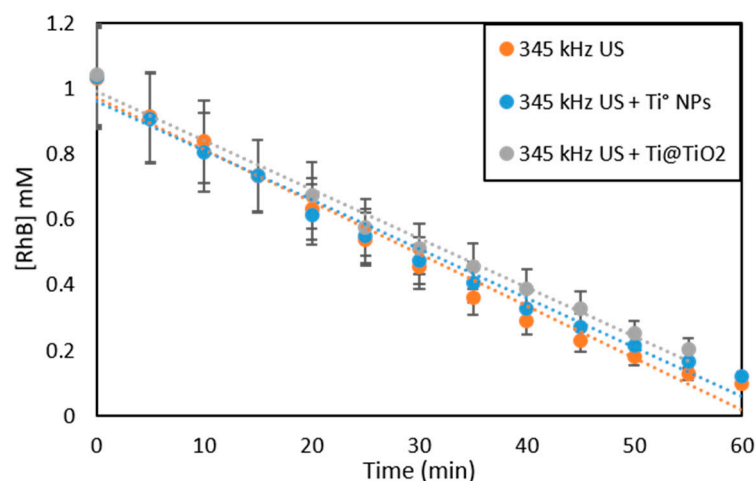


**Figure 6.** Kinetic curves of RhB evolution upon sonolysis of homogeneous RhB solution and sonochemical oxidation of RhB in the presence of  $\text{Ti}^0$  and  $\text{Ti@TiO}_2$  NPs in  $\text{Ar}/20\% \text{O}_2$  at (catalyst concentration  $2 \text{ g L}^{-1}$ ,  $T = 40 \text{ }^\circ\text{C}$ ).

Figure 7 shows better performance of the sonochemical process in the presence of  $\text{Ar}/\text{O}_2$  atmosphere compared to pure  $\text{Ar}$  or air. In addition, sonochemical degradation of RhB is more rapid than that of EDTA even in  $\text{Ar}$  and air (Table 4). In general, kinetic data point out significant difference in sonochemical mechanisms for RhB and EDTA, which can be assigned to the difference in physico-chemical properties of these molecules. It is well known that RhB readily forms dimers in aqueous solutions [27]. These relatively large and hydrophobic dimers enable to accumulate at cavitation bubble/solution interface thus providing RhB degradation not only by oxidizing radicals but also by interfacial pyrolytic decomposition [28].

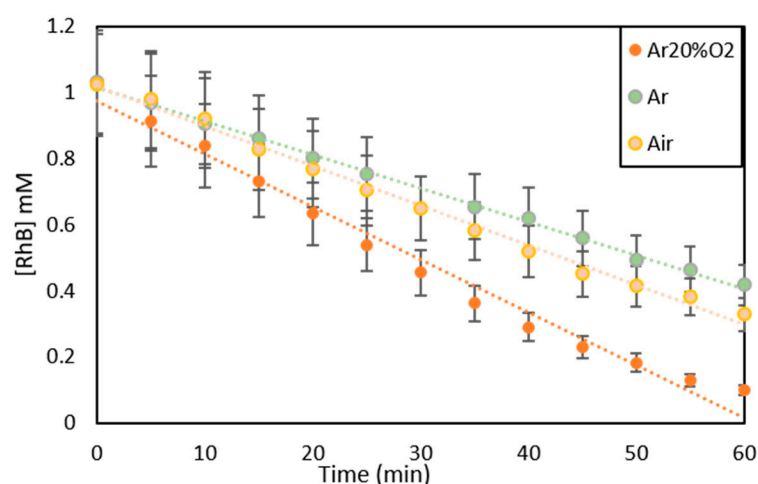


**Figure 7.** Kinetics of RhB evolution upon sonolysis of RhB with 345 kHz US in the absence of any solid particles under different gas atmospheres ( $V_{\text{RhB}} = 200 \text{ mL}$ ,  $T = 40 \text{ }^\circ\text{C}$ ).

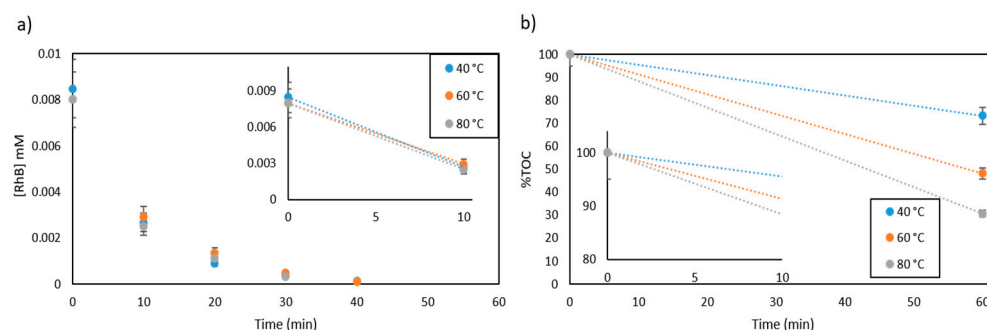
**Table 4.** Comparison of RhB and EDTA degradation rate (R) obtained upon sonolysis by 345 kHz power US at 40 °C obtained under Ar, Ar/20% O<sub>2</sub> and Air.

	Ar 20%O <sub>2</sub>	Ar	Air
R <sub>RhB</sub> (μmol <sup>-1</sup> L <sup>-1</sup> min <sup>-1</sup> )	16 ± 1.3	10 ± 0.3	12 ± 0.6
R <sub>EDTA</sub> (μmol <sup>-1</sup> L <sup>-1</sup> min <sup>-1</sup> )	6.42 ± 0.43	4 ± 0.03	Not calculated

### 2.2.6. RhB Photocatalytic Degradation

In contrast to sonochemistry, at (RhB) = 1 mM photocatalytic degradation is not observed regardless of the chosen experimental conditions, such as temperature, nature of the catalyst and gas mixture (Figure S9). This can be related to the strong light self-absorption by RhB molecules (Figure S7a). It was previously reported that the initial concentration, in this case of RhB, is an important parameter determining the efficiency of photodegradation of the organic pollutant. The high concentration of RhB in photocatalytic processes can result in the decrease of light penetration into the suspension, thus, decreasing the overall efficiency of RhB degradation [29]. At (RhB) = 0.1 mM, some degradation is observed in the presence of Ar/O<sub>2</sub> gas mixture with the rate  $\leq 0.6 \pm 0.1 \mu\text{mol}\cdot\text{L}^{-1}\cdot\text{min}^{-1}$  (Figure S10). However, in pure Ar photocatalytic removal of RhB is not feasible at this concentration.

As the concentration of initial RhB solution is decreased to 0.01 mM, the photocatalytic process over Ti@TiO<sub>2</sub> NPs and under Ar/O<sub>2</sub> atmosphere becomes clearly observable. The initial degradation rate only weakly varies with temperature (Figure 8a) and is equal to  $0.5 \mu\text{mol}\cdot\text{L}^{-1}\cdot\text{min}^{-1}$ . On the other hand, photothermal effect is observed for TOC removal (Figure 8b) and CO<sub>2</sub> emission (Figure 9). Such a difference can be explained by the fact that CO<sub>2</sub> emission (TOC removal) originates from intermediate product degradation, rather than from primary RhB molecule defunctionalisation.

**Figure 8.** Kinetic curves of 0.01 mM RhB degradation and (a) TOC removal (b) in the presence of Ti@TiO<sub>2</sub> NPs under Ar/20% O<sub>2</sub> flux at three different temperatures. Catalyst concentration  $0.12 \text{ g}^{-1}\cdot\text{L}^{-1}$ .

The reaction intermediates of RhB photocatalytic degradation includes 4-(methoxycarbonyl) benzoic acid, 2-(methoxycarbonyl) benzoic acid, phthalic acid, isophthalic acid terephthalic acid, phthalic anhydride, 2-hydroxypentanedioic acid and maleic acid, etc [30]. Then, the products were further transformed to smaller organic products, CO<sub>2</sub> and H<sub>2</sub>O following the similar mechanism as for photocatalytic EDTA degradation (Equations (3)–(10)). It is noteworthy to mention that the photothermal effect is less pronounced with RhB than with EDTA. Replacing Ar/O<sub>2</sub> by Ar or Ti@TiO<sub>2</sub> by Ti<sup>0</sup> leads to a significant drop in RhB degradation rate (Figure S10). In general, the efficiency of RhB photocatalytic degradation is lower than of EDTA, which can be attributed to weaker complexing ability of RhB (or RhB dimer) compared to EDTA. According to the proposed mechanism of photocatalytic process (Equations (3)–(10)), the formation of surface complexes is important for efficient charge transfer after catalyst photoexcitation step.

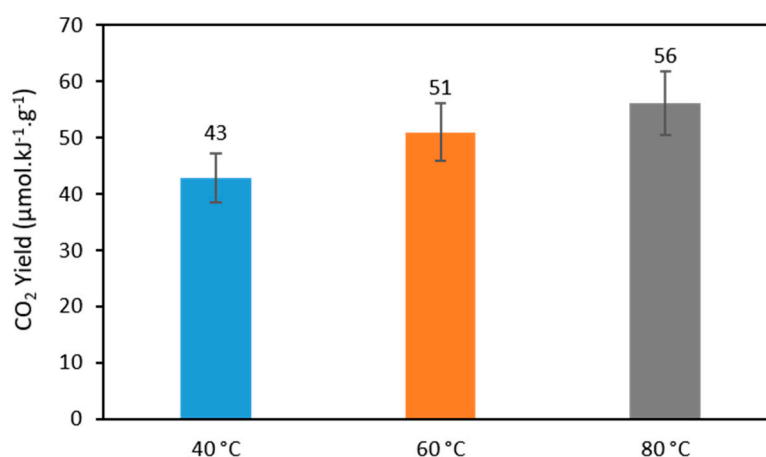


**Figure 9.** Calculated CO<sub>2</sub> yield from the photothermal treatment of 0.01 mM RhB solutions in the presence of Ti@TiO<sub>2</sub> photocatalyst under Ar/20% O<sub>2</sub> atmosphere at 40, 60 and 80 °C (catalyst concentration 0.12 g<sup>-1</sup>.L<sup>-1</sup> V = 60 mL, P<sub>Xe light</sub> = 9.5 W). Emission profiles of CO<sub>2</sub> emission are shown in Figure S14.

### 3. Materials and Methods

#### 3.1. Chemical Reagents

Na<sub>2</sub>H<sub>2</sub>EDTA·2H<sub>2</sub>O (98%, Fluka AG, Hamburg, Germany), Rhodamine B (C<sub>28</sub>H<sub>31</sub>ClN<sub>2</sub>O<sub>3</sub>, for fluorescence, Sigma Aldrich, India), titanium nanopowder (Ti, 99%, Nanostructured & Amorphous Materials, Inc., Los Angeles, CA, USA), TiO<sub>2</sub> anatase (99%, 95% anatase, 5% rutile, US Research Nanomaterials, Inc., Houston, TX, USA) were used as received without further purification. All solutions were prepared with deionized water (Milli-Q, 18.2 MΩ.cm at 25 °C, Darmstadt, Germany). Air, Ar and Ar/O<sub>2</sub> gas mixture with 20 vol.% of O<sub>2</sub> and Ar of 99.999% purity were supplied by Air Liquide (Paris, France).

#### 3.2. Catalyst Preparation

Ti@TiO<sub>2</sub> core-shell nanoparticles (NPs) have been obtained by sonohydrothermal treatment (20 kHz, 200 °C) of commercially available Ti<sup>0</sup> NPs in pure water [18,20]. It is worth noting that Ti<sup>0</sup> NPs are potentially pyrophoric and cannot be used in catalysis as such. In this work, Ti<sup>0</sup> NPs were passivated by storage in contact with air at room temperature for ca. 48 h. In a typical synthesis procedure, 2 g of air passivated Ti<sup>0</sup> NPs are dispersed in 50 mL deionized H<sub>2</sub>O for 5 min using an ultrasonic bath. The dispersion is then transferred into the sonohydrothermal reactor (Figure S13) and heated at 200 °C (autogenic pressure P = 19 bar) under simultaneous ultrasonic treatment (f = 20 kHz, P<sub>ac</sub> = 17 W) for 3 h. After cooling, the treated particles are recovered by centrifugation (12 min, 9000 rpm), washed with deionized water and dried at room temperature under reduced pressure.

#### 3.3. Catalyst Characterization

The crystal phase identification of the as-synthesized particles and air passivated Ti<sup>0</sup> NPs was performed by X-ray diffraction (XRD) analysis. The XRD measurement was done using Bruker D8 Advance X-ray diffractometer equipped with a linear Lynx eye detector (Cu Kα<sub>1,2</sub> radiation, λ = 1.54184 Å). The patterns were collected at room temperature in the range of 10–90 2θ degrees with a step size of 0.02 2θ degree and a counting time of 1.8 s·step<sup>-1</sup>. Rietveld refinement was performed on the XRD patterns to determine the different phase composition of our particles. The structure and morphology were examined by high-resolution transmission electron microscopy (HRTEM) and scanning transmission electron microscopy (STEM) coupled with EDX mapping (SDD Oxford detector, High Wycombe, UK). The analysis was performed using Jeol 2200FS (200 kV, Tokyo, Japan) microscope.

### 3.4. Experimental Setups

#### 3.4.1. Photocatalytic Experiments

Photocatalytic degradation of EDTA and RhB has been performed using commercial anatase TiO<sub>2</sub>, air passivated Ti<sup>0</sup> NPs and the as-synthesized Ti@TiO<sub>2</sub> core-shell NPs. The experiments were carried out in a thermostated glass-made gas-flow cell (Figure S14a) adapted to mass spectroscopic analysis of the outlet gases [18]. For a typical experiment, 7.8 mg of the catalyst was dispersed in an ultrasonic bath ( $P_{el} = 100$  W,  $f = 40$  kHz) in 65 mL of 5 Mm EDTA solution or in 65 mL of  $2.10^{-3}$  to 1 mM (1 to 500 ppm) RhB solutions and then placed into the photoreactor. Photolysis was performed using the white light of ASB-XE-175 W xenon lamp equipped with ozone blocking coatings. The lamp was placed at 8 cm away from the reactor and the light power at this distance was measured by X1-1 Optometer (Gigahertz-Optik GmbH, Türkenfeld, Germany) using UV-3710-4 (300–420 nm) and RW-3705-4 (400–1100 nm) calibrated detectors. The obtained values of light power were equal to  $8.9$  ( $1.07$  W·cm<sup>-2</sup>) and  $0.6$  W ( $0.07$  W·cm<sup>-2</sup>) for vis/NIR and UV spectral ranges respectively, which provides the close spectral match to solar spectrum. The solutions inside the reactor were stirred continuously and the temperature was kept constant at 40, 60 or 80 °C during photolysis. The gas flow (Ar or Ar/20% O<sub>2</sub>) through the reactor was kept constant at  $58$  mL·min<sup>-1</sup> and controlled by a volumetric flowmeter. The gaseous products in the outlet gas were analysed using a Thermo Scientific PRIMA BT mass spectrometer. The H<sub>2</sub> and CO<sub>2</sub> formation rate was quantified using external calibration curves prepared with standard gas mixtures in argon (Messer). During photolysis, sample aliquots are taken at specified time intervals filtered using  $0.2$  µM PTFE filters and used for TOC and UV-vis spectroscopic analysis. The kinetics of RhB photocatalytic degradation are studied following the change in RhB absorption peak at 532 nm. On the other hand, EDTA kinetics are followed following the change in the absorption peak of (Fe-TPTZ)<sup>2+</sup> complex where TPTZ stands for Bis (2,4,6-tripyridyl-s-triazine). Fe-TPTZ has an intense violet blue color. EDTA in the presence of Fe-TPTZ reacts with iron to form a complex, which decreases the color intensity of the mixture. The absorbance is directly proportional to the concentration of EDTA, as shown recently [31].

#### 3.4.2. Sonocatalytic Experiments

For RhB degradation experiments under ultrasonic irradiation, a homemade thermostated glass reactor (Figure S14b) similar to the one reported in our previous work regarding the sonocatalytic degradation of EDTA was used [17]. High frequency ultrasonic treatment is supplied by 345 kHz transducer (25 cm<sup>2</sup>, ELAC Nautik, Kiel, Germany) fixed at the bottom of the glass reactor and connected to a generator with a maximal electric power of 125 W (T&C Power Conversion Inc., Rochester, NY, USA). For a typical degradation process, we use 200 mL of RhB solution with initial concentration of 5–500 mg·L<sup>-1</sup>. An additional amount of  $2$  g·L<sup>-1</sup> of Ti<sup>0</sup> NPs or Ti@TiO<sub>2</sub> NPs is added to the RhB solution and the mixture obtained is dispersed for at least 5 min in an ultrasonic bath ( $P_{el} = 100$  W,  $f = 40$  kHz) and then transferred into the glass reactor. Prior sonochemical treatment, the mixture was saturated with the desired gas (Ar, Ar/20% O<sub>2</sub> or air) for at least 20 min by bubbling through thin plastic tube at  $200$  mL·min<sup>-1</sup> and kept constant throughout the entire experiment time. External control of the reaction temperature was provided by a Huber Unistat Tango thermo-cryostat (Offenburg, Germany). The internal temperature of the reaction mixture was kept constant at 40 °C through the entire ultrasonic treatment and monitored with a Pt 100 probe. Continuous mechanical stirring at a rate of 300 rpm was applied to maintain homogeneous suspension of the catalyst particles in solution. At a defined time interval, sample aliquots were taken and filtered with a  $0.2$  µm PTFE filter to remove solid particles. The filtered solution is then used to follow total organic carbon using a Shimadzu TOC-VCSH analyser calibrated with standard potassium phthalate solution and RhB concentration by absorption peak at 520 nm using a Thermo Scientific Evolution 220 UV-vis spectrophotometer.

#### 4. Conclusions

In summary, this study pointed out that the choice of a suitable treatment process, sonochemistry, sonocatalysis or photocatalysis, for the degradation of organic pollutants in wastewater is highly dependent on the nature of chosen pollutant and the catalyst. For strongly complexing but weakly light absorbing species, like EDTA, photocatalysis is more efficient than sonocatalysis, and the use of catalyst influences greatly the kinetics of both processes. Faster sonocatalytic degradation is obtained in the presence of air passivated Ti<sup>0</sup> NPs under Ar/20% O<sub>2</sub> [17], while photocatalytic degradation of EDTA molecules is more efficient when using a core-shell photocatalyst, Ti@TiO<sub>2</sub>, also in the presence of Ar/20% O<sub>2</sub>. On the other hand, for strongly light absorbing, but weakly complexing, pollutants, like RhB, sonochemistry is much more efficient than photocatalysis. However, the presence of oxygen is required for both systems. The interesting finding of this work is a photothermal effect observed for EDTA, and, in less extent, for RhB degradation. Complementary studies have revealed that the observed photothermal effect of EDTA degradation can be attributed to the enhanced production of oxidizing radicals at higher temperature.

**Supplementary Materials:** The following are available online at <https://www.mdpi.com/article/10.3390/catal11080928/s1>, Figure S1: Kinetic curves of EDTA evolution during photolysis of 5 mM initial EDTA solutions under Ar atmosphere at 40 and 60 °C in the presence of Ti@TiO<sub>2</sub> NPs; Figure S2: Kinetic curves of EDTA evolution (a) and CO<sub>2</sub> emission profile (b) during photolysis of 5 mM initial EDTA solutions under Ar20%O<sub>2</sub> atmosphere at 60 °C in the presence of Ti<sup>0</sup> NPs; Figure S3: Typical carbon dioxide emission profiles obtained upon irradiating 5 mM EDTA solution under the white light of the Xe lamp and in the presence of Ti@TiO<sub>2</sub> catalyst under Ar20%O<sub>2</sub>; Figure S4: Typical carbon dioxide (a) and hydrogen(b) emission profiles obtained upon irradiating 5 mM EDTA solution under the white light of the Xe lamp and in the presence of Ti@TiO<sub>2</sub> catalyst under Ar; Figure S5: By-products of sonocatalytic [21] (a) and photocatalytic [15] (b) EDTA degradation; Figure S6: Evolution of titanium concentration in solution during photocatalytic experiments with 0.25 M H<sub>2</sub>SO<sub>4</sub> solutions over Ti@TiO<sub>2</sub> NPs at different temperatures in the presence of Ar/20%O<sub>2</sub>; Figure S7: Absorption spectrum of 10-2 mM (a), 10-1 mM (b) and 2 10-1 mM (c) RhB solution during sonolysis at 40 °C with 345 kHz in Ar20%O<sub>2</sub>. Major absorption peak of RhB is at 553 nm. [RhB] degradation profiles as a function of time 10-1 and 2 10-1 mM are shown in graph (d); Figure S8: Kinetics of RhB evolution upon ultrasonic treatment under Ar (a) and under Air (b) flux in the presence of solid particles; Figure S9: Variation of RhB concentration upon photothermal treatment of 1 mM RhB solution with and without catalyst under Ar flux at 40 °C (a) and with Ti@TiO<sub>2</sub> at 40 °C and 60 °C with Ar and Ar/20%O<sub>2</sub>; Figure S10: Variation of RhB concentration upon photothermal treatment of 0.1 mM RhB solution with Ti@TiO<sub>2</sub> catalyst under Ar (a) and under Ar/20%O<sub>2</sub> (b); Figure S11: Variation of 0.01 mM initial RhB concentration upon photocatalytic treatment with Ti@TiO<sub>2</sub> under Ar atmosphere (a) and with Ti<sup>0</sup> under Ar/20%O<sub>2</sub> atmosphere (b); Figure S12: Carbon dioxide emission profiles from photothermal treatment of 0.01 mM RhB solutions in the presence of Ti@TiO<sub>2</sub> photocatalyst under Ar/20%O<sub>2</sub> atmosphere at 40, 60 and 80 °C; Figure S13: Graphical sketch of sonohydrothermal reactor; Figure S14: Images of the thermostated photocatalytic cell (a) and the high frequency sonochemical reactor (b).

**Author Contributions:** All authors contributed equally. All authors have read and agreed to the published version of the manuscript.

**Funding:** This research received no external funding.

**Conflicts of Interest:** The authors declare no conflict of interest.

#### References

- Roy, M.; Saha, R. Dyes and their removal technologies from wastewater: A critical review. In *Intelligent Environmental Data Monitoring for Pollution Management*; Elsevier BV: Amsterdam, The Netherlands, 2021; pp. 127–160.
- Ortiz, I.; Rivero, M.J.; Margallo, M. Advanced oxidative and catalytic processes. In *Sustainable Water and Wastewater Processing*; Elsevier BV: Amsterdam, The Netherlands, 2019; pp. 161–201.
- Ullah, H.; Víglašová, E.; Galamboš, M. Visible Light-Driven Photocatalytic Rhodamine B Degradation Using CdS Nanorods. *Processes* **2021**, *9*, 263. [CrossRef]

4. Severa, J.; Bàr, J. *Handbook of Radioactive Contamination and Decontamination*; Elsevier Science: Amsterdam, The Netherlands, 1991; Volume 47.
5. Hinck, M.L.; Ferguson, J.; Puhaakka, J. Resistance of EDTA and DTPA to aerobic biodegradation. *Water Sci. Technol.* **1997**, *35*, 25–31. [CrossRef]
6. Motekaitis, R.J.; Cox, X.B., III; Taylor, P.; Martell, A.E.; Miles, B.; Tvedt, T.J., Jr. Thermal degradation of EDTA chelates in aqueous solution. *Can. J. Chem.* **1982**, *60*, 1207–1213. [CrossRef]
7. Oturan, M.A.; Aaron, J.-J. Advanced oxidation processes in water/wastewater treatment: Principles and applications. A review. *Crit. Rev. Environ. Sci. Technol.* **2014**, *44*, 2577–2641. [CrossRef]
8. Bajpai, P. Emerging technologies for waste water treatment. In *Ind Finish; Pulp and Paper Industry Emerging Waste Water Treatment Technologies*; Kanpur, India, 2017; Volume 51, pp. 93–179.
9. Wang, J.; Wang, Z.; Vieira, C.L.; Wolfson, J.M.; Pingtian, G.; Huang, S. Review on the treatment of organic pollutants in water by ultrasonic technology. *Ultrason. Sonochemistry* **2019**, *55*, 273–278. [CrossRef]
10. Chitra, S.; Paramasivan, K.; Sinha, P.; Lal, K. Ultrasonic treatment of liquid waste containing EDTA. *J. Clean. Prod.* **2004**, *12*, 429–435. [CrossRef]
11. Jorfi, S.; Pourfadakari, S.; Kakavandi, B. A new approach in sono-photocatalytic degradation of recalcitrant textile wastewater using MgO@Zeolite nanostructure under UVA irradiation. *Chem. Eng. J.* **2018**, *343*, 95–107. [CrossRef]
12. Mason, T.J.; Lorimer, J.P. *Applied Sonochemistry: The Uses of Power Ultrasound in Chemistry and Processing*; Wiley: Weinheim, Germany, 2002.
13. Qiu, P.; Park, B.; Choi, J.; Thokchom, B.; Pandit, A.B.; Khim, J. A review on heterogeneous sonocatalyst for treatment of organic pollutants in aqueous phase based on catalytic mechanism. *Ultrason. Sonochem.* **2018**, *45*, 29–49. [CrossRef]
14. Choi, Y.; Lee, D.; Hong, S.; Khan, S.; Darya, B.; Lee, J.-Y.; Chung, J.; Cho, S.-H. Investigation of the synergistic effect of sonolysis and photocatalysis of titanium dioxide for organic dye degradation. *Catalysts* **2020**, *10*, 500. [CrossRef]
15. Babey, P.; Emilio, C.; Ferreyra, R.; Gautier, E.; Gettar, R.; Litter, M. Kinetics and mechanisms of EDTA photocatalytic degradation with TiO<sub>2</sub>. *Water Sci. Technol.* **2001**, *44*, 179–185. [CrossRef]
16. Godt, J.; Scheidig, F.; Grosse-Siestrup, C.; Esche, V.; Brandenburg, P.; Reich, A.; Groneberg, D. The toxicity of cadmium and resulting hazards for human health. *J. Occup. Med. Toxicol.* **2006**, *1*, 22. [CrossRef] [PubMed]
17. El Hakim, S.; Chave, T.; Nikitenko, S.I. Sonocatalytic degradation of EDTA in the presence of Ti and Ti@TiO<sub>2</sub> nanoparticles. *Ultrason. Sonochem.* **2021**, *70*, 105336. [CrossRef] [PubMed]
18. El Hakim, S.; Chave, T.; Nada, A.A.; Roualdes, S.; Nikitenko, S.I. Tailoring noble metal-free Ti@TiO<sub>2</sub> photocatalyst for boosting photothermal hydrogen production. *Front. Catal.* **2021**, *1*, 669260. [CrossRef]
19. Höbel, B.; Von Sonntag, C. OH-Radical induced degradation of ethylenediaminetetraacetic acid (EDTA) in aqueous solution: A pulse radiolysis study. *J. Chem. Soc. Perkin Trans.* **1998**, *2*, 509–514. [CrossRef]
20. Nikitenko, S.I.; Chave, T.; Cau, C.; Brau, H.-P.; Flaud, V. Photothermal Hydrogen production using noble-metal-free Ti@TiO<sub>2</sub> core-shell nanoparticles under visible-NIR light irradiation. *ACS Catal.* **2015**, *5*, 4790–4795. [CrossRef]
21. Parizot, L.; Chave, T.; Galvez, M.-E.; Dutilleul, H.; Da Costa, P.; Nikitenko, S.I. Sonocatalytic oxidation of EDTA in aqueous solutions over noble metal-free Co<sub>3</sub>O<sub>4</sub>/TiO<sub>2</sub> catalyst. *Appl. Catal. B Environ.* **2019**, *241*, 570–577. [CrossRef]
22. Babay, P.A.; Emilio, C.A.; Ferreyra, R.E.; Gautier, E.A.; Gettar, R.T.; Litter, M.I. Kinetics and mechanisms of EDTA photocatalytic degradation with TiO<sub>2</sub> under different experimental conditions. *Int. J. Photoenergy* **2001**, *3*, 193–199. [CrossRef]
23. Tang, W.; Chen, J.; Yin, Z.; Sheng, W.; Lin, F.; Xu, H.; Cao, S. Complete removal of phenolic contaminants from bismuth-modified TiO<sub>2</sub> single-crystal photocatalysts. *Chin. J. Catal.* **2021**, *42*, 347–355. [CrossRef]
24. Wang, F.; Feng, Y.; Chen, P.; Wang, Y.; Su, Y.; Zhang, Q.; Zeng, Y.; Xie, Z.; Liu, H.; Liu, Y.; et al. Photocatalytic degradation of fluoroquinolone antibiotics using ordered mesoporous g-C<sub>3</sub>N<sub>4</sub> under simulated sunlight irradiation: Kinetics, mechanism, and antibacterial activity elimination. *Appl. Catal. B Environ.* **2018**, *227*, 114–122. [CrossRef]
25. Liu, S.-H.; Tang, W.-T.; Chou, P.-H. Microwave-assisted synthesis of triple 2D g-C<sub>3</sub>N<sub>4</sub>/Bi<sub>2</sub>WO<sub>6</sub>/rGO composites for ibuprofen photodegradation: Kinetics, mechanism and toxicity evaluation of degradation products. *Chem. Eng. J.* **2020**, *387*, 124098. [CrossRef]
26. O’Sullivan, D.W.; Tyree, M. The kinetics of complex formation between Ti(IV) and hydrogen peroxide. *Int. J. Chem. Kinet.* **2007**, *39*, 457–461. [CrossRef]
27. Setiawan, D.; Kazaryan, A.; Martoprawiro, M.; Filatov, M. A first principles study of fluorescence quenching in rhodamine B dimers: How can quenching occur in dimeric species? *Phys. Chem. Chem. Phys.* **2010**, *12*, 11238–11244. [CrossRef] [PubMed]
28. Chiha, M.; Merouani, S.; Hamdaoui, O.; Baup, S.; Gondrexon, N.; Pétrier, C. Modeling of ultrasonic degradation of non-volatile organic compounds by Langmuir-type kinetics. *Ultrason. Sonochem.* **2010**, *17*, 773–782. [CrossRef] [PubMed]
29. Akbal, F. Photocatalytic degradation of organic dyes in the presence of titanium dioxide under UV and solar light: Effect of operational parameters. *Environ. Prog.* **2005**, *24*, 317–322. [CrossRef]
30. Zhao, G.; Liu, L.; Li, C.; Yu, J.; Jiao, F. Synthesis, characterization and enhanced visible light photocatalytic activity of Bi<sub>2</sub>WO<sub>6</sub>/Ni-Al layered double hydroxide composites. *J. Mater. Sci. Mater. Electron.* **2018**, *29*, 14008–14021. [CrossRef]
31. Kratochvil, B.; White, M.C. Spectrophotometric determination of microgram quantities of (ethylenedinitrilo)tetraacetic acid with bis(2/4,6-tripyridyl-s-triazine)iron(II). UTC, 1962. *Anal. Chem.* **1965**, *37*, 111–113. Available online: <https://pubs.acs.org/sharingguidelines> (accessed on 29 July 2021). [CrossRef]

## Article

# Preparation of Mn-Doped $\text{Co}_3\text{O}_4$ Catalysts by an Eco-Friendly Solid-State Method for Catalytic Combustion of Low-Concentration Methane

Linshuang Xue<sup>1</sup>, Chenyi Yuan<sup>1</sup>, Shipeng Wu<sup>1</sup>, Zhen Huang<sup>1,\*</sup>, Zhen Yan<sup>2</sup>, Stéphane Streiff<sup>2</sup>, Hualong Xu<sup>1</sup> and Wei Shen<sup>2,\*</sup>

<sup>1</sup> Shanghai Key Laboratory of Molecular Catalysis and Innovative Materials, Laboratory of Advanced Materials and Collaborative Innovation Center of Chemistry for Energy Materials, Department of Chemistry, Fudan University, Shanghai 200433, China

<sup>2</sup> Eco-Efficient Products and Processes Laboratory (E2P2L), UMI 3464 CNRS-Solvay, Shanghai 201108, China

\* Correspondence: huangzhen@fudan.edu.cn (Z.H.); wshen@fudan.edu.cn (W.S.)

**Abstract:** Coalbed methane is a significant source of methane in the atmosphere, which is a potent greenhouse gas with a considerable contribution to global warming, thus it is of great importance to remove methane in coalbed gas before the emission. Exploring the economical non-noble metal catalysts for catalytic methane combustion (CMC) has been a wide concern to mitigate the greenhouse effect caused by the emitted low-concentration methane. Herein, a series of Mn-doped  $\text{Co}_3\text{O}_4$  catalysts have been synthesized by the environmentally friendly solid-state method. As a result, the  $\text{Mn}_{0.05}\text{Co}_1$  catalyst performed the best CMC activity ( $T_{90} = 370\text{ }^\circ\text{C}$ ) and good moisture tolerance (3 vol% steam). The introduction of an appropriate amount of manganese conduced  $\text{Co}_3\text{O}_4$  lattice distortion and transformed  $\text{Co}^{3+}$  to  $\text{Co}^{2+}$ , thus producing more active oxygen vacancies.  $\text{Mn}_{0.05}\text{Co}_1$  exhibited better reducibility and oxygen mobility. In situ studies revealed that methane was adsorbed and oxidized much easier on  $\text{Mn}_{0.05}\text{Co}_1$ , which is the crucial reason for its superior catalytic performance.

**Keywords:** active oxygen; catalytic combustion; low-concentration; methane; Mn- $\text{Co}_3\text{O}_4$ ; solid-state

**Citation:** Xue, L.; Yuan, C.; Wu, S.; Huang, Z.; Yan, Z.; Streiff, S.; Xu, H.; Shen, W. Preparation of Mn-Doped  $\text{Co}_3\text{O}_4$  Catalysts by an Eco-Friendly Solid-State Method for Catalytic Combustion of Low-Concentration Methane. *Catalysts* **2023**, *13*, 529. <https://doi.org/10.3390/catal13030529>

Academic Editors: Juan José Rueda-Márquez, Javier Moreno-Andrés and Irina Levchuk

Received: 29 January 2023  
Revised: 25 February 2023  
Accepted: 3 March 2023  
Published: 5 March 2023



**Copyright:** © 2023 by the authors. Licensee MDPI, Basel, Switzerland. This article is an open access article distributed under the terms and conditions of the Creative Commons Attribution (CC BY) license (<https://creativecommons.org/licenses/by/4.0/>).

## 1. Introduction

Methane ( $\text{CH}_4$ ) is one of the most significant greenhouse gases (GHG), whose global warming potential is about 25 times over a 100-year time horizon and about 72 times over a 20-year time horizon than that of  $\text{CO}_2$ , thus the direct emission of methane can cause a series of severe environmental issues [1,2]. There are many sources of  $\text{CH}_4$  in the atmosphere including biogenic, geogenic, and anthropogenic sources. As the main ingredient of natural gas, one of the largest anthropogenic emissions of  $\text{CH}_4$  comes from the coal mining process [3,4]. This part of  $\text{CH}_4$  is further diluted to 0.1–1.0% after mixing with air during underground mining, resulting in low-concentration coalbed methane. According to the requirements of relevant environmental protection policies,  $\text{CH}_4$  emissions need to be strictly controlled. Catalytic methane combustion (CMC) helps to reduce the emission of  $\text{CH}_4$  to meet the increasingly strict regulations on emissions reduction [5,6]. Therefore, it is of great significance to develop efficient CMC catalysts. Furthermore, the activation of the methane C–H bond in the gas phase usually requires a very high temperature due to the high stability of the molecular structure [7]. As a result, it is necessary to further optimize the low-temperature activity and thermal stability of CMC catalysts, which is in favor of industrial development and environmental protection.

Noble metal catalysts of Pd, Pt, and Rh are enriched with high activity for the catalytic combustion of low-concentration methane, but their industrial applications are restricted due to their low thermal stability, the shortage of resources, and high expense of the raw materials [8–10]. Considering cost control and the easy availability of raw materials,

transition metal (Mn, Fe, Co, Ni, Cu, etc.) oxides are thought to be a feasible substitution for noble metal catalysts as they are prone to realize redox cycles among different oxidation states [9]. The commonly used transition metal oxide catalysts include  $\text{MnO}_x$  [11–13],  $\text{Co}_3\text{O}_4$  [5,6,14],  $\text{CeO}_2$  [15],  $\text{NiO}$  [16], and their mixed components [17–22]. A lot of research has proven that  $\text{Co}_3\text{O}_4$  is one of the most promising transition metal oxides among different CMC catalysts [23,24]. Adding dopants of Ce, Zr, and Mn with higher redox advantages can further enhance catalytic activity by introducing lattice defects and increasing active oxygen species. Specifically, the enhancing effect of Mn is the most remarkable [25–27]. As for Mn–Co composite oxides, different procedures of hydrothermal, co-precipitation, and sol–gel methods are commonly applied to introduce dopants into the support structure. Chang et al. [28] elucidated that the introduction of Mn can promote the formation and mobility of active oxygen as well as the redox cycle between  $\text{Mn}^{4+}/\text{Mn}^{3+}$  and  $\text{Co}^{2+}/\text{Co}^{3+}$ , accelerating the deeper transformation from intermediates to  $\text{CO}_2$  and  $\text{H}_2\text{O}$ .

The synthesis method plays a significant impact on the catalytic performance of transition metal oxide catalysts. Compared with the methods above-mentioned, the solid-state method with simple procedures and easily accessible precursors is quite promising in industrial applications. Moreover, no organic solvent is needed in the preparation process with no harmful wastewater emission [29–31]. Akbari et al. [32] ground the nitrates of Mn and Ba into a paste, resulting in a BaO-doped solid-state mixing catalyst. The decent elemental doping under the solid-state method promoted a favorable regulation of the redox property and bi-component synergistic effect of the catalyst, providing more active oxygen for the reaction [33]. However, the emission of nitrogen oxides ( $\text{NO}_x$ ) is still a problem when nitrates are used as precursors. Synthesizing composite oxides by the solid-state method using carbonates as precursors is a green route without wastewater and exhaust gas. However, the application of this method in CMC catalyst preparation has not been reported.

In this work, a solid-state method with carbonates as precursors was applied to investigate the CMC activities of a series of Mn-doped  $\text{Co}_3\text{O}_4$  catalysts ( $\text{Mn-Co}_3\text{O}_4$ ). This method is environmentally friendly with no wastewater or harmful gas emissions. Various characterization measures were applied to investigate the effect of Mn doping on the chemical state of active components, redox properties, and catalytic performance. Adjusting the Mn doping amount to 5.0% not only resulted in the formation of a Co–Mn solid solution and lattice defects, but also modified the surface properties and increased the active oxygen species of  $\text{Co}_3\text{O}_4$ , which was found to be beneficial for improving the catalytic performance. The cost of a prepared  $\text{Mn}_{0.05}\text{Co}_1$  catalyst was lower than that of noble metals, and it has the advantages of high catalytic activity and good water resistance, so it has a good prospect of industrial application.

## 2. Results and Discussion

### 2.1. Structural and Textural Properties

The morphologies and microstructures of  $\text{Co}_3\text{O}_4$ ,  $\text{MnO}_x$ , and the synthesized  $\text{Mn}_x\text{Co}_1$  ( $x = 0.025, 0.05, \text{ and } 0.1$ ) catalysts were characterized by SEM and HRTEM. Pure  $\text{Co}_3\text{O}_4$  (Figure 1a–c) mainly exhibited spherical and polygonal nanostructures with a diameter of 30–50 nm. On doping a low amount of Mn into  $\text{Co}_3\text{O}_4$ , the morphologies and crystal sizes of the obtained  $\text{Mn}_{0.025}\text{Co}_1$  (Figure 1d–f),  $\text{Mn}_{0.05}\text{Co}_1$  (Figure 1g–i), and  $\text{Mn}_{0.1}\text{Co}_1$  (Figure 1j–l) catalysts became irregular with a wider size distribution (10–50 nm). Moreover, the catalyst edges became rougher and more blurred after Mn doping, implicating that the growth of the crystallite had been restrained and the amount of crystal defects increased. Generally, the formation of crystal defects facilitates the formation of more reactive sites and oxygen vacancies for CMC, thus enhancing the combustion activity of the Mn–Co catalyst [34]. Pure  $\text{MnO}_x$  (Figure 1m–o) showed a random accumulation of worm-like nanograins (20–50 nm). Clear lattice stripes of all catalysts can be seen in the HRTEM photos, indicating a high crystallinity.



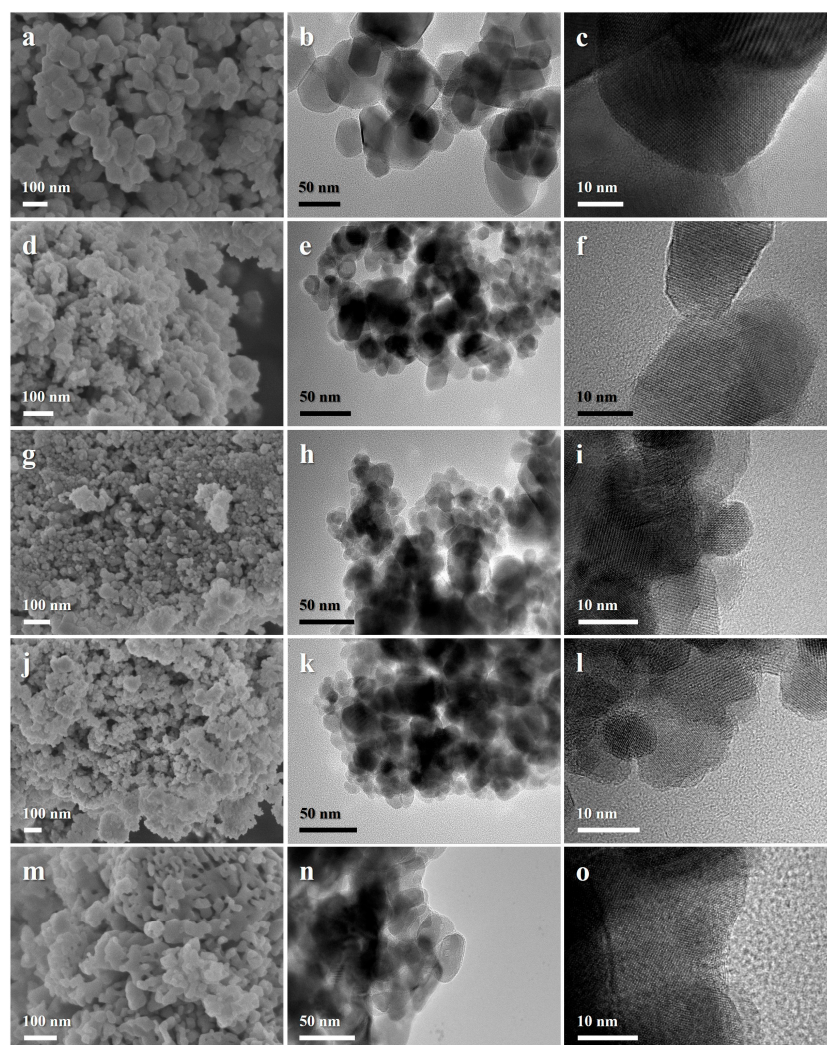


**Figure 1.** SEM and HRTEM images of  $\text{Co}_3\text{O}_4$  (a–c),  $\text{Mn}_{0.025}\text{Co}_1$  (d–f),  $\text{Mn}_{0.05}\text{Co}_1$  (g–i),  $\text{Mn}_{0.1}\text{Co}_1$  (j–l), and  $\text{MnO}_x$  (m–o) catalysts.

The crystalline phase structures of  $\text{Co}_3\text{O}_4$  and  $\text{Mn}_x\text{Co}_1$  were characterized by XRD (Figure 2a). The  $\text{Mn}_x\text{Co}_1$  catalysts mainly exhibited the characteristic diffraction peaks of  $\text{Co}_3\text{O}_4$  (JCPDS No. 42-1467), and almost no obvious characteristic diffraction peaks of  $\text{MnO}_x$  were observed in the XRD patterns, except for the  $\text{Mn}_{0.1}\text{Co}_1$  catalyst, which may be the result of the incorporation of Mn into the  $\text{Co}_3\text{O}_4$  lattice to form a solid solution or the high dispersion of Mn on the surface of  $\text{Co}_3\text{O}_4$  [28]. The main diffraction peaks of the Mn- $\text{Co}_3\text{O}_4$  catalysts were exposed at  $2\theta = 19.0^\circ, 31.3^\circ, 36.8^\circ, 38.7^\circ, 44.8^\circ, 55.8^\circ, 59.4^\circ,$  and  $65.2^\circ$ , which can be attributed to the (111), (220), (311), (222), (400), (422), (511), and (440) facets of the  $\text{Co}_3\text{O}_4$  phase [35–37]. With the increase in the Mn doping amount to 10.0 mol%, weak diffraction peaks at around  $2\theta = 33.0^\circ$  and  $55.0^\circ$  were observed on the  $\text{Mn}_{0.1}\text{Co}_1$  catalyst, which were well-matched with the characteristic diffraction peaks of the  $\text{Mn}_2\text{O}_3$  (JCPDS No. 41-1442) and  $\text{Mn}_3\text{O}_4$  (JCPDS No. 04-0732) phases, respectively. This indicates that increasing the Mn doping amount to a certain extent will lead to the formation of some  $\text{Mn}_2\text{O}_3$  and  $\text{Mn}_3\text{O}_4$  oxides instead of producing a Mn–Co solid solution. When the doping amount of Mn increased, the intensity of the diffraction peak slightly decreased, while the half-peak width slightly rose, resulting in a gradual reduction in the crystal size. The crystal sizes of the prepared catalysts were calculated by the Scherrer equation (Table 1) in which the mean crystal sizes decreased from 34 nm to 25 nm with an increasing Mn doping amount, which is consistent with the microscope images. Smaller crystals may also boost the formation of low-coordinated defect sites that can promote

catalyst activities including surface oxygen vacancies [34]. Based on Mars–van-Krevelen (MvK) mechanisms, the surface-active oxygen species play a decisive role in CH<sub>4</sub> oxidation, providing more assistance for acceleration of the chemical reactions [38]. In addition, the diffraction peak of the Co<sub>3</sub>O<sub>4</sub> (311) facet at 36.8° (Figure 2b) gradually shifted toward lower angles, and the corresponding lattice constant (Figure 2c) increased from 8.0608 Å (Co<sub>3</sub>O<sub>4</sub>) to 8.0809 Å (Mn<sub>0.05</sub>Co<sub>1</sub>), with a maximum increase of 0.25%. Considering the crystal radius of Co<sup>3+</sup> (0.685 Å), which is lower than that of Mn<sup>3+</sup> (high spin, 0.785 Å; low spin, 0.72 Å), substituting Mn<sup>3+</sup> for Co<sup>3+</sup> can result in the expansion of interplanar spacing [39]. Therefore, the shift in the diffraction position and the increase in the lattice constant can be ascribed to the incorporation of Mn ions. Furthermore, incorporating Mn ions also led to the accompanying transformation from Co<sup>3+</sup> into Co<sup>2+</sup> [25,40,41]. All of the mentioned changes directly prove that the doped Mn had been incorporated into the Co<sub>3</sub>O<sub>4</sub> lattice and a Mn–Co solid solution formed. However, further increasing the doping amount to 10.0% (Mn<sub>0.1</sub>Co<sub>1</sub>) resulted in a slight decrease in the lattice constant, indicating no further incorporation of Mn into the Co<sub>3</sub>O<sub>4</sub> lattice and no further formation of the Mn–Co solid solution.

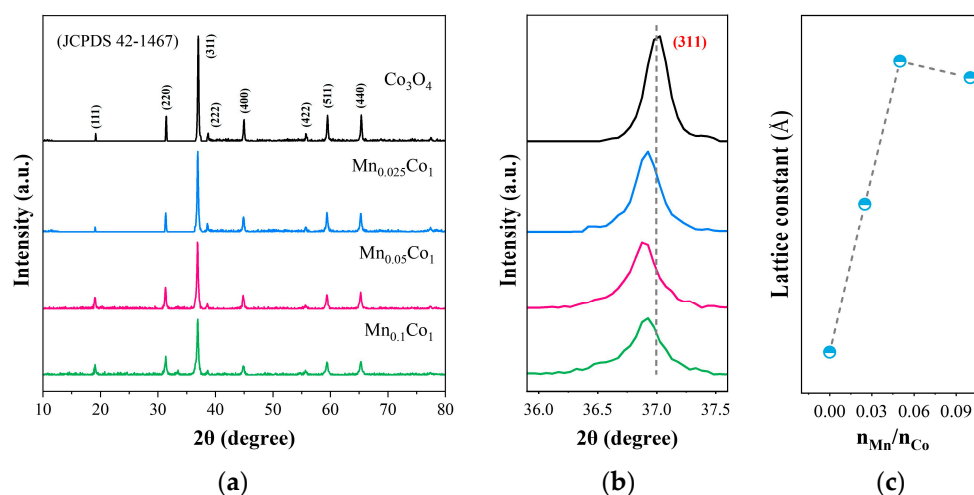


**Figure 2.** Wide-angle (a) and enlarged (b) XRD spectra of the Co<sub>3</sub>O<sub>4</sub> and Mn<sub>x</sub>Co<sub>1</sub> ( $x = 0.025, 0.05, 0.1$ ) catalysts and (c) a variation in the lattice constant of Co<sub>3</sub>O<sub>4</sub> as a function of the mole ratio of Mn/Co.

**Table 1.** Textual properties of the as-obtained catalysts.

Catalyst	Crystallite Size <sup>1</sup> (nm)	Specific Surface Area <sup>2</sup> (m <sup>2</sup> ·g <sup>-1</sup> )	Pore Volume <sup>3</sup> (cm <sup>3</sup> ·g <sup>-1</sup> )	Average Pore Diameter <sup>4</sup> (nm)
Co <sub>3</sub> O <sub>4</sub>	34	14	0.09	39.7
Mn <sub>0.025</sub> Co <sub>1</sub>	30	26	0.20	28.8
Mn <sub>0.05</sub> Co <sub>1</sub>	27	33	0.21	15.6
Mn <sub>0.1</sub> Co <sub>1</sub>	25	39	0.21	11.0
MnO <sub>x</sub>	28	28	0.22	20.5

<sup>1</sup> Calculated from the line broadening of diffraction peaks by the Scherrer equation from XRD patterns. <sup>2</sup> Determined by the BET method. <sup>3</sup> Total pore volume adsorbed at  $P/P_0 = 0.99$ . <sup>4</sup> Determined by the BJH method.

The textual properties of the prepared Co<sub>3</sub>O<sub>4</sub>, Mn<sub>x</sub>Co<sub>1</sub>, and MnO<sub>x</sub> samples were characterized by N<sub>2</sub> adsorption–desorption isotherms. Figures S1 and S2 illustrate the isotherms and the pore size distributions of the catalysts, respectively. Detailed data about the specific surface areas, pore volumes, and mean pore sizes of the catalysts are listed in Table 1. Compared with pure Co<sub>3</sub>O<sub>4</sub>, the Mn–Co<sub>3</sub>O<sub>4</sub> catalysts possess a larger specific surface area and total pore volume as well as a smaller mean pore size. It has been proven that larger specific surface area increases will be beneficial for the transfer of CH<sub>4</sub> molecules inside the catalyst pores and can promote contact between CH<sub>4</sub> molecules and active sites, enhancing the efficiency of CH<sub>4</sub> oxidation [42]. When the doping amount of Mn increased,

the specific surface area increased from  $14 \text{ m}^2 \cdot \text{g}^{-1}$  ( $\text{Co}_3\text{O}_4$ ) to  $26 \text{ m}^2 \cdot \text{g}^{-1}$  ( $\text{Mn}_{0.025}\text{Co}_1$ ),  $33 \text{ m}^2 \cdot \text{g}^{-1}$  ( $\text{Mn}_{0.05}\text{Co}_1$ ), and  $39 \text{ m}^2 \cdot \text{g}^{-1}$  ( $\text{Mn}_{0.1}\text{Co}_1$ ).

## 2.2. Surface Chemical States

The impacts of properties including the surface elemental valence states and oxygen species on the catalytic activities were characterized by XPS. The XPS spectra of Co  $2p_{3/2}$  (Figure 3a) can be divided into two peaks, with which the peak with a binding energy (BE) of 779.4–780.1 eV can be attributed to octahedral  $\text{Co}^{3+}$ , while the other with a higher BE of 780.4–781.1 eV can be assigned to tetrahedral  $\text{Co}^{2+}$  [43,44]. When the doping amount of Mn increased, the  $\text{Co}^{2+}$  ratio ( $\text{Co}^{2+}/(\text{Co}^{2+} + \text{Co}^{3+})$ ) value increased at first and then decreased:  $\text{Mn}_{0.05}\text{Co}_1$  (34.89%) >  $\text{Mn}_{0.025}\text{Co}_1$  (32.16%) >  $\text{Mn}_{0.1}\text{Co}_1$  (28.50%) >  $\text{Co}_3\text{O}_4$  (27.41%), indicating a highest surface  $\text{Co}^{2+}$  content of  $\text{Mn}_{0.05}\text{Co}_1$ . The introduction of a decent amount of Mn into the  $\text{Co}_3\text{O}_4$  lattice will facilitate the formation of crystal defects such as oxygen vacancy, leading to the reduction of neighbored  $\text{Co}^{3+}$  ions into  $\text{Co}^{2+}$ . Excessive  $\text{Co}^{2+}$  can bring about a surface charge imbalance, causing other metal components to shift from a lower valence state to a higher valence state [45]. This further stimulates the redox balance between Co ions and Mn ions, in which the doping of a decent amount of Mn can effectively facilitate the breakage of Co–O bonds and create more oxygen vacancies [46].

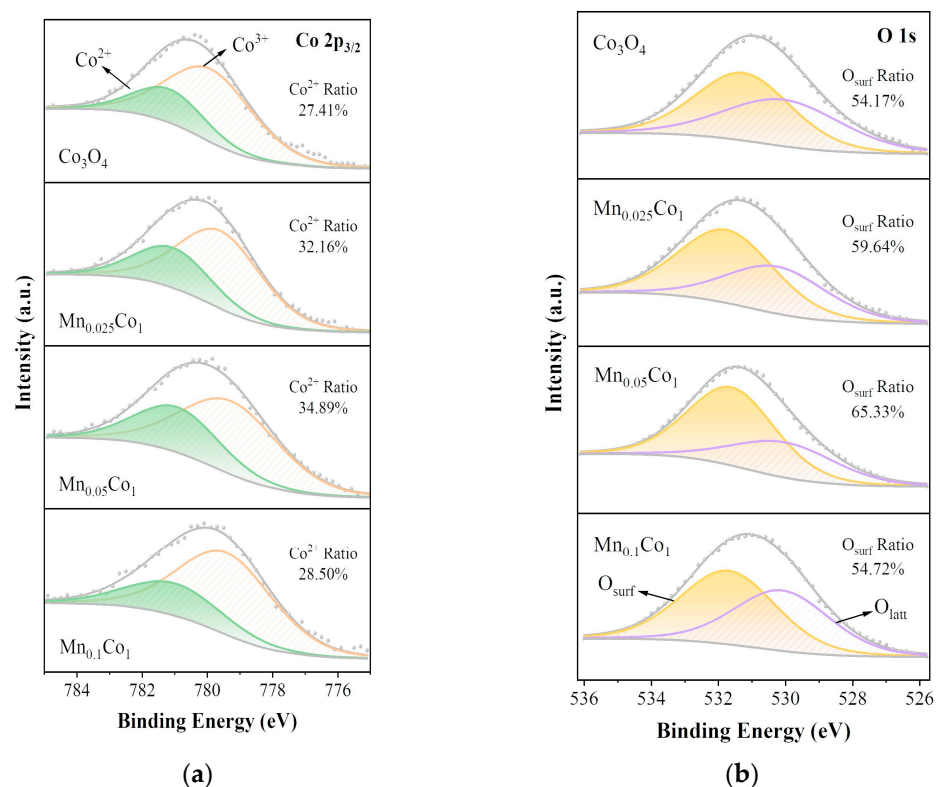


**Figure 3.** XPS spectra for (a) Co  $2p_{3/2}$ , (b) O  $1s$  of  $\text{Co}_3\text{O}_4$ ,  $\text{Mn}_{0.025}\text{Co}_1$ ,  $\text{Mn}_{0.05}\text{Co}_1$ , and  $\text{Mn}_{0.1}\text{Co}_1$  catalysts.

Moreover, the deconvolution of O  $1s$  XPS spectra with two subpeaks is represented in Figure 3b, in which the peaks at 530.8 eV and 529.6 eV can be assigned to the surface-active oxygen species ( $\text{O}_{\text{surf}}$ , e.g.,  $\text{O}_2^-$ ,  $\text{O}^-$ , and  $\text{O}_2^{2-}$ ) associated with the oxygen vacancies and the lattice oxygen ( $\text{O}_{\text{latt}}$ , e.g.,  $\text{O}^{2-}$ ), respectively [47].  $\text{O}_{\text{surf}}$  is the active oxygen species in catalytic oxidation [48]. The formation of active  $\text{O}_{\text{surf}}$  is related to the generation of oxygen vacancies, which is conducive to the adsorption and activation of oxygen molecules [49–51]. As a result, when the doping amount of Mn increases, the  $\text{O}_{\text{surf}}$  ratio ( $\text{O}_{\text{surf}}/(\text{O}_{\text{surf}} + \text{O}_{\text{latt}})$ ) value increases at first—from 54.17% ( $\text{Co}_3\text{O}_4$ ) to 65.33% ( $\text{Mn}_{0.05}\text{Co}_1$ )—and then decreases, suggesting a superior catalytic activity of the  $\text{Mn}_{0.05}\text{Co}_1$  catalyst when compared to other

Mn-Co<sub>3</sub>O<sub>4</sub> catalysts. After being consumed by the oxidation of methane and intermediates, the dissipative surface-active oxygen species can be replenished by the migration of the bulk lattice oxygen species and the supplement of the gaseous O<sub>2</sub>, following the MvK mechanism [21,38]. The active oxygen species released from Co<sub>3</sub>O<sub>4</sub> due to the reduction of Co<sup>3+</sup> will transfer to the Mn species, benefiting the redox reaction cycle (Co<sup>3+</sup> + Mn<sup>3+</sup> ↔ Co<sup>2+</sup> + Mn<sup>4+</sup>), which is responsible for the improved catalytic performance [28,46].

### 2.3. Redox Capabilities

The redox capacities of different catalysts are characterized by H<sub>2</sub>-TPR (Figure 4). The spectrum of pure Co<sub>3</sub>O<sub>4</sub> mainly consists of two reducing peaks, in which the peak at 250–400 °C is attributed to the reduction of Co<sub>3</sub>O<sub>4</sub> to CoO, while the peak at 370–500 °C to the reduction of CoO to Co<sup>0</sup> [52–54]. The spectrum of pure MnO<sub>x</sub> mainly consists of two reducing peaks (300–350 °C and 400–450 °C) as well, which are attributed to the reduction of highly-dispersed MnO<sub>2</sub> and Mn<sup>3+</sup> to Mn<sup>2+</sup>, respectively [40,54,55]. The internal reduction temperatures of Co and Mn oxides are rather close, and thus it is difficult to thoroughly split their respective reducing peaks apart [40,54]. The first peak of Mn<sub>0.05</sub>Co<sub>1</sub> at 328 °C can be assigned to the combined reduction of Co<sup>3+</sup> and Mn<sup>4+</sup> to Co<sup>2+</sup> and Mn<sup>3+</sup>, the second peak at 401 °C is attributed to the continuous combined reduction of Co<sup>2+</sup> and Mn<sup>3+</sup>, while the third peak at 503 °C is attributed to the reduction of Co<sup>2+</sup> to Co<sup>0</sup>. When Mn is doped into Co<sub>3</sub>O<sub>4</sub>, both the first and second reducing peaks of Mn<sub>x</sub>Co<sub>1</sub> (x = 0.025, 0.05, and 0.1) are shifted to lower temperatures, indicating the improvement in the redox capacity, which is beneficial for the CMC process. Combined with the previous results, we suggest that Mn doping can increase the number of oxygen vacancies and active oxygen species, and the oxygen mobility can be correspondingly enhanced, thus causing the reduction profiles to shift to lower temperatures. However, when the Mn doping amount is further increased from 5.0% to 10.0%, the areas of the reduction peaks decrease significantly, indicating the decreased content of oxygen vacancies and surface active oxygen species, which is consistent with the XPS results. The above results show that the redox capacity of Mn<sub>0.05</sub>Co<sub>1</sub> can be improved by Mn doping, which can promote the redox cycles among the reducible Mn–Co species.

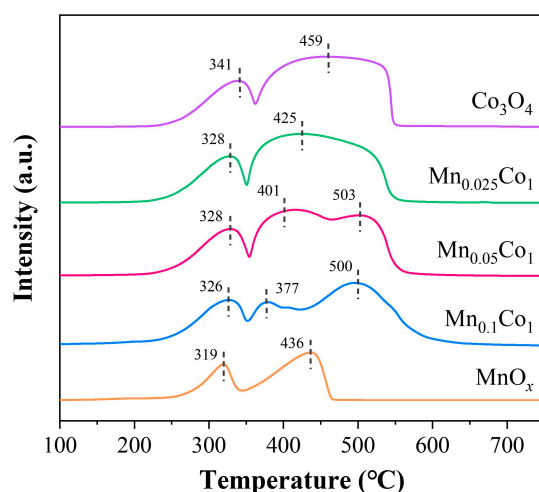


**Figure 4.** H<sub>2</sub>-TPR profiles of Co<sub>3</sub>O<sub>4</sub> and Mn<sub>x</sub>Co<sub>1</sub> (x = 0.025, 0.05, 0.1) catalysts.

To further study the oxygen properties and verify the mobility of oxygen, O<sub>2</sub>-TPD experiments of Co<sub>3</sub>O<sub>4</sub> and Mn<sub>x</sub>Co<sub>1</sub> catalysts were performed, and the results are shown in Figure 5. For all the samples, oxygen desorption peaks appeared at about 600 °C, which can be attributed to lattice oxygen species released from the Co<sub>3</sub>O<sub>4</sub> bulk [56,57]. Pure Co<sub>3</sub>O<sub>4</sub> has a small oxygen desorption peak with a center temperature of 667 °C. After doping a decent amount of manganese into Co<sub>3</sub>O<sub>4</sub>, the desorption temperatures of the composite oxides significantly decreased, indicating the improved oxygen mobility of Mn<sub>x</sub>Co<sub>1</sub>. Moreover,

$\text{Mn}_{0.05}\text{Co}_1$  exhibited the lowest  $\text{O}_2$  desorption temperature at 570 °C, then the desorption temperature rose to 580 °C when the doping amount of manganese was further increased to 0.1, demonstrating that active oxygen vacancies most easily formed on  $\text{Mn}_{0.05}\text{Co}_1$ , which agrees with the XPS results. Based on the above investigations, it can be estimated that the doping of Mn into the  $\text{Co}_3\text{O}_4$  lattice facilitates the release of lattice oxygen at high temperatures, and significantly enhances the redox capacities and oxygen mobility, which is beneficial to promoting CMC activities.

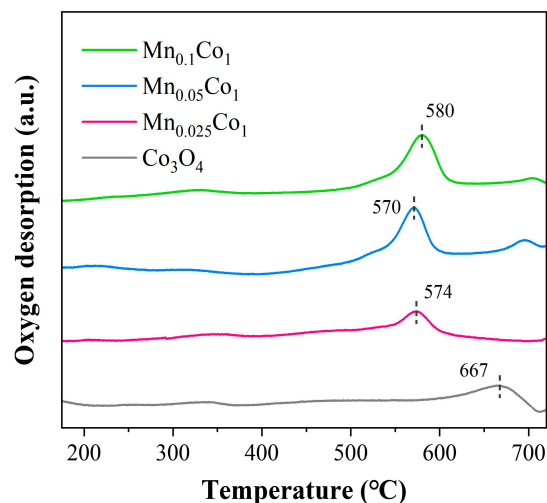


**Figure 5.**  $\text{O}_2$ -TPD profiles of the  $\text{Co}_3\text{O}_4$  and  $\text{Mn}_x\text{Co}_1$  ( $x = 0.025, 0.05, 0.1$ ) catalysts.

#### 2.4. Catalytic Performance for Low-Concentration $\text{CH}_4$ Combustion

The CMC catalytic activities of different catalysts were evaluated (Figure 6) including Mn-doped  $\text{Co}_3\text{O}_4$  with different doping amounts, pure  $\text{Co}_3\text{O}_4$ , and  $\text{MnO}_x$ . The Mn doping amounts in the Mn- $\text{Co}_3\text{O}_4$  samples were 2.5%, 5.0%, 10.0%, and 20.0%, respectively. As shown in Figure 6a, among all of the tested catalysts, pure  $\text{MnO}_x$  showed a low activity for CMC, in which the temperature needed for 50% conversion of  $\text{CH}_4$  ( $T_{50}$ ) was over 408 °C. On the other hand, pure  $\text{Co}_3\text{O}_4$  had good activity, in which  $T_{50}$  was about 333 °C, indicating that in the whole system,  $\text{Co}_3\text{O}_4$  plays a major role in  $\text{CH}_4$  catalytic oxidation. When small amounts of Mn were doped into  $\text{Co}_3\text{O}_4$ , the low-concentration CMC catalytic performances of the obtained Mn- $\text{Co}_3\text{O}_4$  samples were improved to a certain extent. When the doping amount of Mn was increased from 2.5% to 20.0%, the catalytic activity first increased and then decreased. When the doping amount of Mn increased to 20.0%, the activity of  $\text{Mn}_{0.2}\text{Co}_1$  was much lower than that of  $\text{Co}_3\text{O}_4$ , indicating that manganese is no longer easily incorporated into the  $\text{Co}_3\text{O}_4$  lattice to form a Mn-Co solid solution at this time, but mainly exists in the form of aggregated  $\text{Mn}_2\text{O}_3$  oxide, as shown in the XRD pattern of Figure S3. From the experimental results, the  $\text{Mn}_{0.05}\text{Co}_1$  catalyst with the Mn doping amount of 5.0% had the best activity, in which  $T_{50}$  and  $T_{90}$  (the temperature needed for 90%  $\text{CH}_4$  conversion) were 310 °C and 370 °C, respectively. It can be concluded that doping the proper amount of Mn is beneficial to improving the catalytic performance of  $\text{Co}_3\text{O}_4$ .

To compare the catalytic activity differences of the samples more clearly, the temperatures needed for 10%, 50%, and 90%  $\text{CH}_4$  conversion ( $T_{10}$ ,  $T_{50}$ , and  $T_{90}$ ) of all the catalysts as well as their reaction rates per unit area per second at 250 °C are summarized in Table 2. The reaction rates per unit area per second of the relevant catalysts were calculated on the activity data of a  $\text{CH}_4$  conversion lower than 20%. The Arrhenius equations for CMC reactions of  $\text{Co}_3\text{O}_4$ ,  $\text{Mn}_{0.025}\text{Co}_1$ ,  $\text{Mn}_{0.05}\text{Co}_1$ , and  $\text{Mn}_{0.1}\text{Co}_1$  catalysts were calculated according to their reaction rates (Figure 6b). The apparent activation energy of  $\text{CH}_4$  oxidation was determined by the slope of the Arrhenius equation, and for the above catalysts, the activation energies were  $\text{Mn}_{0.1}\text{Co}_1$  ( $109.2 \pm 0.4 \text{ kJ}\cdot\text{mol}^{-1}$ ) >  $\text{Co}_3\text{O}_4$  ( $102.1 \pm 0.2 \text{ kJ}\cdot\text{mol}^{-1}$ ) >  $\text{Mn}_{0.025}\text{Co}_1$  ( $97.2 \pm 0.5 \text{ kJ}\cdot\text{mol}^{-1}$ ) >  $\text{Mn}_{0.05}\text{Co}_1$  ( $88.4 \pm 0.2 \text{ kJ}\cdot\text{mol}^{-1}$ ), which was consistent with the CMC reaction results. This further proves that the  $\text{Mn}_{0.05}\text{Co}_1$  catalyst with a small Mn doping

amount had the highest catalytic activity. It can be concluded that the formation of the Mn–Co solid solution and the increase in the redox pairs of the Co/Mn multi-valence ions can effectively improve the oxygen mobility and increase oxygen vacancies. Although the specific surface area of the  $\text{Mn}_{0.05}\text{Co}_1$  catalyst increases due to manganese incorporation, the more essential reasons for its performance enhancements were the higher oxygen mobility and more oxygen vacancies.

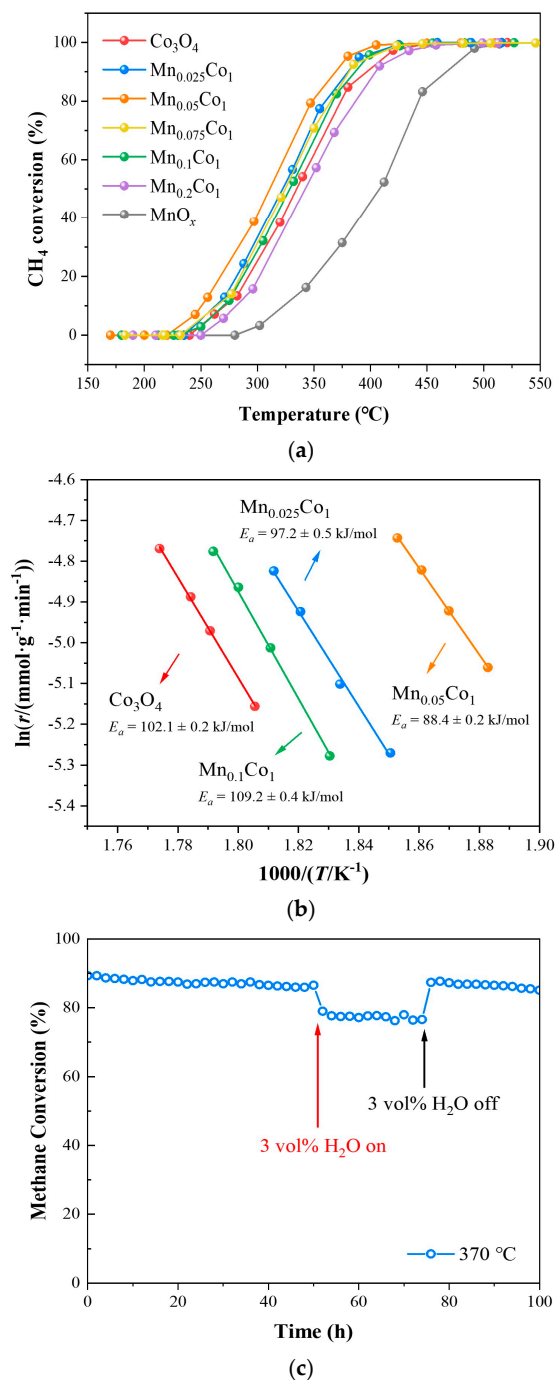


**Figure 6.** (a) Catalytic activities of the  $\text{Co}_3\text{O}_4$ , Mn-doped  $\text{Co}_3\text{O}_4$ , and  $\text{MnO}_x$  samples. (b) Arrhenius plots of the  $\text{CH}_4$  oxidation rates over the  $\text{Co}_3\text{O}_4$  and  $\text{Mn}_x\text{Co}_1$  ( $x = 0.025, 0.05, 0.1$ ) catalysts. (c) Stability test and effect of 3 vol% steam on  $\text{CH}_4$  conversion over the  $\text{Mn}_{0.05}\text{Co}_1$  catalyst at 370 °C. Reaction conditions: 0.5 vol%  $\text{CH}_4$ , 20 vol%  $\text{O}_2$ ,  $\text{N}_2$  as the balance gas. GHSV =  $12,000 \text{ mL g}^{-1} \text{ h}^{-1}$ .

**Table 2.** Catalytic activities over the Co<sub>3</sub>O<sub>4</sub>, Mn<sub>x</sub>Co<sub>1</sub> (x = 0.025, 0.05, and 0.1), and MnO<sub>x</sub> catalysts.

Catalysts	T <sub>10</sub> (°C)	T <sub>50</sub> (°C)	T <sub>90</sub> (°C)	r <sup>1</sup> × 10 <sup>9</sup> (mol·m <sup>-2</sup> ·s <sup>-1</sup> )
Co <sub>3</sub> O <sub>4</sub>	269	333	395	1.57
Mn <sub>0.025</sub> Co <sub>1</sub>	262	321	379	1.63
Mn <sub>0.05</sub> Co <sub>1</sub>	250	310	370	2.14
Mn <sub>0.1</sub> Co <sub>1</sub>	269	328	385	0.66
MnO <sub>x</sub>	323	408	468	0.06

<sup>1</sup> The feed gas was 0.5 vol% CH<sub>4</sub> and 20 vol% O<sub>2</sub>/N<sub>2</sub> at T = 250 °C.

On the other hand, the CMC stability test for the Mn<sub>0.05</sub>Co<sub>1</sub> catalyst with the best performance was carried out at 370 °C (Figure 6c). After continuous reaction for 100 h, the CH<sub>4</sub> conversion was maintained at above 85%, expressing good durability, which provides the potential possibility for its application in the CH<sub>4</sub> treatment industry. To further investigate the water resistance, water vapor (3 vol%) was further introduced after 50 h. The CH<sub>4</sub> conversion of Mn<sub>0.05</sub>Co<sub>1</sub> first decreased from 86.6% to 79% and then fluctuated in the range of 76–78% for 25 h. When the vapor was evacuated, the activity of the Mn<sub>0.05</sub>Co<sub>1</sub> catalyst could be thoroughly recovered to the initial level, giving a CH<sub>4</sub> conversion of 87.4% again, which could be maintained above 85% in the next 25 h of operation. It was found that the methane conversion could quickly increase to the previous level after stopping the water addition and still showed good stability. Based on the above results, we can conclude that the introduction of steam had a certain effect on the CMC reactivity of the Mn<sub>0.05</sub>Co<sub>1</sub> sample, but this effect is reversible because its activity can be recovered after the water is removed, illustrating that the Mn<sub>0.05</sub>Co<sub>1</sub> catalyst has a certain degree of water resistance.

### 2.5. In Situ DRIFTS Study

The CH<sub>4</sub> adsorption processes at room temperature on the Mn<sub>0.05</sub>Co<sub>1</sub> and Co<sub>3</sub>O<sub>4</sub> catalysts over time were observed by in situ DRIFTS spectra (Figure 7a,b). The peaks at 3016 cm<sup>-1</sup> and 1304 cm<sup>-1</sup> were attributed to the C–H vibration of CH<sub>4</sub>, while the peak near 1613 cm<sup>-1</sup> was attributed to the antisymmetric stretching vibrations of formates (HCO or HCOO) [58–60]. For Mn<sub>0.05</sub>Co<sub>1</sub>, the formate species can be instantly well-observed after introducing the CH<sub>4</sub> stream for 1 min, while the intensities of the same peaks on Co<sub>3</sub>O<sub>4</sub> are very weak, indicating that the CH<sub>4</sub> molecules are more easily oxidized by the surface-active lattice oxygen on the Mn<sub>0.05</sub>Co<sub>1</sub> surface under O<sub>2</sub>-free circumstances, which obey the fundamental properties of the MvK mechanism. Furthermore, the surface-active lattice oxygen on Mn<sub>0.05</sub>Co<sub>1</sub> is more reactive than that on Co<sub>3</sub>O<sub>4</sub>. For a more visual comparison of the CH<sub>4</sub> relative adsorption capacity, the peak signals of Mn<sub>0.05</sub>Co<sub>1</sub> and Co<sub>3</sub>O<sub>4</sub> after 15-min of CH<sub>4</sub> adsorption were compared under the same testing conditions after weighing the same amount of samples accurately (Figure S4). Mn<sub>0.05</sub>Co<sub>1</sub> had a higher maximum peak intensity than Co<sub>3</sub>O<sub>4</sub>, suggesting that more CH<sub>4</sub> was absorbed on Mn<sub>0.05</sub>Co<sub>1</sub>, which had a higher surface CH<sub>4</sub> adsorption capacity.

Moreover, the in situ DRIFTS spectra of the Mn<sub>0.05</sub>Co<sub>1</sub> and Co<sub>3</sub>O<sub>4</sub> catalysts with a temperature rise in an atmosphere of 1% CH<sub>4</sub> + O<sub>2</sub> were characterized (Figure 7c,d) to identify the intermediate species and their contents changed during CH<sub>4</sub> oxidation. For Mn<sub>0.05</sub>Co<sub>1</sub>, the peak at 1530 cm<sup>-1</sup> was attributed to formates, while the peaks at 1373 cm<sup>-1</sup>, 1341 cm<sup>-1</sup>, and 1260 cm<sup>-1</sup> were attributed to carbonates. For Co<sub>3</sub>O<sub>4</sub>, the peak at 1530 cm<sup>-1</sup> was attributed to formates, while the peaks at 1371 cm<sup>-1</sup>, 1341 cm<sup>-1</sup>, and 1250 cm<sup>-1</sup> were attributed to carbonates [59–61]. At low temperatures (100–350 °C), a certain amount of formate and carbonate intermediates were detected for Mn<sub>0.05</sub>Co<sub>1</sub>, while almost no intermediates were detected at the same temperature for Co<sub>3</sub>O<sub>4</sub>. Merely a small number of formates and carbonates were detected on the Co<sub>3</sub>O<sub>4</sub> surface with an increase in temperature to 250 °C. On the other hand, at high temperatures (350–450 °C), the intensity of the formate peak signals on the Mn<sub>0.05</sub>Co<sub>1</sub> surface weakened as the temperature increased, and due to the fast reaction depletion at 400 °C, the formate peaks almost

disappeared. At the same time, the peaks at 2300–2400  $\text{cm}^{-1}$  could be observed at 450  $^{\circ}\text{C}$ , which were attributed to the C=O stretch of the vibration of gaseous  $\text{CO}_2$ . This means that the intermediates undergo rapid conversion and are more likely to further oxidize into carbonates and the product  $\text{CO}_2$  on the  $\text{Mn}_{0.05}\text{Co}_1$  surface [62]. The above results indicate that  $\text{Mn}_{0.05}\text{Co}_1$  has a stronger capacity for  $\text{CH}_4$  and  $\text{O}_2$  activation, assisting in the production of intermediates and  $\text{CO}_2$ . This is one of the significant reasons for the CMC performance difference between the two catalysts.

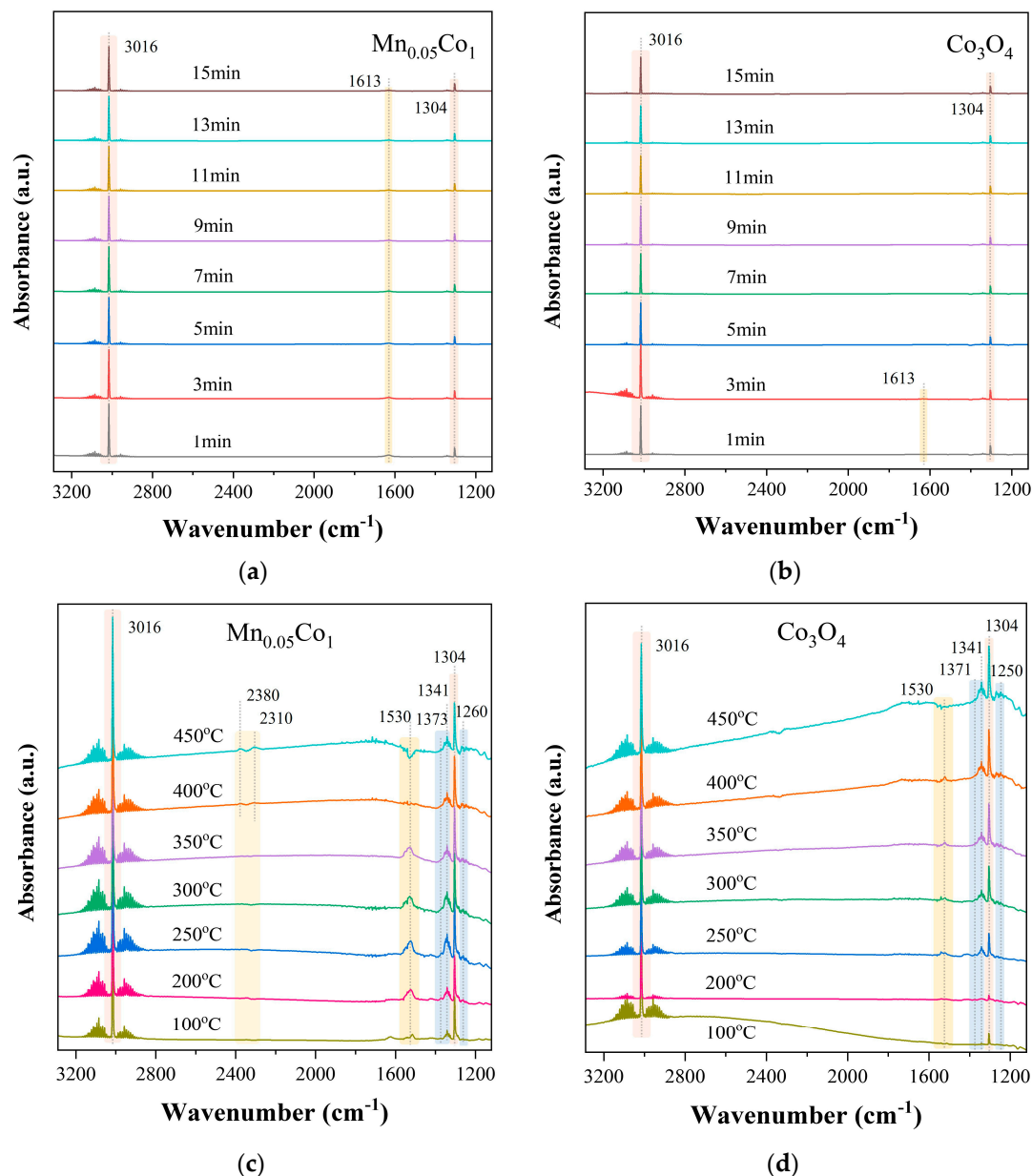


**Figure 7.** In situ DRIFTS spectra of  $\text{CH}_4$  adsorption over the (a)  $\text{Mn}_{0.05}\text{Co}_1$  and (b)  $\text{Co}_3\text{O}_4$  catalysts as a function of time at 30  $^{\circ}\text{C}$ , and the in situ DRIFTS spectra with the temperature increased after  $\text{CH}_4 + \text{O}_2$  adsorption over the (c)  $\text{Mn}_{0.05}\text{Co}_1$  and (d)  $\text{Co}_3\text{O}_4$  catalysts.

### 3. Materials and Methods

#### 3.1. Catalyst Preparation

Basic cobalt carbonate ( $(\text{CoCO}_3)_2 \cdot [\text{Co}(\text{OH})_2]_3 \cdot x\text{H}_2\text{O}$ , 99%) was purchased from Sinopharm (Shanghai, China). Manganese carbonate ( $\text{MnCO}_3$ , 99%) was purchased from Aladdin (Shanghai, China). A series of improved catalysts of Mn-doped  $\text{Co}_3\text{O}_4$  with different doping amounts was synthesized by the solid-state reactions of basic cobalt carbonate and man-



ganese carbonate. In the synthesis procedure, the scaled carbonate precursors were placed in the grinding jar, in which the grinding media of zirconium oxide balls occupied a 1/3 of the whole volume. The precursors were then ground and mixed at room temperature for 8 h using a planetary ball mill at a speed of 200 rpm. The doping amount of Mn was adjusted at the range of 2.5–20.0 mol% than that of Co. The obtained powder was dried overnight at 110 °C and then calcined at 550 °C for 4 h. The obtained mixture after calcination is denoted as  $Mn_xCo_1$ , in which  $x$  stands for the molar ratio of Mn/Co. The reference catalysts of pure  $MnO_x$  and  $Co_3O_4$  samples were synthesized according to the same procedure using basic cobalt carbonate and manganese carbonate, respectively.

### 3.2. Catalyst Characterizations

X-ray powder diffraction (XRD) was carried out on a Bruker AXS D8 diffractometer (AXS D8, Bruker, Madison, WI, USA). The XRD spectra were obtained in the  $2\theta$  of 10–80° to identify the crystal structures of the calcinated samples. The micromorphology of the catalysts was observed by field-emission scanning electron microscopy (FESEM) and high-resolution transmission electron microscopy (HRTEM). FESEM images were obtained on a Gemini 500 microscope (Gemini 500, Zeiss, Oberkochen, Ostalbkreis, Baden-Württemberg, Germany) at a working voltage of 3 kV. HRTEM images were obtained on a Tecnai G2 F20 S-Twin microscope (Tecnai G2 F20 S-Twin, FEI, Waltham, MA, USA) at a working voltage of 200 kV. The specific surface areas (SSA), pore volumes, and pore distributions were characterized by nitrogen adsorption–desorption isotherms on a Quadrasorb evo analyzer (Quadrasorb evo, Quantachrome, Boynton Beach, FL, USA). The pore structure data were then calculated according to the Brunauer–Emmett–Teller (BET) equation and the Barrett–Joyner–Halenda (BJH) model (Quadrasorb evo, Quantachrome, Boynton Beach, FL, USA). X-ray photoelectronic spectroscopy (XPS) was carried out on a PHI 5000C spectrometer (PHI 5000C, ULVCA-PHI, Chanhassen, MN, USA) to identify the surface element composition, valence states, and content of the catalysts. The reductivity and oxygen mobility of the catalysts were characterized by hydrogen temperature-programmed reduction ( $H_2$ -TPR) and oxygen temperature-programmed desorption ( $O_2$ -TPD) on a ChemiSorb 2720 automatic multi-purpose adsorption instrument (Auto Chem II 2720, Micromeritics, Norcross, GA, USA). Before the  $H_2$ -TPR experiments, the 40–60-mesh sample of 100 mg was filled in a quartz tube and pretreated under helium (flow rate 30 mL·min<sup>-1</sup>) at 200 °C for 2 h (heating rate 10 °C·min<sup>-1</sup>). The sample was then cooled to room temperature under a helium atmosphere. After that, the sample was heated under 10%  $H_2$ /Ar to 800 °C (heating rate 10 °C·min<sup>-1</sup>), during which the curve was recorded. In the  $O_2$ -TPD experiments, the 40–60-mesh sample of 100 mg was pretreated under 5%  $O_2$ /He (flow rate 30 mL·min<sup>-1</sup>) at 300 °C for 1 h (heating rate 10 °C·min<sup>-1</sup>). After that, the sample was purged using helium for 0.5 h at 300 °C and then heated to 800 °C with a heating rate of 10 °C·min<sup>-1</sup>, during which the curve was recorded. In situ diffuse reflectance infrared Fourier transform spectroscopy (in situ DRIFTS) was carried out on a Nicolet 6700 spectrometer (Nicolet 6700, Thermo Fisher Scientific, Waltham, MA, USA). Before the experiments, the catalyst was pretreated at 300 °C for 1 h and cooled to 30 °C under helium to obtain the background spectrum. The pre-obtained background spectrum at the respective temperature was deducted in the following adsorption/desorption and transient reaction experiments.

### 3.3. Evaluation of the Catalytic Performance

To evaluate the catalytic activity for the CMC reaction at atmospheric pressure, CMC catalytic experiments toward low-concentration  $CH_4$  were carried out on a fixed-bed reactor. The as-made powder was tablet pressed and sieved (40–60 mesh), and 200 mg of the obtained particles were packed in a quartz tube (inner diameter 4.5 mm). The total flow rate of the feeding gas (0.5 vol%  $CH_4$ , and 20 vol%  $O_2$  with  $N_2$  balanced) was 40 mL·min<sup>-1</sup>, and the gas hourly space velocity (GHSV) was 12,000 mL g<sup>-1</sup> h<sup>-1</sup>. The reaction products

were detected and analyzed online by the FTD detector of a Thermo trace GC Ultra gas chromatography. The CH<sub>4</sub> conversion ( $X_{\text{CH}_4}$ ) was calculated by the following formula:

$$X_{\text{CH}_4}(\%) = \frac{[\text{CH}_4]_{\text{in}} - [\text{CH}_4]_{\text{out}}}{[\text{CH}_4]_{\text{in}}} \times 100\% \quad (1)$$

where  $[\text{CH}_4]_{\text{in}}$  and  $[\text{CH}_4]_{\text{out}}$  are the inlet and outlet CH<sub>4</sub> concentrations at the steady state, respectively.

The CMC reaction rates per unit area per second of the catalysts can be calculated by the following formulas:

$$r(\text{mol} \cdot \text{m}^{-2} \cdot \text{s}^{-1}) = \frac{X_{\text{CH}_4} \cdot q \cdot [\text{CH}_4]_{\text{in}}}{V_m \cdot W \cdot S} \quad (2)$$

$$\ln r = \frac{-E_a}{RT} + C \quad (3)$$

where  $q$ ,  $V_m$ ,  $W$ ,  $S$ ,  $E_a$ ,  $R$ , and  $T$  are the volume flow rate (40 mL·min<sup>-1</sup>), the standard molar volume of gases (22.4 mL·mmol<sup>-1</sup>), catalyst mass (0.2 g), SSA of the catalyst (m<sup>2</sup>·g<sup>-1</sup>), activation energy (kJ·mol<sup>-1</sup>), universal gas constant (8.314 J·mol<sup>-1</sup>·K<sup>-1</sup>), and thermodynamic temperature (K), respectively.

#### 4. Conclusions

In summary, a series of Mn-Co<sub>3</sub>O<sub>4</sub> catalysts with different Mn doping amounts synthesized by a solid-state method was applied for catalytic methane combustion. The XRD and XPS results revealed that the formation of a Co–Mn solid solution could introduce more crystal defects and oxygen vacancies, inducing higher surface concentrations of Co<sup>2+</sup> and active oxygen species. The study of H<sub>2</sub>-TPR and O<sub>2</sub>-TPD analysis indicated the enhancement in redox capacity and oxygen mobility due to more active oxygen vacancies. Compared with the pure Co<sub>3</sub>O<sub>4</sub>, the Mn<sub>0.05</sub>Co<sub>1</sub> sample exhibited superior catalytic performance in low-concentration methane combustion. The  $T_{50}$  and  $T_{90}$  of Mn<sub>0.05</sub>Co<sub>1</sub> were 310 and 370 °C, respectively, which is outstanding as a transition metal catalyst compared with other components. Furthermore, the Mn<sub>0.05</sub>Co<sub>1</sub> catalyst also possessed good stability and water resistance (3 vol% steam). In situ DRIFTS results confirmed that Mn<sub>0.05</sub>Co<sub>1</sub> held stronger capabilities for CH<sub>4</sub> adsorption and provided more abundant active oxygen species for the reaction, which helped to improve the reaction rates and catalytic performance. It can be concluded that the Mn<sub>0.05</sub>Co<sub>1</sub> catalyst not only had a lower cost than noble metal materials, but also had a good performance in the catalytic combustion reaction of low-concentration methane, making it of great research value and industrial application potential. Based on these results, we propose an effective strategy to develop promising high-performance non-noble metal catalysts for low-concentration methane combustion.

**Supplementary Materials:** The following supporting information can be downloaded at: <https://www.mdpi.com/article/10.3390/catal13030529/s1>, Figure S1: N<sub>2</sub> adsorption–desorption isotherms of Co<sub>3</sub>O<sub>4</sub>, Mn<sub>x</sub>Co<sub>1</sub> ( $x = 0.025, 0.05, \text{ and } 0.1$ ) and the MnO<sub>x</sub> catalysts; Figure S2: Pore size distribution profiles of (A) Co<sub>3</sub>O<sub>4</sub>, (B) Mn<sub>0.025</sub>Co<sub>1</sub>, (C) Mn<sub>0.05</sub>Co<sub>1</sub>, (D) Mn<sub>0.1</sub>Co<sub>1</sub>, and (E) MnO<sub>x</sub> catalysts (Method: BJH desorption); Figure S3: The XRD spectra of the Mn<sub>0.2</sub>Co<sub>1</sub> catalyst; Figure S4: In situ DRIFTS spectra of the Mn<sub>0.05</sub>Co<sub>1</sub> and Co<sub>3</sub>O<sub>4</sub> catalysts after CH<sub>4</sub> adsorption for 15 min.

**Author Contributions:** Conceptualization, L.X., C.Y., H.X. and W.S.; Methodology, L.X., C.Y., S.W. and Z.H.; Software, L.X. and C.Y.; Validation, C.Y.; Formal analysis, L.X.; Investigation, L.X., S.W. and Z.H.; Resources, Z.H., H.X. and W.S.; Data curation, C.Y. and S.W.; Writing—original draft preparation, L.X.; Writing—review and editing, L.X., C.Y., Z.H., H.X. and W.S.; Visualization, L.X.; Supervision, Z.Y., S.S., H.X. and W.S.; Project administration, H.X. and W.S.; Funding acquisition, Z.H., H.X. and W.S. All authors have read and agreed to the published version of the manuscript.

**Funding:** This research was funded by Shanghai Science and Technology Committee (Grant No. 14DZ2273900), and the Solvay (China) Co. Ltd.

**Data Availability Statement:** The data is included in the article or Supplementary Materials.

**Conflicts of Interest:** The authors declare no conflict of interest.

## References

1. He, X.; Wallington, T.J.; Anderson, J.E.; Keoleian, G.A.; Shen, W.; De Kleine, R.; Kim, H.C.; Winkler, S. Life-Cycle Greenhouse Gas Emission Benefits of Natural Gas Vehicles. *ACS Sustain. Chem. Eng.* **2021**, *9*, 7813–7823. [CrossRef]
2. Gholami, R.; Smith, K.J. Activity of PdO/SiO<sub>2</sub> catalysts for CH<sub>4</sub> oxidation following thermal treatments. *Appl. Catal. B Environ.* **2015**, *168–169*, 156–163. [CrossRef]
3. Allen, D. Attributing Atmospheric Methane to Anthropogenic Emission Sources. *Acc. Chem. Res.* **2016**, *49*, 1344–1350. [CrossRef] [PubMed]
4. Ercolino, G.; Stelmachowski, P.; Grzybek, G.; Kotarba, A.; Specchia, S. Optimization of Pd catalysts supported on Co<sub>3</sub>O<sub>4</sub> for low-temperature lean combustion of residual methane. *Appl. Catal. B Environ.* **2017**, *206*, 712–725. [CrossRef]
5. De Rivas, B.; López-Fonseca, R.; Jiménez-González, C.; Gutiérrez-Ortiz, J.I. Highly active behaviour of nanocrystalline Co<sub>3</sub>O<sub>4</sub> from oxalate nanorods in the oxidation of chlorinated short chain alkanes. *Chem. Eng. J.* **2012**, *184*, 184–192. [CrossRef]
6. Zhu, Z.; Lu, G.; Zhang, Z.; Guo, Y.; Guo, Y.; Wang, Y. Highly Active and Stable Co<sub>3</sub>O<sub>4</sub>/ZSM-5 Catalyst for Propane Oxidation: Effect of the Preparation Method. *ACS Catal.* **2013**, *3*, 1154–1164. [CrossRef]
7. Dietl, N.; Schlangen, M.; Schwarz, H. Thermal hydrogen-atom transfer from methane: The role of radicals and spin states in oxo-cluster chemistry. *Angew. Chem. Int. Ed. Engl.* **2012**, *51*, 5544–5555. [CrossRef]
8. Choudhary, T.V.; Banerjee, S.; Choudhary, V.R. Catalysts for combustion of methane and lower alkanes. *Appl. Catal. A Gen.* **2002**, *234*, 1–23. [CrossRef]
9. Liotta, L.F.; Wu, H.; Pantaleo, G.; Venezia, A.M. Co<sub>3</sub>O<sub>4</sub> nanocrystals and Co<sub>3</sub>O<sub>4</sub>-MO<sub>x</sub> binary oxides for CO, CH<sub>4</sub> and VOC oxidation at low temperatures: A review. *Catal. Sci. Technol.* **2013**, *3*, 3085–3102. [CrossRef]
10. Kim, S.C.; Shim, W.G. Catalytic combustion of VOCs over a series of manganese oxide catalysts. *Appl. Catal. B Environ.* **2010**, *98*, 180–185. [CrossRef]
11. Huang, Z.; Wei, Y.; Song, Z.; Luo, J.; Mao, Y.; Gao, J.; Zhang, X.; Niu, C.; Kang, H.; Wang, Z. Three-dimensional (3D) hierarchical Mn<sub>2</sub>O<sub>3</sub> catalysts with the highly efficient purification of benzene combustion. *Sep. Purif. Technol.* **2021**, *255*, 117633. [CrossRef]
12. Ji, J.; Lu, X.; Chen, C.; He, M.; Huang, H. Potassium-modulated δ-MnO<sub>2</sub> as robust catalysts for formaldehyde oxidation at room temperature. *Appl. Catal. B Environ.* **2020**, *260*, 118210. [CrossRef]
13. Wang, F.; Dai, H.; Deng, J.; Bai, G.; Ji, K.; Liu, Y. Manganese oxides with rod-, wire-, tube-, and flower-like morphologies: Highly effective catalysts for the removal of toluene. *Environ. Sci. Technol.* **2012**, *46*, 4034–4041. [CrossRef]
14. Li, G.; Zhang, C.; Wang, Z.; Huang, H.; Peng, H.; Li, X. Fabrication of mesoporous Co<sub>3</sub>O<sub>4</sub> oxides by acid treatment and their catalytic performances for toluene oxidation. *Appl. Catal. A Gen.* **2018**, *550*, 67–76. [CrossRef]
15. Zhang, X.; Wei, Y.; Song, Z.; Liu, W.; Gao, C.; Luo, J. Silicotungstic acid modified CeO<sub>2</sub> catalyst with high stability for the catalytic combustion of chlorobenzene. *Chemosphere* **2021**, *263*, 128129. [CrossRef] [PubMed]
16. Wang, H.; Guo, W.; Jiang, Z.; Yang, R.; Jiang, Z.; Pan, Y.; Shanguan, W. New insight into the enhanced activity of ordered mesoporous nickel oxide in formaldehyde catalytic oxidation reactions. *J. Catal.* **2018**, *361*, 370–383. [CrossRef]
17. Cai, T.; Yuan, J.; Zhang, L.; Yang, L.; Tong, Q.; Ge, M.; Xiao, B.; Zhang, X.; Zhao, K.; He, D. Ni-Co-O solid solution dispersed nanocrystalline Co<sub>3</sub>O<sub>4</sub> as a highly active catalyst for low-temperature propane combustion. *Catal. Sci. Technol.* **2018**, *8*, 5416–5427. [CrossRef]
18. Castaño, M.H.; Molina, R.; Moreno, S. Cooperative effect of the Co-Mn mixed oxides for the catalytic oxidation of VOCs: Influence of the synthesis method. *Appl. Catal. A Gen.* **2015**, *492*, 48–59. [CrossRef]
19. Hu, Z.; Qiu, S.; You, Y.; Guo, Y.; Guo, Y.; Wang, L.; Zhan, W.; Lu, G. Hydrothermal synthesis of NiCeO<sub>x</sub> nanosheets and its application to the total oxidation of propane. *Appl. Catal. B Environ.* **2018**, *225*, 110–120. [CrossRef]
20. Luo, M.; Cheng, Y.; Peng, X.; Pan, W. Copper modified manganese oxide with tunnel structure as efficient catalyst for low-temperature catalytic combustion of toluene. *Chem. Eng. J.* **2019**, *369*, 758–765. [CrossRef]
21. Zhang, X.; Zhao, M.; Song, Z.; Zhao, H.; Liu, W.; Zhao, J.; Ma, Z.A.; Xing, Y. The effect of different metal oxides on the catalytic activity of a Co<sub>3</sub>O<sub>4</sub> catalyst for toluene combustion: Importance of the structure–property relationship and surface active species. *New J. Chem.* **2019**, *43*, 10868–10877. [CrossRef]
22. Chen, L.; Jia, J.; Ran, R.; Song, X. Nickel doping MnO<sub>2</sub> with abundant surface pits as highly efficient catalysts for propane deep oxidation. *Chem. Eng. J.* **2019**, *369*, 1129–1137. [CrossRef]
23. Pu, Z.; Zhou, H.; Zheng, Y.; Huang, W.; Li, X. Enhanced methane combustion over Co<sub>3</sub>O<sub>4</sub> catalysts prepared by a facile precipitation method: Effect of aging time. *Appl. Surf. Sci.* **2017**, *410*, 14–21. [CrossRef]
24. Zheng, Y.; Liu, Y.; Zhou, H.; Huang, W.; Pu, Z. Complete combustion of methane over Co<sub>3</sub>O<sub>4</sub> catalysts: Influence of pH values. *J. Alloys Compd.* **2018**, *734*, 112–120. [CrossRef]
25. El-Shobaky, H.G.; Shouman, M.A.; Attia, A.A. Effect of La<sub>2</sub>O<sub>3</sub> and Mn<sub>2</sub>O<sub>3</sub>-doping of Co<sub>3</sub>O<sub>4</sub>/Al<sub>2</sub>O<sub>3</sub> system on its surface and catalytic properties. *Collids Surf. A* **2006**, *274*, 62–70. [CrossRef]
26. Tang, X.; Gao, F.; Xiang, Y.; Yi, H.; Zhao, S. Low temperature catalytic oxidation of nitric oxide over the Mn-CoO<sub>x</sub> catalyst modified by nonthermal plasma. *Catal. Commun.* **2015**, *64*, 12–17. [CrossRef]


27. Wu, M.; Zhan, W.; Guo, Y.; Guo, Y.; Wang, Y.; Wang, L.; Lu, G. An effective Mn–Co mixed oxide catalyst for the solvent-free selective oxidation of cyclohexane with molecular oxygen. *Appl. Catal. A Gen.* **2016**, *523*, 97–106. [CrossRef]
28. Chang, T.; Shen, Z.; Huang, Y.; Lu, J.; Ren, D.; Sun, J.; Cao, J.; Liu, H. Post-plasma-catalytic removal of toluene using MnO<sub>2</sub>–Co<sub>3</sub>O<sub>4</sub> catalysts and their synergistic mechanism. *Chem. Eng. J.* **2018**, *348*, 15–25. [CrossRef]
29. Du Preez, S.P.; Bessarabov, D.G. The effects of bismuth and tin on the mechanochemical processing of aluminum-based composites for hydrogen generation purposes. *Int. J. Hydrogen Energy* **2019**, *44*, 21896–21912. [CrossRef]
30. Farhang, Y.; Taheri-Nassaj, E.; Rezaei, M. Pd doped LaSrCuO<sub>4</sub> perovskite nano-catalysts synthesized by a novel solid state method for CO oxidation and Methane combustion. *Ceram. Int.* **2018**, *44*, 21499–21506. [CrossRef]
31. Medina, B.; Verdério Fressati, M.G.; Gonçalves, J.M.; Bezerra, F.M.; Pereira Scacchetti, F.A.; Moisés, M.P.; Bail, A.; Samulewski, R.B. Solventless preparation of Fe<sub>3</sub>O<sub>4</sub> and Co<sub>3</sub>O<sub>4</sub> nanoparticles: A mechanochemical approach. *Mater. Chem. Phys.* **2019**, *226*, 318–322. [CrossRef]
32. Akbari, E.; Alavi, S.M.; Rezaei, M.; Larimi, A. Barium promoted manganese oxide catalysts in low-temperature methane catalytic combustion. *Int. J. Hydrogen Energy* **2021**, *46*, 5181–5196. [CrossRef]
33. Amol, P.; Amrute, Z.L.; Schreyer, H.; Weidenthaler, C.; Schüth, F. High-surface-area corundum by mechanochemically induced phase transformation of boehmite. *Science* **2019**, *366*, 485–489.
34. Tang, W.; Xiao, W.; Wang, S.; Ren, Z.; Ding, J.; Gao, P.-X. Boosting catalytic propane oxidation over PGM-free Co<sub>3</sub>O<sub>4</sub> nanocrystal aggregates through chemical leaching: A comparative study with Pt and Pd based catalysts. *Appl. Catal. B Environ.* **2018**, *226*, 585–595. [CrossRef]
35. Chen, L.; Hu, J.; Richards, R.; Prikhodko, S.; Kodambaka, S. Synthesis and surface activity of single-crystalline Co<sub>3</sub>O<sub>4</sub> (111) holey nanosheets. *Nanoscale* **2010**, *2*, 1657–1660. [CrossRef] [PubMed]
36. Jiang, Y.; Wu, Y.; Xie, B. Moderate temperature synthesis of nanocrystalline Co<sub>3</sub>O<sub>4</sub> via gel hydrothermal oxidation. *Mater. Chem. Phys.* **2002**, *74*, 234–237. [CrossRef]
37. Zhai, G.; Wang, J.; Chen, Z.; An, W.; Men, Y. Boosting soot combustion efficiency of Co<sub>3</sub>O<sub>4</sub> nanocrystals via tailoring crystal facets. *Chem. Eng. J.* **2018**, *337*, 488–498. [CrossRef]
38. Solsona, B.; Vázquez, I.; Garcia, T.; Davies, T.E.; Taylor, S.H. Complete oxidation of short chain alkanes using a nanocrystalline cobalt oxide catalyst. *Catal. Lett.* **2007**, *116*, 116–121. [CrossRef]
39. Ma, J.; Wang, C.; He, H. Transition metal doped cryptomelane-type manganese oxide catalysts for ozone decomposition. *Appl. Catal. B Environ.* **2017**, *201*, 503–510. [CrossRef]
40. Todorova, S.; Kolev, H.; Holgado, J.P.; Kadinov, G.; Bonev, C.; Pereñíguez, R.; Caballero, A. Complete n-hexane oxidation over supported Mn–Co catalysts. *Appl. Catal. B Environ.* **2010**, *94*, 46–54. [CrossRef]
41. Zheng, Y.; Wang, W.; Jiang, D.; Zhang, L. Amorphous MnO<sub>x</sub> modified Co<sub>3</sub>O<sub>4</sub> for formaldehyde oxidation: Improved low-temperature catalytic and photothermocatalytic activity. *Chem. Eng. J.* **2016**, *284*, 21–27. [CrossRef]
42. Qiu, M.; Zhan, S.; Yu, H.; Zhu, D. Low-temperature selective catalytic reduction of NO with NH<sub>3</sub> over ordered mesoporous Mn<sub>x</sub>Co<sub>3-x</sub>O<sub>4</sub> catalyst. *Catal. Commun.* **2015**, *62*, 107–111. [CrossRef]
43. Chuang, T.J.; Brundle, C.R.; Rice, D.W. Interpretation of the X-ray photoemission spectra of cobalt oxides and cobalt oxide surfaces. *Surf. Sci.* **1976**, *59*, 413–429. [CrossRef]
44. González-Prior, J.; López-Fonseca, R.; Gutiérrez-Ortiz, J.I.; de Rivas, B. Catalytic removal of chlorinated compounds over ordered mesoporous cobalt oxides synthesised by hard-templating. *Appl. Catal. B Environ.* **2018**, *222*, 9–17. [CrossRef]
45. Luo, Y.; Zheng, Y.; Zuo, J.; Feng, X.; Wang, X.; Zhang, T.; Zhang, K.; Jiang, L. Insights into the high performance of Mn–Co oxides derived from metal-organic frameworks for total toluene oxidation. *J. Hazard. Mater.* **2018**, *349*, 119–127. [CrossRef] [PubMed]
46. Li, K.; Xu, D.; Liu, K.; Ni, H.; Shen, F.; Chen, T.; Guan, B.; Zhan, R.; Huang, Z.; Lin, H. Catalytic Combustion of Lean Methane Assisted by Electric Field over Mn<sub>x</sub>Co<sub>y</sub> Catalysts at Low Temperature. *J. Phys. Chem. C* **2019**, *123*, 10377–10388. [CrossRef]
47. Amri, A.; Duan, X.; Yin, C.-Y.; Jiang, Z.-T.; Rahman, M.M.; Pryor, T. Solar absorptance of copper–cobalt oxide thin film coatings with nano-size, grain-like morphology: Optimization and synchrotron radiation XPS studies. *Appl. Surf. Sci.* **2013**, *275*, 127–135. [CrossRef]
48. Huang, Z.; Zhao, M.; Luo, J.; Zhang, X.; Liu, W.; Wei, Y.; Zhao, J.; Song, Z. Interaction in LaO<sub>x</sub>–Co<sub>3</sub>O<sub>4</sub> for highly efficient purification of toluene: Insight into LaO<sub>x</sub> content and synergistic effect contribution. *Sep. Purif. Technol.* **2020**, *251*, 117369. [CrossRef]
49. Jia, J.; Zhang, P.; Chen, L. Catalytic decomposition of gaseous ozone over manganese dioxides with different crystal structures. *Appl. Catal. B Environ.* **2016**, *189*, 210–218. [CrossRef]
50. Zhang, X.; Zhao, J.; Song, Z.; Liu, W.; Zhao, H.; Zhao, M.; Xing, Y.; Ma, Z.; Du, H. The catalytic oxidation performance of toluene over the Ce–Mn–O<sub>x</sub> catalysts: Effect of synthetic routes. *J. Colloid. Interface Sci.* **2020**, *562*, 170–181. [CrossRef] [PubMed]
51. Liu, Y.; Zhao, P.; Sun, L.; Feng, N.; Wang, L.; Wan, H.; Guan, G. Surface Modification of Cobalt–Manganese Mixed Oxide and Its Application for Low-Temperature Propane Catalytic Combustion. *ChemistrySelect* **2021**, *6*, 522–531. [CrossRef]
52. Liotta, L.F.; Di Carlo, G.; Pantaleo, G.; Venezia, A.M.; Deganello, G. Co<sub>3</sub>O<sub>4</sub>/CeO<sub>2</sub> composite oxides for methane emissions abatement: Relationship between Co<sub>3</sub>O<sub>4</sub>–CeO<sub>2</sub> interaction and catalytic activity. *Appl. Catal. B Environ.* **2006**, *66*, 217–227. [CrossRef]

53. Puértolas, B.; Smith, A.; Vázquez, I.; Dejoz, A.; Moragues, A.; Garcia, T.; Solsona, B. The different catalytic behaviour in the propane total oxidation of cobalt and manganese oxides prepared by a wet combustion procedure. *Chem. Eng. J.* **2013**, *229*, 547–558. [CrossRef]
54. Todorova, S.; Naydenov, A.; Kolev, H.; Holgado, J.P.; Ivanov, G.; Kadinov, G.; Caballero, A. Mechanism of complete n-hexane oxidation on silica supported cobalt and manganese catalysts. *Appl. Catal. A Gen.* **2012**, *413–414*, 43–51. [CrossRef]
55. Zhao, Z.; Bao, T.; Zeng, Y.; Wang, G.; Muhammad, T. Efficient cobalt–manganese oxide catalyst deposited on modified AC with unprecedented catalytic performance in CO preferential oxidation. *Catal. Commun.* **2013**, *32*, 47–51. [CrossRef]
56. Morales, M.R.; Barbero, B.P.; Cadús, L.E. Combustion of volatile organic compounds on manganese iron or nickel mixed oxide catalysts. *Appl. Catal. B Environ.* **2007**, *74*, 1–10. [CrossRef]
57. Xue, L.; Zhang, C.; He, H.; Teraoka, Y. Catalytic decomposition of N<sub>2</sub>O over CeO<sub>2</sub> promoted Co<sub>3</sub>O<sub>4</sub> spinel catalyst. *Appl. Catal. B Environ.* **2007**, *75*, 167–174. [CrossRef]
58. Li, J.; Liang, X.; Xu, S.; Hao, J. Catalytic performance of manganese cobalt oxides on methane combustion at low temperature. *Appl. Catal. B Environ.* **2009**, *90*, 307–312. [CrossRef]
59. Schmal, M.; Souza, M.; Alegre, V.; Dasilva, M.; Cesar, D.; Perez, C. Methane oxidation—effect of support, precursor and pretreatment conditions—in situ reaction XPS and DRIFT. *Catal. Today* **2006**, *118*, 392–401. [CrossRef]
60. Xiong, J.; Mo, S.; Song, L.; Fu, M.; Chen, P.; Wu, J.; Chen, L.; Ye, D. Outstanding stability and highly efficient methane oxidation performance of palladium-embedded ultrathin mesoporous Co<sub>2</sub>MnO<sub>4</sub> spinel catalyst. *Appl. Catal. A Gen.* **2020**, *598*, 117571. [CrossRef]
61. Wang, X.; Liu, Y.; Zhang, Y.; Zhang, T.; Chang, H.; Zhang, Y.; Jiang, L. Structural requirements of manganese oxides for methane oxidation: XAS spectroscopy and transition-state studies. *Appl. Catal. B Environ.* **2018**, *229*, 52–62. [CrossRef]
62. Zhao, S.; Li, K.; Jiang, S.; Li, J. Pd–Co based spinel oxides derived from pd nanoparticles immobilized on layered double hydroxides for toluene combustion. *Appl. Catal. B Environ.* **2016**, *181*, 236–248. [CrossRef]

**Disclaimer/Publisher’s Note:** The statements, opinions and data contained in all publications are solely those of the individual author(s) and contributor(s) and not of MDPI and/or the editor(s). MDPI and/or the editor(s) disclaim responsibility for any injury to people or property resulting from any ideas, methods, instructions or products referred to in the content.

## Article

# Photocatalytic CO<sub>2</sub> Reduction to CH<sub>4</sub> and Dye Degradation Using Bismuth Oxychloride/Bismuth Oxyiodide/Graphitic Carbon Nitride (BiO<sub>m</sub>Cl<sub>n</sub>/BiO<sub>p</sub>I<sub>q</sub>/g-C<sub>3</sub>N<sub>4</sub>) Nanocomposite with Enhanced Visible-Light Photocatalytic Activity

Yong-Ming Dai <sup>1</sup>, Wu-Tsan Wu <sup>2</sup>, Yu-Yun Lin <sup>2</sup>, Hsiao-Li Wu <sup>2</sup>, Szu-Han Chen <sup>2</sup>, Jih-Mirn Jehng <sup>3</sup> , Jia-Hao Lin <sup>2</sup>, Fu-Yu Liu <sup>2</sup> and Chiing-Chang Chen <sup>2,\*</sup> 

<sup>1</sup> Department of Chemical and Materials Engineering, National Chin-Yi University of Technology, Taichung 411, Taiwan

<sup>2</sup> Department of Science Education and Application, National Taichung University of Education, Taichung 403, Taiwan

<sup>3</sup> Department of Chemical Engineering, National Chung Hsing University, Taichung 402, Taiwan

\* Correspondence: ccchen@mail.ntcu.edu.tw; Tel.: +886-4-2218-3406; Fax: +886-4-2218-3560

**Abstract:** The use of visible-light-driven photocatalysts in wastewater treatment, photoreduction of CO<sub>2</sub>, green solar fuels, and solar cells has elicited substantial research attention. Bismuth oxyhalide and its derivatives are a group of visible-light photocatalysts that can diminish electron-hole recombination in layered structures and boost photocatalytic activity. The energy bandgap of these photocatalysts lies in the range of visible light. A simple hydrothermal method was applied to fabricate a series of bismuth oxychloride/bismuth oxyiodide/grafted graphitic carbon nitride (BiO<sub>m</sub>Cl<sub>n</sub>/BiO<sub>p</sub>I<sub>q</sub>/g-C<sub>3</sub>N<sub>4</sub>) sheets with different contents of g-C<sub>3</sub>N<sub>4</sub>. The fabricated sheets were characterized through XRD, TEM, SEM-EDS, XPS, UV-vis DRS, PL, and BET. The conversion efficiency of CO<sub>2</sub> reduction to CH<sub>4</sub> of BiO<sub>m</sub>Cl<sub>n</sub>/BiO<sub>p</sub>I<sub>q</sub> of 4.09 μmol g<sup>-1</sup> can be increased to 39.43 μmol g<sup>-1</sup> by compositing with g-C<sub>3</sub>N<sub>4</sub>. It had an approximately 9.64 times improvement. The photodegradation rate constant for crystal violet (CV) dye of BiO<sub>m</sub>Cl<sub>n</sub>/BiO<sub>p</sub>I<sub>q</sub> of  $k = 0.0684$  can be increased to 0.2456 by compositing with g-C<sub>3</sub>N<sub>4</sub>. It had an approximately 3.6 times improvement. The electron paramagnetic resonance results and the quenching effects indicated that <sup>1</sup>O<sub>2</sub>, •OH, h<sup>+</sup>, and •O<sub>2</sub><sup>-</sup> were active species in the aforementioned photocatalytic degradation. Because of their heterojunction, the prepared ternary nanocomposites possessed the characteristics of a heterojunction of type II band alignment.

**Keywords:** composites; photocatalysis; BiO<sub>m</sub>Cl<sub>n</sub>; BiO<sub>p</sub>Br<sub>q</sub>; g-C<sub>3</sub>N<sub>4</sub>; CO<sub>2</sub> reduction

**Citation:** Dai, Y.-M.; Wu, W.-T.; Lin, Y.-Y.; Wu, H.-L.; Chen, S.-H.; Jehng, J.-M.; Lin, J.-H.; Liu, F.-Y.; Chen, C.-C. Photocatalytic CO<sub>2</sub> Reduction to CH<sub>4</sub> and Dye Degradation Using Bismuth Oxychloride/Bismuth Oxyiodide/Graphitic Carbon Nitride (BiO<sub>m</sub>Cl<sub>n</sub>/BiO<sub>p</sub>I<sub>q</sub>/g-C<sub>3</sub>N<sub>4</sub>) Nanocomposite with Enhanced Visible-Light Photocatalytic Activity. *Catalysts* **2023**, *13*, 522. <https://doi.org/10.3390/catal13030522>

Academic Editors: Juan José Rueda-Márquez, Javier Moreno-Andrés and Irina Levchuk

Received: 1 February 2023

Revised: 21 February 2023

Accepted: 1 March 2023

Published: 3 March 2023



**Copyright:** © 2023 by the authors. Licensee MDPI, Basel, Switzerland. This article is an open access article distributed under the terms and conditions of the Creative Commons Attribution (CC BY) license (<https://creativecommons.org/licenses/by/4.0/>).

## 1. Introduction

Semiconductor photocatalysis is an effective green technology because it can completely decompose environmental pollutants under mild conditions. The applications of semiconductor photocatalysts have elicited much scholarly attention for use in the treatment of organic pollutants because these photocatalysts can transform solar energy into chemical energy [1]. In addition, photocatalysts can also be used in the reduction of CO<sub>2</sub> and/or the construction of solar cells [2–6]. Since Fujishima and Honda reported the photocatalytic decomposition of water on the surface of TiO<sub>2</sub>, TiO<sub>2</sub> has been widely studied to degrade pollutants or decompose water. However, the wide band gap (3.0–3.2 eV) of TiO<sub>2</sub> limits its application range [7]. Because the band gap in this range can only be applied to UV light with a small energy proportion in solar energy for photocatalysis, if the band gap can be reduced to below 2.5 eV, visible light can also be applied for photocatalysis, which accounts for a larger proportion of solar energy, and can be used more effectively.

Many semiconductor photocatalysts have been developed, including TiO<sub>2</sub>, Fe<sub>2</sub>O<sub>3</sub>, CuO, and BiOX (X = I, Br, Cl). In particular, BiOX photocatalysts have drawn much research

interest due to their unique electronic structure [8–11]. Bismuth oxychloride (BiOCl) was first discovered in the early 19th century, and other bismuth oxyhalides (e.g., BiOF, BiOBr, and BiOI) have been discovered since then. BiOX crystals contain a layered structure of  $[\text{Bi}_2\text{O}_2]^{2+}$ , which results in them having highly asymmetric electrical, magnetic, and optical properties; thus, BiOX is frequently used in industrial chemicals, such as pharmaceuticals, pigments, and organic catalysts [12,13]. In BiOX crystals, four X and four O atoms surround each Bi atom to form a uniform asymmetric decahedral geometric structure [12].  $[\text{Bi}_2\text{O}_2]^{2+}$  has a strong covalent bond, which connects to the  $[\text{X}]^-$  layer through the van der Waals force along the *c*-axis direction. Weak van der Waals forces and strong covalent bonds lead to the formation of layered structures.  $X_{np}$  ( $n = 3, 4,$  and  $5$  corresponding to  $X = \text{Cl}, \text{Br},$  and  $\text{I}$ , respectively) and  $\text{O}_{2p}$  occupy the top of the valence band of BiOX, and  $\text{Bi}_{6p}$  occupies the conduction band of BiOX [14]. Due to the unique atomic structure of BiOX, it has inherently superior photocatalytic properties. However, many bottlenecks must still be overcome to improve its performance in practical applications.

BiOX with the aforementioned compositions is a heterogeneous compound. There are heterojunctions between  $\text{BiO}_m\text{Cl}_n/\text{BiO}_p\text{I}_q$  and  $g\text{-C}_3\text{N}_4$ . The first study to use  $g\text{-C}_3\text{N}_4$  as a nonmetallic visible-light photocatalyst was published in 2008 [15]. However, because of the high electron–hole recombination rate of  $g\text{-C}_3\text{N}_4$ , its degradation efficiency is low; therefore, many studies have been conducted on composite photocatalysts containing  $g\text{-C}_3\text{N}_4$  [16,17]. Studies have reported that heterojunctions associated with perovskite materials, including  $\text{Bi}_2\text{SiO}_5\text{-}g\text{-C}_3\text{N}_4$  [18],  $\text{SrFeO}_3\text{-}g\text{-C}_3\text{N}_4$  [19],  $\text{BiOI-}g\text{-C}_3\text{N}_4$  [20],  $\text{PbBiO}_2\text{Br/}g\text{-C}_3\text{N}_4$  [21],  $\text{PbBiO}_2\text{I/Bi}_5\text{O}_7\text{I/}g\text{-C}_3\text{N}_4$  [22], and  $\text{PbBiO}_2\text{Br/PbO/}g\text{-C}_3\text{N}_4$  [23], exhibit high photocatalytic activity.

When two or more different band gap photocatalysts are combined together, the heterojunction between their interfaces often has a synergistic effect on their photocatalysis. Many scholars have conducted a lot of research on this phenomenon in the past ten years. For example, Li et al. proposed the concept of a heterostructure of type II band alignment [22,24–26]. In addition, there are also newer descriptions of Z-scheme and S-scheme effects in the literature by Wang et al. [27], Xu et al. [28], and Wang et al. [29].

This study synthesized a  $\text{BiO}_p\text{Cl}_g/\text{BiO}_x\text{I}_y$  compound and composited  $\text{BiO}_p\text{Cl}_g/\text{BiO}_x\text{I}_y$  with  $g\text{-C}_3\text{N}_4$  to separate photogenerated electron holes for achieving enhanced photocatalytic activity. The synthesized and composited photocatalyst materials were studied for the reduction of  $\text{CO}_2$  to  $\text{CH}_4$  and the degradation of CV dyes. At the same time, some discussions were made on the photocatalytic mechanism of prepared ternary nanocomposites.

## 2. Results and Discussion

### 2.1. Characterization of the Produced $\text{BiO}_m\text{Cl}_n/\text{BiO}_p\text{I}_q/g\text{-C}_3\text{N}_4$ Composites

The crystal phases of the 40 samples produced in this study were controlled by varying the sample synthesis ratio, solution pH, and reaction temperature. The hydrothermal time was 12 h; the molar ratio of Cl: I was 1:2 or 2:1; the solution pH was 1, 4, 7, 10, or 13; the reaction temperature was 100, 150, 200, or 250 °C. Table 1 presents the codes of the prepared samples.

#### 2.1.1. XRD Analysis

XRD analysis was conducted to identify the compounds present in the synthesized samples. Each compound has a unique diffraction spectrum, and an analysis of the diffraction spectrum of a sample can indicate its composition.

Figure 1 shows that materials with different weight percentages of  $g\text{-C}_3\text{N}_4$  (0, 2, 5, 10, 12, 15, 18, 20, and 55 wt%) were composited with the compound at a reaction temperature of 150 °C in 4 h. The synthesized samples were used to degrade CV dye to identify the catalyst with the highest degradation efficiency after electron–hole recombination. The XRD results of the BC112-250-4 sample agreed with those of  $\text{Bi}_3\text{O}_4\text{Cl}$  (diffraction peaks at  $2\theta$  values of approximately 9.5°, 24.0°, 29.1°, 29.7°, 31.4°, 41.6°, and 45.2°), BiOCl (diffraction peaks at  $2\theta$  values of approximately 12.0°, 24.1°, 25.9°, 32.5°, 33.5°, 40.9°, 46.7°, 49.7°, 54.1°, 55.1°, and

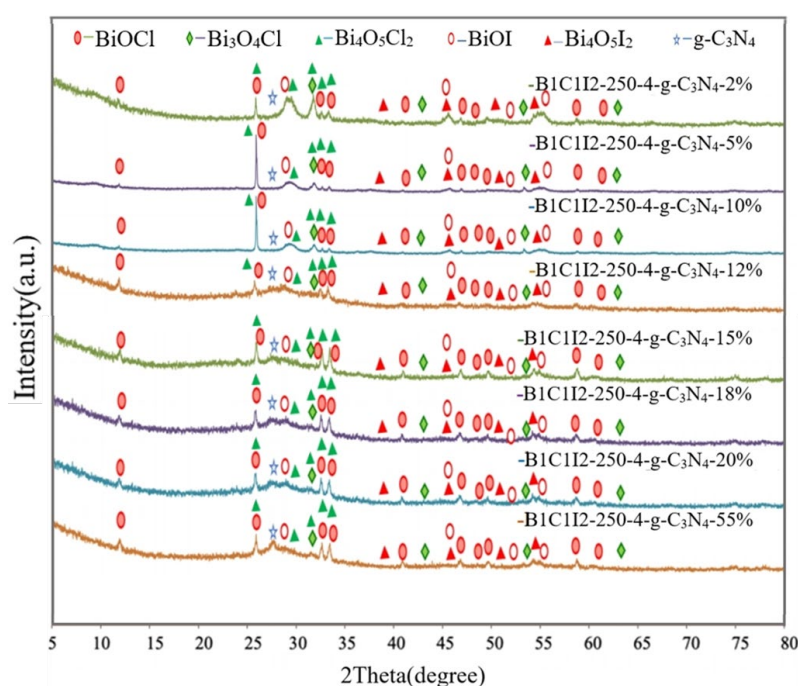
58.6°), BiOI (diffraction peaks at  $2\theta$  values of approximately 9.7°, 29.7°, 31.7°, 45.5°, 51.3°, and 55.3°),  $\text{Bi}_4\text{O}_5\text{I}_2$  (diffraction peaks at  $2\theta$  values of approximately 29.6°, 31.6°, 37.0°, 37.3°, 39.3°, 45.4°, 51.3°, and 55.1°), and  $\text{Bi}_4\text{O}_5\text{I}_2$  (diffraction peaks at  $2\theta$  values of approximately 7.2°, 24.0°, 31.3°, 32.03°, 33.88°, 35.5°, 40.5°, and 41.1°). Thus, the aforementioned sample contains a crystalline phase comprising  $\text{Bi}_3\text{O}_4\text{Cl}$ , BiOI, BiOCl,  $\text{Bi}_4\text{O}_5\text{Cl}_2$ , and  $\text{Bi}_4\text{O}_5\text{I}_2$ . Pure g- $\text{C}_3\text{N}_4$  has a relatively strong diffraction peak at 27°. Small quantities of g- $\text{C}_3\text{N}_4$  were added into the samples, and the strength of the samples decreased with decreases in the weight percentage of the added g- $\text{C}_3\text{N}_4$ . The aforementioned result verified the successful synthesis of heterogenous composite catalysts containing g- $\text{C}_3\text{N}_4$  in this study.

**Table 1.** Codes of the  $\text{BiO}_m\text{Cl}_n/\text{BiO}_p\text{I}_q$  samples produced under various reaction temperatures, different pH values, two KCl:KI molar ratios, and a reaction time of 12 h.

Molar Ratio (Cl:I = 1:2)				
pH	Temperature (°C)			
	100	150	200	250
1	B1C1I2-1-100-12	B1C1I2-1-150-12	B1C1I2-1-200-12	B1C1I2-1-250-12
4	B1C1I2-4-100-12	B1C1I2-4-150-12	B1C1I2-4-200-12	B1C1I2-4-250-12
7	B1C1I2-7-100-12	B1C1I2-7-150-12	B1C1I2-7-200-12	B1C1I2-7-250-12
10	B1C1I2-10-100-12	B1C1I2-10-150-12	B1C1I2-10-200-12	B1C1I2-10-250-12
13	B1C1I2-13-100-12	B1C1I2-13-150-12	B1C1I2-13-200-12	B1C1I2-13-250-12

Molar Ratio (Cl:I = 2:1)				
pH	Temperature (°C)			
	100	150	200	250
1	B1C2I1-1-100-12	B1C2I1-1-150-12	B1C2I1-1-200-12	B1C2I1-1-250-12
4	B1C2I1-4-100-12	B1C2I1-4-150-12	B1C2I1-4-200-12	B1C2I1-4-250-12
7	B1C2I1-7-100-12	B1C2I1-7-150-12	B1C2I1-7-200-12	B1C2I1-7-250-12
10	B1C2I1-10-100-12	B1C2I1-10-150-12	B1C2I1-10-200-12	B1C2I1-10-250-12
13	B1C2I1-13-100-12	B1C2I1-13-150-12	B1C2I1-13-200-12	B1C2I1-13-250-12



**Figure 1.** X-ray diffraction (XRD) patterns of the  $\text{BiO}_m\text{Cl}_n/\text{BiO}_p\text{I}_q/\text{g-C}_3\text{N}_4$  samples with g- $\text{C}_3\text{N}_4$  contents of 2%, 5%, 10%, 12%, 15%, 18%, 20%, and 55% that were prepared under a KCl:KI molar ratio of 1:2, a hydrothermal temperature of 250 °C, a pH of 4, and a reaction time of 12 h.



### 2.1.2. SEM and TEM

SEM and TEM mainly detect the morphology of samples. With the aid of their accessory equipment, functions such as detecting EDS, HR-TEM, and SAED can be added to determine the element composition and crystallinity of the sample. There are a lot of studies in the literature using SEM and TEM to detect the material properties of the bismuth oxyhalide photocatalyst [30–35]. With the different operating conditions for the synthesis of bismuth oxyhalide, the crystalline and morphology of the synthesized samples will also be different.

Figure 2a displays the bright-field TEM image of the BC112-4-250-g-C<sub>3</sub>N<sub>4</sub>-20% sample. The light part of this image represents g-C<sub>3</sub>N<sub>4</sub> and the dark part of this image represents BiOCl and BiOI. The image analysis of the aforementioned composite indicated that BiO<sub>m</sub>Cl<sub>n</sub>/BiO<sub>p</sub>I<sub>q</sub> was embedded in the sheet structure of g-C<sub>3</sub>N<sub>4</sub>. This phenomenon has similar results to BiOBr/g-C<sub>3</sub>N<sub>4</sub> [34]. It showed that g-C<sub>3</sub>N<sub>4</sub> coats other substances to become a wrinkled two-dimensional structure. When C<sub>3</sub>N<sub>4</sub> belongs to an amorphous structure, it becomes difficult to see the state of encapsulation [33]. Figure 2b depicts the HR-TEM image of the aforementioned sample. TEM and XRD analyses indicate that BC112-250-4-g-C<sub>3</sub>N<sub>4</sub>-20% was mainly composed of BiOCl (*d* = 0.368 nm) and BiOI (*d* = 0.281 nm). The aforementioned result is the result of comparing the HR-TEM image and the JCPDS crystallization parameters of XRD. This is good evidence for the crystallization condition of the sample. Figure 2c presents the SAED pattern of this sample. The light spots were arranged in an aperture; therefore, the aforementioned sample was speculated to have a polycrystalline nature, and from the comparison of the pattern with XRD results, it can be proved that the samples in the figure correspond to BiOCl (110) and BiOI (002), respectively. Compared with the result of [34], the crystallinity of our sample is slightly inferior to [34]. Figure 2d illustrates the EDS results of BC112-4-250-g-C<sub>3</sub>N<sub>4</sub>-20%, with the ratio of each element being presented in the inset. The EDS results indicated that the aforementioned sample contained Bi, Cl, I, O, C, and N, which evinced the successful synthesis of BC112-4-250-g-C<sub>3</sub>N<sub>4</sub>-20%.

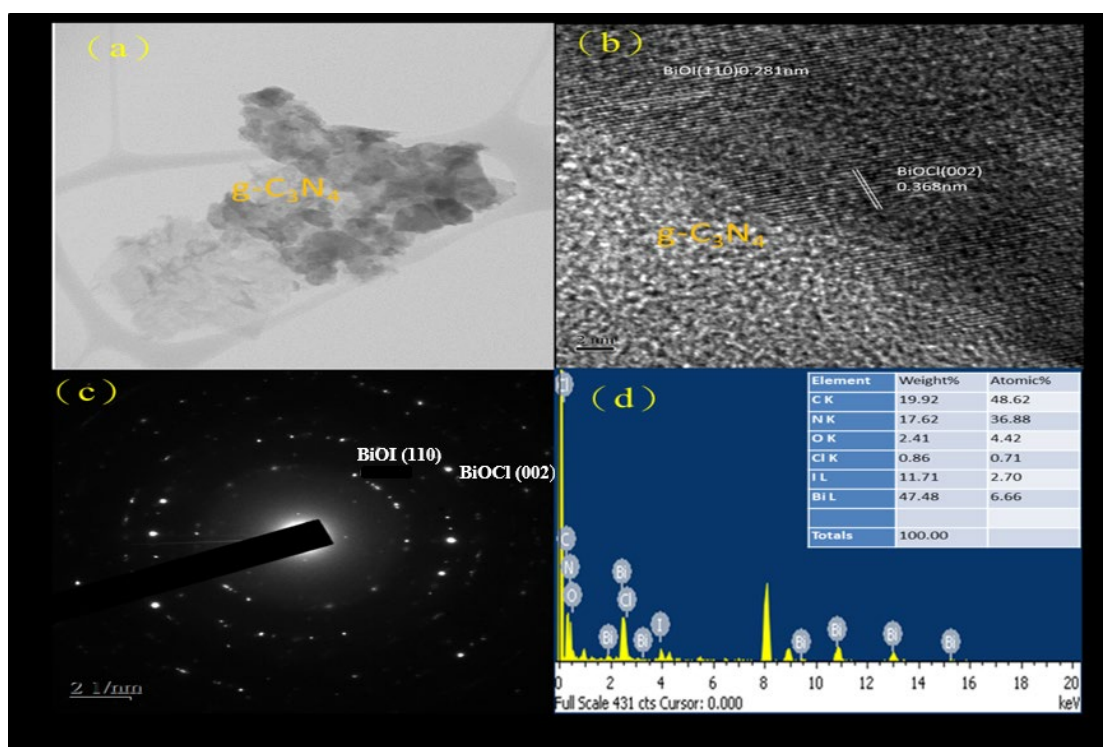


**Figure 2.** (a) FE-TEM image, (b) HR-TEM image, (c) SAD and (d) EDS of the BC112-250-4-g-C<sub>3</sub>N<sub>4</sub>-20% sample prepared using the hydrothermal autoclave method.

### 2.1.3. Analysis of XPS Spectra

In XPS, X-rays are used to excite electrons in the inner shells of atoms for quantitatively analyzing the electronic and chemical states of the elements in a material. Therefore, this method is also called electron spectroscopy for chemical analysis (ESCA). The electronic transition state in the principal quantum orbital can be quantitatively analyzed using XPS, and the electronic transition state in the angular quantum orbital can be examined through the deconvolution of the XPS spectrum. XPS also indicates whether the bonding energy of a substance has changed. An X-ray photoelectron spectrometer can be used to analyze the valence state and configuration of a sample. Moreover, the elemental composition of a sample can be determined from its XPS spectrum. Figure 3a displays the complete XPS spectra of BC1I2-250-4 and BC1I2-250-4-g-C<sub>3</sub>N<sub>4</sub>-20%. As depicted in the aforementioned figure, the photoelectrons used in XPS excited the I 3p, Bi 4p, I 3d, O 1s, Bi 4f, Bi 4d, N 1s, C 1s, Cl 2p, Bi 4f, I 4d, O 2s, and Bi 5d energy levels of the aforementioned samples. Our lab has performed XPS analysis on BiO<sub>x</sub>Cl<sub>y</sub>/BiO<sub>m</sub>Br<sub>n</sub>/g-C<sub>3</sub>N<sub>4</sub> and determined its XPS pattern [31].

Figure 3b displays the Bi 4f diagram of BC1I2-250-4 and BC1I2-250-4-g-C<sub>3</sub>N<sub>4</sub>-20%. In this figure, peaks representing Bi<sup>3+</sup> were located at 158.3 and 163.6 eV and the characteristic peak positions representing Bi<sup>+3-x</sup> were located at 155.9 and 161.3 eV. By contrast, Bi<sup>+3-x</sup> peaks were not observed in [31]. Subtle differences existed in the bonding electronic configurations of Bi in BiO<sub>m</sub>Cl<sub>n</sub>/BiO<sub>p</sub>I<sub>q</sub> and BiO<sub>x</sub>Cl<sub>y</sub>/BiO<sub>m</sub>Br<sub>n</sub>. However, the same trend was observed in the right displacement caused by the addition of g-C<sub>3</sub>N<sub>4</sub> for both aforementioned composites. The aforementioned result was obtained because when Bi was partially synthesized with the iodine element using a high-pressure hydrothermal method, it would be reduced to a low valence state that corresponds to the signals of the 4d<sub>3/2</sub>, 4d<sub>5/2</sub>, 4f<sub>5/2</sub>, 4f<sub>7/2</sub>, and 5d states. Figure 3c shows the O1s peaks of BC1I2-250-4 and BC1I2-250-4-g-C<sub>3</sub>N<sub>4</sub>-20%. The full-width at half-maximum (FWHM) of Bi<sup>+3</sup>-O was 0.9863–1.1920 eV, and the FWHM of Bi<sup>+3-x</sup>-O was 1.7639–2.6427 eV. The BiO<sub>x</sub>Cl<sub>y</sub>/BiO<sub>m</sub>Br<sub>n</sub> spectrum obtained in [31] contained only a single peak, whereas the BiO<sub>m</sub>Cl<sub>n</sub>/BiO<sub>p</sub>I<sub>q</sub> spectrum obtained in this study contained two peaks. This observation was probably because the splitting of Bi into two valence states, namely Bi<sup>+3</sup> and Bi<sup>+3-x</sup>, results in the splitting of O into two valence states. Figure 3d presents the N1s diagram of g-C<sub>3</sub>N<sub>4</sub> and BC1I2-250-4-g-C<sub>3</sub>N<sub>4</sub>-20%. The FWHM of C=NC was 1.1464–1.1773 eV, and the FWHM of N-(C)<sub>3</sub> and HN-(C)<sub>2</sub> was 1.9754–2.133 eV. These results are consistent with those obtained in [31]. Thus, both BiO<sub>m</sub>Cl<sub>n</sub>/BiO<sub>p</sub>I<sub>q</sub> and BiO<sub>x</sub>Cl<sub>y</sub>/BiO<sub>m</sub>Br<sub>n</sub> can be composited with g-C<sub>3</sub>N<sub>4</sub>. Figure 3e displays the Cl 2p narrow spectrum of BC1I2-250-4 and BC1I2-250-4-g-C<sub>3</sub>N<sub>4</sub>-20%, whose Cl 2p peaks were located at 196.8 and 198.7 eV, respectively, which corresponded to 2p<sub>3/2</sub> and 2p<sub>1/2</sub>. The aforementioned peaks are the characteristic peaks of Cl, which agrees with the results of [31]. Figure 3f illustrates the C 1s narrow spectra of BC1I2-250-4-g-C<sub>3</sub>N<sub>4</sub>-20% and g-C<sub>3</sub>N<sub>4</sub>. The C1s spectrum of BC1I2-250-4-g-C<sub>3</sub>N<sub>4</sub>-20% exhibited two peaks that corresponded to binding energies of approximately 284.4 and 287.8 eV. This result agrees with that in [31]. As displayed in Figure 3g, the binding energy of the characteristic positions of I was 617.8–629.7 eV, with the binding energies of 617.8 and 629.7 eV corresponding to I3d<sub>5/2</sub> and I3d<sub>3/2</sub>. This result is in line with those obtained in previous studies for the BiO<sub>x</sub>I<sub>y</sub> [36] and BiO<sub>x</sub>Cl<sub>y</sub>/BiO<sub>m</sub>Br<sub>n</sub>/BiO<sub>p</sub>I<sub>q</sub> [32] composites. A system containing I in the form of PbBiO<sub>2</sub>I/Bi<sub>5</sub>O<sub>7</sub>I/g-C<sub>3</sub>N<sub>4</sub> has a complex but consistent peak distribution in [22].

### 2.1.4. UV–Vis DRS Analysis

The energy bandgaps (*E<sub>g</sub>*) of the samples were calculated from the data obtained using UV–vis DRS and the Tauc plot method [14,37]. Some of the results and discussion of this work are shown in the Supplementary Materials. All *E<sub>g</sub>* were in the visible light range (400 nm < λ < 700 nm, or 1.77 eV < *E<sub>g</sub>* < 3.1 eV). Therefore, it can be expected that the photocatalysts of this work are promising to utilize most of the energy of sunlight for photocatalysis.

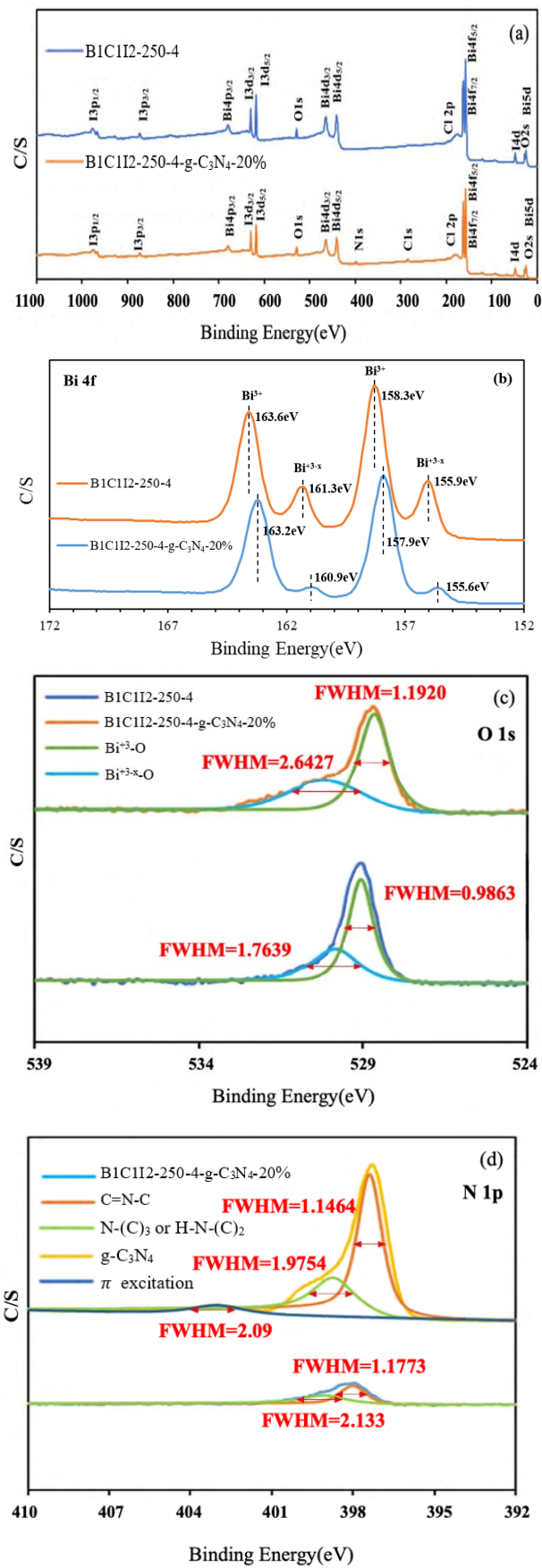
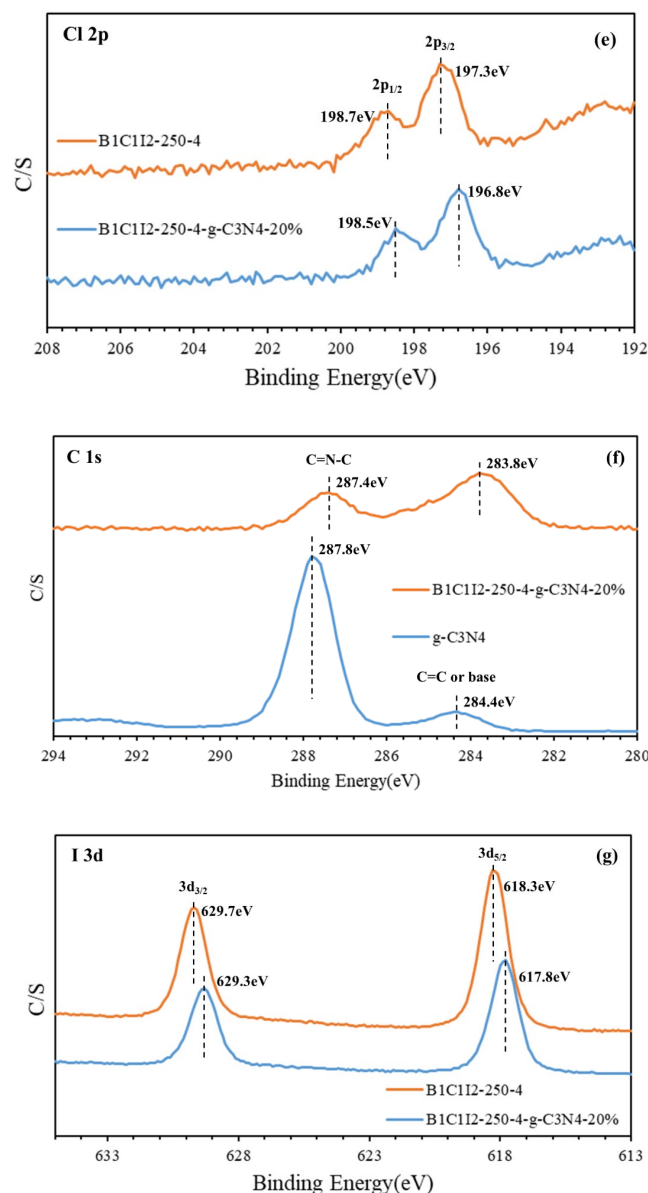
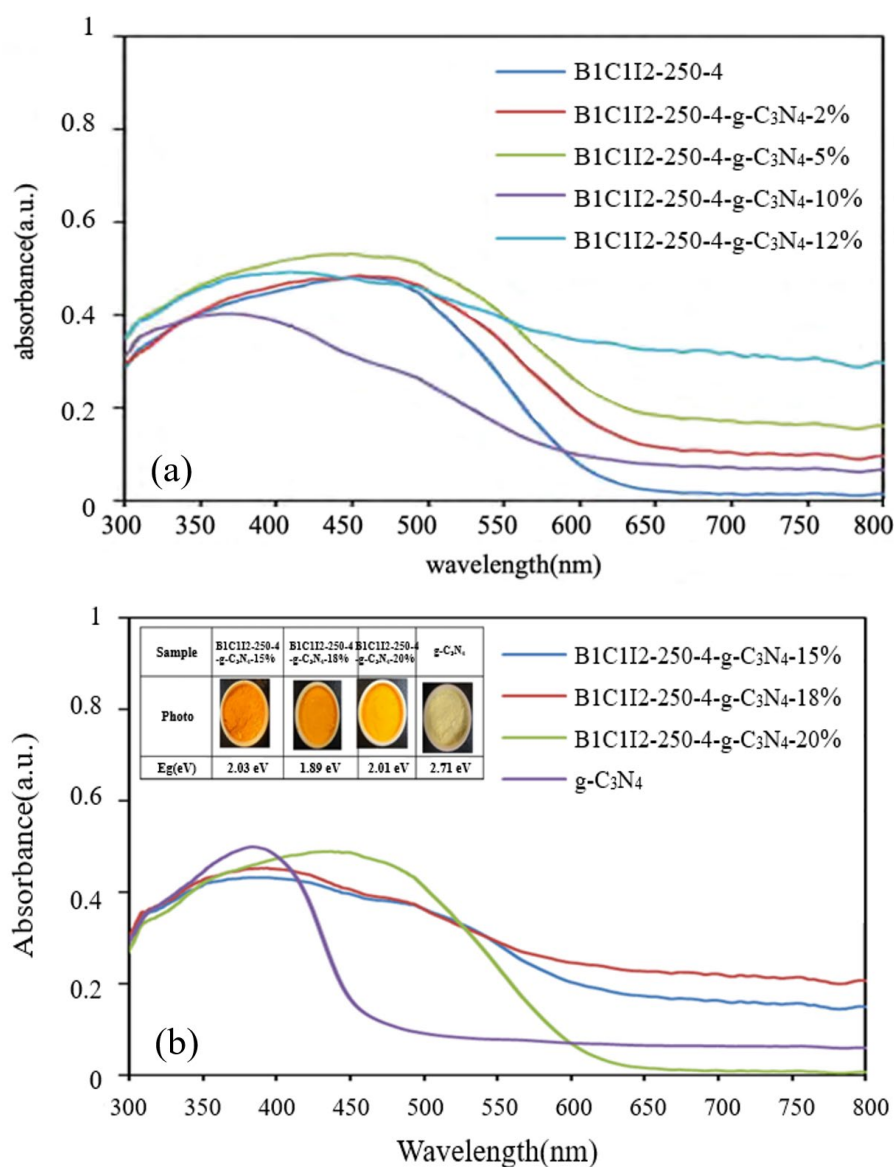


Figure 3. Cont.



**Figure 3.** High-resolution X-ray photoelectron spectroscopy spectra of the BiO<sub>m</sub>Cl<sub>n</sub>/BiO<sub>p</sub>I<sub>q</sub>/g-C<sub>3</sub>N<sub>4</sub>-20% photocatalyst prepared under a KCl:KI molar ratio of 1:2, a hydrothermal temperature of 250 °C, a pH of 4: (a) complete survey, (b) Bi-4f, (c) O-1s, (d) N-1s, (e) Cl-2p, (f) C-1s, and (g) I-3d spectra.

Figure 4 displays the UV–vis spectra of BiO<sub>m</sub>Cl<sub>n</sub>/BiO<sub>p</sub>I<sub>q</sub>/g-C<sub>3</sub>N<sub>4</sub> samples with 2%, 5%, 10%, 12%, 15%, 18%, 20%, and 100% g-C<sub>3</sub>N<sub>4</sub> under a pH of 4 and a hydrothermal temperature of 250 °C. The aforementioned figure indicates that the sample color changed from orange to yellow as the g-C<sub>3</sub>N<sub>4</sub> content in the samples increased; specifically, with such an increase from 0% to 10%, the absorption peak of the sample moved to the left and deviated from the visible light region. However, when the content of g-C<sub>3</sub>N<sub>4</sub> increased to 20%, the absorption peak moved to the right. Thus, the addition of g-C<sub>3</sub>N<sub>4</sub> considerably affected the absorption peaks in the DRS spectra. Similar results were observed in [6] for BC1B1I1 when graphene oxide was added to it. The formation of a heterojunction by using two photocatalysts in different ratios considerably affects the energy bandgap of a material. The  $E_g$  values of B1C1I2-250-4-g-C<sub>3</sub>N<sub>4</sub>-15%, B1C1I2-250-4-g-C<sub>3</sub>N<sub>4</sub>-18%, and B1C1I2-250-4-g-C<sub>3</sub>N<sub>4</sub>-20% (2.03, 1.89, and 2.01 eV, respectively) were less than that of g-C<sub>3</sub>N<sub>4</sub> (2.71 eV). This result indicates that the prepared photocatalysts containing g-C<sub>3</sub>N<sub>4</sub> can absorb more visible light than can pure g-C<sub>3</sub>N<sub>4</sub>.



**Figure 4.** UV-vis absorption spectra of BiOmcIn/BiOpIq/g-C<sub>3</sub>N<sub>4</sub> photocatalysts with different g-C<sub>3</sub>N<sub>4</sub> contents that were prepared under a KCl:KI molar ratio of 1:2, a hydrothermal temperature of 250 °C, and a pH of 4: (a) photocatalysts with g-C<sub>3</sub>N<sub>4</sub> contents of 2%, 5%, 10%, and 12%; (b) photocatalysts with g-C<sub>3</sub>N<sub>4</sub> contents of 15%, 18%, and 20%.

#### 2.1.5. PL Analysis

We used a photo-excited fluorescence spectrometer (PL) to determine the electron–hole recombination rate of the samples because the hydroxyl radicals and oxygen radicals required for photocatalysis originated from the reduction and oxidation of electrons and holes in the photocatalysts. When the electron–hole recombination rate is excessively high, the generation rates of hydroxyl radicals and superoxide radicals affect the photocatalytic efficiency [38]. Therefore, the photocatalytic efficiency can be determined from the results of PL spectroscopy. As displayed in Figure 5, the electron–hole recombination rates of the uncomposed samples were lower than those of the composited samples. The scanning range of the spectrum was 350–600 nm, and the excitation wavelength of 300 nm was used. The electron–hole recombination rate of pure g-C<sub>3</sub>N<sub>4</sub> was higher than those of all the uncomposed samples, and BC1I2-250-4-g-C<sub>3</sub>N<sub>4</sub>-20% had a lower electron–hole recombination rate than pure g-C<sub>3</sub>N<sub>4</sub> did.

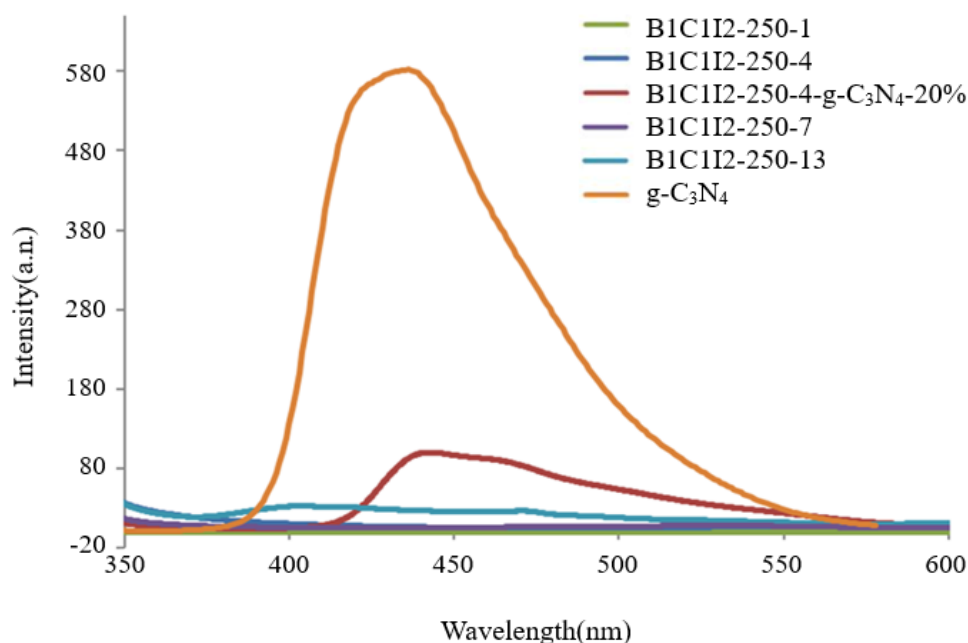


**Figure 5.** Photoluminescence spectra of the BiO<sub>m</sub>Cl<sub>n</sub>/BiOpIq/g-C<sub>3</sub>N<sub>4</sub>–20% photocatalyst prepared under a KCl:KI molar ratio of 1:2, a hydrothermal temperature of 250 °C, and a pH of 4.

Pure g-C<sub>3</sub>N<sub>4</sub> exhibited the highest electron–hole recombination rate in this study. Therefore, when electrons and holes were generated in pure g-C<sub>3</sub>N<sub>4</sub> through photocatalysis, they recombined quickly. Consequently, free radicals that react with CV could not form. However, low electron–hole recombination rates were observed in samples with 0 wt% g-C<sub>3</sub>N<sub>4</sub> (i.e., C1I2-250-1, C1I2-250-4, C1I2-250-7, and C1I2-250-13). The aforementioned result can be attributed to two possibilities: (1) the generated electrons and holes formed free radicals to react with CV, so the recombination of electron holes was very weak; (2) the generated electrons and holes were few in number; therefore, there was no recombination of electrons and holes.

The CV photodegradation efficiency of the samples with 20 wt% g-C<sub>3</sub>N<sub>4</sub> was greater than that of the sample with pure g-C<sub>3</sub>N<sub>4</sub> and those of the B1C1I2-250-1, B1C1I2-250-4, B1C1I2-250-7, and B1C1I2-250-13 samples because the numbers of electrons and holes generated through photocatalysis and the electron–hole recombination rate were higher in the samples with 20 wt% g-C<sub>3</sub>N<sub>4</sub>, which reached the better and more appropriate state.

#### 2.1.6. BET Analysis

The nitrogen gas content in and nitrogen adsorption–desorption isotherm of the BiO<sub>m</sub>Cl<sub>n</sub>/BiOpIq/g-C<sub>3</sub>N<sub>4</sub>–20% sample were used to calculate its pore volume and BET-specific surface area, respectively. As the BET-specific surface area increased, the reaction area on the sample surface increased, which affected the reaction rate. As displayed in Figure 6, the nitrogen adsorption–desorption isotherm of the aforementioned sample was a type IV isotherm with an H3 hysteresis loop [39–42] (as defined by the International Union of Pure and Applied Chemistry). The hysteresis loop of this isotherm ( $P/P_0 > 0.8$ ) indicates that the aforementioned sample contained mesopores (size = 2–50 nm) and macropores (size  $\geq 50$  nm). Using the Barrett–Joyner–Halenda method, we computed the BET-specific surface area to be 17.4356 m<sup>2</sup>/g and the average pore size to be 27.76 nm. [43]

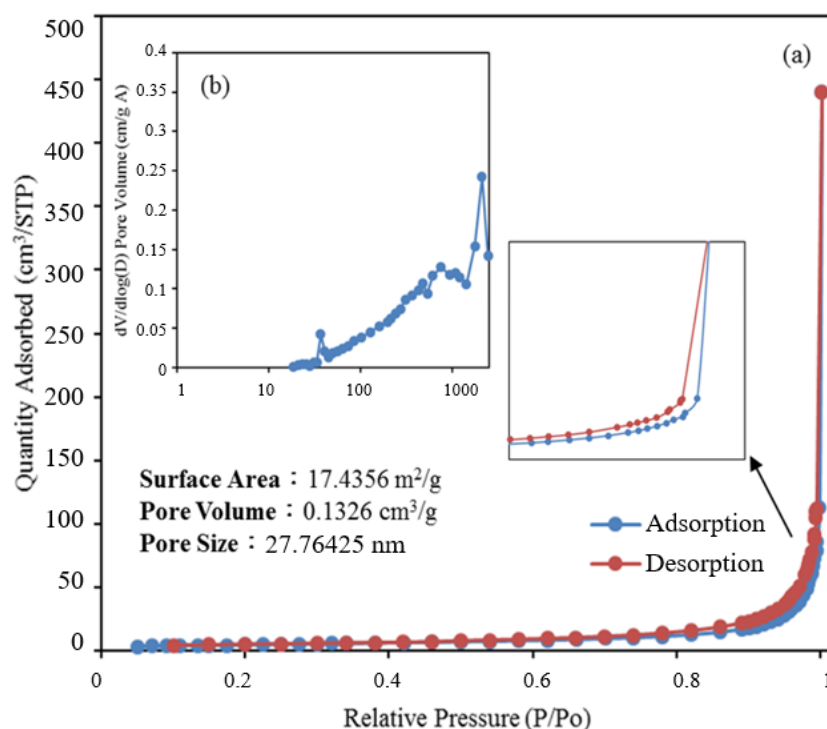


**Figure 6.** (a) Nitrogen adsorption–desorption isotherms and (b) the corresponding pore-size distribution curve (inset) for BiOmCln/BiOpIq/g-C<sub>3</sub>N<sub>4</sub>–20% photocatalyst prepared under a KCl:KI molar ratio of 1:2, a hydrothermal temperature of 250 °C, and a pH of 4.

Samples with appropriate pore sizes and a large specific surface area contain numerous surface activation sites, which promote product and reactant transfer. An appropriate pore size and large specific surface area can result in high electron–hole separation and a high photoenergy yield, which result in improved photocatalysis.

## 2.2. Photocatalytic Activity

### 2.2.1. Photocatalytic Reduction of CO<sub>2</sub>

The application of semiconductor photocatalysts in carbon dioxide reduction, water splitting, and nitrogen fixation is an important topic at present. The mechanism for the above applications is that semiconductor photocatalysts have a tunable solar absorption range to support photo-excited electrons to reach feasible reduction potentials for the above applications [44–46]. Despite various strategies including the semiconductor heterojunction, heteroatom doping, defect engineering, new semiconductor synthesis, and morphology control that have been used to improve the segregation performance of photogenerated charges, the photocatalytic design to achieve efficient reduction, splitting, and fixation of extremely stable CO<sub>2</sub>, H<sub>2</sub>O, and N<sub>2</sub> is still very challenging [47–49]. Generally, it is very difficult for a single catalyst to generate a sufficient number of photogenerated electrons or active species for CO<sub>2</sub> conversion, so the photocatalytic CO<sub>2</sub> reduction efficiency of the single catalyst is generally poor. Furthermore, it is also a challenge to utilize visible light or solar radiation and achieve efficient charge separation and robust redox capabilities [50,51].

Figure 7 shows the results of CO<sub>2</sub> reduction by B1C1I2, B1C1I2/g-C<sub>3</sub>N<sub>4</sub>, and g-C<sub>3</sub>N<sub>4</sub>. This result shows that the CO<sub>2</sub>–CH<sub>4</sub> conversion efficiency of the composite B1C1I2/g-C<sub>3</sub>N<sub>4</sub> was much better than those of the individual B1C1I2 and g-C<sub>3</sub>N<sub>4</sub>. The conversion efficiency of CO<sub>2</sub> reduction to CH<sub>4</sub> of BiO<sub>m</sub>Cl<sub>n</sub>/BiO<sub>p</sub>I<sub>q</sub> of 4.09 μmol g<sup>−1</sup>h<sup>−1</sup> can be increased to 39.43 μmol g<sup>−1</sup> by compositing with g-C<sub>3</sub>N<sub>4</sub>. It had an approximately 9.64 times improvement.

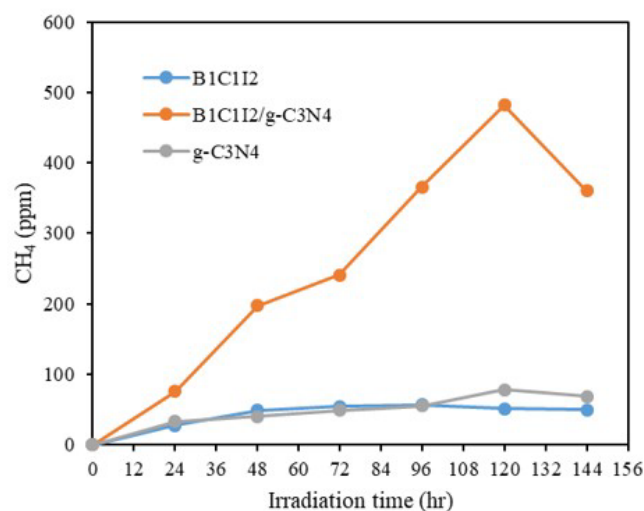


**Figure 7.** Photocatalytic reduction of CO<sub>2</sub> as a function of irradiation time over B1C1I2, B1C1I2/g-C<sub>3</sub>N<sub>4</sub>, and g-C<sub>3</sub>N<sub>4</sub>.

### 2.2.2. Photocatalytic Degradation of CV

The photocatalytic effects of photocatalysts are key to the degradation of organic pollutants. In this study, CV dye was degraded using the prepared samples under different conditions to investigate their photocatalytic degradation effects. Moreover, the sample with the best photocatalytic degradation effect was identified. As displayed in Figure 8, the signal intensity of CV at 591 nm gradually weakened when it was degraded by using the prepared samples; thus, CV was successfully degraded by these samples. The original maximum absorption peak of CV dye was at 591 nm; however, the spectrum of this dye exhibited a hypsochromic shift as the irradiation time increased. CV may have undergone a structural change, which also indicates that this dye was successfully degraded by the prepared photocatalyst samples [52,53]. Jiang et al. [54] and Liao et al. [55] detailed the mechanism underlying the photocatalytic degradation of CV under visible-light irradiation. The aforementioned authors have indicated that photocatalysis enables CV dyes to form N-demethylated intermediates. Moreover, the conjugated chromophores of CV dyes can be cleaved through BiO<sub>m</sub>Cl<sub>n</sub>/BiO<sub>p</sub>I<sub>q</sub>/g-C<sub>3</sub>N<sub>4</sub> photocatalysis [53].

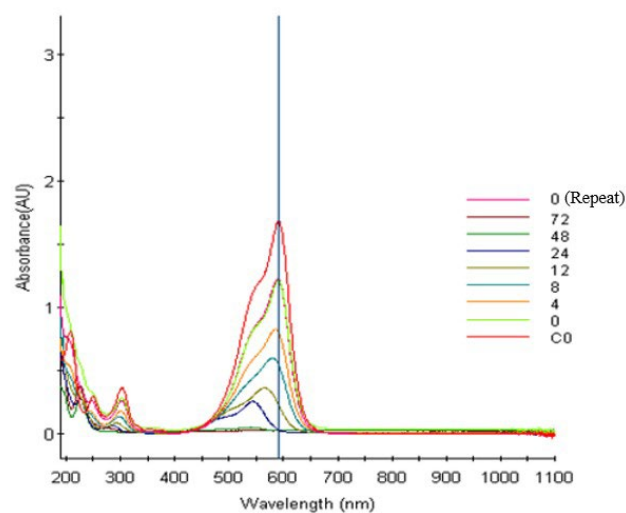


**Figure 8.** Temporal variations in the UV-vis adsorption of the aqueous BiO<sub>m</sub>Cl<sub>n</sub>/BiO<sub>p</sub>I<sub>q</sub>/g-C<sub>3</sub>N<sub>4</sub>-20% photocatalyst prepared under a KCl:KI molar ratio of 1:2, a hydrothermal temperature of 250 °C, and a pH of 4 during the photocatalytic degradation of CV on the photocatalyst under visible-light irradiation.



Figure 9 presents the CV degradation efficiency diagram of  $\text{BiO}_m\text{Cl}_n/\text{BiO}_p\text{I}_q$  for a Cl:I ratio of 1:2, a hydrothermal temperature of 250 °C, and different pH values. The degraded pollutant in this study was 100 mL of 10 ppm of CV dye. By using relevant first-order kinetic equations ( $(dC_t/dt) = kC_t$  and  $\ln(C_0/C_t) = kt$ , where  $C_t$  is concentration of the CV dye at time  $t$  and  $k$  is the reaction rate constant), we determined the  $k$  and  $R^2$  values for different pH values. Specifically, for the pH values of 1, 4, 7, 10, and 13, the  $k$  values were 0.017, 0.068, 0.035, 0.033, and 0.015  $\text{h}^{-1}$ , respectively, and the  $R^2$  values were above 0.90 (Table 2),  $\text{BiO}_m\text{Cl}_n/\text{BiO}_p\text{I}_q$  had a superior photocatalytic degradation effect at a pH of 4. It was also found from the literature that under similar synthesis conditions, a Cl: I (or Br) ratio of 1:2, a hydrothermal temperature of 250 °C, and pH = 4,  $\text{BiO}_p\text{I}_q$  (BC1I2-250-4,  $k = 0.068 \text{ h}^{-1}$ ) gave slightly better results than for  $\text{BiO}_x\text{Cl}_y/\text{BiO}_m\text{Br}_n$  (BC1B2-250-4,  $k = 0.043 \text{ h}^{-1}$ ) [31].

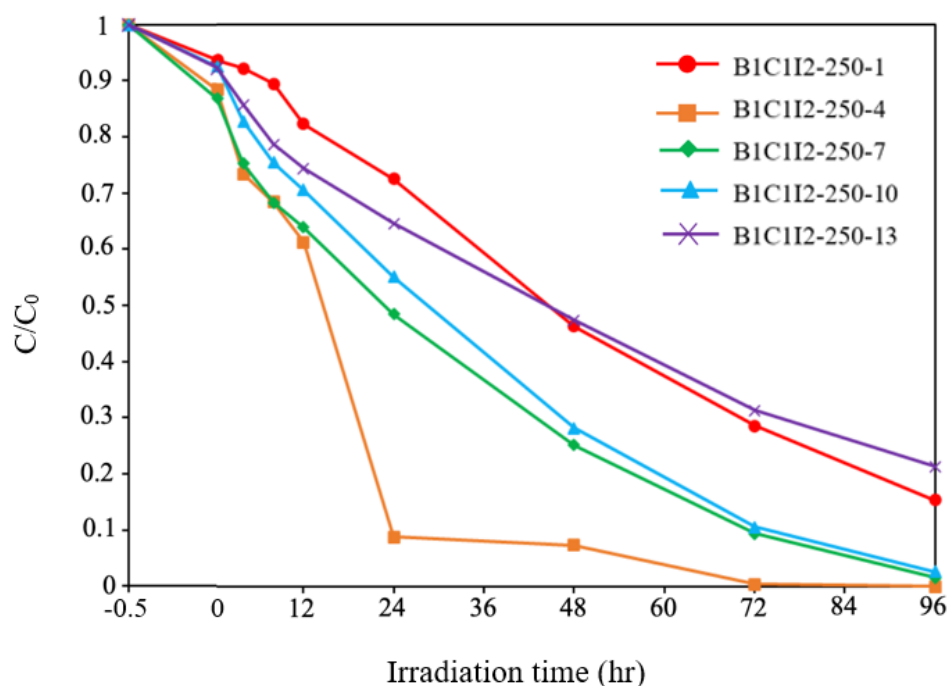


**Figure 9.** Photodegradation of CV with the irradiation time on various  $\text{BiO}_m\text{Cl}_n/\text{BiO}_p\text{I}_q$  photocatalysts prepared under a KCl:KI molar ratio of 1:2, a pH of 1–13, and a hydrothermal temperature of 250 °C.

**Table 2.** Rate constants for the pseudo-first-order degradation of CV on the prepared  $\text{BiO}_m\text{Cl}_n/\text{BiO}_p\text{I}_q$  photocatalysts under visible-light irradiation.

Cl I = 1 2										
Temperature (°C)	pH									
	1		4		7		10		13	
	$k$ ( $\text{h}^{-1}$ )	$R^2$	$k$ ( $\text{h}^{-1}$ )	$R^2$	$k$ ( $\text{h}^{-1}$ )	$R^2$	$k$ ( $\text{h}^{-1}$ )	$R^2$	$k$ ( $\text{h}^{-1}$ )	$R^2$
100	0.01	0.974	0.034	0.982	0.027	0.986	0.043	0.977	0.008	0.903
150	0.021	0.939	0.036	0.977	0.026	0.986	0.025	0.974	0.008	0.903
200	0.005	0.812	0.033	0.984	0.031	0.979	0.035	0.986	0.013	0.994
250	0.017	0.973	0.068	0.983	0.035	0.945	0.033	0.961	0.015	0.997

Figure 10 displays the degradation efficiency graph of the  $\text{BiO}_m\text{Cl}_n/\text{BiO}_p\text{I}_q/\text{g-C}_3\text{N}_4$  samples with  $\text{g-C}_3\text{N}_4$  contents of 20%, 40%, 60%, and 80% for a Cl:I ratio of 1:2, a pH of 4, and a reaction temperature of 250 °C. To ensure that the CV dye was completely adsorbed by the prepared catalysts, the first 30 min of the degradation reaction was conducted in a dark room. Figure 10 indicates that C1I2-250-4- $\text{g-C}_3\text{N}_4$ -20% had a superior photocatalytic effect on the other adopted samples. By using relevant first-order kinetic

equations  $(dC_t/dt) = -kC_t$  and  $\ln(C_0/C_t) = kt$ , we determined the  $k$  and  $R^2$  values for different g-C<sub>3</sub>N<sub>4</sub> contents. For g-C<sub>3</sub>N<sub>4</sub> contents of 20%, 40%, 60%, and 80%, the  $k$  values were determined to be 0.2456, 0.1943, 0.1041, and 0.0584 h<sup>-1</sup>, respectively, and the  $R^2$  values were determined to be above 0.9. Compared with the results of BiO<sub>x</sub>Cl<sub>y</sub>/BiO<sub>m</sub>Br<sub>n</sub>/g-C<sub>3</sub>N<sub>4</sub> ( $k = 0.0282\sim 0.0710$  h<sup>-1</sup>) [4], the results of BiO<sub>m</sub>Cl<sub>n</sub>/BiO<sub>p</sub>I<sub>q</sub>/g-C<sub>3</sub>N<sub>4</sub> were much better.

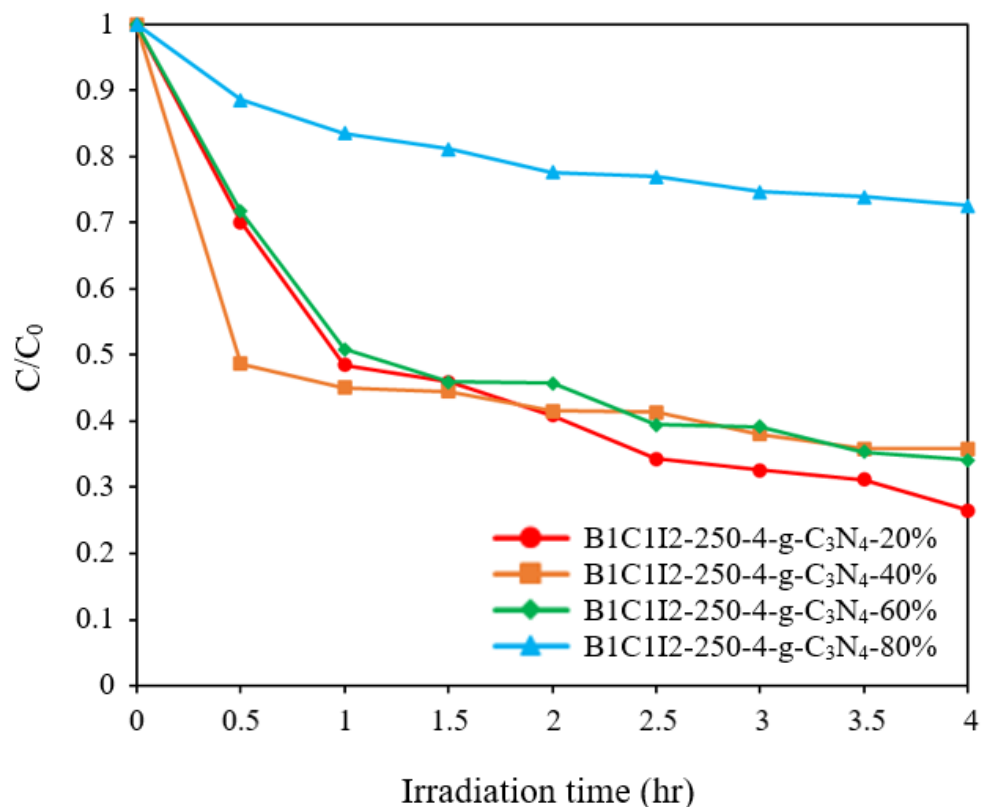


**Figure 10.** Photodegradation of CV with the irradiation time on BiO<sub>m</sub>Cl<sub>n</sub>/BiO<sub>p</sub>I<sub>q</sub>/g-C<sub>3</sub>N<sub>4</sub> samples with g-C<sub>3</sub>N<sub>4</sub> contents of 20–80% that were prepared under a KCl:KI molar ratio of 1:2, a pH of 4, and a hydrothermal temperature of 250 °C.

The aforementioned results were in line with the PL results. When the proportion of g-C<sub>3</sub>N<sub>4</sub> was 20%, optimal numbers of electrons and holes were generated through photocatalysis and an optimal electron–hole recombination rate was achieved. The photocatalytic efficiency at a g-C<sub>3</sub>N<sub>4</sub> content of 80% was considerably lower than that at a g-C<sub>3</sub>N<sub>4</sub> content of 20% (Figure 10). The reason can be inferred from the mechanism that when the content of g-C<sub>3</sub>N<sub>4</sub> increased from 0.5% to 20%, the generation of •OH increased. However, when the content of g-C<sub>3</sub>N<sub>4</sub> was further increased to 80%, the formation of •OH decreased. Equations (1) and (2) describe photocatalytic CV degradation by active substances over multiple cycles.

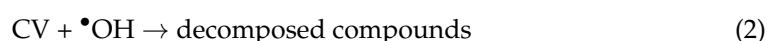
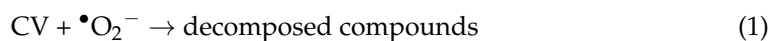


Table 3 presents a summary of the results of all the irradiation experiments. Among the samples without g-C<sub>3</sub>N<sub>4</sub>, the BC2I1-100-4, BC1I2-250-4, and BC2I1-150-4 samples had the top three degradation efficiencies. Among all the samples, the C1I2-250-4-g-C<sub>3</sub>N<sub>4</sub>-20% sample had the highest degradation efficiency. The degradation efficiency of this sample exceeded that of the uncomposited C2I1-100-4 sample by more than three times.

**Table 3.** Rate constants for the pseudo-first-order degradation of CV on the prepared BiO<sub>m</sub>Cl<sub>n</sub>/BiO<sub>p</sub>I<sub>q</sub>/g-C<sub>3</sub>N<sub>4</sub> samples under visible-light irradiation.

Photocatalyst	<i>k</i> (h <sup>-1</sup> )	R <sup>2</sup>
BC2I1-100-4-g-C3N420%	0.0208	0.8935
BC2I1-100-4-g-C3N440%	0.0349	0.92
BC2I1-100-4-g-C3N460%	0.0244	0.9958
BC2I1-100-4-g-C3N480%	0.0331	0.9843
g-C3N4	0.0162	0.9027
BC1I2-250-4-g-C3N420%	0.2456	0.9732
BC1I2-250-4-g-C3N440%	0.1041	0.9767
BC1I2-250-4-g-C3N460%	0.1943	0.9938
BC1I2-250-4-g-C3N480%	0.0584	0.9887
BC2I1-150-4-g-C3N420%	0.0125	0.9027
BC2I1-150-4-g-C3N440%	0.0349	0.8125
BC2I1-150-4-g-C3N460%	0.0244	0.9841
BC2I1-150-4-g-C3N480%	0.0347	0.9786
BC1I2-250-4-g-C3N40.5%	0.0868	0.9859
BC1I2-250-4-g-C3N41%	0.1962	0.9421
BC1I2-250-4-g-C3N42%	0.1656	0.9896
BC1I2-250-4-g-C3N45%	0.0514	0.9849
BC1I2-250-4-g-C3N410%	0.0373	0.9339
BC1I2-250-4-g-C3N412%	0.0462	0.9811
BC1I2-250-4-g-C3N415%	0.0474	0.9565
BC1I2-250-4-g-C3N418%	0.0399	0.944
BC1I2-250-4-g-C3N425%	0.0492	0.9346
BC1I2-250-4-g-C3N430%	0.0462	0.9811

We used fluorescent lamps with very weak light intensity to conduct experiments, which can prove that the new composite material produced by bismuth oxyhalide photocatalyst composite g-C<sub>3</sub>N<sub>4</sub> can still exert the photodegradation effect under weak visible-light sources. (More “Photocatalytic degradation of CV” can be found in the Supplementary Materials).

### 2.2.3. Reuse of BiOCl/BiOI/g-C<sub>3</sub>N<sub>4</sub>

Reuse rate tests were conducted to determine the reuse rate and stability of the prepared catalysts. Each of the prepared photocatalysts was used to photodegrade 10 ppm of CV dye five times. Subsequently, we recovered the remaining catalyst, filtered it with distilled water, and dried it for 24 h in an oven. Figure 11a displays the reuse efficiency of the BiO<sub>m</sub>Cl<sub>n</sub>/BiO<sub>p</sub>I<sub>q</sub>/g-C<sub>3</sub>N<sub>4</sub> catalyst with 20% g-C<sub>3</sub>N<sub>4</sub> for the degradation of CV dye under a Cl:I ratio of 1:2, a pH of 4, and a hydrothermal temperature of 250 °C. The degradation efficiency of the aforementioned catalyst remained above 90.5% even after it was used three times for photodegradation; thus, this catalyst can be reused. The aforementioned result is similar to a result obtained in [52]. Figure 11b presents the XRD patterns of BC1I2-4-250-g-C<sub>3</sub>N<sub>4</sub>-20% before use and after five times of use. The aforementioned catalyst exhibited a similar crystal phase after five times of use, which indicates that this catalyst had satisfactory stability.

In terms of practicality, a re-usability of only three times represents that the stability of the material needs to be strengthened. However, from the perspective of innovative research, this does not deny the fact that the experiment is reproducible. There are some studies in the literature that used various surface modification or doping trace element methods to improve the stability of photocatalysts. The primary goal of this experiment was to confirm the reproducibility of this innovative photocatalyst. Its stability may be related to the bonding strength between the crystalline elements of its material, or it may also be related to its own crystalline stability. How to strengthen the stability of this innovative photocatalyst and improve its feasibility in practical application can be listed as a project for future work.

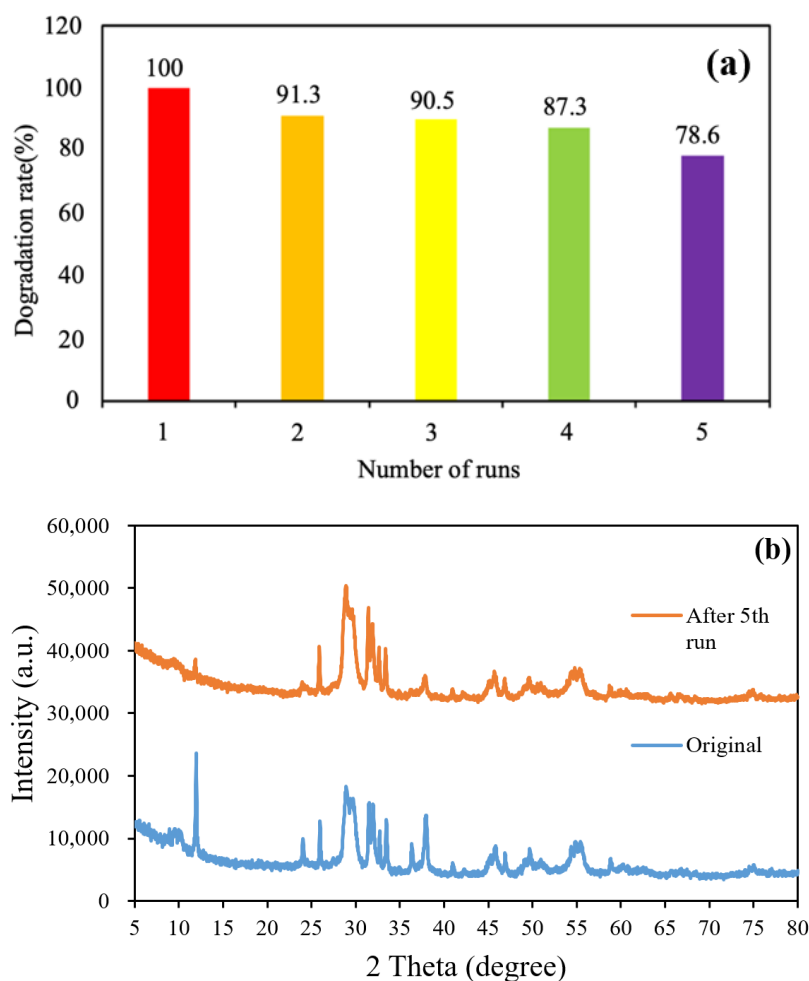


**Figure 11.** (a) Cycling runs in the photocatalytic degradation of CV in the presence of the BiO<sub>m</sub>Cl<sub>n</sub>/BiO<sub>p</sub>I<sub>q</sub>/g-C<sub>3</sub>N<sub>4</sub>-20% photocatalyst prepared under a KCl:KI molar ratio of 1:2, a hydrothermal temperature of 250 °C, and a pH of 4. (b) XRD patterns of the aforementioned photocatalyst before use and after five times of use.

#### 2.2.4. Verification of Active Species and EPR Analysis

Scavengers can be used to confirm the presence of main free radicals produced by catalysts during photocatalytic reactions. Different photocatalytic effects may occur when different radical scavengers are added during the photodegradation reaction. Studies have demonstrated that the main free radicals generated by the synthesized catalysts are trapped free radicals [56,57]. In this study, an experiment was conducted in which IPA, BQ, SA, and AO were used as the scavengers of hydroxyl radicals ( $\bullet\text{OH}$ ), superoxide radicals ( $\bullet\text{O}_2^-$ ), singlet oxygen ( $^1\text{O}_2$ ), and holes ( $\text{h}^+$ ), respectively. Figure 12a displays the variations in the dye concentration changes for the BC112-250-4-g-C<sub>3</sub>N<sub>4</sub>-20% photocatalyst when different capture agents were used. In this figure, the Y-axis ( $1-\eta$ ) represents  $(\Delta C_0 - \Delta C_s)/\Delta C_0 \times 100\%$ , where  $\Delta C_0$  is the CV concentration change without scavenger illumination for 96 h, and  $\Delta C_s$  is the CV concentration change with scavenger illumination for 96 h. The higher the  $(1-\eta)$ , the more obvious the change in the CV degradation rate. This meant that the specified active species was captured obviously by the corresponding scavenger. This implied that the specified active species plays an increasingly important role in the photodegradation of CV solution. The proportions of BQ and AO in the aforementioned photocatalysts were 23.5% and 13.2%, respectively. Thus, the main active species produced by the photodegradation reaction of BC112-250-4-g-C<sub>3</sub>N<sub>4</sub>-20% was the  $\bullet\text{O}_2^-$  superoxide radical; however, the  $\text{h}^+$ ,  $\bullet\text{OH}$ , and  $^1\text{O}_2$  species also exerted an influence.

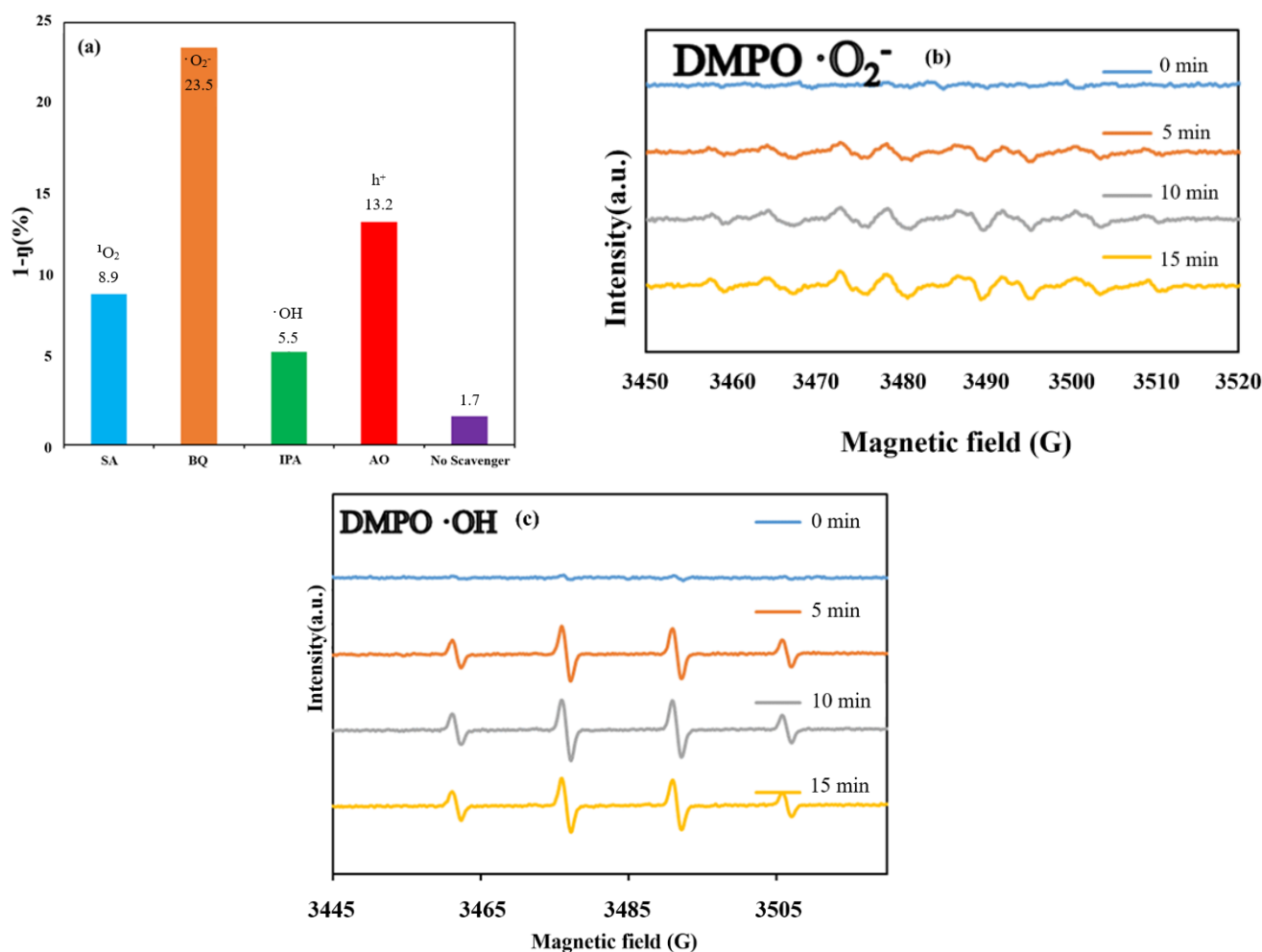


**Figure 12.** (a) Variations in the dye concentration with the irradiation time on the BiOmCln/BiOpIq/g-C<sub>3</sub>N<sub>4</sub>-20% photocatalyst prepared under a KCl:KI molar ratio of 1:2, a hydrothermal temperature of 250 °C, and a pH of 4 when using different scavengers (i.e., sodium azide, p-benzoquinone, ammonium oxalate, and isopropanol). Electron paramagnetic resonance spectra for (b) DMPO-•O<sub>2</sub><sup>-</sup> and (c) DMPO-•OH on the aforementioned catalyst under visible-light irradiation.

EPR spectroscopy can be used to detect the •OH and •O<sub>2</sub><sup>-</sup> radicals produced through the reactions of photogenerated holes and electrons with H<sub>2</sub>O and O<sub>2</sub> during the photocatalytic degradation process [57,58]. We used 5,5-dimethyl-1-pyrroline N-oxide (DMPO) as a free radical scavenger to produce photocatalytic degradation. DMPO when dissolved in an aqueous solution can be used to detect whether a catalyst produces •OH during a photocatalytic reaction. Moreover, DMPO dissolved in methanol solution can be used to identify the production of •O<sub>2</sub><sup>-</sup> by a catalyst in a photocatalytic reaction.

Figure 12b displays the EPR spectrum of the BC112-4-250-g-C<sub>3</sub>N<sub>4</sub>-20% sample in a solution of DMPO in methanol. The results in the aforementioned figure indicate the absence of any detected EPR signal when the aforementioned sample was in the dark room, and the characteristic •O<sub>2</sub><sup>-</sup> peak appeared after 5 min of illumination. Thus, the aforementioned catalyst contained the •O<sub>2</sub><sup>-</sup> active species. Figure 12c depicts the EPR spectrum of the aforementioned sample in an aqueous solution containing DMPO. No EPR signal was observed in the dark room, and a characteristic 1:2:2:1 peak appeared after 5 min of illumination. These results indicate that the aforementioned catalyst contained the •OH active species.

A comparison of the results displayed in Figure 12a–c with the results presented in the literature [2,38] indicated that the EPR signal of •OH was relatively stable and had a more

consistent trend with that of the scavenger method for measuring active species. The EPR signal of  $\bullet\text{O}_2^-$  was relatively unstable. Although the EPR signal of  $\bullet\text{O}_2^-$  appeared to be weak,  $\bullet\text{O}_2^-$  was a dominant active species in the aforementioned photocatalyst [38].

### 2.3. Schematic of Bandgap Structures of BiOCl/BiOI/g-C<sub>3</sub>N<sub>4</sub>

Figure 13 depicts a schematic of a hypothetical mechanism of the photocatalytic effect of BiO<sub>m</sub>Cl<sub>n</sub>/BiO<sub>p</sub>I<sub>q</sub>/g-C<sub>3</sub>N<sub>4</sub> in the reduction of CO<sub>2</sub> (Figure 13a) and photocatalytic degradation of a CV aqueous solution dye (Figure 13b). Figure 13a clarifies the mechanism approach, which can optimize the overall CO<sub>2</sub> conversion rate. Through thermodynamic or kinetic control, the selectivity of the whole product can be improved [59]. Figure 13b illustrates the photosensitization and photocatalytic processes of the aforementioned photocatalyst. When irradiating BiO<sub>m</sub>Cl<sub>n</sub>/BiO<sub>p</sub>I<sub>q</sub>/g-C<sub>3</sub>N<sub>4</sub> with light, the electrons in the valence band of g-C<sub>3</sub>N<sub>4</sub> are excited and move to the conduction band of g-C<sub>3</sub>N<sub>4</sub>. These electrons are transported first to the conduction band of BiOCl and then to the conduction band of BiOI. The aforementioned electrons generate  $\bullet\text{O}_2^-$  when they react with O<sub>2</sub> during transportation. If these electrons are transferred back to g-C<sub>3</sub>N<sub>4</sub>, the electron–hole recombination rate can be effectively reduced.

The BiOCl/BiOI/g-C<sub>3</sub>N<sub>4</sub> photocatalyst is a three-phase composite material. The experimental results showed that the photocatalytic activity of the derived composite BiOCl/BiOI/g-C<sub>3</sub>N<sub>4</sub> exceeded the activity of the individual components of BiOCl/BiOI by about 9.64 times for CO<sub>2</sub> reduction and 3.6 times for photocatalysis degradation of CV. Therefore, there may be a synergistic effect between BiOCl/BiOI and g-C<sub>3</sub>N<sub>4</sub>. In fact, many researchers have indicated that there is a synergistic effect in a composite material comprising two contacting semiconductors [49,60]. The above effect is ascribed to the effective charge transfer achieved at the interface of the two semiconductors. The described phenomenon may produce the effectiveness of photo-excited electron–hole separation, thereby increasing photocatalytic activity. The charge transfer process is driven by the corresponding relationship of the band potentials. Therefore, a suitable band potential constitutes a prerequisite related to the synergistic effect of the composite photocatalyst.

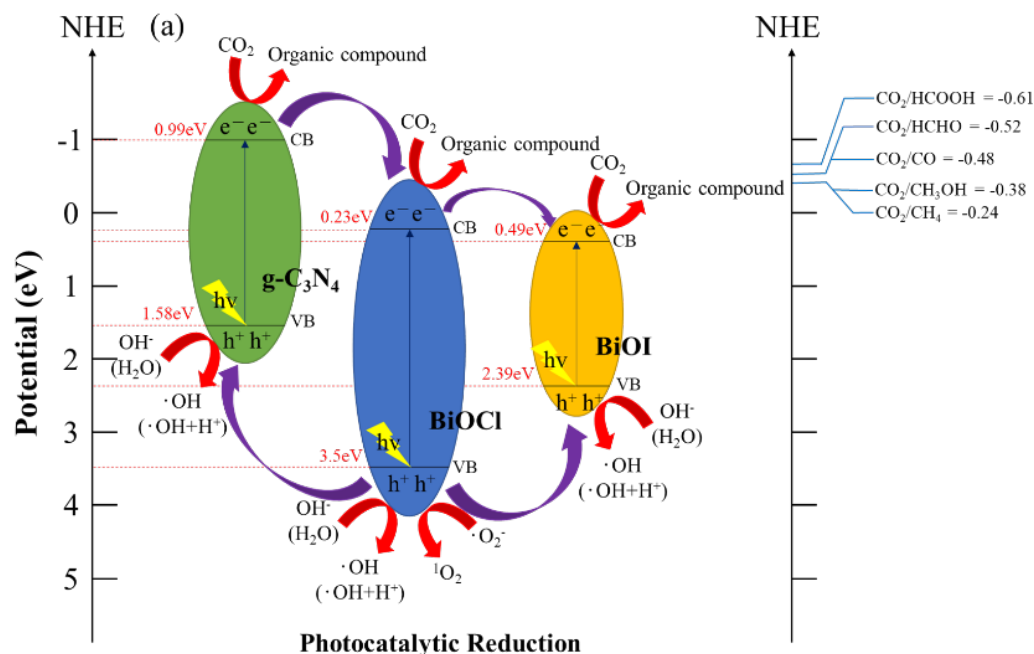
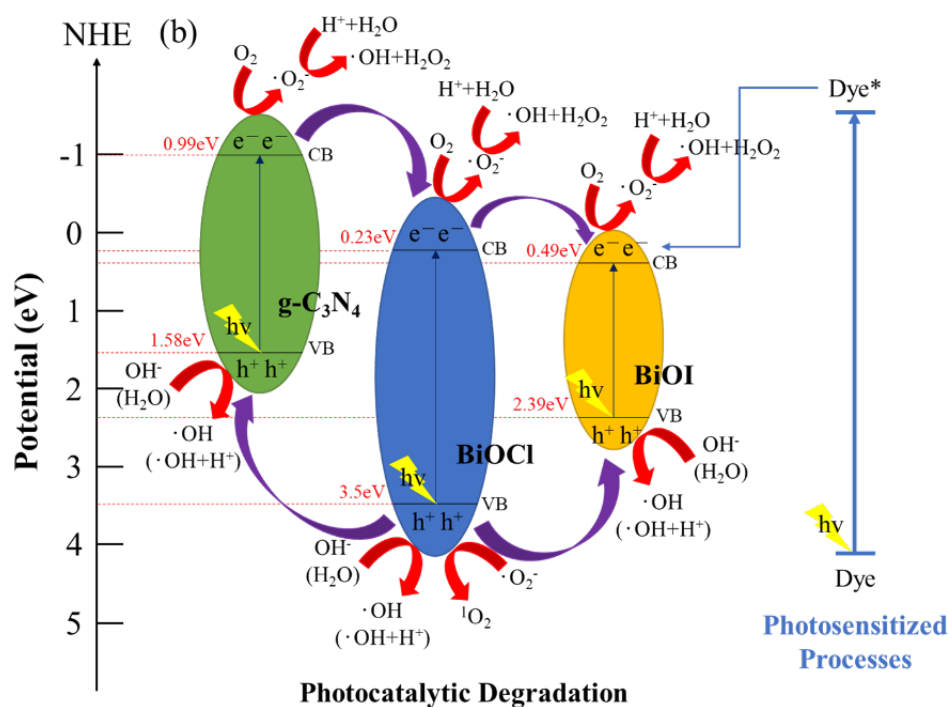


Figure 13. Cont.



**Figure 13.** Band structure diagram and possible charge separation processes of the BiOx/g-C<sub>3</sub>N<sub>4</sub>-20% photocatalyst prepared under a KCl:KI molar ratio of 1:2, a hydrothermal temperature of 250 °C, and a pH of 4 for (a) photocatalytic reduction of CO<sub>2</sub> and (b) photocatalytic degradation of dye.

The prerequisite for decomposing CV dyes is that the electrons in the conduction band of BiOX (X = Cl, I) are transferred to the bulk solution, and react with the aqueous solution to form reactive oxygen species, so the photocatalysis and photosensitization processes can be carried out simultaneously. These photogenerated and photosensitive electrons leaving the material interface, after reaching the bulk solution, interact with the photocatalyst-surface-dwelling oxygen; then,  $\bullet\text{O}_2^-$  radicals are generated. The  $\bullet\text{O}_2^-$  radicals are very unstable. It quickly reacts with  $\text{H}^+$  ions to form hydroxyl radicals. The  $\text{h}^+$  holes will also enter the bulk solution after leaving the valence band interface, react with  $\text{OH}^-$  ions (or  $\text{H}_2\text{O}$ ), and generate hydroxyl radicals [61]. The mechanism of  $^1\text{O}_2$  generation is also related to  $\bullet\text{O}_2^-$ . Through the action of cationic substances (including  $\text{h}^+$ ) and superoxide  $\bullet\text{O}_2^-$ , one electron in  $\bullet\text{O}_2^-$  is transferred to the cationic substance to generate  $^1\text{O}_2$  active species [62]. Although  $^1\text{O}_2$  does not play any important role in CO<sub>2</sub> reduction and CV degradation, we can still see its presence in active species detection experiments.

In the literature about the mechanism of degradation of CV dyes in the presence of photocatalysts by ultraviolet irradiation, it is believed that nitrogen-centered and carbon-centered free radicals are formed first. Then, there is the opportunity for N-dealkylation and disruption of the dye chromophore structure [35,54,60]. In this study, photocatalytic degradation was carried out with more practical visible light as the light source instead of UV irradiation to degrade the hydroxylated compounds of CV. It was confirmed by this study that the intermediates produced by the semiconductor photocatalyst we used under the catalysis of visible-light irradiation were the same as the intermediates produced by irradiation with ultraviolet light in the literature. In this study, it is believed that photosensitization and photocatalysis will proceed simultaneously during the reaction. The generation of  $\bullet\text{O}_2^-$  radicals is caused by the reaction of photosensitive and photogenerated electrons  $\text{e}^-$  on the surface of the photocatalyst. The generation of  $\bullet\text{OH}$  radicals is caused by the reaction of  $\text{h}^+$ - $\text{OH}^-$  (or  $\text{H}_2\text{O}$ ) and  $\bullet\text{O}_2^-$ - $\text{H}^+$ . From the experiments of active species, we can see that the two main free radical oxidants ( $\bullet\text{OH}$  and  $\bullet\text{O}_2^-$ ) in this work are dominated by  $\bullet\text{O}_2^-$ .

In the electron transportation process,  $h^+$  oxidizes  $OH^-$  and  $H_2O$  to produce  $\bullet OH$ . These free radicals further degrade and react with CV dyes, which results in the formation of mineralized products and the CV dyes absorbing light energy for photosensitization reactions to improve the photocatalytic effect. Because of their heterostructures, the prepared ternary nanocomposites possess the characteristics of heterostructures of type II band alignment [22,24]. Therefore, the Z-scheme effect [63] of improving photocatalytic degradation is achieved.

### 3. Experimental

#### 3.1. Materials

Potassium chloride (KCl), potassium iodide (KI; Katayama, Osaka, Japan),  $Bi(NO_3)_3 \cdot 5H_2O$  (Sigma-Aldrich, St. Louis, MO, USA), 2-hydroxybenzoic acid (2-HBA, Katayama, Osaka, Japan), CV dye (TCI), p-benzoquinone (BQ; Alfa Aesar, Ward Hill, MA, USA), ammonium oxalate (AO; Osaka, Japan), sodium azide (SA; Sigma-Aldrich, St. Louis, MO, USA), and isopropanol (IPA; Merck, Rahway, NJ, USA) were used in the absence of further purification. Moreover, sodium hydroxide, reagent-grade nitric acid, and high-performance liquid-chromatography-grade methanol were from Merck.

#### 3.2. Instruments and Analytical Methods

An MAC Science MXP18 instrument (MAC Science Co., Ltd., Tokyo, Japan), was used with  $Cu-K\alpha$  radiation at a current of 80 mA and a working voltage of 40 kV to obtain X-ray diffraction (XRD) spectra. A Scinco SA-13.1 spectrophotometer (Scinco Co., Ltd., Seoul, Republic of Korea) was adopted to measure ultraviolet UV-DRS ( $k = 300\text{--}800$  nm) spectra at room temperature. A JEOL-2010 microscope (JEOL Ltd., Tokyo, Japan) with an accelerating voltage of 200 kV was used to perform high-resolution transmission electron microscopy (HR-TEM), field emission transmission electron microscopy (TEM), selected-area electron diffraction (SAED), and electron-dispersive X-ray spectroscopy (EDS). A JEOL JSM-7401F (JEOL Ltd., Tokyo, Japan) microscope with an accelerating voltage of 15 kV was adopted to conduct field emission scanning electron microscopy (FE-SEM)–EDS. Photoluminescence (PL) measurements were performed on a Hitachi F-7000 (Hitachi, Ltd., Tokyo, Japan) device. A Micromeritics Gemini (Gemini-V, Micromeritics, USA) automated system was used with the adsorbate being nitrogen gas at liquid nitrogen temperature for measuring the samples' Brunauer–Emmett–Teller (BET) specific surface areas ( $S_{BET}$ ). An instrument manufactured by ULVAC-PHI (ULVAC PHI INC. Kanagawa, Japan) was adopted to conduct high-resolution X-ray photoelectron spectroscopy (HR-XPS). Finally, an Agilent 5310A frequency counter operating in the X band and a Bruker ER200D spectrometer (Bruker, Karlsruhe, Germany) were used to record the electron paramagnetic resonance (EPR) spectra.

#### 3.3. Synthesis of Different $BiO_mCl_n/BiO_pI_q/g-C_3N_4$ Composites

The method described as follows was used to produce  $BiO_mCl_n/BiO_pI_q$  composites. In a 50 mL flask, we mixed 5 mmol  $Bi(NO_3)_3 \cdot 5H_2O$  with 5 mL of 4 M  $HNO_3$ . Then, we added 2 M NaOH dropwise to the aforementioned mixture to adjust its pH value to 1, 4, 7, 10, and 13. Subsequently, 3 M KI and 3 M KCl were added into the aforementioned mixture in a ratio of 2:1 or 1:2. We vigorously stirred the resulting solution for 30 min before transferring it into a 30 mL Teflon-lined autoclave, which we heated to 200, 150, or 100 °C over 30 min; then, we maintained the respective temperature for 24 h and finally left it to naturally cool to room temperature. The formulation of the aforementioned reaction parameters is based on the most appropriate operating conditions and intervals summed up by our laboratory for many years of research on hydrothermal methods [1–6]. After it was cooled to room temperature, we filtered the solution to collect the solid precipitate. During filtration, the precipitate was washed with deionized water for other ionic substances to be removed from it. The precipitate was subsequently dried at 60 °C until the next day. Different  $BiO_mCl_n/BiO_pBr_q$  composites could be produced according to the reaction



temperature and pH. Table 1 presents our coding of the samples prepared under various reaction temperatures, pH values, and molar ratios.

Melamine was calcined in a muffle furnace under atmospheric conditions to synthesize  $g\text{-C}_3\text{N}_4$  powder directly. A total of 5 g of melamine was placed into an alumina crucible with a lid, which was subsequently heated to 520 °C in 4 h at a heating rate of 10 °C/min. After the crucible was cooled to room temperature, the powdered  $g\text{-C}_3\text{N}_4$  was obtained.

The method described as follows was used to produce  $\text{BiO}_m\text{Cl}_n/\text{BiO}_p\text{I}_q/g\text{-C}_3\text{N}_4$  composites. Binary Bi oxyhalide was composited with materials having different weight percentages of  $g\text{-C}_3\text{N}_4$  (10, 20, 30, 40, 50, 60, 70, 80, and 90 wt%). First,  $\text{BiO}_m\text{Cl}_n/\text{BiO}_p\text{I}_q$  was dissolved in 10 mL of ethylene glycol to produce solution A. Second,  $g\text{-C}_3\text{N}_4$  was dissolved in 10 mL of ethylene glycol to produce solution B. Third, solutions A and B were mixed, stirred for 30 min, autoclaved, and then heated in an oven to 150 °C over 4 h. The total amount of  $\text{BiO}_m\text{Cl}_n/\text{BiO}_p\text{I}_q$  and  $g\text{-C}_3\text{N}_4$  in each batch was 0.2 g. Subsequently, we filtered the mixture before drying and ground it to obtain  $\text{BiO}_m\text{Cl}_n/\text{BiO}_p\text{I}_q/g\text{-C}_3\text{N}_4$ .

### 3.4. Photocatalytic Experiments

#### 3.4.1. Reduction of $\text{CO}_2$

A three-necked flask was charged with 300 mL of an aqueous solution of 1 N NaOH and 0.1 g of photocatalyst. Then, we used a compressed steel cylinder containing  $\text{CO}_2$  (99.99%) with a mass flow controller at a delivery rate of 500 mL/min for 1 h to adjust the  $\text{CO}_2$  content of the aqueous solution to saturation. Photocatalyst reduction of  $\text{CO}_2$  was carried out under a light source. In the process of  $\text{CO}_2$  reduction, 1 mL of the gas above the solution was drawn out with a syringe needle every 24 h, and then injected into the GC. The concentration of  $\text{CH}_4$  reduced from  $\text{CO}_2$  was obtained from GC analysis.

#### 3.4.2. Degradation of Dye

In the conducted photocatalytic experiments, 100 mL of 10 ppm of CV dye was used as the degradation product and 0.05 g of  $\text{BiO}_m\text{Cl}_n/\text{BiO}_p\text{I}_q/g\text{-C}_3\text{N}_4$  was used as the photocatalyst. The solution was irradiated under a 15 W visible fluorescent light to produce a photocatalytic reaction. Prior to the beginning of the photocatalytic reaction, the solution was stirred in a dark room with a magnet for 30 min. After we confirmed the absorption–desorption equilibrium of the dye and catalyst at room temperature, stirring was continued and degradation occurred under irradiation with visible light. A 5 mL sample of the solution was obtained at different intervals (4, 8, 12, 24, 48, 72, and 96 h) and centrifuged at 4000 rpm for 30 min after which it became clear. The concentration of the CV aqueous solution was measured using a Scinco S-3000 spectrophotometer (Photo Diode Array UV–visible, UV–vis PDA). Absorption bands of the CV dye were located at 591.

## 4. Conclusions

In this study, the  $\text{BiO}_m\text{Cl}_n/\text{BiO}_p\text{I}_q/g\text{-C}_3\text{N}_4$  photocatalyst was successfully produced using a high-pressure hydrothermal method, as verified by XRD results. The DRS results indicated that the addition of  $g\text{-C}_3\text{N}_4$  effectively reduced the bandgap value of the aforementioned photocatalyst and made it easier for the photocatalyst to absorb visible light. The TEM analysis indicated that  $g\text{-C}_3\text{N}_4$  was successfully composited with  $\text{BiO}_m\text{Cl}_n/\text{BiO}_p\text{I}_q$ . The BET analysis indicated that the adsorption–desorption isotherm of  $\text{BiO}_m\text{Cl}_n/\text{BiO}_p\text{I}_q/g\text{-C}_3\text{N}_4$  was in agreement with those of mesoporous catalysts. In an analysis of the degradation rate of the prepared catalyst with and without  $g\text{-C}_3\text{N}_4$ , the addition of  $g\text{-C}_3\text{N}_4$  increased the degradation rate of the photocatalyst by up to three times. In reuse tests,  $\text{BiO}_m\text{Cl}_n/\text{BiO}_p\text{I}_q/g\text{-C}_3\text{N}_4$  had a degradation efficiency of 90.5% after its third use, which indicated that this catalyst was recyclable. Moreover, XRD results indicated that the aforementioned catalyst had the same crystal phase even after being used multiple times, which indicated that this catalyst had high stability. The conversion efficiency of  $\text{CO}_2$  reduction to  $\text{CH}_4$  of  $\text{BiO}_m\text{Cl}_n/\text{BiO}_p\text{I}_q$  of  $4.09 \mu\text{mol g}^{-1}$  can be increased to  $39.43 \mu\text{mol g}^{-1}$  by compositing with  $g\text{-C}_3\text{N}_4$ . It had an approximately 9.64 times improvement. The

photodegradation rate constant for CV of BiO<sub>m</sub>Cl<sub>n</sub>/BiO<sub>p</sub>I<sub>q</sub> can be increased to 0.2456 by complexation with g-C<sub>3</sub>N<sub>4</sub>. It had an approximately 3.6 times improvement.

**Supplementary Materials:** The following supporting information can be downloaded at: <https://www.mdpi.com/article/10.3390/catal13030522/s1>, Figure S1: XRD patterns of the BiO<sub>m</sub>Cl<sub>n</sub>/BiO<sub>p</sub>I<sub>q</sub> samples prepared under a KCl:KI molar ratio of 1:2, a pH of 1–13, a reaction time of 12 h, and a hydrothermal temperature of 100 °C; Figure S2: XRD patterns of the BiO<sub>m</sub>Cl<sub>n</sub>/BiO<sub>p</sub>I<sub>q</sub> samples prepared under a KCl:KI molar ratio of 1:2, a pH of 1–13, a reaction time of 12 h, and a hydrothermal temperature of 150 °C; Figure S3: XRD patterns of the BiO<sub>m</sub>Cl<sub>n</sub>/BiO<sub>p</sub>I<sub>q</sub> samples prepared under a KCl:KI molar ratio of 1:2, a pH of 1–13, a reaction time of 12 h, and a hydrothermal temperature of 200 °C; Figure S4: XRD patterns of the BiO<sub>m</sub>Cl<sub>n</sub>/BiO<sub>p</sub>I<sub>q</sub> samples prepared under a KCl:KI molar ratio of 1:2, a pH of 1–13, a reaction time of 12 h, and a hydrothermal temperature of 250 °C; Figure S5: XRD patterns of the BiO<sub>m</sub>Cl<sub>n</sub>/BiO<sub>p</sub>I<sub>q</sub> samples prepared under a KCl:KI molar ratio of 2:1, a pH of 1–13, a reaction time of 12 h, and a hydrothermal temperature of 100 °C; Figure S6: XRD patterns of the BiO<sub>m</sub>Cl<sub>n</sub>/BiO<sub>p</sub>I<sub>q</sub> samples prepared under a KCl:KI molar ratio of 2:1, a pH of 1–13, a reaction time of 12 h, and a hydrothermal temperature of 150 °C; Figure S7: XRD patterns of the BiO<sub>m</sub>Cl<sub>n</sub>/BiO<sub>p</sub>I<sub>q</sub> samples prepared under a KCl:KI molar ratio of 2:1, a pH of 1–13, a reaction time of 12 h, and a hydrothermal temperature of 200 °C; Figure S8: XRD patterns of the BiO<sub>m</sub>Cl<sub>n</sub>/BiO<sub>p</sub>I<sub>q</sub> samples prepared under a KCl:KI molar ratio of 2:1, a pH of 1–13, a reaction time of 12 h, and a hydrothermal temperature of 250 °C; Figure S9: Scanning electron microscopy images of the BiO<sub>m</sub>Cl<sub>n</sub>/BiO<sub>p</sub>I<sub>q</sub>/g-C<sub>3</sub>N<sub>4</sub>-20% samples prepared using the hydrothermal autoclave method under a KCl:KI molar ratio of 1:2, different pH values, a reaction time of 12 h, and a hydrothermal temperature of 250 °C; Figure S10: UV–vis absorption spectra of the BiO<sub>m</sub>Cl<sub>n</sub>/BiO<sub>p</sub>I<sub>q</sub> photocatalysts prepared under a KCl:KI molar ratio of 1:2, a hydrothermal temperature of 250 °C, and various pH values; Figure S11: UV–vis absorption spectra of the BiO<sub>m</sub>Cl<sub>n</sub>/BiO<sub>p</sub>I<sub>q</sub> photocatalysts prepared under a KCl:KI molar ratio of 1:2, a pH of 1–13, and a hydrothermal temperature of 250 °C; Table S1: Chemical and physical properties of the BC1I2-4-250-g-C<sub>3</sub>N<sub>4</sub>-20% sample.

**Author Contributions:** Conceptualization, C.-C.C.; methodology, S.-H.C. and F.-Y.L.; software, H.-L.W.; validation, S.-H.C. and Y.-Y.L.; formal analysis, H.-L.W.; investigation, J.-M.J.; resources, J.-M.J.; data curation, H.-L.W. and J.-H.L.; writing—original draft preparation, Y.-M.D. and W.-T.W.; writing—review and editing, C.-C.C., Y.-M.D., W.-T.W. and Y.-Y.L.; visualization, S.-H.C.; supervision, C.-C.C.; project administration, Y.-M.D.; funding acquisition, C.-C.C. All authors have read and agreed to the published version of the manuscript.

**Funding:** This research was funded by the Ministry of Science and Technology (Grant No.: MOST-109-2113-M-142 -001), Taiwan.

**Data Availability Statement:** The data is included in the article or Supplementary Materials.

**Acknowledgments:** We thank the Ministry of Science and Technology of Taiwan (MOST-109-2113-M-142 -001) for financially supporting this study, and thank the Instrumentation Center of Chung Hsing University, Taiwan (MOST110-2731-M-005-001, EM022400, EPR000000400); Instrumentation Center at National Tsing Hua University, Taiwan (MOST110-2731-M-007-001, ESCA00002603); Precious Instrument Utilization Center at National Central University, Taiwan (MOST110-2731-M-008-001, ESCA00001005) for utilization of precious instruments.

**Conflicts of Interest:** The authors declare no conflict of interest.

## References

1. Lee, D.H.; Porta, M.; Jacobs, D.R.; Vandenberg, L.N., Jr. Chlorinated persistent organic pollutants, obesity, and type 2 diabetes. *Endocr. Rev.* **2014**, *35*, 557–601. [CrossRef] [PubMed]
2. Chen, H.L.; Liu, F.Y.; Xiao, X.; Hu, J.; Gao, B.; Zou, D.; Chen, C.C. Visible-light-driven photocatalysis of carbon dioxide and organic pollutants by MFeO<sub>2</sub> (M = Li, Na, or K). *J. Colloid Interface Sci.* **2021**, *601*, 758–772. [CrossRef] [PubMed]
3. Liu, F.Y.; Dai, Y.M.; Chen, F.H.; Chen, C.C. Lead bismuth oxybromide/graphene oxide: Synthesis, characterization, and photocatalytic activity for removal of carbon dioxide, crystal violet dye, and 2-hydroxybenzoic acid. *J. Colloid Interface Sci.* **2020**, *562*, 112–124. [CrossRef] [PubMed]
4. He, J.; Liu, J.; Hou, Y.; Wang, Y.; Yang, S.; Yang, H.G. Surface chelation of cesium halide perovskite by dithiocarbamate for efficient and stable solar cells. *Nat. Commun.* **2020**, *11*, 4237. [CrossRef] [PubMed]
5. Ramirez, D.; Velilla, E.; Montoya, J.F.; Jaramillo, F. Mitigating scalability issues of perovskite photovoltaic technology through a p-i-n meso-structured solar cell architecture. *Sol. Energy Mater. Sol. Cells* **2019**, *195*, 191–197. [CrossRef]

6. Zheng, J.; Lei, Z. Incorporation of CoO nanoparticles in 3D marigold flower-like hierarchical architecture MnCo<sub>2</sub>O<sub>4</sub> for highly boosting solar light photo-oxidation and reduction ability. *Appl. Catal. B Environ.* **2018**, *237*, 1–8. [CrossRef]
7. Yin, R.; Li, Y.; Zhong, K.; Yao, H.; Zhang, Y.; Lai, K. Multifunctional property exploration: Bi<sub>4</sub>O<sub>5</sub>I<sub>2</sub> with high visible light photocatalytic performance and a large nonlinear optical effect. *RSC Adv.* **2019**, *9*, 4539–4544. [CrossRef]
8. Chang, C.; Zhu, L.; Wang, S.; Chu, X.; Yue, L. Novel mesoporous graphite carbon nitride/BiOI heterojunction for enhancing photocatalytic performance under visible-light irradiation. *Appl. Mater. Interfaces* **2014**, *6*, 5083–5093. [CrossRef]
9. Ye, L.; Su, Y.; Jin, X.; Xie, H.; Zhang, C. Recent advances in BiOX (X = Cl, Br and I) photocatalysts: Synthesis, modification, facet effects and mechanisms. *Environ. Sci. Nano* **2014**, *1*, 90–112. [CrossRef]
10. Bai, Y.; Wang, P.Q.; Liu, J.Y.; Liu, X.J. Enhanced photocatalytic performance of direct Z-scheme BiOCl-g-C<sub>3</sub>N<sub>4</sub> photocatalysts. *RSC Adv.* **2014**, *4*, 19456. [CrossRef]
11. Bu, Y.; Xu, J.; Li, Y.; Liu, Q.; Zhang, X. Enhanced photocatalytic activity of BiOI under visible light irradiation by the modification of MoS<sub>2</sub>. *RSC Adv.* **2017**, *7*, 42398–42406. [CrossRef]
12. Bhachu, D.S.; Moniz, S.J.A.; Sathasivam, S.; Scanlon, D.O.; Walsh, A.; Bawaked, S.M.; Mokhtar, M.; Obaid, A.Y.; Parkin, I.P.; Tang, J.; et al. Bismuth oxyhalides: Synthesis, structure and photoelectrochemical activity. *Chem. Sci.* **2016**, *7*, 4832–4841. [CrossRef]
13. Singh, M.; Kumar, A.; Krishnan, V. Influence of different bismuth oxyhalides on the photocatalytic activity of graphitic carbon nitride: A comparative study under natural sunlight. *Mater. Adv.* **2020**, *1*, 1262–1272. [CrossRef]
14. Zheng, M.; Ma, X.; Hu, J.; Zhang, X.; Duan, W. Novel recyclable BiOBr/Fe<sub>3</sub>O<sub>4</sub>/RGO composites with remarkable visible-light photocatalytic activity. *RSC Adv.* **2020**, *10*, 19961–19973. [CrossRef]
15. Wang, X.; Maeda, K.; Thomas, A.; Takanabe, K.; Xin, G.; Carlsson, J.; Domen, K.; Antonietti, M. A metal-free polymeric photocatalyst for hydrogen production from water under visible light. *Nat. Mater.* **2008**, *8*, 76–80. [CrossRef]
16. Jiang, D.; Chen, L.; Zhu, J.; Chen, M.; Shi, W.; Xie, J. Novel p-n heterojunction photocatalyst constructed by porous graphite-like C<sub>3</sub>N<sub>4</sub> and nanostructured BiOI: Facile synthesis and enhanced photocatalytic activity. *Dalton Trans.* **2013**, *42*, 15726–15734. [CrossRef]
17. Zhao, Z.; Sun, Y.; Dong, F. Graphitic carbon nitride based nano composites: A review. *Nanoscale* **2015**, *7*, 15–37. [CrossRef]
18. Yang, C.T.; Lee, W.W.; Lin, H.P.; Dai, Y.M.; Chi, H.T.; Chen, C.C. A novel heterojunction photocatalyst, Bi<sub>2</sub>SiO<sub>5</sub>/g-C<sub>3</sub>N<sub>4</sub> synthesis, characterization, photocatalytic activity, and mechanism. *RSC Adv.* **2016**, *6*, 40664. [CrossRef]
19. Lin, H.P.; Chen, C.C.; Lee, W.W.; Lai, Y.Y.; Chen, J.Y.; Chen, Y.Q.; Fu, J.Y. Synthesis of a SrFeO<sub>3-x</sub>/g-C<sub>3</sub>N<sub>4</sub> heterojunction with improved visible-light photocatalytic activities in chloramphenicol and crystal violet degradation. *RSC Adv.* **2016**, *6*, 2323. [CrossRef]
20. Chou, S.Y.; Chen, C.C.; Dai, Y.M.; Lin, J.H.; Lee, W.W. Novel synthesis of bismuth oxyiodide/graphitic carbon nitride nanocomposites with enhanced visible-light photocatalytic activity. *RSC Adv.* **2016**, *6*, 33478–33491. [CrossRef]
21. Wang, B.; Di, J.; Liu, G.; Yin, S.; Xia, J.; Zhang, Q.; Li, H. Novel mesoporous graphitic carbon nitride modified PbBiO<sub>2</sub>Br porous microspheres with enhanced photocatalytic performance. *J. Colloid Interface Sci.* **2017**, *507*, 310–322. [CrossRef] [PubMed]
22. Lee, A.H.; Wang, Y.C.; Chen, C.C. Composite photocatalyst, tetragonal lead bismuth oxyiodide/bismuth oxyiodide/graphitic carbon nitride synthesis, characterization, and photocatalytic activity. *J. Colloid Interface Sci.* **2019**, *533*, 319–332. [CrossRef] [PubMed]
23. Wang, Y.C.; Lee, A.H.; Chen, C.C. Perovskite-like photocatalyst, PbBiO<sub>2</sub>/BrPbO/g-C<sub>3</sub>N<sub>4</sub> synthesis, characterization, and visible-light-driven photocatalytic activity. *J. Taiwan Inst. Chem. Eng.* **2018**, *93*, 315–328. [CrossRef]
24. Li, Z.; Feng, J.; Yan, S.; Zou, Z. Solar fuel production: Strategies and new opportunities with nanostructures. *Nano Today* **2015**, *10*, 468–486. [CrossRef]
25. Huang, H.; Pradhan, B.; Hofkens, J.; Roeyfaers, M.B.J.; Steele, J.A. Solar-driven metal halide perovskite photocatalysis: Design, stability, and performance. *Energy Lett.* **2020**, *5*, 1107–1123. [CrossRef]
26. Chen, S.; Huang, D.; Cheng, M.; Lei, L.; Chen, Y.; Zhou, C.; Deng, R.; Li, B. Surface and interface engineering of two-dimensional bismuth-based photocatalysts for ambient molecule activation. *J. Mater. Chem. A* **2021**, *9*, 196–233. [CrossRef]
27. Wang, B.; Zhao, J.; Chen, H.; Weng, Y.X.; Tang, H.; Chen, Z.; Zhu, W.; She, Y.; Xia, J.; Li, H. Unique Z-scheme carbonized polymer dots/Bi<sub>4</sub>O<sub>5</sub>Br<sub>2</sub> hybrids for efficiently boosting photocatalytic CO<sub>2</sub> reduction. *Appl. Catal. B Environ.* **2021**, *293*, 120128. [CrossRef]
28. Xu, Q.; Zhang, L.; Cheng, B.; Fan, J.; Yu, J. S-scheme heterojunction photocatalyst. *Chem* **2020**, *6*, 1543–1559. [CrossRef]
29. Wang, Y.; Wang, K.; Wang, J.; Wu, X.; Zhang, G. Sb<sub>2</sub>WO<sub>6</sub>/BiOBr 2D nanocomposite S-scheme photocatalyst for NO removal. *J. Mater. Sci. Technol.* **2020**, *56*, 236–243. [CrossRef]
30. Chen, C.C.; Fu, J.Y.; Chang, J.L.; Huang, S.T.; Yeh, T.W.; Huang, J.T.; Huang, P.H.; Liu, F.Y.; Chen, L.W. Bismuth oxyfluoride/bismuth oxyiodide nanocomposites enhance visible-light-driven photocatalytic activity. *J. Colloid Interface Sci.* **2018**, *532*, 375–386. [CrossRef]
31. Chou, Y.C.; Lin, Y.Y.; Lu, C.S.; Liu, F.Y.; Lin, J.H.; Chen, F.H.; Chen, C.C.; Wu, W.T. Controlled hydrothermal synthesis of BiO<sub>x</sub>Cl<sub>y</sub>/BiO<sub>m</sub>Br<sub>n</sub>/g-C<sub>3</sub>N<sub>4</sub> composites exhibiting visible-light photocatalytic activity. *J. Environ. Manag.* **2021**, *297*, 113256. [CrossRef]
32. Siao, C.W.; Lee, W.L.W.; Dai, Y.M.; Chung, W.H.; Hung, J.T.; Hung, P.H.; Lin, W.Y.; Chen, C.C. BiO<sub>x</sub>Cl<sub>y</sub>/BiO<sub>m</sub>Br<sub>n</sub>/BiO<sub>p</sub>I<sub>q</sub>/GO quaternary composites syntheses and application of visible-light-driven photocatalytic activities. *J. Colloid Interface Sci.* **2019**, *544*, 25–36. [CrossRef]

33. Wang, X.J.; Wang, Q.; Li, F.T.; Yang, W.Y.; Zhao, Y.; Hao, Y.J.; Liu, S.J. Novel BiOCl–C<sub>3</sub>N<sub>4</sub> heterojunction photocatalysts: In situ preparation via an ionic-liquid-assisted solvent-thermal route and their visible-light photocatalytic activities. *Chem. Eng. J.* **2013**, *234*, 361–371. [CrossRef]
34. Ye, L.; Liu, J.; Jiang, Z.; Peng, T.; Zan, L. Facets coupling of BiOBr-g-C<sub>3</sub>N<sub>4</sub> composite photocatalyst for enhanced visible-light-driven photocatalytic activity. *Appl. Catal. B Environ.* **2013**, *142–143*, 1–7. [CrossRef]
35. Jiang, Y.R.; Lin, H.P.; Chung, W.H.; Dai, Y.M.; Lin, W.Y.; Chen, C.C. Controlled hydrothermal synthesis of BiO<sub>x</sub>Cl<sub>y</sub>/BiO<sub>m</sub>I<sub>n</sub> composites exhibiting visible-light photocatalytic degradation of crystal violet. *J. Hazard. Mater.* **2015**, *283*, 787–805. [CrossRef]
36. Lee, W.W.; Lu, C.S.; Chuang, C.W.; Chen, Y.J.; Fu, J.Y.; Siao, C.W.; Chen, C.C. Synthesis of bismuth oxyiodides and their composites: Characterization, photocatalytic activity, and degradation mechanisms. *RSC Adv.* **2015**, *5*, 23450–23463. [CrossRef]
37. Xiao, X.; Liu, C.; Hu, R.; Zuo, X.; Nan, J.; Li, L.; Wang, L. Oxygen-rich bismuth oxyhalides: Generalized one-pot synthesis, band structures and visible-light photocatalytic properties. *J. Mater. Chem.* **2012**, *22*, 22840–22843. [CrossRef]
38. Chen, C.C.; Chen, T.T.; Shaya, J.; Wu, C.L.; Lu, C.S. Bi<sub>12</sub>SiO<sub>20</sub>/g-C<sub>3</sub>N<sub>4</sub> heterojunctions: Synthesis, characterization, photocatalytic activity for organic pollutant degradation, and mechanism. *J. Taiwan Inst. Chem. Eng.* **2021**, *123*, 228–244. [CrossRef]
39. Li, T.B.; Chen, G.; Zhou, C.; Shen, Z.Y.; Jin, R.C.; Sun, J.X. New photocatalyst BiOCl/BiOI composites with highly enhanced visible light photocatalytic performances. *Dalton Trans.* **2011**, *40*, 6751–6758. [CrossRef]
40. Song, L.; Zhang, S.; Wei, Q. Porous BiOI sonocatalysts: Hydrothermal synthesis, characterization, sonocatalytic, and kinetic properties. *Ind. Eng. Chem. Res.* **2012**, *51*, 1193–1197. [CrossRef]
41. Zhu, L.P.; Liao, G.H.; Bing, N.C.; Wang, L.L.; Yang, Y.; Xie, H.Y. Self-assembled 3D BiOCl architectures: Tunable synthesis and characterization. *CrystEngComm* **2010**, *2*, 3791–3796. [CrossRef]
42. Sing, K.S.W.; Everett, D.H.; Haul, R.A.W.; Moscou, L.; Pierotti, R.A.; Rouquerol, J.; Siemieniewska, T. Reporting physisorption data for gas/solid systems with special reference to the determination of surface area and porosity (Recommendations 1984). *Pure Appl. Chem.* **1985**, *57*, 603–619. [CrossRef]
43. Tian, Z.; Yang, X.; Chen, Y.; Huang, H.; Hu, J.; Wen, B. Fabrication of alveolate g-C<sub>3</sub>N<sub>4</sub> with nitrogen vacancies via cobalt introduction for efficient photocatalytic hydrogen evolution. *Int. J. Hydrog. Energy* **2020**, *45*, 24792–24806. [CrossRef]
44. Xu, S.; Carter, E.A. Theoretical insights into heterogeneous (photo) electrochemical CO<sub>2</sub> reduction. *Chem. Rev.* **2019**, *119*, 6631–6669. [CrossRef] [PubMed]
45. Huang, J.; Mensi, M.; Oveisi, E.; Mantella, V.; Buonsanti, R. Structural sensitivities in bimetallic catalysts for electrochemical CO<sub>2</sub> reduction revealed by Ag-Cu nanodimers. *J. Am. Chem. Soc.* **2019**, *141*, 2490–2499. [CrossRef]
46. Parvanian, A.M.; Sadeghi, N.; Rafiee, A.; Shearer, C.J.; Jafarian, M. Application of porous materials for CO<sub>2</sub> reutilization: A review. *Energies* **2022**, *15*, 63. [CrossRef]
47. Xie, C.; Niu, Z.; Kim, D.; Li, M.; Yang, P. Surface and interface control in nanoparticle catalysis. *Chem. Rev.* **2020**, *120*, 1184–1249. [CrossRef]
48. Gao, C.; Low, J.; Long, R.; Kong, T.; Zhu, J.; Xiong, Y. Heterogeneous single-atom photocatalysts: Fundamentals and applications. *Chem. Rev.* **2020**, *120*, 12175–12216. [CrossRef]
49. Wei, X.; Akbar, M.U.; Raza, A.; Li, G. A review on bismuth oxyhalide based materials for photocatalysis. *Nanoscale Adv.* **2021**, *3*, 3353–3372. [CrossRef]
50. Wang, L.; Chen, W.; Zhang, D.; Du, Y.; Amal, R.; Qiao, S.; Wu, J.; Yin, Z. Surface strategies for catalytic CO<sub>2</sub> reduction: From two-dimensional materials to nanoclusters to single atoms. *Chem. Soc. Rev.* **2019**, *48*, 5310–5349. [CrossRef]
51. Yang, L.; Peng, Y.; Luo, X.; Dan, Y.; Ye, J.; Zhou, Y.; Zou, Z. Beyond C<sub>3</sub>N<sub>4</sub> π-conjugated metal-free polymeric semiconductors for photocatalytic chemical transformations. *Chem. Soc. Rev.* **2021**, *50*, 2147–2172. [CrossRef]
52. Siao, C.W.; Chen, H.L.; Chen, L.W.; Chang, J.L.; Yeh, T.W.; Chen, C.C. Controlled hydrothermal synthesis of bismuth oxychloride-bismuth oxybromide-bismuth oxyiodide composites exhibiting visible-light photocatalytic degradation of 2-hydroxybenzoic acid and crystal violet. *J. Colloid Interface Sci.* **2018**, *526*, 322–336. [CrossRef]
53. Li, K.L.; Lee, W.W.; Lu, C.S.; Dai, Y.M.; Chou, S.Y.; Chen, H.L.; Lin, H.P.; Chen, C.C. Synthesis of BiOBr, Bi<sub>3</sub>O<sub>4</sub>Br, and Bi<sub>12</sub>O<sub>17</sub>Br<sub>2</sub> by controlled hydrothermal method and their photocatalytic properties. *J. Taiwan Inst. Chem. Eng.* **2014**, *45*, 2688–2697. [CrossRef]
54. Jiang, Y.R.; Chou, S.Y.; Chang, J.L.; Huang, S.T.; Lin, H.P.; Chen, C.C. Hydrothermal synthesis of bismuth oxybromide–bismuth oxyiodide composites with high visible light photocatalytic performance for the degradation of CV and phenol. *RSC Adv.* **2015**, *5*, 30851–30860. [CrossRef]
55. Liao, Y.H.B.; Wang, J.X.; Lin, J.S.; Chung, W.H.; Lin, W.Y.; Chen, C.C. Synthesis, photocatalytic activities and degradation mechanism of Bi<sub>2</sub>WO<sub>6</sub> toward crystal violet dye. *Catal. Today* **2011**, *174*, 148–159. [CrossRef]
56. Oppong, S.O.B.; Opoku, F.; Govender, P.P. Remarkable Enhancement of Eu–TiO<sub>2</sub>–GO Composite for Photodegradation of Indigo Carmine: A Design Method Based on Computational and Experimental Perspectives. *Catal. Lett.* **2020**, *151*, 1111–1126. [CrossRef]
57. Chen, L.W.; Chen, H.L.; Lu, C.S.; Huang, S.T.; Yeh, T.W.; Chen, C.C. Preparation of perovskite-like PbBiO<sub>2</sub>I/g-C<sub>3</sub>N<sub>4</sub> exhibiting visible-light-driven activity. *Catal. Today* **2021**, *375*, 472–483. [CrossRef]
58. Dimitrijevic, N.M.; Vijayan, B.K.; Poluektov, O.G.; Rajh, T.; Gray, K.A.; He, H.; Zapol, P. Role of water and carbonates in photocatalytic transformation of CO<sub>2</sub> to CH<sub>4</sub> on titania. *J. Am. Chem. Soc.* **2011**, *133*, 3964–3971. [CrossRef]
59. Gandhi, R.; Moses, A.; Sundar Baral, S. Fundamental study of the photocatalytic reduction of CO<sub>2</sub>: A short review of thermodynamics, kinetics and mechanisms. *Chem. Process Eng.* **2022**, *43*, 223–228.

60. Li, H.; Zhou, Y.; Tu, W.; Ye, J.; Zou, Z. State-of-the-art progress in diverse heterostructured photocatalysts toward promoting photocatalytic performance. *Adv. Funct. Mater.* **2015**, *25*, 998–1013. [CrossRef]
61. Fan, H.J.; Lu, C.S.; Lee, W.L.; Chiou, M.R.; Chen, C.C. Mechanistic pathways differences between P25-TiO<sub>2</sub> and Pt-TiO<sub>2</sub> mediated CV photodegradation. *J. Hazard. Mater.* **2011**, *185*, 227–235. [CrossRef] [PubMed]
62. He, W.; Jia, H.; Wamer, W.G.; Zheng, Z.; Li, P.; Callahan, J.H.; Yin, J.-J. Predicting and identifying reactive oxygen species and electrons for photocatalytic metal sulfide micro–nano structures. *J. Catal.* **2014**, *320*, 97–105. [CrossRef]
63. Wang, Y.; Huang, H.; Zhang, Z.; Wang, C.; Yang, Y.; Li, Q.; Xu, D. Lead-free perovskite Cs<sub>2</sub>AgBiBr<sub>6</sub>@g-C<sub>3</sub>N<sub>4</sub> Z-scheme system for improving CH<sub>4</sub> production in photocatalytic CO<sub>2</sub> reduction. *Appl. Catal. B Environ.* **2021**, *282*, 119570. [CrossRef]

**Disclaimer/Publisher’s Note:** The statements, opinions and data contained in all publications are solely those of the individual author(s) and contributor(s) and not of MDPI and/or the editor(s). MDPI and/or the editor(s) disclaim responsibility for any injury to people or property resulting from any ideas, methods, instructions or products referred to in the content.

MDPI  
St. Alban-Anlage 66  
4052 Basel  
Switzerland  
Tel. +41 61 683 77 34  
Fax +41 61 302 89 18  
[www.mdpi.com](http://www.mdpi.com)

*Catalysts* Editorial Office  
E-mail: [catalysts@mdpi.com](mailto:catalysts@mdpi.com)  
[www.mdpi.com/journal/catalysts](http://www.mdpi.com/journal/catalysts)







Academic Open  
Access Publishing

[mdpi.com](http://mdpi.com)

ISBN 978-3-0365-8794-3